UNIVERSITY OF SÃO PAULO

INSTITUTE OF GEOCIENCES

Tectono-metamorphic evolution of the Embu Terrane and the adjacent terranes at the Southern Ribeira Belt

DINA ISABEL GUERREIRO CABRITA

Doctoral Thesis presented to the Postgraduate program of the Geoscience Institute as part of the requirements for the degree of Doctor of Sciences

Postgraduate Area: Igneous and Metamorphic Petrology

Advisor: Prof. Dr. Frederico Meira Faleiros

SÃO PAULO

2022

Serviço de Biblioteca e Documentação do IGc/USP
Ficha catalográfica gerada automaticamente com dados fornecidos pelo(a) autor(a)
via programa desenvolvido pela Seção Técnica de Informática do ICMC/USP

Bibliotecários responsáveis pela estrutura de catalogação da publicação:
Sonia Regina Yole Guerra - CRB-8/4208 | Anderson de Santana - CRB-8/6658

Cabrita, Dina Isabel Guerreiro
Tectono-metamorphic evolution of the Embu Terrane and the adjacent terranes at the Southern Ribeira Belt / Dina Isabel Guerreiro Cabrita; orientador Frederico Meira Faleiros. -- São Paulo, 2022.
356 p.

Tese (Doutorado - Programa de Pós-Graduação em Mineralogia e Petrologia) -- Instituto de Geociências, Universidade de São Paulo, 2022.

1. High-grade metamorphism. 2. Petrochronology. 3. Accretionary orogen. 4. Transcurrent deformation. 5. West Gondwana. I. Faleiros, Frederico Meira, orient. II. Título.

UNIVERSIDADE DE SÃO PAULO
INSTITUTO DE GEOCIÊNCIAS

"Tectono-metamorphic evolution of the Embu Terrane and the adjacent terranes at the Southern Ribeira Belt"

DINA ISABEL GUERREIRO CABRITA

Orientador: Prof. Dr. Frederico Meira Faleiros

Tese de Doutorado

Nº 648

COMISSÃO JULGADORA

Dr. Frederico Meira Faleiros

Dra. Inês Pereira

Dra. Carla Cristine Porcher

Dra. Alice Westin Teixeira

Dr. Telmo Bento dos Santos

SÃO PAULO
2022

ACKNWLEDGMENTS

Dear reader, the doctoral thesis I present here as a single author is a result from a collective effort that may not be directly reflected in the following dozen pages. To begin with, I would like to express my sincere gratitude to the São Paulo Research Foundation (FAPESP), as this thesis would not have been possible without the financial support from the grants 2015/26645-3, 2018/21824-5 and 2019/10457-4.

During this doctoral journey, I was welcomed by a legion of human beings who helped me in every way possible. My first and greatest recognition is to my main supervisor – Frederico Faleiros – for presenting me with this challenging research topic and for the ongoing support. I hope that the partnership can continue in future works. This gratitude extends to my two formal abroad supervisors – Luca Menegon and Peter Cawood – for the support during my stay at the University of Plymouth (United Kingdom) and Monash University (Australia) and to my informal supervisor – Ginaldo Campanha – for guiding me in understanding the Apiaí Terrane mess. I would also like to extend my gratitude to the professors I came across during this doctoral journey, including my doctoral paper reviewers. Their immense knowledge and great experience challenge and encourage me to constantly improve myself.

I equally like to express my sincere recognition to all the technical staff for their support in my study and help in acquiring and processing giant quantities of data. Due to them, I developed a keen and never-ending interest in working in laboratories. A very special thanks to Paulinho, Renato, Luís, Vasco and Samuel (Samuca) from the sample preparation section, Isaac Sayeg and Artur Onoe from the scanning electron microscope, José Paulo Sertek from the X-ray fluorescence, Marcos Mansueto and Leandro Moraes from the electron microprobe, Kei Sato from SHRIMP within IGc-USP and Massimo Raveggi of Monash Isotopia Facility Laboratory.

To my fellow earth science postgraduate students and early career research mates, among them – Juliana Pertille, Maria Thereza Yogi, Bruno Ribeiro, Vanessa Mucivuna, Mariana Ambrosio, Luanna Chmyz, Karine Arena, Gustavo Garcia, Luiza Garcia, Joana Cipriano and Marta Codeço – I thank them for the happy distractions/mentoring. Last (but never least), my special appreciation goes to my family and childhood friends for resting my mind outside of academia. Without their tremendous understanding and constant daily life presence, it would be impossible for me to move abroad so many times. I am fortunate to have them as my safe haven.

RESUMO

O metamorfismo em conjunto com o magmatismo e a deformação fornecem informações importantes para a compreensão da evolução tectônica de cinturões orogênicos. Este estudo é particularmente importante na Faixa Ribeira de idade Neoproterozóica, onde existem atualmente modelos tectônicos contrastantes. Modelos envolvendo múltiplas acreções foram os mais aceitos até recentemente. No entanto, estudos recentes propõem um modelo de evolução intracontinental para a Faixa Ribeira. O Terreno Embu e as unidades adjacentes são áreas cruciais para investigar os modelos controversos acima, uma vez que representa uma unidade importante dentro da Faixa Ribeira. Para tanto, esta tese investigou a evolução tectônica do Terreno Embu, do Grupo Votuverava a noroeste e o limite sudeste do Terreno Embu, a Zona de Cisalhamento Cubatão por meio de um estudo envolvendo análise química mineral e de rocha total, orientação cristalográfica preferencial de quartzo e petrocronologia. Os dados desta contribuição revelam uma história evolutiva distinta entre o Grupo Votuverava e o Terreno Embu. Rochas ígneas máficas do Grupo Votuverava registram a existência de dois eventos magmáticos no Mesoproterozóico (1490-1475 Ma e 1300-1260 Ma), caracterizados por razões Th/Yb acima de N-MORB, baixas razões Ta/Yb e Nb/La, baixas concentrações de Nb e Zr, anomalia negativa de Nb, εNdt de -3 a +6 e idade do modelo Nd T_{DM} entre 2110-1500 Ma, que são características de magmatismo relacionado a ambientes de arco magmático. No Terreno Embu, um terceiro evento magmático é registrado durante o Neoproterozóico (900 Ma) com rochas máficas toleíticas caracterizadas por baixos enriquecimentos em LREE, anomalia negativa de Nb, baixos teores de Nb e Zr e baixas razões Nb/La e Zr/Y, consistentes com basaltos relacionados a ambientes de arco magmático. Além disso, os dados metamórficos das rochas metassedimentares do Terreno Embu demonstraram um evento metamórfico de alto grau entre 810-760 Ma representado pelas zonas da silimanita, silimanita-K-feldspato e cordierita com condições P-T entre 750–805 °C e 3,6–9,2 kbar, concomitante à atividade ígnea registrada durante este período. Finalmente, os dados petrocronológicos da zona de cisalhamento de Cubatão indicaram condições de temperatura média de 460–520 °C e 4,5–9,5 kbar, consistentes com microestruturas de recristalização de quartzo indicativas de recristalização de rotação do subgrão entre 610–570 Ma. A atividade da zona de cisalhamento de Cubatão é síncrona com o período principal de atividade de outras zonas de cisalhamento dúctil da Faixa Ribeira. Este período coincide com o período principal de atividade de outras zonas de cisalhamento

regionais, volumoso magmatismo granítico e metamorfismo regional na Faixa Ribeira, indicando participação ativa das zonas de cisalhamento transcorrentes nos processos orogênicos. Os dados desta contribuição registram vários períodos de acreção e convergência e, portanto, não são consistentes com um modelo de evolução único intracontinental.

Palavras-chave: Metamorfismo de alto grau, Petrocronologia, Orógeno acrescionário, Deformação transcorrente, Gondwana Ocidental

ABSTRACT

Metamorphism coupled with magmatism and deformation provides key information in understanding the evolutionary tectonic setting of orogenic belts. This study is particularly important in Neoproterozoic Ribeira Belt, where there are currently contrasting tectonic models. Models involving multiple long-lived terrane accretion have been the most accepted until recently. However, recent studies propose an intracontinental setting model for the belt. The Embu Terrane and the adjacent units are crucial areas to investigate the above controversial models once it represents a major unit within Ribeira Belt. For this purpose, this thesis investigated the geotectonic evolution of Embu Terrane, the adjacent northwestern Votuverava Group and the Embu Terrane southeastern limit, the crustal-scale Cubatão Shear Zone by a multi-method study involving whole-rock and mineral chemical analysis, quartz crystallographic fabric analysis, and petrochronology. The data in this contribution reveal a distinct evolutionary history between the Votuverava Group and Embu Terrane. Mafic igneous rocks from the Votuverava Group record the existence of two Mesoproterozoic magmatic events at (1490-1475 Ma and 1300-1260 Ma), which are characterized by Th / Yb ratios above N-MORB, low Ta / Yb and Nb / La ratios, low Nb and Zr concentrations, negative Nb anomaly, εNd_t of -3 to +6, an Nd T_{DM} model age between 2110-1500 Ma, which are characteristics of arc-related magmatism. In the Embu Terrane, a third magmatic event is recorded during the Neoproterozoic (900 Ma) with tholeiitic mafic rocks characterized by low enrichments in LREE, negative Nb anomaly, low Nb and Zr contents and low Nb / La and Zr /Y ratios, consistent with arc-related basalts. Additionally, the metamorphic data from the Embu Terrane metasedimentary rocks demonstrated a high-grade metamorphic event between 810–760 Ma represented by sillimanite, sillimanite–K-feldspar, and cordierite zones. Petrochronological data indicate that the high-grade metamorphic rocks within the Embu Terrane attained conditions between 750–805 °C and 3.6–9.2 kbar, concomitant with igneous activity recorded during this period. Finally, petrochronological data from the crustal-scale Cubatão Shear Zone indicated medium-temperature conditions of 460–520 °C and 4.5–9.5 kbar, consistent with quartz recrystallization microstructures indicative of subgrain rotation recrystallization between 610–570 Ma. The CSZ activity is coeval with the main period of activity of other ductile shear zones from the Ribeira Belt. This period coincides with the main period of other regional shear zones activity, voluminous granitic magmatism, and regional

metamorphism in the Ribeira Belt, indicating active participation of the transcurrent shear zones in the orogenic processes. The data in this contribution record multiple periods of accretion and convergence settings and, therefore, is not consistent with a single intracontinental evolutionary setting.

Keywords: High-grade metamorphism, Petrochronology, Accretionary orogen, Transcurrent deformation, West Gondwana

SUMMARY

1. INTRODUCTION

1.1. Motivation

Metamorphism coupled with magmatism and deformation provides vital information in understanding the evolutionary history of orogenic systems, leading to interpretations of the tectonic evolution of orogens and their orogenic belts (Brown, 2009). This relationship is particularly important for the orogens and belts that formed West Gondwana, especially the Ribeira Belt, part of the Brasiliano-Pan-African Orogen. The Brasiliano-Pan-African Orogen comprises a system of orogenic belts that build up West Gondwana during the Neoproterozoic (Heilbron and Machado, 2003; Alkmim et al., 2006; Gray et al., 2008; Arena et al., 2017; Pertille et al., 2017; Hartmann et al., 2019). The South American counterpart of the Brasiliano-Pan-African Orogen is formed by three major physiographic entities, known as Borborema, Tocantins and Mantiqueira structural provinces (Brito Neves et al., 2021).

Together with Araçuaí and Dom Feliciano belts, the Ribeira Belt form the Mantiqueira Province that extends along the SE coast of Brazil and Uruguay (Almeida et al., 1981; Brito Neves et al., 2021). Tectonic evolutionary models involving multiple long-lived terrane accretion related to accretionary to collisional settings for the Ribeira Belt have been the most accepted ones until recent years. These models involve successive and multiple terrane accretion associated with long-lived subduction of a large Adamastor Ocean between the Paranapanema, São Francisco, Congo and Luís Alves cratons that culminate in continental collision at ca. 600 Ma (Brito Neves et al., 1999; Campos Neto, 2000; Campanha and Brito Neves, 2004; Fuck et al., 2008; Heilbron et al., 2008, 2020; Faleiros et al., 2011; Caxito et al., 2021).

However, recent studies have questioned this tectonic setting, renewing older concepts related to an intracontinental tectonic setting for the orogen (Torquato and Cordani, 1981; Porada, 1989). These recent studies reinforce the intracontinental model where the basins of the Ribeira Belt were developed in an intracontinental setting and were inverted as a consequence of cratonic collisions between ca. 650–600 Ma, which would have given origin to collisional belts, followed by transcurrent tectonics with associated granitic magmatism between ca. 600–560 Ma (Meira et al., 2015, 2019a). Similar ideas are being developed for other parts of the orogen (Fossen et al., 2020; Konopásek et al., 2020; Percival et al., 2022).

The Embu Terrane and the adjacent terranes of the Southern Ribeira Belt represent a crucial area of this orogenic system. The Embu Terrane is one of the geotectonic units with the most significant spatial expression of the Ribeira Belt, mainly in its western portion and the eastern boundary of the Cubatão Shear Zone, where we propose to investigate in this project. Therefore, a multidisciplinary study in this area will contribute to discussing the above-described controversy for the Southern Ribeira Belt and consequently for the tectonic setting that formed West Gondwana.

1.2. Objectives

Based on the above motivation, the objectives of this thesis were:

(i) The study of chemistry, age and tectonic setting of mafic rocks in the Embu Terrane and Votuverava Group by whole-rock geochemistry, whole-rock Sm–Nd isotopic geochemistry and zircon U–Pb–Hf geochronology.

(ii) The study of the metamorphic record in the southwestern portion of the Embu Terrane using petrochronological data from metasedimentary rocks.

(iii) The deformational and thermochronological evolution of the crustal-scale Cubatão Shear Zone and its role during orogenetic processes related to West Gondwana assembly. This study involved the acquisition of data from quartz crystallographic preferred orientation using electron backscatter diffraction (EBSD), phase equilibria modelling, and apatite and zircon U–Pb isotopes and trace element concentrations.

(iv) The integration of the results and use of this data to interpret large-scale tectonic processes and their implications for the tectonic evolution of the Embu Complex and, consequently, for the tectonic setting that formed Ribeira Belt.

1.3. Location of the studied area

The studied area is located in São Paulo state, southeast of the São Paulo city. It corresponds to a NE-SW section, covering the Itapecerica da Serra, Embu-Guaçu, São Lourenço da Serra, Juquitiba, Pedro de Toledo, Miracatu, Juquiá, Registro, Sete Barras and Eldorado municipalities. The main access from São Paulo city was through BR-116

Régis Bittencourt highway (Fig. 1.1). In addition, several municipal roads allowed a better access to the area interior.

The northern and southern portions of the study area are dominated by native Atlantic Forest and banana and palm heart plantations, respectively. The key outcrops were mainly located on road crosscuts or secondarily in waterfalls and quarries.

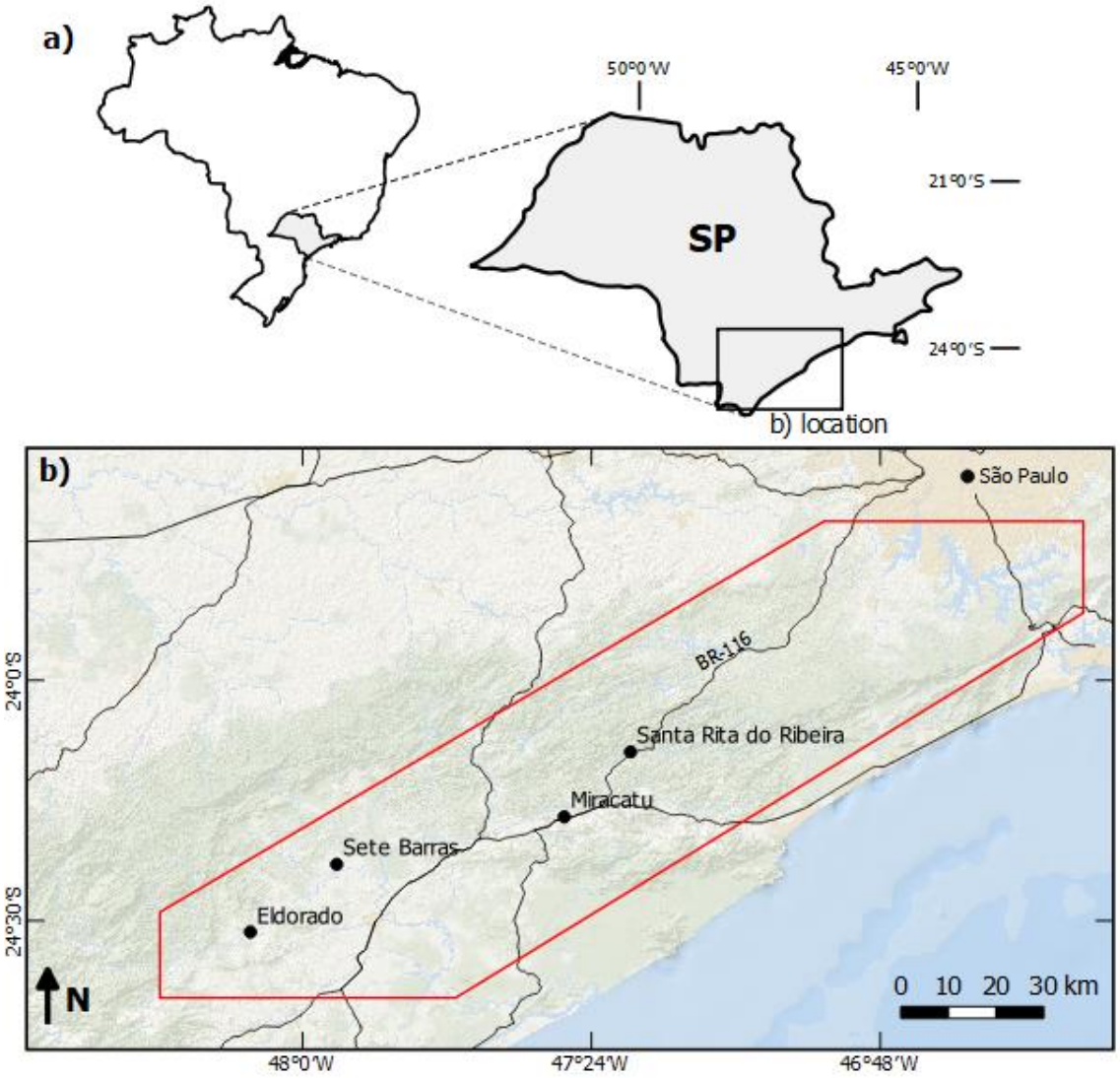

Figure 1.1. a) Map with São Paulo state borders indicating the position of b) figure (black rectangle); b) location of the studied area (in red), including its main roads access. Geographic coordinates, WGS84 datum. Source: ESRI Maps.

1.4. Thesis structure

This thesis is divided into six chapters. Chapter 1 presents the motivation of the thesis, objectives and location of the studied area. Chapter 2 presents a description of the analytical methods adopted. The results acquired with this research are presented in three

manuscripts (Chapters 3 to 5), two of which are published and one that is prepared for submission in peer-reviewed scientific journals. Results chapters sequence reflects the geological time processes evolution within the studied area.

Chapter 3 presents the manuscript entitled “Meso to Neoproterozoic multiple terrane accretion: insights from mafic magmatism in the Ribeira Belt, Brasiliano-Pan-African Orogen”. The data presented in this chapter investigates the role of Embu Complex and Votuverava Group mafic rocks in the tectonic setting of the mafic magmatism in Ribeira Belt and in Brasiliano-Pan-African Orogen, which records processes related to West Gondwana assembly with minor records of Rodinia assembly. The evolutionary history from Rodinia to West Gondwana assembly is still poorly known. Considering this, studying the chemistry and chronology of mafic magmatism in Meso to Neoproterozoic terranes adds new data to unravel the tectonic setting for the time interval.

Chapter 4 is focused on detailing the metamorphism of the Embu Complex by presenting the manuscript entitled “Petrochronological constraints and tectonic implications of Tonian metamorphism in the Embu Complex, Ribeira Belt, Brazil”, published in Precambrian Research (DOI: 10.1016/j.precamres.2021.106315). This work reports a record of orogenic processes within the time period between Rodinia break-up and West Gondwana assembly, using a combined metamorphic and geochronological study in the Embu Complex. The results indicate an 830-760 Ma high-grade metamorphic event related to accretionary to collisional settings.

Chapter 5 is focused on a quantitative multi-method study (quantitative structural analyses, phase-equilibria modelling and zircon and apatite U–Pb–REE analyses) of the transcurrent deformation during the Neoproterozoic orogenic processes. To reach this goal, we use the Cubatão Shear Zone (CSZ) as a study case, which corresponds to a transcurrent crustal-scale shear zone related to West Gondwana assembly. The data and discussion regarding this topic are presented in the manuscript "Deformation, thermochronology and tectonic significance of the crustal-scale Cubatão Shear Zone, Ribeira Belt, Brazil”, published in Tectonophysics (DOI: 10.1016/j.tecto.2022.229278). The results demonstrate that the CSZ was active during the collision stages related to the assembly of West Gondwana.

Finally, Chapter 6 compiles results and discussion developed through chapters 3 to 5 in a brief integrative conclusion of the thesis. Additionally, remaining and new open questions are highlighted in the hope to develop future research.

2. METHODS AND MATERIALS

For the development of this research, the following methods were used:

2.1. Bibliographic Research

The initial objective of the bibliographical research was to review the geological knowledge of the study area, aiming to integrate all the information generated in it. Bibliographical research was also crucial in acquiring expertise related to the applied methods and materials. For that purpose, articles published in scientific journals, abstracts published in annals of events, theses, dissertations and books were searched.

2.2. Fieldwork

To obtain data for this research, 68 outcrops were described. The objectives were to characterize different lithotypes and structures in the area, obtain structural data and collect hand samples. Geological and structural data and rock samples were collected for laboratory analysis during the fieldwork. A total of 107 samples were collected.

The fieldwork was mainly concentrated in two areas. The first one was in the western portion of the Embu Complex since the metasedimentary rocks present in this area have rarely been the subject of petrological and geochronological studies. The other fieldwork area was along the Cubatão Shear Zone, which is responsible for the contact between the Embu and Apiaí terranes to the northwest with the Costeiro and Curitiba terranes to the southeast.

For accomplishing this activity, standard tools for geology works were used: compass, navigation GPS, geologist hammer, slitter, digital camera and material for sample collection. The travel to the area was made by rented car, and the budget came from the technical reserve of the FAPESP scholarship.

2.3. Microscopic Petrography

A detailed petrographic description of selected samples was done in 90 thin sections using a magnifying glass and a petrographic microscope with plane-polarized and crossed-polarized lights. Microscopic petrography allowed the identification and detailed description of mineral phases, metamorphic assemblages, microstructures and qualitative crystallographic fabric. It also contributed to selecting samples suitable for geochemical, geothermobarometric and geochronological analysis.

The thin sections were prepared at the NAP Geoanalítica Laboratory, University of São Paulo, and described in an Olympus BX50 petrographic microscope. Photomicrographs were obtained with an Olympus Evolt E-330 and Zeiss AxioCam MRc cameras.

2.4. Whole-rock chemical analysis

Seventeen representative rock samples (Table 2.1) were selected to measure the major elements by X-ray fluorescence analysis on a fused glass disc. The prior treatment of the samples for whole-rock chemical analysis comprised the steps of sample fragmentation, removal of the altered portions and comminution in hydraulic press and agate mill to achieve a particle size less than 200 mesh. X-ray fluorescence analyses were performed using a PANalytical AXIOS MAX Advanced X-ray fluorescence (XRF) spectrometer of the X-ray fluorescence laboratory, NAP Geoanalítica at the University of São Paulo (Brazil). The steps detailing the analytical routine are described in Mori et al. (1999).

Additionally, in 12 samples, trace elements were analysed on a pressed powder pellet and measured by a Perkin Elmer/SciexTM quadrupole Elan-6100/DRC ICP-MS. JGb-1 (gabbro) and BR (basalt) reference materials were used as quality control standards. The analytical procedures follow the detailed description of Navarro et al. (2008). The geochemical diagrams were produced using the GCDkit program (Janoušek et al., 2006). The tables with the whole-rock chemical analysis are presented in Appendix A, B and C.

2.5. Mineral chemical analysis

The chemical compositions of biotite, muscovite, garnet, feldspars and cordierite of five samples (Table 2.1) were determined through spot analyses in a JEOL JXA-FE-8530 EMPA (electron microprobe analyser) at the NAP Geoanalítica Laboratory, University of São Paulo. The operating conditions were 15.0 kV accelerating voltage and a 20 nA beam current. The beam diameter for biotite, muscovite and garnet punctual analysis was set to 5µm. For feldspars and cordierite, the beam diameter was set to 10µm. Additionally, wavelength dispersive spectrometry (WDS) compositional maps of Fe, Mn and Mg in garnet (for samples 45A and 12A) were obtained under the following operating conditions: 15.0 kV accelerating voltage, 300 nA beam current and a dwell time of 25ms.

Mineral structural formulas were calculated according to Deer et al. (2013), using spreadsheets written by the author using the software Excel. The tables with the chemical compositions of the analysed minerals are presented in Appendix B and C.

2.6. Quartz crystallographic fabric analysis

Quartz crystallographic preferred orientation was collected in two samples from the Cubatão Shear Zone (Table 2.1) by electron backscatter diffraction (EBSD) analysis. During petrographic description, representative areas of deformational microstructures in the thin section were selected for the analysis.

For EBSD analyses, a final polishing stage was done in the polished thin sections using a colloidal silica solution to remove surface damage. After that, they were carbon-coated. EBSD analyses were performed in a JEOL 7001 FE SEM with an EBSD detector (AZTec acquisition software, Oxford Instruments) at Plymouth Electron Microscopy Centre (PEMC), United Kingdom. The setup used a 70º tilt in the microscope chamber to the horizontal position, voltage of 20 kV, probe current of 12 nA and working distance of 20 mm. The step size ranged from 0.8 to 1.5 µm, and was chosen according to subgrain and recrystallized grain size allowing a maximum population of grains to be measured.

Raw EBSD data were processed using HKL Channel 5 software (Oxford Instruments), with a noise reduction being applied in all maps. Subsets with one-point-per-grain were generated to plot the pole figures of the following crystallographic directions and planes: <001> (c axes); {100} (m, prism planes); ⟨110⟩ (a axes); {101} (r rhomb planes); and {011'} (z rhomb planes). Pole figures are oriented with the X parallel to the stretching lineation, and the Z parallel to the pole to the foliation. Pole figures and misorientation axis distribution in crystal coordinates are presented in the lower hemisphere stereographic projections and contoured with a half width of 15° using multiple uniform distribution technique. Misorientation data are displayed as misorientation angle distribution histograms, showing the relative frequency of misorientation angles.

2.7. Phase equilibria modelling

The whole-rock and mineral chemical data were used to construct isochemical phase diagrams for five samples from the Embu Complex and Cubatão Shear Zone (Table

2.1) using the Perple_X software (Connolly, 2005) and the internally consistent thermodynamic database of Holland and Powell (2011) (hp11ver.dat, tc-ds61 in Perple_X). Depending on the sample, the minerals involved in pseudosection construction include mica, staurolite, biotite, chlorite, garnet, ilmenite, feldspar, cordierite, orthopyroxene, epidote, spinel and silicate liquid (melt). The following solution models were used: Mica (W), St (W), Bi (W), Chl (W), Gt (W), Crd (W), Opx (W), Ilm(W) and melt (W) (White et al., 2014), feldspar (Fuhrman and Lindsley, 1988), Sp (WPC) (White et al., 2002) and Ep (HP11).

Fe^{3+} was considered in each modelled bulk composition due to the presence of Fe^{3+} minerals, and to constrain the content, we used T-X_{O2} diagrams. Additionally, the H_2O content was considered a saturated component or estimated so that the modelled rock composition was saturated in H_2O immediately below the solidus. P_2O_5 and MnO were neglected due to their low contents. The calculations were undertaken in the NCKFMASHTO(Na_2O-CaO-K_20-FeO-MgO-Al_2O_3-SiO_2-H_2O-TiO_2-O_2) and NCKFMASHT (Na_2O-CaO-K_2O-FeO-MgO-Al_2O_3-SiO_2-H_2O-TiO_2) chemical model systems using the measured bulk rock composition.

2.8. U–Pb geochronology, trace element and Lu–Hf analysis

Geochronological data was obtained from mineral concentrate mounts and in situ thin sections in 20 rock samples (Table 2.1). U–Pb isotopic ages were determined in monazite, zircon and apatite, the majority coupled with trace element compositions analysis (U–Pb–REE).

Zircon grains were separated using standard mineral separation techniques, including heavy liquids, before being mounted in epoxy and polished. Monazite and apatite were measured in situ in thin section. Secondary electron (SE), backscattered electrons (BSE) and cathodoluminescence (CL) images were obtained using a FEI-QUANTA 250 FEG scanning electron microscope equipped with a Centaurus Mono CL3+ spectroscope at the University of São Paulo, Brazil and in a Philips FEI XL30 scanning electron microscope equipped with a Gatan CL detector at the Earth-Sciences Electron Microscopy and in-situ X-ray Microanalysis at the University of Melbourne, Australia.

Zircon grains from three metasedimentary rocks (FM-27, AN-26A, AN-47) were analysed for U–Pb at the University of São Paulo, Brazil. Analysis of samples AN-26A

and AN-47 were performed on a Finnigan Neptune LA-MC-ICP-MS equipped with 9 Faraday detectors, 6 multi-ion counting and 1 secondary electron multiplier. The operating conditions were 60 seconds of ablation time, 6 mJ laser energy, 25% T attenuator value 6 Hz repetition rate and 29 µm spot size. Elemental fractionation and instrumental mass discrimination for LA-MC-ICP-MS analyses were calibrated using the standard zircon GJ-1 and monitored by measurements of NIST 612 glass, following the procedures described in (Sato et al., 2014). Raw data were reduced off-line with corrections for background, instrumental mass bias drift and common Pb. Analysis of sample FM-27 was carried out using a SHRIMP-IIe machine at the University of São Paulo, Brazil. Correction for common Pb was made based on the measured ^{204}Pb. The U–Pb ratios obtained by SHRIMP were calibrated against the standard zircon Temora (^{206}Pb/^{238}U age of 417 Ma, Black et al., 2004) and followed the procedures described by (Williams, 1997). U–Pb ages were calculated using the Isoplot 3.0 program (Ludwig, 2003).

U–Pb ages and trace element compositions of monazite (45A, 12A, 10A, FM02B), apatite (samples FM02B, DC-37B, DC-39A, DC-41B and DC-46D), and zircon (samples 45A, 10A, DC-39A, DC-46B and DC-41D) were obtained via Laser Ablation Split-Stream inductively coupled plasma mass spectrometer (LASS-ICP-MS) at the Monash Isotopia Facility, School of Earth, Atmosphere and Environment, Monash University. The experiments used an ASI-RESOlution ArF 193 nm excimer laser ablation system coupled to a Thermo Scientific iCAP-Q Quadruple ICP-MS for trace elements and a Thermo Scientific iCAP-TQ Triple-Quadruple ICP-MS for U–Pb isotopes. For zircon and monazite, the laser parameters were as follows: a spot size of 30 µm, fluence of ~4 J.cm-2 at 8 Hz. For apatite, a 30 µm spot size was used, with a fluence of 8 J.cm-2 at 8 Hz. Trace element compositions were obtained with a background of 20-seconds prior to ablation, followed by a 30-second ablation.

Additionally, for four samples, U–Pb was also collected with Lu–Hf isotopes using an ASI-RESOlution ArF 193 nm excimer laser ablation system coupled to a Thermo Scientific iCAP-TQ Triple-Quadruple ICP-MS for U–Pb isotopes and a Thermo Scientific Neptune Plus MC-ICPMS for Lu–Hf isotopes. The operating conditions were 30 seconds ablation time, 4.8 mJ laser energy, 50% T attenuator value 8 Hz repetition rate and 35 µm spot size.

During all sessions, standards were interspersed with unknowns. For zircon U–Pb ages, Plesovice and Mud Tank zircon were the primary standard with Temora 1 (417 Ma,

Black et al., 2003), Plesovice zircon (337 ± 0.4 Ma, Sláma et al. 2008), GJ1 (601 Ma, Jackson et al., 2004), Mud Tank (732 Ma, Black and Gulson, 1978) and 91500 zircon (1068 ± 5 Ma, Orihashi et al. (2008) as quality control. For monazite and apatite, the primary standards were MADel, with 44069 (425 Ma, Aleinikoff et al., 2006) and Madagascar apatite (485 Ma, Thomson et al., 2012) as secondary standards. For the trace element analyses, the NIST 610 glass standard was used as primary, with NIST 612, BCR2, ATHO, and BHVO used as secondary standards. The Lu–Hf ratios were calibrated using the MADEL standard (Payne et al., 2008).

Data reduction was performed in the Iolite 3 software package (Paton et al., 2011), using the U_Pb_Geochron4 and Trace_Elements data reduction schemes for U–Pb isotopes. For the Lu–Hf isotopes, we used the Hf_isotopes data reduction scheme with a mass bias for Yb corrected with a $^{173}Yb/^{171}Yb$ of 1.132685 (Chu et al., 2002) and mass bias for Hf corrected with a $^{179}Hf/^{177}Hf$ of 0.7325 (Guillot et al., 2009). ^{42}Ca was used as internal calibration for apatite and monazite, and ^{14}Si was used as internal calibration for zircon.

U–Pb ages were calculated using the IsoplotR program (version 3.7) (Vermeesch, 2018). For the apatite, the ^{204}Pb non-corrected radiogenic isotopes ratios were plotted in the Tera-Wasserburg Concordia diagrams, and the ages were calculated from the lower intercept of discordia model-1. All data were plotted in the Wetherill Concordia diagrams for monazite and zircon. Ages and respective uncertainties are stated as 2 σ (95 % confidence).

2.9. Rb–Sr geochronology

In situ biotite and muscovite Rb–Sr analyses were performed on two different samples (Table 2.1). Isotopic data were carried by Laser Ablation ICPMS at the Monash Isotopia Facility, School of Earth, Atmosphere and Environment, Monash University. The micas were analysed using a Thermo ICAPTQ Triple Quadrupole ICP-MS The mass spectrometer was coupled with an ASI Resolution 193 nm excimer laser equipped with a dual volume Laurin Technic S155 ablation cell. The minerals were ablated in a He atmosphere with laser operated at a repetition rate 10 Hz, 100 µm spot size and approximately 3 Jcm^{-2} of laser energy at the sample. Each analysis began with a 20-second measurement of the gas background, followed by 30s with the laser switched on ablating the sample.

It has been shown that Triple Quadrupole ICPMS technology is efficient in dealing with isobaric interferences, and in specific, it has been shown that it is useful for in-situ Rb-Sr geochronology where ^{87}Rb and ^{87}Sr directly overlap. The introduction of an oxidising gas such as O_2 or N_2O into the mass spectrometer ion path promotes Sr oxidisation but leaves Rb essentially unaffected, allowing the possibility of measuring Sr isotopes as oxidised reaction products and overcoming the isobaric interference of ^{87}Rb with ^{87}Sr (Hogmalm et al., 2017; Murphy et al., 2020). The analyses used N_2O as a reaction gas as being more efficient than O_2 in oxydising Sr (Hogmalm et al., 2017; Murphy et al., 2020) and analysed the following masses: ^{39}K, ^{41}K, $^{43}Ca^{16}O$, $^{44}Ca^{16}O$, ^{85}Rb, $^{86}Sr^{16}O$, $^{87}Sr^{16}O$, $^{88}Sr^{16}O$. Dwell time for ^{39}K, ^{41}K, $^{43}Ca^{16}O$, $^{44}Ca^{16}O$ was 5 ms, for ^{85}Rb 50 ms, $^{86}Sr^{16}O$, $^{87}Sr^{16}O$ 120 ms and for $^{88}Sr^{16}O$ 20 ms.

The raw data was reduced using the Iolite 3 software (Paton et al., 2011), and the final integrated raw counts were exported and further processed using an excel spreadsheet for drift correction and the calculation of the $^{87}Rb/^{86}Sr$ and $^{87}Sr/^{86}Sr$. For the $^{87}Sr/^{86}Sr$, NIST 610 was used as the main primary calibration standard, whereas for the $^{87}Rb/^{86}Sr$, the Mica-Mg pressed pellet was used. The recommended values used for these standards are reported by (Hogmalm et al., 2017). The analytical uncertainties were estimated using the internal and external precision obtained during the course of analyses of the calibration standards. For the $^{87}Sr/^{86}Sr$, the external precision of NIST 610 of all the analytical sessions (24 analyses) was added in quadratic addition to the internal precision of selected single analyses of the same standard. For the $^{87}Rb/^{86}Sr$, the same statistical approach was used, but in this case, the uncertainties were estimated using internal and external precision of the Mica-Mg (24 analyses) standard. Relative uncertainties ranged between 1.55 - 2.03% for the $^{87}Rb/^{86}Sr$ and 0.53% for the $^{87}Sr/^{86}Sr$, both at 1 sigma level.

2.10. Elementary and isotopic geochemistry

Whole-rock Sm and Nd concentration acquisitions and isotopic compositions were performed on five samples (Table 2.1) using a Thermo-Neptune mass spectrometer (ICP-MS) at the University of São Paulo (Brazil). The Sm and Nd concentrations were obtained by isotopic dissolution, and the $^{143}Nd/^{144}Nd$ ratios were normalised to the value of 0.7219 from the ratio $^{146}Nd/^{144}Nd$ (Depaolo, 1981). The $\varepsilon Nd(0)$ corresponds to the actual value and was calculated by the equation: $\{[(^{143}Nd/^{144}Nd)sam/\ 0.512638]-1\} * 104$, in which $^{143}Nd/^{144}Nd$ CHUR (chondritic uniform reservoir) is 0.512638 (Hamilton

et al., 1983). The value for the $^{143}Nd/^{144}Nd$ ratio from the standard JNDi-1 during the analysing period was 0.512096 ± 0.000005.

Table 2.1. Summary of the methods used per sample in this work.

	Whole-rock chemistry		Mineral chemistry	Quartz EBSD	Phase equilibria modelling	Geochronology and mineral trace element composition						Isotopic geochemistry
						Monazite	Zircon			Apatite	Muscovite + biotite	
	Major elements	Major + REE elements				U–Pb–REE	U–Pb	U–Pb–REE	U–Pb–Hf	U–Pb–REE	Rb–Sr	whole-rock Sm–Nd
Chapter 3		DC-22D DC-70A DC-70B DC-71A DC-72A DC-73A GI-14 FM-06 FM-07 FM-08 WSP-04 WSP-13							WSP-04 DC-09A GI-14 DC-22D			DC-09A FM-06 FM-08A WSP-13 DC-22D
Chapter 4	10A 12A 45A		10A 12A 45A		10A 12A 45A	12A 45A FM-02B	FM-27	45A 10A AN-26A AN-47		FM-02B	12A (bt + ms) 45A (bt)	
Chapter 5	DC-33C DC-41B		DC-33C DC-41B	DC-33B DC-41B	DC-33C DC-41B			DC-39A DC-46B DC-41D		DC-37B DC-39A DC-41B DC-46D		

3. EVIDENCE OF MESO- TO NEOPROTEROZOIC TERRANE ACCRETION IN RIBEIRA BELT, BRAZIL: INSIGHTS FROM JUVENILE MAFIC MAGMATISM FROM THE VOTUVERAVA GROUP AND EMBU COMPLEX

Dina I. G. Cabrita[a]*, Frederico M. Faleiros[a], Peter A. Cawood[b], Ginaldo A. C. Campanha[a], Bruno V. Ribeiro[b, c], Maria T. A. G. Yogi[d]

[a] Instituto de Geociências, Universidade de São Paulo, Rua do Lago 562, São Paulo, SP, CEP 05508-080, Brazil

[b] School of Earth, Atmosphere and Environment, Monash University, Melbourne, VIC 3800, Australia

[c] Curtin University, Timescales of Mineral Systems Group, School of Earth and Planetary Sciences, Perth, WA 6845, Australia

[d] Department of Earth Sciences, Carleton University, Ottawa, ON, Canada

* Corresponding author: dina_cabrita@yahoo.com

Abstract

Terranes of the Neoproterozoic Ribeira Belt provide a record of processes related to West Gondwana assembly. However, the evolutionary history of the belt in the preceding Rodinia supercontinent and its role in the transition to West Gondwana assembly is poorly known. New geochemical and geochronological data of mafic magmatism from Meso- to early Neoproterozoic rock units (1500-900 Ma) integrated with published data provides new constrains to unravel the tectonic setting of the Ribeira Belt. Data from the Votuverava Group and Embu Complex from the southern Ribeira Belt record three distinct periods of juvenile magmatism. The mafic rocks from the Votuverava Group define the oldest magmatism at Calymmian (1490-1475 Ma) and Ectasian (1300-1260 Ma). Both age groups display Th/Yb ratios above N-MORB, low Ta/Yb and Nb/La ratios, low Nb and Zr concentrations, negative Nb anomaly, $\varepsilon Nd_{(t)}$ of +2.25 to +4.01 an Nd two-stage T_{DM} model age spanning 1629-1471 Ma which are characteristic of juvenile mantle source arc-related magmatism. The third event occurred in the early Tonian (900 Ma) and is recorded in the mafic rocks from the Embu Complex. Geochemical data indicate that

the mafic rocks belong to the tholeiitic series with low LREE enrichment, negative Nb and Ta anomalies, low Nb and Zr contents and low Nb/La and Zr/Y ratios, consistent with arc-related basalts. Whole-rock Sm–Nd isotopic data yield $\varepsilon Nd_{(t)}$ of +0.72 and Nd two-stage T_{DM} model age of 1921 Ma, with Hf isotopes indicating juvenile mantle sources to the mafic magmatism with εHf_T between + 4.5 and + 17.2. Thus, mafic rocks from the southern Ribeira Belt record multiple periods of accretion and convergence settings associated with assembly of Rodinia and Gondwana.

Keywords: Geochemistry; U-Pb-Hf isotopes; Arc basalts; Accretionary orogen; Brasiliano-Pan-African Orogen; Rodinia and West Gondwana assembly

3.1. Introduction

In association with sediment accumulation, the geochemical and isotopic study of mafic magmatism in orogenic belts provides vital information to interpret their tectonic settings (Mullen, 1983; Pearce and Cann, 1973; Pearce et al., 1975; Wilson, 1989; Xia and Li, 2019). Such data is potentially critical in resolving contrasting tectonic models for the Ribeira Belt in the Brasiliano-Pan-African Orogen. The current dominant model associated with the setting of the Ribeira Belt suggests multiple terrane accretion phases related to accretionary to collisional settings associated with long-lived subduction of a large Adamastor Ocean, between the Paranapanema, São Francisco, Congo and Luís Alves cratons that culminate in continental collision at ca. 600 Ma (Brito Neves et al., 1999; Campos Neto, 2000; Caxito et al., 2022; Faleiros et al., 2011a; Heilbron et al., 2020). In contrast, tectonic models invoking earlier concepts related to an intracontinental tectonic setting for the orogen (Porada, 1989; Torquato and Cordani, 1981) have been recently proposed (Fossen et al., 2020; Konopásek et al., 2020; Meira, 2014; Meira et al., 2019b, 2019a, 2015; Percival et al., 2022). These studies propose the orogen formed in an extensional rift basin setting followed by cratonic collisions between 650–600 Ma, which would have given origin to collisional belts, followed by transcurrent tectonics with associated granitic magmatism between 600–560 Ma.

We resolve these end-member tectonic models through new whole-rock geochemistry, whole-rock Sm–Nd isotopes and zircon U-Pb-Hf isotopic data from a series of mafic rocks of the Mesoproterozoic Votuverava Group and Neoproterozoic

Embu Complex from the southern Ribeira Belt. Based on this data, we propose multiple periods of terrane accretion between Rodinia and West Gondwana assembly.

3.2. Regional setting

The Ribeira Belt corresponds to one of the orogenic belts in the Brasiliano-Pan-African Orogen, and records geodynamic processes that overlap with, and are related to, Neoproterozoic break-up of Rodinia and West Gondwana assembly (Brito Neves et al., 1999) (Fig. 3.1a and b). The South American component of the Brasiliano-Pan-African Orogen is formed by three major physiographic entities, known as Borborema, Tocantins and Mantiqueira structural provinces (Brito Neves et al., 2021), sometimes designated as the Brasiliano Orogen, Brasiliano fold systems or Brasiliano structural provinces (Arena et al., 2017; Brito Neves et al., 2021; Cerva-Alves et al., 2020; Hartmann et al., 2019; Pertille et al., 2017; Pinto et al., 2021; Werle et al., 2020).

Together with Araçuaí and Dom Feliciano belts, the Ribeira Belt form the Mantiqueira Province that extends along the SE coast of Brazil and Uruguay (Almeida et al., 1981; Brito Neves et al., 2021). The Ribeira Belt extends more than 1400 km along the South Atlantic margin and is approximately 300 km wide in its central segment (e.g., Almeida et al., 1973; Almeida and Hasui, 1984; Brito Neves et al., 2014). The belt is formed by several terranes juxtaposed by a system of an anastomosing network of brittle-ductile to ductile shear zones, mainly with a dextral shear sense (Faleiros et al., 2022). The southern part of the belt comprises, from the northwest to the southeast, the Embu, Apiaí and Curitiba terranes (Fig. 3.1c).

3.2.1. Apiaí Terrane

The Apiaí Terrane is a composite terrane formed by restricted Paleoproterozoic orthogneiss cores (Betara, Perau, Tigre, Anta Gorda and Apiaí-Mirim) and five distinct metasedimentary successions with ages ranging from late Calymmian to Ediacaran (Campanha et al., 2015; Faleiros, 2008; Faleiros et al., 2011a). The metasedimentary rock successions include: (1) the Itaiacoca Group composed by phyllite with intercalations of arkose and rhyolite and carbonate formations with minimum depositional ages of 1030-908 Ma apart from the metavolcanic upper units with ages of 645-628 Ma (Forero-Ortega et al., 2020; Siga Júnior et al., 2009); (2) the Água Clara Formation, mainly composed of impure marble with subordinate intercalations of phyllite, schist and mafic rocks with

depositional ages of ca. 1500-1470 Ma (Weber et al., 2004); (3) the Lageado Group formed by an alternation of siliciclastic and carbonate formations with a depositional age between 1200-880 Ma (Campanha et al., 2016); (4) the Iporanga Formation composed of rhythmite with siltstone, and sandstone conglomerate intercalations deposited between 590-580 Ma (Campanha and Sadowski, 2002) and (5) the Votuverava Group formed by fine-grained pelitic successions deposited during the Calymmian (1490-1475 Ma) ages (Campanha et al., 2015; Siga Júnior et al., 2011a).

The Votuverava Group is the largest unit from the Apiaí Terrane. It overlies Paleoproterozoic granitic and gneissic rocks (Betara and Tigre nuclei) outcropping as elongated domes in the core of regional open anticlines with ca. 2200 and 1770-1750 Ma zircon U-Pb ages (Cury et al., 2002; Yogi, 2019). The group comprises metamorphosed fine-grained pelitic successions (slate, phyllite and schist), generally interpreted as distal turbidites, interbedded with mafic rocks, considered to be deposited during the Calymmian (1490-1475 Ma) based on zircon U–Pb ages (Campanha et al., 2015; Siga Júnior et al., 2011a). The fine-grained pelitic successions were subdivided into several units (Betara, Perau, Rubuquara, Nhunguara, Piririca and Ribeirão das Pedras) (Perrotta, 1996; Perrotta et al., 2005) as well as undivided units of mica schist and garnet mica schist (Faleiros et al., 2011b), and are covered by the Serra das Andorinhas Formation, which is composed of carbonate-bearing schist with marble, quartzite and calciosilicatic lenses (Campanha, 1991; Campanha et al., 1986; Faleiros et al., 2012, 2011b).

A large number of mafic and metavolcanic intercalations also occur within the Votuverava Group, as well as subordinate occurrences of quartzite, conglomerate and calc-silicate rocks, and minor thin layers of iron formations, chert, Pb–Zn–Ag–Cu sulfide and Au deposits. Available geochemical and geochronological analyses of mafic rocks. Based on this data, a magmatic event at ca. 1490 Ma is inferred to be related to an oceanic back-arc basin environment of an accretionary orogen (Campanha et al., 2015). Additionally, zircon U–Pb ages of ca. 1300 Ma from mafic rocks are presented by Campanha et al. (2019) for the easternmost portion of the Votuverava Group, but the tectonic significance of these rocks was not explored. A Barrovian-type metamorphism varying from lower greenschist to medium amphibolite facies conditions is recorded with ages between 820–790 Ma and 615–565 Ma (Campanha et al., 2019; Yogi, 2019).

3.2.2. Embu Terrane

The Embu Terrane comprises the Paleoproterozoic Rio Capivari Complex (Fernandes, 1991; Babinski et al., 2001; Maurer, 2016), the Embu Complex, and Cryogenian to Ediacaran granitoids (Janasi et al., 2003; Alves et al., 2013; Alves et al., 2016). The terrane is bounded by four major units interpreted as composite terranes: Apiaí, Curitiba and Costeiro terranes and the São Roque Domain (Fig. 3.1). The Embu Complex is composed of an association of metasedimentary rocks that include paragneiss, mica schist, quartz schist, quartzite and calc-silicate rocks with concordant intercalations of ultramafic and mafic rocks deformed at lower to upper amphibolite facies conditions. The high-grade metamorphic rocks are represented by migmatitic paragneiss with near-peak metamorphic conditions constrained to 770 to 780 ºC and 8.5 to 9.2 kbar. Partial melting led to the formation of in situ and in source granitic leucosomes, and geochronological data indicates that the high-grade metamorphic event occurred between 830–760 Ma (Cabrita et al., 2021). Orthogneisses of ca. 810–780 Ma occur within the complex (Cordani et al., 2002; Vlach, 2008).

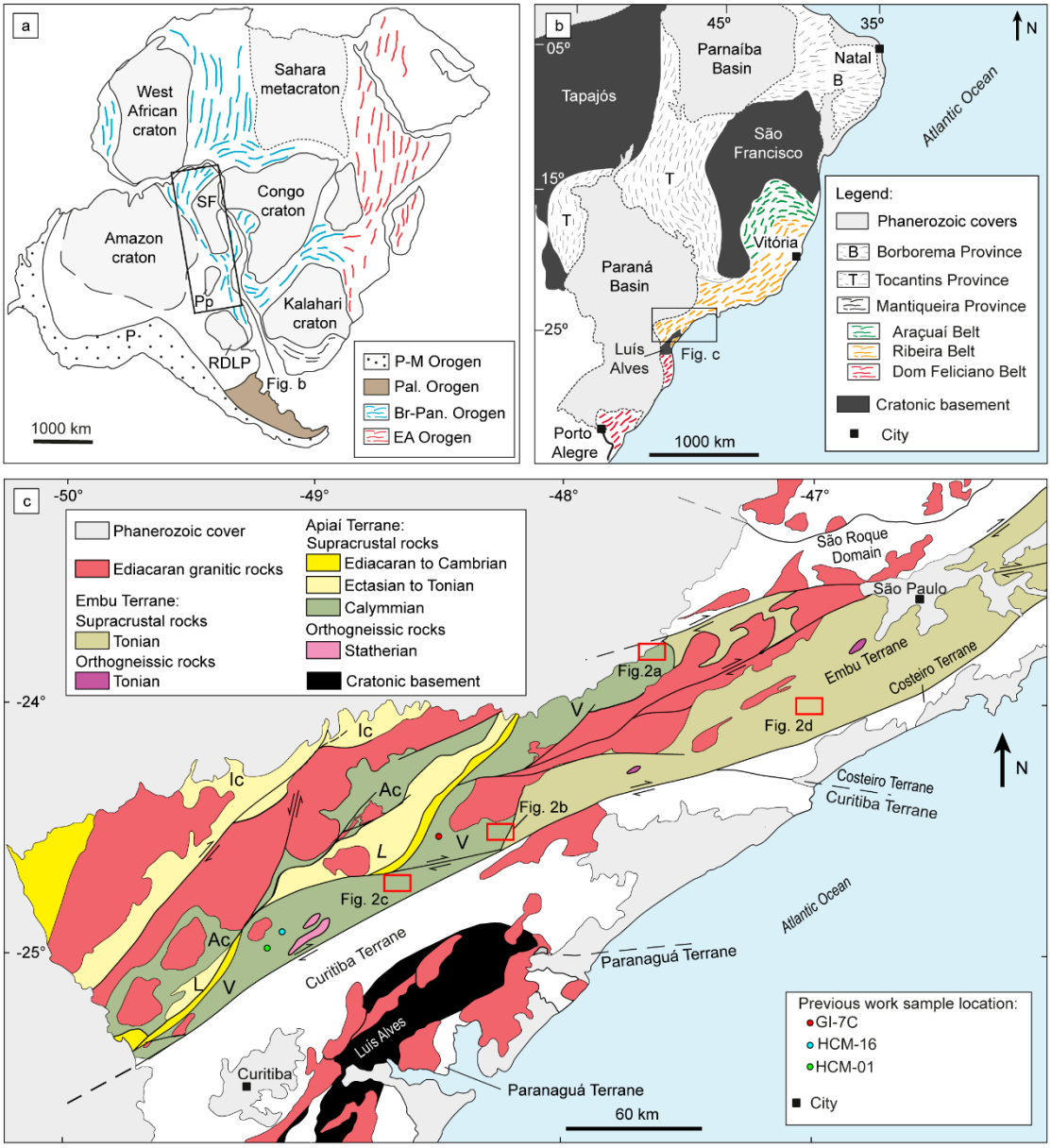

Figure 3.1. Location maps of the study area. a) Location of the studied area in West Gondwana. Abbreviations include: Cratons: SF = São Francisco; Pp = Paranapanema; RDLP = Rio de la Plata. Proterozoic orogens: Br-Pan = Brasiliano-Pan-African; EA = East African. Other units: Pal. = Paleozoic; P-M = Paleozoic-Mezosoic Modified from Gray et al. (2008) and Li et al. (2008); b) Geotectonic sketch map of the South American counterpart of the Brasiliano-Pan-African Orogen, showing the subdivision in three major provinces; c) Geotectonic map of the southern portion of the Ribeira Belt with location of the study area and shear zones ages. Modified from Campanha et al. (2015). The maps use geographical coordinates in degrees (WGS-84 datum).

3.3. Analytical methods and procedures

Whole-rock geochemical analysis was performed at the NAP-Geoanalítica Facility at the University of São Paulo (Brazil). Samples were crushed and milled using a jaw crusher and a disc mill at the X-ray Fluorescence Laboratory. Major and minor element oxides were measured on fused pellets by X-ray fluorescence analysis using a PANalytical AXIOS MAX Advanced X-ray fluorescence (XRF) spectrometer. The analytical procedures follow the detailed description in Mori et al. (1999). Trace elements were measured on pressed pellets by a Perkin Elmer/SciexTM quadrupole Elan-6100/DRC ICP-MS. JGb-1 (gabbro) and BR (basalt) reference materials were used as quality control standards. The analytical procedures follow the detailed description of (Navarro et al., 2008). The geochemical diagrams were produced using the GCDkit program (Janoušek et al., 2006). The data are presented in Supplementary Material 1.

Zircon grains for U–Pb–Hf analyses were extracted and selected using standard mineral separation procedures including rock crushing, milling and sieving using 0.150–0.063 mm fractions. The samples were passed on Frantz isodynamic magnetic separator at 1.2 A. The non-magnetic separate was selected for density separation using heavy liquids (tetrabromoethane), from which the zircons were hand-picked and mounted in epoxy and polished. Cathodoluminescence (CL) images were obtained using an FEI-QUANTA 250 FEG scanning electron microscope equipped with a Centaurus Mono CL3+ spectroscope at the University of São Paulo, Brazil.

For samples FM-06, DC-09A and DC-22D, zircon U–Pb isotopic analyses were performed at the University of São Paulo, Brazil using a SHRIMP-IIe instrument. The setup configuration includes a 25 μm spot-size following the methods proposed in Sato et al. (2014). Correction for common Pb was made based on the ^{204}Pb measured. The U–Pb ratios obtained by SHRIMP were calibrated against the standard zircon TEMORA (Black et al., 2003) and followed the procedures described by Williams, 1997. Uncertainties are stated at 1 σ level.

Zircon U–Pb–Hf isotopic analyses from samples GI-14, DC-09A, WSP-13 and DC-22D were performed at the Monash Isotopia Facility at the Earth, Atmosphere & Environment School (Monash University, Australia) using a laser ablation split stream LASS-ICP-MS setup following the methods described in Mulder et al. (2021) and Ribeiro et al. (2020). The data were collected using an ASI-RESOlution ArF 193 nm excimer laser ablation system coupled to a Thermo Scientific iCAP-TQ Triple-Quadruple

ICP-MS to measure U–Pb isotopes and a Thermo Scientific Neptune Plus MC-ICPMS to measure Lu–Hf isotopes. The operating conditions were 30 seconds ablation time, 4.8 mJ laser energy, 50 % attenuation, 8 Hz repetition rate and 35 µm spot size. For U–Pb isotopes, we used Plesovice zircon as primary reference material (337 ± 0.4 Ma, Sláma et al., 2008), and GJ1 zircon (601 Ma, Jackson et al., 2004) and 91500 zircon (1068 ± 5 Ma, Orihashi et al., 2008) as secondary reference materials. During all sessions, standards were interspersed with unknowns. The Lu and Hf isotopes were calibrated against Mud Tank zircon (Woodhead and Hergt, 2005) as primary reference material. Data reduction was performed using Iolite 3 software (Paton et al., 2011) using the U_Pb_Geochron4 data reduction scheme with down-hole fractionation modelled with a smoothed cubic spline. Uncertainties are stated at 1 σ level. For the Lu–Hf isotopes, we used the Hf_isotopes data reduction scheme with mass bias for Yb corrected with a $^{173}Yb/^{171}Yb$ of 1.132685 (Chu et al., 2002) and mass bias for Hf corrected with a $^{179}Hf/^{177}Hf$ of 0.7325 (Guillot et al., 2009). The present-day depleted mantle ratios of $^{176}Hf/^{177}Hf$ (0.28325), $^{176}Lu/^{177}Hf$ (0.0384), the average continental crust $^{176}Lu/^{177}Hf$ (0.0113) and the ^{176}Lu decay constant of 1.867×10^{-11} year^{-1} were used to calculate Hf model ages (T_{DM1}, T_{DM2}) as recommended by Vervoort and Blichert-Toft (1999). U–Pb ages were calculated using the IsoplotR program (version 3.7) (Vermeesch, 2018). Only analyses that have 10 % or less discordance were plotted on the concordia diagrams. The results from zircon reference materials are presented in Supplementary Material 2 and CL images in Supplementary Material 3.

Whole-rock Sm and Nd concentrations and isotopic compositions were performed for four mafic rocks from the Votuverava Group and one mafic rock from the Embu Complex (DC-22D) using a Thermo-Neptune multi-collector inductively coupled plasma mass spectrometer (MC-ICP-MS) at the University of São Paulo, Brazil. The Sm and Nd concentrations were obtained by isotopic dissolution, and the $^{143}Nd/^{144}Nd$ ratios were normalised to the value of 0.7219 from the ratio $^{146}Nd/^{144}Nd$ (Depaolo, 1981). The $\varepsilon Nd_{(0)}$ corresponds to the actual value and was calculated by the equation: {[($^{143}Nd/^{144}Nd$)sam/ 0.512638]−1} * 104, in which $^{143}Nd/^{144}Nd_{CHUR}$ (chondritic uniform reservoir) is 0.512638 (Hamilton et al., 1983). The value for the $^{143}Nd/^{144}Nd$ ratio from the standard JNDi-1 during the analysing period was 0.512096 ± 0.000005. Initial ratios of 87Sr/86Sr and $^{143}Nd/^{144}Nd$ were calculated based on zircon U–Pb ages. We calculated $\varepsilon Nd_{(t)}$, T_{DM1} (single-stage) and T_{DM2} (two-stage) based on zircon U–Pb ages using GCDkit software (Janoušek et al., 2006), the results of which are presented in Supplementary Material 4.

3.4. Field relationships and petrography

The sample locations from the studied mafic rocks of the Votuverava Group and the Embu Complex are shown in Figure 3.2. Mafic rocks outcrop lenses are concordant with the main tectonic structures of the host rocks, indicating coeval deformation and obliterating original rock relations.

In the Votuverava Group, four different mafic units from distinct portions of the group were studied (Fig. 3.2a-c). The mafic rock units have lenticular shapes concordant with the host rock structural trends with 2-3 km length. Samples WSP-13 and WSP-04 were collected in the Pilar do Sul region (Fig. 3.2a) from mafic rock units hosted by paragneiss and quartz-biotite-muscovite schist, respectively. Sample WSP-13 is a schistose amphibolite primarily composed of hornblende and plagioclase and sample WSP-04 is an amphibolite primarily composed of actinolite, epidote, plagioclase and titanite.

Mafic rock samples DC-09, FM-06, FM-07 and FM-08 of the Votuverava Group outcrops within Serra das Andorinhas schist units (Sete Barras – Eldorado region, Fig. 3.2b and Fig. 3.3a-c) that alternate between fine-grained phyllite and schist. Mafic rock samples are dark greenish and have a dominant isotropic structure but sometimes subtle local metamorphic foliation is also present (samples DC-09 and FM-08). They are composed of hornblende and plagioclase with quartz, opaque oxide minerals, and titanite, epidote and zircon occurring as accessory phases. The greenish hornblende, with euhedral to anhedral shape and grain-size ranging from 50 to 500 μm, is the major phase (60 to 80 %) (Fig. 3.3d, e). Fine-grained plagioclase (10 to 30 μm) with euhedral to subhedral shape make up to 20-30 % of the rock. Sample GI-14 is an epidote-actinolite amphibolite and the surrounding unit is a mica schist with muscovite, chlorite and biotite with local occurrences of garnet.

In the Embu Complex, the mafic rock unit (samples DC-22D, DC-70A, DC-70B, DC-71A, DC-72A, DC-73A, DC-73B) is hosted by a paragneiss unit and display a NE-elongated structure parallel to the structural orientation of the belt with around 500 m length. It is dark in colour and is fine- to medium-grained (0.01 to 3 mm). In most of the samples, the mineral phases define an incipient metamorphic foliation, although isotropic structure is also common (e.g., sample DC-73B). Hornblende and plagioclase are the main minerals in these rocks. Opaque oxide minerals, quartz, titanite and zircon occur as accessory phases. Medium- to coarsed-grained hornblende grains are euhedral to

subhedral, present brownish colour and comprise ca. 70 % of the rock. Fine-grained (10 to 30 µm) plagioclase grains are euhedral subhedral to euhedral and make up to 20 % of the rock.

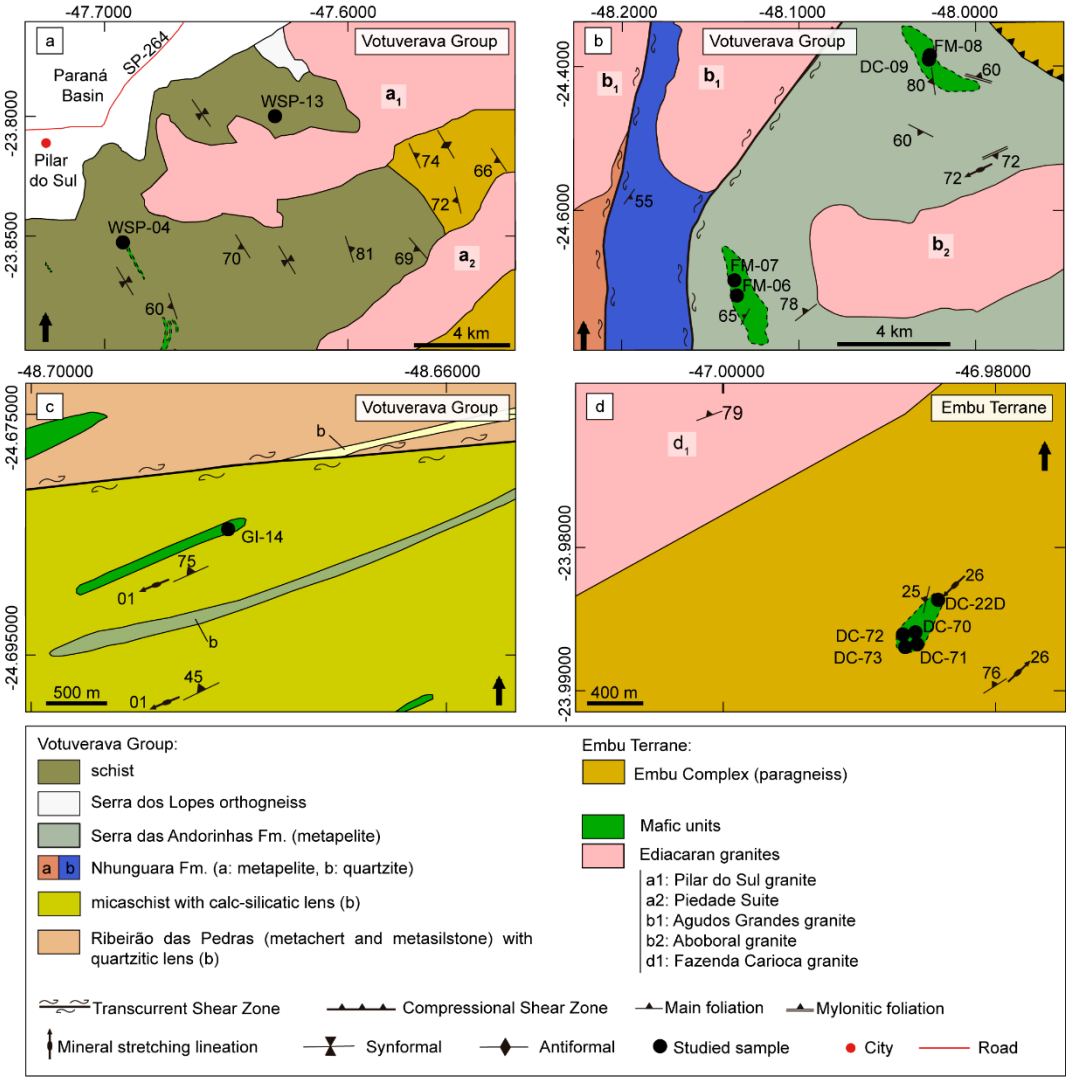

Figure 3.2. Geological maps with the location of the mafic units and analyzed samples. Black arrows indicate the North. Geographic coordinates, WGS84 datum. a) Adapted from Stein et al. (1983); b) and c) Adapted from Caltabellota et al. (2017) and d) mafic outcrop from the Embu Complex. Adapted from Perrotta et al. (2005).

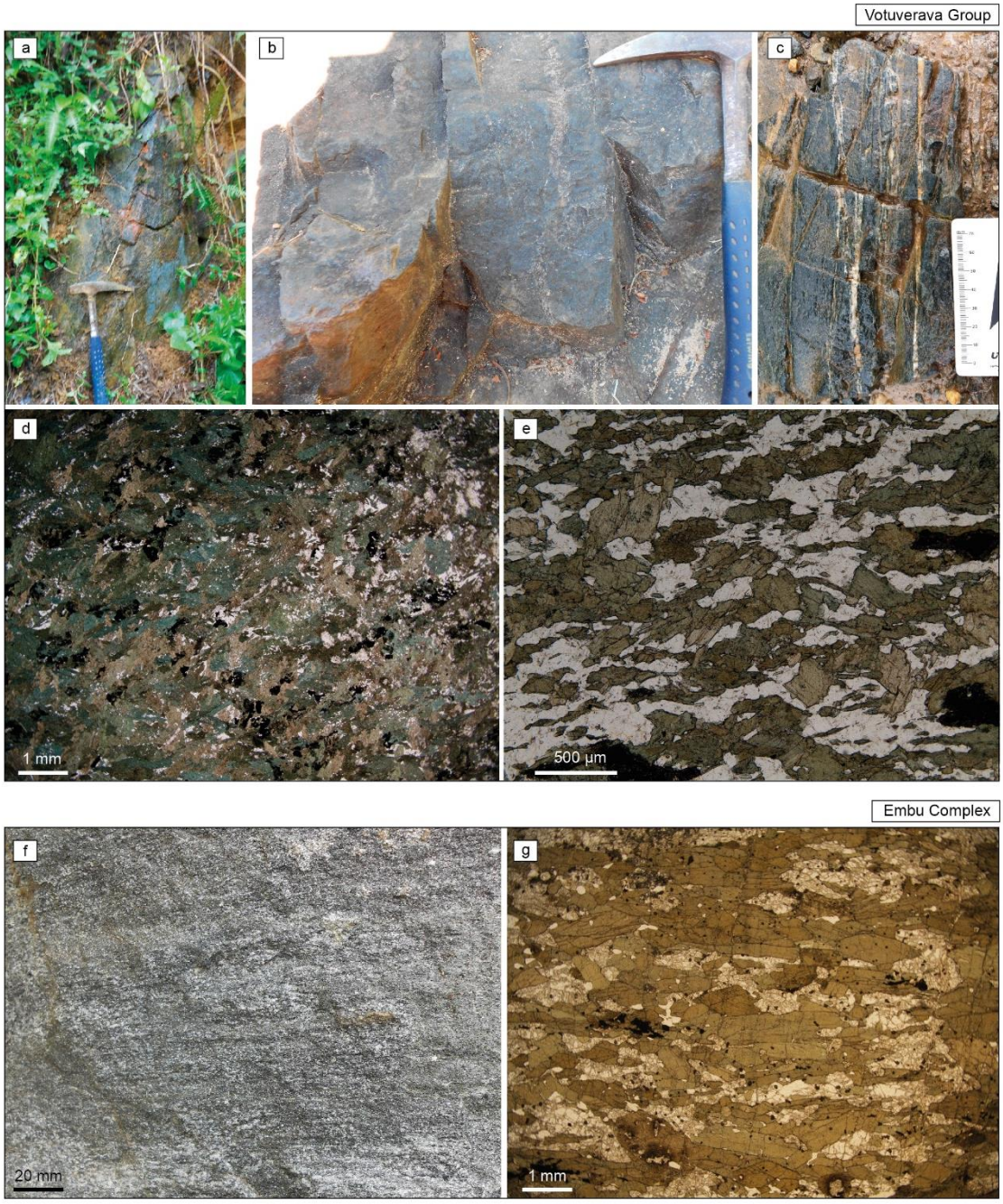

Figure 3.3. Field photographs and photomicrographs from the mafic rocks from the Votuverava Group and Embu Complex. a) Outcrop from the mafic unit of the samples FM-06 and FM-07 (sample DC-01); b) Mafic outcrop of the sample FM-07; c) Mafic outcrop with felsic lenses (DC-09 outcrop); d) Photomicrograph of the fine-grained metamafic rocks from the Votuverava Group (sample FM-06) under plane-polarised light; e) Photomicrograph of the medium to coarse-grained mafic rocks from the Votuverava Group (sample FM-08) under plane-polarised light; f) Hand sample from the mafic rock from the Embu Complex (samples DC-73); g) Medium to coarse-grained hornblende under plane-polarised light.

3.5. Whole-rock geochemistry

Five mafic rock samples of the Votuverava Group (GI-14, FM-06, FM-07, FM-08, WSP-13) and seven mafic rock samples of the Embu Complex (DC-22D, DC-70A, DC-70B, DC-71A, DC-72A, DC-73A, DC-73B) were selected for geochemical analysis, including major and trace element compositions. The results are presented in figures 3.4 and 3.5 and table 1 of Supplementary Material 1. Published whole-rock geochemical data (Campanha et al., 2015; Faleiros et al., 2011b) were added to figures 3.4 and 3.5 and are described together with the data presented in this paper.

To evaluate the effect of the regional metamorphism, hydrothermal alteration, metasomatism and weathering, we plotted the MgO content against the Ca/Al ratio (Hollocher et al., 2012). Our samples have an average MgO content of 7 % and Ca/Al ratios of ~0.6, plotting within the igneous rocks field (Supplementary Material 1). Additionally, to evaluate the alteration and element mobility effect on the trace elements, we used the correlation between Zr and elements used in the below described diagrams (Nb, Yb, Ti, V, Th and Ta), which is widely accepted to assess element mobility (Pearce et al., 1992; Polat et al., 2002). Our samples present Nb, Yb, Ti, V, Th and Ta concentrations well-correlated with Zr (Supplementary Material 1), suggesting that the regional metamorphism and other secondary processes did not significantly disturb the whole-rock geochemical system (i.e., major and minor elements). Thus, the geochemical data, including the interelement ratios, can be used to constrain the origin and evolution of the mafic rocks.

Mafic rocks of the Votuverava Group present two distinct geochemical signatures based on Nb/Yb and Ti/V ratios (Fig. 3.4a): the B1-B2 group present low Nb/Yb (< 4) and Ti/V (< 25) ratios whereas B3 group display higher Nb/Yb (> 4) and Ti/V (> 25) ratios. Group names follow the ones from Campanha et al. (2015). B1-B2 group is enriched in titanite, plagioclase and quartz and depleted in titanomagnetite and ilmenite when compared to the B3 group.

In most of the samples, the SiO_2 and $Na_2O + K_2O$ content vary from 45 to 50 % and 1 to 4 %, respectively, expected characteristics for subalkaline basic rocks (Fig. 3.4b and Supplementary Material 1). Sample FM-07 presents the lowest SiO_2 content (45 %), plotting in the ultrabasic field together with two more samples from the B1-B2 group. The FeO_{total} / MgO versus SiO_2 diagram evidence a tholeiitic signature for the greater part of the samples (Fig. 3.4c) and three samples from the group B1-B2 plotted in the calc-

alkaline series. All the samples have metaluminous affinity highlighted in the A / NK versus A / CNK diagram (Fig. 3.4d).

Zr and Nb concentrations vary between 60–146 ppm and 2–17 ppm, respectively. The Nb/La and the Zr/Y ratios vary between 0.6–1.6 and 1.8–4.9, respectively (Supplementary Material 1). The REE-chondrite normalised pattern from the mafic rocks of the Votuverava Group present two distinct patterns (Fig. 3.5a): B1-B2 group (including samples FM-06 and FM-07) presents a near flat pattern with slight LREE to HREE enrichment, whereas B3 group (including samples GI-14 and WSP-13) presents a moderate LREE to HREE depletion. The incompatible elements spider diagrams normalised by the N-MORB (Sun and McDonough, 1989) show a more fractionated pattern in the low field strength elements (LFSE) compared to the high field strength elements (HFSE). All the samples present negative Nb anomaly (Fig. 3.5b).

The mafic rock samples of the Embu Complex have SiO_2 and $Na_2O + K_2O$ content varying from 47–49 % and 2–3 %, respectively, pointing to a subalkaline basic composition (Supplementary Material 1, Fig. 3.4a). A tholeiitic signature is suggested in the FeO_{total}/MgO versus SiO_2 diagram (Fig. 3.4b) with metaluminous affinity as indicated in the A/NK versus A/CNK diagram (Fig. 4c). Zr and Nb concentrations vary between 42–62 ppm and 1.9–3.4 ppm, respectively. Additionally, the Nb/La and the Zr/Y ratios vary between 0.3–0.7 and 2.2–3.8, respectively (Supplementary Material 1). The REE-chondrite normalised patterns from the Embu Complex present slight depletion trend from LREE to HREE (Fig. 3.5c). The incompatible elements spider diagram normalised by the N-MORB shows slight enrichment of incompatible elements with a more fractionated pattern in the low field strength elements (LFSE) compared to the high field strength elements (HFSE). All the samples present a negative Nb anomaly (Fig. 3.5d).

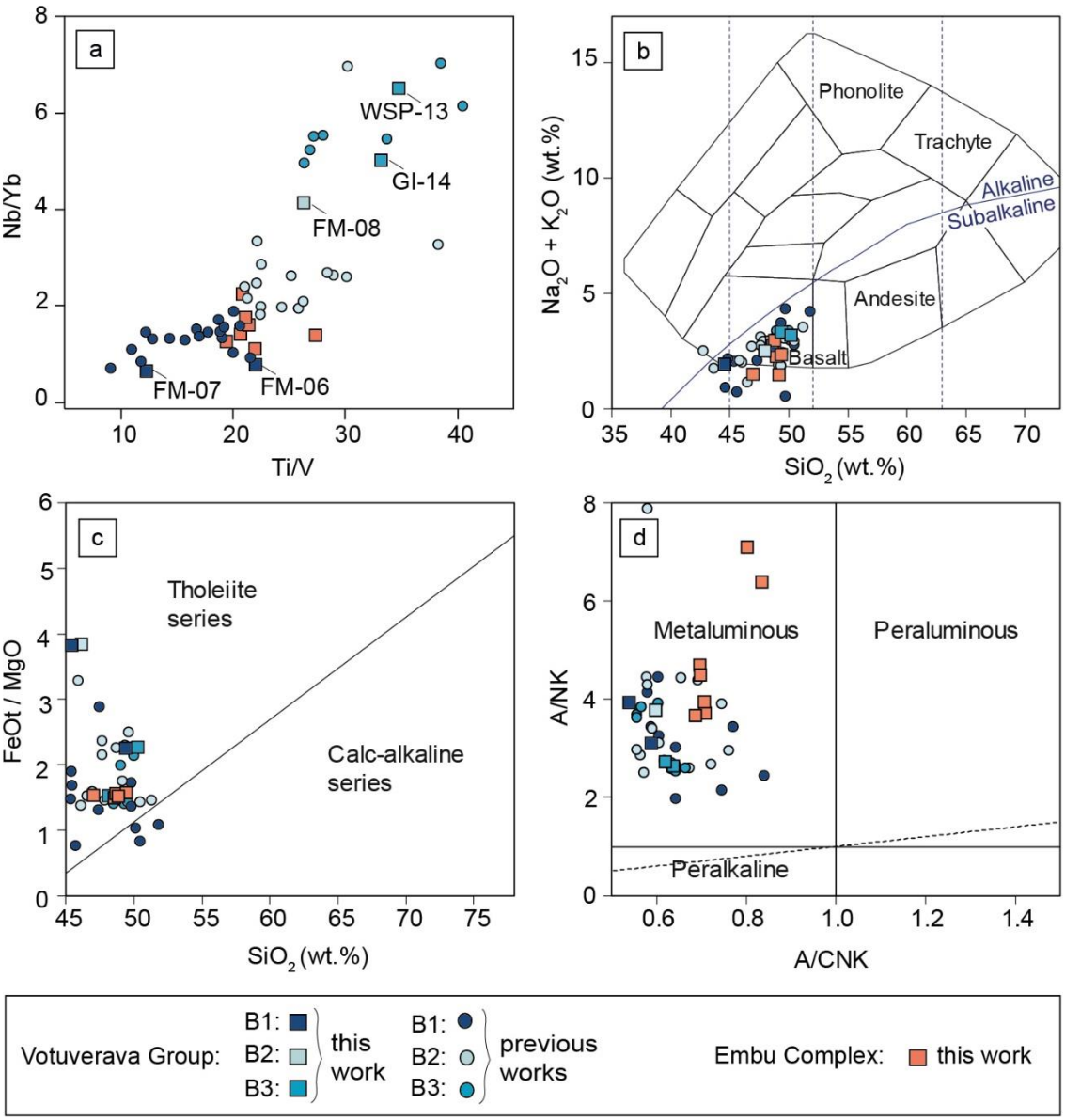

Figure 3.4. Geochemical diagrams from the Embu Terrane and Apiaí Terrane. B1, B2 and B3 data are from Faleiros et al. (2011) and Campanha et al. (2015). a) Ti/V vS Nb/Yb diagram; b) Total alkalis vs SiO2 (TAS) diagram, Cox et al. (1979). Sample GD396D has a SiO2 lower than 35 wt.% and is not on the diagram. Vertical lines correspond from left to right to ultrabasic, basic, intermediate and acid fields; c) SiO2 vs FeO / MgO3 diagram, Miyashiro (1974). Samples GD396D and GD487 have a SiO2 lower than 45 wt.% and are not on the diagram; d) A/CNK vs A/NK discrimination diagram, Shand (1943).

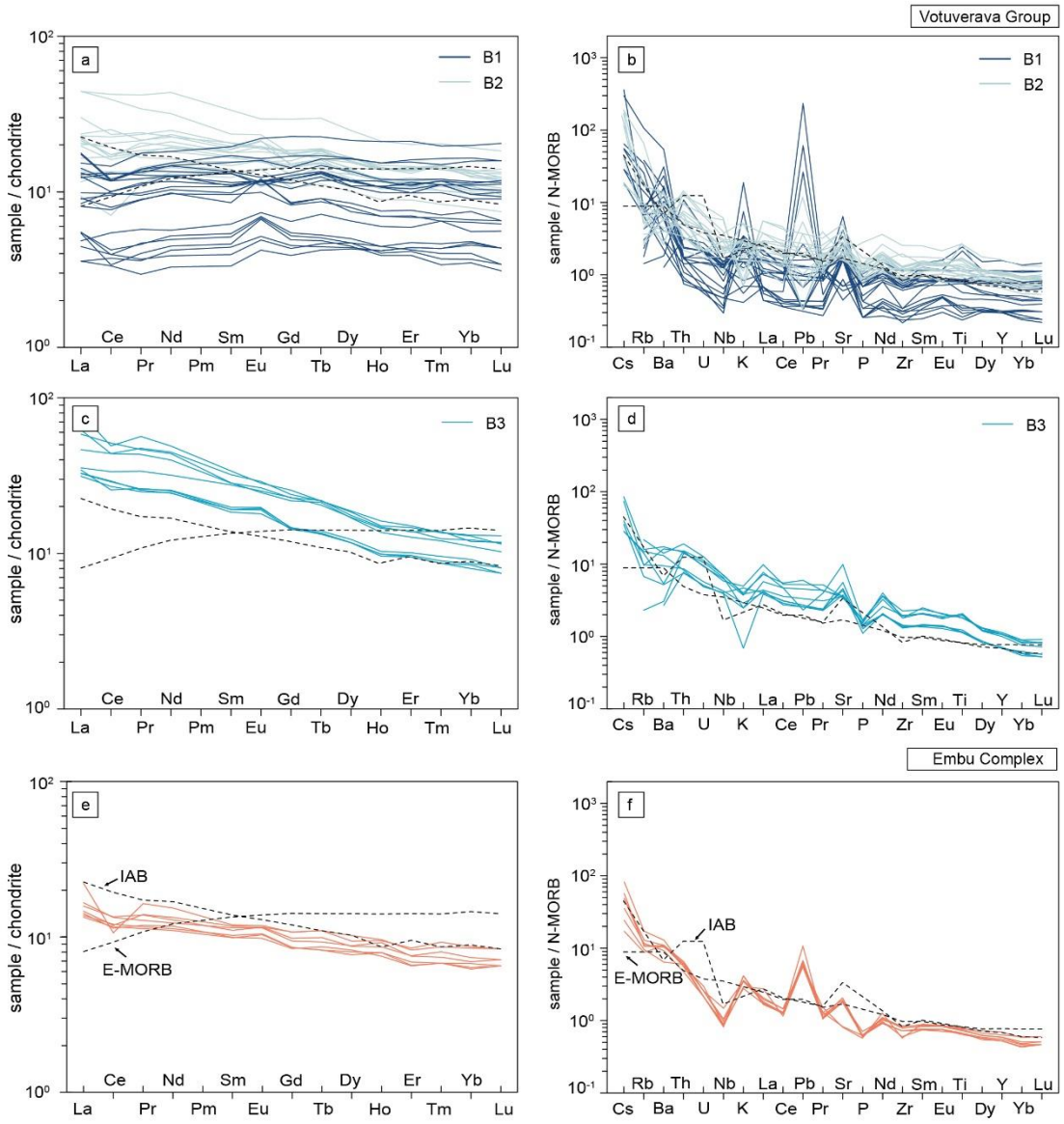

Figure 3.5. Normalised trace element spider diagrams for the mafic rocks from Votuverava Group and Embu Complex. a, c and, e) REE spider diagram with normalised values from chondrite (Boynton, 1984); b, d and, f) incompatible elements spider diagram normalised by the N-MORB (Sun and McDonough, 1989). Values for E-MORB are from Sun and McDonough (1989) and values for island arc basalt (IAB) are from Kelemen et al. (2007).

3.6. Zircon U–Pb–Hf geochronology

Three samples of the Votuverava Group (WSP-04, DC-09A and GI-14) and one sample from the Embu Complex (DC-22D) were selected for zircon U–Pb–Hf geochronology via LASS-ICP-MS. Additionally, sample FM-06 from the Votuverava Group was selected for zircon U–Pb geochronology via SHRIMP. Measured isotopic

ratios and calculated ages are given in Supplementary Material 2 and illustrated CL images are presented in s in Supplementary Material 3, and results presented below.

3.6.1. Votuverava Group

Sample WSP-04 has zircon grains with a xenomorphic habit with compositionally poorly zoned or sector zoned internal textures. Fifty-two zircon grains were analysed with Th/U ratios span 0.10–1.49, suggesting a magmatic origin (Rubatto et al., 2009). Most of the data yield $^{206}Pb/^{238}U$ ages spanning 1200-1300 Ma, and 52 analyses define an upper intercept age of 1267 ± 7 Ma and lower intercept of 506 ± 16 Ma (MSWD = 1.30; Fig. 3.6a). A total of 45 analysis with ± 10 % age discordance have a suprachondritic signature with εHf_T varying from +1.3 to +10.7 and a two-stage T_{DM} Hf model age of ca. 1522 Ma (Fig. 3.6b).

Zircon grains from sample DC-09A are euhedral to subhedral with sizes varying from 50 and 150 µm. Most grains are fractured and present a dark homogeneous luminescence in CL images. Sporadically, diffuse and sector zoning and are also present. Recrystallised rims (lower than 15 µm) are scarce. Th/U ratios varying from 0.64 to 1.61 (Supplementary Material 2), which support a magmatic origin. Twelve analyses define a linear array with an upper intercept age of 1278 ± 8 Ma and lower intercept age of 792 ± 41 Ma (MSWD = 1.40; Fig. 3.6c). Seven zircon Lu-Hf analysis with ± 10 % age discordance define a suprachondritic signature with εHf_T ranging from +2.9 to +12.5 with a two-stage T_{DM} Hf model age of ca. 1438 Ma (Fig. 3.6d).

Sample FM-06 has zircon grains with a subhedral prismatic shape and size ranging from 100 to 200 µm with few presenting internal fractures. Most grains present homogeneous dark luminescence and a secondary group of grains with bright luminescence, sometimes with sector to oscillatory zoning. The measured U concentrations vary from 55 to 829 ppm, Th from 72 to 1218 ppm and Th/U ratios vary from 0.61 to 1.52 (Supplementary Material 2) indicating a magmatic origin. Twenty-one spot analyses were carried out on 20 zircon grains and seven spots yield a concordia age of 1295 ± 3 Ma (MSWD = 1.40; Fig. 3.6e and f).

Zircon grains from sample GI-14 have an elongated prismatic shape with a size ranging from 50 to 150 µm. The Th/U ratios span 0.27–1.57, suggesting a magmatic origin. Two populations of grains are identified based on textures observed in the CL images. The dominant population has homogeneous low luminescence and yields an upper intercept age of 1296 ± 6 Ma and a lower intercept age of 23 ± 32 Ma (MSWD =

2.10, n = 24; Fig. 3.6g). The secondary group has high luminescence and oscillatory zoning (grains 5, 6, 10 and 11) and define a concordia age of 2170 ± 7 Ma (MSWD = 0.03, n = 5; Fig. 3.6g). The Lu-Hf isotopes from both groups are also distinct, in which the youngest and dominant zircon group is mostly suprachondritic with εHf_T varying from -0.3 and +9.5 and two-stage T_{DM} Hf model age of ca. 1540 Ma (n=20), whereas the older zircon grains are dominantly subchondritic with εHf_T varying -7.9 to -11.4 (Fig. 3.6h).

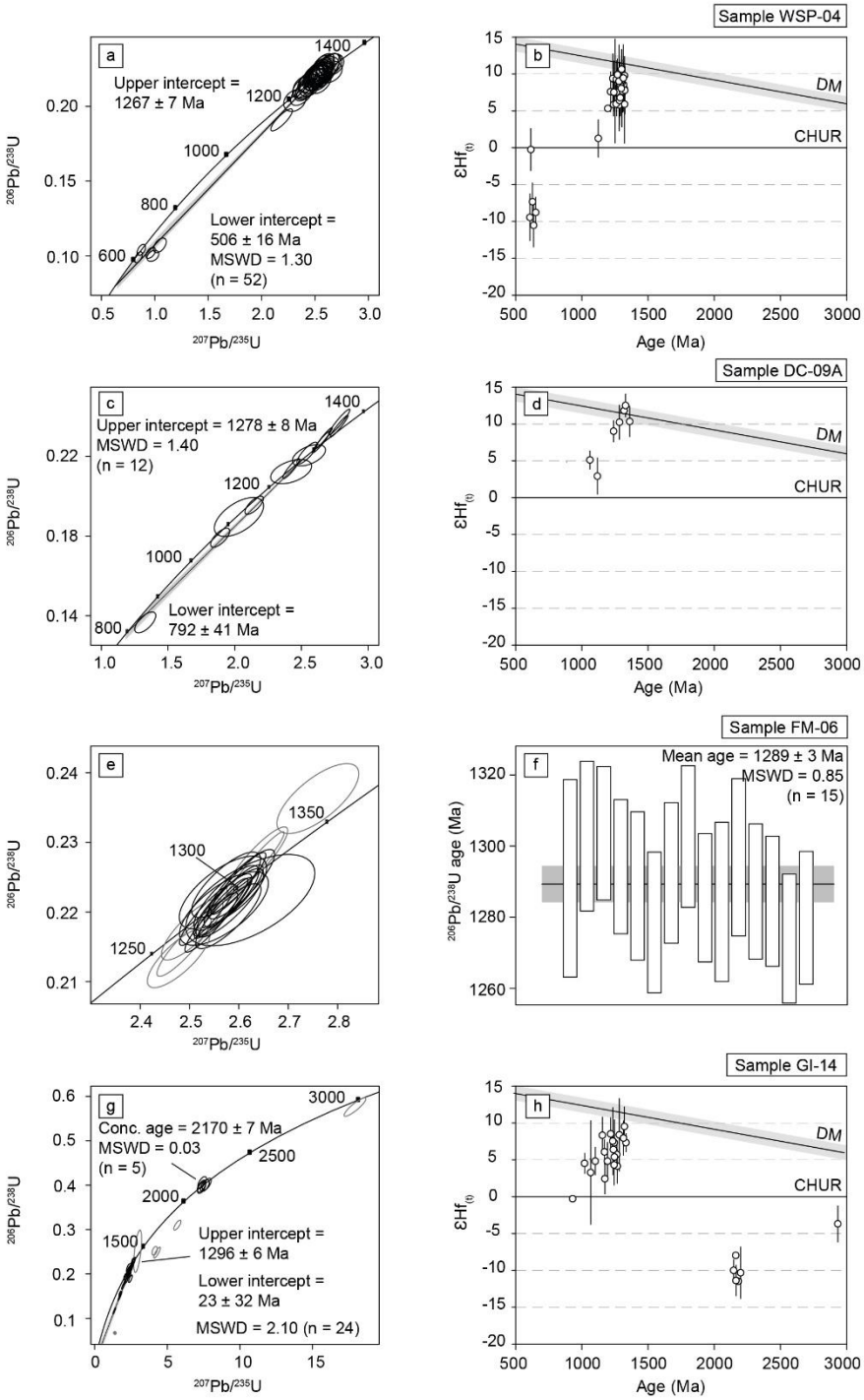

Figure 3.6. U–Pb–Hf data of analysed zircons from mafic samples of the Votuverava Group (Apiaí Terrane). a, c, e, and g) Wetherill diagrams. Data-point error ellipses are 2σ. b, d, f, and h) $\varepsilon Hf_{(t)}$ plotted against zircon single ages for the analysed samples. CHUR = chondrite reservoir, DM = depleted mantle.

3.6.2. Embu Complex

Zircon grains from sample DC-22D are euhedral to subhedral with 90 to 230 µm in length and present some fractures. Most of them show homogeneous dark luminescence with a minor diffusive to sector compositional zoning (Supplementary Material 3). Fifteen spot analyses were carried out from 14 zircon grains. The zircon grains have moderate to high U (145–911 ppm) and Th (167–3330 ppm) contents, and Th/U ratios between 0.81–4.30, indicating a magmatic origin (Supplementary Material 2). All of the analytical spots are over the Concordia, and 13 analyses define a concordia age of 890 ± 2 Ma (MSWD = 0.31; Fig. 3.7a). These zircon grains are dominantly suprachondritic with εHf_T between +4.5 and +17.2 with a two-stage T_{DM} Hf model age of ca. 1185 Ma (Fig. 3.7b).

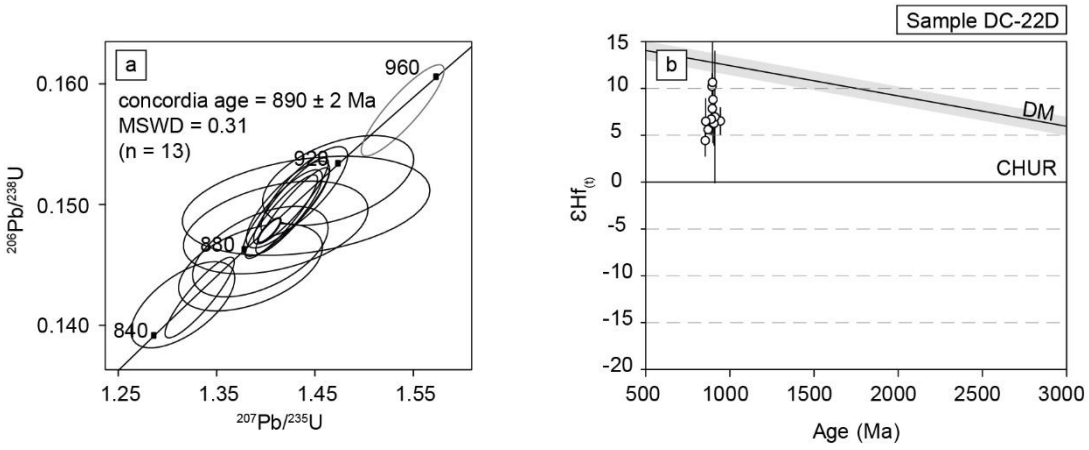

Figure 3.7. a) Wetherill diagrams with zircon U-Pb data from sample DC-22D of the Embu Terrane; b) εHf(t) plotted against zircon single ages for sample DC-22D from the Embu Terrane. CHUR = chondrite reservoir, DM = depleted mantle.

3.7. Whole-rock Sm–Nd

Four mafic rock samples of the Votuverava Group (DC-09A, FM-06, FM-08A, WSP-13) and one sample from the Embu Complex (DC-22D) were selected for whole-rock Sm–Nd analyses. The analytical results are in Supplementary Material 4.

The mafic rock samples of the the Votuverava Group yield a two-stage Nd T_{DM} model ages between ca. 1629 to 1471 Ma with εNd(t) between +2.25 to +4.01 calculated with the zircon U-Pb ages defined in this paper (Fig 3.8). The rock mafic sample of the

Embu Complex (DC-22D) yield a two-stage Nd T_{DM} model age of 1921 Ma and εNd(t) of +0.72 (Fig. 3.8).

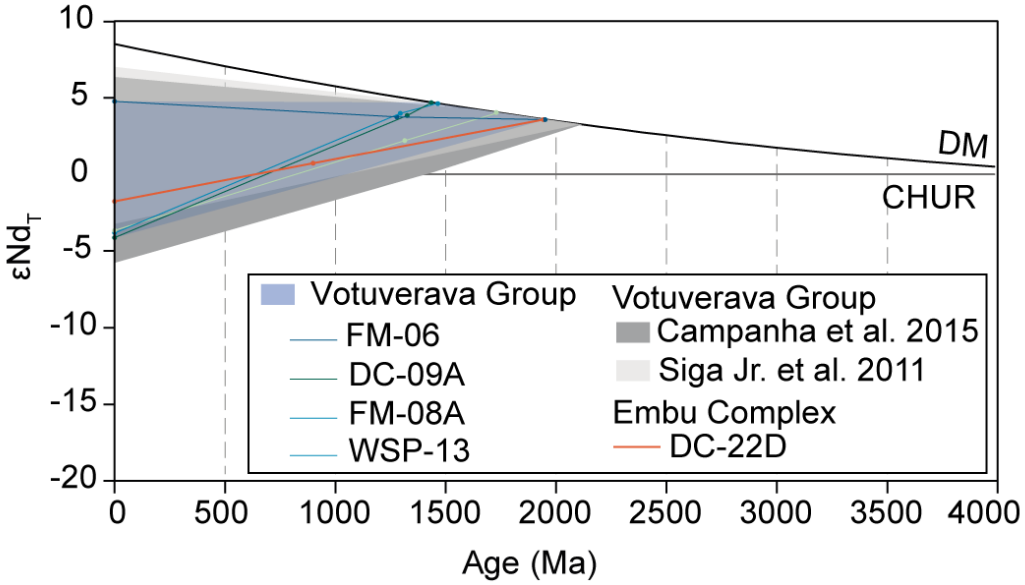

Figure 3.8. Nd isotope evolution diagram for the analysed samples from the Votuverava Group and Embu Complex. CHUR = chondrite reservoir, DM = depleted mantle.

3.8. Discussion

3.8.1. Timing and petrogenesis of the Mesoproterozoic mafic rocks from the Votuverava Group (Apiaí Terrane)

The compilation of new and published igneous zircon U-Pb data from mafic rocks of the Votuverava Group demonstrates the existence of Calymmian (1490-1475 Ma) and Ectasian (1300-1260 Ma) ages. Rhyacian zircon grains from sample GI-14 yielding a concordia age of 2198 ± 16 Ma and dominant subchondritic εHf_T are interpreted as xenocrysts.

The chronology and geochemistry of the Calymmian magmatic event in the Votuverava Group was initially recognized by Campanha et al. (2015) in the Rubuquara Formation (concordia age of 1488 ± 4 Ma, sample GI-7C) and by Siga Jr. et al. (2011) in the Perau Formation (upper intercept ages of 1451 ± 39 Ma and 1479 ± 92 Ma, samples HCM-01 and HCM-16, respectively). These mafic rocks samples from the Perau and Rubuquara formations have a B1-B2 geochemical signature with the direct link between B1-B2 geochemical signature and Calymmian age given by sample GI-7C. For this

reason, we interpret that all the mafic samples presented in the Perau and Rubuquara formations are related to the Calymmian magmatic event. The B1-B2 group is defined by Th/Yb ratios (0.09 to 0.72, average of 0.23) above N-MORB values, low Ta/Yb (0.07 to 0.54, average of 0.11) (Fig. 3.10a), and Nb/La ratios (0.56 to 0.68), low Nb concentration (2.3 to 3.2 ppm), low Zr concentration (60 to 81 ppm) and the negative Nb anomaly. Additionally, these mafic rocks have a $\varepsilon Nd_{(t)}$ of +2.25 to +4.01, two-stage Nd T_{DM} model ages of ca. 1629-1471 Ma presenting a strong negative correlation between Sm–Nd and $\varepsilon Nd_{(t)}$ (Campanha et al., 2015; Siga Júnior et al., 2011b, 2011a), indicating a major contribution of juvenile mantle sources with minor and variable participation of crustal material. These geochemical data are characteristics of convergent tectonic settings, mainly oceanic island arc-related basalts (Fig. 3.10a) (e.g., Xia and Li, 2019; Xia, 2014).

The Ectasian magmatic event has distinct geochemical signatures in different units. All mafic rock samples from the Serra das Andorinhas Formation (Votuverava Group) have a B1-B2 geochemical signature, with the direct link between geochemical signature and Ectasian ages constrained by samples FM-06 and DC-09A. In the two dominant informal units (schist and mica-schist units) as well as in the Nhunguara Formation there is an overlap of B1-B2 geochemical signature with a B3 geochemical signature.

The B3 geochemical signature is marked by higher Th/Yb (0.52 to 0.99, average of 0.65) and Ta/Yb ratios (0.36 to 0.47, average of 0.41) with moderate depletion trend from LREE to HREE compared to the B1-B2 group. These petrogenetic data have affinity with E-MORB basalts. Additionally, zircon Hf and whole-rock Nd isotopes have a dominant suprachondritic signature with a low crustal residence time. In schist and mica-schist units, the direct link between B3 geochemical signature and Ectasian age is constrained by samples GI-14 and WSP-13 (this work), while in the Nhunguara Formation the direct link between B3 geochemical signature and Ectasian age is constrained by sample GD-456 from Campanha et al. (2015). Zircon Hf isotopes from the Ectasian B3 geochemical signature indicate that the mafic rocks are derived from juvenile mantle sources (e.g., sample GI-14 with $\varepsilon Hf_{(t)}$ values of -0.3 to + 9.5). All the other samples present similar zircon suprachondritic Hf isotopic signatures, suggesting that the Ectasian magmatic event has an overall juvenile mantle-derived origin.

3.8.2. Timing and petrogenesis of the Neoproterozoic mafic rocks from the Embu Complex (Embu Terrane)

New zircon U–Pb data from the mafic rocks of the Embu Complex presented in this paper define a crystallization age of 890 ± 2 Ma (Fig. 3.7). This is the first reported age from mafic rocks of the Embu Terrane, being older than the oldest metamorphic grain (850 ± 5 Ma) and younger than the younger detrital grains (974 ± 12 Ma) reported in the Embu Terrane (Campanha et al., 2019; Costa et al., 2017; Duffles et al., 2016; Meira et al., 2015). Thus, the basic magmatic event occurred concomitantly or immediately after the Embu Complex deposition. Although this relationship is still uncertain, it is clear that the basic magmatic event is prior to the Tonian regional metamorphic dated at 810–760 Ma in the Embu Terrane (Cabrita et al., 2021).

Based on the FeO_{total}/MgO versus SiO_2 diagram, the mafic rock samples of the Embu Complex have a tholeiitic signature (Fig. 3.4c). The Th/Yb versus Ta/Yb diagram allows the distinction between continental intraplate and arc-related settings (Ducea et al., 2015; Wilson, 2007; Xia and Li, 2019), with all the mafic rock samples of the Embu Complex having affinity with ocean island arc-related basalts (Fig. 3.10a). Furthermore, the Ti/V ratio indicates the degree of partial melting and fractional crystallisation of the magma (Shervais, 1982). The mafic rock samples of the Embu Complex present a Ti/V ratio of ~ 22 indicating affinity with arc-related to mid-ocean ridges melts (Fig. 3.10b). Although almost all the samples from Embu are plotted inside the mid-ocean ridges melts field, the TiO_2 content is consistent with island arc settings.

Likewise, the Nb and Zr are incompatible during melting but conservative during subduction and are usually low in arc-related basalts (Pearce, 1996). The arc-related basalts have an Nb and Zr content lower than 8 and 130 ppm, respectively. Also, the Zr/Y and Nb/La ratios lower than 3.3 and 0.9, respectively, are also common in the arc-related basalts (Xia and Li, 2019; Xia, 2014). The low Nb and Zr content (1.9 to 3.4 and 42 to 62 ppm, respectively) and low Nb/La and the Zr/Y ratios (0.3 to 0.7 and 2.2 to 3.8, respectively) on the Embu Complex samples suggest arc-related affinity. Moreover, the low enrichment in LREE and the negative Nb anomaly from the mafic samples of the Embu Complex indicate arc affinity (Pearce, 2008). Considering the spectrum of geochemical data, we interpret the mafic rock samples of the Embu Complex to be related to subduction-related convergent settings. Like the Votuverava Group, the suprachondritic zircon εHf_T between +4.5 and +17.2 and whole-rock $\varepsilon Nd_{(t)}$ value of 0.73 from the mafic rocks of the Embu Terrane indicate a mantle-derived juvenile source.

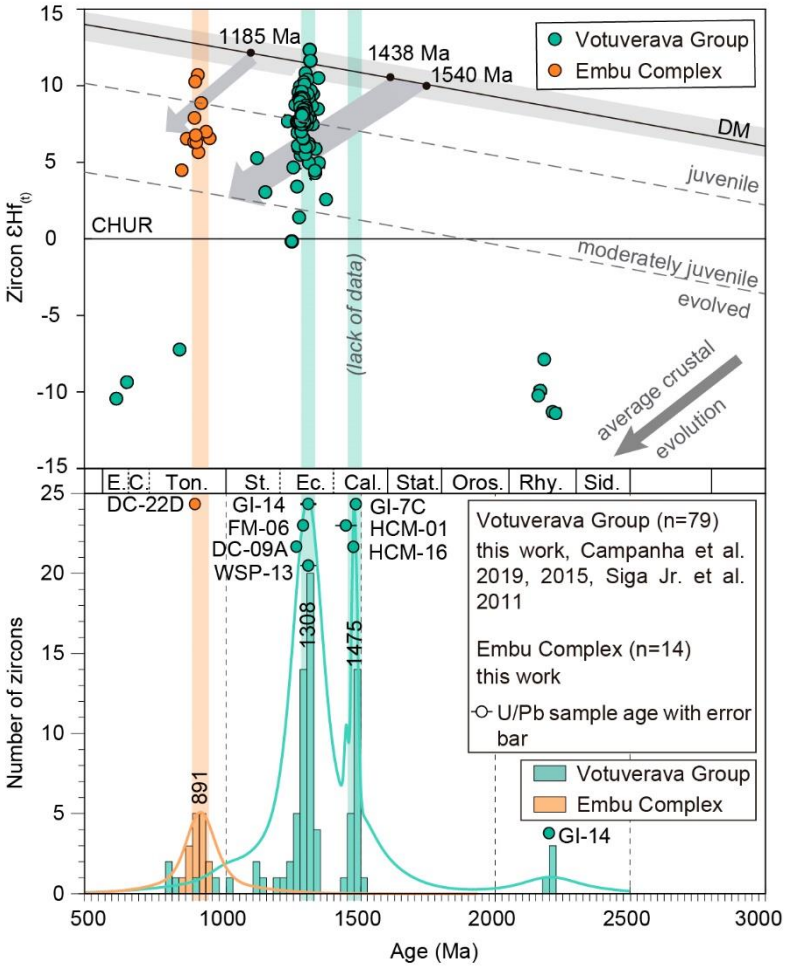

Figure 3.9. Histogram with probability density curves for zircon ages from studied samples of the Apiaí and Embu Terranes. Bins = 25 Ma. Samples from Votuverava Group: this work (samples GI-14, FM-06 and DC-09A), (Campanha et al., 2019): sample WSP-13, Campanha et al. (2015): sample GI-7C, Siga Júnior et al. (2011): samples HCM-01 and HCM-16.

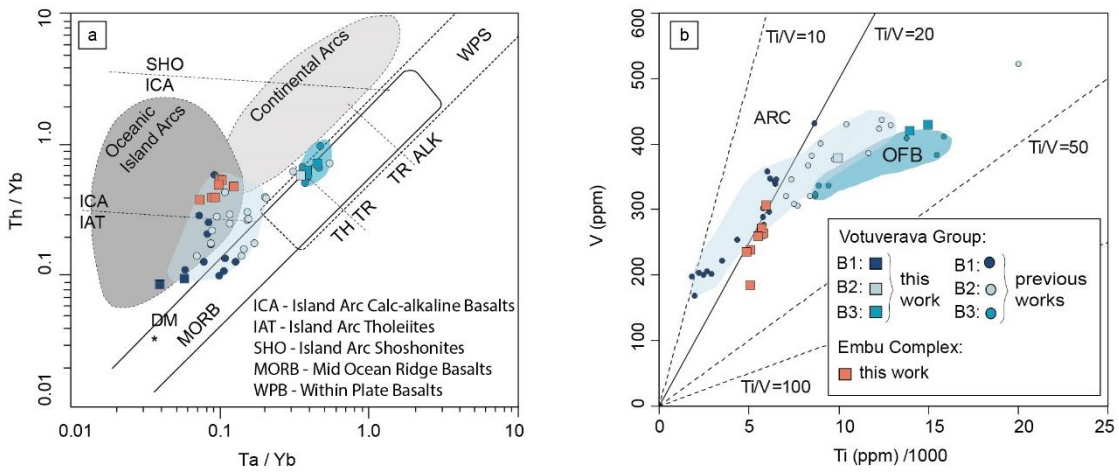

Figure 3.10. Geotectonic discriminant diagrams for the mafic rocks from the Embu Complex. and Votuverava Group. a) Th / Yb – Nb / Yb diagram, (Pearce, 2008); b) V versus Ti /1000 diagram, (Shervais, 1982). Abbreviations: TH - Tholeiitic series; TR = Transitional series; ALK = Alkaline series; ICA = Island Arc Calc-alkaline Basalts; IAT = Island Arc Tholeiites; SHO = Island Arc Shoshonites; MORB = Mid Ocean Ridge Basalts; WPB = Within Plate Basalts; CAB = calc-alkaline basalts; BABB = back-arc basin basalts; AB = alkali basalts; ARC = arc basalts; OFB = ocean floor basalts.

3.8.3. Implications for the Meso- to Neoproterozoic tectonic evolution

Magmatic activity is widespread in the Ribeira Belt, representing different tectonic stages of the belt (Janasi et al., 2016a, 2016b). In this paper, we highlighted that the mafic rocks from the southern Ribeira Belt record multiple periods of accretion and convergence settings from the Meso- to early Neoproterozoic, being a key area to investigate the transition between Rodinia and West Gondwana assembly.

The two oldest magmatic events are recorded in the Votuverava Group. The Calymmian (ca. 1490-1475 Ma) is recorded in the mafic rock units hosted in schist and mica-schist units, and the Ectasian (ca. 1300-1260 Ma) mafic rock units hosted in the Serra das Andorinhas Formation. The Calymmian magmatic event was inferred as related to magmatic activity in a back-arc basin environment of an accretionary orogen (Campanha et al., 2015, 2019). However, the new geochemical and isotopic data presented here demonstrate that Calymmian and Ectasian magmatic episodes are consistent with arc-related magmatism, highlighting the distinction between those units and supporting the model of two distinct episodes of arc-related magmatism related to the accretion of two distinct basins within the Votuverava Group, linked to the accretion and convergence processes that built Rodinia. In addition, tholeiitic MORB-like magmatism

between ca. 1000–880 Ma and related to the initial break-up of Rodinia passive margin and the formation of the Brasiliano oceans is described in Lajeado (Apiaí Gabbro) and Itaiacoca groups (Campanha et al., 2016; Siga Júnior et al., 2009). Orthogneiss dated at ca. 810–780 Ma and of unknown tectonic setting occur between Apiaí and Embu terranes (Serra dos Lopes orthogneiss, Leite, 2003) and within the Embu Terrane (Cordani et al., 2002; Vlach, 2008).

A convergent setting is also recorded in the mafic rocks of the Embu Complex during the Tonian period, with geochemical data highlighting arc relate affinity. In this period, the metasedimentary rocks of the southern portion of this terrane were deposited between 970–850 Ma (Campanha et al., 2019) and metamorphosed at ca. 810–760 Ma (Cabrita et al., 2021). Record of igneous activity coeval with the Tonian metamorphic event is recorded by orthogneiss outcrops derived from a granodioritic to tonalitic protolith with igneous crystallisation ages ranging from 810 to 780 Ma (Cordani et al., 2002; Silva, 2017). Further evidence of Tonian felsic magmatism is also recorded in a two-mica granite (Juquiá granite) with a crystallisation age of 799 ± 5 Ma (Passarelli et al., 2019), a meta-aplite with a crystallisation age of 783 ± 6 Ma, and a metagranite with a crystallisation age of 768 ± 8 Ma (Meira et al., 2015). This Tonian magmatism is interpreted to be related to convergent settings related to the West Gondwana assembly (Cordani et al., 2002; Passarelli et al., 2019; Silva, 2017).

Arc-related magmatic activity from the Tonian to Ediacaran periods is also described in other units of the Ribeira Belt. In the northern Ribeira Belt, the Serra da Prata, Rio Negro, and Rio Doce magmatic arcs are evidence of a complex evolution of a subduction zone system (Corrales et al., 2020; Heilbron et al., 2020; Peixoto et al., 2017). In the central Ribeira Belt, the Barreiro Suite represents a late Tonian tholeiitic intraplate magmatic event at ca. 766 Ma (Heilbron et al., 2019). Late Tonian within-plate tholeiitic to alkaline mafic magmatism is also described in the Costeiro Complex (Meira et al., 2019b).

In addition, evidences of oceanic crust during Ediacaran period (Tassinari et al., 2001) and high-pressure and low-pressure paired belt metamorphism (Faleiros et al., 2011a; Ricardo et al., 2020) are described in the Ribeira Belt as well as in other parts of the Mantiqueira Province (Amaral et al., 2020; Arena et al., 2017; Hartmann et al., 2019; Werle et al., 2020). This scenario is consistent with a period of accretion and convergence settings from the Mesoproterozoic to Neoproterozoic related to subduction processes in the Southern Ribeira Belt.

3.9. Conclusions

The mafic rocks from the southern Ribeira Belt record multiple periods of accretion and convergence settings from the Meso- to early Neoproterozoic, being a key area to investigate the transition between Rodinia and West Gondwana assembly. The data in this contribution expose the existence of three distinct periods of accretion and convergence processes from the Meso- to Neoproterozoic in the southern Ribeira Belt, related to the Rodinia and West Gondwana assembly.

The mafic rocks from the Votuverava Group define the oldest magmatism at Calymmian (1490-1475 Ma) and Ectasian (1300-1260 Ma) with juvenile characteristics indicated by Th / Yb ratios above N-MORB, low Ta / Yb and Nb / La ratios, low Nb and Zr concentrations, negative Nb anomaly, $\varepsilon Nd_{(t)}$ of +2.25 to +4.01 an Nd T_{DM} model age between 1629-1471 Ma, which are characteristics of juvenile mantle source arc-related magmatism related to convergent tectonic settings.

The third event occurred in the early Tonian (900 Ma) and is recorded in the mafic rocks from the Embu Complex. Geochemical data indicate that the mafic rocks belong to the tholeiitic series with low LREE enrichments, negative Nb anomaly, low Nb and Zr contents and low Nb / La and Zr /Y ratios, consistent with arc-related basalts. Whole-rock Sm–Nd isotopic data yield εNd_T of 0.72 and Nd T_{DM} two-stage model age of 1921 Ma, with Hf isotopes indicating juvenile mantle sources to the mafic magmatism with εHf_T between + 4.5 and + 17.2. Therefore, mafic rocks from the southern Ribeira Belt record multiple periods of accretion and convergence settings associated with the assembly of Rodinia and West Gondwana.

Acknowledgments

Financial support was provided by grants 2019/10457-4, 2015/26645-3 and 2015/04487-7, São Paulo Research Foundation (FAPESP). FMF and GACC thank the research productivity grants 307732/2019-3 and 305701/2019-3, National Council of Technological and Scientific Development (CNPq). BVR and PAC acknowledge financial support from the Australian Research Council (grant FL160100168).

3.10. References

Aleinikoff, J.N., Schenck, W.S., Plank, M.O., Srogi, L.A., Fanning, C.M., Kamo, S.L., Bosbyshell, H., 2006. Deciphering igneous and metamorphic events in high-grade

rocks of the Wilmington complex, Delaware: Morphology, cathodoluminescence and backscattered electron zoning, and SHRIMP U-Pb geochronology of zircon and monazite. Bulletin of the Geological Society of America 118, 39–64. https://doi.org/10.1130/B25659.1

Alkmim, F.F., Marshak, S., Pedrosa-Soares, A.C., Peres, G.G., Cruz, S.C.P., Whittington, A., 2006. Kinematic evolution of the Araçuaí-West Congo orogen in Brazil and Africa: Nutcracker tectonics during the Neoproterozoic assembly of Gondwana. Precambrian Research 149, 43–64. https://doi.org/10.1016/j.precamres.2006.06.007

Almeida, F.F.M. De, Hasui, Y., Brito Neves, B.B. De, Fuck, R.A., 1981. Brazilian structural provinces: An introduction. Earth-Science Reviews 17, 1–29. https://doi.org/10.1016/0012-8252(81)90003-9

Almeida, F.F.M., Amaral, G., Cordani, U.G., Kawashita, K., 1973. The Precambrian Evolution of the South American Cratonic Margin South of the Amazon River. The South Atlantic 1, 411–446. https://doi.org/10.1007/978-1-4684-3030-1_11

Almeida, F.F.M., Hasui, Y., 1984. O pré-cambriano do Brasil. Edgard Blucher.

Alsop, G.I., Holdsworth, R.E., 2004. Shear zones — an introduction and overview. Geological Society, London, Special Publications 224, 1 LP – 9. https://doi.org/10.1144/GSL.SP.2004.224.01.01

Alves, A., Janasi, V. de A., Campos Neto, M. da C., 2016. Sources of granite magmatism in the Embu Terrane (Ribeira Belt, Brazil): Neoproterozoic crust recycling constrained by elemental and isotope (Sr-Nd-Pb) geochemistry. Journal of South American Earth Sciences 68, 205–223. https://doi.org/10.1016/j.jsames.2015.10.014

Alves, A., Janasi, V. de A., Campos Neto, M. da C., Heaman, L., Simonetti, A., 2013. U-Pb geochronology of the granite magmatism in the embu terrane: Implications for the evolution of the central ribeira belt, SE Brazil. Precambrian Research 230, 1–12. https://doi.org/10.1016/j.precamres.2013.01.018

Amaral, L., Caxito, F. de A., Pedrosa-Soares, A.C., Queiroga, G., Babinski, M., Trindade, R., Lana, C., Chemale, F., 2020. The Ribeirão da Folha ophiolite-bearing accretionary wedge (Araçuaí orogen, SE Brazil): New data for Cryogenian

plagiogranite and metasedimentary rocks. Precambrian Research 336, 105522. https://doi.org/10.1016/j.precamres.2019.105522

Arena, K.R., Hartmann, L.A., Lana, C., 2017. Tonian emplacement of ophiolites in the southern Brasiliano Orogen delimited by U-Pb-Hf isotopes of zircon from metasomatites. Gondwana Research 49, 296–332. https://doi.org/10.1016/j.gr.2017.05.018

Babinski, M., Tassinari, C.C.G., Nutman, A.P., Sato, K., Pimentel, M.M., Iyer, S.S., 2001. U/Pb shrimp zircon ages of migmatites from the basement of the Embu Complex, Ribeira Fold Belt, Brazil: indications for ~1.4-1.3 Ga Pb-Pb and Rb-Sr "isochron" ages of no geological meaning. III South American Symposium on Isotope Geology. Pucón.

Bartoli, O., 2017. Phase equilibria modelling of residual migmatites and granulites: An evaluation of the melt-reintegration approach. Journal of Metamorphic Geology 35, 919–942. https://doi.org/10.1111/jmg.12261

Basei, M.A.S., Frimmel, H.E., Nutman, A.P., Preciozzi, F., 2008. West Gondwana amalgamation based on detrital zircon ages from Neoproterozoic Ribeira and Dom Feliciano belts of South America and comparison with coeval sequences from SW Africa. Geological Society, London, Special Publications 294, 239–256.

Basei, M.A.S., Siga, O., Machiavelli, A., Mancini, F., 1992. Evolução tectônica dos terrenos entre os cinturões ribeira e dom feliciano (PR-SC). Revista Brasileira de Geociências 22, 216–221.

Bell, E.A., Boehnke, P., Barboni, M., Harrison, T.M., 2019. Tracking chemical alteration in magmatic zircon using rare earth element abundances. Chemical Geology 510, 56–71. https://doi.org/10.1016/j.chemgeo.2019.02.027

Black, L.P., Gulson, B.L., 1978. The age of the Mud Tank carbonatite, Strangways Range, Northern Territory. BMR J. Austral. Geol. Geophy. 3, 227–232. https://doi.org/10.1016/j.apenergy.2015.11.040

Black, L.P., Kamo, S.L., Allen, C.M., Aleinikoff, J.N., Davis, D.W., Korsch, R.J., Foudoulis, C., 2003. TEMORA 1: a new zircon standard for Phanerozoic U-Pb geochronology. Chemical Geology 155–170.

Bose, S., Ghosh, G., Kawaguchi, K., Das, K., Mondal, A.K., Banerjee, A., 2021. Zircon and monazite geochronology from the Rengali-Eastern Ghats Province: Implications for the tectonic evolution of the eastern Indian terrane. Precambrian Research 355, 106080. https://doi.org/10.1016/j.precamres.2020.106080

Boynton, W. V., 1984. Cosmochemistry of the rare earth elements: meteorite studies. Rare Earth Element Geochemistry. Elsevier B.V., 63–114. https://doi.org/10.1016/b978-0-444-42148-7.50008-3

Brito Neves, B.B., Campos Neto, M.D.C., Fuck, R.A., 1999. From Rodinia to Western Gondwana: An approach to the Brasiliano-Pan African cycle and orogenic collage. Episodes 22, 155–166. https://doi.org/10.18814/epiiugs/1999/v22i3/002

Brito Neves, B.B. de, Fuck, R.A., 2013. Neoproterozoic evolution of the basement of the South-American platform. Journal of South American Earth Sciences 47, 72–89. https://doi.org/10.1016/j.jsames.2013.04.005

Brito Neves, B.B. de, Fuck, R.A., Campanha, G.A. da C., 2021. Basement inliers of the Brasiliano structural provinces of South America. Journal of South American Earth Sciences 110, 103392. https://doi.org/10.1016/j.jsames.2021.103392

Brito Neves, B.B. de, Fuck, R.A., Pimentel, M.M., 2014. The Brasiliano collage in South America: a review. Brazilian Journal of Geology 44, 493–518. https://doi.org/10.5327/Z2317-4889201400030010

Brown, M., 2009. Metamorphic patterns in orogenic systems and the geological record. Geological Society, London, Special Publications 318, 37 LP – 74. https://doi.org/10.1144/SP318.2

Cabrita, D., Salamuni, E., Lagoeiro, L., 2017. Fabric evolution of polydeformed orthogneisses and quartzites along the Curitiba Shear Zone, Curitiba Domain, Southern Brazil. Journal of South American Earth Sciences 77. https://doi.org/10.1016/j.jsames.2017.05.010

Cabrita, D.I.G., Faleiros, F.M., Cawood, P.A., Campanha, G.A.C., Yogi, M.T.A.G., Wainwright, A.N., Raveggi, M., Almeida, V. V., 2021. Petrochronological constraints and tectonic implications of Tonian metamorphism in the Embu Complex, Ribeira Belt, Brazil. Precambrian Research 363.

https://doi.org/10.1016/j.precamres.2021.106315

Caltabellota, F.P., Lopes, A.P., Brumatti, M., Rodrigues da Silva, A.D., Lima, R.A.P., Severino, R.R., Andrade, J.J.C., Palmeira, L.C.M., Mapa, F.B., Marque, I.P., Turra, B.B., Costa, V.S., Campos, F.F., Ferrari, V.C., Mendes, D., 2017. Mapa Geológico de Integração do ARIM Vale do Ribeira (SP e PR). Escala 1:250.000.

Campanha, G.A. da C., 2002. O Papel do Sistema de Zonas de Cisalhamento Transcorrentes na Configuração da Porção Meridional da Faixa Ribeira. Lecturer Thesis, University of São Paulo.

Campanha, G.A. da C., 1991. Tectônica Proterozóica no Alto e Médio Vale do Ribeira, estados de São Paulo e Paraná. Doctoral Thesis. University of São Paulo.

Campanha, G.A. da C., Brito Neves, B.B., 2004. Frontal and oblique tectonics in the Brazilian Shield. Episodes 27, 255–259. https://doi.org/10.1016/S1342-937X(05)70391-9

Campanha, G.A. da C., Faleiros, F.M., Basei, M.A.S., Tassinari, C.C.G., Nutman, A., Vasconcelos, P., 2015. Geochemistry and age of mafic rocks from the Votuverava Group, southern Ribeira Belt, Brazil: Evidence for 1490Ma oceanic back-arc magmatism. Precambrian Research 266, 530–550. https://doi.org/10.1016/j.precamres.2015.05.026

Campanha, G.A. da C., Sadowski, G.R., 2002. Determinações da deformação finita em rochas metassedimentares da faixa ribeira na região de Iporanga e Apiaí, SP. Revista Brasileira de Geociências 32, 107–118.

Campanha, G.A. da C., Sadowski, G.R., 1999. Tectonics of the southern portion of the Ribeira Belt (Apiai Domain). Precambrian Research 98, 31–51. https://doi.org/10.1016/S0301-9268(99)00027-3

Campanha, G.A.C., Basei, M.S., Faleiros, F.M., Nutman, A.P., 2016. The Mesoproterozoic to early Neoproterozoic passive margin Lajeado Group and Apiaí Gabbro, Southeastern Brazil. Geoscience Frontiers 7, 683–694. https://doi.org/10.1016/j.gsf.2015.08.004

Campanha, G.A.C., Faleiros, F.M., Cawood, P.A., Cabrita, D.I.G., Ribeiro, B. V, Basei,

M.A.S., 2019. The Tonian Embu Complex in the Ribeira Belt (Brazil): revision , depositional age and setting in Rodinia and West Gondwana. Precambrian Research 320, 31–45. https://doi.org/10.1016/j.precamres.2018.10.010

Campanha, G.A.C., Gimenez Filho, A., Caetano, S.L.V., Pires, F.A., Dantas, A.S.L., Teixeira, A.L., Dehira, L.K., 1986. Geologia e estratigrafia da região das folhas Iporanga e Gruta do Diabo, Vale do Ribeira, São Paulo. Congresso Brasileiro de Geologia. Sociedade Brasileira de Geologia, Goiânia, 1058–1073.

Campos Neto, M. da C., Figueiredo, M.C.., 1995. The Rio Doce Orogeny, Southeastern Brazil. Journal of South American Earth Sciences 8, 143–162. https://doi.org/10.1016/0895-9811(95)00002-W

Campos Neto, M.D.C., 2000. Orogenic systems from Southwestern Gondwana: an approach to Brasiliano Pan African cycle and orogenic collage in Southeastern Brazil. Tectonic Evolution of South America. Rio de Janeiro, 335–365.

Cavalcante, C., Lagoeiro, L., Fossen, H., Egydio-Silva, M., Morales, L.F.G., Ferreira, F., Conte, T., 2018. Temperature constraints on microfabric patterns in quartzofeldsphatic mylonites, Ribeira belt (SE Brazil). Journal of Structural Geology 115, 243–262. https://doi.org/10.1016/j.jsg.2018.07.013

Cawood, P.A., Hawkesworth, C.J., Dhuime, B., 2012. Detrital zircon record and tectonic setting. Geology 40, 875–878. https://doi.org/10.1130/G32945.1

Cawood, P.A., Strachan, R.A., Pisarevsky, S.A., Gladkochub, D.P., Murphy, J.B., 2016. Linking collisional and accretionary orogens during Rodinia assembly and breakup: Implications for models of supercontinent cycles. Earth and Planetary Science Letters 449, 118–126. https://doi.org/10.1016/j.epsl.2016.05.049

Caxito, F.A., Heilbron, M., Valeriano, C.M., Bruno, H., Pedrosa-Soares, A., Alkmim, F.F., Chemale, F., Hartmann, L.A., Dantas, E., Basei, M.A.S., 2021. Integration of elemental and isotope data supports a neoproterozoic adamastor ocean realm. Geochemical Perspectives Letters 17, 6–10. https://doi.org/10.7185/GEOCHEMLET.2106

Ceccato, A., Pennacchioni, G., Menegon, L., Bestmann, M., 2017. Crystallographic control and texture inheritance during mylonitization of coarse grained quartz veins.

Lithos 290–291, 210–227. https://doi.org/10.1016/j.lithos.2017.08.005

Cerva-Alves, T., Hartmann, L.A., Remus, M. V.D., Lana, C., 2020. Integrated ophiolite and arc evolution, southern Brasiliano Orogen. Precambrian Research 341, 105648. https://doi.org/10.1016/j.precamres.2020.105648

Chetty, T.R.K., 2017. Chapter 1 - Orogens. In: Proterozoic Orogens of India: A Critical Window to Gondwana. Elsevier, 1–34. https://doi.org/https://doi.org/10.1016/B978-0-12-804441-4.00001-8

Chu, N.C., Taylor, R.N., Chavagnac, V., Nesbitt, R.W., Boella, R.M., Milton, J.A., German, C.R., Bayon, G., Burton, K., 2002. Hf isotope ratio analysis using multi-collector inductively coupled plasma mass spectrometry: An evaluation of isobaric interference corrections. Journal of Analytical Atomic Spectrometry 17, 1567–1574. https://doi.org/10.1039/b206707b

Condie, K.C., 2003. Supercontinents, superplumes and continental growth: The Neoproterozoic record. Geological Society Special Publication 206, 1–21. https://doi.org/10.1144/GSL.SP.2003.206.01.02

Connolly, J.A.D., 2005. Computation of phase equilibria by linear programming: A tool for geodynamic modeling and its application to subduction zone decarbonation. Earth and Planetary Science Letters 236, 524–541. https://doi.org/10.1016/j.epsl.2005.04.033

Conte, T., Cavalcante, C., Lagoeiro, L.E., Fossen, H., Silveira, C.S., 2020. Quartz textural analysis from an anastomosing shear zone system: Implications for the tectonic evolution of the Ribeira belt, Brazil. Journal of South American Earth Sciences 103, 102750. https://doi.org/10.1016/j.jsames.2020.102750

Cordani, U.G., Coutinho, J.M. V, Nutman, A.P., 2002. Geochronological constraints on the evolution of the Embu Complex São Paulo, Brazil. Journal of South American Earth Sciences 14, 903–910. https://doi.org/10.1016/S0895-9811(01)00083-9

Corrales, F.F.P., Dussin, I.A., Heilbron, M., Bruno, H., Bersan, S., Valeriano, C.M., Pedrosa-Soares, A.C., Tedeschi, M., 2020. Coeval high Ba-Sr arc-related and OIB Neoproterozoic rocks linking pre-collisional magmatism of the Ribeira and Araçuaí orogenic belts, SE-Brazil. Precambrian Research 337, 105476.

https://doi.org/10.1016/j.precamres.2019.105476

Costa, R.V. da, Johannes Trouw, R.A., Marimon, R.S., Nepomuceno, F., Mendes, J.C., Dantas, E., 2020. São Bento do Sapucaí Shear Zone: Constraining age and P-T conditions of a collisional Neoproterozoic oblique shear zone, Ribeira Orogen, Brazil. Journal of South American Earth Sciences 98, 102418. https://doi.org/10.1016/j.jsames.2019.102418

Costa, R.V., Trouw, R.A.J., Mendes, J.C., Geraldes, M., Tavora, A., Nepomuceno, F., de Araújo Junior, E.B., 2017. Proterozoic evolution of part of the Embu Complex , eastern S a state , SE Brazil. Journal of South American Earth Sciences 79, 170–188. https://doi.org/10.1016/j.jsames.2017.08.003

Cota de Freitas, N., Almeida, J., Heilbron, M., Cutts, K., Dussin, I., 2021. The Cabo Frio Thrust: A folded suture zone, Ribeira belt, SE Brazil. Journal of Structural Geology 149, 104379. https://doi.org/https://doi.org/10.1016/j.jsg.2021.104379

Cury, L.F., Kaulfuss, G.A., Siga Júnior, O., Basei, M.A.S., Harara, O.M., Sato, K., 2002. Idades U-Pb (Zircões) de 1.75 Ga em granitóides alcalinos deformados dos núcleos Betara e Tigre: evidências de regimes extensionais do estateriano na Faixa Apiaí. Geologia USP - Serie Cientifica 2, 95–108. https://doi.org/10.5327/S1519-874X2002000100009

Da Silva, L.C., McNaughton, N.J., Armstrong, R., Hartmann, L.A., Fletcher, I.R., 2005. The neoproterozoic Mantiqueira Province and its African connections: A zircon-based U-Pb geochronologic subdivision for the Brasiliano/Pan-African systems of orogens. Precambrian Research 136, 203–240. https://doi.org/10.1016/j.precamres.2004.10.004

Deer, W.A., Howie, R.A., Zussman, J., 2013. An introduction to the rock-forming minerals, Mineralogical Society of Great Britain and Ireland

Depaolo, D.J., 1981. Neodymium isotopes in the Colorado Front Range and crust-mantle evolution in the Proterozoic. Nature 291, 193–196. https://doi.org/10.1038/291193a0

Ducea, M.N., Saleeby, J.B., Bergantz, G., 2015. The architecture, chemistry, and evolution of continental magmatic arcs. Annual Review of Earth and Planetary

Sciences 43, 299–331. https://doi.org/10.1146/annurev-earth-060614-105049

Duffles, P., Trouw, R.A.J., Mendes, J.C., Gerdes, A., Vinagre, R., 2016. U-Pb age of detrital zircon from the Embu sequence, Ribeira belt, Se Brazil. Precambrian Research 278, 69–86. https://doi.org/10.1016/j.precamres.2016.03.007

Egydio-Silva, M., Vauchez, A., Bascou, J., Hippertt, J., 2002. High-temperature deformation in the Neoproterozoic transpressional Ribeira belt, southeast Brazil. Tectonophysics 352, 203–224. https://doi.org/10.1016/S0040-1951(02)00197-X

Faleiros, F.M., 2008. Evolução de Terrenos Tectono-Metamórficos da Serrania do Ribeira e Planalto Alto Turvo (SP, PR). Doctoral Thesis, University of São Paulo.

Faleiros, F.M., Campanha, G.A. da C., Bello, R.M. da S., Fuzikawa, K., 2010. Quartz recrystallization regimes, c-axis texture transitions and fluid inclusion reequilibration in a prograde greenschist to amphibolite facies mylonite zone (Ribeira Shear Zone, SE Brazil). Tectonophysics 485, 193–214. https://doi.org/10.1016/j.tecto.2009.12.014

Faleiros, F.M., Campanha, G.A. da C., Martins, L., Vlach, S., Vasconcelos, P.M., 2011a. Ediacaran high-pressure collision metamorphism and tectonics of the southern Ribeira Belt (SE Brazil): Evidence for terrane accretion and dispersion during Gondwana assembly. Precambrian Research 189, 263–291. https://doi.org/10.1016/j.precamres.2011.07.013

Faleiros, F.M., Campanha, G.A.C., Pavan, M., Almeida, V. V., Rodrigues, S.W.O., Araújo, B.P., 2016. Short-lived polyphase deformation during crustal thickening and exhumation of a collisional orogen (Ribeira Belt, Brazil). Journal of Structural Geology 93, 106–130. https://doi.org/10.1016/j.jsg.2016.10.006

Faleiros, F.M., Ferrari, V.C., Costa, V.S., Da Cruz Campanha, G.A., 2011b. Geochemistry and Petrogenesis of Metabasites from the Votuverava Group (Apiaí Terrane, Southern Ribeira Belt): Evidence of a Calymmian Back-arc Basin. Geologia USP - Serie Cientifica 11, 135–155. https://doi.org/10.5327/Z1519-874X2011000200008

Faleiros, F.M., Morais, S.M., Costa, V.S., 2012. Geologia e recursos minerais da folha Apiaí SG.22-X-B-V: escala 1:100.000: estados de São Paulo e Paraná. CPRM,

Programa de Levantamentos Geológicos Básicos do Brasil.

Faleiros, F.M., Ribeiro, B. V, Campanha, G.A.C., Cawood, P.A., Cabrita, D.I.G., Yogi, M.T.A.G., Milani, L.A., Lemos-Santos, D. V, Almeida, V. V, Rodrigues, S.W.O., Malta, I.S., Forero-Ortega, A.J., 2022. Strain Partitioning along Terrane Bounding and Intraterrane Shear Zones: Constraints from a Long-Lived Transpressional System in West Gondwana (Ribeira Belt, Brazil). Lithosphere 2021, 2103213. https://doi.org/10.2113/2022/2103213

Fassbinder, E., 1990. Análise estrutural da Falha Lancinha, Estado do Paraná. Master Thesis, University of São Paulo.

Fernandes, A.J., 1991. O Complexo Embu no Leste do Estado de São Paulo: Contribuição ao Conhecimento da Litoestratigrafia e da Evolução Estrutural e Metamórfica. Universidade de São Paulo. Master Thesis, University of São Paulo.

Forero-Ortega, A.J., Campanha, G.A.C., Faleiros, F.M., Yogi, M.T.A.G., 2020. Pure shear-dominated transpression and vertical extrusion in a strike-slip fault splay from the Itapirapuã Shear Zone, Ribeira Belt, Brazil. Tectonophysics 786, 228455. https://doi.org/10.1016/j.tecto.2020.228455

Forero-Ortega, A.J., Faleiros, F.M., 2018. Ediacaran (570-615 Ma) back-arc basin basaltic volcanism in the ltaiacoca Group, Ribeira Belt, Brazil: a remnant of the Adamastor Ocean. South American Symposium on Isotope Geology. Cochabamba.

Fossen, H., Cavalcante, C., Konopásek, J., Meira, V.T., de Almeida, R.P., Hollanda, M.H.B.M., Trompette, R., 2020. A critical discussion of the subduction-collision model for the Neoproterozoic Araçuaí-West Congo orogen. Precambrian Research 343. https://doi.org/10.1016/j.precamres.2020.105715

Fossen, H., Cavalcante, G.C.G., 2017. Shear zones – A review., Earth-Science Reviews. https://doi.org/10.1016/j.earscirev.2017.05.002

Fuck, R.A., Brito Neves, B.B., Schobbenhaus, C., 2008. Rodinia descendants in South America. Precambrian Research 160, 108–126. https://doi.org/10.1016/j.precamres.2007.04.018

Fuhrman, M.L., Lindsley, D.H., 1988. Ternary-Feldspar Modeling and Thermometry.

American Mineralogist 73, 201–215.

Gain, S.E.M., Gréau, Y., Henry, H., Belousova, E., Dainis, I., Griffin, W.L., O'Reilly, S.Y., 2019. Mud Tank Zircon: Long-Term Evaluation of a Reference Material for U-Pb Dating, Hf-Isotope Analysis and Trace Element Analysis. Geostandards and Geoanalytical Research 43, 339–354. https://doi.org/10.1111/ggr.12265

Gilgannon, J., Fusseis, F., Menegon, L., Regenauer-Lieb, K., Buckman, J., 2017. Hierarchical creep cavity formation in an ultramylonite and implications for phase mixing. Solid Earth 8, 1193–1209. https://doi.org/10.5194/se-8-1193-2017

Giraldo, S.J., Trouw, R.A.J., Duffles, P., Vinagre da Costa, R., Ibañez Mejia, M., Schwantes Marimon, R., 2019. Structural analysis combined with new geothermobarometric and geochronological results of the Além Paraíba shear zone, between Três Rios and Bananal, Ribeira Orogen, SE Brazil. Journal of South American Earth Sciences 90, 118–136. https://doi.org/10.1016/j.jsames.2018.11.018

Gray, D.R., Foster, D.A., Meert, J.G., Goscombe, B.D., Armstrong, R., Trouw, R.A.J., Passchier, C.W., 2008. A Damara orogen perspective on the assembly of southwestern Gondwana. Geological Society Special Publication 294, 257–278. https://doi.org/10.1144/SP294.14

Guillot, S., Hattori, K., Agard, P., Schwartz, S., Vidal, O., 2009. Exhumation Processes in Oceanic and Continental Subduction Contexts: A Review. Subduction Zone Geodynamics. 103–118. https://doi.org/10.1007/978-3-540-87974-9

Hackspacher, P.C., Dantas, E.L., Spoladore, Â., Fetter, A.H., Oliveira, M.A.F. de, 2000. Evidence of Neoproterozoic Backarc Basin Development in the Central Ribeira Belt, Southeastern Brazil: New Geochronological and Geochemical Constraints From the São Roque - Açungui Groups. Revista Brasileira de Geociências 30, 110–114.

Hamilton, P.J., O'Nions, R.K., Bridgwater, D., Nutman, A., 1983. Sm-Nd studies of Archaean metasediments and metavolcanics from West Greenland and their implications for the Earth's early history. Earth and Planetary Science Letters 62, 263–272. https://doi.org/10.1016/0012-821X(83)90089-4

Hartmann, L.A., Werle, M., Michelin, C.R.L., Lana, C., Queiroga, G.N., Castro, M.P.,

Arena, K.R., 2019. Proto-Adamastor ocean crust (920 Ma) described in Brasiliano Orogen from coetaneous zircon and tourmaline. Geoscience Frontiers 10, 1623–1633. https://doi.org/10.1016/j.gsf.2018.09.018

Heilbron, M., Machado, N., 2003. Timing of terrane accretion in the Neoproterozoic-Eopaleozoic Ribeira orogen (SE Brazil). Precambrian Research 125, 87–112.

Heilbron, M., Oliveira, C., Lobato, M., De Morisson Valeriano, C., Dussin, I., Dantas, E., Simonetti, A., Bruno, H., Corrales, F., Socoloff, E., 2019. The Barreiro suite in the central Ribeira Belt (SE-Brazil): A late Tonian tholeiitic intraplate magmatic event in the distal passive margin of the São Francisco Paleocontinent. Brazilian Journal of Geology 49, 1–21. https://doi.org/10.1590/2317-4889201920180129

Heilbron, M., Valeriano, C.D.M., Peixoto, C., Neubauer, F., Dussin, I., Corrales, F., Bruno, H., Cesar, J., Almeida, H. De, Guilherme, L., 2020. Neoproterozoic magmatic arc systems of the central Ribeira belt, SE-Brazil, in the context of the West-Gondwana pre-collisional history: A review. Journal of South American Earth Sciences 102710. https://doi.org/10.1016/j.jsames.2020.102710

Heilbron, M., Valeriano, C.M., Tassinari, C.C.G., Almeida, J., Tupinambá, M., Siga Jr, O., Trouw, R., 2008. Correlation of Neoproterozoic terranes between Ribeira Belt, SE Brazil and its African counterpart: comparative tectonic evolution and open questions., West Gondwana: Pre-Cenozoic Correlations Across the South Atlantic Region. https://doi.org/10.1144/SP294.12

Henrique-Pinto, R., De Assis Janasi, V., Da Cruz Campanha, G.A., 2018. U-Pb dating, Lu-Hf isotope systematics and chemistry of zircon from the Morro do Polvilho meta-trachydacite: Constraints on sources of magmatism and on the depositional age of the São Roque Group. Geologia USP - Serie Cientifica 18, 45–56. https://doi.org/10.11606/issn.2316-9095.v18-125793

Henrique-Pinto, R., Janasi, V.A., Vasconcellos, A.C.B.C., Sawyer, E.W., Barnes, S., Basei, M.A.S., Tassinari, C.C.G., 2015. Zircon provenance in meta-sandstones of the São Roque Domain : Implications for the Proterozoic evolution of the Ribeira Belt , SE Brazil. Precambrian Research 256, 271–288. https://doi.org/10.1016/j.precamres.2014.11.014

Hippertt, J., Egydio-Silva, M., 1996. New polygonal grains formed by dissolution-redeposition in quartz mylonite. Journal of Structural Geology 18, 1345–1352. https://doi.org/10.1016/S0191-8141(96)00047-8

Hogmalm, K.J., Zack, T., Karlsson, A.K.O., Sjöqvist, A.S.L., Garbe-Schönberg, D., 2017. In situ Rb-Sr and K-Ca dating by LA-ICP-MS/MS: An evaluation of N2O and SF6 as reaction gases. Journal of Analytical Atomic Spectrometry 32, 305–313. https://doi.org/10.1039/c6ja00362a

Holland, T.J.B., Powell, R., 2011. An improved and extended internally consistent thermodynamic dataset for phases of petrological interest, involving a new equation of state for solids. Journal of Metamorphic Geology 29, 333–383. https://doi.org/10.1111/j.1525-1314.2010.00923.x

Hollocher, K., Robinson, P., Walsh, E., Roberts, D., 2012. Geochemistry of amphibolite-facies volcanics and gabbros of the støren nappe in extensions west and southwest of Trondheim, Western Gneiss Region, Norway: A key to correlations and paleotectonic settings. American Journal of Science 312, 357–416. https://doi.org/10.2475/04.2012.01

Jackson, S.E., Pearson, N.J., Griffin, W.L., Belousova, E.A., 2004. The application of laser ablation-inductively coupled plasma-mass spectrometry to in situ U-Pb zircon geochronology. Chemical Geology 211, 47–69. https://doi.org/10.1016/j.chemgeo.2004.06.017

Jäger, E, 1979. Introduction to Geochronology BT - Lectures in Isotope Geology. In: Jäger, Emilie, Hunziker, J.C. (Eds.). Springer Berlin Heidelberg, Berlin, Heidelberg, 1–12.

Janasi, V. de A., Alves, A., Vlach, S.R.F., Leite, R.J., 2003. Granitos Peraluminosos da Porção Central da Faixa Ribeira, Estado de São Paulo: Sucessivos Eventos de Reciclagem da Crosta Continental no Neoproterozóico. Geologia USP - Serie Cientifica 3, 13–24.

Janasi, V. de A., Andrade, S., Vasconcellos, A.C.B.C., Henrique-Pinto, R., Ulbrich, H.H.G.J., 2016. Timing and sources of granite magmatism in the Ribeira Belt, SE Brazil: Insights from zircon in situ U–Pb dating and Hf isotope geochemistry in

granites from the São Roque Domain. Journal of South American Earth Sciences 68, 224–247. https://doi.org/10.1016/j.jsames.2015.11.009

Janasi, V. de A., Ulbrich, H.H.G.J., 1991. Late Proterozoic granitoid magmatism in the state of São Paulo, southeastern Brazil. Precambrian Research 51, 351–374.

Janasi, V.A., Leite, R.J., Van Schmus, W.R., 2001. U-Pb chronostratigraphy of the granitic magmatism in the Agudos Grandes Batholith (West of São Paulo, Brazil) - Implications for the evolution of the Ribeira Belt. Journal of South American Earth Sciences 14, 363–376. https://doi.org/10.1016/S0895-9811(01)00034-7

Janoušek, V., Farrow, C.M., Erban, V., 2006. Interpretation of whole-rock geochemical data in igneous geochemistry: Introducing Geochemical Data Toolkit (GCDkit). Journal of Petrology 47, 1255–1259. https://doi.org/10.1093/petrology/egl013

Juliani, C., Hackspacher, P., Dantas, E.L., Fetter, A.H., 2000. the Mesoproterozoic Volcano-Sedimentary Serra Do Itaberaba Group of the Central Ribeira Belt, São Paulo State, Brazil: Implications for the Age of the Overlying São Roque Group. Revista Brasileira de Geociências 30, 082–086. https://doi.org/10.25249/0375-7536.2000301082086

Kelsey, D.E., Clark, C., Hand, M., 2008. Thermobarometric modelling of zircon and monazite growth in melt-bearing systems: Examples using model metapelitic and metapsammitic granulites. Journal of Metamorphic Geology 26, 199–212. https://doi.org/10.1111/j.1525-1314.2007.00757.x

Kilian, R., Heilbronner, R., Stünitz, H., 2011. Quartz grain size reduction in a granitoid rock and the transition from dislocation to diffusion creep. Journal of Structural Geology 33, 1265–1284. https://doi.org/10.1016/j.jsg.2011.05.004

Konopásek, J., Cavalcante, C., Fossen, H., Janoušek, V., 2020. Adamastor – an ocean that never existed? Earth-Science Reviews 205, 103201. https://doi.org/10.1016/j.earscirev.2020.103201

Leandro, R., 2016. Caracterização Tectonoestratigráfica da Sequência Terrígena da Formação Capiru Na Região de Morro Grande, Colombo - Pr., Dissertação de Mestrado. Universidade Federal do Paraná. https://doi.org/10.1017/CBO9781107415324.004

Leite, R.J., 2003. Petrogênese e geocronologia U-Pb do magmatismo granítico tardi- a pós-orogênico no batólito Agudos Grandes (SP). Doctoral Thesis, University of São Paulo.

Leite, R.J., Heaman, L.M., de Assis Janasi, V., Martins, L., Creaser, R.A., 2007. The late- to postorogenic transition in the Neoproterozoic Agudos Grandes Granite Batholith (Apiaí Domain, SE Brazil): Constraints from geology, mineralogy, and U-Pb geochronology. Journal of South American Earth Sciences 23, 193–212. https://doi.org/10.1016/j.jsames.2006.09.022

Li, Z.X., Bogdanova, S. V., Collins, A.S., Davidson, A., De Waele, B., Ernst, R.E., Fitzsimons, I.C.W., Fuck, R.A., Gladkochub, D.P., Jacobs, J., Karlstrom, K.E., Lu, S., Natapov, L.M., Pease, V., Pisarevsky, S.A., Thrane, K., Vernikovsky, V., 2008. Assembly, configuration, and break-up history of Rodinia: A synthesis. Precambrian Research 160, 179–210. https://doi.org/10.1016/j.precamres.2007.04.021

Lobato, M., Heilbron, M., Torós, B., Ragatky, D., Dantas, E., 2015. Provenance of the Neoproterozoic high-grade metasedimentary rocks of the arc-related Oriental Terrane of the Ribeira belt: Implications for Gondwana amalgamation. Journal of South American Earth Sciences 63, 260–278. https://doi.org/10.1016/j.jsames.2015.07.019

Ludwig, K.R., 2003. A Geochronological Toolkit for Microsoft Excel. Berkeley Geochronology Center, Special Publication. 4, 71.

Machado, R., Dehler, N.M., Vasconcelos, P., 2007. 40Ar/39Ar ages (600-570 Ma) of the Serra do Azeite transtensional shear zone: Evidence for syncontractional extension in the Cajati area, southern Ribeira belt. Anais Da Academia Brasileira de Ciências 79, 713–723.

Maurer, V.C., 2016. Caracterização geocronológica (U-Pb), geoquímica e isotópica 9Sr, Nd, Hf) do Complexo Rio Capivari no Terreno Embu. Master Thesis, University of São Paulo.

Meira, V.T., 2014. Evolução Tectono-Metamórfica Neoproterozóica dos Complexos Embu e Costeiro no Contexto de Formação do Gondwana Ocidental (Leste do Estado de São Paulo). Doctoral Thesis, University of São Paulo.

Meira, V.T., Garcia-Casco, A., Hyppolito, T., Juliani, C., Schorscher, J.H.D., 2019a. Tectono-Metamorphic Evolution of the Central Ribeira Belt, Brazil: A Case of Late Neoproterozoic Intracontinental Orogeny and Flow of Partially Molten Deep Crust During the Assembly of West Gondwana. Tectonics 38, 3182–3209. https://doi.org/10.1029/2018TC004959

Meira, V.T., García-Casco, A., Juliani, C., Almeida, R.P., Schorscher, J.H.D., 2015. The role of intracontinental deformation in supercontinent assembly: Insights from the Ribeira Belt, Southeastern Brazil (Neoproterozoic West Gondwana). Terra Nova 27, 206–217. https://doi.org/10.1111/ter.12149

Meira, V.T., Garcia-Casco, A., Juliani, C., Schorscher, J.H.D., 2019b. Late Tonian within-plate mafic magmatism and Ediacaran partial melting and magmatism in the Costeiro Domain, Central Ribeira Belt, Brazil. Precambrian Research 334, 105440. https://doi.org/10.1016/j.precamres.2019.105440

Mora, C.A.S., Campanha, G.A. da C., Wemmer, K., 2013. Microstructures and K-Ar illite fine-fraction ages of the cataclastic rocks associated to the Camburu Shear Zone, Ribeira Belt, Southeastern Brazil. Brazilian Journal of Geology 43, 607–622. https://doi.org/10.5327/z2317-48892013000400003

Mori, P.E., Reeves, S., Correia, C.T., Haukka, M., 1999. Development of a fused glass disc XRF facility and comparison with pressed powder pellet technique at Instituto de Geociências, São Paulo University. Revista Brasileira de Geociencias 29, 441–446. https://doi.org/10.5327/rbg.v29i3.715

Mullen, E.D., 1983. MnO/TiO2/P2O5: a minor element discriminant for basaltic rocks of oceanic environments and its implications for petrogenesis. Earth and Planetary Science Letters 62, 53–62. https://doi.org/10.1016/0012-821X(83)90070-5

Murphy, D.T., Allen, C.M., Ghidan, O., Dickson, A., Hu, W.P., Briggs, E., Holder, P.W., Armstrong, K.F., 2020. Analysing Sr isotopes in low-Sr samples such as single insects with inductively coupled plasma tandem mass spectrometry using N2O as a reaction gas for in-line Rb separation. Rapid Communications in Mass Spectrometry 34, 1–12. https://doi.org/10.1002/rcm.8604

Navarro, M.S., Andrade, S., Ulbrich, H., Gomes, C.B., Girardi, V.A.V., 2008. The direct

determination of rare earth elements in basaltic and related rocks using ICP-MS: Testing the efficiency of microwave oven sample decomposition procedures. Geostandards and Geoanalytical Research 32, 167–180. https://doi.org/10.1111/j.1751-908X.2008.00840.x

Neumann, B., 2000. Texture development of recrystallised quartz polycrystals unravelled by orientation and misorientation characteristics. Journal of Structural Geology 22, 1695–1711. https://doi.org/10.1016/S0191-8141(00)00060-2

O'Sullivan, G., Chew, D., Kenny, G., Henrichs, I., Mulligan, D., 2020. The trace element composition of apatite and its application to detrital provenance studies. Earth-Science Reviews 201, 103044. https://doi.org/10.1016/j.earscirev.2019.103044

O'Sullivan, G.J., Thakurdin, Y., Bolhar, R., Horváth, P., Hoare, B.C., Collerson, K.D., 2021. The Great Falls Tectonic Zone after the assembly of Laurentia: evidence for long-term tectonic stability from xenolith apatite. Lithos 384–385, 105977. https://doi.org/10.1016/j.lithos.2021.105977

Orihashi, Y., Nakai, S., Hirata, T., 2008. U-Pb age determination for seven standard zircons using inductively coupled plasma-mass spectrometry coupled with frequency quintupled Nd-YAG (λ = 213 nm) laser ablation system: Comparison with LA-ICP-MS zircon analyses with a NIST glass reference materia. Resource Geology 58, 101–123. https://doi.org/10.1111/j.1751-3928.2008.00052.x

Oriolo, S., Oyhantçabal, P., Wemmer, K., Siegesmund, S., 2017. Contemporaneous assembly of Western Gondwana and final Rodinia break-up: Implications for the supercontinent cycle. Geoscience Frontiers 8, 1431–1445. https://doi.org/10.1016/j.gsf.2017.01.009

Oyhantçabal, P., Wagner-Eimer, M., Wemmer, K., Schulz, B., Frei, R., Siegesmund, S., 2012. Paleo- and Neoproterozoic magmatic and tectonometamorphic evolution of the Isla Cristalina de Rivera (Nico Pérez Terrane, Uruguay). International Journal of Earth Sciences 101, 1745–1762. https://doi.org/10.1007/s00531-012-0757-4

Passarelli, C.R., Basei, M.A.S., Prazeres-Filho, H.J., Siga, O., Szabó, G.A.J., Marco-Neto, J., 2007. Structural and geochronological constraints on the evolution of the Juréia Massif, Registro Domain, State of São Paulo, Brazil. Anais Da Academia

Brasileira de Ciencias 79, 441–455. https://doi.org/10.1590/s0001-37652007000300008

Passarelli, C.R., Basei, M.A.S., Wemmer, K., Siga Júnior, O., Oyhantc, P., 2011. Major shear zones of southern Brazil and Uruguay : escape tectonics in the eastern border of Rio de La plata and Paranapanema cratons during the Western Gondwana amalgamation. International Journal of Earth Sciences 100, 391–414. https://doi.org/10.1007/s00531-010-0594-2

Passarelli, C.R., Verma, S.K., Mcreath, I., Basei, M.Â.S., Siga Júnior, O., 2019. Tracing the history from Rodinia break-up to the Gondwana amalgamation in the Embu Terrane, southern Ribeira Belt, Brazil. Lithos. https://doi.org/10.1016/j.lithos.2019.05.024

Passchier, C.W., Trouw, R.A.J., 2005. Microtectonics. Springer Berlin Heidelberg.

Patiño Douce, A.E., Harris, N., 1998. Experimental constraints on Himalayan anatexis. Journal of Petrology 39, 689–710. https://doi.org/10.1093/petroj/39.4.689

Paton, C., Hellstrom, J., Paul, B., Woodhead, J., Hergt, J., 2011. Iolite: Freeware for the visualisation and processing of mass spectrometric data. Journal of Analytical Atomic Spectrometry 26, 2508–2518. https://doi.org/10.1039/c1ja10172b

Payne, J.L., Hand, M., Barovich, K.M., Wade, B.P., 2008. Temporal constraints on the timing of high-grade metamorphism in the northern Gawler Craton: Implications for assembly of the Australian Proterozoic. Australian Journal of Earth Sciences 55, 623–640. https://doi.org/10.1080/08120090801982595

Pearce, J.A., 2008. Geochemical fingerprinting of oceanic basalts with applications to ophiolite classification and the search for Archean oceanic crust. Lithos 100, 14–48. https://doi.org/10.1016/j.lithos.2007.06.016

Pearce, J.A., 1996. A User's Guide to Basalto Discriminant Diagrams., Geological Association of Canada, Short Course Notes.

Pearce, J.A., Cann, J.R., 1973. Tectonic setting of basic volcanic rocks determined using trace element analyses. Earth and Planetary Science Letters 19, 290–300. https://doi.org/10.1016/0012-821X(73)90129-5

Pearce, J.A., Thirlwall, M.F., Ingram, G., Murton, B.J., Arculus, R.J., Van Der Laan, S.R., 1992. Isotopic evidence for the origin of boninites and related rocks drilled in the Izu-Bonin (Ogasawara) Forearc, Leg 125. Proc., Scientific Results, ODP, Leg 125, Bonin/Mariana Region 125, 237–262. https://doi.org/10.2973/odp.proc.sr.125.134.1992

Pearce, T.H., Gorman, B.E., Birkett, T.C., 1975. The TiO_2-K_2O-P_2O_5 Diagram: A Method of Discriminating Between Oceanic and Non-Oceanic Basalts. Earth and Planetary Science Letters 24, 419–426.

Peixoto, C. de A., Heilbron, M., Ragatky, D., Armstrong, R., Dantas, E., de Morisson Valeriano, C., Simonetti, A., 2017. Tectonic evolution of the Juvenile Tonian Serra da Prata magmatic arc in the Ribeira belt, SE Brazil: Implications for early west Gondwana amalgamation. Precambrian Research 302, 221–254. https://doi.org/10.1016/j.precamres.2017.09.017

Percival, J.J., Konopásek, J., Anczkiewicz, R., Ganerød, M., Sláma, J., de Campos, R.S., Bitencourt, M. de F., 2022. Tectono-Metamorphic Evolution of the Northern Dom Feliciano Belt Foreland, Santa Catarina, Brazil: Implications for Models of Subduction-Driven Orogenesis. Tectonics 41, e2021TC007014. https://doi.org/https://doi.org/10.1029/2021TC007014

Perrotta, M.M., 1996. Potencial aurífero de uma região no Vale do Ribeira, São Paulo, estimado por modelagem de dados geológicos, geoquiuímicos, geofísicos e de sensores remotos num sistema de informações geográficas, Doctoral Thesis, University of São Paulo.

Perrotta, M.M., Salvador, E.D., Lopes, R.C., D'Agostino, L.Z., Peruffo, N., Gomes, S.D., Sachs, L.L.B., Meira, V.T., Garcia, M.G.M., Lacerda Filho, J.V., 2005. Mapa geológico do estado de São Paulo. CPRM, Escala: 1:750.000.

Pertille, J., Hartmann, L.A., Santos, J.O.S., N.J., M., Armstrong, R., 2017. Reconstructing the Cryogenian–Ediacaran evolution of the Porongos fold and thrust belt, Southern Brasiliano Orogen, based on Zircon U–Pb–Hf–O isotopes. International Geology Review 59, 1532–1560. https://doi.org/10.1080/00206814.2017.1285257

Philipp, R.P., Pimentel, M.M., Chemale, F., 2016. Tectonic evolution of the Dom

Feliciano Belt in Southern Brazil: Geological relationships and U-Pb geochronology. Brazilian Journal of Geology 46, 83–104. https://doi.org/10.1590/2317-4889201620150016

Pinto, V.M., Debruyne, D., Hartmann, L.A., Queiroga, G.N., Lana, C., Fragoso César, B.A.M., Porcher, C., Castro, M.P., Laux, J., 2021. Metamorphic evolution of a Tonian eclogite associated with an island arc of the southern Brasiliano Orogen. Precambrian Research 366. https://doi.org/10.1016/j.precamres.2021.106414

Polat, A., Hofmann, A.W., Rosing, M.T., 2002. Boninite-like volcanic rocks in the 3.7-3.8 Ga isua greenstone belt, West Greenland: Geochemical evidence for intra-oceanic subduction zone processes in the early earth. Chemical Geology 184, 231–254. https://doi.org/10.1016/S0009-2541(01)00363-1

Porada, H., 1989. Pan-African rifting and orogenesis in Southern Equatorial Africa and Eastern Brazil. Precambrian Research 44, 103–136. https://doi.org/10.1016/0301-9268(89)90078-8

Porcher, C., Egydio-silva, M., Fernandes, L., Vauchez, A., 1995. Dados prelimineres do metamorfismo M1 da Faixa Ribeira: Região de Três Rios e Santo Antônio de Pádua (RJ). In: V Simpósio Nacional de Estudos Tectônicos. Gramado, 71–73.

Prazeres Filho, H.J. dos, 2005. Caracterização geológica e petrogenética do batólito granítico Três Córregos (PR-SP): geoquímica isotópica (Nd-Sr-Pb), idades (ID-TIMS/SHRIMP) e $d^{18}O$ em zircão. Doctoral Thesis, University of São Paulo.

Ramsay, J.G., 1980. Shear zone geometry: A review. Journal of Structural Geology 2, 83–99. https://doi.org/10.1016/0191-8141(80)90038-3

Ribeiro, B. V., Finch, M.A., Cawood, P.A., Faleiros, F.M., Murphy, T.D., Simpson, A., Glorie, S., Tedeschi, M., Armit, R., Barrote, V.R., 2021. From microanalysis to supercontinents: insights from the Rio Apa Terrane into the Mesoproterozoic SW Amazonian Craton evolution during Rodinia assembly. Journal of Metamorphic Geology. https://doi.org/10.1111/jmg.12641

Ribeiro, B. V., Lagoeiro, L., Faleiros, F.M., Hunter, N.J.R., Queiroga, G., Raveggi, M., Cawood, P.A., Finch, M., Campanha, G.A.C., 2020a. Strain localization and fluid-assisted deformation in apatite and its influence on trace elements and U–Pb

systematics. Earth and Planetary Science Letters 545, 116421. https://doi.org/10.1016/j.epsl.2020.116421

Ribeiro, B. V., Mulder, J.A., Faleiros, F.M., Kirkland, C.L., Cawood, P.A., O'Sullivan, G., Campanha, G.A.C., Finch, M.A., Weinberg, R.F., Nebel, O., 2020b. Using apatite to resolve the age and protoliths of mid-crustal shear zones: A case study from the Taxaquara Shear Zone, SE Brazil. Lithos 378–379, 105817. https://doi.org/10.1016/j.lithos.2020.105817

Ribeiro, B. V, Faleiros, F.M., Campanha, G.A.C., Lagoeiro, L., Weinberg, R.F., Hunter, N.J.R., 2019. Tectonophysics Kinematics , nature of deformation and tectonic setting of the Taxaquara Shear Zone , a major transpressional zone of the Ribeira Belt (SE Brazil). Tectonophysics 751, 83–108. https://doi.org/10.1016/j.tecto.2018.12.025

Ricardo, B.S., Faleiros, F.M., Moraes, R., Siga Júnior, O., Campanha, G.A.C., 2020. Tectonic implications of juxtaposed high- and low-pressure metamorphic field gradient rocks in the Turvo-Cajati Formation, Curitiba Terrane, Ribeira Belt, Brazil. Precambrian Research 345, 105766. https://doi.org/10.1016/j.precamres.2020.105766

Rubatto, D., Hermann, J., Berger, A., Engi, M., 2009. Protracted fluid-induced melting during Barrovian metamorphism in the Central Alps. Contributions to Mineralogy and Petrology 158, 703–722. https://doi.org/10.1007/s00410-009-0406-5

Sadowski, G.R., 1991. A megafalha de Cubatão no Sudeste Brasileiro. Boletim IG, Instituto de Geociências 22, 15–28.

Sadowski, G.R., Motidome, M.J., 1987. Brazilian megafaults. Revista Geologica de Chile 31, 61–75.

Sadowski, H.G.R.&, 1976. Considerações sobre a estratigrafia do Pré-Cambriano na Região de São Paulo. Boletim IG, Instituto de Geociências 9, 107–112.

Santiago, R., Caxito, F. de A., Pedrosa-Soares, A., Neves, M.A., Dantas, E.L., 2020. Tonian island arc remnants in the northern Ribeira orogen of Western Gondwana: The Caxixe batholith (Espírito Santo, SE Brazil). Precambrian Research 351, 105944. https://doi.org/10.1016/j.precamres.2020.105944

Santos, L. da R., Leandro, R., Bahniuk, A., Cury, L.F., 2018. Low-temperature metamorphism in the Capiru Formation, Morro Grande Synform, Southern Ribeira Belt. Brazilian Journal of Geology 48, 95–113. https://doi.org/10.1590/2317-4889201820170090

Santosh, M., Maruyama, S., Sato, K., 2009. Anatomy of a Cambrian suture in Gondwana: Pacific-type orogeny in southern India? Gondwana Research 16, 321–341. https://doi.org/10.1016/j.gr.2008.12.012

Sato, K., Siga, O., Da Silva, J.A., McReath, I., Dunyi, L., Iizuka, T., Rino, S., Hirata, T., Sproesser, W., Basei, M.A.S., 2009. In situ isotopic analyses of U and Pb in zircon by remotely operated SHRIMP II, and Hf by LA-ICP-MS: An example of dating and genetic evolution of zircon by 176Hf/177Hf from the Ita quarry in the Atuba Complex, Se Brazil. Geologia USP - Serie Cientifica 9, 61–69.

Sato, K., Siga, O., Nutman, A.P., Basei, M.A.S., McReath, I., Kaulfuss, G., 2003. The Atuba Complex, Southern South American platform: Archean components and paleoproterozoic to neoproterozoic tectonothermal events. Gondwana Research 6, 251–263. https://doi.org/10.1016/S1342-937X(05)70974-6

Sawyer, E.W., 2008. Atlas of Migmatites. Canadian Science Publishing. https://doi.org/10.1139/9780660197876

Schulz, B., 2021. Monazite Microstructures and Their Interpretation in Petrochronology. Frontiers in Earth Science 9. https://doi.org/10.3389/feart.2021.668566

Shervais, J.W., 1982. TiV plots and the petrogenesis of modern and ophiolitic lavas. Earth and Planetary Science Letters 59, 101–118. https://doi.org/10.1016/0012-821X(82)90120-0

Siga Junior, O., 1995. Domínios Tectônicos do Sudeste do Paraná e Nordeste de Santa Catarina: Geocronologia e Evolução crustal. Doctoral Thesis, University of São Paulo.

Siga Júnior, O., Angelo, Basei, S., Sato, K., Passarelli, C.R., Nutman, A., Mcreath, I., Prazeres Filho, H.J. dos, 2011a. Calymmian (1 .50 e 1.45 Ga) magmatic records in Votuverava and Perau sequences , south-southeastern Brazil : Zircon ages and Nd e Sr isotopic geochemistry. Journal of South American Earth Sciences 32, 301–308.

https://doi.org/10.1016/j.jsames.2011.03.015

Siga Júnior, O., Basei, M.A.S., Nutman, A., Sato, K., McReath, I., Passarelli, C.R., Liu, D., 2011b. Extensional and Colisional Magmatic Records in the Apiaí Terrane, South-Southeastern Brazil: Integration of Geochronological U-Pb Zircon Ages. Geologia USP - Serie Cientifica 11, 149–175.

Siga Júnior, O., Basei, M.A.S., Passarelli, C.R., Sato, K., Cury, L.F., McReath, I., 2009. Lower and Upper Neoproterozoic magmatic records in Itaiacoca Belt (Paraná-Brazil): Zircon ages and lithostratigraphy studies. Gondwana Research 15, 197–208. https://doi.org/10.1016/j.gr.2008.11.002

Siga Júnior, O., Basei, M.A.S., Reis Neto, J.M., Machiavelli, A., Harara, O.M., 1995. O complexo Atuba: um cinturão paleoproterozóico intensamente retrabalhado no Neoproterozóico. Boletim IG-USP. Série Científica 26, 69. https://doi.org/10.11606/issn.2316-8986.v26i0p69-98

Siga Júnior, O., Cury, L.F., Mcreath, I., Maria, L., Leite, D.A., Sato, K., Basei, M.A.S., Passarelli, C.R., 2011c. Geology and geochronology of the Betara region in south-southeastern Brazil: Evidence for possible Statherian (1.80 – 1.75 Ga) and Calymmian (1.50 –1.45 Ga) extension events. Gondwana Research 19, 260–274. https://doi.org/10.1016/j.gr.2010.06.003

Silva, B.Y.B., 2017. Evolução Tectônica Da Porção Central Do Terreno Embu Ao Norte Da Zona De Cisalhamento Taxaquara-Guararema Terreno Embu Ao Norte Da Zona De Cisalhamento Taxaquara-Guararema. Master Thesis, University of São Paulo.

Sláma, J., Košler, J., Condon, D.J., Crowley, J.L., Gerdes, A., Hanchar, J.M., Horstwood, M.S.A., Morris, G.A., Nasdala, L., Norberg, N., Schaltegger, U., Schoene, B., Tubrett, M.N., Whitehouse, M.J., 2008. Plešovice zircon - A new natural reference material for U-Pb and Hf isotopic microanalysis. Chemical Geology 249, 1–35. https://doi.org/10.1016/j.chemgeo.2007.11.005

Sobrinho, J.M.A., Janasi, V.A., Simonetti, A., 2011. The Ilha Anchieta Quartz Monzonite : the southernmost expression of ca . 500 Ma post-collisional magmatism in the Ribeira Belt. Anais Da Academia Brasileira de Ciencias 83, 891–906.

Spear, F.S., Kohn, M.J., Cheney, J.T., 1999. P -T paths from anatectic pelites.

Contributions Mineral Petrology 134, 17–32.

Stallard, A., Shelley, D., 1995. Quartz c-axes parallel to stretching directions in very low-grade metamorphic rocks. Tectonophysics 249, 31–40. https://doi.org/10.1016/0040-1951(95)00040-T

Stein, D.P., Campanha, G.A. da C., Fernandes, L.A., 1983. Geologia da Folha Pilar do Sul (SF.23-Y-C-IV-4). Estado de São Paulo. São Paulo.

Stipp, M., Stünitz, H., Heilbronner, R., Schmid, S.M., 2002. The eastern Tonale fault zone: A "natural laboratory" for crystal plastic deformation of quartz over a temperature range from 250 to 700 °C. Journal of Structural Geology 24, 1861–1884. https://doi.org/10.1016/S0191-8141(02)00035-4

Sun, S.S., McDonough, W.F., 1989. Chemical and isotopic systematics of oceanic basalts: Implications for mantle composition and processes. Geological Society Special Publication 42, 313–345. https://doi.org/10.1144/GSL.SP.1989.042.01.19

Tassinari, C.C.G., 1988. As idades das rochas e dos eventos metamórficos da porção sudeste do estado de São Paulo e sua evolução crustal. Doctoral Thesis, University of São Paulo.

Tassinari, C.C.G., Campos Neto, M. da C., 1988. Precambrian continental crust evolution of Southeastern São Paul State, Brazil, based on isotopic evidence. Geochim. Brasil 2, 175–183.

Tassinari, C.C.G., Munhá, J.M.U., Ribeiro, A., Correia, C.T., 2001. Neoproterozoic oceans in the Ribeira belt (southeastern Brazil): The Pirapora do bom Jesus ophiolitic complex. Episodes 24, 245–251. https://doi.org/10.18814/epiiugs/2001/v24i4/004

Thomson, S.N., Gehrels, G.E., Ruiz, J., Buchwaldt, R., 2012. Routine low-damage apatite U-Pb dating using laser ablation-multicollector- ICPMS. Geochemistry, Geophysics, Geosystems 13, 1–23. https://doi.org/10.1029/2011GC003928

Torquato, J.R., Cordani, 1981. Brazil-Africa geological links. Earth Science Reviews 17, 155–176. https://doi.org/10.1016/0012-8252(81)90010-6

Trouw, R.A.J., Peternel, R., Ribeiro, A., Heilbron, M., Vinagre, R., Duffles, P., Trouw,

C.C., Fontainha, M., Kussama, H.H., 2013. A new interpretation for the interference zone between the southern Brasília belt and the central Ribeira belt, SE Brazil. Journal of South American Earth Sciences 48, 43–57. https://doi.org/10.1016/j.jsames.2013.07.012

Tsunogae, T., Uthup, S., Nyirongo, M.W., Takahashi, K., Rahman, M.S., Liu, Q., Takamura, Y., Tsutsumi, Y., 2021. Neoproterozoic crustal growth in southern Malawi: New insights from petrology, geochemistry, and U–Pb zircon geochronology, and implications for the Kalahari Craton–Congo Craton amalgamation. Precambrian Research 352, 106007. https://doi.org/10.1016/j.precamres.2020.106007

Tupinambá, M., Heilbron, M., Valeriano, C., Júnior, R.P., de Dios, F.B., Machado, N., Silva, L.G. do E., de Almeida, J.C.H., 2012. Juvenile contribution of the Neoproterozoic Rio Negro Magmatic Arc (Ribeira Belt, Brazil): Implications for Western Gondwana amalgamation. Gondwana Research 21, 422–438. https://doi.org/10.1016/j.gr.2011.05.012

Vauchez, A., Tommasi, A., Silva, A., Trompette, R., 1992. Tectônica de escape na terminação de um craton: A Faixa Ribeira. Congresso Brasileiro de Geologia. 373–374.

Vermeesch, P., 2018. IsoplotR: A free and open toolbox for geochronology. Geoscience Frontiers 9, 1479–1493. https://doi.org/10.1016/j.gsf.2018.04.001

Viegas, G., Menegon, L., Archanjo, C., 2016. Brittle grain-size reduction of feldspar, phase mixing and strain localization in granitoids at mid-crustal conditions (Pernambuco shear zone, NE Brazil). Solid Earth 7, 375–396. https://doi.org/10.5194/se-7-375-2016

Vieira, S.R.S.S., 1996. Estudo de processos metamórfico-metassomáticos nos Complexos Embu e Pilar no Bloco Juquitiba, SP. Doctoral Thesis, University of São Paulo.

Vlach, S., 2008. Mineralogia, análise e datação de monazita com microssonda eletrônica e aplicações. Lecturer Thesis, University of São Paulo.

Weber, W., Siga Junior, O., Sato, K., Neto, J.M. dos R., Basei, M.Â.S., Nutman, A.P., 2004. A Formação Água Clara na região de Araçaíba-SP: registro de uma bacia

Mesoproterozoica. Boletim IG, Instituto de Geociências, USP 4, 101–110.

Werle, M., Hartmann, L.A., Queiroga, G.N., Lana, C., Pertille, J., Michelin, C.R.L., Remus, M.V.D., Roberts, M., Castro, M.P., Leandro, C.G., Savian, J.F., 2020. Oceanic crust and mantellic evidence on the evolution of tonian-cryogenian ophiolites, southern Brasiliano Orogen. Precambrian Research 351, 105979. https://doi.org/10.1016/j.precamres.2020.105979

White, R.W., Powell, R., Halpin, J.A., 2004. Spatially-focussed melt formation in aluminous metapelites from Broken Hill, Australia. Journal of Metamorphic Geology 22, 825–845. https://doi.org/10.1111/j.1525-1314.2004.00553.x

White, R.W., Powell, R., Holland, T.J.B., 2001. Calculation of partial melting equilibria in the system Na2O-CaO-K2O-FeO-MgO-Al2O3-SiO2-H2O (NCKFMASH). Journal of Metamorphic Geology 19, 139–153. https://doi.org/10.1046/j.0263-4929.2000.00303.x

White, R.W., Powell, R., Johnson, T.E., 2014. The effect of Mn on mineral stability in metapelites revisited: New a-x relations for manganese-bearing minerals. Journal of Metamorphic Geology 32, 809–828. https://doi.org/10.1111/jmg.12095

Williams, I.S., 1997. U-Th-Pb Geochronology by Ion Microprobe., Applications of Microanalytical Techniques to Understanding Mineralizing Processes. https://doi.org/10.5382/Rev.07.01

Wilson, M., 1989. Igneous Petrogenesis, Journal of Chemical Information and Modeling. Chapman & Hall.

Wilson, M. (B. M., 2007. Igneous petrogenesis. Dordrecht : Springer, [2007] ©2007.

Xia, L., Li, X., 2019. Basalt geochemistry as a diagnostic indicator of tectonic setting. Gondwana Research 65, 43–67. https://doi.org/10.1016/j.gr.2018.08.006

Xia, L.Q., 2014. The geochemical criteria to distinguish continental basalts from arc related ones. Earth-Science Reviews 139, 195–212. https://doi.org/10.1016/j.earscirev.2014.09.006

Yogi, M.T., 2019. Thermobaric and kinematic evolution of Anta Gorda Anticlinorium , Ribeira Belt : metamorphism record and shear deformation in a transpressional

setting. Master Thesis, University of São Paulo.

4. PETROCHRONOLOGICAL CONSTRAINTS AND TECTONIC IMPLICATIONS OF TONIAN METAMORPHISM IN THE EMBU COMPLEX, RIBEIRA BELT, BRAZIL

Dina I. G. Cabrita[a]*, Frederico M. Faleiros[a], Peter A. Cawood[b], Ginaldo A.C. Campanha[a], M. Thereza A.G. Yogi[c], Ashlea N. Wainwright[d], Massimo Raveggi[b], Vidyã V. Almeida[e]

[a] Instituto de Geociências, Universidade de São Paulo, Rua do Lago 562, São Paulo SP, Brazil

[b] School of Earth, Atmosphere and Environment, Monash University, Melbourne, VIC, Australia

[c] Department of Earth Sciences, Carleton University, Ottawa, ON, Canada

[d] School of Earth Sciences, University of Melbourne, Parkville, VIC, Australia

[e] CPRM – Geological Survey of Brazil, Rua Costa 55, Consolação, São Paulo SP, Brazil

*Corresponding author: dina_cabrita@usp.br

Abstract

The Embu Complex of the Ribeira Belt, southeast Brazil, provides records of orogenic processes within the time period between Rodinia break-up and West Gondwana assembly. Recent studies have questioned the accretionary setting for the belt, suggesting an intracontinental setting. In this paper, we present new petrological, U–Pb and Rb-Sr data from metasedimentary rocks of the Embu Complex, discussing the implications for the tectonic evolution from Rodinia to West Gondwana in the Ribeira Belt. Sillimanite, sillimanite–K-feldspar and cordierite zones represent the high-grade metamorphic zones for the metamorphic event identified in the southern portion of the Embu Complex. Petrological and thermodynamic modelling data indicate that the high-grade metamorphic rocks of the complex attained conditions between 750–805 ºC and 3.6–9.2 kbar. Monazite and zircon U–Pb data indicate that the high-grade metamorphic event occurred between 810–760 Ma, concomitant with igneous activity recorded during this period. In addition, zircon and apatite U–Pb ages, as well as, biotite and muscovite Rb–

Sr ages, between 675–550 Ma record a slow cooling rate of 4.4 ºC/Ma for the period between 675 and 640 Ma, and a late stage of shear zones development. These results reinforce the accretion of distinct units within the Ribeira Belt during the Neoproterozoic Era.

Keywords: high-grade metamorphism; U–Pb geochronology; phase equilibria modelling; Rodinia; West Gondwana.

4.1. Introduction

Rodinia break-up and West Gondwana assembly are recorded in several Neoproterozoic orogenic belts in South America and Africa (e.g. Brasília, Araçuaí, Ribeira and Dom Feliciano, Gariep, Damara, Kaoko and West Congo belts). The Ribeira Belt, in southern Brazil, is composed of a number of terranes interpreted to record a convergent plate setting related to multiple accretionary events with the neighboring craton (e.g. Paranapanema Craton), and is associated with the assembly of West Gondwana during the Neoproterozoic Era (Campos Neto and Figueiredo, 1995; Cordani et al., 2002; Heilbron and Machado, 2003; Basei et al., 2008; Faleiros et al., 2011a; Brito Neves et al., 2014). Recent studies have questioned this tectonic setting for the Ribeira Belt, and suggested an Ediacaran intracontinental setting for the belt (Meira et al., 2015, 2019a, 2019b) as well as for other surrounding Neoproterozoic orogenic belts (Fossen et al., 2020; Konopásek et al., 2020). The Embu Complex of the Ribeira Belt can provide additional information towards resolving the setting of the belt as it constitutes a major segment of the belt providing robust metamorphic and geochronological data.

In this paper, we aim to reconstruct the metamorphic history of the Embu Complex and discuss the implications of these results for orogenic models of the Ribeira Belt during Rodinia break-up and West Gondwana assembly. We present: (1) detailed petrology and P–T metamorphic data, determined by phase equilibria modelling, to constrain the metamorphic peak conditions; (2) monazite, zircon and apatite U–Pb age data and trace element compositions to determine the timing of metamorphism; and (3) in situ Rb–Sr muscovite and biotite dating to investigate the cooling history of the Embu Complex. The results from this work, integrated with published data, indicate an 810–760 Ma high-grade metamorphic event that is related to accretion terrane processes during the Neoproterozoic Era.

4.2. Regional setting

The Embu Complex is part of the Embu Terrane within the Southern and Central Ribeira Belt and comprises a crustal segment orientated parallel to the S-SE trending Brazilian coastline deformed during the Neoproterozoic Brasiliano-Pan African Orogeny (e.g., Brito Neves et al., 2014) (Fig. 4.1). The Embu Terrane comprises the Paleoproterozoic Rio Capivari Complex (Fernandes, 1991; Babinski et al., 2001; Maurer, 2016), the Embu Complex, and Cryogenian to Ediacaran granitoids (Janasi et al., 2003; Alves et al., 2013, 2016). The terrane is bounded by four major units interpreted as composite terranes: Apiaí, Curitiba and Costeiro terranes and the São Roque Domain (Fig. 4.1). The complex is composed of an association of metasedimentary rocks that includes paragneiss, mica schist, quartz schist, quartzite and calc-silicate rocks with concordant intercalations of metaultramafic and metamafic rocks that experienced lower to upper amphibolite facies conditions. Orthogneisses, dated at ca. 810–780 Ma (Tonian) occur within the complex (Cordani et al., 2002; Vlach, 2008).

The Apiaí Terrane is formed by the amalgamation of different units with ages ranging from late Calymmian (ca. 1500–1400 Ma: Água Clara and Votuverava Groups), Stenian to Tonian (1200–880 Ma: Lajeado Group), Tonian (1000–900 Ma: part of the Itaiacoca Group), and Ediacaran (630–580 Ma: part of the Itaiacoca Group and the Iporanga Formation), during the Neoproterozoic Brasiliano-Pan African Orogeny (Faleiros, 2008; Faleiros et al., 2011a; Campanha et al., 2015). In the Votuverava Group, which is juxtaposed with the Embu Complex, monazite U–Pb and Ar-Ar hornblende geochronology record a metamorphic event between 615 to 565 Ma (Yogi, 2019). Arc-related, collisional and post-collisional granitic magmatism is recorded in three main batholiths (Agudos Grandes, Cunhaporanga and Três Corregos) with ages spanning between 640 to 565 Ma (Janasi et al., 2001; Prazeres Filho, 2005; Leite et al., 2007; Mora et al., 2013) (Fig. 4.2).

The Curitiba Terrane is composed of migmatitic orthogneisses of Rhyacian age from the Atuba Complex (ca. 2200–2100 Ma; Siga Junior, 1995; Siga Júnior et al., 1995, 2009; Sato et al., 2003, 2009), interpreted as a fragment of a Paleoproterozoic mobile belt reworked in the Neoproterozoic, and two supracrustal units with largely Neoproterozoic sedimentation ages. One of them, the Capiru Formation has a maximum depositional age of 1080 Ma (Leandro, 2016) and was deformed under low-temperature conditions (250–350 ºC) (Santos et al., 2018). The other unit, the Turvo-Cajati Formation, has a maximum

depositional age of ca. 640–630 Ma, and was deformed and metamorphosed under greenschist to granulite facies conditions at 600-580 Ma (Faleiros et al., 2011, 2016; Ricardo et al., 2020).

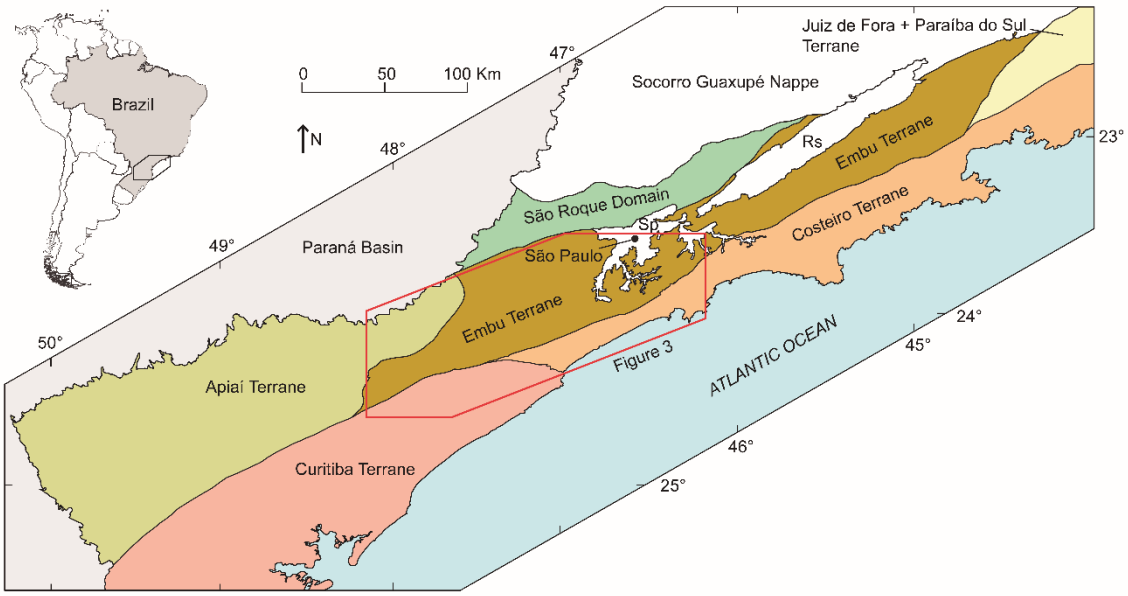

Figure 4.1. Geotectonic sketch map of the Ribeira Belt, showing the subdivision in terranes and the studied area (red polygon). Terranes of the Ribeira Belt are colored. Abbreviations include: Sp = São Paulo Basin, Rs = Resende Basin. Modified from Campanha et al. (2019).

The Costeiro Terrane, occurs along the Atlantic coast and comprises the Costeiro Complex and syn to post-collisional granitoids. The Costeiro Complex comprises high-grade migmatitic metapelites and metapsammites, calcsilicate rocks, orthogneisses and boudins of amphibolites. The metasedimentary rocks have a maximum depositional age of 670–650 Ma (Meira et al., 2015) but an amphibolite sample gives a Tonian magmatic age of 790–750 Ma (Meira et al., 2019b). The syn-collisional granitoids are garnet-bearing two mica leucogranites and, hornblende-bearing granitoids emplaced at 600–560 Ma (Janasi and Ulbrich, 1991; Janasi et al., 2003; Meira, 2014; Meira et al., 2019a). The post-collisional granitoids include the Ilha Anchieta monzogranite and charnockitic rocks (Janasi and Ulbrich, 1991; Sobrinho et al., 2011). The Costeiro Terrane is correlated to the Oriental Terrane in the northern Ribeira Belt, which is composed of metasedimentary successions (Italva and São Fidelis Group), arc-related rocks (Serra da Prata and Rio

Negro complexes) and syn to post-collisional granitoids (Heilbron and Machado, 2003; Tupinambá et al., 2012; Lobato et al., 2015; Peixoto et al., 2017).

The São Roque Domain is composed by different metavolcano-sedimentary successions; the São Roque and Serra do Itaberaba groups (Juliani et al., 2000; Henrique-Pinto et al., 2018). The São Roque Group is considered to be a passive continental margin succession with a basal unit (Boturuna Formation) composed of metarkose interlayered with polymictic metaconglomerate, meta-quartz arenite and small bodies of metavolcanic rocks deposited ca. 1800–1750 Ma (Sadowski, 1976; Henrique-Pinto et al., 2015), and an upper unit (Piragibu Fornation) composed of meta-mudstones interbedded with metawackes, which may correspond to rhythmic turbidity deposits with an unknown age (Tassinari et al., 2001). There is also a younger unit, the Pirapora do Bom Jesus Formation, which is interpreted as an ophiolitic complex emplaced during the Ediacaran (ca. 628 Ma) (Tassinari et al., 2001) or as a back-arc basin (Hackspacher et al., 2000) (Fig. 4.2). The Serra do Itaberaba Group is a volcano-sedimentary succession with MORB-like magmatism interpreted as a back-arc basin with depositional ages of 1500–1400 Ma (Juliani et al., 2000).

The inferred maximum depositional age of the Embu Complex metasedimentary succession, based on detrital zircon U–Pb data, varies along strike, ranging from ca. 1100 to 785 Ma. In the north, sedimentation occurred between ca. 1000 and 785 Ma (Duffles et al., 2016; Costa et al., 2017), in the central portion maximum depositional ages of ca. 1100 Ma (Meira et al., 2015) and 980 to 800 Ma (Silva, 2017) are reported, whereas in the southern portion the possible depositional interval is 970–850 Ma (Campanha et al., 2019) (Fig. 4.2). Ages of metamorphic events are controversial. Tonian metamorphic ages are sporadically reported in Embu Complex and range from 805 ± 6 Ma in zircon (Silva, 2017) to ca.790 Ma in monazite (Vlach, 2008). In the southwest portion of the complex metamorphic zircon overgrowths with ages spanning 820–790 Ma are dominant (Campanha et al., 2019). However, the majority of the metamorphic zircon U–Pb ages from the Embu Complex are Cryogenian to Ediacaran. Published zircon U–Pb metamorphic ages are within the intervals of 630–600 Ma and 600–560 Ma (Meira, 2014; Meira et al., 2019a), 670–640 Ma, 620–600 Ma and 580–570 Ma (Duffles et al., 2016), and 705–660 and 607–577 Ma (Silva, 2017). Despite numerous metamorphic ages, it is unclear what age range is related to the main regional metamorphism recorded in the Embu Complex. Tonian granodioritic to tonalitic orthogneisses of unknown regional expression were described and interpreted as evidence of compressional (Cordani et al.,

2002; Silva, 2017) or extensional (Meira et al., 2015) environments. A two-mica peraluminous granite (Juquiá granite), dated at ca. 799 Ma, is interpreted as a part of the first magmatic event in the Embu Complex, and related to the final stages of the Rodina break-up or the initial stages of an ocean formation in the region (Passarelli et al., 2019). These rocks assemblages were intruded by Cryogenian to Ediacaran granitic plutons ranging in age from ca. 680 Ma to ca. 580 Ma, which are interpreted to be related to an evolving accretionary to collisional event (Janasi et al., 2001, 2016; Alves et al., 2013, 2016; Passarelli et al., 2019) or to an intracontinental orogeny (Meira et al., 2019b, 2019a).

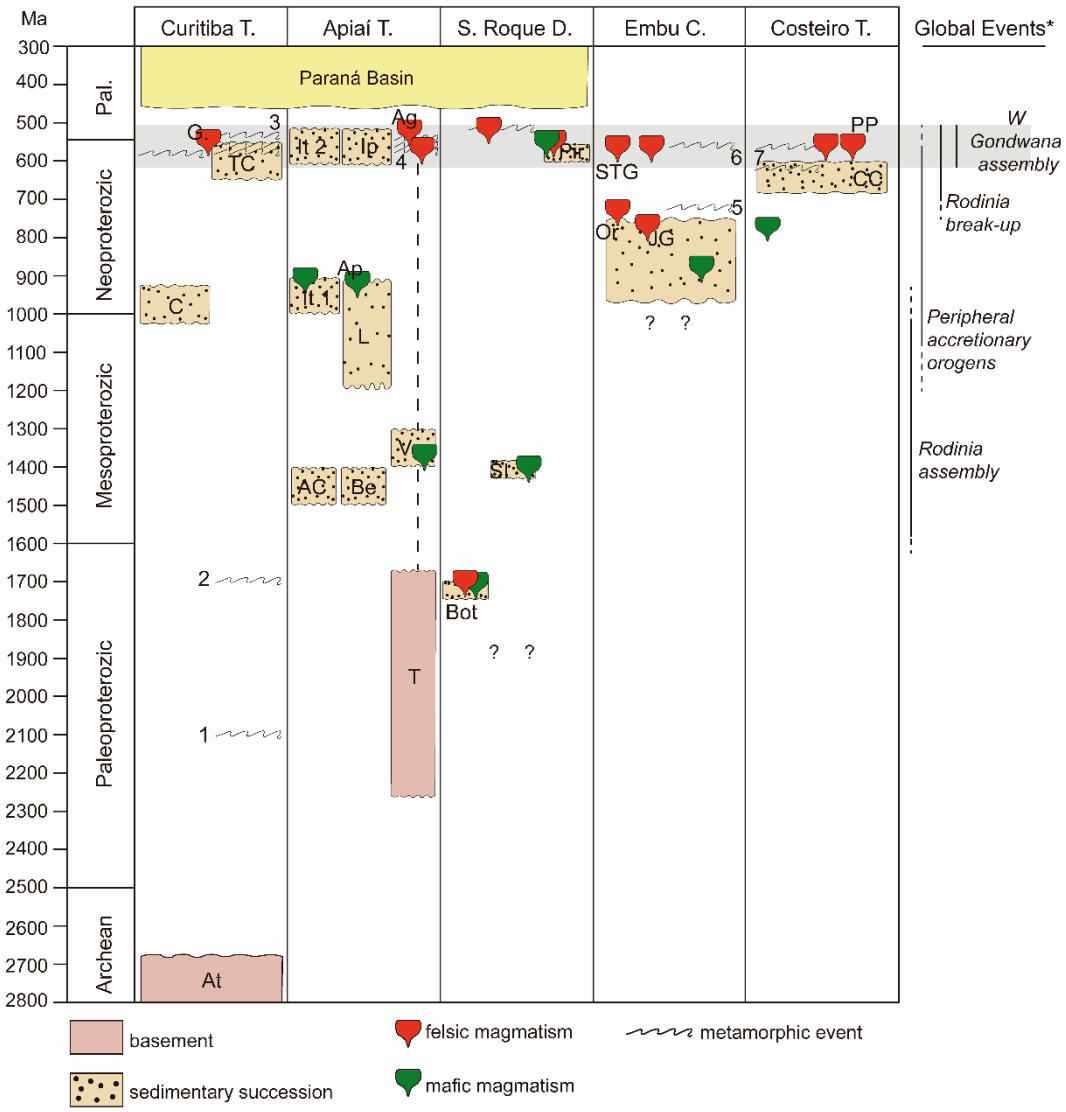

Figure 4.2. Time-space diagram outlining the depositional, metamorphic and igneous ages in the Ribeira Belt. Abbreviations: At - Atuba Complex (3.1–2.7 Ga) (Sato et al., 2009); C - Capiru Formation (maximum depositional age of 1.08 Ga) (Leandro, 2016); TC - Turvo-Cajati Formation (Faleiros, personal communication); G - Graciosa Province;

T - Tigre Gneiss; AC - Água Clara Formation; Be - Betara Formation; V - Votuverava Group (volcanic rocks with an age of 1400 Ma) (Campanha et al., 2015); depositional age 1.4–1.3 Ga (Campanha et al., 2019); L - Lajeado Group; It - Itaiacoca Group; Ap - Apiaí Gabbro; I - Iporanga Formation; Ag - Agudos Grandes Batholit (610– 565 Ma) (Janasi et al., 2001); Bot - Boturuna Formation (1.75–1.80 Ga) (Henrique-Pinto et al., 2015; Henrique-Pinto et al., 2018); SI - Serra do Itaberaba Group (1.4–1.5 Ga) (Juliani et al., 2000); Pir - Pirapora do Bom Jesus Formation (ca. 628 Ma) (Hackspacher et al., 2000; Tassinari et al., 2001); JQ - Juquiá Granite (Passarelli et al., 2019); Or - Ortogneiss (Cordani et al., 2002, this work); STG - Sete Barras Granite (Passarelli et al., 2019); CC - Costeiro Complex (maximum depositional age of 670–650 Ma) (Meira et al., 2015); PP - Pico do Papagaio Batholit (Meira, 2014). Mafic magmatism with an age of 750–790 Ma (Meira et al., 2019b). *from (Cawood et al., 2016). Metamorphic data from: 1 and 2. (Siga Júnior et al., 1995); 3. (Faleiros et al., 2011); 4. (Yogi, 2019); 5. (Vlach, 2008; Campanha et al., 2019, this work); 6. (Campanha et al., 2019, this work); 7. (Meira et al., 2015; Meira et al., 2019a).

4.3. Analytical methods

Petrological and geochronological studies were performed on representative samples of metapelites recording distinct metamorphic grades. Whole rock and mineral chemical analyses were performed at the NAP–Geoanalítica Facility, University of São Paulo, Brazil. Monazite, zircon and apatite U–Pb dating and trace element geochemistry were performed simultaneously via Laser Ablation Split-Stream, as well as mica Rb-Sr dating, by the laser ablation triple quadrupole inductively coupled plasma mass spectrometer (LA-TQ-ICPMS) at the Isotopia Laboratory, School of Earth, Atmosphere and Environment, Monash University, Australia. Additional zircon U–Pb dating was conducted by sensitive high-resolution ion microprobe (SHRIMP) at the University of São Paulo. Calculation of U–Pb and Rb-Sr ages and plotting of results were done using isoplotR (Vermeesch, 2018). Thermodynamic modelling was performed with Perple_X software, version 6.7.5 (Connolly, 2005) using bulk compositions of representative metapelite samples, obtained from X-ray fluorescence analyses. Detailed analytical methods are described in Supplementary Information A.

4.4. Embu Complex lithotypes

The dominant lithotypes in the study area are metapelites, which contain minor intercalations of metamafic, orthogneiss and mylonitic rocks (Fig. 4.3). Greyish orthogneiss of granodioritic to tonalitic composition occurs as discontinuous lenses up to 10 m long in outcrops and up to 2 km in map view (Fig. 4.3). They are composed of

plagioclase, K-feldspar, biotite, hornblende and quartz, together with accessory zircon and opaque minerals and with a foliation defined by the preferred orientation of biotite and hornblende. Lenses of granitic leucosomes concordant with the S_1 foliation and with thickness from 2 to 40 cm are common.

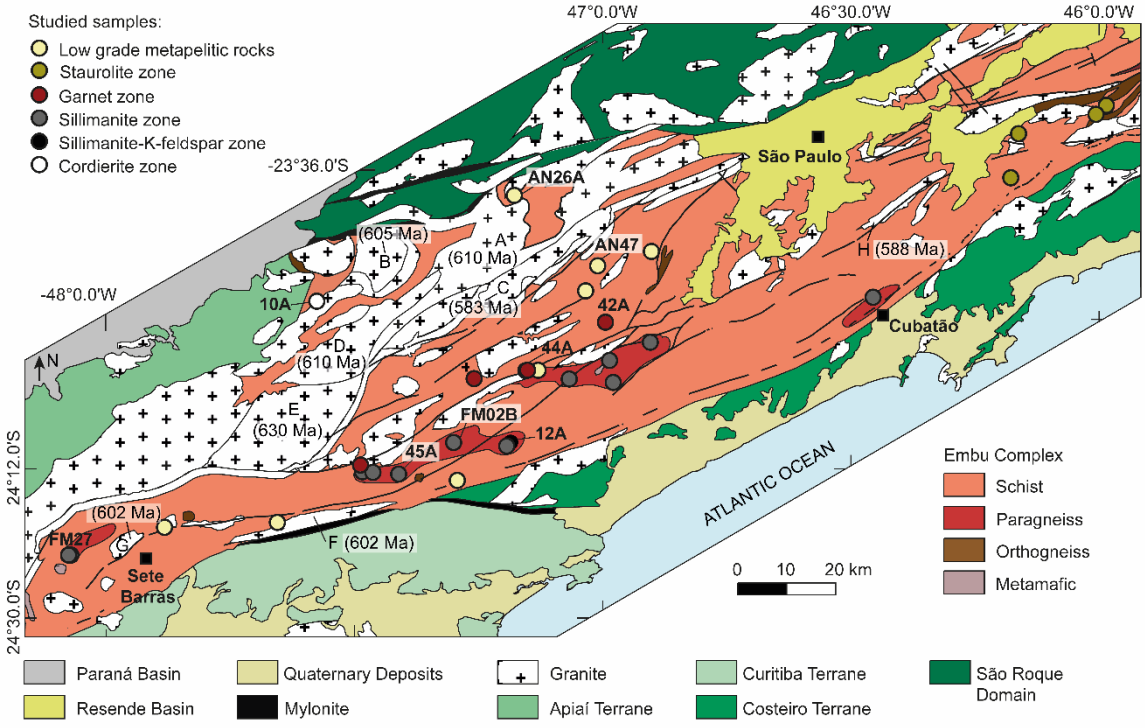

Figure 4.3. Geological map of southwestern Embu Terrane showing the site of studied samples. A: Ibiúna granite (Janasi et al., 2001); B: Piedade Suite (Janasi et al., 2001); C: Caucaia granite (Alves et al., 2013); D: Tapiraí granite (Janasi et al., 2001); E: Jurupará granite (Janasi et al., 2001); F: Juquiá granite (Passarelli et al., 2019); G: Sete Barras granite (Passarelli et al., 2019); H: Mauá granite (Filipov and Janasi, 2001). Geographic coordinates, WGS84 datum. Modified from Perrotta et al. (2005).

The metapelites comprise schists and paragneisses. Locally, quartzite and calcsilicate rocks are also present. Mica schist is the dominant rock type from the Embu Complex and is composed of biotite, muscovite, garnet and quartz (Fig. 4.4a and b). It has a fine-grained lepidoblastic texture defined by the preferred orientation of muscovite and biotite, defining an S_{cs} continuous schistosity. The schistosity has a planar geometry, with a mean orientation of N50ºE with a spread up to N80ºE and a dominant dip of ~70º southeast and a secondary dip direction to the northwest. Locally, the S_{cs} is folded and cut by an asymmetric crenulation cleavage S_{cr}. Tourmaline and opaque minerals are

common secondary phases. Locally, staurolite is also present. The paragneiss is a dark-coloured, fine to medium-grained lepidoblastic rock (Fig. 4.4c, d and e), sometimes with millimetre-scale alternations of white and grey bands (Fig 4.4d and e). White bands are composed of K-feldspar, plagioclase, sillimanite and quartz and grey bands by fine-grained biotite, muscovite, sillimanite, quartz and plagioclase. Cordierite is locally present.

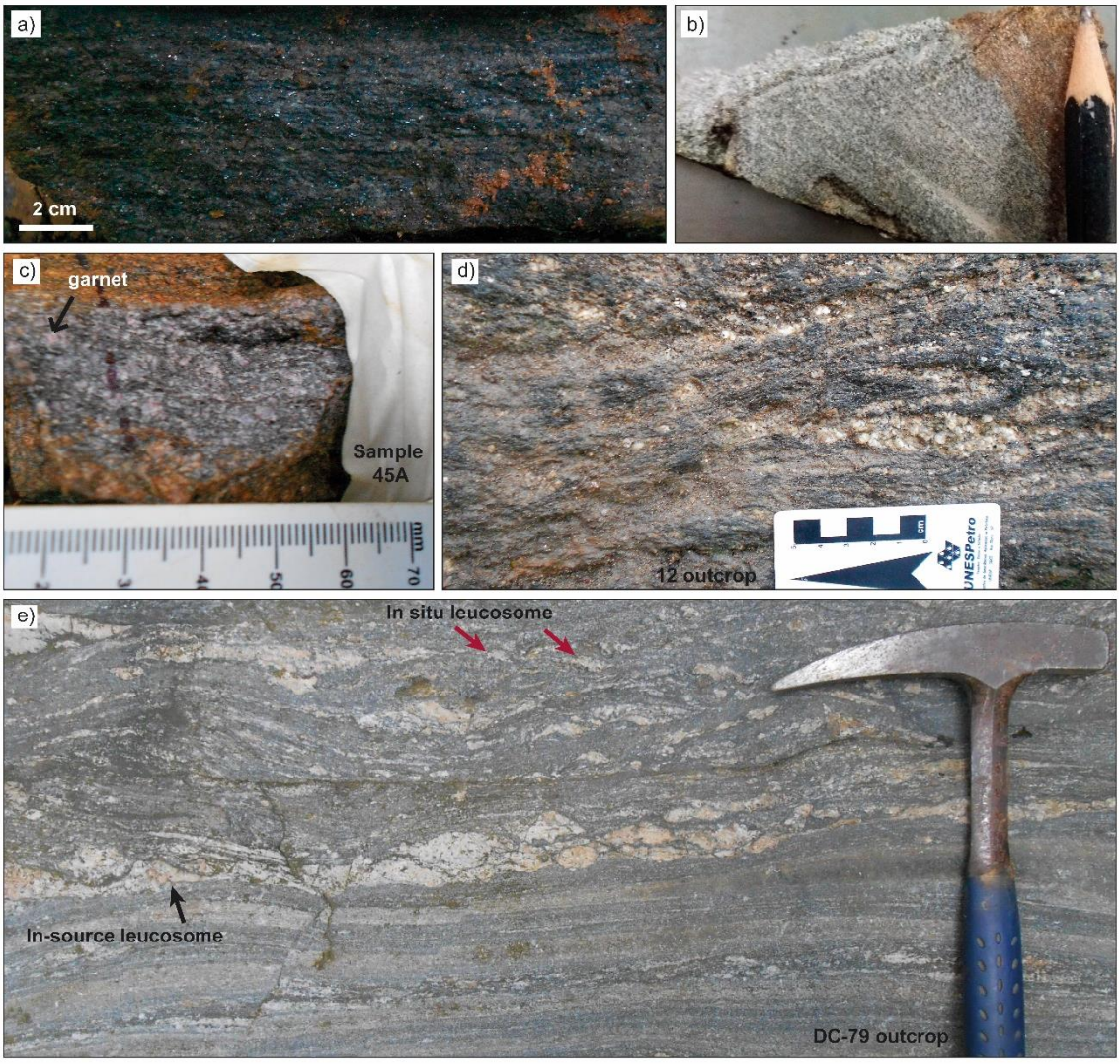

Figure 4.4. photographs showing the different dominant rock types from the Embu Complex. a) and b) schist, the dominant metapelite in the westernmost portion of the Embu Complex; c), d) and e) dark-coloured, medium to coarse-grained, granoblastic paragneiss.

Granitic leucosomes are present in most of the metapelites, but are more abundant in the paragneiss. They are medium to coarse-grained, granoblastic and range between 1

and 20 cm in thickness. The leucosomes occur as in situ and in-source according to the classification of Sawyer (2008). In situ leucosomes are composed of aggregates of quartz + plagioclase + cordierite with grains up to 0.5 mm or with K-feldspar megacrystals up to 1 cm long (Fig. 4.4e, red arrows). In-source leucosomes occur parallel to the S_{cs} foliation, usually have a lenticular shape and are composed of aggregates of quartz + plagioclase + K-feldspar with grains of up to 2 mm (Fig. 4.4e, black arrow).

4.5. Metamorphism

4.5.1. Sample description

Based on sample descriptions and petrographic observations, five regional metamorphic zones were recognized in the metapelites: garnet, staurolite, sillimanite, sillimanite–K-feldspar and cordierite zones (Fig. 4.3). To the south of São Paulo city, the metamorphic grade increases from NW to SE. Staurolite zone rocks are primarily composed of biotite, muscovite, staurolite, garnet and quartz, and only occur to the east of São Paulo city (Fig. 4.3). Lower grade metapelitic rocks composed of biotite, muscovite, quartz and opaque oxide minerals occur associated with major shear zones throughout the studied area.

Representative samples of the high-grade metamorphic zones (sillimanite, sillimanite–K-feldspar and cordierite zones) were studied in detail. AFM diagrams are presented in Supplementary Information B. Mineral chemical analyses were performed on three representative samples, and one each from the sillimanite (sample 45A), sillimanite–K-feldspar (sample 12A), and cordierite zones (sample 10A). Mineral chemical analyses were conducted on biotite, garnet, K-feldspar, plagioclase and cordierite (Supplementary Information C).

Sillimanite zone

Sillimanite zone sample 45A has a medium to coarse-grained (0.03 to 2.0 mm) granolepidoblastic texture and contain the mineral assemblage quartz + biotite + garnet + sillimanite + plagioclase + titanite + leucosome. Zircon, monazite and ilmenite occur as accessory minerals. Biotite and sillimanite have a preferred orientation, defining the S_{cs} schistosity (Fig. 4.5c). Biotite from sample 45A has a Ti content of 0.19–0.24 apfu and a X_{Mg} of 0.54–0.57 (X_{Mg}= (Mg / (Fe + Mg)) (Fig. 6a). Garnet occurs as rounded

porphyroblasts (0.05 to 1.5 mm) and is partially replaced by retrograde biotite along with fractures. The X_{Alm} content increases (from 0.72 to 0.75) and the X_{Pyr} content decreases (0.20 to 0.25) towards the rim (Fig. 4.6b).

Sillimanite–K-feldspar zone

Sillimanite–K-feldspar zone sample 12A has a medium to coarse-grained granolepidoblastic texture constituted by the assemblage quartz + biotite + sillimanite + garnet + K-feldspar + plagioclase + leucosome (Fig. 4.5d, e and f). Zircon, monazite and ilmenite occur as accessory minerals. Biotite and sillimanite define the S_{cs} schistosity. Garnet porphyroblasts (50 to 2500 µm) have an anhedral shape being replaced by quartz and biotite. Some K-feldspar grains contain rounded quartz inclusions. Biotite from sample 12A has a Ti content of 0.19 to 0.24 apfu (Fig. 4.6a). Garnet rim-core-rim analytical chemical profile and the X-ray element map show a flat profile with a weak X_{Sps} enrichment and X_{Pyp} and depletion towards the rim (Fig. 4.6c). K-feldspar is homogeneous in composition with X_{Or} varying between 0.86 and 0.92 (where X_{Or} = K / (Ca + Na + K)).

Cordierite zone

Cordierite zone rocks (sample 10A) are restricted in the study area, corresponding to a transitional vein-structured migmatite. The residue is formed by biotite + sillimanite + cordierite + K-feldspar + plagioclase + quartz + ilmenite, and presents a fine to medium-grained lepidoblastic texture. The preferred orientation of biotite + muscovite + sillimanite defines the S_{cs} foliation. Biotite has an intermediary Ti content (0.15–0.21 apfu) and lower values of X_{Mg} (0.31–0.36) compared with the other samples (Fig. 6a). The leucosome presents a medium to coarse-grained granoblastic texture and occurs as in situ and in-source leucosomes according to the classification of Sawyer (2008) (Fig. 4.5g). In situ leucosomes are composed of quartz + plagioclase + cordierite with grains up to 0.5 mm.

Cordierite occurs as a matrix phase with sillimanite inclusions. Cordierite has an X_{Mg} content between 0.49 and 0.51 (where X_{Mg} = Mg / (Fe + Mg)). In-source leucosomes are composed of quartz + plagioclase + K-feldspar with grains up to 2 mm. K-feldspar is

homogeneous in composition with X_{Or} varying between 0.85 and 0.92. The anorthite content in plagioclase varies from An_1 to An_{25}.

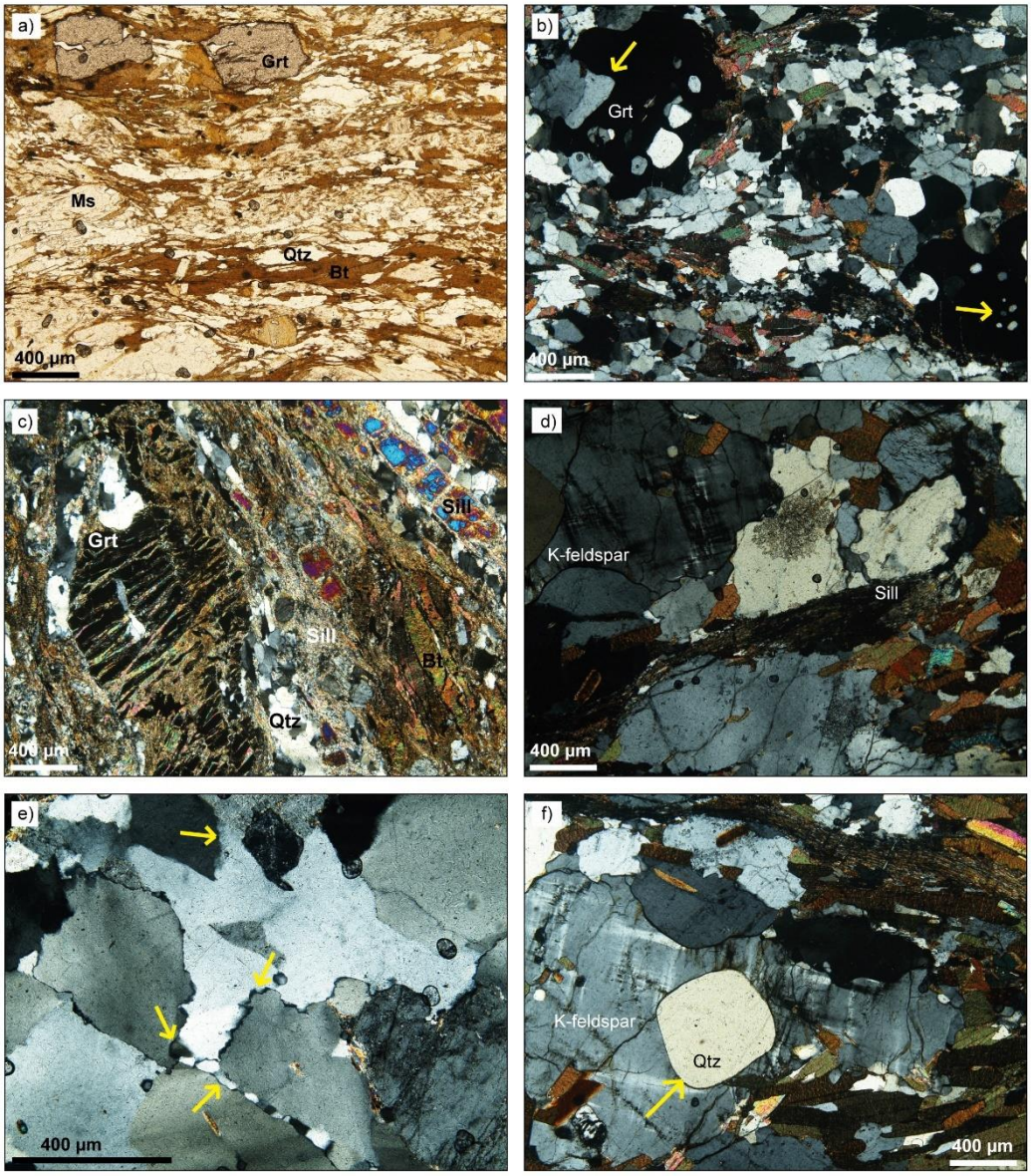

Figure 4.5. Photomicographs of the representative from lithotypes from the Embu Complex. a) biotite + muscovite + quartz + garnet + tourmaline assemblage representing low-grade metapelitic rocks; b) coarse-grained garnet being partial consumed to form quartz; c) quartz + biotite + garnet + sillimanite + plagioclase + titanite mineral assemblage representing sillimanite zone; d) K-feldspar and sillimanite occurrence indicate the fluid-absent muscovite melting reaction; e) evidence of partial melting by the corroded quartz grains along the rims; f) evidence of partial melting by the K-feldspar surrounding corroded grains of quartz recording melt around quartz grain; g) vein-structured migmatite from cordierite zone (sample 10A). The residue is formed by biotite + sillimanite + cordierite + K-feldspar + plagioclase + quartz + ilmenite. The leucosome presents a medium to coarse-grained granoblastic texture and occurs as in situ and in-source leucosomes.

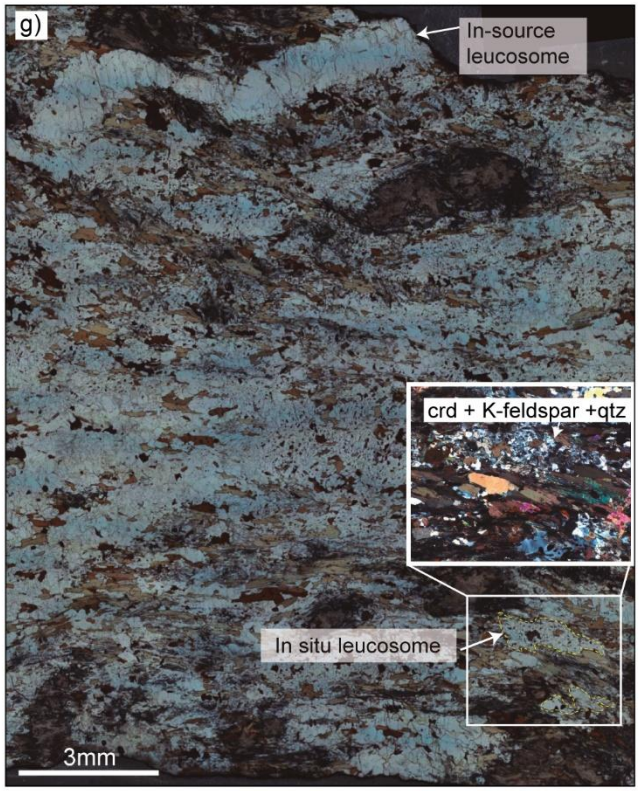

Figure 4.5. *cont.*

4.5.2. Phase equilibria modelling and P–T conditions

The metamorphic P–T conditions of the three highest metamorphic grade assemblages (sillimanite, sillimanite–K-feldspar and cordierite zones) were constrained based on the quantitative P–T isochemical phase diagrams and mineral compositional isopleths and modes calculated using the Perple_X software, version 6.7.5 (Connolly, 2005). The isochemical phase diagrams were calculated using the measured XRF bulk rock composition for samples 12A and 10A, and a melt reintegrated composition for sample 45A (see section 5.2.1), presented in Supplementary Information D. Analytical procedures for isochemical phase diagram modelling are described in Supplementary Information A.

Sillimanite zone

The presence of sillimanite and trondhjemitic leucosomes, and the absence of muscovite and K-feldspar suggest that sample 45A reached the fluid-present muscovite melting reaction (1) within the stability field of sillimanite, but the rock did not cross the fluid-absent muscovite melting reaction (2) (Spear et al., 1999).

muscovite + albite + quartz + H_2O = sillimanite + liquid (1)

muscovite + albite + quartz = sillimanite + K-feldspar + liquid (2)

Sample 45A comprises a residual neosome where all the leucosome was extracted, as indicated by the scarcity of feldspar and the absence of muscovite. Leucosome depletion is reflected in the measured bulk rock composition, which is poor in Na_2O and CaO contents (0.07 and 0.17 wt.%, respectively). The modeled bulk composition was recalculated by adding an amount of 8 vol.% of melt, equivalent to the 8 vol. % proportion of leucosome measured in outcrop, taking the melt composition produced in experimental melting of a metapelite sample under conditions of 750 ºC, 6 kbar and 1 wt.% of added water (Patiño Douce and Harris, 1998) and using the single-step melt-reintegration method (White et al., 2004; Bartoli, 2017). The P–T pseudosection of sample 45A is shown in Fig. 4.7a, with the modeled bulk composition indicated on the bottom. Garnet, biotite, feldspar and quartz are the dominant phases in most of the fields. Muscovite is stable over a restricted P–T range of 650–750 °C and above 8.7 kbar. The peak metamorphic assemblage is represented by the field biotite + garnet + sillimanite + plagioclase + ilmenite + quartz + melt and is stable between 700 to 790 ºC and 5.6 to 8.5 kbar. The peak assemblage field was contoured with compositional isopleths of X_{Alm} and X_{Grs} in garnet and X_{Mg} in biotite and the measured compositions indicate conditions of 750–780 ºC and 7.5–8.5 kbar (Fig. 4.7a, yellow field).

Sillimanite–K-feldspar zone

The presence of sillimanite and K-feldspar and abundant outcrop-scale granitic leucosomes in sample 12A is evidence for partial melting by the fluid-absent muscovite melting reaction (2). Figure 4.7b shows the equilibria mineral assemblages modelled for sample 12A. Biotite is stable throughout most of the P–T range except at the higher T and lower P extremity. The peak metamorphic assemblage is represented by the field biotite + garnet + sillimanite + K-feldspar + melt + quartz + ilmenite, and is stable within 760–860 ºC and 4.9–9.1 kbar. Compositional isopleths of X_{Alm} and X_{Grs} in garnet and X_{Mg} in biotite were calculated and the measured compositions constrain conditions of 770–780 ºC and 8.5–9.2 kbar (Fig. 4.7b, orange field).

Cordierite zone

The presence of cordierite, K-feldspar and granitic leucosome in sample 10A is evidence for a fluid-absent biotite melting reaction producing peritectic cordierite and K-feldspar. The P–T pseudosection computed for the sample 10A is shown in figure 4.8. The peak metamorphic assemblage is represented by the narrow field biotite + cordierite + plagioclase + K-feldspar + melt + quartz + ilmenite, which is stable between 745–810 ºC and 2.8–4.5 kbar. The intersection of compositional isopleths of X_{Mg} in biotite and cordierite and Ti in biotite constrain conditions of 775–805 ºC and 3.6–4.5 kbar (Fig. 4.8, red field).

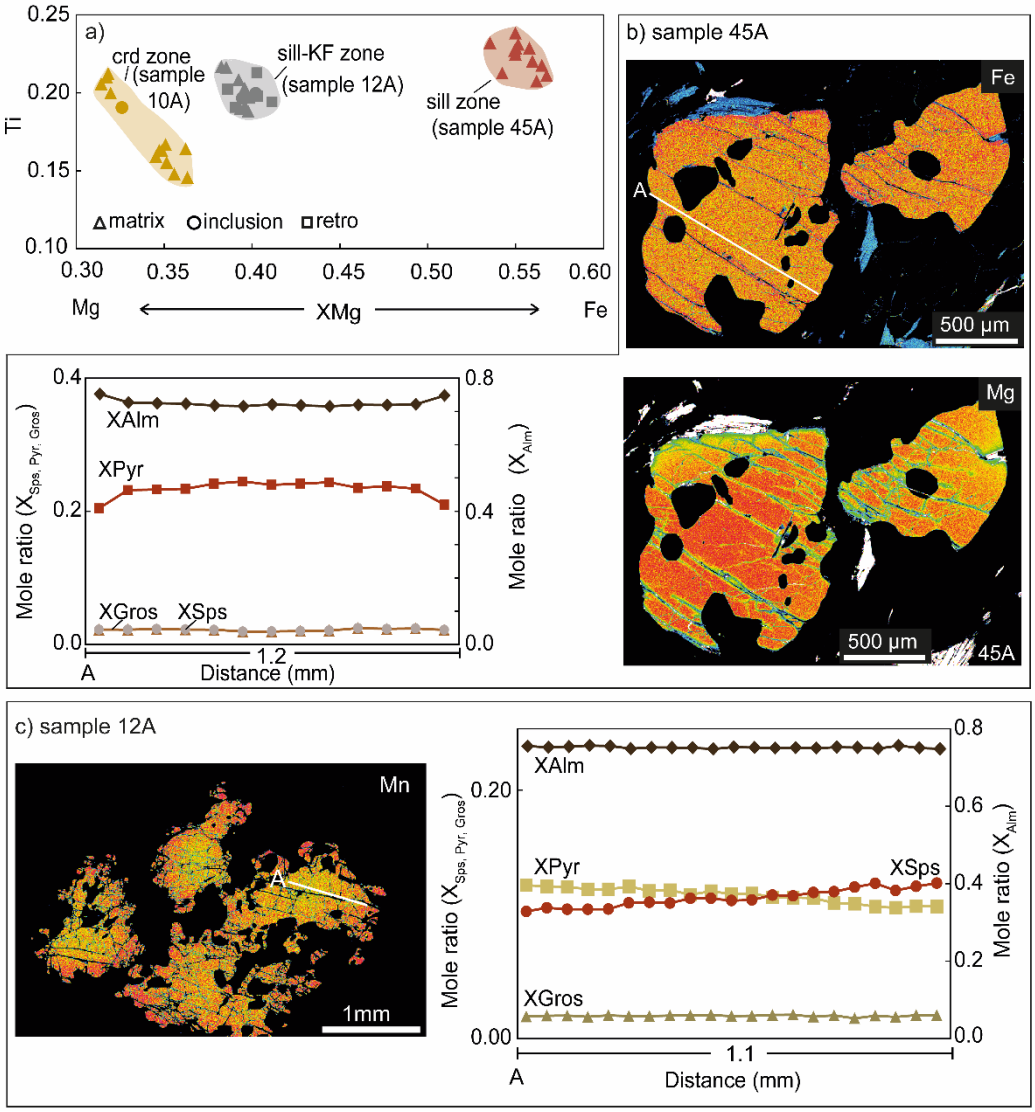

Figure 4.6. Mineral chemical data from the representative samples of the high-grade metamorphic zones. a) XMg and Ti contents for matrix biotite; b) garnet chemical data from sample 45A, including X-ray element maps of Fe and Mg and representative chemical zoning profiles showing the variations in almandine, pyrope, grossular and spessartine contents and c) garnet chemical data from sample 12A, including, X-ray element maps of Mn and the representative chemical zoning profiles.

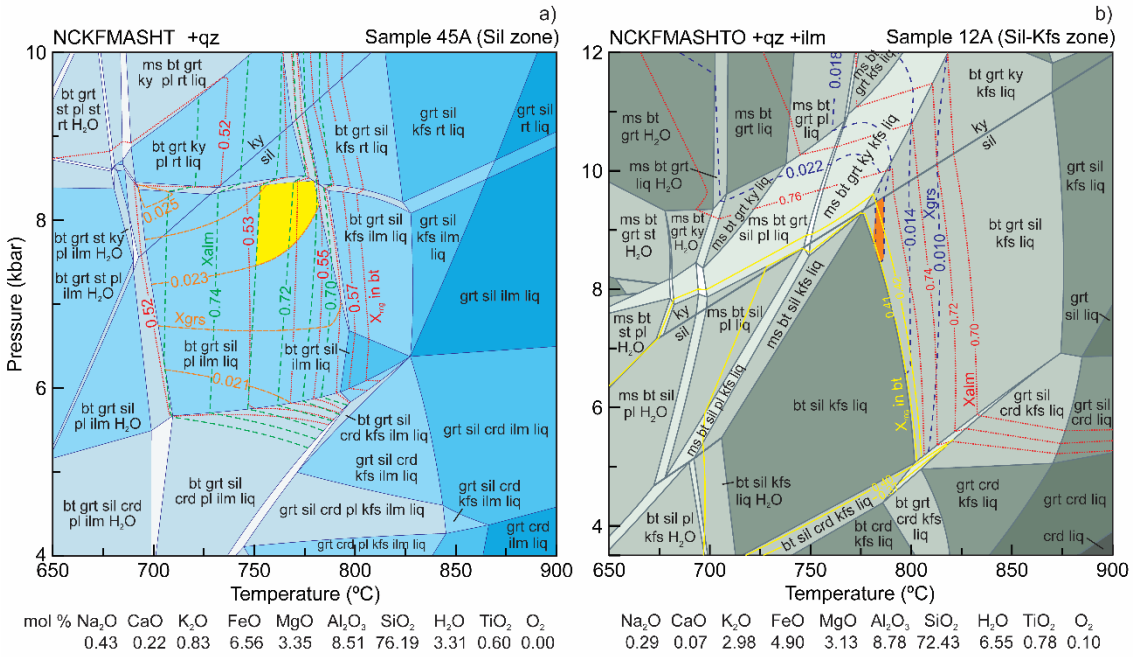

Figure 4.7. P–T equilibrium assemblage diagrams of sample 45A of the sillimanite zone (a) and sample 12A of the sillimanite-K-feldspar zone (b). Also shown are the best-fit peak P-T conditions estimated using intersections of compositional isopleths of garnet and biotite within the stability field of peak mineral assemblages observed in thin sections. Modelled bulk compositions are indicated at the bottom of each diagram. Abbreviatures for minerals after (Whitney and Evans, 2010).

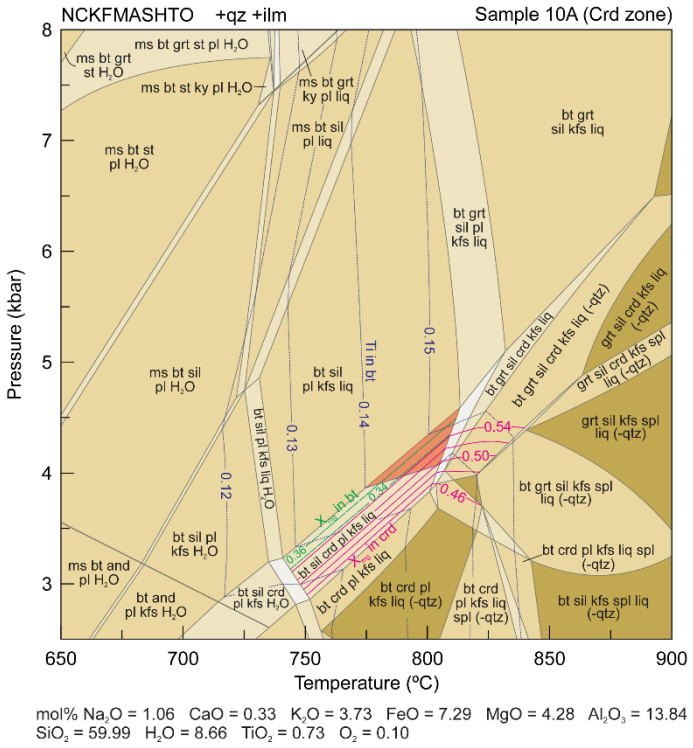

Figure 4.8. P–T pseudosection for sample 10A (cordierite zone). Modelled compositions are indicated at the bottom of the diagram. Also shown are the best-fit peak P–T conditions estimated using intersections of compositional isopleths of XMg in cordierite and Ti and XMg in biotite within the stability field of peak mineral assemblage observed in thin section. Abbreviatures for minerals after (Whitney and Evans, 2010).

4.6. Geochronology and mineral trace element composition

4.6.1. Monazite composition and U–Pb age data

Three representative samples of metasedimentary rocks from the Embu Complex were analyzed for in situ monazite U–Pb geochronology and trace element composition. Samples 45A and FM02B are representative of the sillimanite zone and sample 12A of the sillimanite–K-feldspar zone. Sample descriptions and monazite BSE images are presented in Supplementary Information B and E, respectively. We plotted all the data on concordia diagrams, displaying data discarded from the age calculation with grey ellipses. The table with isotopic ratios and ages are presented in Supplementary Information F. Analytical procedures for U–Pb geochronology and trace element analysis are described in Supplementary Information A.

Monazite grains from all the samples have anhedral to subhedral shapes with a grain size between 10 and 80 µm. They are divided into four different types of textural domains. Type-1 monazite grains occur as inclusions in garnet or at the margin of the garnet. Type-2 monazite occurs as inclusion in biotite in all samples. Type-3 monazite occurs in contact with apatite in sample FM02B and type-4 monazite is the dominant textural domain, occurring dispersed in the matrix of all samples.

Sample 45A presents three different types of monazite, type-1, type-2 and type-4 (Fig. 4.9a). Grain shapes range from anhedral to rounded and grain size vary from 20 to 50 µm in type-1 and type-2 and from 20 to 200 µm in type-4. All monazite types present a homogeneous internal texture in CL images (Fig. 4.9b). Twenty-eight REE and U–Pb spot analyses were obtained from 27 zircon grains. The chondrite normalized REE pattern has a strong depletion trend from LREE to HREE with a strong negative Eu anomaly and a spread in HREE from 10^0 to 10^2 (Fig. 4.9b). Some grains also present a positive Er and Yb anomaly. All the analyses are distributed around the concordia line between 850-690 Ma, with a large concentration of data ca. 770-760 Ma (Fig. 4.9c). The oldest age, 831 ± 23 Ma, corresponds to type-1 monazite, which occurs as an inclusion in garnet near a fracture (Fig. 4.9a, grain 02) All other type-1 monazite spots define the large concentration of data at ca. 770-760 Ma. Type-2 monazite (n=2) also plots within this concentration of data. Additionally, although the majority type-1 and type-2 monazites are enriched in HREE compared to the majority of type-4 monazites, they all overlap and we interpret all the monazite types as being in chemical equilibrium within the peak metamorphic assemblage.

Sample FM02B presents the four monazite types (Fig. 4.9d). All of the types present shapes varying from rounded anhedral to subhedral and a grain size varying from 20 to 400 µm. Internal textures vary from homogeneous to cloudy irregular zoning (Fig. 4.9e). Forty-one REE and U–Pb spot analyses were obtained from 26 zircon grains. The chondrite normalized REE pattern has a strong depletion trend from LREE to HREE with a strong negative Eu anomaly and a spread in HREE from 10^1 to 10^2 (Fig. 4.9e). The analyses are concentrated on the concordia line between 800-690 Ma, with a large concentration of data ca. 770 Ma (Fig. 4.9c). We interpret all the monazite types being in chemical equilibrium with the peak metamorphic assemblage, and there is overlap of the chondrite normalized REE pattern and age between the four different monazite types. Excluding 10 visible discordant spots, 33 spots define a $^{206}Pb/^{238}U$ concordia age of 754 ± 1 Ma (MSWD = 0.17). A similar age with a large MSWD is defined including the visible discordant spots (Fig. 4.9f).

Sample 12A presents type-2 and type-4 monazite (Fig 4.9g). Type-2 has a predominant subhedral shape and type-4 a rounded anhedral shape. However, both shapes occur in both monazite types. In addition, both monazite types present a grain size varying from 15 to 100 µm and a dominant homogeneous internal texture, but irregular zoning textures also occur (Fig. 4.9h). Twenty-seven REE and U–Pb spot analyses were obtained from 25 zircon grains. The chondrite normalized REE patterns have a strong depletion trend from LREE to HREE with a strong negative Eu anomaly and a concentration in HREE between 10^2 to 10^3 (Fig. 4.9h). The oldest $^{206}Pb/^{238}U$ age (831 ± 14 Ma) corresponds to a type-2 monazite (Fig. 4.8h, grain 21) but the remaining type-2 monazite ages overlap with type-4 monazite ages, as well as for the REE content. Considering this, we interpret all the monazite types being in chemical equilibrium within the peak metamorphic assemblage. All the spots (excluding one visible discordant spot) define a concordia age of 768 ± 1 Ma (MSWD = 0.3) (Fig. 4.9i).

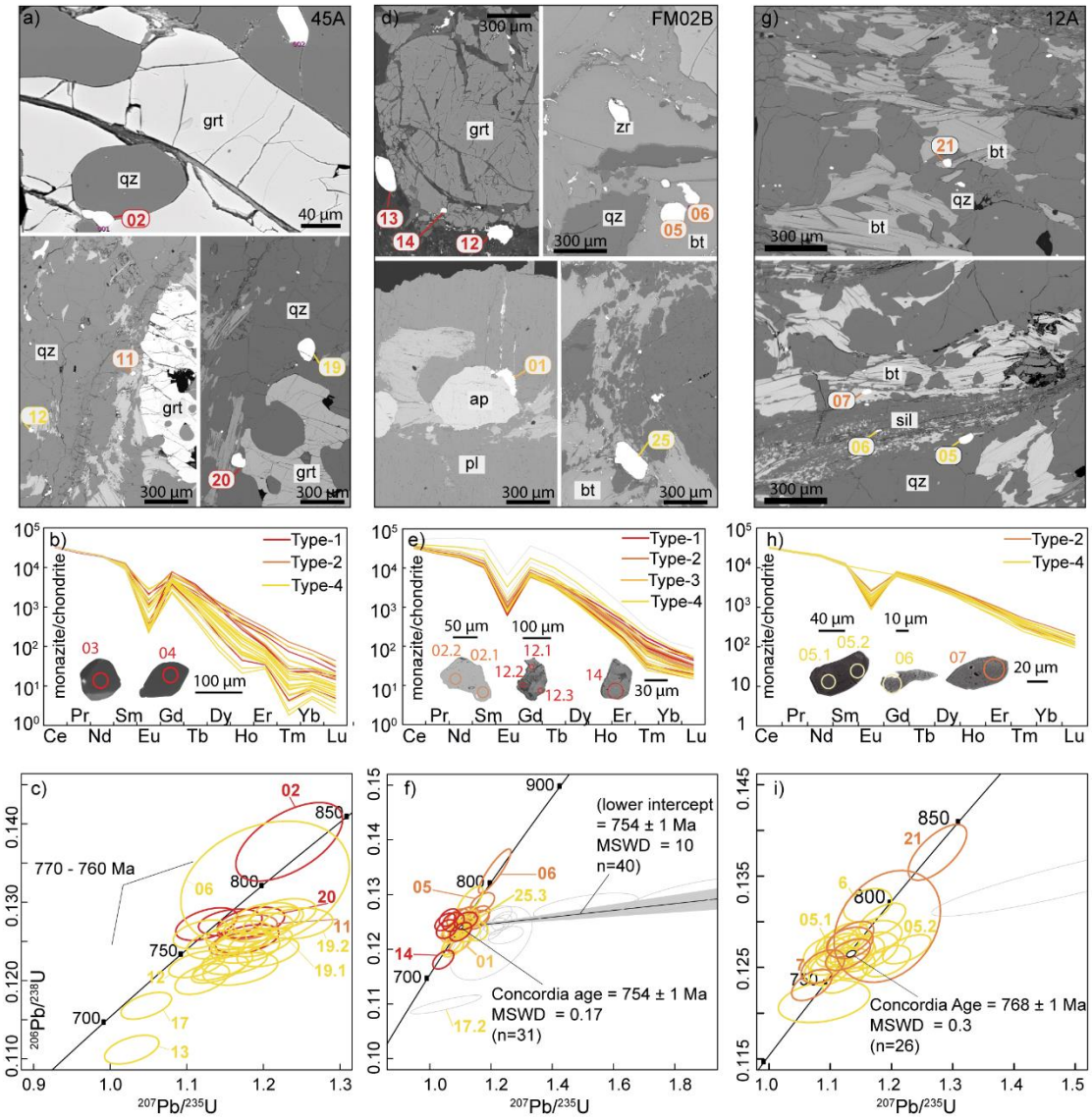

Figure 4.9. Monazite representative BSE images, trace element composition and U–Pb isotopic ages from metasedimentary samples of the Embu Complex. a) d) and g) representative BSE images of the different monazite types described for samples 45A, FM02B and 12A, respectively; b), e) and h) chondrite normalized diagram of the REE composition for the samples 045A, FM02B and 12A, respectively, with monazite types distinguished by different ellipses colours. c), f) and i) concordia diagrams for the samples 45A, FM02B and 12A, respectively, with monazite types distinguished by different ellipses colours. Grey ellipses represent discordant data. Data-point error ellipses are 2σ.

4.6.2. Zircon composition and U–Pb age data

Zircon grains from five representative samples of metasedimentary rocks (45A, FM-27, 10A, AN-26A, AN-47) of the Embu Complex were analyzed for U–Pb geochronology. Additionally, trace element concentrations were acquired on grains from

samples 45A and 10A. Samples 45A and FM-27 are paragneisses representative of the sillimanite zone, sample 10A is representative of the cordierite zone and samples AN-26A and AN-47 are quartzites. Sample descriptions are in Supplementary Information B and CL images in Supplementary Information E. We plotted all the data on concordia diagrams, displaying the data with a discordance level equal to or higher than 5 % with grey ellipses. Tables with isotopic ratios and ages are shown in Supplementary Information F. Analytical procedures for U–Pb geochronology and trace element analysis are described in Supplementary Information A.

Sample 45A presents zircon grains with external morphology ranging from subhedral to rounded. The main internal textures are a dark and compositionally homogeneous rounded nucleus overgrown by a lighter thin rim (Fig. 4.10a). Thirty-one REE and U–Pb spot analyses were obtained from 26 zircon grains, with 29 concordant data points. The chondrite normalized REE patterns have a trend of enrichment from LREE to HREE with a strong negative Eu anomaly in the majority of the grains. Some grains present a positive Eu anomaly whereas others have a positive Ce anomaly. All the analyses are distributed on or close to concordia between 810-700 Ma. The Th/U ratio of the concordant spots range from 0.02 to 0.09. As the U–Pb data are dispersed within this age interval, we combined textural and trace composition analysis to extract meaningful ages. The difference in Eu pattern has no relationship with the age distribution (Fig. 4.10a). Additionally, there is no correlation between Th/U ratio and age. We analyzed more than one spot in grains that present two distinct textural domains (grains 11, 17, 19, 20, 26, Fig. 9a) and the data show a relationship between the two distinct textural domains and age, within the range of 810-740 Ma and 710-695 Ma (Fig. 4.10a). Using the textural criteria, we calculate the ages for these two distinct domains. Twenty analyses of the older group yield a concordia age of 776 ± 1 Ma (MSWD = 5.8) (Fig. 4.10a) and four analyses of the younger group (spots 14.1, 17.1, 19.2 and 20.2) yield a $^{206}Pb/^{238}U$ weighted mean age of 700 ± 3 Ma (MSWD = 0.92) (Fig. 4.10a).

Sample FM-27 presents rounded zircon grains with partially resorbed cores with oscillatory compositional zoning (lower U contents) and dark homogeneous rims with higher U contents (Fig. 4.10b). Fifteen U–Pb analyses were performed on the cores and rims (Fig. 4.10b). Assuming a maximum of ± 5 % discordance, 10 data points are concordant. The Th/U ratio of the concordant spots range from 0.01 to 1.17. Four analyses (spots 3.1, 6.1, 8.1, 13.1) of high-U of zircon rims have Th/U ratio lower than 0.1 and

define a concordia age of 790 ± 5 Ma (MSWD = 0.09; Fig. 4.10b). The remaining analyses span the age interval from 2004 ± 7 to 1165 ± 18 Ma (Fig. 4.10b).

Sample 10A has zircons with a grain size ranging between 50 and 100 µm with a subhedral to anhedral shape. The internal texture is similar to the previous sample with a lower U oscillatory compositional zoned core with a dark high U and compositionally homogeneous rim (Fig. 4.10c). Frequently, the cores are being consumed to form the rims (49 and 72). Eighty-seven REE and U–Pb spot analyses were obtained from 86 zircon grains, with 19 concordant data points. The Th/U ratio of the concordant spots range from 0.01 to 1.61. The U–Pb data show two discordant trends (1º and 2º, Fig. 4.10c) with similar lower intercept trends and concordant with the $^{206}Pb/^{238}U$ individual ages for the rims with Th/U ratio lower than 0.1 (spots 14.1, 49.1, 72.1, figure 4.10c). The first intercept has a lower MSWD and a higher number of spots compared to the second and present a lower intercept age of 724 ± 4 Ma (MSWD=9.1, n=70). The chondrite normalized REE pattern has an enrichment trend from LREE to HREE with positive and negative Ce and Eu anomalies. The rims 14.1, 49.1, 72.1 present the highest depletion in LREE compared with the remaining concordant data.

In addition to the zircon U–Pb data collected in this work, we interpreted published metamorphic U–Pb data from two more samples (AN-26A and AN-47) from Campanha et al. (2019). Those samples constrain the depositional age of the Embu Complex between 970 and 850 Ma. However, their rims were not the focus of the work. Below, we describe the rims of those two samples.

Sample AN-26A presents prismatic to rounded zircons. The majority of zircon grains show a core-rim structure in CL images. The cores display oscillatory zoning with high luminescence and the rims are homogeneous with low luminescence (Fig. 4.10d). Ten spot analyses were conducted on nine zircon rims. The Th/U ratio of the concordant spots range from 0.004 to 0.87. All analytical spots define a linear array on concordia between 800-610 Ma. The dominant zircon texture corresponds to the core-rim structure and are related to the highest concentration of ages between 800-700 Ma (Fig. 4.10d).

The zircon grains from sample AN-47 are rounded or prismatic in shape with sizes from 100 to 180 µm. The majority of zircon grains show a core-rim structure in CL images. Both core and rim display oscillatory zoning, although the luminescence in the core is higher than at the rim, being partially resorbed. Nineteen spot analyses were conducted on rims of eighteen zircon grains. The Th/U ratio of the concordant spots range from 0.02 to 0.28. We used the textural differences between grains combined with Th/U

ratios lower than 0.1 to calculate an age. Ten rim spots in grains with a core-rim structure define a concordia age of at 827 ± 2 Ma (MSWD = 5.2) (Fig. 4.10e).

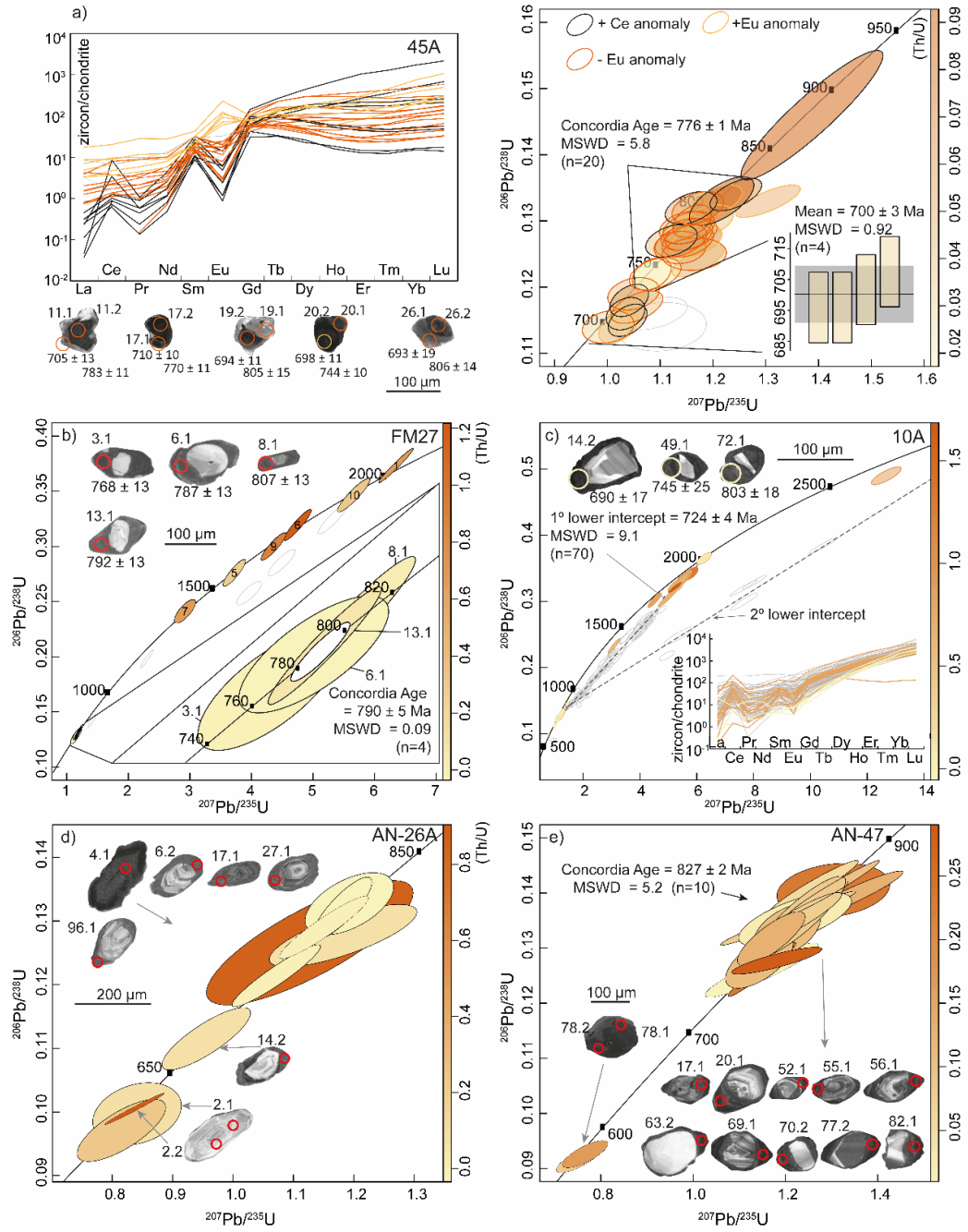

Figure 4.10. U–Pb isotopic age distributions of analyzed zircons from metasedimentary samples of the Embu Complex. Grey ellipses represent discordant data. a) chondrite normalized diagram of the REE composition for sample 45A with representative CL images of the zircon grains with spots colour according to Ce and Eu anomalies. At the left concordia diagram for this sample is shown. Positive Ce and Eu anomalies and negative Eu anomaly are distinguished by different ellipses contours. Data-point ellipses are 2σ; b) concordia diagram for sample FM27. Data-point ellipses are 1σ; c) concordia diagram and chondrite normalized diagram of the REE composition for sample 10A, highlighting the three younger rims with light orange. Data-point ellipses are 2σ; d) and e) concordia diagram of the non-detrital spots of the samples AN-26A and AN-47, respectively. Data-point ellipses are 1σ.

4.6.3. Apatite composition and U–Pb age data

One representative sample (FM02B) of metasedimentary rock from the sillimanite zone was analyzed for in situ apatite U–Pb geochronology and trace element composition. Apatite BSE images and isotopic ratios and ages for the analyses are shown in Supplementary Information E and F, respectively. Apatite grains are euhedral to subhedral with a grain size between 40 and 400 µm. Most grains are dispersed in the matrix (Fig. 4.11a, apatite 50 and 51), sometimes in contact with biotite (Fig.4.11a, apatite 23 to 29), monazite (Fig. 4.11a, apatite 24) and garnet. Occasionally, apatite is included in biotite and biotite also occurs included in apatite, highlighting the coexistence of these two phases. Sample description is in Supplementary Information B. Analytical procedures for U–Pb geochronology and trace element analysis are described in Supplementary Information A.

Sixty-one analyses from 58 apatite grains were acquired. The ^{204}Pb non-corrected radiogenic isotopes ratios were plotted in a Tera-Wasserburg diagram (Fig. 4.11b). Only five visibly discordant data were excluded (spots 09.1, 09.2, 39, 42 and 53) from the age calculation (Fig. 4.10b, grey ellipses). Data present a common dispersion trend along the inverse isochron and the lower intercept yields an age of 550 ± 9 Ma (MSWD = 2.9). The chondrite normalized REE pattern has a positive and negative trend for LREE and HREE, respectively with notable negative Eu anomaly (Fig. 4.11c).

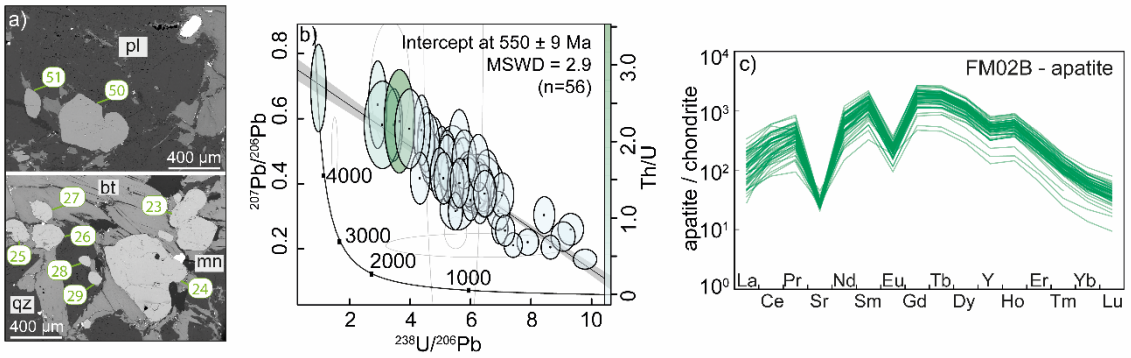

Figure 4.11. Apatite textures, U–Pb age and composition data from metasedimentary sample FM02B. a) Representative BSE images. b) Tera-Wasserburg concordia diagram coloured according to the Th/U ratio. Grey ellipses represent visible discordant data. Data-point error symbols are 2σ. c) chondrite normalized diagram of the REE composition.

4.6.4. Muscovite and biotite Rb–Sr age data

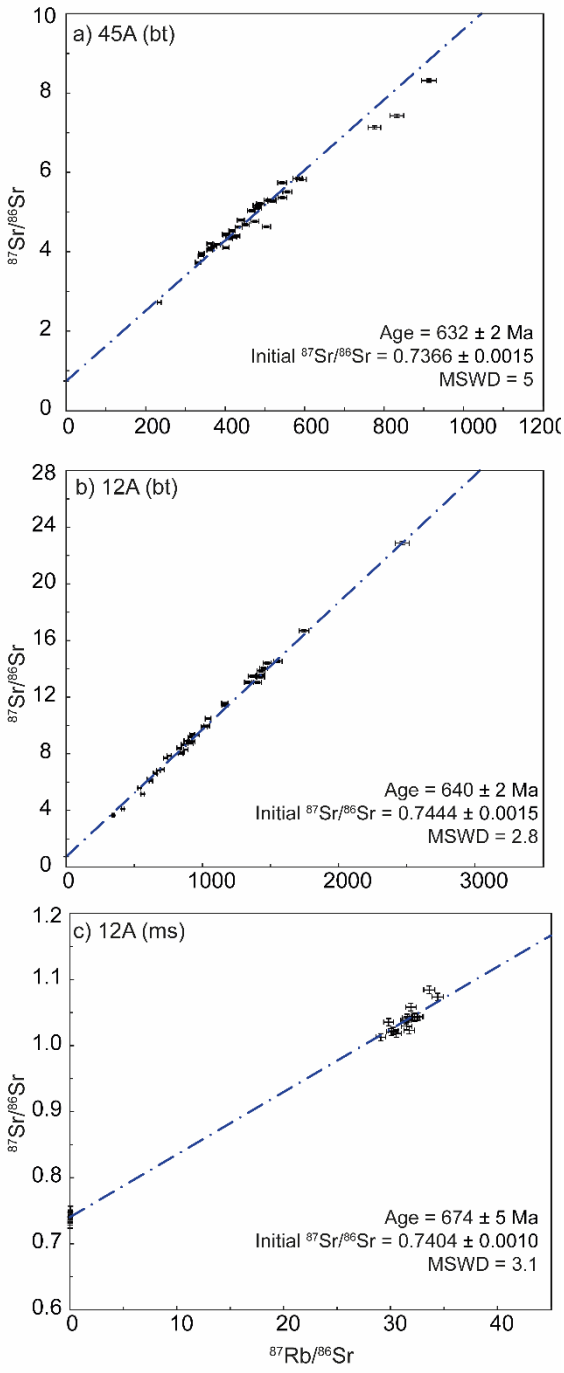

Figure 4.12. Rb–Sr isochrones from metasedimentary samples of the Embu Complex. a) biotite from sample 45A; b) biotite from sample 12A; c) muscovite from the sample 12A. Data-point error symbols are 1σ.

Two representative samples (045A, 12A) of metasedimentary rocks from the sillimanite and sillimanite–K-feldspar zones, respectively, were analyzed for in situ mica Rb–Sr isotope analysis. Biotite was analyzed in both samples, whereas muscovite was analyzed only in sample 12A. Table with isotopic ratios is shown in Supplementary Information F. The biotite from sample 45A presents average $^{87}Rb/^{86}Sr$ and $^{87}Sr/^{86}Sr$ values of 474.1681 and 9.9050, respectively. Micas from sample 012A present average $^{87}Rb/^{86}Sr$ values of 1014.0506 (biotite) and 31.5886 (muscovite) and $^{87}Sr/^{86}Sr$ values of 9.8797 (biotite) and 1.0395 (muscovite). Analytical procedures for in situ Rb–Sr dating are described in Supplementary Information A.

Three different isochrons were created using the monazite $^{87}Rb/^{86}Sr$ as an anchor point. The biotite isochron from sample 45A yielded an age of 632 ± 2 Ma (MSWD = 5) with an initial $^{87}Rb/^{86}Sr$ from monazite of 0.0040 (Fig. 4.12a). The biotite isochron from sample 12A yielded an age of 640 ± 2 Ma (MSWD = 2.8) with an initial $^{87}Rb/^{86}Sr$ from monazite of 0.0488 (Fig. 4.12b) and the muscovite isochron yielded and age of 674 ± 5 Ma (MSWD = 3.1) with an initial $^{87}Rb/^{86}Sr$ from monazite of 0.0488 (Fig. 4.12c).

4.7. Discussion

4.7.1. Tonian metamorphic evolution for the Embu Complex

The three studied metamorphic zones from the Embu Complex reveal two distinct baric regimes: medium- to high pressure in the sillimanite (750–780 ºC and 7.5–8.5 kbar) and sillimanite–K-feldspar (770–780 ºC and 8.5–9.2 kbar) zones and low pressure in the cordierite zone (775–805 ºC and 3.6–4.5 kbar). Similar low pressure P–T conditions were described for the central portion of the Embu Complex (Vieira, 1996) (Fig. 4.13).

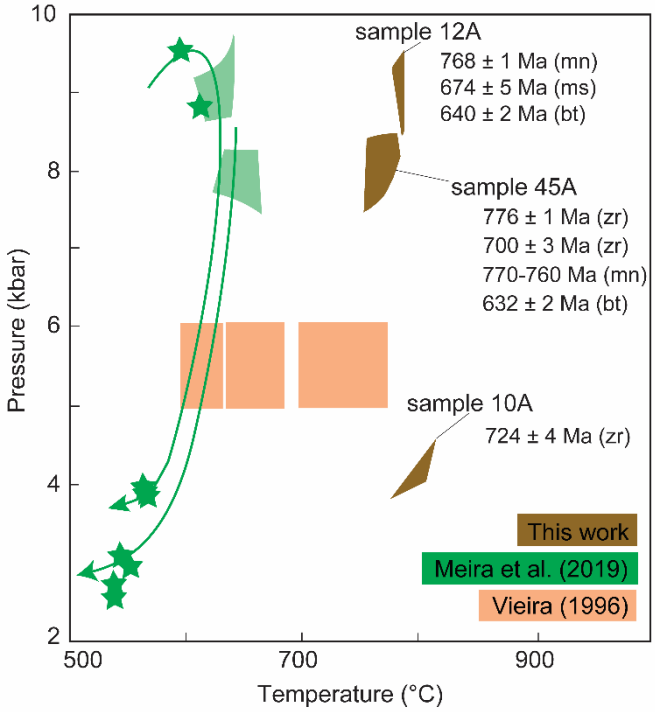

Figure 4.13. Summary of the P-T-t conditions for the samples modeled in this work for the Embu Complex. Samples 12A (garnet zone) and 10A record the highest and lowest pressure condition, respectively. Mz = monazite; zr = zircon; ms = muscovite and bt = biotite. For the samples 12A, 45A and 10A, monazite and zircon data are U–Pb ages and biotite and muscovite data are Rb–Sr isochron ages. Additional published data is also showed.

The prograde P–T evolution of a metapelitic rock is usually preserved in mineral growth zoning or in mineral inclusions. However, the garnet zoning profiles of the high-grade metamorphic zones from the Embu Complex rocks (Fig. 4.6), show a weak to absent compositional zoning. Moreover, biotite grains included in garnet porphyroblasts have a similar compositional trend of X_{Mg} and Ti compared to the biotite in the matrix. Finally, type-1 monazite (included or at the garnet margins) has a chondrite normalized REE pattern and age equal to other monazite types (Fig. 4.9). These lines of evidence indicate that the growth zoning and path were not preserved and the thermodynamic equilibrium was reached within the metamorphic peak stage. Thus, there is no preserved record of the burial and thermal relaxation episodes of the Embu Complex evolution.

The four monazite types present indistinguishable chondrite normalized REE patterns and ages suggesting they were in chemical equilibrium with the peak metamorphic assemblage (Fig. 4.9). Furthermore, there is no relationship between distinct internal textures and ages, and the cloudy patchy areas of BSE images are typical of high-grade monazite (Schulz, 2021). Two distinct textural domains in zircon grains from sample 45A present distinct ages, 776 ± 1 Ma (MSWD = 5.8) and 700 ± 3 Ma (MSWD = 0.92) but with identical chondrite normalized REE patterns (Fig. 4.9). We interpret this feature as a subsequent recrystallization texture within the peak metamorphic assemblage and indicative of a protracted period for high-grade metamorphic conditions with two zircon growth stages.

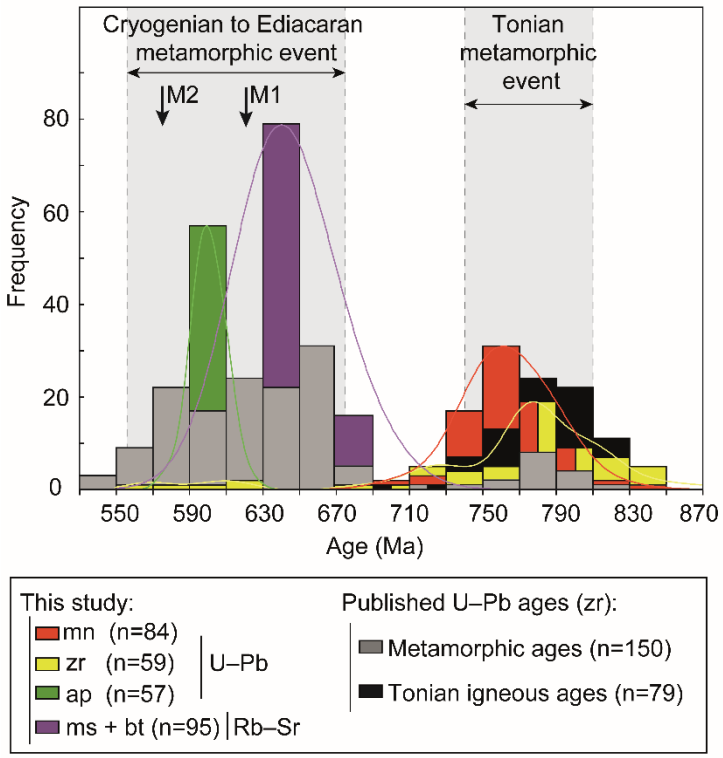

Figure 4.14. Histogram of metamorphic and Tonian igneous ages for the Embu Complex. Zircon U–Pb ages are either 206Pb/238U and 207Pb/235U. The average trendline for the ages acquired in this work is aldo represented. Apatite U–Pb and muscovite and biotite Rb–Sr ages correspond to isochron ages. M1 and M2 correspond to the two Ediacaran metamorphic events of Meira et al. (2015), (Meira et al., 2019a). Abbreviations: mn: monazite; zr: zircon; ap: apatite; ms: muscovite; bt: biotite. Published metamorphic and Tonian igneous ages are from Vlach (2008), Duffles et al. (2016), Silva (2017), Meira et al. (2019a) and Cordani et al. (2002), Silva (2017).

Monazite and zircon U–Pb data from the sillimanite-bearing rocks reveal that this high-grade metamorphic event occurred between 850-690 Ma (Fig. 4.9, 10 and 4.14), with a high concentration of ages at 810–760 Ma (Fig. 4.14), giving a time span of at least ca. 50 Ma for the high-grade conditions at suprasolidus conditions. This time interval is in agreement with monazite chemical ages of 792 ± 7 Ma, 794 ± 10 Ma and 789 ± 10 Ma obtained for paragneiss samples (Vlach, 2008). Metamorphic zircon U–Pb ages are on average 20-50 Ma older than monazite ages, including sample 45A, where both monazite and zircon were dated. This feature is

also described in other Proterozoic terranes (Oyhantçabal et al., 2012; Bose et al., 2021), reflecting distinct grain growth between the minerals (Kelsey et al., 2008).

4.7.2. Tonian magmatism in the Embu Complex

Orthogneiss outcrops derived from a granodioritic to tonalitic protolith are described in the Embu Complex with igneous crystallization ages ranging from 810 to 780 Ma (Cordani et al., 2002; Silva, 2017). Further evidence of felsic magmatism is also recorded in a two-mica granite (Juquiá granite) with a crystallization age of 799 ± 5 Ma (Passarelli et al., 2019), a meta-aplite with a crystallization age of 783 ± 6 Ma, and a metagranite with a crystallization age of 768 ± 8 Ma (Meira et al., 2015). The combination of these ages suggests that the Embu Complex have experienced a period of ca. 40 Ma of igneous activity between 810-770 Ma.

Tonian igneous activity is concomitant with the high-grade metamorphic event documented here and involved a with a period of at least ca. 40 Ma in high-temperature suprasolidus conditions. The majority of the authors relate this magmatism to the final stages of the Rodina break-up and/or the initial stages of a subduction and ocean consumption in the region (Cordani et al., 2002; Silva, 2017; Passarelli et al., 2019). Alternatively, this magmatism has also been related to extensional tectonics and lithospheric thinning (Meira et al., 2015). More isotopic and geochemical data over the orthogneiss rocks of the Embu Complex are needed to clarify this question.

4.7.3. Cryogenian to Ediacaran metamorphic evolution for the Embu Complex

Cryogenian to Ediacaran ages between 675 and 550 Ma are recorded in zircon and apatite U–Pb and biotite and muscovite Rb–Sr data (Fig. 4.10, 4.11, 4.13 and Table 4.1). Six single grain zircon U–Pb ages between 680 and 565 Ma are recorded in two quartzite samples (AN-26A and AN-47) where a relationship with the defined metamorphic zones has not been established. Despite the textural equilibrium of zircon with the main metamorphic mineral assemblage of Embu Complex rocks, these data suggest that these grains are not in chemical equilibrium with the main metamorphic mineral assemblage. This age interval could be associated with the Cryogenian to Ediacaran metamorphic event described for the eastern portion of the Embu Terrane (Meira et al., 2015, 2019a; Duffles et al., 2016; Costa et al., 2017).

Muscovite Rb–Sr age of 674 ± 5 Ma (sample 12A) and biotite Rb–Sr ages of 640 ± 2 Ma (sample 12A) and 632 ± 2 Ma (sample 45A) were obtained for sillimanite-bearing rocks (Fig. 4.11, 4.12 and Table 4.1). The time interval between the high-grade metamorphic conditions recorded in zircon and monazite U–Pb data (810–760 Ma) and biotite and muscovite Rb-Sr data (675-630 Ma) point to a slow cooling path that lasts at least 85 Ma. Considering the average ages and closure temperatures of the Rb–Sr isotopic system for muscovite (500 ± 50 ºC) and biotite (350 ± 50 ºC) (Jäger, 1979), a slow cooling rate of 4.4 ºC/Ma was calculated for sample 12A, where both minerals were analyzed, for the interval between 674 and 640 Ma. These data strongly suggest a retrograde cooling path for the Embu Complex. Using apatite U–Pb closure temperatures of 460–500 ºC (Ribeiro et al., 2020b), the apatite age of 550 ± 9 Ma obtained for sample FM02B correlates with the timing of low-grade regional shear zones estimated in the southern Ribeira Belt

Published data from the eastern portion of the Embu Complex show that the main high-grade metamorphism occurred from Cryogenian to Ediacaran (Meira et al., 2015, 2019a; Duffles et al., 2016; Costa et al., 2017).. A single zircon spot yielding a Tonian metamorphic age of 786 ± 99 Ma is described by Costa et al. (2017). Meira et al. (2015, 2019a) interpret that two metamorphic events, an intermediate-pressure metamorphism (M1) and a low-pressure metamorphism (M2) occurred at ca. 620 Ma and 575 Ma, respectively (Fig. 13). However, the petrological and geochronological data acquired in this work do not record these two distinct Ediacaran groups of metamorphic events.

Meira et al. (2019a) quantified near isothermal decompression paths from 8–10 kbar at 610–650 ºC to 3–4 kbar at 550–570 ºC for the northeastern portion of the Embu Complex. Similar isothermal decompression paths explain the baric regime variation quantified in this work. The last low-pressure high-temperature regime recorded in Embu Complex rocks overlaps the regional metamorphic regime recorded in the Costeiro Terrane (Fig. 4.1), which has been interpreted as an oceanic arc terrane with contribution of juvenile granitic magmatism followed by syn and post-collisional magmatism (Heilbron et al. 2020, and references therein).

Cryogenian to Ediacaran metamorphism is also the main regional metamorphism recorded in all the Ribeira Belt units (Campos Neto and Figueiredo, 1995; Campanha and Sadowski, 1999; Cordani et al., 2002; Heilbron et al., 2008; Faleiros et al., 2011a; Trouw et al., 2013; Meira et al., 2015, 2019a; Duffles et al., 2016; Ricardo et al., 2020). Our data reinforces that the magnitude of the Cryogenian to Ediacaran metamorphism increases

from SW to NE in the Embu Complex obliterating the Tonian metamorphism in the northeast portion of the complex.

Table 4.1. Summary of the geochronological data obtained in this work.

Sample	Lithotype	Metamorphic zone	Method	Mineral	Age (Ma)	Type of age
45A	Paragneisse	Sillimanite	U-Pb (in situ)	Monazite	770-760	Interval age
			U-Pb (in mount)	Zircon	776 ± 1	Concordia
					700 ± 3	Mean age
			Rb-Sr (in situ)	Biotite	632 ± 2	Isochron
FM02B	Paragneisse	Sillimanite	U-Pb (in situ)	Monazite	754 ± 1	Concordia
				Apatite	550 ± 9	Lower intercept
12A	Paragneisse	Sillimanite–K-feldspar	U-Pb (in situ)	Monazite	768 ± 1	Concordia
			Rb-Sr (in situ)	Biotite	640 ± 2	Isochron
				Muscovite	674 ± 5	Isochron
FM-27	Paragneisse	Sillimanite	U-Pb (in mount)	Zircon	790 ± 5	Concordia
10A	Paragneisse	Cordierite	U-Pb (in mount)	Zircon	724 ± 4	Lower intercept
AN-47	Quartzite	-	U-Pb (in mount)	Zircon	827 ± 2	Concordia

4.7.4. Comparison with neighbouring terranes in the southern Ribeira Belt

The southern Embu Complex has a depositional interval between 970-900 Ma with a detrital age signature distinct from the neighbouring terranes and cratons (Campanha et al., 2019). This suggests it was isolated from these blocks, which is consistent with a peripheral or external location with respect to Rodinia rather than an intracontinental setting. Additionally, the relatively short-time difference between accumulation of the southern Embu Terrane (970-900 Ma) and its Tonian high-grade metamorphic event documented in this work (810–760 Ma) is consistent with the terrane being located at or close to a convergent plate boundary (Cawood et al., 2012);

The metasedimentary deposition and volcanic ages of the neighbouring terranes are distinct, with Statherian ages for the basal units of the São Roque Group (Henrique-Pinto et al., 2015, 2018), Calymian ages for the Votuverava and Serra de Itaberaba groups (Juliani et al., 2000; Campanha et al., 2015) and Ediacaran ages for the Curitiba Terrane

(Ricardo et al., 2020). Additionally, all contacts between these units are tectonic, characterized by regional shear zones (Fig. 4.1). All these lines of evidence favour a terrane collage model for the Ribeira Belt evolution from the Tonian to Ediacaran.

4.7.5. Implications for Rodinia and West Gondwana

Accretionary and collisional processes during the Tonian are recognized in South America and other continents (Siga Júnior et al., 2011; Brito Neves and Fuck, 2013; Brito Neves et al., 2014). They were responsible for the formation and reworking of several crustal segments, including metavolcanic-sedimentary successions and magmatic arc associations, and are associated with the top-down processes related to subduction processes and the development of accretionary orogens around the periphery of the Rodinia supercontinent (Cawood et al., 2016; Oriolo et al., 2017).

The Tonian depositional (970–900 Ma), metamorphic (810–760 Ma) and magmatic (810–770 Ma) activity recorded in the Embu Complex, as well as its age of assembly with the Apiaí Terrane, suggest that the unit was in a peripheral position in the Rodinia supercontinent (Campanha et al., 2019). Thus, the Embu Complex represents an older accretionary event during the Tonian along the Rodinia margin that evolved to a collisional orogeny during the Ediacaran related to the West Gondwana assembly, as indicated by the widespread presence of Ediacaran zircon metamorphic overgrowths (Meira et al., 2015, 2019a; Duffles et al., 2016; Costa et al., 2017; Campanha et al., 2019, this work).

Early Tonian magmatic events recorded in the belts around the São Francisco-Congo, Rio de la Plata and Kalahari cratons have been interpreted as processes at convergent plate boundaries (Peixoto et al., 2017; Passarelli et al., 2019; Cerva-Alves et al., 2020; Santiago et al., 2020; Werle et al., 2020; Tsunogae et al., 2021). The metavolcano-sedimentary sequence of the Italva Group and Serra da Prata magmatic events in the northern Ribeira Belt are interpreted as a record of arc generation and convergence processes around the São Francisco-Congo cratons between 856–838 Ma (Peixoto et al., 2017). The Cachoeira Sequence and Juréia Massif in the Ribeira Belt could represent similar accretionary processes in the southern Ribeira Belt (Passarelli et al., 2007, 2019). In the Dom Feliciano Belt, the Passinho and São Gabriel magmatic units are interpreted as related with ocean closure processes during the Tonian (Philipp et al., 2016; Arena et al., 2017; Hartmann et al., 2019; Cerva-Alves et al., 2020; Werle et al., 2020).

4.8. Conclusions

Based on petrography, phase equilibria modelling, monazite, apatite and zircon U–Pb age data and trace element compositions, and in situ Rb–Sr dating for the metapelites of the Embu Complex in its westernmost portion, we recognize the following:

1. Sillimanite, sillimanite–K-feldspar and cordierite zones represent the high-grade metamorphic zones of the metamorphic event in the southern portion of the Embu Complex. Petrological and thermodynamic modelling data indicate that the high-grade metamorphic rocks of the complex attained conditions between 750–805 ºC and 3.6–9.2 kbar.

2. Monazite and zircon U–Pb data indicate that the high-grade metamorphic event occurred over ca. 40 Ma, between 810–760 Ma. Igneous activity from 810–770 Ma is concomitant with the high-grade metamorphic event.

3. Zircon and apatite U–Pb ages, and biotite and muscovite Rb–Sr data record ages between 675–550 Ma, representing a slow cooling rate of 4.4 ºC/Ma for the period between 675 and 640 Ma, and a late stage of shear zones development.

4. Results from this work reinforce the accretion of distinct units within the Ribeira Belt between Rodinia break-up and West Gondwana assembly.

Acknowledgements

We thank Mauricio Pavan, Isaac Malta, Bruna Coldebella, Mariana Ambrosio, Gabriel Kuhlmann and Adriano Reis for their help with the fieldwork. We also thanks Renato de Moraes, Kathryn Cutts and Mikaella Balis for comments and suggestions that have helped us to improve the manuscript. Financial support was provided by São Paulo Research Foundation (FAPESP) grants 2019/10457-4 and 2015/26645-3. Frederico Faleiros and Ginaldo Campanha thank the research productivity grants 307732/2019-3 and 305701/2019-3, of the National Council of Technological and Scientific Development (CNPq), respectively. Peter Cawood acknowledges support from Australian Research Council grant FL160100168.

4.9. References

Aleinikoff, J.N., Schenck, W.S., Plank, M.O., Srogi, L.A., Fanning, C.M., Kamo, S.L., Bosbyshell, H., 2006. Deciphering igneous and metamorphic events in high-grade

rocks of the Wilmington complex, Delaware: Morphology, cathodoluminescence and backscattered electron zoning, and SHRIMP U-Pb geochronology of zircon and monazite. Bulletin of the Geological Society of America 118, 39–64. https://doi.org/10.1130/B25659.1

Alkmim, F.F., Marshak, S., Pedrosa-Soares, A.C., Peres, G.G., Cruz, S.C.P., Whittington, A., 2006. Kinematic evolution of the Araçuaí-West Congo orogen in Brazil and Africa: Nutcracker tectonics during the Neoproterozoic assembly of Gondwana. Precambrian Research 149, 43–64. https://doi.org/10.1016/j.precamres.2006.06.007

Almeida, F.F.M. De, Hasui, Y., Brito Neves, B.B. De, Fuck, R.A., 1981. Brazilian structural provinces: An introduction. Earth-Science Reviews 17, 1–29. https://doi.org/10.1016/0012-8252(81)90003-9

Almeida, F.F.M., Amaral, G., Cordani, U.G., Kawashita, K., 1973. The Precambrian Evolution of the South American Cratonic Margin South of the Amazon River. The South Atlantic 1, 411–446. https://doi.org/10.1007/978-1-4684-3030-1_11

Almeida, F.F.M., Hasui, Y., 1984. O pré-cambriano do Brasil. Edgard Blucher.

Alsop, G.I., Holdsworth, R.E., 2004. Shear zones — an introduction and overview. Geological Society, London, Special Publications 224, 1 LP – 9. https://doi.org/10.1144/GSL.SP.2004.224.01.01

Alves, A., Janasi, V. de A., Campos Neto, M. da C., 2016. Sources of granite magmatism in the Embu Terrane (Ribeira Belt, Brazil): Neoproterozoic crust recycling constrained by elemental and isotope (Sr-Nd-Pb) geochemistry. Journal of South American Earth Sciences 68, 205–223. https://doi.org/10.1016/j.jsames.2015.10.014

Alves, A., Janasi, V. de A., Campos Neto, M. da C., Heaman, L., Simonetti, A., 2013. U-Pb geochronology of the granite magmatism in the embu terrane: Implications for the evolution of the central ribeira belt, SE Brazil. Precambrian Research 230, 1–12. https://doi.org/10.1016/j.precamres.2013.01.018

Amaral, L., Caxito, F. de A., Pedrosa-Soares, A.C., Queiroga, G., Babinski, M., Trindade, R., Lana, C., Chemale, F., 2020. The Ribeirão da Folha ophiolite-bearing accretionary wedge (Araçuaí orogen, SE Brazil): New data for Cryogenian

plagiogranite and metasedimentary rocks. Precambrian Research 336, 105522. https://doi.org/10.1016/j.precamres.2019.105522

Arena, K.R., Hartmann, L.A., Lana, C., 2017. Tonian emplacement of ophiolites in the southern Brasiliano Orogen delimited by U-Pb-Hf isotopes of zircon from metasomatites. Gondwana Research 49, 296–332. https://doi.org/10.1016/j.gr.2017.05.018

Babinski, M., Tassinari, C.C.G., Nutman, A.P., Sato, K., Pimentel, M.M., Iyer, S.S., 2001. U/Pb shrimp zircon ages of migmatites from the basement of the Embú Complex, Ribeira Fold Belt, Brazil: indications for ~1.4-1.3 Ga Pb-Pb and Rb-Sr "isochron" ages of no geological meaning. III South American Symposium on Isotope Geology. Pucón.

Bartoli, O., 2017. Phase equilibria modelling of residual migmatites and granulites: An evaluation of the melt-reintegration approach. Journal of Metamorphic Geology 35, 919–942. https://doi.org/10.1111/jmg.12261

Basei, M.A.S., Frimmel, H.E., Nutman, A.P., Preciozzi, F., 2008. West Gondwana amalgamation based on detrital zircon ages from Neoproterozoic Ribeira and Dom Feliciano belts of South America and comparison with coeval sequences from SW Africa. Geological Society, London, Special Publications 294, 239–256.

Basei, M.A.S., Siga, O., Machiavelli, A., Mancini, F., 1992. Evolução tectônica dos terrenos entre os cinturões ribeira e dom feliciano (PR-SC). Revista Brasileira de Geociências 22, 216–221.

Bell, E.A., Boehnke, P., Barboni, M., Harrison, T.M., 2019. Tracking chemical alteration in magmatic zircon using rare earth element abundances. Chemical Geology 510, 56–71. https://doi.org/10.1016/j.chemgeo.2019.02.027

Black, L.P., Gulson, B.L., 1978. The age of the Mud Tank carbonatite, Strangways Range, Northern Territory. BMR J. Austral. Geol. Geophy. 3, 227–232. https://doi.org/10.1016/j.apenergy.2015.11.040

Black, L.P., Kamo, S.L., Allen, C.M., Aleinikoff, J.N., Davis, D.W., Korsch, R.J., Foudoulis, C., 2003. TEMORA 1: a new zircon standard for Phanerozoic U-Pb geochronology. Chemical Geology 155–170.

Bose, S., Ghosh, G., Kawaguchi, K., Das, K., Mondal, A.K., Banerjee, A., 2021. Zircon and monazite geochronology from the Rengali-Eastern Ghats Province: Implications for the tectonic evolution of the eastern Indian terrane. Precambrian Research 355, 106080. https://doi.org/10.1016/j.precamres.2020.106080

Boynton, W. V., 1984. Cosmochemistry of the rare earth elements: meteorite studies. Rare Earth Element Geochemistry. Elsevier B.V., 63–114. https://doi.org/10.1016/b978-0-444-42148-7.50008-3

Brito Neves, B.B., Campos Neto, M.D.C., Fuck, R.A., 1999. From Rodinia to Western Gondwana: An approach to the Brasiliano-Pan African cycle and orogenic collage. Episodes 22, 155–166. https://doi.org/10.18814/epiiugs/1999/v22i3/002

Brito Neves, B.B. de, Fuck, R.A., 2013. Neoproterozoic evolution of the basement of the South-American platform. Journal of South American Earth Sciences 47, 72–89. https://doi.org/10.1016/j.jsames.2013.04.005

Brito Neves, B.B. de, Fuck, R.A., Campanha, G.A. da C., 2021. Basement inliers of the Brasiliano structural provinces of South America. Journal of South American Earth Sciences 110, 103392. https://doi.org/10.1016/j.jsames.2021.103392

Brito Neves, B.B. de, Fuck, R.A., Pimentel, M.M., 2014. The Brasiliano collage in South America: a review. Brazilian Journal of Geology 44, 493–518. https://doi.org/10.5327/Z2317-4889201400030010

Brown, M., 2009. Metamorphic patterns in orogenic systems and the geological record. Geological Society, London, Special Publications 318, 37 LP – 74. https://doi.org/10.1144/SP318.2

Cabrita, D., Salamuni, E., Lagoeiro, L., 2017. Fabric evolution of polydeformed orthogneisses and quartzites along the Curitiba Shear Zone, Curitiba Domain, Southern Brazil. Journal of South American Earth Sciences 77. https://doi.org/10.1016/j.jsames.2017.05.010

Cabrita, D.I.G., Faleiros, F.M., Cawood, P.A., Campanha, G.A.C., Yogi, M.T.A.G., Wainwright, A.N., Raveggi, M., Almeida, V. V., 2021. Petrochronological constraints and tectonic implications of Tonian metamorphism in the Embu Complex , Ribeira Belt , Brazil. Precambrian Research 363.

https://doi.org/10.1016/j.precamres.2021.106315

Caltabellota, F.P., Lopes, A.P., Brumatti, M., Rodrigues da Silva, A.D., Lima, R.A.P., Severino, R.R., Andrade, J.J.C., Palmeira, L.C.M., Mapa, F.B., Marque, I.P., Turra, B.B., Costa, V.S., Campos, F.F., Ferrari, V.C., Mendes, D., 2017. Mapa Geológico de Integração do ARIM Vale do Ribeira (SP e PR). Escala 1:250.000.

Campanha, G.A. da C., 2002. O Papel do Sistema de Zonas de Cisalhamento Transcorrentes na Configuração da Porção Meridional da Faixa Ribeira. University of São Paulo.

Campanha, G.A. da C., 1991. Tectônica Proterozóica no Alto e Médio Vale do Ribeira, estados de São Paulo e Paraná. Universidade de São Paulo.

Campanha, G.A. da C., Brito Neves, B.B., 2004. Frontal and oblique tectonics in the Brazilian Shield. Episodes 27, 255–259. https://doi.org/10.1016/S1342-937X(05)70391-9

Campanha, G.A. da C., Faleiros, F.M., Basei, M.A.S., Tassinari, C.C.G., Nutman, A., Vasconcelos, P., 2015. Geochemistry and age of mafic rocks from the Votuverava Group, southern Ribeira Belt, Brazil: Evidence for 1490Ma oceanic back-arc magmatism. Precambrian Research 266, 530–550. https://doi.org/10.1016/j.precamres.2015.05.026

Campanha, G.A. da C., Sadowski, G.R., 2002. Determinações da deformação finita em rochas metassedimentares da faixa ribeira na região de Iporanga e Apiaí, SP. Revista Brasileira de Geociências 32, 107–118.

Campanha, G.A. da C., Sadowski, G.R., 1999. Tectonics of the southern portion of the Ribeira Belt (Apiai Domain). Precambrian Research 98, 31–51. https://doi.org/10.1016/S0301-9268(99)00027-3

Campanha, G.A.C., Basei, M.S., Faleiros, F.M., Nutman, A.P., 2016. The Mesoproterozoic to early Neoproterozoic passive margin Lajeado Group and Apiaí Gabbro, Southeastern Brazil. Geoscience Frontiers 7, 683–694. https://doi.org/10.1016/j.gsf.2015.08.004

Campanha, G.A.C., Faleiros, F.M., Cawood, P.A., Cabrita, D.I.G., Ribeiro, B. V, Basei,

M.A.S., 2019. The Tonian Embu Complex in the Ribeira Belt (Brazil): revision , depositional age and setting in Rodinia and West Gondwana. Precambrian Research 320, 31–45. https://doi.org/10.1016/j.precamres.2018.10.010

Campanha, G.A.C., Gimenez Filho, A., Caetano, S.L.V., Pires, F.A., Dantas, A.S.L., Teixeira, A.L., Dehira, L.K., 1986. Geologia e estratigrafia da região das folhas Iporanga e Gruta do Diabo, Vale do Ribeira, São Paulo. Congresso Brasileiro de Geologia. Sociedade Brasileira de Geologia, Goiânia, 1058–1073.

Campos Neto, M. da C., Figueiredo, M.C.., 1995. The Rio Doce Orogeny, Southeastern Brazil. Journal of South American Earth Sciences 8, 143–162. https://doi.org/10.1016/0895-9811(95)00002-W

Campos Neto, M.D.C., 2000. Orogenic systems from Southwestern Gondwana: an approach to Brasiliano Pan African cycle and orogenic collage in Southeastern Brazil. Tectonic Evolution of South America. Rio de Janeiro, 335–365.

Cavalcante, C., Lagoeiro, L., Fossen, H., Egydio-Silva, M., Morales, L.F.G., Ferreira, F., Conte, T., 2018. Temperature constraints on microfabric patterns in quartzofeldsphatic mylonites, Ribeira belt (SE Brazil). Journal of Structural Geology 115, 243–262. https://doi.org/10.1016/j.jsg.2018.07.013

Cawood, P.A., Hawkesworth, C.J., Dhuime, B., 2012. Detrital zircon record and tectonic setting. Geology 40, 875–878. https://doi.org/10.1130/G32945.1

Cawood, P.A., Strachan, R.A., Pisarevsky, S.A., Gladkochub, D.P., Murphy, J.B., 2016. Linking collisional and accretionary orogens during Rodinia assembly and breakup: Implications for models of supercontinent cycles. Earth and Planetary Science Letters 449, 118–126. https://doi.org/10.1016/j.epsl.2016.05.049

Caxito, F.A., Heilbron, M., Valeriano, C.M., Bruno, H., Pedrosa-Soares, A., Alkmim, F.F., Chemale, F., Hartmann, L.A., Dantas, E., Basei, M.A.S., 2021. Integration of elemental and isotope data supports a neoproterozoic adamastor ocean realm. Geochemical Perspectives Letters 17, 6–10. https://doi.org/10.7185/GEOCHEMLET.2106

Ceccato, A., Pennacchioni, G., Menegon, L., Bestmann, M., 2017. Crystallographic control and texture inheritance during mylonitization of coarse grained quartz veins.

Lithos 290–291, 210–227. https://doi.org/10.1016/j.lithos.2017.08.005

Cerva-Alves, T., Hartmann, L.A., Remus, M. V.D., Lana, C., 2020. Integrated ophiolite and arc evolution, southern Brasiliano Orogen. Precambrian Research 341, 105648. https://doi.org/10.1016/j.precamres.2020.105648

Chetty, T.R.K., 2017. Chapter 1 - Orogens. In: Chetty, T.R.K.B.T.-P.O. of I. (Ed.), Proterozoic Orogens of India: A Critical Window to Gondwana. Elsevier, 1–34. https://doi.org/https://doi.org/10.1016/B978-0-12-804441-4.00001-8

Chu, N.C., Taylor, R.N., Chavagnac, V., Nesbitt, R.W., Boella, R.M., Milton, J.A., German, C.R., Bayon, G., Burton, K., 2002. Hf isotope ratio analysis using multi-collector inductively coupled plasma mass spectrometry: An evaluation of isobaric interference corrections. Journal of Analytical Atomic Spectrometry 17, 1567–1574. https://doi.org/10.1039/b206707b

Condie, K.C., 2003. Supercontinents, superplumes and continental growth: The Neoproterozoic record. Geological Society Special Publication 206, 1–21. https://doi.org/10.1144/GSL.SP.2003.206.01.02

Connolly, J.A.D., 2005. Computation of phase equilibria by linear programming: A tool for geodynamic modeling and its application to subduction zone decarbonation. Earth and Planetary Science Letters 236, 524–541. https://doi.org/10.1016/j.epsl.2005.04.033

Conte, T., Cavalcante, C., Lagoeiro, L.E., Fossen, H., Silveira, C.S., 2020. Quartz textural analysis from an anastomosing shear zone system: Implications for the tectonic evolution of the Ribeira belt, Brazil. Journal of South American Earth Sciences 103, 102750. https://doi.org/10.1016/j.jsames.2020.102750

Cordani, U.G., Coutinho, J.M. V, Nutman, A.P., 2002. Geochronological constraints on the evolution of the Embu Complex São Paulo, Brazil. Journal of South American Earth Sciences 14, 903–910. https://doi.org/10.1016/S0895-9811(01)00083-9

Corrales, F.F.P., Dussin, I.A., Heilbron, M., Bruno, H., Bersan, S., Valeriano, C.M., Pedrosa-Soares, A.C., Tedeschi, M., 2020. Coeval high Ba-Sr arc-related and OIB Neoproterozoic rocks linking pre-collisional magmatism of the Ribeira and Araçuaí orogenic belts, SE-Brazil. Precambrian Research 337, 105476.

https://doi.org/10.1016/j.precamres.2019.105476

Costa, R.V. da, Johannes Trouw, R.A., Marimon, R.S., Nepomuceno, F., Mendes, J.C., Dantas, E., 2020. São Bento do Sapucaí Shear Zone: Constraining age and P-T conditions of a collisional Neoproterozoic oblique shear zone, Ribeira Orogen, Brazil. Journal of South American Earth Sciences 98, 102418. https://doi.org/10.1016/j.jsames.2019.102418

Costa, R.V., Trouw, R.A.J., Mendes, J.C., Geraldes, M., Tavora, A., Nepomuceno, F., de Araújo Junior, E.B., 2017. Proterozoic evolution of part of the Embu Complex , eastern S a state , SE Brazil. Journal of South American Earth Sciences 79, 170–188. https://doi.org/10.1016/j.jsames.2017.08.003

Cota de Freitas, N., Almeida, J., Heilbron, M., Cutts, K., Dussin, I., 2021. The Cabo Frio Thrust: A folded suture zone, Ribeira belt, SE Brazil. Journal of Structural Geology 149, 104379. https://doi.org/https://doi.org/10.1016/j.jsg.2021.104379

Cury, L.F., Kaulfuss, G.A., Siga Júnior, O., Basei, M.A.S., Harara, O.M., Sato, K., 2002. Idades U-Pb (Zircões) de 1.75 Ga em granitóides alcalinos deformados dos núcleos Betara e Tigre: evidências de regimes extensionais do estateriano na Faixa Apiaí. Geologia USP - Serie Cientifica 2, 95–108. https://doi.org/10.5327/S1519-874X2002000100009

Da Silva, L.C., McNaughton, N.J., Armstrong, R., Hartmann, L.A., Fletcher, I.R., 2005. The neoproterozoic Mantiqueira Province and its African connections: A zircon-based U-Pb geochronologic subdivision for the Brasiliano/Pan-African systems of orogens. Precambrian Research 136, 203–240. https://doi.org/10.1016/j.precamres.2004.10.004

Deer, W.A., Howie, R.A., Zussman, J., 2013. An introduction to the rock-forming minerals.

Depaolo, D.J., 1981. Neodymium isotopes in the Colorado Front Range and crust-mantle evolution in the Proterozoic. Nature 291, 193–196. https://doi.org/10.1038/291193a0

Ducea, M.N., Saleeby, J.B., Bergantz, G., 2015. The architecture, chemistry, and evolution of continental magmatic arcs. Annual Review of Earth and Planetary

Sciences 43, 299–331. https://doi.org/10.1146/annurev-earth-060614-105049

Duffles, P., Trouw, R.A.J., Mendes, J.C., Gerdes, A., Vinagre, R., 2016. U-Pb age of detrital zircon from the Embu sequence, Ribeira belt, Se Brazil. Precambrian Research 278, 69–86. https://doi.org/10.1016/j.precamres.2016.03.007

Egydio-Silva, M., Vauchez, A., Bascou, J., Hippertt, J., 2002. High-temperature deformation in the Neoproterozoic transpressional Ribeira belt, southeast Brazil. Tectonophysics 352, 203–224. https://doi.org/10.1016/S0040-1951(02)00197-X

Faleiros, F.M., 2008. Evolução de Terrenos Tectono-Metamórficos da Serrania do Ribeira e Planalto Alto Turvo (SP, PR). Universidade de São Paulo.

Faleiros, F.M., Campanha, G.A. da C., Bello, R.M. da S., Fuzikawa, K., 2010. Quartz recrystallization regimes, c-axis texture transitions and fluid inclusion reequilibration in a prograde greenschist to amphibolite facies mylonite zone (Ribeira Shear Zone, SE Brazil). Tectonophysics 485, 193–214. https://doi.org/10.1016/j.tecto.2009.12.014

Faleiros, F.M., Campanha, G.A. da C., Martins, L., Vlach, S., Vasconcelos, P.M., 2011a. Ediacaran high-pressure collision metamorphism and tectonics of the southern Ribeira Belt (SE Brazil): Evidence for terrane accretion and dispersion during Gondwana assembly. Precambrian Research 189, 263–291. https://doi.org/10.1016/j.precamres.2011.07.013

Faleiros, F.M., Campanha, G.A.C., Pavan, M., Almeida, V. V., Rodrigues, S.W.O., Araújo, B.P., 2016. Short-lived polyphase deformation during crustal thickening and exhumation of a collisional orogen (Ribeira Belt, Brazil). Journal of Structural Geology 93, 106–130. https://doi.org/10.1016/j.jsg.2016.10.006

Faleiros, F.M., Ferrari, V.C., Costa, V.S., Da Cruz Campanha, G.A., 2011b. Geochemistry and Petrogenesis of Metabasites from the Votuverava Group (Apiaí Terrane, Southern Ribeira Belt): Evidence of a Calymmian Back-arc Basin. Geologia USP - Serie Cientifica 11, 135–155. https://doi.org/10.5327/Z1519-874X2011000200008

Faleiros, F.M., Morais, S.M., Costa, V.S., 2012. Geologia e recursos minerais da folha Apiaí SG.22-X-B-V: escala 1:100.000: estados de São Paulo e Paraná.

Faleiros, F.M., Ribeiro, B. V, Campanha, G.A.C., Cawood, P.A., Cabrita, D.I.G., Yogi, M.T.A.G., Milani, L.A., Lemos-Santos, D. V, Almeida, V. V, Rodrigues, S.W.O., Malta, I.S., Forero-Ortega, A.J., 2022. Strain Partitioning along Terrane Bounding and Intraterrane Shear Zones: Constraints from a Long-Lived Transpressional System in West Gondwana (Ribeira Belt, Brazil). Lithosphere 2021, 2103213. https://doi.org/10.2113/2022/2103213

Fassbinder, E., 1990. Análise estrutural da Falha Lancinha, Estado do Paraná. Universidade de São Paulo.

Fernandes, A.J., 1991. O Complexo Embu no Leste do Estado de São Paulo: Contribuição ao Conhecimento da Litoestratigrafia e da Evolução Estrutural e Metamórfica. Universidade de São Paulo.

Forero-Ortega, A.J., Campanha, G.A.C., Faleiros, F.M., Yogi, M.T.A.G., 2020. Pure shear-dominated transpression and vertical extrusion in a strike-slip fault splay from the Itapirapuã Shear Zone, Ribeira Belt, Brazil. Tectonophysics 786, 228455. https://doi.org/10.1016/j.tecto.2020.228455

Forero-Ortega, A.J., Faleiros, F.M., 2018. Ediacaran (570-615 Ma) back-arc basin basaltic volcanism in the ltaiacoca Group, Ribeira Belt, Brazil: a remnant of the Adamastor Ocean. South American Symposium on Isotope Geology. Cochabamba.

Fossen, H., Cavalcante, C., Konopásek, J., Meira, V.T., de Almeida, R.P., Hollanda, M.H.B.M., Trompette, R., 2020. A critical discussion of the subduction-collision model for the Neoproterozoic Araçuaí-West Congo orogen. Precambrian Research 343. https://doi.org/10.1016/j.precamres.2020.105715

Fossen, H., Cavalcante, G.C.G., 2017. Shear zones – A review., Earth-Science Reviews. https://doi.org/10.1016/j.earscirev.2017.05.002

Fuck, R.A., Brito Neves, B.B., Schobbenhaus, C., 2008. Rodinia descendants in South America. Precambrian Research 160, 108–126. https://doi.org/10.1016/j.precamres.2007.04.018

Fuhrman, M.L., Lindsley, D.H., 1988. Ternary-Feldspar Modeling and Thermometry. American Mineralogist 73, 201–215.

Gain, S.E.M., Gréau, Y., Henry, H., Belousova, E., Dainis, I., Griffin, W.L., O'Reilly, S.Y., 2019. Mud Tank Zircon: Long-Term Evaluation of a Reference Material for U-Pb Dating, Hf-Isotope Analysis and Trace Element Analysis. Geostandards and Geoanalytical Research 43, 339–354. https://doi.org/10.1111/ggr.12265

Gilgannon, J., Fusseis, F., Menegon, L., Regenauer-Lieb, K., Buckman, J., 2017. Hierarchical creep cavity formation in an ultramylonite and implications for phase mixing. Solid Earth 8, 1193–1209. https://doi.org/10.5194/se-8-1193-2017

Giraldo, S.J., Trouw, R.A.J., Duffles, P., Vinagre da Costa, R., Ibañez Mejia, M., Schwantes Marimon, R., 2019. Structural analysis combined with new geothermobarometric and geochronological results of the Além Paraíba shear zone, between Três Rios and Bananal, Ribeira Orogen, SE Brazil. Journal of South American Earth Sciences 90, 118–136. https://doi.org/10.1016/j.jsames.2018.11.018

Gray, D.R., Foster, D.A., Meert, J.G., Goscombe, B.D., Armstrong, R., Trouw, R.A.J., Passchier, C.W., 2008. A Damara orogen perspective on the assembly of southwestern Gondwana. Geological Society Special Publication 294, 257–278. https://doi.org/10.1144/SP294.14

Guillot, S., Hattori, K., Agard, P., Schwartz, S., Vidal, O., 2009. Exhumation Processes in Oceanic and Continental Subduction Contexts: A Review. Subduction Zone Geodynamics. 103–118. https://doi.org/10.1007/978-3-540-87974-9

Hackspacher, P.C., Dantas, E.L., Spoladore, Â., Fetter, A.H., Oliveira, M.A.F. de, 2000. Evidence of Neoproterozoic Backarc Basin Development in the Central Ribeira Belt, Southeastern Brazil: New Geochronological and Geochemical Constraints From the São Roque - Açungui Groups. Revista Brasileira de Geociências 30, 110–114.

Hamilton, P.J., O'Nions, R.K., Bridgwater, D., Nutman, A., 1983. Sm-Nd studies of Archaean metasediments and metavolcanics from West Greenland and their implications for the Earth's early history. Earth and Planetary Science Letters 62, 263–272. https://doi.org/10.1016/0012-821X(83)90089-4

Hartmann, L.A., Werle, M., Michelin, C.R.L., Lana, C., Queiroga, G.N., Castro, M.P., Arena, K.R., 2019. Proto-Adamastor ocean crust (920 Ma) described in Brasiliano

Orogen from coetaneous zircon and tourmaline. Geoscience Frontiers 10, 1623–1633. https://doi.org/10.1016/j.gsf.2018.09.018

Heilbron, M., Machado, N., 2003. Timing of terrane accretion in the Neoproterozoic-Eopaleozoic Ribeira orogen (SE Brazil). Precambrian Research 125, 87–112.

Heilbron, M., Oliveira, C., Lobato, M., De Morisson Valeriano, C., Dussin, I., Dantas, E., Simonetti, A., Bruno, H., Corrales, F., Socoloff, E., 2019. The Barreiro suite in the central Ribeira Belt (SE-Brazil): A late Tonian tholeiitic intraplate magmatic event in the distal passive margin of the São Francisco Paleocontinent. Brazilian Journal of Geology 49, 1–21. https://doi.org/10.1590/2317-4889201920180129

Heilbron, M., Valeriano, C.D.M., Peixoto, C., Neubauer, F., Dussin, I., Corrales, F., Bruno, H., Cesar, J., Almeida, H. De, Guilherme, L., 2020. Neoproterozoic magmatic arc systems of the central Ribeira belt, SE-Brazil, in the context of the West-Gondwana pre-collisional history: A review. Journal of South American Earth Sciences 102710. https://doi.org/10.1016/j.jsames.2020.102710

Heilbron, M., Valeriano, C.M., Tassinari, C.C.G., Almeida, J., Tupinambá, M., Siga Jr, O., Trouw, R., 2008. Correlation of Neoproterozoic terranes between Ribeira Belt, SE Brazil and its African counterpart: comparative tectonic evolution and open questions., West Gondwana: Pre-Cenozoic Correlations Across the South Atlantic Region. https://doi.org/10.1144/SP294.12

Henrique-Pinto, R., De Assis Janasi, V., Da Cruz Campanha, G.A., 2018. U-Pb dating, Lu-Hf isotope systematics and chemistry of zircon from the Morro do Polvilho meta-trachydacite: Constraints on sources of magmatism and on the depositional age of the São Roque Group. Geologia USP - Serie Cientifica 18, 45–56. https://doi.org/10.11606/issn.2316-9095.v18-125793

Henrique-Pinto, R., Janasi, V.A., Vasconcellos, A.C.B.C., Sawyer, E.W., Barnes, S., Basei, M.A.S., Tassinari, C.C.G., 2015. Zircon provenance in meta-sandstones of the São Roque Domain : Implications for the Proterozoic evolution of the Ribeira Belt , SE Brazil. Precambrian Research 256, 271–288. https://doi.org/10.1016/j.precamres.2014.11.014

Hippertt, J., Egydio-Silva, M., 1996. New polygonal grains formed by dissolution-

redeposition in quartz mylonite. Journal of Structural Geology 18, 1345–1352. https://doi.org/10.1016/S0191-8141(96)00047-8

Hogmalm, K.J., Zack, T., Karlsson, A.K.O., Sjöqvist, A.S.L., Garbe-Schönberg, D., 2017. In situ Rb-Sr and K-Ca dating by LA-ICP-MS/MS: An evaluation of N2O and SF6 as reaction gases. Journal of Analytical Atomic Spectrometry 32, 305–313. https://doi.org/10.1039/c6ja00362a

Holland, T.J.B., Powell, R., 2011. An improved and extended internally consistent thermodynamic dataset for phases of petrological interest, involving a new equation of state for solids. Journal of Metamorphic Geology 29, 333–383. https://doi.org/10.1111/j.1525-1314.2010.00923.x

Hollocher, K., Robinson, P., Walsh, E., Roberts, D., 2012. Geochemistry of amphibolite-facies volcanics and gabbros of the støren nappe in extensions west and southwest of Trondheim, Western Gneiss Region, Norway: A key to correlations and paleotectonic settings. American Journal of Science 312, 357–416. https://doi.org/10.2475/04.2012.01

Jackson, S.E., Pearson, N.J., Griffin, W.L., Belousova, E.A., 2004. The application of laser ablation-inductively coupled plasma-mass spectrometry to in situ U-Pb zircon geochronology. Chemical Geology 211, 47–69. https://doi.org/10.1016/j.chemgeo.2004.06.017

Jäger, E, 1979. Introduction to Geochronology BT - Lectures in Isotope Geology. In: Jäger, Emilie, Hunziker, J.C. (Eds.). Springer Berlin Heidelberg, Berlin, Heidelberg, 1–12.

Janasi, V. de A., Alves, A., Vlach, S.R.F., Leite, R.J., 2003. Granitos Peraluminosos da Porção Central da Faixa Ribeira, Estado de São Paulo: Sucessivos Eventos de Reciclagem da Crosta Continental no Neoproterozóico. Geologia USP - Serie Cientifica 3, 13–24.

Janasi, V. de A., Andrade, S., Vasconcellos, A.C.B.C., Henrique-Pinto, R., Ulbrich, H.H.G.J., 2016. Timing and sources of granite magmatism in the Ribeira Belt, SE Brazil: Insights from zircon in situ U–Pb dating and Hf isotope geochemistry in granites from the São Roque Domain. Journal of South American Earth Sciences 68,

224–247. https://doi.org/10.1016/j.jsames.2015.11.009

Janasi, V. de A., Ulbrich, H.H.G.J., 1991. Late Proterozoic granitoid magmatism in the state of São Paulo, southeastern Brazil. Precambrian Research 51, 351–374.

Janasi, V.A., Leite, R.J., Van Schmus, W.R., 2001. U-Pb chronostratigraphy of the granitic magmatism in the Agudos Grandes Batholith (West of São Paulo, Brazil) - Implications for the evolution of the Ribeira Belt. Journal of South American Earth Sciences 14, 363–376. https://doi.org/10.1016/S0895-9811(01)00034-7

Janoušek, V., Farrow, C.M., Erban, V., 2006. Interpretation of whole-rock geochemical data in igneous geochemistry: Introducing Geochemical Data Toolkit (GCDkit). Journal of Petrology 47, 1255–1259. https://doi.org/10.1093/petrology/egl013

Juliani, C., Hackspacher, P., Dantas, E.L., Fetter, A.H., 2000. the Mesoproterozoic Volcano-Sedimentary Serra Do Itaberaba Group of the Central Ribeira Belt, São Paulo State, Brazil: Implications for the Age of the Overlying São Roque Group. Revista Brasileira de Geociências 30, 082–086. https://doi.org/10.25249/0375-7536.2000301082086

Kelsey, D.E., Clark, C., Hand, M., 2008. Thermobarometric modelling of zircon and monazite growth in melt-bearing systems: Examples using model metapelitic and metapsammitic granulites. Journal of Metamorphic Geology 26, 199–212. https://doi.org/10.1111/j.1525-1314.2007.00757.x

Kilian, R., Heilbronner, R., Stünitz, H., 2011. Quartz grain size reduction in a granitoid rock and the transition from dislocation to diffusion creep. Journal of Structural Geology 33, 1265–1284. https://doi.org/10.1016/j.jsg.2011.05.004

Konopásek, J., Cavalcante, C., Fossen, H., Janoušek, V., 2020. Adamastor – an ocean that never existed? Earth-Science Reviews 205, 103201. https://doi.org/10.1016/j.earscirev.2020.103201

Leandro, R., 2016. Caracterização Tectonoestratigráfica da Sequência Terrígena da Formação Capiru Na Região de Morro Grande, Colombo - Pr., Dissertação de Mestrado. Universidade Federal do Paraná. https://doi.org/10.1017/CBO9781107415324.004

Leite, R.J., 2003. Petrogênese e geocronologia U-Pb do magmatismo granítico tardi- a pós-orogênico no batólito Agudos Grandes (SP). Universidade de São Paulo.

Leite, R.J., Heaman, L.M., de Assis Janasi, V., Martins, L., Creaser, R.A., 2007. The late- to postorogenic transition in the Neoproterozoic Agudos Grandes Granite Batholith (Apiaí Domain, SE Brazil): Constraints from geology, mineralogy, and U-Pb geochronology. Journal of South American Earth Sciences 23, 193–212. https://doi.org/10.1016/j.jsames.2006.09.022

Li, Z.X., Bogdanova, S. V., Collins, A.S., Davidson, A., De Waele, B., Ernst, R.E., Fitzsimons, I.C.W., Fuck, R.A., Gladkochub, D.P., Jacobs, J., Karlstrom, K.E., Lu, S., Natapov, L.M., Pease, V., Pisarevsky, S.A., Thrane, K., Vernikovsky, V., 2008. Assembly, configuration, and break-up history of Rodinia: A synthesis. Precambrian Research 160, 179–210. https://doi.org/10.1016/j.precamres.2007.04.021

Lobato, M., Heilbron, M., Torós, B., Ragatky, D., Dantas, E., 2015. Provenance of the Neoproterozoic high-grade metasedimentary rocks of the arc-related Oriental Terrane of the Ribeira belt: Implications for Gondwana amalgamation. Journal of South American Earth Sciences 63, 260–278. https://doi.org/10.1016/j.jsames.2015.07.019

Ludwig, K.R., 2003. A Geochronological Toolkit for Microsoft Excel. Berkeley Geochronology Center, Special Publication. 4, 71.

Machado, R., Dehler, N.M., Vasconcelos, P., 2007. 40Ar/39Ar ages (600-570 Ma) of the Serra do Azeite transtensional shear zone: Evidence for syncontractional extension in the Cajati area, southern Ribeira belt. Anais Da Academia Brasileira de Ciencias 79, 713–723.

Maurer, V.C., 2016. Caracterização geocronológica (U-Pb), geoquímica e isotópica 9Sr, Nd, Hf) do Complexo Rio Capivari no Terreno Embu. Universidade de São Paulo.

Meira, V.T., 2014. Evolução Tectono-Metamórfica Neoproterozóica dos Complexos Embu e Costeiro no Contexto de Formação do Gondwana Ocidental (Leste do Estado de São Paulo). Universidade de São Paulo.

Meira, V.T., Garcia-Casco, A., Hyppolito, T., Juliani, C., Schorscher, J.H.D., 2019a. Tectono-Metamorphic Evolution of the Central Ribeira Belt, Brazil: A Case of Late

Neoproterozoic Intracontinental Orogeny and Flow of Partially Molten Deep Crust During the Assembly of West Gondwana. Tectonics 38, 3182–3209. https://doi.org/10.1029/2018TC004959

Meira, V.T., García-Casco, A., Juliani, C., Almeida, R.P., Schorscher, J.H.D., 2015. The role of intracontinental deformation in supercontinent assembly: Insights from the Ribeira Belt, Southeastern Brazil (Neoproterozoic West Gondwana). Terra Nova 27, 206–217. https://doi.org/10.1111/ter.12149

Meira, V.T., Garcia-Casco, A., Juliani, C., Schorscher, J.H.D., 2019b. Late Tonian within-plate mafic magmatism and Ediacaran partial melting and magmatism in the Costeiro Domain, Central Ribeira Belt, Brazil. Precambrian Research 334, 105440. https://doi.org/10.1016/j.precamres.2019.105440

Mora, C.A.S., Campanha, G.A. da C., Wemmer, K., 2013. Microstructures and K-Ar illite fine-fraction ages of the cataclastic rocks associated to the Camburu Shear Zone, Ribeira Belt, Southeastern Brazil. Brazilian Journal of Geology 43, 607–622. https://doi.org/10.5327/z2317-48892013000400003

Mori, P.E., Reeves, S., Correia, C.T., Haukka, M., 1999. Development of a fused glass disc XRF facility and comparison with pressed powder pellet technique at Instituto de Geociências, São Paulo University. Revista Brasileira de Geociencias 29, 441–446. https://doi.org/10.5327/rbg.v29i3.715

Mullen, E.D., 1983. MnO/TiO2/P2O5: a minor element discriminant for basaltic rocks of oceanic environments and its implications for petrogenesis. Earth and Planetary Science Letters 62, 53–62. https://doi.org/10.1016/0012-821X(83)90070-5

Murphy, D.T., Allen, C.M., Ghidan, O., Dickson, A., Hu, W.P., Briggs, E., Holder, P.W., Armstrong, K.F., 2020. Analysing Sr isotopes in low-Sr samples such as single insects with inductively coupled plasma tandem mass spectrometry using N2O as a reaction gas for in-line Rb separation. Rapid Communications in Mass Spectrometry 34, 1–12. https://doi.org/10.1002/rcm.8604

Navarro, M.S., Andrade, S., Ulbrich, H., Gomes, C.B., Girardi, V.A.V., 2008. The direct determination of rare earth elements in basaltic and related rocks using ICP-MS: Testing the efficiency of microwave oven sample decomposition procedures.

Geostandards and Geoanalytical Research 32, 167–180. https://doi.org/10.1111/j.1751-908X.2008.00840.x

Neumann, B., 2000. Texture development of recrystallised quartz polycrystals unravelled by orientation and misorientation characteristics. Journal of Structural Geology 22, 1695–1711. https://doi.org/10.1016/S0191-8141(00)00060-2

O'Sullivan, G., Chew, D., Kenny, G., Henrichs, I., Mulligan, D., 2020. The trace element composition of apatite and its application to detrital provenance studies. Earth-Science Reviews 201, 103044. https://doi.org/10.1016/j.earscirev.2019.103044

O'Sullivan, G.J., Thakurdin, Y., Bolhar, R., Horváth, P., Hoare, B.C., Collerson, K.D., 2021. The Great Falls Tectonic Zone after the assembly of Laurentia: evidence for long-term tectonic stability from xenolith apatite. Lithos 384–385, 105977. https://doi.org/10.1016/j.lithos.2021.105977

Orihashi, Y., Nakai, S., Hirata, T., 2008. U-Pb age determination for seven standard zircons using inductively coupled plasma-mass spectrometry coupled with frequency quintupled Nd-YAG (λ = 213 nm) laser ablation system: Comparison with LA-ICP-MS zircon analyses with a NIST glass reference materia. Resource Geology 58, 101–123. https://doi.org/10.1111/j.1751-3928.2008.00052.x

Oriolo, S., Oyhantçabal, P., Wemmer, K., Siegesmund, S., 2017. Contemporaneous assembly of Western Gondwana and final Rodinia break-up: Implications for the supercontinent cycle. Geoscience Frontiers 8, 1431–1445. https://doi.org/10.1016/j.gsf.2017.01.009

Oyhantçabal, P., Wagner-Eimer, M., Wemmer, K., Schulz, B., Frei, R., Siegesmund, S., 2012. Paleo- and Neoproterozoic magmatic and tectonometamorphic evolution of the Isla Cristalina de Rivera (Nico Pérez Terrane, Uruguay). International Journal of Earth Sciences 101, 1745–1762. https://doi.org/10.1007/s00531-012-0757-4

Passarelli, C.R., Basei, M.A.S., Prazeres-Filho, H.J., Siga, O., Szabó, G.A.J., Marco-Neto, J., 2007. Structural and geochronological constraints on the evolution of the Juréia Massif, Registro Domain, State of São Paulo, Brazil. Anais Da Academia Brasileira de Ciencias 79, 441–455. https://doi.org/10.1590/s0001-37652007000300008

Passarelli, C.R., Basei, M.A.S., Wemmer, K., Siga Júnior, O., Oyhantc, P., 2011. Major shear zones of southern Brazil and Uruguay : escape tectonics in the eastern border of Rio de La plata and Paranapanema cratons during the Western Gondwana amalgamation. International Journal of Earth Sciences 100, 391–414. https://doi.org/10.1007/s00531-010-0594-2

Passarelli, C.R., Verma, S.K., Mcreath, I., Basei, M.Â.S., Siga Júnior, O., 2019. Tracing the history from Rodinia break-up to the Gondwana amalgamation in the Embu Terrane, southern Ribeira Belt, Brazil. Lithos. https://doi.org/10.1016/j.lithos.2019.05.024

Passchier, C.W., Trouw, R.A.J., 2005. Microtectonics. Springer Berlin Heidelberg.

Patiño Douce, A.E., Harris, N., 1998. Experimental constraints on Himalayan anatexis. Journal of Petrology 39, 689–710. https://doi.org/10.1093/petroj/39.4.689

Paton, C., Hellstrom, J., Paul, B., Woodhead, J., Hergt, J., 2011. Iolite: Freeware for the visualisation and processing of mass spectrometric data. Journal of Analytical Atomic Spectrometry 26, 2508–2518. https://doi.org/10.1039/c1ja10172b

Payne, J.L., Hand, M., Barovich, K.M., Wade, B.P., 2008. Temporal constraints on the timing of high-grade metamorphism in the northern Gawler Craton: Implications for assembly of the Australian Proterozoic. Australian Journal of Earth Sciences 55, 623–640. https://doi.org/10.1080/08120090801982595

Pearce, J.A., 2008. Geochemical fingerprinting of oceanic basalts with applications to ophiolite classification and the search for Archean oceanic crust. Lithos 100, 14–48. https://doi.org/10.1016/j.lithos.2007.06.016

Pearce, J.A., 1996. A User's Guide to Basalto Discriminant Diagrams., Geological Association of Canada, Short Course Notes.

Pearce, J.A., Cann, J.R., 1973. Tectonic setting of basic volcanic rocks determined using trace element analyses. Earth and Planetary Science Letters 19, 290–300. https://doi.org/10.1016/0012-821X(73)90129-5

Pearce, J.A., Thirlwall, M.F., Ingram, G., Murton, B.J., Arculus, R.J., Van Der Laan, S.R., 1992. Isotopic evidence for the origin of boninites and related rocks drilled in

the Izu-Bonin (Ogasawara) Forearc, Leg 125. Proc., Scientific Results, ODP, Leg 125, Bonin/Mariana Region 125, 237–262. https://doi.org/10.2973/odp.proc.sr.125.134.1992

Pearce, T.H., Gorman, B.E., Birkett, T.C., 1975. The TiO_2-K_2O-P_2O_5 Diagram: A Method of Discriminating Between Oceanic and Non-Oceanic Basalts. Earth and Planetary Science Letters 24, 419–426.

Peixoto, C. de A., Heilbron, M., Ragatky, D., Armstrong, R., Dantas, E., de Morisson Valeriano, C., Simonetti, A., 2017. Tectonic evolution of the Juvenile Tonian Serra da Prata magmatic arc in the Ribeira belt, SE Brazil: Implications for early west Gondwana amalgamation. Precambrian Research 302, 221–254. https://doi.org/10.1016/j.precamres.2017.09.017

Percival, J.J., Konopásek, J., Anczkiewicz, R., Ganerød, M., Sláma, J., de Campos, R.S., Bitencourt, M. de F., 2022. Tectono-Metamorphic Evolution of the Northern Dom Feliciano Belt Foreland, Santa Catarina, Brazil: Implications for Models of Subduction-Driven Orogenesis. Tectonics 41, e2021TC007014. https://doi.org/https://doi.org/10.1029/2021TC007014

Perrotta, M.M., 1996. POTENCIAL AURÍFERO DE UMA REGIÃO NO VALE DO RIBEIRA , SÃO PAULO , ESTIMADO POR MODELAGEM DE DADOS GEOLÓGICOS , SISTEMA DE INFORMAÇÕES GEOGRÁFICAS . Mônica Mazzini Perrotta Tese de Doutoramento Programa de Pós-Graduação em Geoquími. Universidade de São Paulo.

Perrotta, M.M., Salvador, E.D., Lopes, R.C., D'Agostino, L.Z., Peruffo, N., Gomes, S.D., Sachs, L.L.B., Meira, V.T., Garcia, M.G.M., Lacerda Filho, J.V., 2005. Mapa geológico do estado de São Paulo. Escala: 1:750.000.

Pertille, J., Hartmann, L.A., Santos, J.O.S., N.J., M., Armstrong, R., 2017. Reconstructing the Cryogenian–Ediacaran evolution of the Porongos fold and thrust belt, Southern Brasiliano Orogen, based on Zircon U–Pb–Hf–O isotopes. International Geology Review 59, 1532–1560. https://doi.org/10.1080/00206814.2017.1285257

Philipp, R.P., Pimentel, M.M., Chemale, F., 2016. Tectonic evolution of the Dom Feliciano Belt in Southern Brazil: Geological relationships and U-Pb

geochronology. Brazilian Journal of Geology 46, 83–104. https://doi.org/10.1590/2317-4889201620150016

Pinto, V.M., Debruyne, D., Hartmann, L.A., Queiroga, G.N., Lana, C., Fragoso César, B.A.M., Porcher, C., Castro, M.P., Laux, J., 2021. Metamorphic evolution of a Tonian eclogite associated with an island arc of the southern Brasiliano Orogen. Precambrian Research 366. https://doi.org/10.1016/j.precamres.2021.106414

Polat, A., Hofmann, A.W., Rosing, M.T., 2002. Boninite-like volcanic rocks in the 3.7-3.8 Ga isua greenstone belt, West Greenland: Geochemical evidence for intra-oceanic subduction zone processes in the early earth. Chemical Geology 184, 231–254. https://doi.org/10.1016/S0009-2541(01)00363-1

Porada, H., 1989. Pan-African rifting and orogenesis in Southern Equatorial Africa and Eastern Brazil. Precambrian Research 44, 103–136. https://doi.org/10.1016/0301-9268(89)90078-8

Porcher, C., Egydio-silva, M., Fernandes, L., Vauchez, A., 1995. Dados prelimineres do metamorfismo M1 da Faixa Ribeira: Região de Três Rios e Santo Antônio de Pádua (RJ). V Simpósio Nacional de Estudos Tectônicos. Gramado, 71–73.

Prazeres Filho, H.J. dos, 2005. Caracterização geológica e petrogenética do batólito granítico Três Córregos (PR-SP): geoquímica isotópica (Nd-Sr-Pb), idades (ID-TIMS/SHRIMP) e d18'O em zircão. https://doi.org/10.11606/T.44.2005.tde-29102015-131336

Ramsay, J.G., 1980. Shear zone geometry: A review. Journal of Structural Geology 2, 83–99. https://doi.org/10.1016/0191-8141(80)90038-3

Ribeiro, B. V., Finch, M.A., Cawood, P.A., Faleiros, F.M., Murphy, T.D., Simpson, A., Glorie, S., Tedeschi, M., Armit, R., Barrote, V.R., 2021. From microanalysis to supercontinents: insights from the Rio Apa Terrane into the Mesoproterozoic SW Amazonian Craton evolution during Rodinia assembly. Journal of Metamorphic Geology. https://doi.org/10.1111/jmg.12641

Ribeiro, B. V., Lagoeiro, L., Faleiros, F.M., Hunter, N.J.R., Queiroga, G., Raveggi, M., Cawood, P.A., Finch, M., Campanha, G.A.C., 2020a. Strain localization and fluid-assisted deformation in apatite and its influence on trace elements and U–Pb

systematics. Earth and Planetary Science Letters 545, 116421. https://doi.org/10.1016/j.epsl.2020.116421

Ribeiro, B. V., Mulder, J.A., Faleiros, F.M., Kirkland, C.L., Cawood, P.A., O'Sullivan, G., Campanha, G.A.C., Finch, M.A., Weinberg, R.F., Nebel, O., 2020b. Using apatite to resolve the age and protoliths of mid-crustal shear zones: A case study from the Taxaquara Shear Zone, SE Brazil. Lithos 378–379, 105817. https://doi.org/10.1016/j.lithos.2020.105817

Ribeiro, B. V, Faleiros, F.M., Campanha, G.A.C., Lagoeiro, L., Weinberg, R.F., Hunter, N.J.R., 2019. Tectonophysics Kinematics , nature of deformation and tectonic setting of the Taxaquara Shear Zone , a major transpressional zone of the Ribeira Belt (SE Brazil). Tectonophysics 751, 83–108. https://doi.org/10.1016/j.tecto.2018.12.025

Ricardo, B.S., Faleiros, F.M., Moraes, R., Siga Júnior, O., Campanha, G.A.C., 2020. Tectonic implications of juxtaposed high- and low-pressure metamorphic field gradient rocks in the Turvo-Cajati Formation, Curitiba Terrane, Ribeira Belt, Brazil. Precambrian Research 345, 105766. https://doi.org/10.1016/j.precamres.2020.105766

Rubatto, D., Hermann, J., Berger, A., Engi, M., 2009. Protracted fluid-induced melting during Barrovian metamorphism in the Central Alps. Contributions to Mineralogy and Petrology 158, 703–722. https://doi.org/10.1007/s00410-009-0406-5

Sadowski, G.R., 1991. A megafalha de Cubatão no Sudeste Brasileiro. Boletim IG, Instituto de Geociências 22, 15–28.

Sadowski, G.R., Motidome, M.J., 1987. Brazilian megafaults. Revista Geologica de Chile 31, 61–75.

Sadowski, H.G.R.&, 1976. Considerações sobre a estratigrafia do Pré-Cambriano na Região de São Paulo. Boletim IG, Instituto de Geociências 9, 107–112.

Santiago, R., Caxito, F. de A., Pedrosa-Soares, A., Neves, M.A., Dantas, E.L., 2020. Tonian island arc remnants in the northern Ribeira orogen of Western Gondwana: The Caxixe batholith (Espírito Santo, SE Brazil). Precambrian Research 351, 105944. https://doi.org/10.1016/j.precamres.2020.105944

Santos, L. da R., Leandro, R., Bahniuk, A., Cury, L.F., 2018. Low-temperature metamorphism in the Capiru Formation, Morro Grande Synform, Southern Ribeira Belt. Brazilian Journal of Geology 48, 95–113. https://doi.org/10.1590/2317-4889201820170090

Santosh, M., Maruyama, S., Sato, K., 2009. Anatomy of a Cambrian suture in Gondwana: Pacific-type orogeny in southern India? Gondwana Research 16, 321–341. https://doi.org/10.1016/j.gr.2008.12.012

Sato, K., Siga, O., Da Silva, J.A., McReath, I., Dunyi, L., Iizuka, T., Rino, S., Hirata, T., Sproesser, W., Basei, M.A.S., 2009. In situ isotopic analyses of U and Pb in zircon by remotely operated SHRIMP II, and Hf by LA-ICP-MS: An example of dating and genetic evolution of zircon by 176Hf/177Hf from the Ita quarry in the Atuba Complex, Se Brazil. Geologia USP - Serie Cientifica 9, 61–69.

Sato, K., Siga, O., Nutman, A.P., Basei, M.A.S., McReath, I., Kaulfuss, G., 2003. The Atuba Complex, Southern South American platform: Archean components and paleoproterozoic to neoproterozoic tectonothermal events. Gondwana Research 6, 251–263. https://doi.org/10.1016/S1342-937X(05)70974-6

Sawyer, E.W., 2008. Atlas of Migmatites. Canadian Science Publishing. https://doi.org/10.1139/9780660197876

Schulz, B., 2021. Monazite Microstructures and Their Interpretation in Petrochronology. Frontiers in Earth Science 9. https://doi.org/10.3389/feart.2021.668566

Shervais, J.W., 1982. TiV plots and the petrogenesis of modern and ophiolitic lavas. Earth and Planetary Science Letters 59, 101–118. https://doi.org/10.1016/0012-821X(82)90120-0

Siga Junior, O., 1995. Domínios Tectônicos do Sudeste do Paraná e Nordeste de Santa Catarina: Geocronologia e Evolução crustal. Universidade de São Paulo.

Siga Júnior, O., Angelo, Basei, S., Sato, K., Passarelli, C.R., Nutman, A., Mcreath, I., Prazeres Filho, H.J. dos, 2011a. Calymmian (1 .50 e 1.45 Ga) magmatic records in Votuverava and Perau sequences , south-southeastern Brazil : Zircon ages and Nd e Sr isotopic geochemistry. Journal of South American Earth Sciences 32, 301–308. https://doi.org/10.1016/j.jsames.2011.03.015

Siga Júnior, O., Basei, M.A.S., Nutman, A., Sato, K., McReath, I., Passarelli, C.R., Liu, D., 2011b. Extensional and Colisional Magmatic Records in the Apiaí Terrane, South-Southeastern Brazil: Integration of Geochronological U-Pb Zircon Ages. Geologia USP - Serie Cientifica 11, 149–175.

Siga Júnior, O., Basei, M.A.S., Passarelli, C.R., Sato, K., Cury, L.F., McReath, I., 2009. Lower and Upper Neoproterozoic magmatic records in Itaiacoca Belt (Paraná-Brazil): Zircon ages and lithostratigraphy studies. Gondwana Research 15, 197–208. https://doi.org/10.1016/j.gr.2008.11.002

Siga Júnior, O., Basei, M.A.S., Reis Neto, J.M., Machiavelli, A., Harara, O.M., 1995. O complexo Atuba: um cinturão paleoproterozóico intensamente retrabalhado no Neoproterozóico. Boletim IG-USP. Série Científica 26, 69. https://doi.org/10.11606/issn.2316-8986.v26i0p69-98

Siga Júnior, O., Cury, L.F., Mcreath, I., Maria, L., Leite, D.A., Sato, K., Basei, M.A.S., Passarelli, C.R., 2011c. Geology and geochronology of the Betara region in south-southeastern Brazil: Evidence for possible Statherian (1.80 – 1.75 Ga) and Calymmian (1.50 –1.45 Ga) extension events. Gondwana Research 19, 260–274. https://doi.org/10.1016/j.gr.2010.06.003

Silva, B.Y.B., 2017. Evolução Tectônica Da Porção Central Do Terreno Embu Ao Norte Da Zona De Cisalhamento Taxaquara-Guararema Terreno Embu Ao Norte Da Zona De Cisalhamento Taxaquara-Guararema. University of São Paulo.

Sláma, J., Košler, J., Condon, D.J., Crowley, J.L., Gerdes, A., Hanchar, J.M., Horstwood, M.S.A., Morris, G.A., Nasdala, L., Norberg, N., Schaltegger, U., Schoene, B., Tubrett, M.N., Whitehouse, M.J., 2008. Plešovice zircon - A new natural reference material for U-Pb and Hf isotopic microanalysis. Chemical Geology 249, 1–35. https://doi.org/10.1016/j.chemgeo.2007.11.005

Sobrinho, J.M.A., Janasi, V.A., Simonetti, A., 2011. The Ilha Anchieta Quartz Monzonite : the southernmost expression of ca . 500 Ma post-collisional magmatism in the Ribeira Belt. Anais Da Academia Brasileira de Ciencias 83, 891–906.

Spear, F.S., Kohn, M.J., Cheney, J.T., 1999. P -T paths from anatectic pelites. Contributions Mineral Petrology 134, 17–32.

Stallard, A., Shelley, D., 1995. Quartz c-axes parallel to stretching directions in very low-grade metamorphic rocks. Tectonophysics 249, 31–40. https://doi.org/10.1016/0040-1951(95)00040-T

Stein, D.P., Campanha, G.A. da C., Fernandes, L.A., 1983. Geologia da Folha Pilar do Sul (SF.23-Y-C-IV-4). Estado de São Paulo. São Paulo.

Stipp, M., Stünitz, H., Heilbronner, R., Schmid, S.M., 2002. The eastern Tonale fault zone: A "natural laboratory" for crystal plastic deformation of quartz over a temperature range from 250 to 700 °C. Journal of Structural Geology 24, 1861–1884. https://doi.org/10.1016/S0191-8141(02)00035-4

Sun, S.S., McDonough, W.F., 1989. Chemical and isotopic systematics of oceanic basalts: Implications for mantle composition and processes. Geological Society Special Publication 42, 313–345. https://doi.org/10.1144/GSL.SP.1989.042.01.19

Tassinari, C.C.G., 1988. As idades das rochas e dos eventos metamórficos da porção sudeste do estado de São Paulo e sua evolução crustal. Universidade de São Paulo.

Tassinari, C.C.G., Campos Neto, M. da C., 1988. Precambrian continental crust evolution of Southeastern São Paul State, Brazil, based on isotopic evidence. Geochim. Brasil 2, 175–183.

Tassinari, C.C.G., Munhá, J.M.U., Ribeiro, A., Correia, C.T., 2001. Neoproterozoic oceans in the Ribeira belt (southeastern Brazil): The Pirapora do bom Jesus ophiolitic complex. Episodes 24, 245–251. https://doi.org/10.18814/epiiugs/2001/v24i4/004

Thomson, S.N., Gehrels, G.E., Ruiz, J., Buchwaldt, R., 2012. Routine low-damage apatite U-Pb dating using laser ablation-multicollector- ICPMS. Geochemistry, Geophysics, Geosystems 13, 1–23. https://doi.org/10.1029/2011GC003928

Torquato, J.R., Cordani, 1981. Brazil-Africa geological links. Earth Science Reviews 17, 155–176. https://doi.org/10.1016/0012-8252(81)90010-6

Trouw, R.A.J., Peternel, R., Ribeiro, A., Heilbron, M., Vinagre, R., Duffles, P., Trouw, C.C., Fontainha, M., Kussama, H.H., 2013. A new interpretation for the interference zone between the southern Brasília belt and the central Ribeira belt, SE Brazil.

Journal of South American Earth Sciences 48, 43–57. https://doi.org/10.1016/j.jsames.2013.07.012

Tsunogae, T., Uthup, S., Nyirongo, M.W., Takahashi, K., Rahman, M.S., Liu, Q., Takamura, Y., Tsutsumi, Y., 2021. Neoproterozoic crustal growth in southern Malawi: New insights from petrology, geochemistry, and U–Pb zircon geochronology, and implications for the Kalahari Craton–Congo Craton amalgamation. Precambrian Research 352, 106007. https://doi.org/10.1016/j.precamres.2020.106007

Tupinambá, M., Heilbron, M., Valeriano, C., Júnior, R.P., de Dios, F.B., Machado, N., Silva, L.G. do E., de Almeida, J.C.H., 2012. Juvenile contribution of the Neoproterozoic Rio Negro Magmatic Arc (Ribeira Belt, Brazil): Implications for Western Gondwana amalgamation. Gondwana Research 21, 422–438. https://doi.org/10.1016/j.gr.2011.05.012

Vauchez, A., Tommasi, A., Silva, A., Trompette, R., 1992. Tectônica de escape na terminação de um craton: A Faixa Ribeira. Congresso Brasileiro de Geologia. 373–374.

Vermeesch, P., 2018. IsoplotR: A free and open toolbox for geochronology. Geoscience Frontiers 9, 1479–1493. https://doi.org/10.1016/j.gsf.2018.04.001

Viegas, G., Menegon, L., Archanjo, C., 2016. Brittle grain-size reduction of feldspar, phase mixing and strain localization in granitoids at mid-crustal conditions (Pernambuco shear zone, NE Brazil). Solid Earth 7, 375–396. https://doi.org/10.5194/se-7-375-2016

Vieira, S.R.S.S., 1996. Estudo de processos metamórfico-metassomáticos nos Complexos Embu e Pilar no Bloco Juquitiba, SP. Universidade de São Paulo.

Vlach, S., 2008. Mineralogia, análise e datação de monazita com microssonda eletrônica e aplicações. Universidade de São Paulo.

Weber, W., Siga Junior, O., Sato, K., Neto, J.M. dos R., Basei, M.Â.S., Nutman, A.P., 2004. A Formação Água Clara na região de Araçaíba-SP: registro de uma bacia Mesoproterozoica. Boletim IG, Instituto de Geociências, USP 4, 101–110.

Werle, M., Hartmann, L.A., Queiroga, G.N., Lana, C., Pertille, J., Michelin, C.R.L., Remus, M.V.D., Roberts, M., Castro, M.P., Leandro, C.G., Savian, J.F., 2020. Oceanic crust and mantellic evidence on the evolution of tonian-cryogenian ophiolites, southern Brasiliano Orogen. Precambrian Research 351, 105979. https://doi.org/10.1016/j.precamres.2020.105979

White, R.W., Powell, R., Halpin, J.A., 2004. Spatially-focussed melt formation in aluminous metapelites from Broken Hill, Australia. Journal of Metamorphic Geology 22, 825–845. https://doi.org/10.1111/j.1525-1314.2004.00553.x

White, R.W., Powell, R., Holland, T.J.B., 2001. Calculation of partial melting equilibria in the system Na2O-CaO-K2O-FeO-MgO-Al2O3-SiO2-H2O (NCKFMASH). Journal of Metamorphic Geology 19, 139–153. https://doi.org/10.1046/j.0263-4929.2000.00303.x

White, R.W., Powell, R., Johnson, T.E., 2014. The effect of Mn on mineral stability in metapelites revisited: New a-x relations for manganese-bearing minerals. Journal of Metamorphic Geology 32, 809–828. https://doi.org/10.1111/jmg.12095

Williams, I.S., 1997. U-Th-Pb Geochronology by Ion Microprobe., Applications of Microanalytical Techniques to Understanding Mineralizing Processes. https://doi.org/10.5382/Rev.07.01

Wilson, M., 1989. Igneous Petrogenesis, Journal of Chemical Information and Modeling. Chapman & Hall.

Wilson, M. (B. M., 2007. Igneous petrogenesis. Dordrecht : Springer, [2007] ©2007.

Xia, L., Li, X., 2019. Basalt geochemistry as a diagnostic indicator of tectonic setting. Gondwana Research 65, 43–67. https://doi.org/10.1016/j.gr.2018.08.006

Xia, L.Q., 2014. The geochemical criteria to distinguish continental basalts from arc related ones. Earth-Science Reviews 139, 195–212. https://doi.org/10.1016/j.earscirev.2014.09.006

Yogi, M.T., 2019. Thermobaric and kinematic evolution of Anta Gorda Anticlinorium , Ribeira Belt : metamorphism record and shear deformation in a transpressional setting. São Paulo University.

5. DEFORMATION, THERMOCHRONOLOGY AND TECTONIC SIGNIFICANCE OF THE CRUSTAL-SCALE CUBATÃO SHEAR ZONE, RIBEIRA BELT, BRAZIL

Dina I. G. Cabrita[a]*, Frederico M. Faleiros[a], Bruno V. Ribeiro[b,c], Luca Menegon[d], Peter A. Cawood[b], Ginaldo A. C. Campanha[a]

[a] Instituto de Geociências, Universidade de São Paulo, Rua do Lago 562, CEP 05508-080, São Paulo SP, Brazil

[b] School of Earth, Atmosphere and Environment, Monash University, Melbourne, VIC 3800, Australia

[c] Curtin University, Timescales of Mineral Systems Group, School of Earth and Planetary Sciences, Perth, WA 6845, Australia

[d] The Njord Centre, Department of Geosciences, University of Oslo, Postbox 1047, Blindern, 0316 Oslo, Norway

*Corresponding author: dina_cabrita@yahoo.com

Abstract

Crustal-scale shear zones are key structures in orogenic belts linked to the assembly of West Gondwana. The Cubatão Shear Zone (CSZ) represents a significant segment of a crustal-scale transcurrent shear zone system that cuts Paleoproterozoic to Neoproterozoic units in the Ribeira Belt (SE Brazil). Despite its tectonic importance, the relationship between transcurrent deformation and orogenesis is still controversial. This work aims to understand this relationship by integrating the transcurrent deformation history of the CSZ with regional orogenic processes through structural analyses, phase-equilibria modelling, and zircon and apatite U–Pb–REE analyses. The results indicate that the CSZ developed within a transpressional setting with a dominant subhorizontal stretching lineation at medium-temperature conditions of 460–520 ºC and 4.5–9.5 kbar, consistent with quartz recrystallisation microstructures indicative of subgrain rotation recrystallisation. Igneous-type apatite from the mylonites of the CSZ record ages of ca.

610–570 Ma, which are interpreted as reset ages due to ductile deformation at medium-temperature conditions. Zircon U–Pb geochronology indicates that mylonites are sourced from the Juquiá Granite and the Atuba Complex. The CSZ activity is coeval with the main period of activity of other ductile shear zones from the Ribeira Belt, as indicated by available geochronological data. This age interval coincides with the main period of other regional shear zones activity, voluminous granitic magmatism, regional metamorphism and convergence of the cratons surrounding the Ribeira Belt, indicating active participation of the transcurrent shear zones in the orogenic processes that built up West Gondwana.

Keywords: transcurrent deformation; quartz EBSD; phase equilibria modelling; West Gondwana

.

5.1. Introduction

Shear zones localise deformation within the crust and operate at scales ranging from microscopic to tectonic plates boundaries (Ramsay, 1980; Alsop and Holdsworth, 2004; Fossen and Cavalcante, 2017; Faleiros et al., 2021). Additionally, shear zones are key structures in all types of tectonic settings, including orogenic belts, where they separate terranes with distinct tectonic, metamorphic, and paleogeographic histories (Condie, 2003; Santosh et al., 2009; Faleiros et al., 2011a, 2016; Chetty, 2017). For example, the orogenic belts that formed West Gondwana, and specially the Ribeira Belt, consist of allochthonous terranes juxtaposed by a crustal-scale transcurrent shear system (e.g.,, Sadowski and Motidome, 1987; Campanha and Sadowski, 1999; Egydio-Silva et al., 2002; Basei et al., 2008; Passarelli et al., 2011; Costa de Freitas et al., 2021; Faleiros et al., 2021).

The Cubatão Shear Zone (CSZ) represents a key segment of this shear zone system within the Ribeira Belt, with an exposed length of ca. 450 km, been interpreted as a Neoproterozoic suture zone (Basei et al., 2008; Passarelli et al., 2011; Ricardo et al., 2020). However, despite its major coverage and tectonic significance, no work has quantified its deformation and petrochronological evolution, which can provide vital clues for understanding the role of localised shear zones in crustal deformation.

Our study focuses on the role of transcurrent deformation during orogenenic processes related to West Gondwana assembly, exemplified by the CSZ. We present a multi-method study involving quartz crystallographic preferred orientation using electron backscatter diffraction (EBSD), phase equilibria modelling, and apatite and zircon U–Pb isotopes and trace element concentrations. The results demonstrate that the CSZ was active during the main period of activity of other ductile shear zones from the Ribeira Belt, indicating active participation of the transcurrent shear zones in the orogenic processes that built up West Gondwana.

5.2. Geological context

5.2.1. Ribeira Belt

The Ribeira Belt comprises a crustal segment orientated parallel to the S-SE trending coastline of Brazil. The evolutionary history of the belt overlaps with, and is related to Rodinia break-up and assembly of West Gondwana (e.g., Almeida et al., 1973; Almeida and Hasui, 1984; Brito Neves et al., 2014) (Fig. 5.1a and b). The southern portion of the belt comprises, from northwest to southeast, the Embu, Costeiro, Apiaí and Curitiba terranes (Fig. 5.1c).

The Embu Terrane is composed by Paleoproterozoic gneiss (Rio Capivari Complex), the Embu Complex and Tonian to Ediacaran granitoids (Fernandes, 1991; Babinski et al., 2001; Janasi et al., 2003; Alves et al., 2013, 2016; Maurer, 2016; Campanha et al., 2019; Meira et al., 2019a). The Embu Complex is an association of early Tonian metasedimentary rocks with intercalations of orthogneiss and metamafic rocks deformed during the Tonian (under high-temperature conditions) and the Ediacaran to Cryogenian (Cordani et al., 2002; Vlach, 2008; Campanha et al., 2019). The Costeiro Terrane is composed by the Costeiro Complex and syn to post-tectonic granites. The Costeiro Complex comprises Ediacaran high-grade metamorphic rocks, including orthogneiss, metatexitic to diatexitic metapelites/semipelites, metapsammites, calcsilicate rocks and boudins of amphibolites (Meira, 2014; Meira et al., 2015, 2019a).

The Curitiba Terrane is composed of the Atuba Complex, Cryogenian to Ediacaran metasedimentary successions (Turvo-Cajati and Capiru formations) and granitoids. The Atuba Complex is composed of a Paleoproterozoic tonalite-trondhjemite-granodiorite type migmatitic orthogneiss that underwent two main episodes of high-grade metamorphism during the Rhyacian (2100–2000 Ma) and Cryogenian to Ediacaran (650–

550 Ma) (Siga Júnior, 1995; Siga Júnior et al., 1995; Sato et al., 2003, 2009; Faleiros et al., 2011). Finally, the Apiaí Terrane comprises Paleoproterozoic gneisses and granites, a series of metasedimentary units deposited from the Calymmian to Ediacaran and granitoids from the Cryogenian to Ediacaran (Hackspacher et al., 2000; Campanha and Sadowski, 2002; Weber et al., 2004; Basei et al., 2008; Siga Júnior et al., 2009, 2011a, 2011b; Campanha et al., 2015, 2016; Forero-Ortega and Faleiros, 2018). Metamorphic activity spans between 615–565 Ma (Yogi, 2019) and igneous activity between 640–565 Ma (Janasi et al., 2001; Prazeres Filho, 2005).

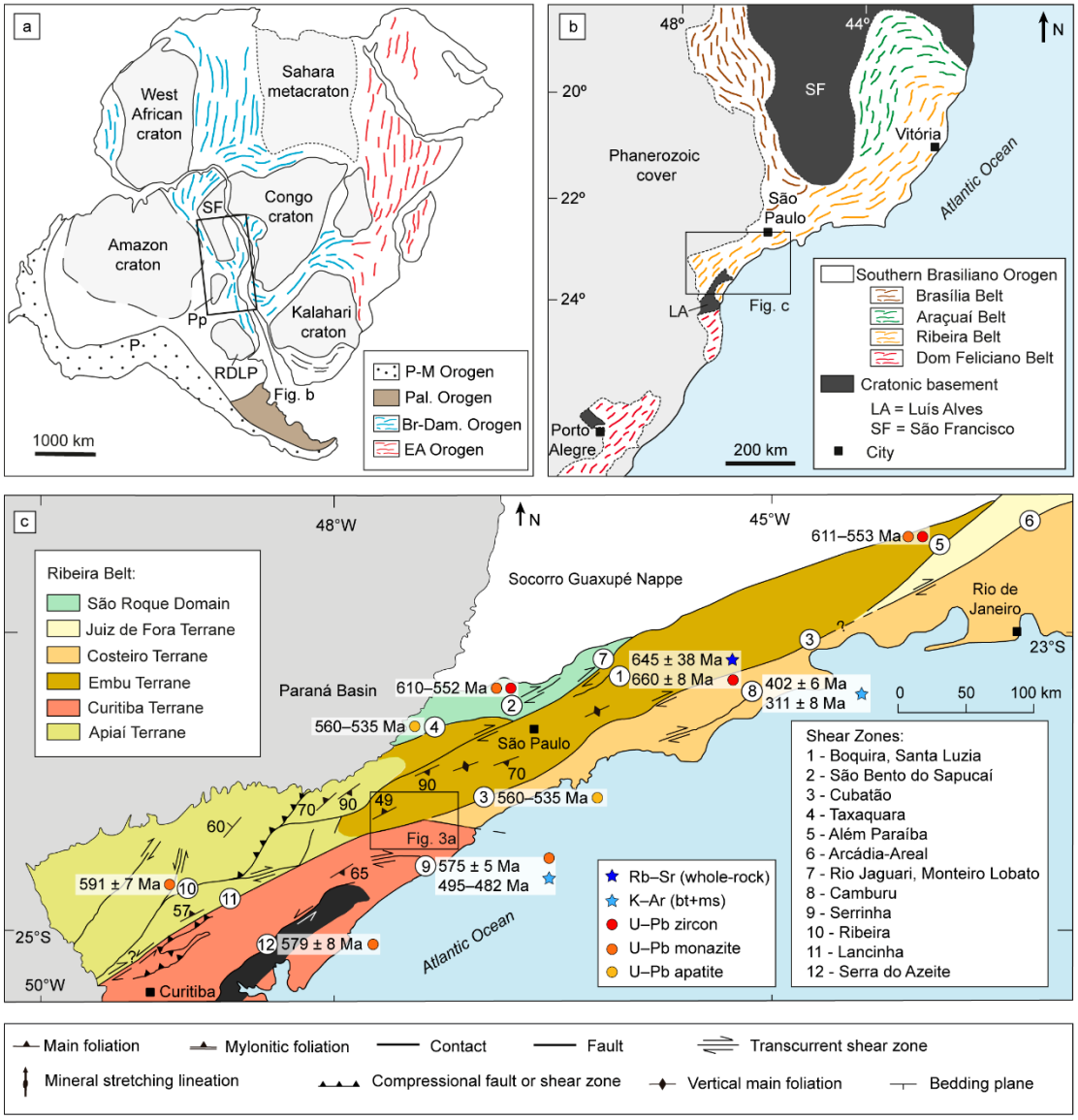

Figure 5.1. Location maps of the study area. a) Location of the studied area in West Gondwana. Abbreviations include: Cratons: Am = Amazonian; SF = S˜ao Francisco; Pp = Paranapanema; RDLP = Rio de la Plata.Proterozoic orogens: Br-Dam = Brasiliano-Damara; EA = East African. Other units: Pal. = Paleozoic; P-M = Paleozoic- Mezosoic Modified from Gray et al. (2008) and Li et al. (2008). b) Geotectonic sketch map of the Southern Brasiliano Orogen, showing the subdivision in belts. c) Geotectonic map of the

southern portion of the Ribeira Belt with location of the study area and shear zones ages. Modified from Campanha et al. (2019). Ages are from: 1 - Tassinari (1988); 2 - Costa et al., 2020; 3 – this work; 4 - Ribeiro et al. (2020); 5 - Giraldo et al. (2019); 8 - Mora et al. (2013); 9 - Passarelli et al. (2011); 10 - Faleiros et al. (2010); 12 - Faleiros et al. (2011). The maps use geographical coordinates in degrees (WGS-84 datum).

5.2.2. Brazilian Southeastern Shear Zone System

The transcurrent Brazilian Southeastern Shear Zone System (Sadowski, 1991; Basei et al., 1992, 2008; Campanha, 2002; Passarelli et al., 2011) cuts Meso to Neoproterozoic metasedimentary successions and large volumes of granitic plutons in the Ribeira Belt, and is related to the late stages of West Gondwana assembly (Vauchez et al., 1992; Porcher et al., 1995; Faleiros et al., 2011a, 2016; Passarelli et al., 2011). The Cubatão Shear Zone is the main branch of the system, composed of an anastomosing network of brittle-ductile to ductile shear zones (Fig. 1c), largely with dextral shear sense. The Lancinha and Além Paraíba shear zones along with the Cubatão Shear Zone are thought to be segments of the one system (Fig. 5.1c) with an exposed length > 900 km (Sadowski, 1991; Passarelli et al., 2011).

The level of crustal exposure along the Brazilian Southeastern Shear Zone System becomes progressively deeper from the southwest to the northeast. In the southwest, the shear zone system displays greenschist facies conditions interpreted as preservation of an upper crustal structural level (e.g., Lancinha, Ribeira and Curitiba shear zones) (Fassbinder, 1990; Faleiros et al., 2010; Cabrita et al., 2017; Conte et al., 2020), whereas amphibolite facies conditions occur in the central portion, inferred as a mid-crustal structural level (e.g., Taxaquara Shear Zone and the northwestern portion of the Lancinha Shear Zone) (Ribeiro et al., 2019, 2020b, 2020a; Conte et al., 2020). Granulite facies conditions were reached in the northeast (e.g., Além Paraíba Shear Zone) (Sadowski and Motidome, 1987; Sadowski, 1991; Egydio-Silva et al., 2002; Cavalcante et al., 2018; Giraldo et al., 2019). In detail, however, data support a more complex structure and evolutionary history, with coexistence and alternation between ductile and brittle fabrics formed at contrasting crustal levels (Faleiros et al., 2010, 2016; Cabrita et al., 2017).

Available geochronological data for the various segments of the shear zonesystem indicate activity from the Ediacaran to Cambrian (Fig. 5.2). The oldest deformation ages are zircon U–Pb age of 660 ± 8 Ma and whole-rock Rb-Sr age of 645 ± 38 Ma in mylonite from the Boquira Shear Zone (Tassinari and Campos Neto, 1988) and zircon U–Pb ages

between 610–552 Ma in the São Bento do Sapucaí Shear Zone (Costa et al., 2020). Monazite U–Th–Pb_T age of 579 ± 8 Ma is recorded for the Serra do Azeite Shear Zone (Faleiros et al., 2011a), zircon and monazite U–Pb ages between 611–553 Ma in the Além Paraíba Shear Zone (Giraldo et al., 2019) and apatite U–Pb ages of 560-535 Ma in the Taxaquara Shear Zone (Ribeiro et al., 2020b). Younger reactivations in brittle conditions were identified by the K–Ar method with ages of 402 ± 6 Ma and 311 ± 8 Ma in cataclasites from the Camburu Shear Zone (Mora et al., 2013) (Fig. 5.2).

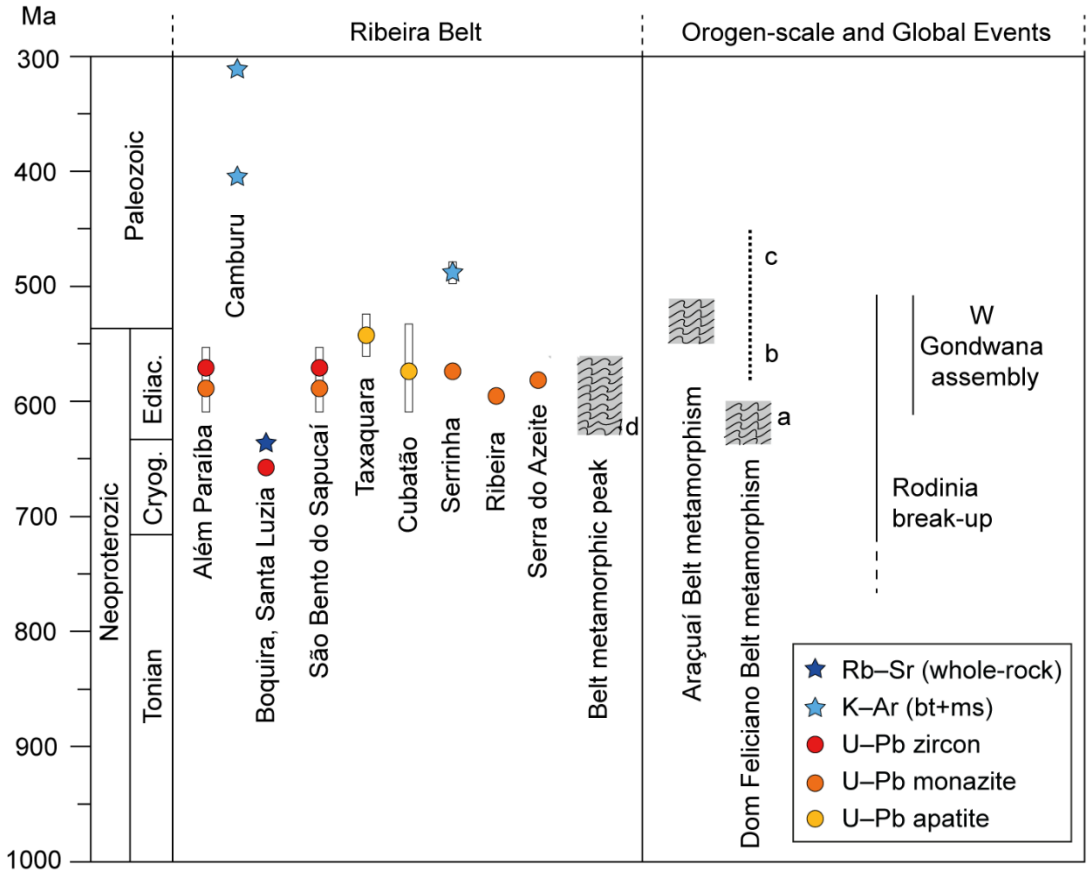

Figure 5.2. Time-space diagram with geochronological data of shear zones from Ribeira Belt and orogenic belts metamorphic ages. Shear zones symbology and age are the same presented in Fig. 5.1. Metamorphic ages are from: a, b and c are from Oyhantçabal et al. (2011) and Oriolo et al., 2016 and d = Brito Neves et al. (2021). a = Main collisional stage; b = Orogen-parallel sinistral shearing; c = E-NE-striking dextral shearing. Dom Feliciano Belt geochronological data are from Oriolo et al. (2016), Araçuaí Belt data from Alkmim et al. (2017) and Rodinia and W Gondwana assembly from Cawood et al. (2016).

5.2.3. Cubatão Shear Zone

The Cubatão Shear Zone (CSZ) is a crustal-scale, dextral, transcurrent and ductile structure that comprises a mylonitic zone of up to 1 km wide over a length of ca. 450 km

(Fig. 5.1c). The CSZ displays a NE-SW structural trend parallel to the main orientation of the surrounding units. Additionally, the CSZ separates the Embu Terrane (in the northwest) from the Costeiro Terrane (northeast) and Curitiba Terrane (southeast) (Fig. 5.1c).

This contribution studies a sector where the CSZ separates the Embu Terrane from the Curitiba Terrane. The studied sector was selected once it corresponds to a key area to investigate the deformation over ca. 8 km CSZ length and displays semi-continuous rock exposure (Fig. 5.3a and b). Sampling sites are located along a national highway (BR-116) presenting individual outcrops with rock exposures of ca. 20–100 m along strike exposures extending in a NE-SW orientation. In this region, deformation associated with the CSZ primarily affected rocks from the Juquiá Granite (Fig. 5.3a), a pluton with a zircon U–Pb crystallisation age of 799 ± 5 Ma (Passarelli et al., 2019) by which a transition from undeformed to highly deformed rocks can be mapped. However, in outcrops with the greatest deformation zone of the CSZ, quartz-feldspar ultramylonites cannot be unequivocally attributed to the Juquiá Granite (Embu Terrane) or the Atuba Complex (Curitiba Terrane) without the aid of geochronological data.

The studied outcrops present sheared rocks ranging from protomylonite to ultramylonite. The protolith, preserved in the less deformed domains, consists primarily of a biotite orthogneiss with monzogranitic composition (Fig. 5.4a), and subordinate amphibolite and schist lenses. The orthogneiss is fine to medium-grained with alternation of millimeter to centimeter-thick biotite-rich and quartz-rich layers. Biotite-rich layers are leuco to mesocratic, and present centimeter euhedral K-feldspar in a fine to medium-grained matrix composed of plagioclase, quartz, biotite and subordinate K-feldspar. The protomylonite (Fig. 5.4b and c) shows an alternation between felsic (grain size up to 1 cm) and mafic layers (ca. 10 µm). Quartz veins occur parallel or subparallel to the mylonitic foliation with thickness up to 3 cm.

In the studied sector of the CSZ, the mylonitic foliation (S_m) strikes ENE-WSW and dips at a high-agle (>80º) towards the NW (with subordinate dips to SE) (Fig. 5.3c) . The mylonitic fabric contains a stretching lineation (L_m) that plunges from ca. 0º to 73º (with a predominance of low-angle plunges) towards ENE and WSW (Fig. 5.3c and Fig. 5.4b and e, yellow dashed lines).

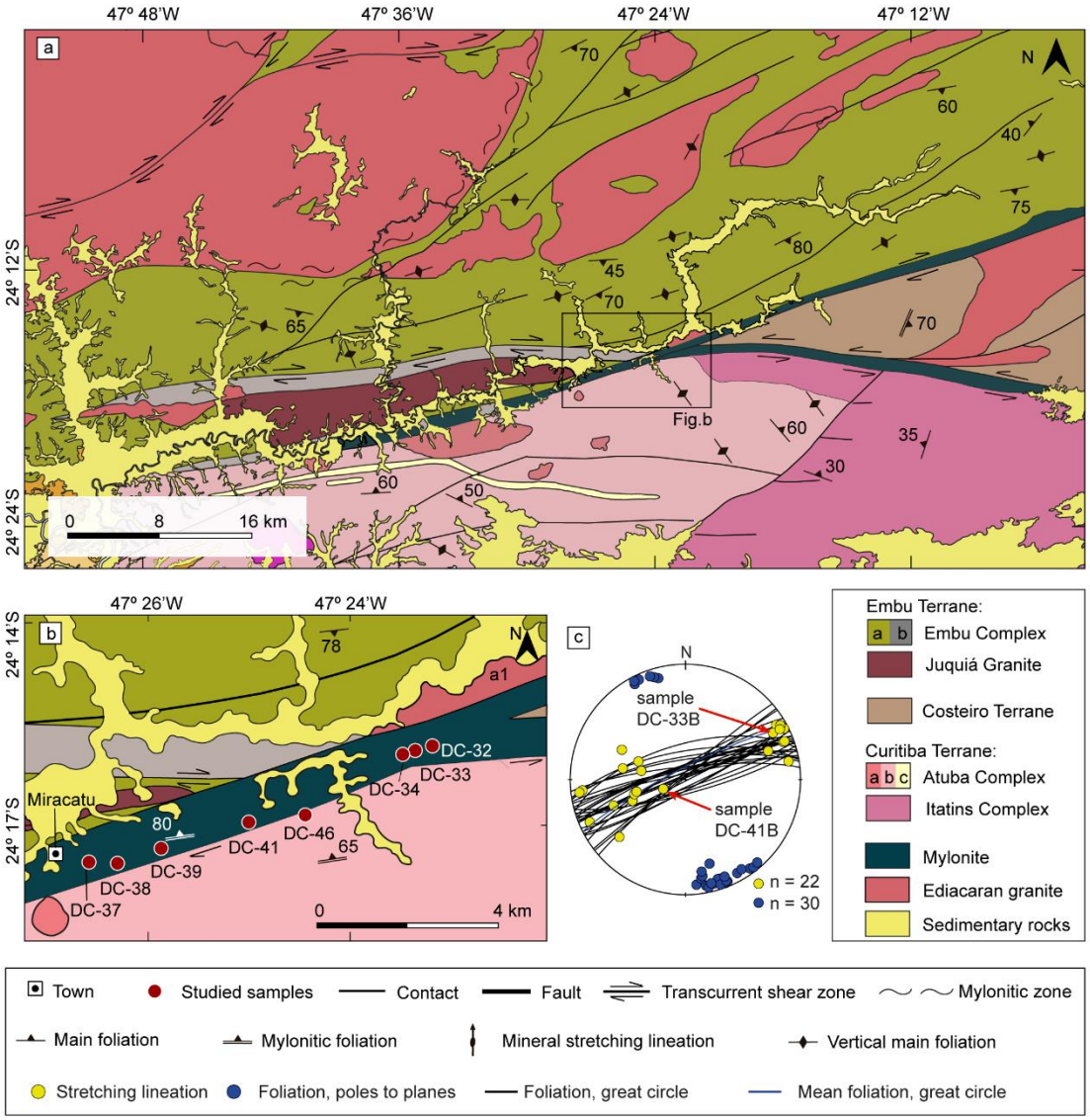

Figure 5.3. Geological maps and stereo plot of the studied area. a) Regional geological and structural map. b) Inset map indicating the location of analysed samples. Embu Terrane: a: paragneiss; b: schist; Atuba Complex: a: diatexite; b gneiss; c: quartzite. Ediacaran granites: a1: Pedro Barros granite. Geographic coordinates, SIRGAS 2000 datum. Modified from Caltabellota et al. (2017). c) Stereoplot with structural data for the studied area. Data is equal-area, lower hemisphere.

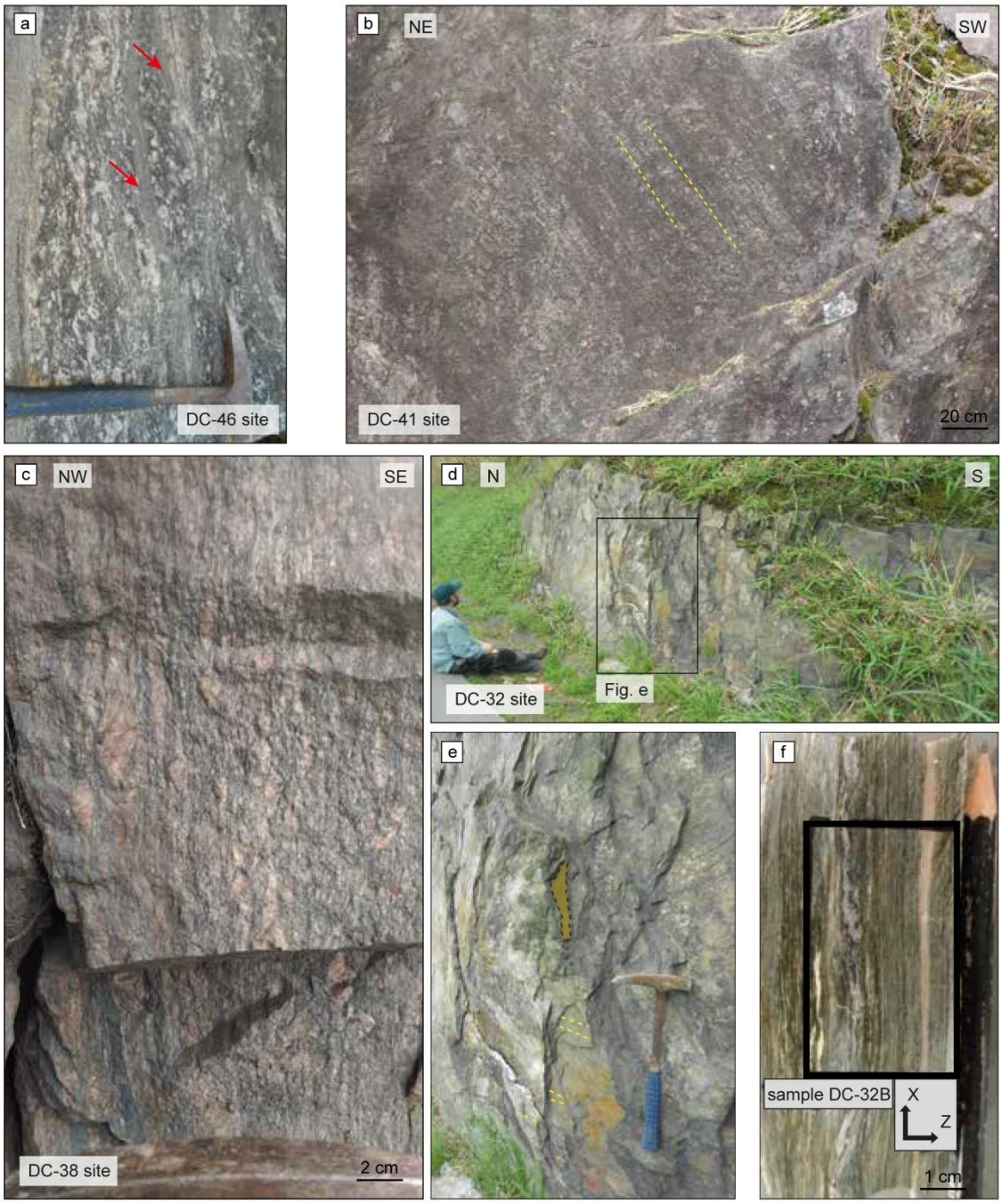

Figure 5.4. Cubatão Shear Zone field site examples. a) Ultramylonite (red arrows) where the protolith (biotite orthogneiss) can be inferred in the less deformed portions; b) Field location where sample DC-41B was obtained with high-angle plunge highlighted by the yellow dashed lines; c) Protomylonite example; d) Field location for site DC-32, which is similar to the site for samples DC-33B and DC-33C; e) Inset photograph showing the high-angle mylonitic foliation (brownish polygon) and the low-angle plunge of the stretching lineation (yellow dashed lines); f) Sample site for ultramylonite sample DC-32B. (For interpretation of the references to colour in this figure legend, the reader is referred to the web version of this article.)

5.3. Methods

Methods used to analyse the CSZ included: (1) quartz quantitative microstructural analysis using electron backscatter diffraction (EBSD), (2) phase diagram modelling, and (3) apatite and zircon trace element analysis and U–Pb geochronology. Studied samples for each of the methods are shown in Table 5.1 and analytical details for methods are presented in Supplementary Material 1.

Electron backscatter diffraction analyses were performed to determine crystallographic preferred orientation of recrystallised quartz to identify the dominant deformation mechanisms during mylonite development. EBSD analyses were performed on a JEOL 7001 FE SEM with an EBSD detector (AZTec acquisition software, Oxford Instruments) at Plymouth Electron Microscopy Centre (PEMC), United Kingdom. Raw EBSD data were processed using HKL Channel 5 software (Oxford Instruments), with noise reduction applied to all maps.

Isochemical phase diagrams were constructed for bulk rock compositions using the Perple_X software (Connolly, 2005) and the internally consistent thermodynamic database of Holland and Powell (Holland and Powell, 2011) (hp11ver.dat in Perple_X) (hp11ver.dat, tc-ds61in Perple_X). The calculations were undertaken using the measured bulk rock composition determined by X-ray fluorescence analysis using a PANalytical AXIOS MAX Advanced X-ray fluorescence (XRF) spectrometer at the University of São Paulo (Brazil). Chemical compositions of minerals were determined with a JEOL JXA-FE-8530 EMPA (electron microprobe analyser) at the University of São Paulo.

To constrain element mobility and timing of deformation of the CSZ, apatite and zircon grains were analysed for trace element compositions and U–Pb isotopic ages. Apatite grains were analysed in five samples (Table 5.1). Samples DC-37B and DC-41B were measured in situ in thin section, and samples DC-39A and DC-46D were measured in mounts of grain separates. The analyses were carried out using a laser ablation split-stream inductively coupled plasma mass spectrometer (LASS-ICP-MS) at the Monash Isotopia Facility, School of Earth, Atmosphere and Environment, Monash University, Australia. The experiments used an ASI-RESOlution ArF 193 nm excimer laser ablation system coupled to a Thermo Scientific iCAP Q ICP-MS for trace elements measurements and to a Thermo Scientific iCAP-TQ ICP-MS for U and Pb isotope measurements. Data reduction was performed in the Iolite 3 software package (Paton et al., 2011), and U–Pb ages were calculated using the IsoplotR program (version 3.7) (Vermeesch, 2018). Ages

and respective uncertainties are stated at 2 σ (95 % confidence). Isotopic data are presented in Supplementary Information 4. The apatite U–Pb data are presented with Tera-Wasserburg diagrams with no common-Pb correction.

Table 5.1. Summary of the methods applied in each studied sample.

Sample	Mylonite type	Protolith	Mineral assemblage	Quartz EBSD	Phase equilibria modelling	Apatite U–Pb–REE	Zircon U–Pb–REE
DC-32A	Ultramylonite	?	ms, bt, Kfs, plg, q, cc, mn	-	-	-	-
DC-33B	Ultramylonite	?	ms, bt, Kfs, plg, q, ep, tit, mn	X	-	-	-
DC-33C	Ultramylonite	?	ms, bt, Kfs, plg, q, ep, tit, mn	-	X	-	-
DC-37B	Mylonite	Tonatite /Granodiorite	ms, bt, Kfs,ep, plg, q, tit, ap	-	-	X	-
DC-39A	Mylonite	Tonatite /Granodiorite	bt, chl, sill, Kfs, q, ap, mn	-	-	X	X
DC-41B	Mylonite	Tonatite /Granodiorite	ms, bt, Kfs, plg, q, ep, tit, ap, mn	X	X	X	-
DC-41D	Protomylonite	Granite	ms, bt, Kfs, plg, q, ep, tit, ap, zr				X
DC-46D	Protomylonite	Granite	ms, bt, Kfs, plg, q, ep, ap, zr	-	-	X	X

5.4. Results

5.4.1. Sample petrography and microstructures

Eleven samples were studied in this work. The mineral assemblages of each sample are described in Table 5.1.

The studied samples vary from proto to ultramylonite. Samples DC-37B, DC-39A, DC-41 (B and D) and DC-46D are protomylonites to mylonites with a millimetric to centimetric alternation between felsic quartz-feldspar and mafic biotite-rich lenticular bands (Fig. 5a). Felsic bands are composed of K-feldspar porphyroclasts and quartz and mafic bands by fine-grained elongated biotite, sericite, titanite and tourmaline. Apatite, zircon and monazite occur as accessory minerals. Muscovite and biotite define the L_m and

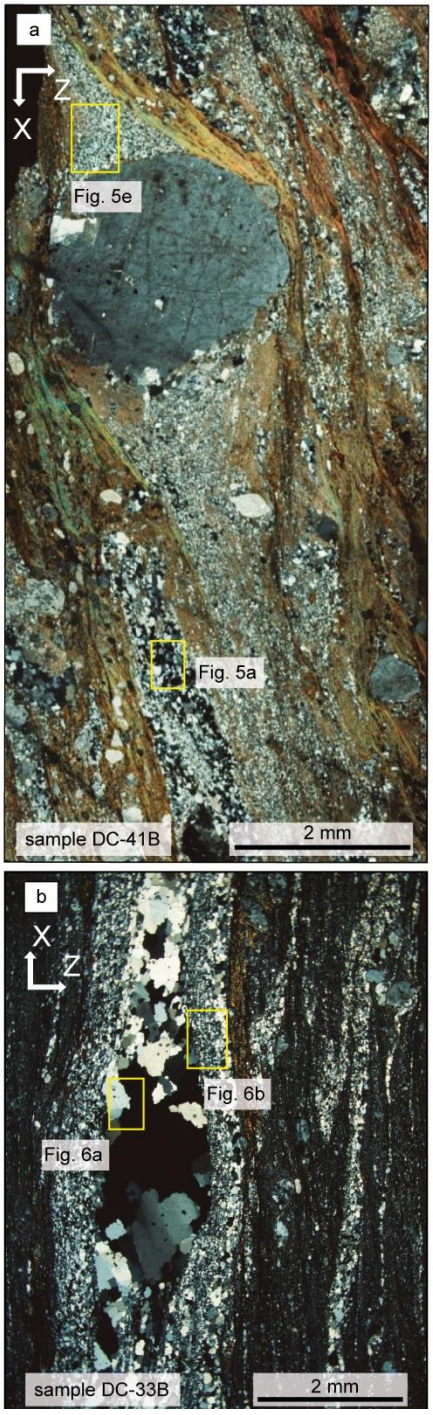

Figure 5.5. Photomicrographs from Cubatão Shear Zone mylonites showing different microstructures. a) coarse to medium-grained mylonite showing an alternation between protomylonite felsic and ultramylonite mafic bands; b) Fine-grained mylonite formed by a fine matrix formed by quartz and K-feldspar. The yellow rectangles locate the EBSD maps.

have grain size ranging from 20 to 100 µm. Plagioclase is fine-grained (up to 10 µm) and dispersed in the matrix along with quartz and epidote. K-feldspar porphyroclasts are rounded with length up to 2 mm, and lack evidence of intracrystalline deformation as well as no evidence of dynamic recrystallisation. Sometimes K-feldspar grains present fractures filled by quartz veins. Strain shadows composed of quartz and muscovite around K-feldspar are common (Fig. 5.5a). Quartz is recrystallised, occurring as interlobated to polygonal granoblastic aggregates or as aggregates of fine-grained new grains (up to 50 µm). Sample DC-41B has a granolepidobastic texture and contains the assemblage muscovite + biotite + K-feldspar + quartz + plagioclase + epidote + ilmenite + titanite. K-feldspar is homogeneous in composition with X_{Or} varying between 0.94 and 0.96 (where X_{Or} = K / (Ca + Na + K)).

Samples DC-32A, DC-33B and DC-33C are ultramylonites, composed of muscovite + biotite + K-feldspar + quartz + plagioclase + epidote + ilmenite + titanite. Muscovite and biotite define discontinuous layers parallel to the mylonitic foliation, and have grain size ranging from 10 to 50 µm. K-feldspar occurs as rounded porphyroclasts up to 500 µm in all ultramilonite samples. Fine-grained K-feldspar grains up to 20 µm in size occur only in the matrix of sample DC-33B. Both feldspar textures present similar composition, with X_{Or} varying between 0.96 and 0.98. Plagioclase is fine-grained and dispersed in the matrix along with quartz and epidote. Quartz occurs recrystallised as interlobate to polygonal granoblastic aggregates or as an

aggregate of fine-grained new grains. Several veins with a range of 2-300 cm occur parallel to the mylonitic foliation. In the core of larger veins, quartz forms an interlobated granoblastic aggregate with thicker rims formed by an aggregate of fine-grained new grains (Fig. 5.5b).

5.4.2. Quartz EBSD

EBSD analysis was performed on two representative samples of the CSZ to investigate the dominant deformation mechanisms in mylonites with different plunging lineations (Fig. 5.3c). Sample DC-41B (Fig. 5.5a) has a steeply plunging lineation whereas sample DC-33B (Fig. 5.5b) has a subhorizontal lineation. These two representative samples were selected as representative of mylonites from the shear zone, so that the dominant deformation mechanism of quartz during shearing could be identified.

Two quartz microstructures are present in sample DC-41B (subvertical L_m): (a) recrystallised aggregate (Fig. 5.5a, map 1 and Fig. 5.6a), and (b) strain shadows around K-feldspar porphyroclast (Fig. 5.5a, map 2 and 5.6b). The area of map 1 shows bimodal grain size distribution with one maximum at ca. 20 µm and a second maximum at ca. 6 µm (Fig. 5.6c). The misorientation angle distribution for correlated pairs has a high frequency of misorientation up to 10° (Fig. 5.6d). A lower concentration of correlated grains at ca. 60º is interpreted as the result of Dauphiné twinning. Additionally, the uncorrelated misorientation angle distribution is close to the theoretical random curve. The pole figure shows a weak CPO of the c-axis (Fig. 5.6d), with a maximum near the periphery of the pole figure, rotated at ca. 30º from the Z-direction with the dextral sense of shear.

The quartz strain shadow area (Fig. 5.6e, map 2) shows a bimodal grain size distribution with a small difference between the two populations (Fig. 5.6f). High concentration of low-angle misorientations (up to 10º) occurs between correlated pairs, whereas the uncorrelated misorientation angle distribution (as well as the correlated distribution for misorientations >10º) is close to the theoretical random curve (Fig. 5.6g). The c-axis CPO is weak and characterised by scattered orientations. One cluster of weak maxima is subparallel to the instantaneous stretching axis for the dextral sense of shear of the sample and to the dominant mineral elongation direction in the strain shadow (Fig. 5.6h).

Three different grain size portions of a quartz vein transposed into the S_m were analysed in sample DC-33B (subhorizontal L_m, Fig. 5.5b): a) an inner area (Fig. 5.5b, map 1, and Fig. 5.7a) with a coarse grain size average of ca. 300 µm; b) an adjacent fine grained area where quartz is mixed with other phases (Fig. 5.7a, map 2, subset 2) with a grain size up to 10 µm; and c) an outer medium grain size portion (Fig. 5.7a, map 2, subset 1) with an average grain size of 30 µm, where quartz occurs in largely monophase recrystallised ribbons. Coarse grains are oriented with their c-axis between the X and Y-axis of the pole figure (Fig. 5.7c, map 1). This area contains a high concentration of low-angle boundaries up to 10º for correlated and uncorrelated grains (Fig. 5.7d, map 1). They reflect the misorientation bands and subgrains represented by the white lines in Figure 7a. A second concentration of ca. 60º misorientation angles also occurs and reflects the presence of Dauphiné twins. In crystal coordinates, low and high angle misorientation axes (21-10º and 21-80º) show high density near the c-axis (Fig. 5.7e, map1), which is the rotation axis of the prism <a> slip system (e.g., Neumann, 2000).

The adjacent fine-grained area (Fig. 5.7b) has a c-axis maximum near the Y-axis, with a dispersion of orientation in both subsets (Fig. 5.7c). The correlated misorientation angle distributions show high concentration of low-angle misorientations (up to 10º) (Fig. 5.7c). These misorientations likely reflect the presence of subgrains, and misorientations of 60º indicative of the presence of Dauphine twins. Additionally, the distribution of both correlated and uncorrelated pairs is close to the theoretical random curve for misorientations >20º. In crystal coordinates, low-angle misorientation axes in both subsets (Fig. 5.7e, map 2, subset 1 and 2) show high density near the c-axis, which is the rotation axis of the prism <a> slip system. Subset 1 also shows a secondary maximum centered on the pole to the {m} prism, which is the rotation axis of the prism <c> slip system (Neumann, 2000). Medium angle orientations (11 to 20º) also show a secondary concentration towards the <r> and <z> directions.

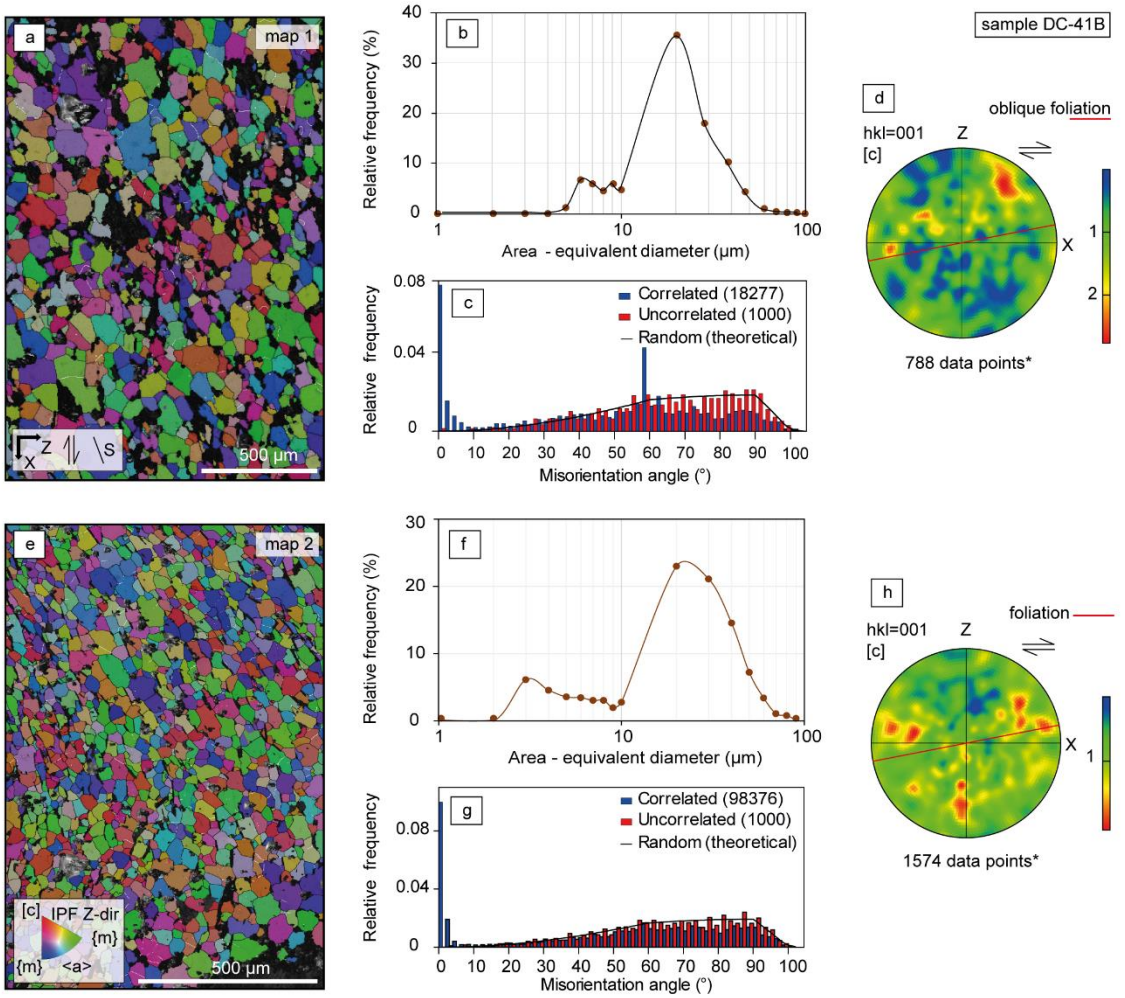

Figure 5.6. EBSD data of the sample with steeply plunging lineation (DC-041B). a) map 1 and map 2, respectively. Orientation map according to the inverse pole figure with respect to the pole to the mylonitic foliation (Z-direction); c) map 1 grain size distribution; d) map 1 misorientation angle distribution for correlated and uncorrelated misorientations; e) map 1 quartz pole figure. Stereographic projection, lower hemisphere. Total: Exp. densities (mud) min = 0.15, max = 2.77. *data are plotted as one point per grain (includes Dauphin´e twins); f) map 2, grain size distribution; g) map 2, misorientation angle distribution for correlated and uncorrelated misorientations; h) map 2, quartz pole figure, Stereographic projection, lower hemisphere. Total: Exp. densities (mud) min = 0.14, max = 2.07.

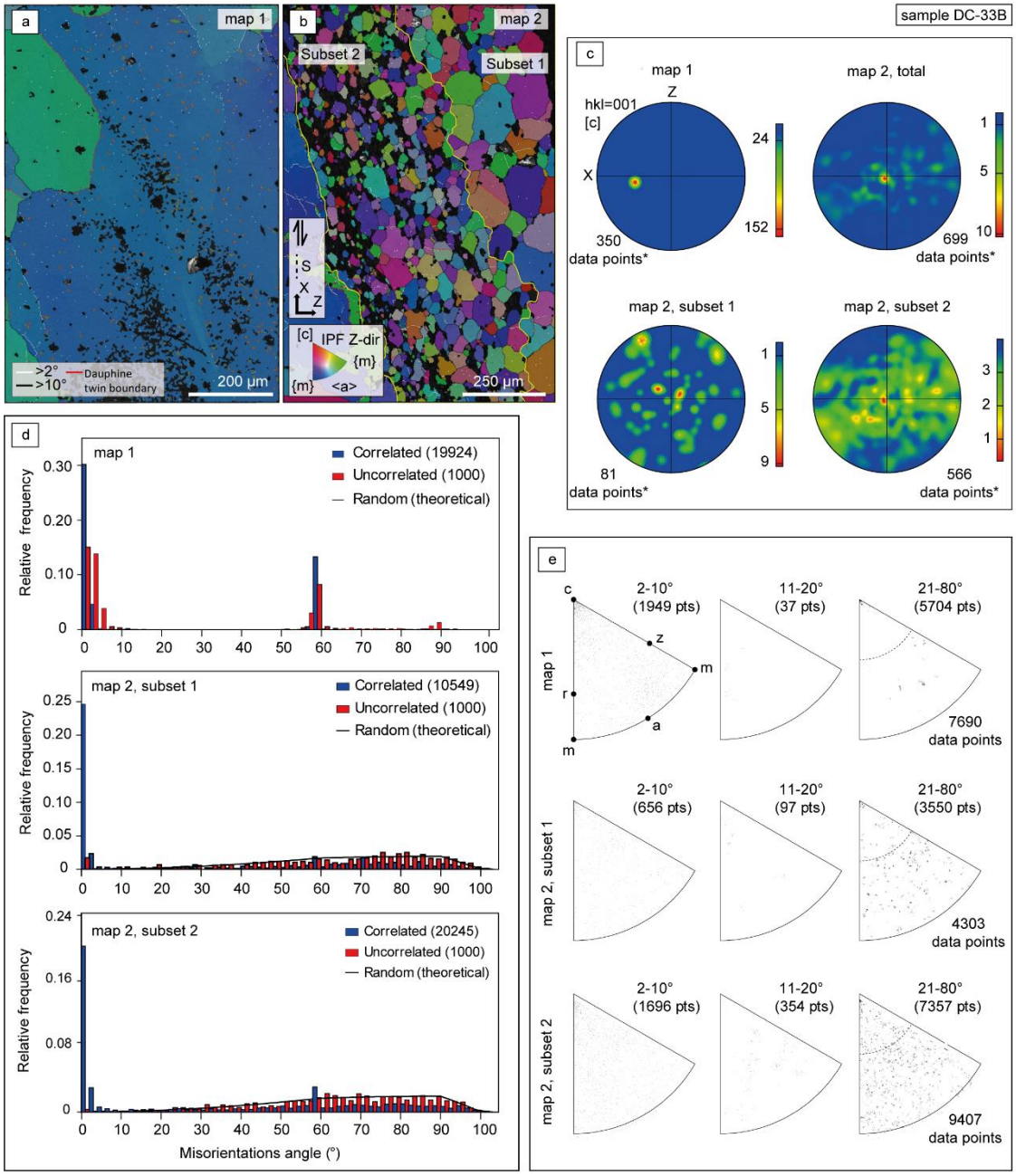

Figure 5.7. EBSD data of the sample with subhorizontal lineation (DC-33B). a) Orientation maps according to the inverse pole figure with respect to the pole to the mylonitic foliation (Z-direction); b) Quartz pole figures, stereographic projection, lower hemisphere. *data are plotted as one point per grain (includes Dauphin´e twins); c) Misorientation angle distribution for correlated and uncorrelated misorientations; d) Misorientation axis in crystal coordinates.

5.4.3. Phase equilibria modelling

Samples DC-41B with subvertical L_m, and sample DC-33C with subhorizontal L_m from the southwestern sector were selected for phase equilibria modelling aiming to

constrain the P-T deformation conditions (bulk rock and mineral compositions are in Supplementary Material 2). The phase-diagrams for both samples span 250-650 °C and 1-11 kbar (Fig. 5.8).

In the phase equilibria diagram of sample DC-41B, biotite, muscovite, feldspar and quartz are the dominant minerals in most fields, with epidote and titanite stable below 500 °C (Fig. 5.8a). The equilibrium mineral assemblage (muscovite + biotite + K-feldspar + quartz + plagioclase + epidote + ilmenite + titanite) is stable between ca. 300-600 ºC and 1-11 kbar in the modelled phase diagram. The compositional isopleths of Si between 3.19-3.28 apfu (atoms per formula unit) and Mg content between 0.21-0.27 apfu in muscovite constrain a P-T field between 350-570 ºC and 3.3-8.6 kbar (Fig. 5.8a).

The phase equilibria diagram of sample DC-33C has a similar topology compared to that of sample DC-41B, with epidote and titanite stable over a restricted temperature range below 500 °C. The mineral assemblage in equilibrium with deformation (muscovite + biotite + K-feldspar + plagioclase + epidote + ilmenite + titanite + quartz) is stable between 250-600 ºC and 1-11 kbar. The compositional isopleths of Si content in muscovite between 3.24-3.44 apfu and Mg content in biotite between 0.92-0.97 apfu define a P-T field at 300-510 ºC and 2.4-9.5 kbar (Fig. 5.8b).

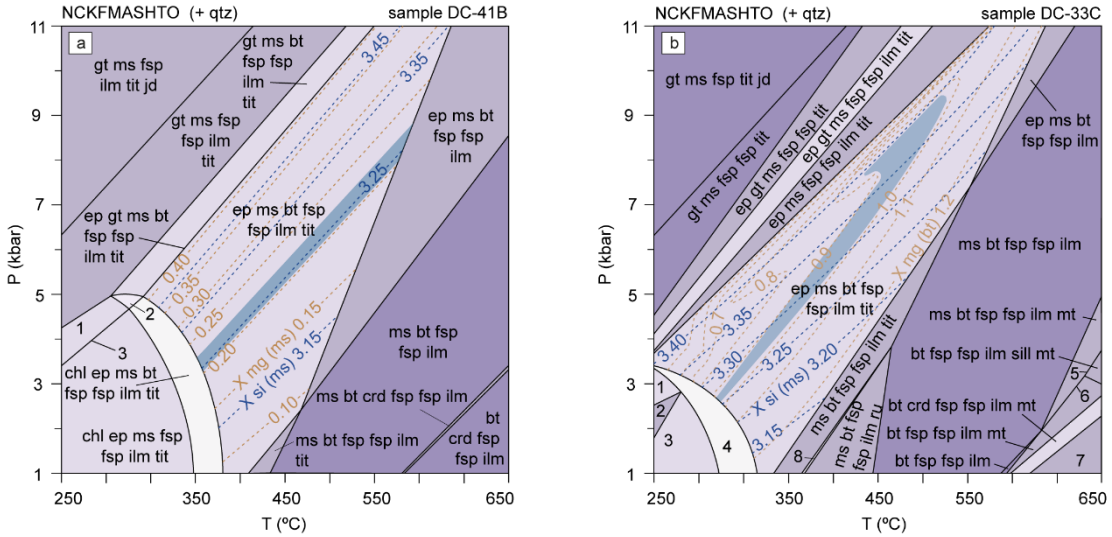

Figure 5.8. P-T pseudosection for the coarse to medium-grained mylonite (sample DC-41B) with a steelply plunging lineation a) and the fine-grained mylonite with a subhorizontal lineation in NCKFMASHTO system (sample DC-33C), b). Numbers for the fields: 1. melt ms bt fsp fsp ilm sill q mt; 2. melt ms bt fsp fsp ilm q mt H2O; 3. ms bt fsp fsp ilm sill q mt H2O; 4. melt bt fsp fsp ilm sill q mt H2O; 5. melt bt fsp fsp ilm q mt.

5.4.4. Apatite petrography, trace element concentrations and U–Pb ages

Apatite has a dominantly prismatic euhedral to subhedral shape but rounded, elongated and irregular shapes are also present. Apatite is generally oriented parallel to the mylonitic foliation with predominant grain size between 100–200 µm. The association of apatite either surrounded by titanite and ilmenite or forming strain shadows around apatite as; strain shadows of biotite and muscovite around apatite also occur. Homogeneous internal texture is dominant, but sector and zoning textures are also observed in BSE and CL images (Supplementary Material 3).

Apatite grains from sample DC-37B are characterised by concave chondrite-normalised REE patterns, displaying prominent negative Sr and Eu anomalies and positive U anomaly (Fig. 5.9a). Most grains lie within felsic granitoid (S) and high-grade metamorphic (HM) compositions (Fig. 5.9b). The U–Pb data have wide distribution along the isochron, defining a single inverse isochron with a lower intercept age of 573 ± 9 Ma (MSWD = 0.35) (Fig. 5.9c).

Apatite grains from sample DC-39A are characterised by chondrite-normalised REE contents around 1000 and flat patterns with negative Sr and Eu anomalies and positive U anomaly (Fig. 5.9d). All trace element compositions are related to high-grade metamorphic apatite (Fig. 5.9e). Spot analyses are spread in the isochron, defining a single inverse isochron with a lower intercept age of 603 ± 7 Ma (MSWD = 0.42) (Fig. 5.9f).

Apatite grains from sample DC-41B display concave chondrite-normalised REE patterns with a slight depletion in the HREE, also marked by positive U anomaly and moderate negative Sr and Eu anomalies (Fig. 5.9g). One apatite crystal lacks negative Sr anomaly. In the classification diagram, this apatite set lies in the metamorphic composition fields between the low to high-grade metamorphic compositions (Fig. 5.9h). The U–Pb data are widely spread along a single inverse isochron line, yielding a lower intercept age of 591 ± 6 Ma (MSWD = 1.3, n = 41) (Fig. 5.9i).

Apatite grains from sample DC-46D are characterised by nearly flat chondrite-normalised REE patterns, with slight depletions in the HREE, positive U anomaly and negative Sr and Eu anomalies (Fig. 5.9j). All apatite grains are related to high-grade metamorphic compositions according to the classification diagram (Fig. 5.9k), defining a single inverse isochron in the Tera-Wasserburg diagram, yielding a lower intercept age of 610 ± 8 Ma (MSWD = 0.38) (Fig. 5.9l).

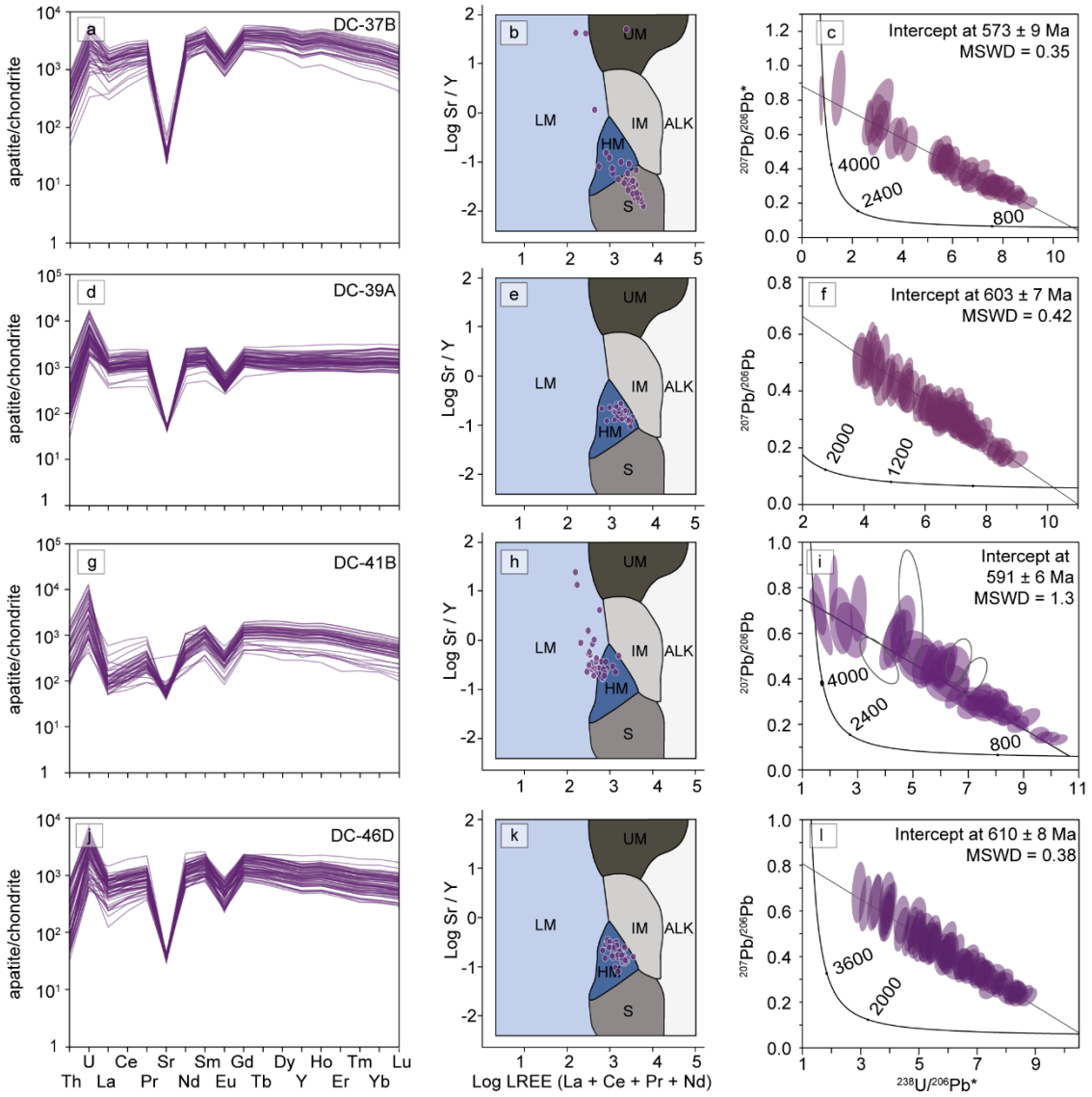

Figure 5.9. Apatite chrondrite normalised, classification and Tera-Wasserburg diagrams from the CSZ mylonites. * REE chondrite normalised diagrams (a, d, g and j) were calculated using values from McDonough and Sun (1995) and apatite classification diagrams follow O'Sullivan et al. (2020). Abbreviations in the apatite classification diagram: S = felsic granitoids; HM = high-grade metamorphic, leucosome and anatectic rocks; IM = mafic granitoids-to-mafic igneous rocks; ALK = syenites and other alkali-rich igneous rocks and UM = low and medium-grade metamorphic and metasomatised rocks. Ellipse uncertainties are 2σ.

5.4.5. Zircon petrography, trace element concentrations and U–Pb ages

We collected U–Pb isotopes and trace element data of zircon grains from three mylonite samples (DC-39A, DC-46D and DC-41D), commonly presenting a combination of common-Pb, Pb loss and hydrothermal alteration. The latter is well illustrated in the chondrite-normalised rare earth element diagrams with light rare earth element

enrichment (LREE; Fig. 5.10), which was quantitatively identified by using the light rare earth element index (LREE-I =Dy/Nd + Dy/Sm; Bell et al., 2019). Zircon grains from sample DC-39A are prismatic to subhedral with grain size ranging from 80-300 µm. Internal textures vary from core-rim to homogeneous. Zircon grains with core-rim texture present a high luminescence, week sector zoning core and a homogeneous low luminescence rim. Homogeneous zircon grains also present low luminescence.

We collected a total of 44 zircon U–Pb -REE data, from which only two have a typical zircon REE pattern with LREE-I greater than 30, which is typically associated with igneous zircons (Bell et al., 2019) (Fig. 5.10a). Additionally, the majority of the U–Pb data present influence of common-Pb and Pb loss evident in the Tera-Wasserburg diagram (Fig. 5.10b). Nevertheless, a subset of 10 zircon grains defines a discordia trend in the Wetherill diagram yielding an upper intercept age of 2277 ± 26 Ma and a lower intercept age of 604 ± 13 Ma (MSWD = 3.2) (Fig. 5.10c).

Zircon grains from mylonite sample DC-46D have also being affected by hydrothermal processes with 51 out of 61 data indicating LREE enrichment with LREE-I < 30 (Fig. 5.10D). In respect to the zircon U–Pb data, a total of 21 out of 61 U–Pb are within the concordance limit between 90-110 %. Disregarding two outliers, the concordant U–Pb data define a discordia trend in the Wetherill diagram yielding an upper intercept age of 782 ± 28 Ma and a lower intercept age of 237 ± 80 Ma (recent Pb loss) (MSWD = 1.6) (Fig. 5.10e). By removing the zircon grains affected by hydrothermal processes, the discordia trend yield an upper intercept age of 726 ± 15 Ma (MSWD = 1.5) anchored to zero (recent Pb loss). In general terms, the upper intercept from both data treatments match within error.

The great majority (41 out of 45) of the zircon grains from sample DC-41D were affected by hydrothermal processes as indicated in the chondrite-normalised REE diagram (Fig. 5.10g). From these, a subset of 10 zircon U–Pb data within the concordance limit (90-110 %) define a discordia trend yielding an upper intercept age of 856 ± 44 Ma and a lower intercept age of 269 ± 67 Ma (recent Pb loss) (MSWD = 4.2) (Fig. 5.10h). By removing the zircon grains affected by hydrothermal processes, the discordia trend yields an upper intercept age of 755 ± 45 Ma and a lower intercept age of 346 ± 97 Ma (MSWD = 3.7) (Fig. 5.10i). Despite the poor statistics and high errors, the upper intercept ages match with those from sample DC-46D considering uncertainties.

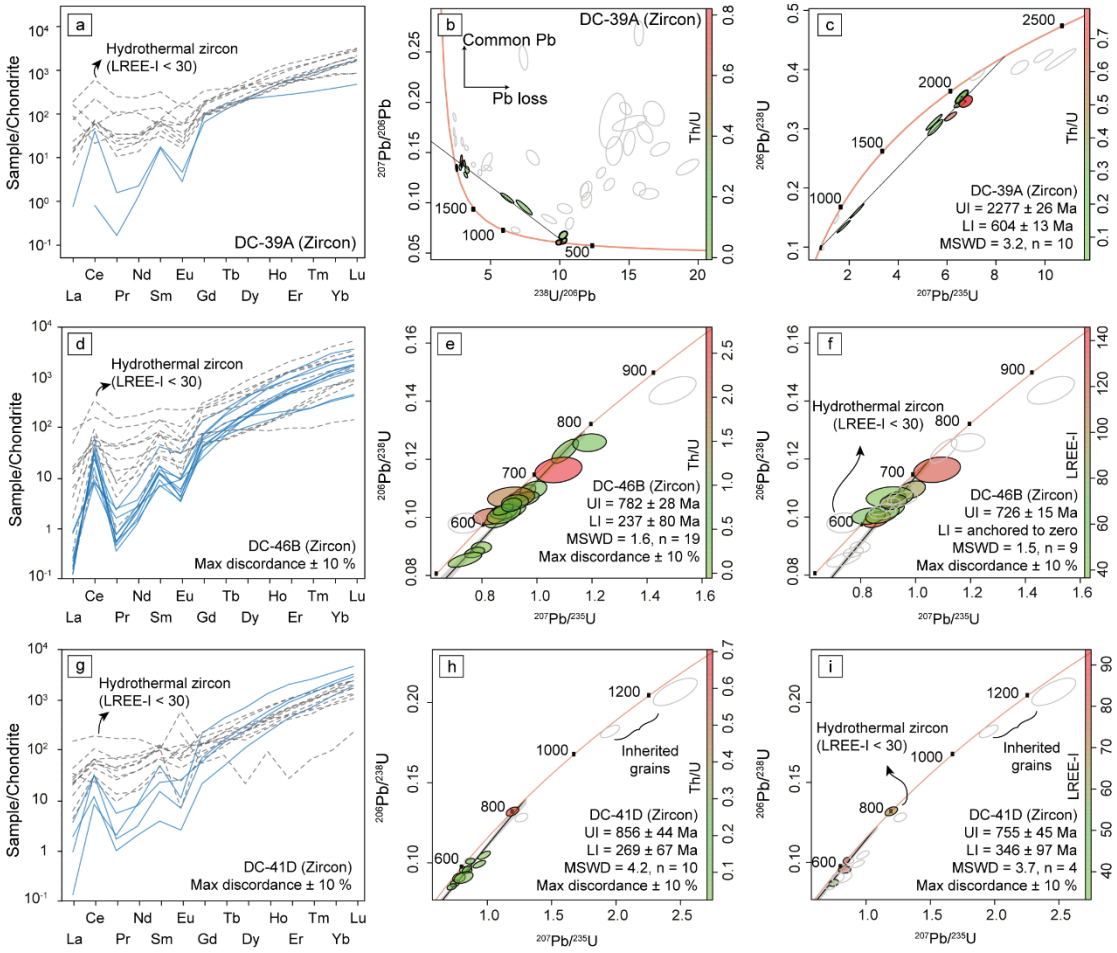

Figure 5.10. Zircon U-Pb-REE data from Cubatão Shear Zone. REE chondrite normalised diagrams (a, d and g) were calculated using values from McDonough and Sun (1995) Ellipse uncertainties are 2σ.

5.5. Discussion

5.5.1. CSZ deformational and thermal conditions

Mylonites of the CSZ present quartz deformation microstructures consistent with those from medium-temperature deformational conditions. Medium-temperature deformation mechanisms are recognised in quartz aggregates in the matrix and quartz veins, accompanied by grain size reduction. In addition, quartz-filled strain shadows around K-feldspar porphyroclasts indicate grain growth related to the dissolution precipitation creep mechanism (Passchier and Trouw, 2005). The c-axis maximum parallel to the elongation direction of quartz grains in the strain shadows is attributed to crystallography controlled by growth during precipitation (Stallard and Shelley, 1995; Hippertt and Egydio-Silva, 1996; Kilian et al., 2011). The high concentration of low-

angle misorientation for the samples analysed by EBSD is consistent with recrystallisation-accommodated dislocation creep. Moreover, the occurrence of low-angle boundaries defining polygonal regions in the interior of larger quartz grains supports recrystallisation primarily by progressive subgrain rotation.

The EBSD analysis of quartz aggregates in the vein of sample DC-33B (Fig. 5.5e and Fig. 5.7b) records evidence of grain size reduction by subgrain rotation, with phase mixing within recrystallised layers. These microstructures are evidence of progressive dismembering of the initial quartz vein during deformation at medium-temperature conditions (e.g.,, Kilian et al., 2011; Viegas et al., 2016; Gilgannon et al., 2017). The presence of clusters of misorientation axes near the c-axis and {m} prism for low-angle misorientations in the coarse host grain (Fig. 5.7e) suggests that deformation started at high to medium-temperature conditions, at which the prism <a> and prism <c> slip systems were active, and evolved to lower temperature conditions.

The activity of SGR in quartz indicates deformation temperatures between 400º and 520º, depending on the strain rate (Stipp et al., 2002; Faleiros et al., 2010). Combining the modelled pseudosections with quartz microstructures and, apatite U–Pb resetting (see section 5.5.2), the P-T conditions for the mylonites are constrained at 460-520 ºC and 4.5-9.5 kbar.

5.5.2. CSZ time constraints

The samples used for zircon and apatite U–Pb dating include less deformed rocks that can be petrographically attributed to the Juquiá Granite (samples DC-41D and DC-46D) and more intensely deformed rocks (samples DC-39A and DC-37B) that cannot be clearly attributed to the Juquiá Granite or the Atuba Complex without the aid of geochronological data. Defining the protolith ages is fundamental to interpret the significance of apatite U–Pb ages in our study, once the medium-temperature deformation quantified in our samples (460-520 ºC) is expected to reset apatite U–Pb system in response to shearing deformation (e.g., Ribeiro et al., 2020a, b; Ribeiro et al., 2021).

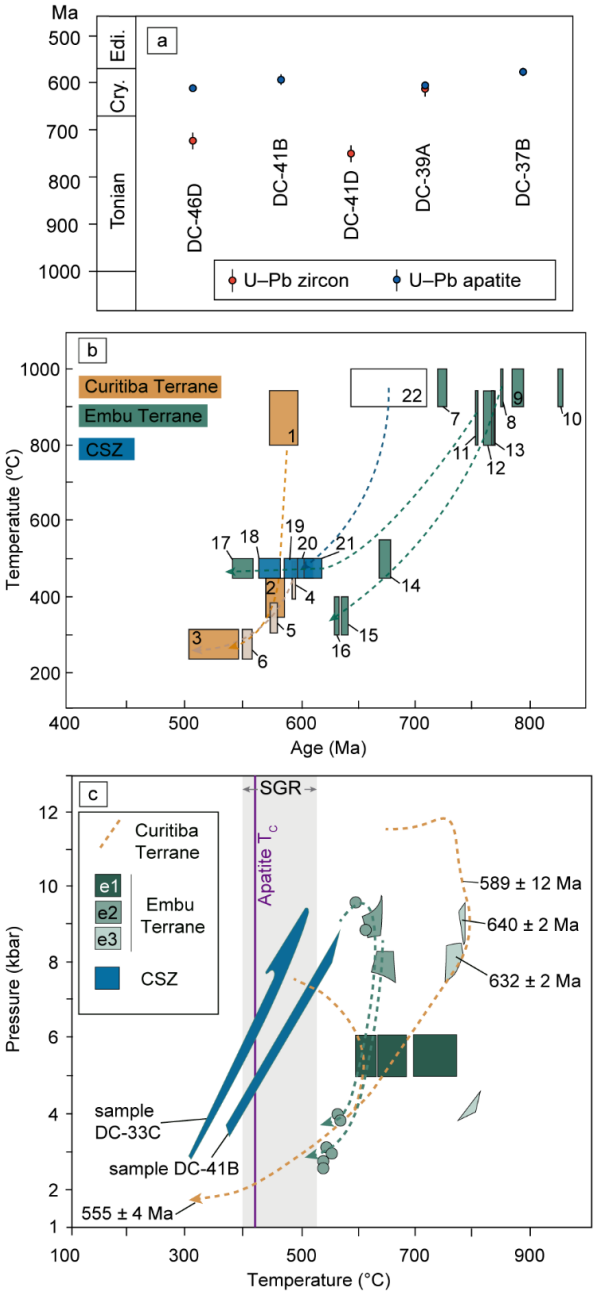

Figure 5.11. Petrocronological evolution for the CSZ and adjacent units. a) summary of the ages obtained in this work; b) temperature-time diagram with data from previous works (1 to 17) and from this work (18 to 22). 1 and 2 monazite U-Th-Pb, Faleiros et al. (2011); 3. biotite K-Ar, Campagnoli (1996); 4. hornblende Ar-Ar, Machado et al. (2007); 5. muscovite Ar-Ar, Campagnoli (1996); 6. biotite Ar-Ar, Faleiros et al. (2011); 7 to 17 are from Cabrita et al. (2021); 7. sample 10A, zircon U-Pb; 8. sample 45A, zircon U-Pb; 9. sample FM-27, zircon U-Pb; 10. sample AN-47, zircon U-Pb; 11. sample FM02B, monazite U-Pb; 12. sample 45A, monazite U-Pb; 13. sample 12A, monazite U-Pb; 14. sample 12A, muscovite Rb-Sr; 15. sample 12A, biotite Rb-Sr; 16. sample 45A, biotite Rb-Sr; 17. sample FM02B, apatite U-Pb; 18. sample DC-37B (apatite U-Pb); 19. sample DC-41B, apatite U-Pb; 20. Sample DC-39A, apatite U-Pb; 21. DC-46D, apatite U-Pb; 22. Sample DC-39A, zircon U-Pb; c) Pressure-temperature diagram. Published data are from: e1 = Vieira (1996); e2 = Meira et al. (2019); e3 = Cabrita et al. (2021). Legend; Tc = closure temperature; SGR = subgrain rotation.

The zircon U–Pb upper intercept ages obtained for samples DC-46D (782 ± 28 Ma) and DC-41D (856 ± 44 Ma (Fig. 5.10e and h), although imprecise due to hydrothermal alteration, are consistent with the zircon U–Pb crystallisation age of 799 ± 5 Ma obtained for an undeformed sample of the Juquiá Granite (Passarelli et al., 2019). This similarity establishes that this pluton is the protolith for these mylonite samples. Conversely, the zircon U–Pb ages of 2277 ± 26 Ma (upper intercept) and 604 ± 13 Ma (lower intercept) obtained for sample DC-39A is a typical geochronological pattern recognised in the Atuba Complex rocks (Fig. 5.10c). The upper intercept is commonly

interpreted to represent the Paleoproterozoic igneous crystallisation age affected by a Neoproterozoic thermal/metamorphic overprint represented by the lower intercept age (Sato et al., 2003, 2009).

Apatite grains from four mylonite samples of the CSZ are mostly characterised by concave chondrite-normalised REE patterns with contents around 10^2-10^3, typical of igneous apatite (see O'Sullivan et al., 2020 for apatite REE signatures). However, the majority of the apatite grains plot within the high-grade metamorphic field in the apatite classification diagram (Fig. 5.9). The high-grade metamorphic field in the apatite classification diagram was constrained with rocks that experienced anatexis, forming apatite with REE that resemble those from S-type granitoids leading to potential misclassification as discussed elsewhere (O'Sullivan et al., 2020, 2021; Ribeiro et al., 2021). The apatite high REE content and mostly concave shape with predominance of medium-REE (MREE) are suggestive of igneous origin, which is consistent with the absence of high-grade metamorphism in the mylonites of the CSZ.

The apatite U–Pb ages obtained for the mylonite samples span ca. 610-570 Ma (Fig. 5.11a), being ca. 200 Ma younger than the zircon crystallisation ages obtained for samples DC-41D and DC-46D (Juquiá Granite protolith) and matching the metamorphic lower intercept ages obtained for sample DC-39A (Atuba Complex protolith). These data unequivocally indicate that the U–Pb apatite system were reset during the medium-temperature (460-520 ºC) ductile deformation along the CSZ without affecting the original igneous chemistry (e.g., Ribeiro et al., 2020b). Therefore, apatite records the medium-temperature deformational history of the CSZ between 610–570 Ma, giving a time span of ca. 40 Ma for the ductile activity.

5.5.3. Tectonic implications

Available geochronological and geological data indicate that the CSZ had a fundamental role in the tectonic compartmentation of the southern Ribeira Belt, which is highlighted for the metasedimentary rock assemblages of distinct ages present in each terrane (Fig. 1). Detrital and volcanic zircon U–Pb age data indicate that metasedimentary rocks to the north of the CSZ present Paleoproterozoic to early Tonian depositional ages (e.g., 1760 Ma (São Roque Group; Henrique-Pinto et al., 2015, 2018), 1470-1490 Ma (Votuverava Group; Campanha et al., 2015), and 970-850 Ma (Embu Complex; Campanha et al., 2019)). Conversely, the metasedimentary rock units to the south of the

CSZ present detrital zircon age populations as young as the late Cryogenian (ca. 650 Ma in the Costeiro Terrane; Meira et al., 2015) and Cryogenian-Ediacaran transition (640-630 Ma in the Curitiba Terrane; Ricardo et al., 2020).

Ricardo et al. (2020) used these data combined with the record of paired high-pressure/low-pressure metamorphic field gradients and detrital zircon signatures of convergent margin settings for the Curitiba Terrane metasedimentary rocks to support the model that the Lancinha-Cubatão shear zone represents an Edicaran suture zone, as firstly proposed by Basei et al. (1992, 2008). On the other hand, Meira's et al. (2015) intracontinental model for the southern and central Ribeira Belt implicitly proposes that all metasedimentary units belong to a single rift-related sedimentary basin deposited from 640 to 600 Ma. In a revised intracontinental model, Meira et al. (2019) propose a long-lived rift-related sedimentary basin deposited from ca. 700 Ma (Embu Terrane metasedimentary rocks) to ca. 640 Ma (Costeiro Terrane metasedimentary rocks) that was deformed by an intracontinental compressional event at 640-600 Ma and an extensional and wrench tectonic stage at 600-560 Ma. The shear zone system, including the CSZ would be developed at this late stage.

The data acquired in this work demonstrate that the CSZ activity overlaps with the deformational history of the adjoining northern Embu Terrane block and is coeval with the metamorphism in the adjoining southern Curitiba Terrane block. Within the Embu Terrane, the deformation of the CSZ overprints the cooling metamorphic path at 610 Ma (Fig. 5.11b). Within this terrane, the Embu Complex records a Tonian high-grade metamorphic P-T conditions of 750–805 ºC and 3.6–9.2 kbar at 810–760 Ma with a slow cooling path lasting at least 85 Ma recorded by biotite and muscovite Rb–Sr ages (Vlach, 2008; Cabrita et al., 2021). Additionally, the CSZ ductile activity was coeval with the Ediacaran metamorphism within the Curitiba Terrane (Atuba Complex and Turvo-Cajati Formation) at 630-585 Ma (Sato et al., 2003, 2009; Machado et al., 2007; Faleiros et al., 2011a, 2016; Ricardo et al., 2020). The Turvo-Cajati Formation presents high-pressure granulite rocks that evolved from low-temperature and high-temperature eclogite facies rocks and attained peak metamorphic conditions of ~800 ºC and 9.5-12 kbar at 600-585 Ma (Faleiros et al., 2011, 2016; Ricardo et al., 2020), which coincides with the main stage of activation of the CSZ (Fig. 5.11c).

The ductile activity period of the CSZ (610–570 Ma) is related to, and coeval with the timing of transcurrent shearing of other segments of the crustal-scale Brazilian Southeastern Shear Zone System, such as the Serra do Azeite Shear Zone (Machado et

al., 2007; Faleiros et al., 2011a) and Além Paraíba Shear Zone (Egydio-Silva et al., 2002; Giraldo et al., 2019) (Fig. 5.2). In addition, ductile transcurrent activity is also coeval with the main episodes of granitic magmatism and regional metamorphism for the Ribeira Belt (630–590 Ma) (Brito Neves et al., 2021), highlighting the interaction between deformation, metamorphism and magmatic activity, and therefore, the active role of the transcurrent system in the orogenesis of Ribeira Belt.

Available data demonstrate a long and complex evolutionary history for the transcurrent system, with a ductile activity extending over ca. 115 Ma between 650–535 Ma (Tassinari, 1988; Faleiros et al., 2011a; Passarelli et al., 2011; Giraldo et al., 2019; Costa et al., 2020; Ribeiro et al., 2020b) (Fig. 5.2). Some shear zones were coeval with Ediacaran regional metamorphism in the Ribeira Belt, such as the Ribeira Shear Zone (591±7 Ma; Faleiros et al. 2011), Serra do Azeite Shear Zone (579 ± 8 Ma; Faleiros et al., 2011), Serrinha Shear Zone (575 ± 5 Ma; Passarelli et al., 2008). Other shear zones (e.g., Taxaquara shear zone) were only active during the late stages of the orogenic activity constraining the younger age for the ductile period at 560-535 Ma (Ribeiro et al., 2020b). Therefore, the apatite U–Pb ages from mylonite of the CSZ (610–570 Ma) indicate that this structure was coeval with the main period of other regional shear zones activity, granitic magmatism and regional metamorphism and convergence of the cratons surrounding the Ribeira Belt, indicating active participation of the transcurrent shear zones in the orogenic processes that built up West Gondwana.

5.6. Conclusions

The crustal-scale CSZ was developed in an overall transpressional shear zone system setting with dominant vertical mylonitic foliation and subhorizontal stretching lineation. Additionally, the CSZ juxtaposes distinct rock units with microstructures, and metamorphic mineral assemblage indicative of medium-temperature deformation conditions, recording ductile deformation conditions of 460–520 ºC and 4.5–9.5 kbar active between ca. 610–570 Ma within the studied area. Zircon geochronology indicate that mylonites are sourced from the Juquiá Granite (ca. 799 Ma) and the Atuba Complex (ca. 2100 Ma). These results indicate that the CSZ was active during the main period of activity of other ductile shear zones, granitic magmatism and regional metamorphism and convergence of the cratons surrounding the Ribeira Belt, indicating active participation of the transcurrent shear zones in the orogenic processes that built up West Gondwana.

The study presented in this contribution was crucial for the above findings, highlighting the need for similar studies in other major crustal-scale shear zones in orogenic belts worldwide.

Acknowledgements

Dina Cabrita and Frederico Faleiros thank the São Paulo Research Foundation (FAPESP – grants number: 2019/10457-4, 2018/21824-5, 2018/10012-0, 2015/26645-3 and 2015/04487-7). Special thanks to Léo Hartmann, Haakon Fossen, and Renata Schmitt for suggestions and manuscript revision. Frederico Faleiros also thanks to the National Council of Technological and Scientific Development (CNPq) for the research productivity grant 307732/2019-3, and Ginaldo Campanha for grant 305701/2019-3. Peter Cawood and Bruno Ribeiro acknowledge the Australian Research Council for grant FL160100168.

5.7. References

Aleinikoff, J.N., Schenck, W.S., Plank, M.O., Srogi, L.A., Fanning, C.M., Kamo, S.L., Bosbyshell, H., 2006. Deciphering igneous and metamorphic events in high-grade rocks of the Wilmington complex, Delaware: Morphology, cathodoluminescence and backscattered electron zoning, and SHRIMP U-Pb geochronology of zircon and monazite. Bulletin of the Geological Society of America 118, 39–64. https://doi.org/10.1130/B25659.1

Alkmim, F.F., Marshak, S., Pedrosa-Soares, A.C., Peres, G.G., Cruz, S.C.P., Whittington, A., 2006. Kinematic evolution of the Araçuaí-West Congo orogen in Brazil and Africa: Nutcracker tectonics during the Neoproterozoic assembly of Gondwana. Precambrian Research 149, 43–64. https://doi.org/10.1016/j.precamres.2006.06.007

Almeida, F.F.M. De, Hasui, Y., Brito Neves, B.B. De, Fuck, R.A., 1981. Brazilian structural provinces: An introduction. Earth-Science Reviews 17, 1–29. https://doi.org/10.1016/0012-8252(81)90003-9

Almeida, F.F.M., Amaral, G., Cordani, U.G., Kawashita, K., 1973. The Precambrian Evolution of the South American Cratonic Margin South of the Amazon River. The South Atlantic 1, 411–446. https://doi.org/10.1007/978-1-4684-3030-1_11

Almeida, F.F.M., Hasui, Y., 1984. O pré-cambriano do Brasil.

Alsop, G.I., Holdsworth, R.E., 2004. Shear zones — an introduction and overview. Geological Society, London, Special Publications 224, 1 LP – 9. https://doi.org/10.1144/GSL.SP.2004.224.01.01

Alves, A., Janasi, V. de A., Campos Neto, M. da C., 2016. Sources of granite magmatism in the Embu Terrane (Ribeira Belt, Brazil): Neoproterozoic crust recycling constrained by elemental and isotope (Sr-Nd-Pb) geochemistry. Journal of South American Earth Sciences 68, 205–223. https://doi.org/10.1016/j.jsames.2015.10.014

Alves, A., Janasi, V. de A., Campos Neto, M. da C., Heaman, L., Simonetti, A., 2013. U-Pb geochronology of the granite magmatism in the embu terrane: Implications for the evolution of the central ribeira belt, SE Brazil. Precambrian Research 230, 1–12. https://doi.org/10.1016/j.precamres.2013.01.018

Amaral, L., Caxito, F. de A., Pedrosa-Soares, A.C., Queiroga, G., Babinski, M., Trindade, R., Lana, C., Chemale, F., 2020. The Ribeirão da Folha ophiolite-bearing accretionary wedge (Araçuaí orogen, SE Brazil): New data for Cryogenian plagiogranite and metasedimentary rocks. Precambrian Research 336, 105522. https://doi.org/10.1016/j.precamres.2019.105522

Arena, K.R., Hartmann, L.A., Lana, C., 2017. Tonian emplacement of ophiolites in the southern Brasiliano Orogen delimited by U-Pb-Hf isotopes of zircon from metasomatites. Gondwana Research 49, 296–332. https://doi.org/10.1016/j.gr.2017.05.018

Babinski, M., Tassinari, C.C.G., Nutman, A.P., Sato, K., Pimentel, M.M., Iyer, S.S., 2001. U/Pb shrimp zircon ages of migmatites from the basement of the Embú Complex, Ribeira Fold Belt, Brazil: indications for ~1.4-1.3 Ga Pb-Pb and Rb-Sr "isochron" ages of no geological meaning. III South American Symposium on Isotope Geology. Pucón.

Bartoli, O., 2017. Phase equilibria modelling of residual migmatites and granulites: An evaluation of the melt-reintegration approach. Journal of Metamorphic Geology 35, 919–942. https://doi.org/10.1111/jmg.12261

Basei, M.A.S., Frimmel, H.E., Nutman, A.P., Preciozzi, F., 2008. West Gondwana amalgamation based on detrital zircon ages from Neoproterozoic Ribeira and Dom Feliciano belts of South America and comparison with coeval sequences from SW Africa. Geological Society, London, Special Publications 294, 239–256.

Basei, M.A.S., Siga, O., Machiavelli, A., Mancini, F., 1992. Evolução tectônica dos terrenos entre os cinturões ribeira e dom feliciano (PR-SC). Revista Brasileira de Geociências 22, 216–221.

Bell, E.A., Boehnke, P., Barboni, M., Harrison, T.M., 2019. Tracking chemical alteration in magmatic zircon using rare earth element abundances. Chemical Geology 510, 56–71. https://doi.org/10.1016/j.chemgeo.2019.02.027

Black, L.P., Gulson, B.L., 1978. The age of the Mud Tank carbonatite, Strangways Range, Northern Territory. BMR J. Austral. Geol. Geophy. 3, 227–232. https://doi.org/10.1016/j.apenergy.2015.11.040

Black, L.P., Kamo, S.L., Allen, C.M., Aleinikoff, J.N., Davis, D.W., Korsch, R.J., Foudoulis, C., 2003. TEMORA 1: a new zircon standard for Phanerozoic U-Pb geochronology. Chemical Geology 155–170.

Bose, S., Ghosh, G., Kawaguchi, K., Das, K., Mondal, A.K., Banerjee, A., 2021. Zircon and monazite geochronology from the Rengali-Eastern Ghats Province: Implications for the tectonic evolution of the eastern Indian terrane. Precambrian Research 355, 106080. https://doi.org/10.1016/j.precamres.2020.106080

Boynton, W. V., 1984. Cosmochemistry of the rare earth elements: meteorite studies. Rare Earth Element Geochemistry. Elsevier B.V., 63–114. https://doi.org/10.1016/b978-0-444-42148-7.50008-3

Brito Neves, B.B., Campos Neto, M.D.C., Fuck, R.A., 1999. From Rodinia to Western Gondwana: An approach to the Brasiliano-Pan African cycle and orogenic collage. Episodes 22, 155–166. https://doi.org/10.18814/epiiugs/1999/v22i3/002

Brito Neves, B.B. de, Fuck, R.A., 2013. Neoproterozoic evolution of the basement of the South-American platform. Journal of South American Earth Sciences 47, 72–89. https://doi.org/10.1016/j.jsames.2013.04.005

Brito Neves, B.B. de, Fuck, R.A., Campanha, G.A. da C., 2021. Basement inliers of the Brasiliano structural provinces of South America. Journal of South American Earth Sciences 110, 103392. https://doi.org/10.1016/j.jsames.2021.103392

Brito Neves, B.B. de, Fuck, R.A., Pimentel, M.M., 2014. The Brasiliano collage in South America: a review. Brazilian Journal of Geology 44, 493–518. https://doi.org/10.5327/Z2317-4889201400030010

Brown, M., 2009. Metamorphic patterns in orogenic systems and the geological record. Geological Society, London, Special Publications 318, 37 LP – 74. https://doi.org/10.1144/SP318.2

Cabrita, D., Salamuni, E., Lagoeiro, L., 2017. Fabric evolution of polydeformed orthogneisses and quartzites along the Curitiba Shear Zone, Curitiba Domain, Southern Brazil. Journal of South American Earth Sciences 77. https://doi.org/10.1016/j.jsames.2017.05.010

Cabrita, D.I.G., Faleiros, F.M., Cawood, P.A., Campanha, G.A.C., Yogi, M.T.A.G., Wainwright, A.N., Raveggi, M., Almeida, V. V., 2021. Petrochronological constraints and tectonic implications of Tonian metamorphism in the Embu Complex , Ribeira Belt , Brazil. Precambrian Research 363. https://doi.org/10.1016/j.precamres.2021.106315

Caltabellota, F.P., Lopes, A.P., Brumatti, M., Rodrigues da Silva, A.D., Lima, R.A.P., Severino, R.R., Andrade, J.J.C., Palmeira, L.C.M., Mapa, F.B., Marque, I.P., Turra, B.B., Costa, V.S., Campos, F.F., Ferrari, V.C., Mendes, D., 2017. Mapa Geológico de Integração do ARIM Vale do Ribeira (SP e PR). Escala 1:250.000.

Campanha, G.A. da C., 2002. O Papel do Sistema de Zonas de Cisalhamento Transcorrentes na Configuração da Porção Meridional da Faixa Ribeira. University of São Paulo.

Campanha, G.A. da C., 1991. Tectônica Proterozóica no Alto e Médio Vale do Ribeira, estados de São Paulo e Paraná. Universidade de São Paulo.

Campanha, G.A. da C., Brito Neves, B.B., 2004. Frontal and oblique tectonics in the Brazilian Shield. Episodes 27, 255–259. https://doi.org/10.1016/S1342-937X(05)70391-9

Campanha, G.A. da C., Faleiros, F.M., Basei, M.A.S., Tassinari, C.C.G., Nutman, A., Vasconcelos, P., 2015. Geochemistry and age of mafic rocks from the Votuverava Group, southern Ribeira Belt, Brazil: Evidence for 1490Ma oceanic back-arc magmatism. Precambrian Research 266, 530–550. https://doi.org/10.1016/j.precamres.2015.05.026

Campanha, G.A. da C., Sadowski, G.R., 2002. Determinações da deformação finita em rochas metassedimentares da faixa ribeira na região de Iporanga e Apiaí, SP. Revista Brasileira de Geociências 32, 107–118.

Campanha, G.A. da C., Sadowski, G.R., 1999. Tectonics of the southern portion of the Ribeira Belt (Apiai Domain). Precambrian Research 98, 31–51. https://doi.org/10.1016/S0301-9268(99)00027-3

Campanha, G.A.C., Basei, M.S., Faleiros, F.M., Nutman, A.P., 2016. The Mesoproterozoic to early Neoproterozoic passive margin Lajeado Group and Apiaí Gabbro, Southeastern Brazil. Geoscience Frontiers 7, 683–694. https://doi.org/10.1016/j.gsf.2015.08.004

Campanha, G.A.C., Faleiros, F.M., Cawood, P.A., Cabrita, D.I.G., Ribeiro, B. V, Basei, M.A.S., 2019. The Tonian Embu Complex in the Ribeira Belt (Brazil): revision , depositional age and setting in Rodinia and West Gondwana. Precambrian Research 320, 31–45. https://doi.org/10.1016/j.precamres.2018.10.010

Campanha, G.A.C., Gimenez Filho, A., Caetano, S.L.V., Pires, F.A., Dantas, A.S.L., Teixeira, A.L., Dehira, L.K., 1986. Geologia e estratigrafia da região das folhas Iporanga e Gruta do Diabo, Vale do Ribeira, São Paulo. Congresso Brasileiro de Geologia. Sociedade Brasileira de Geologia, Goiânia, 1058–1073.

Campos Neto, M. da C., Figueiredo, M.C.., 1995. The Rio Doce Orogeny, Southeastern Brazil. Journal of South American Earth Sciences 8, 143–162. https://doi.org/10.1016/0895-9811(95)00002-W

Campos Neto, M.D.C., 2000. Orogenic systems from Southwestern Gondwana: an approach to Brasiliano Pan African cycle and orogenic collage in Southeastern Brazil. Tectonic Evolution of South America. Rio de Janeiro, 335–365.

Cavalcante, C., Lagoeiro, L., Fossen, H., Egydio-Silva, M., Morales, L.F.G., Ferreira, F.,

Conte, T., 2018. Temperature constraints on microfabric patterns in quartzofeldsphatic mylonites, Ribeira belt (SE Brazil). Journal of Structural Geology 115, 243–262. https://doi.org/10.1016/j.jsg.2018.07.013

Cawood, P.A., Hawkesworth, C.J., Dhuime, B., 2012. Detrital zircon record and tectonic setting. Geology 40, 875–878. https://doi.org/10.1130/G32945.1

Cawood, P.A., Strachan, R.A., Pisarevsky, S.A., Gladkochub, D.P., Murphy, J.B., 2016. Linking collisional and accretionary orogens during Rodinia assembly and breakup: Implications for models of supercontinent cycles. Earth and Planetary Science Letters 449, 118–126. https://doi.org/10.1016/j.epsl.2016.05.049

Caxito, F.A., Heilbron, M., Valeriano, C.M., Bruno, H., Pedrosa-Soares, A., Alkmim, F.F., Chemale, F., Hartmann, L.A., Dantas, E., Basei, M.A.S., 2021. Integration of elemental and isotope data supports a neoproterozoic adamastor ocean realm. Geochemical Perspectives Letters 17, 6–10. https://doi.org/10.7185/GEOCHEMLET.2106

Ceccato, A., Pennacchioni, G., Menegon, L., Bestmann, M., 2017. Crystallographic control and texture inheritance during mylonitization of coarse grained quartz veins. Lithos 290–291, 210–227. https://doi.org/10.1016/j.lithos.2017.08.005

Cerva-Alves, T., Hartmann, L.A., Remus, M. V.D., Lana, C., 2020. Integrated ophiolite and arc evolution, southern Brasiliano Orogen. Precambrian Research 341, 105648. https://doi.org/10.1016/j.precamres.2020.105648

Chetty, T.R.K., 2017. Chapter 1 - Orogens. In: Chetty, T.R.K.B.T.-P.O. of I. (Ed.), Proterozoic Orogens of India: A Critical Window to Gondwana. Elsevier, 1–34. https://doi.org/https://doi.org/10.1016/B978-0-12-804441-4.00001-8

Chu, N.C., Taylor, R.N., Chavagnac, V., Nesbitt, R.W., Boella, R.M., Milton, J.A., German, C.R., Bayon, G., Burton, K., 2002. Hf isotope ratio analysis using multi-collector inductively coupled plasma mass spectrometry: An evaluation of isobaric interference corrections. Journal of Analytical Atomic Spectrometry 17, 1567–1574. https://doi.org/10.1039/b206707b

Condie, K.C., 2003. Supercontinents, superplumes and continental growth: The Neoproterozoic record. Geological Society Special Publication 206, 1–21.

https://doi.org/10.1144/GSL.SP.2003.206.01.02

Connolly, J.A.D., 2005. Computation of phase equilibria by linear programming: A tool for geodynamic modeling and its application to subduction zone decarbonation. Earth and Planetary Science Letters 236, 524–541. https://doi.org/10.1016/j.epsl.2005.04.033

Conte, T., Cavalcante, C., Lagoeiro, L.E., Fossen, H., Silveira, C.S., 2020. Quartz textural analysis from an anastomosing shear zone system: Implications for the tectonic evolution of the Ribeira belt, Brazil. Journal of South American Earth Sciences 103, 102750. https://doi.org/10.1016/j.jsames.2020.102750

Cordani, U.G., Coutinho, J.M. V, Nutman, A.P., 2002. Geochronological constraints on the evolution of the Embu Complex São Paulo, Brazil. Journal of South American Earth Sciences 14, 903–910. https://doi.org/10.1016/S0895-9811(01)00083-9

Corrales, F.F.P., Dussin, I.A., Heilbron, M., Bruno, H., Bersan, S., Valeriano, C.M., Pedrosa-Soares, A.C., Tedeschi, M., 2020. Coeval high Ba-Sr arc-related and OIB Neoproterozoic rocks linking pre-collisional magmatism of the Ribeira and Araçuaí orogenic belts, SE-Brazil. Precambrian Research 337, 105476. https://doi.org/10.1016/j.precamres.2019.105476

Costa, R.V. da, Johannes Trouw, R.A., Marimon, R.S., Nepomuceno, F., Mendes, J.C., Dantas, E., 2020. São Bento do Sapucaí Shear Zone: Constraining age and P-T conditions of a collisional Neoproterozoic oblique shear zone, Ribeira Orogen, Brazil. Journal of South American Earth Sciences 98, 102418. https://doi.org/10.1016/j.jsames.2019.102418

Costa, R.V., Trouw, R.A.J., Mendes, J.C., Geraldes, M., Tavora, A., Nepomuceno, F., de Araújo Junior, E.B., 2017. Proterozoic evolution of part of the Embu Complex , eastern S a state , SE Brazil. Journal of South American Earth Sciences 79, 170–188. https://doi.org/10.1016/j.jsames.2017.08.003

Cota de Freitas, N., Almeida, J., Heilbron, M., Cutts, K., Dussin, I., 2021. The Cabo Frio Thrust: A folded suture zone, Ribeira belt, SE Brazil. Journal of Structural Geology 149, 104379. https://doi.org/https://doi.org/10.1016/j.jsg.2021.104379

Cury, L.F., Kaulfuss, G.A., Siga Júnior, O., Basei, M.A.S., Harara, O.M., Sato, K., 2002.

Idades U-Pb (Zircões) de 1.75 Ga em granitóides alcalinos deformados dos núcleos Betara e Tigre: evidências de regimes extensionais do estateriano na Faixa Apiaí. Geologia USP - Serie Cientifica 2, 95–108. https://doi.org/10.5327/S1519-874X2002000100009

Da Silva, L.C., McNaughton, N.J., Armstrong, R., Hartmann, L.A., Fletcher, I.R., 2005. The neoproterozoic Mantiqueira Province and its African connections: A zircon-based U-Pb geochronologic subdivision for the Brasiliano/Pan-African systems of orogens. Precambrian Research 136, 203–240. https://doi.org/10.1016/j.precamres.2004.10.004

Deer, W.A., Howie, R.A., Zussman, J., 2013. An introduction to the rock-forming minerals.

Depaolo, D.J., 1981. Neodymium isotopes in the Colorado Front Range and crust-mantle evolution in the Proterozoic. Nature 291, 193–196. https://doi.org/10.1038/291193a0

Ducea, M.N., Saleeby, J.B., Bergantz, G., 2015. The architecture, chemistry, and evolution of continental magmatic arcs. Annual Review of Earth and Planetary Sciences 43, 299–331. https://doi.org/10.1146/annurev-earth-060614-105049

Duffles, P., Trouw, R.A.J., Mendes, J.C., Gerdes, A., Vinagre, R., 2016. U-Pb age of detrital zircon from the Embu sequence, Ribeira belt, Se Brazil. Precambrian Research 278, 69–86. https://doi.org/10.1016/j.precamres.2016.03.007

Egydio-Silva, M., Vauchez, A., Bascou, J., Hippertt, J., 2002. High-temperature deformation in the Neoproterozoic transpressional Ribeira belt, southeast Brazil. Tectonophysics 352, 203–224. https://doi.org/10.1016/S0040-1951(02)00197-X

Faleiros, F.M., 2008. Evolução de Terrenos Tectono-Metamórficos da Serrania do Ribeira e Planalto Alto Turvo (SP, PR). Universidade de São Paulo.

Faleiros, F.M., Campanha, G.A. da C., Bello, R.M. da S., Fuzikawa, K., 2010. Quartz recrystallization regimes, c-axis texture transitions and fluid inclusion reequilibration in a prograde greenschist to amphibolite facies mylonite zone (Ribeira Shear Zone, SE Brazil). Tectonophysics 485, 193–214. https://doi.org/10.1016/j.tecto.2009.12.014

Faleiros, F.M., Campanha, G.A. da C., Martins, L., Vlach, S., Vasconcelos, P.M., 2011a. Ediacaran high-pressure collision metamorphism and tectonics of the southern Ribeira Belt (SE Brazil): Evidence for terrane accretion and dispersion during Gondwana assembly. Precambrian Research 189, 263–291. https://doi.org/10.1016/j.precamres.2011.07.013

Faleiros, F.M., Campanha, G.A.C., Pavan, M., Almeida, V. V., Rodrigues, S.W.O., Araújo, B.P., 2016. Short-lived polyphase deformation during crustal thickening and exhumation of a collisional orogen (Ribeira Belt, Brazil). Journal of Structural Geology 93, 106–130. https://doi.org/10.1016/j.jsg.2016.10.006

Faleiros, F.M., Ferrari, V.C., Costa, V.S., Da Cruz Campanha, G.A., 2011b. Geochemistry and Petrogenesis of Metabasites from the Votuverava Group (Apiaí Terrane, Southern Ribeira Belt): Evidence of a Calymmian Back-arc Basin. Geologia USP - Serie Cientifica 11, 135–155. https://doi.org/10.5327/Z1519-874X2011000200008

Faleiros, F.M., Morais, S.M., Costa, V.S., 2012. Geologia e recursos minerais da folha Apiaí SG.22-X-B-V: escala 1:100.000: estados de São Paulo e Paraná.

Faleiros, F.M., Ribeiro, B. V, Campanha, G.A.C., Cawood, P.A., Cabrita, D.I.G., Yogi, M.T.A.G., Milani, L.A., Lemos-Santos, D. V, Almeida, V. V, Rodrigues, S.W.O., Malta, I.S., Forero-Ortega, A.J., 2022. Strain Partitioning along Terrane Bounding and Intraterrane Shear Zones: Constraints from a Long-Lived Transpressional System in West Gondwana (Ribeira Belt, Brazil). Lithosphere 2021, 2103213. https://doi.org/10.2113/2022/2103213

Fassbinder, E., 1990. Análise estrutural da Falha Lancinha, Estado do Paraná. Universidade de São Paulo.

Fernandes, A.J., 1991. O Complexo Embu no Leste do Estado de São Paulo: Contribuição ao Conhecimento da Litoestratigrafia e da Evolução Estrutural e Metamórfica. Universidade de São Paulo.

Forero-Ortega, A.J., Campanha, G.A.C., Faleiros, F.M., Yogi, M.T.A.G., 2020. Pure shear-dominated transpression and vertical extrusion in a strike-slip fault splay from the Itapirapuã Shear Zone, Ribeira Belt, Brazil. Tectonophysics 786, 228455.

https://doi.org/10.1016/j.tecto.2020.228455

Forero-Ortega, A.J., Faleiros, F.M., 2018. Ediacaran (570-615 Ma) back-arc basin basaltic volcanism in the ltaiacoca Group, Ribeira Belt, Brazil: a remnant of the Adamastor Ocean. South American Symposium on Isotope Geology. Cochabamba.

Fossen, H., Cavalcante, C., Konopásek, J., Meira, V.T., de Almeida, R.P., Hollanda, M.H.B.M., Trompette, R., 2020. A critical discussion of the subduction-collision model for the Neoproterozoic Araçuaí-West Congo orogen. Precambrian Research 343. https://doi.org/10.1016/j.precamres.2020.105715

Fossen, H., Cavalcante, G.C.G., 2017. Shear zones – A review., Earth-Science Reviews. https://doi.org/10.1016/j.earscirev.2017.05.002

Fuck, R.A., Brito Neves, B.B., Schobbenhaus, C., 2008. Rodinia descendants in South America. Precambrian Research 160, 108–126. https://doi.org/10.1016/j.precamres.2007.04.018

Fuhrman, M.L., Lindsley, D.H., 1988. Ternary-Feldspar Modeling and Thermometry. American Mineralogist 73, 201–215.

Gain, S.E.M., Gréau, Y., Henry, H., Belousova, E., Dainis, I., Griffin, W.L., O'Reilly, S.Y., 2019. Mud Tank Zircon: Long-Term Evaluation of a Reference Material for U-Pb Dating, Hf-Isotope Analysis and Trace Element Analysis. Geostandards and Geoanalytical Research 43, 339–354. https://doi.org/10.1111/ggr.12265

Gilgannon, J., Fusseis, F., Menegon, L., Regenauer-Lieb, K., Buckman, J., 2017. Hierarchical creep cavity formation in an ultramylonite and implications for phase mixing. Solid Earth 8, 1193–1209. https://doi.org/10.5194/se-8-1193-2017

Giraldo, S.J., Trouw, R.A.J., Duffles, P., Vinagre da Costa, R., Ibañez Mejia, M., Schwantes Marimon, R., 2019. Structural analysis combined with new geothermobarometric and geochronological results of the Além Paraíba shear zone, between Três Rios and Bananal, Ribeira Orogen, SE Brazil. Journal of South American Earth Sciences 90, 118–136. https://doi.org/10.1016/j.jsames.2018.11.018

Gray, D.R., Foster, D.A., Meert, J.G., Goscombe, B.D., Armstrong, R., Trouw, R.A.J.,

Passchier, C.W., 2008. A Damara orogen perspective on the assembly of southwestern Gondwana. Geological Society Special Publication 294, 257–278. https://doi.org/10.1144/SP294.14

Guillot, S., Hattori, K., Agard, P., Schwartz, S., Vidal, O., 2009. Exhumation Processes in Oceanic and Continental Subduction Contexts: A Review. Subduction Zone Geodynamics. 103–118. https://doi.org/10.1007/978-3-540-87974-9

Hackspacher, P.C., Dantas, E.L., Spoladore, Â., Fetter, A.H., Oliveira, M.A.F. de, 2000. Evidence of Neoproterozoic Backarc Basin Development in the Central Ribeira Belt, Southeastern Brazil: New Geochronological and Geochemical Constraints From the São Roque - Açungui Groups. Revista Brasileira de Geociências 30, 110–114.

Hamilton, P.J., O'Nions, R.K., Bridgwater, D., Nutman, A., 1983. Sm-Nd studies of Archaean metasediments and metavolcanics from West Greenland and their implications for the Earth's early history. Earth and Planetary Science Letters 62, 263–272. https://doi.org/10.1016/0012-821X(83)90089-4

Hartmann, L.A., Werle, M., Michelin, C.R.L., Lana, C., Queiroga, G.N., Castro, M.P., Arena, K.R., 2019. Proto-Adamastor ocean crust (920 Ma) described in Brasiliano Orogen from coetaneous zircon and tourmaline. Geoscience Frontiers 10, 1623–1633. https://doi.org/10.1016/j.gsf.2018.09.018

Heilbron, M., Machado, N., 2003. Timing of terrane accretion in the Neoproterozoic-Eopaleozoic Ribeira orogen (SE Brazil). Precambrian Research 125, 87–112.

Heilbron, M., Oliveira, C., Lobato, M., De Morisson Valeriano, C., Dussin, I., Dantas, E., Simonetti, A., Bruno, H., Corrales, F., Socoloff, E., 2019. The Barreiro suite in the central Ribeira Belt (SE-Brazil): A late Tonian tholeiitic intraplate magmatic event in the distal passive margin of the São Francisco Paleocontinent. Brazilian Journal of Geology 49, 1–21. https://doi.org/10.1590/2317-4889201920180129

Heilbron, M., Valeriano, C.D.M., Peixoto, C., Neubauer, F., Dussin, I., Corrales, F., Bruno, H., Cesar, J., Almeida, H. De, Guilherme, L., 2020. Neoproterozoic magmatic arc systems of the central Ribeira belt, SE-Brazil, in the context of the West-Gondwana pre-collisional history: A review. Journal of South American Earth Sciences 102710. https://doi.org/10.1016/j.jsames.2020.102710

Heilbron, M., Valeriano, C.M., Tassinari, C.C.G., Almeida, J., Tupinambá, M., Siga Jr, O., Trouw, R., 2008. Correlation of Neoproterozoic terranes between Ribeira Belt, SE Brazil and its African counterpart: comparative tectonic evolution and open questions., West Gondwana: Pre-Cenozoic Correlations Across the South Atlantic Region. https://doi.org/10.1144/SP294.12

Henrique-Pinto, R., De Assis Janasi, V., Da Cruz Campanha, G.A., 2018. U-Pb dating, Lu-Hf isotope systematics and chemistry of zircon from the Morro do Polvilho meta-trachydacite: Constraints on sources of magmatism and on the depositional age of the São Roque Group. Geologia USP - Serie Cientifica 18, 45–56. https://doi.org/10.11606/issn.2316-9095.v18-125793

Henrique-Pinto, R., Janasi, V.A., Vasconcellos, A.C.B.C., Sawyer, E.W., Barnes, S., Basei, M.A.S., Tassinari, C.C.G., 2015. Zircon provenance in meta-sandstones of the São Roque Domain : Implications for the Proterozoic evolution of the Ribeira Belt , SE Brazil. Precambrian Research 256, 271–288. https://doi.org/10.1016/j.precamres.2014.11.014

Hippertt, J., Egydio-Silva, M., 1996. New polygonal grains formed by dissolution-redeposition in quartz mylonite. Journal of Structural Geology 18, 1345–1352. https://doi.org/10.1016/S0191-8141(96)00047-8

Hogmalm, K.J., Zack, T., Karlsson, A.K.O., Sjöqvist, A.S.L., Garbe-Schönberg, D., 2017. In situ Rb-Sr and K-Ca dating by LA-ICP-MS/MS: An evaluation of N2O and SF6 as reaction gases. Journal of Analytical Atomic Spectrometry 32, 305–313. https://doi.org/10.1039/c6ja00362a

Holland, T.J.B., Powell, R., 2011. An improved and extended internally consistent thermodynamic dataset for phases of petrological interest, involving a new equation of state for solids. Journal of Metamorphic Geology 29, 333–383. https://doi.org/10.1111/j.1525-1314.2010.00923.x

Hollocher, K., Robinson, P., Walsh, E., Roberts, D., 2012. Geochemistry of amphibolite-facies volcanics and gabbros of the støren nappe in extensions west and southwest of Trondheim, Western Gneiss Region, Norway: A key to correlations and paleotectonic settings. American Journal of Science 312, 357–416. https://doi.org/10.2475/04.2012.01

Jackson, S.E., Pearson, N.J., Griffin, W.L., Belousova, E.A., 2004. The application of laser ablation-inductively coupled plasma-mass spectrometry to in situ U-Pb zircon geochronology. Chemical Geology 211, 47–69. https://doi.org/10.1016/j.chemgeo.2004.06.017

Jäger, E, 1979. Introduction to Geochronology BT - Lectures in Isotope Geology. In: Jäger, Emilie, Hunziker, J.C. (Eds.). Springer Berlin Heidelberg, Berlin, Heidelberg, 1–12.

Janasi, V. de A., Alves, A., Vlach, S.R.F., Leite, R.J., 2003. Granitos Peraluminosos da Porção Central da Faixa Ribeira, Estado de São Paulo: Sucessivos Eventos de Reciclagem da Crosta Continental no Neoproterozóico. Geologia USP - Serie Cientifica 3, 13–24.

Janasi, V. de A., Andrade, S., Vasconcellos, A.C.B.C., Henrique-Pinto, R., Ulbrich, H.H.G.J., 2016. Timing and sources of granite magmatism in the Ribeira Belt, SE Brazil: Insights from zircon in situ U–Pb dating and Hf isotope geochemistry in granites from the São Roque Domain. Journal of South American Earth Sciences 68, 224–247. https://doi.org/10.1016/j.jsames.2015.11.009

Janasi, V. de A., Ulbrich, H.H.G.J., 1991. Late Proterozoic granitoid magmatism in the state of São Paulo, southeastern Brazil. Precambrian Research 51, 351–374.

Janasi, V.A., Leite, R.J., Van Schmus, W.R., 2001. U-Pb chronostratigraphy of the granitic magmatism in the Agudos Grandes Batholith (West of São Paulo, Brazil) - Implications for the evolution of the Ribeira Belt. Journal of South American Earth Sciences 14, 363–376. https://doi.org/10.1016/S0895-9811(01)00034-7

Janoušek, V., Farrow, C.M., Erban, V., 2006. Interpretation of whole-rock geochemical data in igneous geochemistry: Introducing Geochemical Data Toolkit (GCDkit). Journal of Petrology 47, 1255–1259. https://doi.org/10.1093/petrology/egl013

Juliani, C., Hackspacher, P., Dantas, E.L., Fetter, A.H., 2000. the Mesoproterozoic Volcano-Sedimentary Serra Do Itaberaba Group of the Central Ribeira Belt, São Paulo State, Brazil: Implications for the Age of the Overlying São Roque Group. Revista Brasileira de Geociências 30, 082–086. https://doi.org/10.25249/0375-7536.2000301082086

Kelsey, D.E., Clark, C., Hand, M., 2008. Thermobarometric modelling of zircon and monazite growth in melt-bearing systems: Examples using model metapelitic and metapsammitic granulites. Journal of Metamorphic Geology 26, 199–212. https://doi.org/10.1111/j.1525-1314.2007.00757.x

Kilian, R., Heilbronner, R., Stünitz, H., 2011. Quartz grain size reduction in a granitoid rock and the transition from dislocation to diffusion creep. Journal of Structural Geology 33, 1265–1284. https://doi.org/10.1016/j.jsg.2011.05.004

Konopásek, J., Cavalcante, C., Fossen, H., Janoušek, V., 2020. Adamastor – an ocean that never existed? Earth-Science Reviews 205, 103201. https://doi.org/10.1016/j.earscirev.2020.103201

Leandro, R., 2016. Caracterização Tectonoestratigráfica da Sequência Terrígena da Formação Capiru Na Região de Morro Grande, Colombo - Pr., Dissertação de Mestrado. Universidade Federal do Paraná. https://doi.org/10.1017/CBO9781107415324.004

Leite, R.J., 2003. Petrogênese e geocronologia U-Pb do magmatismo granítico tardi- a pós-orogênico no batólito Agudos Grandes (SP). Universidade de São Paulo.

Leite, R.J., Heaman, L.M., de Assis Janasi, V., Martins, L., Creaser, R.A., 2007. The late- to postorogenic transition in the Neoproterozoic Agudos Grandes Granite Batholith (Apiaí Domain, SE Brazil): Constraints from geology, mineralogy, and U-Pb geochronology. Journal of South American Earth Sciences 23, 193–212. https://doi.org/10.1016/j.jsames.2006.09.022

Li, Z.X., Bogdanova, S. V., Collins, A.S., Davidson, A., De Waele, B., Ernst, R.E., Fitzsimons, I.C.W., Fuck, R.A., Gladkochub, D.P., Jacobs, J., Karlstrom, K.E., Lu, S., Natapov, L.M., Pease, V., Pisarevsky, S.A., Thrane, K., Vernikovsky, V., 2008. Assembly, configuration, and break-up history of Rodinia: A synthesis. Precambrian Research 160, 179–210. https://doi.org/10.1016/j.precamres.2007.04.021

Lobato, M., Heilbron, M., Torós, B., Ragatky, D., Dantas, E., 2015. Provenance of the Neoproterozoic high-grade metasedimentary rocks of the arc-related Oriental Terrane of the Ribeira belt: Implications for Gondwana amalgamation. Journal of South American Earth Sciences 63, 260–278.

https://doi.org/10.1016/j.jsames.2015.07.019

Ludwig, K.R., 2003. A Geochronological Toolkit for Microsoft Excel. Berkeley Geochronology Center, Special Publication. 4, 71.

Machado, R., Dehler, N.M., Vasconcelos, P., 2007. 40Ar/39Ar ages (600-570 Ma) of the Serra do Azeite transtensional shear zone: Evidence for syncontractional extension in the Cajati area, southern Ribeira belt. Anais Da Academia Brasileira de Ciencias 79, 713–723.

Maurer, V.C., 2016. Caracterização geocronológica (U-Pb), geoquímica e isotópica 9Sr, Nd, Hf) do Complexo Rio Capivari no Terreno Embu. Universidade de São Paulo.

Meira, V.T., 2014. Evolução Tectono-Metamórfica Neoproterozóica dos Complexos Embu e Costeiro no Contexto de Formação do Gondwana Ocidental (Leste do Estado de São Paulo). Universidade de São Paulo.

Meira, V.T., Garcia-Casco, A., Hyppolito, T., Juliani, C., Schorscher, J.H.D., 2019a. Tectono-Metamorphic Evolution of the Central Ribeira Belt, Brazil: A Case of Late Neoproterozoic Intracontinental Orogeny and Flow of Partially Molten Deep Crust During the Assembly of West Gondwana. Tectonics 38, 3182–3209. https://doi.org/10.1029/2018TC004959

Meira, V.T., García-Casco, A., Juliani, C., Almeida, R.P., Schorscher, J.H.D., 2015. The role of intracontinental deformation in supercontinent assembly: Insights from the Ribeira Belt, Southeastern Brazil (Neoproterozoic West Gondwana). Terra Nova 27, 206–217. https://doi.org/10.1111/ter.12149

Meira, V.T., Garcia-Casco, A., Juliani, C., Schorscher, J.H.D., 2019b. Late Tonian within-plate mafic magmatism and Ediacaran partial melting and magmatism in the Costeiro Domain, Central Ribeira Belt, Brazil. Precambrian Research 334, 105440. https://doi.org/10.1016/j.precamres.2019.105440

Mora, C.A.S., Campanha, G.A. da C., Wemmer, K., 2013. Microstructures and K-Ar illite fine-fraction ages of the cataclastic rocks associated to the Camburu Shear Zone, Ribeira Belt, Southeastern Brazil. Brazilian Journal of Geology 43, 607–622. https://doi.org/10.5327/z2317-48892013000400003

Mori, P.E., Reeves, S., Correia, C.T., Haukka, M., 1999. Development of a fused glass disc XRF facility and comparison with pressed powder pellet technique at Instituto de Geociências, São Paulo University. Revista Brasileira de Geociencias 29, 441–446. https://doi.org/10.5327/rbg.v29i3.715

Mullen, E.D., 1983. MnO/TiO2/P2O5: a minor element discriminant for basaltic rocks of oceanic environments and its implications for petrogenesis. Earth and Planetary Science Letters 62, 53–62. https://doi.org/10.1016/0012-821X(83)90070-5

Murphy, D.T., Allen, C.M., Ghidan, O., Dickson, A., Hu, W.P., Briggs, E., Holder, P.W., Armstrong, K.F., 2020. Analysing Sr isotopes in low-Sr samples such as single insects with inductively coupled plasma tandem mass spectrometry using N2O as a reaction gas for in-line Rb separation. Rapid Communications in Mass Spectrometry 34, 1–12. https://doi.org/10.1002/rcm.8604

Navarro, M.S., Andrade, S., Ulbrich, H., Gomes, C.B., Girardi, V.A.V., 2008. The direct determination of rare earth elements in basaltic and related rocks using ICP-MS: Testing the efficiency of microwave oven sample decomposition procedures. Geostandards and Geoanalytical Research 32, 167–180. https://doi.org/10.1111/j.1751-908X.2008.00840.x

Neumann, B., 2000. Texture development of recrystallised quartz polycrystals unravelled by orientation and misorientation characteristics. Journal of Structural Geology 22, 1695–1711. https://doi.org/10.1016/S0191-8141(00)00060-2

O'Sullivan, G., Chew, D., Kenny, G., Henrichs, I., Mulligan, D., 2020. The trace element composition of apatite and its application to detrital provenance studies. Earth-Science Reviews 201, 103044. https://doi.org/10.1016/j.earscirev.2019.103044

O'Sullivan, G.J., Thakurdin, Y., Bolhar, R., Horváth, P., Hoare, B.C., Collerson, K.D., 2021. The Great Falls Tectonic Zone after the assembly of Laurentia: evidence for long-term tectonic stability from xenolith apatite. Lithos 384–385, 105977. https://doi.org/10.1016/j.lithos.2021.105977

Orihashi, Y., Nakai, S., Hirata, T., 2008. U-Pb age determination for seven standard zircons using inductively coupled plasma-mass spectrometry coupled with frequency quintupled Nd-YAG (λ = 213 nm) laser ablation system: Comparison with

LA-ICP-MS zircon analyses with a NIST glass reference materia. Resource Geology 58, 101–123. https://doi.org/10.1111/j.1751-3928.2008.00052.x

Oriolo, S., Oyhantçabal, P., Wemmer, K., Siegesmund, S., 2017. Contemporaneous assembly of Western Gondwana and final Rodinia break-up: Implications for the supercontinent cycle. Geoscience Frontiers 8, 1431–1445. https://doi.org/10.1016/j.gsf.2017.01.009

Oyhantçabal, P., Wagner-Eimer, M., Wemmer, K., Schulz, B., Frei, R., Siegesmund, S., 2012. Paleo- and Neoproterozoic magmatic and tectonometamorphic evolution of the Isla Cristalina de Rivera (Nico Pérez Terrane, Uruguay). International Journal of Earth Sciences 101, 1745–1762. https://doi.org/10.1007/s00531-012-0757-4

Passarelli, C.R., Basei, M.A.S., Prazeres-Filho, H.J., Siga, O., Szabó, G.A.J., Marco-Neto, J., 2007. Structural and geochronological constraints on the evolution of the Juréia Massif, Registro Domain, State of São Paulo, Brazil. Anais Da Academia Brasileira de Ciencias 79, 441–455. https://doi.org/10.1590/s0001-37652007000300008

Passarelli, C.R., Basei, M.A.S., Wemmer, K., Siga Júnior, O., Oyhantc, P., 2011. Major shear zones of southern Brazil and Uruguay : escape tectonics in the eastern border of Rio de La plata and Paranapanema cratons during the Western Gondwana amalgamation. International Journal of Earth Sciences 100, 391–414. https://doi.org/10.1007/s00531-010-0594-2

Passarelli, C.R., Verma, S.K., Mcreath, I., Basei, M.Â.S., Siga Júnior, O., 2019. Tracing the history from Rodinia break-up to the Gondwana amalgamation in the Embu Terrane, southern Ribeira Belt, Brazil. Lithos. https://doi.org/10.1016/j.lithos.2019.05.024

Passchier, C.W., Trouw, R.A.J., 2005. Microtectonics. Springer Berlin Heidelberg.

Patiño Douce, A.E., Harris, N., 1998. Experimental constraints on Himalayan anatexis. Journal of Petrology 39, 689–710. https://doi.org/10.1093/petroj/39.4.689

Paton, C., Hellstrom, J., Paul, B., Woodhead, J., Hergt, J., 2011. Iolite: Freeware for the visualisation and processing of mass spectrometric data. Journal of Analytical Atomic Spectrometry 26, 2508–2518. https://doi.org/10.1039/c1ja10172b

Payne, J.L., Hand, M., Barovich, K.M., Wade, B.P., 2008. Temporal constraints on the timing of high-grade metamorphism in the northern Gawler Craton: Implications for assembly of the Australian Proterozoic. Australian Journal of Earth Sciences 55, 623–640. https://doi.org/10.1080/08120090801982595

Pearce, J.A., 2008. Geochemical fingerprinting of oceanic basalts with applications to ophiolite classification and the search for Archean oceanic crust. Lithos 100, 14–48. https://doi.org/10.1016/j.lithos.2007.06.016

Pearce, J.A., 1996. A User's Guide to Basalto Discriminant Diagrams., Geological Association of Canada, Short Course Notes.

Pearce, J.A., Cann, J.R., 1973. Tectonic setting of basic volcanic rocks determined using trace element analyses. Earth and Planetary Science Letters 19, 290–300. https://doi.org/10.1016/0012-821X(73)90129-5

Pearce, J.A., Thirlwall, M.F., Ingram, G., Murton, B.J., Arculus, R.J., Van Der Laan, S.R., 1992. Isotopic evidence for the origin of boninites and related rocks drilled in the Izu-Bonin (Ogasawara) Forearc, Leg 125. Proc., Scientific Results, ODP, Leg 125, Bonin/Mariana Region 125, 237–262. https://doi.org/10.2973/odp.proc.sr.125.134.1992

Pearce, T.H., Gorman, B.E., Birkett, T.C., 1975. The TiO_2-K_2O-P_2O_5 Diagram: A Method of Discriminating Between Oceanic and Non-Oceanic Basalts. Earth and Planetary Science Letters 24, 419–426.

Peixoto, C. de A., Heilbron, M., Ragatky, D., Armstrong, R., Dantas, E., de Morisson Valeriano, C., Simonetti, A., 2017. Tectonic evolution of the Juvenile Tonian Serra da Prata magmatic arc in the Ribeira belt, SE Brazil: Implications for early west Gondwana amalgamation. Precambrian Research 302, 221–254. https://doi.org/10.1016/j.precamres.2017.09.017

Percival, J.J., Konopásek, J., Anczkiewicz, R., Ganerød, M., Sláma, J., de Campos, R.S., Bitencourt, M. de F., 2022. Tectono-Metamorphic Evolution of the Northern Dom Feliciano Belt Foreland, Santa Catarina, Brazil: Implications for Models of Subduction-Driven Orogenesis. Tectonics 41, e2021TC007014. https://doi.org/https://doi.org/10.1029/2021TC007014

Perrotta, M.M., 1996. POTENCIAL AURÍFERO DE UMA REGIÃO NO VALE DO RIBEIRA , SÃO PAULO , ESTIMADO POR MODELAGEM DE DADOS GEOLÓGICOS , SISTEMA DE INFORMAÇÕES GEOGRÁFICAS . Mônica Mazzini Perrotta Tese de Doutoramento Programa de Pós-Graduação em Geoquími. Universidade de São Paulo.

Perrotta, M.M., Salvador, E.D., Lopes, R.C., D'Agostino, L.Z., Peruffo, N., Gomes, S.D., Sachs, L.L.B., Meira, V.T., Garcia, M.G.M., Lacerda Filho, J.V., 2005. Mapa geológico do estado de São Paulo. Escala: 1:750.000.

Pertille, J., Hartmann, L.A., Santos, J.O.S., N.J., M., Armstrong, R., 2017. Reconstructing the Cryogenian–Ediacaran evolution of the Porongos fold and thrust belt, Southern Brasiliano Orogen, based on Zircon U–Pb–Hf–O isotopes. International Geology Review 59, 1532–1560. https://doi.org/10.1080/00206814.2017.1285257

Philipp, R.P., Pimentel, M.M., Chemale, F., 2016. Tectonic evolution of the Dom Feliciano Belt in Southern Brazil: Geological relationships and U-Pb geochronology. Brazilian Journal of Geology 46, 83–104. https://doi.org/10.1590/2317-4889201620150016

Pinto, V.M., Debruyne, D., Hartmann, L.A., Queiroga, G.N., Lana, C., Fragoso César, B.A.M., Porcher, C., Castro, M.P., Laux, J., 2021. Metamorphic evolution of a Tonian eclogite associated with an island arc of the southern Brasiliano Orogen. Precambrian Research 366. https://doi.org/10.1016/j.precamres.2021.106414

Polat, A., Hofmann, A.W., Rosing, M.T., 2002. Boninite-like volcanic rocks in the 3.7-3.8 Ga isua greenstone belt, West Greenland: Geochemical evidence for intra-oceanic subduction zone processes in the early earth. Chemical Geology 184, 231–254. https://doi.org/10.1016/S0009-2541(01)00363-1

Porada, H., 1989. Pan-African rifting and orogenesis in Southern Equatorial Africa and Eastern Brazil. Precambrian Research 44, 103–136. https://doi.org/10.1016/0301-9268(89)90078-8

Porcher, C., Egydio-silva, M., Fernandes, L., Vauchez, A., 1995. Dados prelimineres do metamorfismo M1 da Faixa Ribeira: Região de Três Rios e Santo Antônio de Pádua (RJ). V Simpósio Nacional de Estudos Tectônicos. Gramado, 71–73.

Prazeres Filho, H.J. dos, 2005. Caracterização geológica e petrogenética do batólito granítico Três Córregos (PR-SP): geoquímica isotópica (Nd-Sr-Pb), idades (ID-TIMS/SHRIMP) e d18'O em zircão. https://doi.org/10.11606/T.44.2005.tde-29102015-131336

Ramsay, J.G., 1980. Shear zone geometry: A review. Journal of Structural Geology 2, 83–99. https://doi.org/10.1016/0191-8141(80)90038-3

Ribeiro, B. V., Finch, M.A., Cawood, P.A., Faleiros, F.M., Murphy, T.D., Simpson, A., Glorie, S., Tedeschi, M., Armit, R., Barrote, V.R., 2021. From microanalysis to supercontinents: insights from the Rio Apa Terrane into the Mesoproterozoic SW Amazonian Craton evolution during Rodinia assembly. Journal of Metamorphic Geology. https://doi.org/10.1111/jmg.12641

Ribeiro, B. V., Lagoeiro, L., Faleiros, F.M., Hunter, N.J.R., Queiroga, G., Raveggi, M., Cawood, P.A., Finch, M., Campanha, G.A.C., 2020a. Strain localization and fluid-assisted deformation in apatite and its influence on trace elements and U–Pb systematics. Earth and Planetary Science Letters 545, 116421. https://doi.org/10.1016/j.epsl.2020.116421

Ribeiro, B. V., Mulder, J.A., Faleiros, F.M., Kirkland, C.L., Cawood, P.A., O'Sullivan, G., Campanha, G.A.C., Finch, M.A., Weinberg, R.F., Nebel, O., 2020b. Using apatite to resolve the age and protoliths of mid-crustal shear zones: A case study from the Taxaquara Shear Zone, SE Brazil. Lithos 378–379, 105817. https://doi.org/10.1016/j.lithos.2020.105817

Ribeiro, B. V, Faleiros, F.M., Campanha, G.A.C., Lagoeiro, L., Weinberg, R.F., Hunter, N.J.R., 2019. Tectonophysics Kinematics , nature of deformation and tectonic setting of the Taxaquara Shear Zone , a major transpressional zone of the Ribeira Belt (SE Brazil). Tectonophysics 751, 83–108. https://doi.org/10.1016/j.tecto.2018.12.025

Ricardo, B.S., Faleiros, F.M., Moraes, R., Siga Júnior, O., Campanha, G.A.C., 2020. Tectonic implications of juxtaposed high- and low-pressure metamorphic field gradient rocks in the Turvo-Cajati Formation, Curitiba Terrane, Ribeira Belt, Brazil. Precambrian Research 345, 105766. https://doi.org/10.1016/j.precamres.2020.105766

Rubatto, D., Hermann, J., Berger, A., Engi, M., 2009. Protracted fluid-induced melting during Barrovian metamorphism in the Central Alps. Contributions to Mineralogy and Petrology 158, 703–722. https://doi.org/10.1007/s00410-009-0406-5

Sadowski, G.R., 1991. A megafalha de Cubatão no Sudeste Brasileiro. Boletim IG, Instituto de Geociências 22, 15–28.

Sadowski, G.R., Motidome, M.J., 1987. Brazilian megafaults. Revista Geologica de Chile 31, 61–75.

Sadowski, H.G.R.&, 1976. Considerações sobre a estratigrafia do Pré-Cambriano na Região de São Paulo. Boletim IG, Instituto de Geociências 9, 107–112.

Santiago, R., Caxito, F. de A., Pedrosa-Soares, A., Neves, M.A., Dantas, E.L., 2020. Tonian island arc remnants in the northern Ribeira orogen of Western Gondwana: The Caxixe batholith (Espírito Santo, SE Brazil). Precambrian Research 351, 105944. https://doi.org/10.1016/j.precamres.2020.105944

Santos, L. da R., Leandro, R., Bahniuk, A., Cury, L.F., 2018. Low-temperature metamorphism in the Capiru Formation, Morro Grande Synform, Southern Ribeira Belt. Brazilian Journal of Geology 48, 95–113. https://doi.org/10.1590/2317-4889201820170090

Santosh, M., Maruyama, S., Sato, K., 2009. Anatomy of a Cambrian suture in Gondwana: Pacific-type orogeny in southern India? Gondwana Research 16, 321–341. https://doi.org/10.1016/j.gr.2008.12.012

Sato, K., Siga, O., Da Silva, J.A., McReath, I., Dunyi, L., Iizuka, T., Rino, S., Hirata, T., Sproesser, W., Basei, M.A.S., 2009. In situ isotopic analyses of U and Pb in zircon by remotely operated SHRIMP II, and Hf by LA-ICP-MS: An example of dating and genetic evolution of zircon by 176Hf/177Hf from the Ita quarry in the Atuba Complex, Se Brazil. Geologia USP - Serie Cientifica 9, 61–69.

Sato, K., Siga, O., Nutman, A.P., Basei, M.A.S., McReath, I., Kaulfuss, G., 2003. The Atuba Complex, Southern South American platform: Archean components and paleoproterozoic to neoproterozoic tectonothermal events. Gondwana Research 6, 251–263. https://doi.org/10.1016/S1342-937X(05)70974-6

Sawyer, E.W., 2008. Atlas of Migmatites. Canadian Science Publishing. https://doi.org/10.1139/9780660197876

Schulz, B., 2021. Monazite Microstructures and Their Interpretation in Petrochronology. Frontiers in Earth Science 9. https://doi.org/10.3389/feart.2021.668566

Shervais, J.W., 1982. TiV plots and the petrogenesis of modern and ophiolitic lavas. Earth and Planetary Science Letters 59, 101–118. https://doi.org/10.1016/0012-821X(82)90120-0

Siga Junior, O., 1995. Domínios Tectônicos do Sudeste do Paraná e Nordeste de Santa Catarina: Geocronologia e Evolução crustal. Universidade de São Paulo.

Siga Júnior, O., Angelo, Basei, S., Sato, K., Passarelli, C.R., Nutman, A., Mcreath, I., Prazeres Filho, H.J. dos, 2011a. Calymmian (1 .50 e 1.45 Ga) magmatic records in Votuverava and Perau sequences , south-southeastern Brazil : Zircon ages and Nd e Sr isotopic geochemistry. Journal of South American Earth Sciences 32, 301–308. https://doi.org/10.1016/j.jsames.2011.03.015

Siga Júnior, O., Basei, M.A.S., Nutman, A., Sato, K., McReath, I., Passarelli, C.R., Liu, D., 2011b. Extensional and Colisional Magmatic Records in the Apiaí Terrane, South-Southeastern Brazil: Integration of Geochronological U-Pb Zircon Ages. Geologia USP - Serie Cientifica 11, 149–175.

Siga Júnior, O., Basei, M.A.S., Passarelli, C.R., Sato, K., Cury, L.F., McReath, I., 2009. Lower and Upper Neoproterozoic magmatic records in Itaiacoca Belt (Paraná-Brazil): Zircon ages and lithostratigraphy studies. Gondwana Research 15, 197–208. https://doi.org/10.1016/j.gr.2008.11.002

Siga Júnior, O., Basei, M.A.S., Reis Neto, J.M., Machiavelli, A., Harara, O.M., 1995. O complexo Atuba: um cinturão paleoproterozóico intensamente retrabalhado no Neoproterozóico. Boletim IG-USP. Série Científica 26, 69. https://doi.org/10.11606/issn.2316-8986.v26i0p69-98

Siga Júnior, O., Cury, L.F., Mcreath, I., Maria, L., Leite, D.A., Sato, K., Basei, M.A.S., Passarelli, C.R., 2011c. Geology and geochronology of the Betara region in south-southeastern Brazil: Evidence for possible Statherian (1.80 – 1.75 Ga) and Calymmian (1.50 –1.45 Ga) extension events. Gondwana Research 19, 260–274.

https://doi.org/10.1016/j.gr.2010.06.003

Silva, B.Y.B., 2017. Evolução Tectônica Da Porção Central Do Terreno Embu Ao Norte Da Zona De Cisalhamento Taxaquara-Guararema Terreno Embu Ao Norte Da Zona De Cisalhamento Taxaquara-Guararema. University of São Paulo.

Sláma, J., Košler, J., Condon, D.J., Crowley, J.L., Gerdes, A., Hanchar, J.M., Horstwood, M.S.A., Morris, G.A., Nasdala, L., Norberg, N., Schaltegger, U., Schoene, B., Tubrett, M.N., Whitehouse, M.J., 2008. Plešovice zircon - A new natural reference material for U-Pb and Hf isotopic microanalysis. Chemical Geology 249, 1–35. https://doi.org/10.1016/j.chemgeo.2007.11.005

Sobrinho, J.M.A., Janasi, V.A., Simonetti, A., 2011. The Ilha Anchieta Quartz Monzonite : the southernmost expression of ca . 500 Ma post-collisional magmatism in the Ribeira Belt. Anais Da Academia Brasileira de Ciencias 83, 891–906.

Spear, F.S., Kohn, M.J., Cheney, J.T., 1999. P -T paths from anatectic pelites. Contributions Mineral Petrology 134, 17–32.

Stallard, A., Shelley, D., 1995. Quartz c-axes parallel to stretching directions in very low-grade metamorphic rocks. Tectonophysics 249, 31–40. https://doi.org/10.1016/0040-1951(95)00040-T

Stein, D.P., Campanha, G.A. da C., Fernandes, L.A., 1983. Geologia da Folha Pilar do Sul (SF.23-Y-C-IV-4). Estado de São Paulo. São Paulo.

Stipp, M., Stünitz, H., Heilbronner, R., Schmid, S.M., 2002. The eastern Tonale fault zone: A “natural laboratory” for crystal plastic deformation of quartz over a temperature range from 250 to 700 °C. Journal of Structural Geology 24, 1861–1884. https://doi.org/10.1016/S0191-8141(02)00035-4

Sun, S.S., McDonough, W.F., 1989. Chemical and isotopic systematics of oceanic basalts: Implications for mantle composition and processes. Geological Society Special Publication 42, 313–345. https://doi.org/10.1144/GSL.SP.1989.042.01.19

Tassinari, C.C.G., 1988. As idades das rochas e dos eventos metamórficos da porção sudeste do estado de São Paulo e sua evolução crustal. Universidade de São Paulo.

Tassinari, C.C.G., Campos Neto, M. da C., 1988. Precambrian continental crust evolution

of Southeastern São Paul State, Brazil, based on isotopic evidence. Geochim. Brasil 2, 175–183.

Tassinari, C.C.G., Munhá, J.M.U., Ribeiro, A., Correia, C.T., 2001. Neoproterozoic oceans in the Ribeira belt (southeastern Brazil): The Pirapora do bom Jesus ophiolitic complex. Episodes 24, 245–251. https://doi.org/10.18814/epiiugs/2001/v24i4/004

Thomson, S.N., Gehrels, G.E., Ruiz, J., Buchwaldt, R., 2012. Routine low-damage apatite U-Pb dating using laser ablation-multicollector- ICPMS. Geochemistry, Geophysics, Geosystems 13, 1–23. https://doi.org/10.1029/2011GC003928

Torquato, J.R., Cordani, 1981. Brazil-Africa geological links. Earth Science Reviews 17, 155–176. https://doi.org/10.1016/0012-8252(81)90010-6

Trouw, R.A.J., Peternel, R., Ribeiro, A., Heilbron, M., Vinagre, R., Duffles, P., Trouw, C.C., Fontainha, M., Kussama, H.H., 2013. A new interpretation for the interference zone between the southern Brasília belt and the central Ribeira belt, SE Brazil. Journal of South American Earth Sciences 48, 43–57. https://doi.org/10.1016/j.jsames.2013.07.012

Tsunogae, T., Uthup, S., Nyirongo, M.W., Takahashi, K., Rahman, M.S., Liu, Q., Takamura, Y., Tsutsumi, Y., 2021. Neoproterozoic crustal growth in southern Malawi: New insights from petrology, geochemistry, and U–Pb zircon geochronology, and implications for the Kalahari Craton–Congo Craton amalgamation. Precambrian Research 352, 106007. https://doi.org/10.1016/j.precamres.2020.106007

Tupinambá, M., Heilbron, M., Valeriano, C., Júnior, R.P., de Dios, F.B., Machado, N., Silva, L.G. do E., de Almeida, J.C.H., 2012. Juvenile contribution of the Neoproterozoic Rio Negro Magmatic Arc (Ribeira Belt, Brazil): Implications for Western Gondwana amalgamation. Gondwana Research 21, 422–438. https://doi.org/10.1016/j.gr.2011.05.012

Vauchez, A., Tommasi, A., Silva, A., Trompette, R., 1992. Tectônica de escape na terminação de um craton: A Faixa Ribeira. Congresso Brasileiro de Geologia. 373–374.

Vermeesch, P., 2018. IsoplotR: A free and open toolbox for geochronology. Geoscience Frontiers 9, 1479–1493. https://doi.org/10.1016/j.gsf.2018.04.001

Viegas, G., Menegon, L., Archanjo, C., 2016. Brittle grain-size reduction of feldspar, phase mixing and strain localization in granitoids at mid-crustal conditions (Pernambuco shear zone, NE Brazil). Solid Earth 7, 375–396. https://doi.org/10.5194/se-7-375-2016

Vieira, S.R.S.S., 1996. Estudo de processos metamórfico-metassomáticos nos Complexos Embu e Pilar no Bloco Juquitiba, SP. Universidade de São Paulo.

Vlach, S., 2008. Mineralogia, análise e datação de monazita com microssonda eletrônica e aplicações. Universidade de São Paulo.

Weber, W., Siga Junior, O., Sato, K., Neto, J.M. dos R., Basei, M.Â.S., Nutman, A.P., 2004. A Formação Água Clara na região de Araçaíba-SP: registro de uma bacia Mesoproterozoica. Boletim IG, Instituto de Geociências, USP 4, 101–110.

Werle, M., Hartmann, L.A., Queiroga, G.N., Lana, C., Pertille, J., Michelin, C.R.L., Remus, M.V.D., Roberts, M., Castro, M.P., Leandro, C.G., Savian, J.F., 2020. Oceanic crust and mantellic evidence on the evolution of tonian-cryogenian ophiolites, southern Brasiliano Orogen. Precambrian Research 351, 105979. https://doi.org/10.1016/j.precamres.2020.105979

White, R.W., Powell, R., Halpin, J.A., 2004. Spatially-focussed melt formation in aluminous metapelites from Broken Hill, Australia. Journal of Metamorphic Geology 22, 825–845. https://doi.org/10.1111/j.1525-1314.2004.00553.x

White, R.W., Powell, R., Holland, T.J.B., 2001. Calculation of partial melting equilibria in the system Na2O-CaO-K2O-FeO-MgO-Al2O3-SiO2-H2O (NCKFMASH). Journal of Metamorphic Geology 19, 139–153. https://doi.org/10.1046/j.0263-4929.2000.00303.x

White, R.W., Powell, R., Johnson, T.E., 2014. The effect of Mn on mineral stability in metapelites revisited: New a-x relations for manganese-bearing minerals. Journal of Metamorphic Geology 32, 809–828. https://doi.org/10.1111/jmg.12095

Williams, I.S., 1997. U-Th-Pb Geochronology by Ion Microprobe., Applications of

Microanalytical Techniques to Understanding Mineralizing Processes. https://doi.org/10.5382/Rev.07.01

Wilson, M., 1989. Igneous Petrogenesis, Journal of Chemical Information and Modeling. Chapman & Hall.

Wilson, M. (B. M., 2007. Igneous petrogenesis. Dordrecht : Springer, [2007] ©2007.

Xia, L., Li, X., 2019. Basalt geochemistry as a diagnostic indicator of tectonic setting. Gondwana Research 65, 43–67. https://doi.org/10.1016/j.gr.2018.08.006

Xia, L.Q., 2014. The geochemical criteria to distinguish continental basalts from arc related ones. Earth-Science Reviews 139, 195–212. https://doi.org/10.1016/j.earscirev.2014.09.006

Yogi, M.T., 2019. Thermobaric and kinematic evolution of Anta Gorda Anticlinorium , Ribeira Belt : metamorphism record and shear deformation in a transpressional setting. São Paulo University.

6. FINAL CONSIDERATIONS

6.1. Integrative concluding remarks

The multidisciplinary study in the Embu Terrane and the adjacent terranes of the Southern Ribeira Belt brought crucial contributions to discussing the conflicting tectonic settings for the Ribeira Belt (presented in Chapter 1).

The evolutionary history and tectonic setting from Rodinia to West Gondwana assembly within Southern Ribeira Belt through the study of mafic magmatism recorded in Apiaí and Embu Terranes are presented in Chapter 3. The chemistry and chronology data of mafic rocks demonstrate the existence of two distinct periods of accretion and convergence processes in this period. The two oldest ones, related to Rodinia assembly, from the Calymmian (1490-1475 Ma) and Ectasian (1300-1260 Ma), are recorded in the mafic rocks from the Votuverava Group. Both events are characterized by a geochemical group with Th / Yb above N-MORB values, low Nb / La ratio, low Nb and Zr concentrations, and Nb anomaly, which are characteristics of arc-related magmatism related to convergent tectonic settings.

A third period of accretion and convergence during the Tonian is recorded in the Embu Terrane. Within this period, the metasedimentary rocks of the southern portion of this terrane were deposited between 970–850 Ma (Campanha et al., 2019) and metamorphosed at 810–760 Ma (Cabrita et al., 2021). Chapter 3 investigate the geochemical data of the mafic igneous rocks from the Embu Terrane. Geochemical data of the Embu Terrane mafic rocks indicate that they belong to the tholeiitic series with low enrichments in LREE, negative Nb and Ta anomalies, low Nb and Zr contents and low Nb / La and Zr /Y ratios, consistent with arc-related basalts. Whole-rock Sm–Nd isotopic data show a εNd(t) a value of 0.73 and an Nd TDM model age of 1941 Ma, with Hf isotopes indicating juvenile mantle sources to the basic magmatism.

The metamorphic data related to the Tonian accretionary to collisional setting is unveiled in Chapter 4. The data demonstrate the existence of a high-grade metamorphic event represented by sillimanite, sillimanite–K-feldspar and cordierite zones. Petrological and thermodynamic modelling data indicate that the high-grade metamorphic rocks within the Embu Terrane attained conditions between 750–805 °C and 3.6–9.2 kbar. Monazite and zircon U–Pb data indicate that this high-grade metamorphic event occurred between 810–760 Ma, concomitant with igneous activity recorded during this period. Several lines of evidence favour an accretionary setting for the the Embu Terrane during

the Tonian. The southern Embu Terrane has a depositional interval between 970–900 Ma with a detrital age signature distinct from the neighbouring terranes and cratons (Campanha et al., 2019). This suggests it was isolated from these blocks, which is consistent with a peripheral or external location with respect to Rodinia rather than an intracontinental setting. Additionally, the relatively short-time difference between the accumulation of the southern Embu Terrane (970–900 Ma) and its Tonian high-grade metamorphic event documented in this work (810–760 Ma) is consistent with the terrane being located at or close to a convergent plate boundary (Cawood et al., 2012). Moreover, the metasedimentary deposition and volcanic ages of the neighbouring terranes are distinct, with Statherian ages for the basal units of the São Roque Group (Henrique-Pinto et al., 2015; Henrique- Pinto et al., 2018), Calymian-Ectasian ages for the Votuverava and Serra de Itaberaba groups (Juliani et al., 2000; Campanha et al., 2015) and Ediacaran ages for the Turvo-Cajati Formation of the Curitiba Terrane (Ricardo et al., 2020).

The Cryogenian to Ediacaran period is the one most well documented in the whole Ribeira Belt. This period is represented by pre, syn and post-orogenic extensive granitic magmatism associated with a Barrovian metamorphism, a crustal-scale transcurrent system and minor supracrustal rocks. This period is associated with anorogenic A-type granitoid magmatism and pull-apart continental sedimentary and volcanic basins. The role of transcurrent deformation in the Cryogenian to Ediacaran was investigated in Chapter 5, exemplified by the Cubatão Shear Zone. The Cubatão Shear Zone is a key segment of the transcurrent system within the Ribeira Belt, with an exposed length of ca. 450 km. However, despite its major coverage and tectonic significance, no work has quantified its deformation and petrochronological evolution until the present contribution.

Chapter 4 results indicate that the Cubatão Shear Zone developed within a transpressional setting with a dominant subhorizontal stretching lineation at medium-temperature conditions of 460–520 °C and 4.5–9.5 kbar, consistent with quartz recrystallisation microstructures indicative of subgrain rotation recrystallisation. Igneous-type apatite from the mylonites of the CSZ record ages of ca. 610–570 Ma, which are interpreted as reset ages due to ductile deformation at medium-temperature conditions. Zircon U-Pb geochronology indicates that mylonites are sourced from the Juquiá Granite and the Atuba Complex. The CSZ activity is coeval with the main period of activity of other ductile shear zones from the Ribeira Belt, as indicated by available geochronological data. This age interval coincides with the main period of other regional shear zones activity, voluminous granitic magmatism, regional metamorphism and

convergence of the cratons surrounding the Ribeira Belt, indicating active participation of the transcurrent shear zones in the orogenic processes that built up West Gondwana. The data in this contribution record multiple periods of accretion and convergence settings from the Rodinia to West Gondwana, not consistent with a single intracontinental orogeny.

6.2. Future research

Tonian igneous activity is partially concomitant with the high-grade metasedimentary rocks from the Embu Terrane. However, it is still vital to study the chemistry of these rocks (e.g., orthogneisses) to better constrain the Tonian accretionary event proposed by this work. Additionally, an investigation detailing Tonian anatexis is an unexplored topic, such as melt compositional diversity (or not), melting reactions, volume of melt produced and spatial variation of the melt.

7. BIBLIOGRAPHICAL REFERENCES

Almeida, F.F.M. de, 1953. Botucatu, a triassic desert of South America. In: Comptes Rendus of Int. Geol. Congr., 19, Argel, 1953, XIX Session, fasc. VII. pp. 9–24, Algerie.

Almeida F.F.M. de, Amaral G., Cordani U.G., Kawashita K. 1973. The Precambrian evolution of the South American cratonic margin south of the Amazon River. In: Nairn A.E.M., Stehli F.G.1973. The Oceanic Basin and Margin. Plenum Press, New York, 1:411-446.

Almeida F.F.M.; Hasui Y., Brito Neves B.B. 1976. The Upper Precambrian of South America.Bol.IG. – USP, São Paulo, 7:45-80.

Almeida F.F.M. de, Hasui Y. 1984.O pré-cambriano do Brasil. Edgard Blucher Ltda. São Paulo, 378pp.

Basei M.A.S., Siga Júnior, O., Machiavelli, A., Mancini, F., 1992. Evolução tectônica dos Terrenos entre os cinturões Ribeira e Dom Feliciano (PR-SC). Revista Brasileira de Geociências, v. 22, p. 216–221.

Brito Neves B.B. de, Cordani U.G. 1991.Tectonic evolution of South America during the Late Proterozoic. Precambrian Research, Amsterdam, 53: 23-40.

Brito Neves B.B., Campos Neto, M.C., Fuck, R.A., 1999. From Rodinia to Western Gondwana: an approach to the Brasiliano–Pan African Cycle and orogenic collage. Episodes, v. 22, p. 155–166.

Campanha G.A.C., Sadowski G.R. 1999. Tectonics of the Southern portion of the Ribeira Belt (Apiaí Domain).Precambrian Research, Amsterdam, 98: 31-51.

Campanha, G.A.C., Brito Neves, B.B., 2004. Frontal and oblique tectonics in the Brazilian shield. Episodes, v. 27, p. 255–259.

Campanha G.A.C., Faleiros F.M., Cawood P.A., Cabrita D.I.G., Ribeiro B.V., Basei M.A.S. 2019. The Tonian Embu Complex in the Ribeira Belt (Brazil): revision, depositional age and setting in Rodinia and West Gondwana. Precambrian Research, Amsterdam, 320: 31-45.

Campos Neto M.C., Figueiredo M.C.H. 1995. The Rio Doce Orogeny, Southeastern Brazil.Journal of South American Earth Sciences, Londres, 8(2): 143-162.

Campos Neto, M.C., 2000. Orogenicsystems from Southwestern Gondwana: an approach to Brasiliano–Pan AfricanCycle and orogenic collage inSoutheastern Brazil. In: Tectonic Evolution of South America (U.G.Cordani, E.J. Milani, A. Thomaz Filhoand

D.A. Campos, eds), 31thInternational Geological Congress, Rio de Janeiro, Brazil, p. 335–368.

Cordani, U. G., Nutman, A. P. 2002. Geochronological constraints on the evolution of the Embu Complex. Journal of South American Earth Sciences, Amsterdam, v. 14, p. 903-910.

Costa, R.V., Trouw, R.A.J., Mendes, J.C., Geraldes, M., Tavora, A., Nepomuceno, F., Araújo Junior, E.B.A. 2017. Proterozoic evolution of part of the Embu Complex, eastern Sao Paulo state, SE Brazil. Journal of South American Earth Sciences v.79, p. 170 -188

CPRM. 1981. Projeto Integração e Detalhe Geológico no Vale Ribeira. Relatório Final Integração Geológica, volume II, anexo I, 12-Folha Campo Largo (SG.22-X-C-III).

Deer, W. A, R. A. Howie and J. Zussman. 1992. An Introduction to the Rock-forming Minerals. Harlow, Essex, England : New York, NY: Longman Scientific & Technical.

Duffles, P., 2013. Petrografia, geoquímica e geocronologia do Complexo Embu e rochas intrusivas associadas, folhas Lorena e Delfim Moreira (1:50.000), estados de SP e MG. Tese de Doutorado-UFRJ-Instituto de Geociências, Rio de Janeiro.

Duffles, P., Trouw, R.A.J, Mendes, J.C., Gerdes, A., Vinagre, R. 2016. U–Pb age of detrital zircon from the Embu sequence, Ribeira belt, SE Brazil. Precambrian Research 278, 69–86.

Ebert H.D., Hasui Y., Costa J.B.S. 1991. O caráter transpressivo do Cinturão de Cisalhamento Rio Paraíba do Sul. Boletim do III Simpósio Nacional de Estudos Tectônicos, IGCE/UNESP-SBG/SP, Rio Claro-SP, 139-141.

Ebert H.D., Hasui Y. 1998. Transpressional tectonics and strain partitioning during oblique collision between three plates in the Precambrian of southeast Brazil. In: Holdsworth R.E., Strachan R.A.,

Faleiros, F.M., 2008. Evolução de Terrenos tectono-metamórficos da Serrania do Ribeira e Planalto Alto Turvo (SP, PR). Tese de Doutorado, Instituto de Geociências, Universidade de São Paulo, 306 pp.

Faleiros, F.M., Campanha, G.A.C, Martins, L., Vlach, S.R.F., Vasconcelos, P.M., 2011. Ediacaran high-pressure collision metamorphism and tectonics of the southern Ribeira Belt: evidence for terrane accretion and dispersion during Gondwana assembly. Precambrian Research, v. 189, p. 263–291.

Faleiros, F. M.; Campanha, G. A. C.; Pavan, M. ; Almeida, V.V. ; Rodrigues, S. W. O. ; Araujo, B. P. 2016. Short-lived polyphase deformation during crustal thickening and exhumation of a collisional orogen (Ribeira Belt, Brazil). Journal of Structural Geology, v. 93, p. 106-130.

Fernandes A.J. Campos Neto M. da C., Figueiredo M.C.H.1990. O Complexo Embu no leste do estado de São Paulo: limites e evolução geológica. In: Congresso Brasileiro de Geologia, 36, Natal, Anais..., SBG, 6: 2755-2763

Fernandes J.A. 1991. O Complexo Embu no leste do Estado de São Paulo: contribuição ao conhecimento da litoestratigrafia e da evolução estrutural e metamórfica. Dissertaçºao de Mestrado. Instituto de Geociências, Universidade de São Paulo.

Fuck, R.A., Brito Neves, B.B., Schobbenhaus, C., 2008. Rodinia descendants in South America. Precambrian Research, v. 160, p. 108–126

Fragoso Cesar A.R.S. 1993. As placas Brasilianas do Sul e Sudeste da Plataforma Sul-Americana. Anais do IV Simpósio Nacional de Estudos Tectônicos, Belo Horizonte, 12:183-188.

Hasui Y. 1975. Evolução polifásica do Pré-cambriano a oeste da capital paulista. Bol. IG. – USP: Sér. Cient., São Paulo, 6: 95-108.

Hasui, Y.; Dantas, A. S. L.; Carneiro, C. D. R., Bistrich, C.A. 1981. O embasamento Pré-cambriano e EoPaleozóico em São Paulo. In: Instituto de Pesquisas Tecnológicas de São Paulo. Mapa geológico do Estado de São Paulo, escala 1.500.000. São Paulo: IPT, V.1, P. 12-45.

Heilbron M., Rocha A.D., Silva L.G.E., Nogueira J.R., Trouw R.A.J., Polónia J.A.L. 1994. Compartimentação tectônica da seção Conceição do Ibitipoca-Valença (RJ), segmento central da Faixa Ribeira. Resumos Expandidos do XXXVIII Congresso Brasileiro de Geologia, Camburiú, Sociedade Brasileira de Geologia, 2: 55-56.

Heilbron M., Valeriano C. M., Valladares C.S., Machado N. 1995. A Orogênese Brasiliana no segmento central da Faixa Ribeira, Brasil. Revista Brasileira de Geociências, São Paulo, Sociedade Brasileira de Geologia, 24(4): 249-266.

Heilbron, M., Valeriano, C.M., Tassinari,C.C.G., Almeida, J.C.H., Tupinambá, M., Siga, O., Jr. and Trouw, R.A.J.,2008. Correlation of Neoproterozoic terranes between Ribeira Belt, SE Brazil and its African counterpart: comparative tectonic evolution and open questions. In: West Gondwana: pre-Cenozoic Correlations Across the South Atlantic Region (R.J. Pankhurst, R.A.J. Trouw, B.B. Brito-Neves and M.J. de Wit, eds). Geological Society of London.Spec. Publ., 294, 211–238.

Launeau, P., Robin, P.-Y.F., 2005. Determination of fabric and strain ellipsoids from measured sectional ellipses—implementation and applications. J. Struct. Geol. 27, 2223–2233.

Meira, V.T., 2014. Evolução tectono-metamórfica neoproterozoica dos complexos Embu e Costeiro no context de Formação do Gondwana Ocidental (Leste do Estado de São Paulo). Tese de Doutorado, Instituto de Geociências, Universidade de São Paulo, 266 pp.

Meira, V.T., García-Casco A., Juliani C., Almeida R.P., Hans, J, Schorscher D., 2015. The role of intracontinental deformation in supercontinent assembly: insights from the Ribeira Belt, Southeastern Brazil (Neoproterozoic West Gondwana). Terra Nova, 0(0): 1-12.

Mori, P.E. et al. 1999. Development of a fused glass disc XRF facility and comparasion with pressed powder pellet technique at Instituto de Geociências, São Paulo University. Revista Brasileira de Geologia, v.29, nº3, p. 441-446.

Passarelli C.R., Basei M.A.S., Campos Neto M.da C., Siga Jr. O., Prazeres Filho J. dos 2004. Geocronologia e Geologia Isotópica dos Terrenos Pré-Cambrianos da Porção Sul-Oriental do Estado de São Paulo. Bol. IG. – USP: Sér. Cient., São Paulo, 4(1):55-74.

Passarelli, C.R., Basei, M.A.S., Wemmer, K.,Siga Jr, O., Oyhantçabal, P., 2011. Major shear zones of southern Brazil and Uruguay:escape tectonics in the eastern border of Rio de La plata and Paranapanema cratons during the Western Gondwana amalgamation. International Journal of Earth Sciences, v. 100, p. 391–414.

Perrotta, M. M.; Salvador, E. D., Lopes, R.C., Dagostino, L. Z., Peruffo, N., Gomes, S. D., Lacerda Filho, J. V. 2006. Mapa Geológico do Estado de São Paulo, escala 1:750.000.

Rogers J.J.W., Unrug R., Sultan M. 1995.Tectonic assembly of Gondwana.Journal of Geodynamics, Londres, 19(1): 1-34.

Sadowski G.R. 1984. Estado da arte do tema: Geologia Estrutural de grandes falhamentos. Anais do XXXIII Congresso Brasileiro de Geologia, Rio de Janeiro, Sociedade Brasileira de Geociências, 1:767-793.

Sadowski G. R., Motidome M. 1987. Brazilian megafaults. Revista Geologica de Chile 31, 61-75.

Sadowski G.R. 1991. A megafalha de Cubatão. Bol. IG-USP, Sér. Cient. 22:15-28.

Siga Jr. O., Basei M.A.S., Reis Neto J.M., Machiavelli A., Harara O.M. 1995. O Complexo Atuba: um cinturão Paleoproterozóico intensamente retrabalhado no Neoproterozóico. Bol. IG. – USP: Sér. Cient., São Paulo, 26: 69-98.

Soares P.C. 1987. Sequências tecto-sedimentares e tectônica deformadora no centro-oeste do Escudo Paranaense. Atas do III Simpósio Sul-Brasileiro de Geologia, Curitiba, 2: 743-771.

Soares P.C., Rostirolla S.P. 1997. Tectônica de escape tardicolisional nos Cinturões Ribeira e Dom Feliciano. Anais do VI Simpósio Nacional de Estudos Tectônicos, Pirenópolis, Sociedade Brasileira de Geologia - Núcleo Brasília, 1: 65-78.

Spear, F.S., Cheney, J.T., Pyle, J.M., Harrison, T.M., Layne, G., 2008. Monazite geochronology in central New England: evidence for a fundamental terrane boundary. Journal of Metamorphic Geology, v. 26, p. 317–329.

Trouw R.A.J., Ribeiro A., Paciullo F.V.P. 1994. A faixa Alto Rio Grande reinterpretada como a zona de interferência entre a Faixa Brasília e Faixa Ribeira. Boletim de Resumos Expandidos do XXXVIII Congresso Brasileiro de Geologia, Camboriú, Sociedade Brasileira de Geologia, 1:234-235.

Vieira, S. R. S. and Tassinari, C.C.G., 1988. Estudo petrológico e geocronológico das rochas da região de Embu-Guaçu, Estado de São Paulo. In: CONGR. BRAS. GEOL., 35. Anais... Belém, SGB, 3:1391-1399.

Vieira, S.R.S.S., 1989. Estudo lito-estrutural da Região de Embu-Guaçu-Parelheiros, São Paulo. Dissertação de Mestrado, Instituto de Geociências, Universidade de São Paulo, 122p.

Vieira, S.R.S.S., Coutinho, J.M.V., Alves, F.R. 1990. Geologia e evolução geológica da região de Embú-Guaçú-Parelheiros, SP. Revista Brasileira de Geociências, v. 20, p. 277–281.

Vieira, S.R.S.S., Coutinho, J.M.V., Alves, F.R. 1992. Considerações sobre o metamorfismo das rochas da região de Embú-Guaçú - Parelheiros, SP. Revista Brasileira de Geociências, v. 22, p. 82–92.

Vieira S.R.S.S. 1996. Estudo de processos metamórfico-metassomáticos nos Complexos Embu e Pilar no Bloco Juquitiba, SP. Tese de Doutoramento, Instituto de Geociências, Universidade de São Paulo, 144 pp.

Vlach, S.R.F., 2001. Microprobe monazite constrainst for an early (ca. 790 Ma) Brasiliano Orogeny: The Embu Terrane, Southeastern Brazil. In: South American Symposium on isotope Geology, 3, Pucón. Extended Abstracts, p. 265-268.

Vlach, S.R.F., 2008. Mineralogia, análise e datação de monazite e xenotima com microssonda eletrônica e aplicações. Tese de Livre-Docência, Instituto de Geociências, Universidade de São Paulo, 186p

APPENDIX A – SUPPLEMNETARY MATERIAL OF CHAPTER 3

Supplementary Material 1

Table 1. Major and trace element geochemical data for metamafic rocks from the Embu Complex. Oxides are in wt% and trace elements in ppm.

	Embu Terrane							Apiaí Terrane				
Sample	DC22D	DC70A	DC70B	DC71A	DC72A	DC73A	DC73B	GI-14	FM-06	FM-07	FM-08	WSP-13
SiO_2	47	49	49	49	49	49	49	49	46	45	48	50
TiO_2	0.99	0.97	0.95	0.84	0.85	0.91	0.81	2.326	3.079	2.715	1.66	2.495
Al_2O_3	16.59	14.87	16.95	17.16	17.50	16.84	17.28	14.06	12.68	12.09	14.71	13.91
Fe_2O_3	12.93	13.19	11.06	11.75	11.38	11.75	11.12	14.27	21	22.61	12.12	14.67
MnO	0.19	0.21	0.17	0.17	0.16	0.17	0.16	0.206	0.273	0.254	0.18	0.224
MgO	7.62	7.64	6.39	7.09	6.59	6.73	6.60	5.7	4.92	5.31	7.17	5.83
CaO	10.10	8.52	11.42	10.79	11.21	11.23	11.28	9.22	9.62	10.67	11.41	9.56
Na_2O	1.25	1.27	2.02	2.60	2.55	2.10	2.65	2.98	2.31	1.72	2.11	2.9
K_2O	0.25	0.21	0.25	0.30	0.20	0.26	0.30	0.36	0.25	0.21	0.37	0.28
P_2O_5	0.07	0.07	0.07	0.07	0.07	0.08	0.07	0.18	0.12	0.08	0.12	0.17
LOI	3.09	3.08	0.90	0.68	0.43	0.67	1.22	1.23	0.42	0.31	0.87	0.44
Total	100.08	98.96	99.12	99.97	99.58	100.12	100.30	99.87	100.8	100.5	98.79	100.7
K_2O + Na_2O	1.5	1.5	2.3	2.9	2.8	2.4	3.0	3.3	2.6	1.9	2.5	3.2
Sc	33.3	37.8	29.8	27.5	26.6	29.2	27	34	52	49	39	36
Rb	7.23	6.17	5.96	6.51	5.35	4.9	9.65	9	4	5	10	8
Sr	74	72.6	172	185	165	162	160	319	160	159	338	325
Y	17.6	19.3	16.4	15.3	14.6	16.3	14.6	31.9	44	31.9	21.9	30
Zr	60	42	58	44	53	62	53	134	81	60	89	146
Nb	2.3	2.0	3.4	2.0	2.1	2.4	1.9	13.7	3.2	2.3	8.2	16.6
Cs	0.34	0.34	0.4	0.25	0.17	0.12	0.58	0.6	0.3	0.2	1.1	0.2

Ba	69.1	67.7	65.6	58.2	40.4	68.9	81.5	110	76	95	83	34
La	4.54	6.88	4.9	4.39	4.27	5.15	4.16	24.7	4.74	4.1	9.6	11
Ce	9.61	8.59	10.9	9.21	9.75	10.8	9.4	39.7	11.8	9.48	22.3	27.1
Pr	1.7	2	1.69	1.45	1.42	1.56	1.38	6.89	2.16	1.71	3.22	4.12
Nd	8.02	9.22	7.73	7.05	6.78	7.38	6.6	29.4	10.9	9.16	14.2	19.1
Sm	2.29	2.33	2.15	1.94	2	2.23	1.93	6.61	3.8	3.34	3.77	5.38
Eu	0.85	0.87	0.85	0.72	0.77	0.84	0.76	2.08	1.62	1.2	1.35	1.85
Gd	2.79	2.78	2.54	2.18	2.22	2.44	2.21	6.6	5.87	4.39	4.24	5.93
Tb	0.52	0.52	0.47	0.41	0.39	0.44	0.39	1.03	1.07	0.81	0.67	0.97
Dy	3.03	3.29	2.8	2.65	2.47	2.83	2.58	6.03	6.89	5.28	3.94	5.49
Ho	0.68	0.69	0.62	0.54	0.57	0.66	0.57	1.16	1.51	1.1	0.76	1.04
Er	1.78	1.73	1.59	1.37	1.45	1.58	1.38	3.16	4.43	3.26	2.2	2.93
Tm	0.3	0.28	0.26	0.22	0.22	0.24	0.22	0.441	0.638	0.484	0.299	0.402
Yb	1.81	1.77	1.54	1.41	1.3	1.45	1.33	2.74	4.15	3.29	1.98	2.55
Lu	0.27	0.27	0.23	0.21	0.21	0.23	0.21	0.418	0.659	0.509	0.296	0.375
Hf	0.71	0.58	0.6	0.58	0.58	0.61	0.54	3.9	2.6	1.8	2.5	3.9
Pb	1.89	1.71	1.84	2.03	1.66	1.67	3.22	< 5	< 5	< 5	< 5	< 5
Th	0.72	0.67	0.74	0.56	0.72	0.78	0.66	1.75	0.39	0.28	1.16	1.85
V	307	264	271	184	238	259	235	420	841	1347	379	430
Mo	<0,01	<0,01	<0,01	<0,01	<0,01	<0,01	<0,01	< 2	< 2	< 2	< 2	< 2
Ta	0.16	0.13	0.19	0.13	0.13	0.15	0.13	1.06	0.24	0.13	0.69	1.15
W	0.07	0.02	<0,01	0.4	<0,01	<0,01	<0,01	1.6	3.7	1.7	2.4	1.4
U	0.12	0.14	0.12	0.1	0.1	0.12	0.1	0.45	0.11	0.1	0.33	0.53
Nb/La	0.50	0.29	0.70	0.45	0.49	0.47	0.45	0.55	0.68	0.56	0.85	1.51
Zr/Nb	27	21	17	22	25	25	28	10	25	26	11	9
Y/Nb	8	10	5	8	7	7	8	2	14	14	3	2
Zr/Y	3.4	2.2	3.5	2.9	3.6	3.8	3.6	4.2	1.8	1.9	4.1	4.9

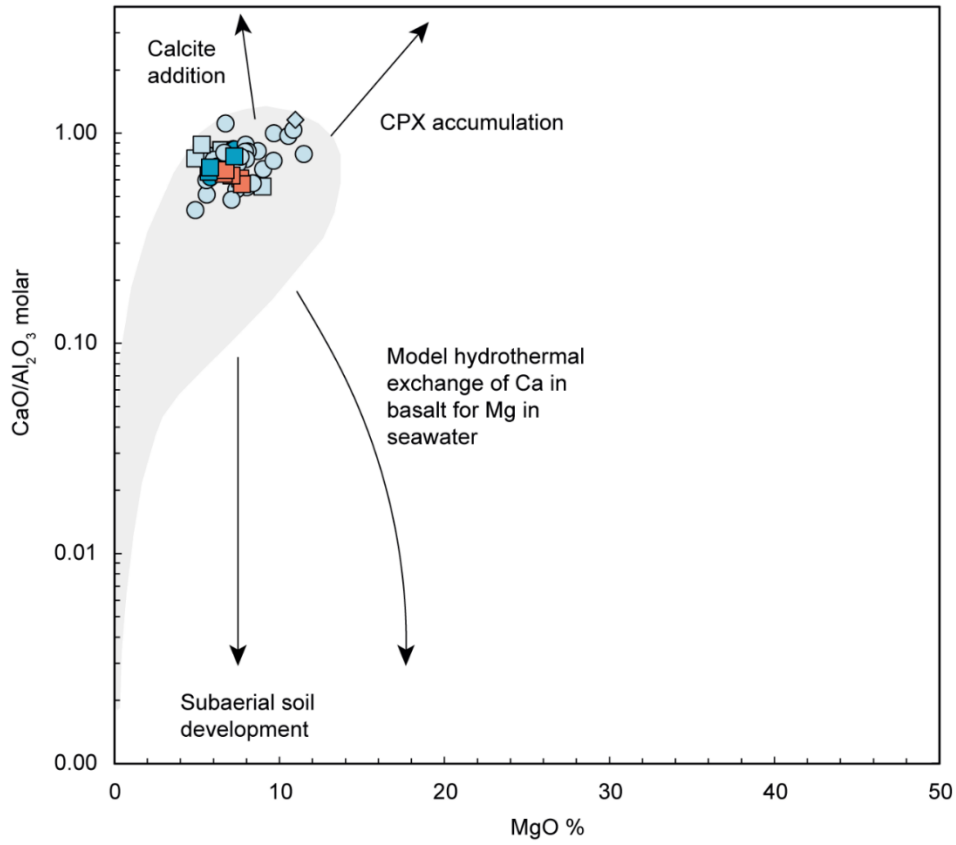

Figure 1. Major oxides chemical alteration diagram from Hollocher et al. 2012.

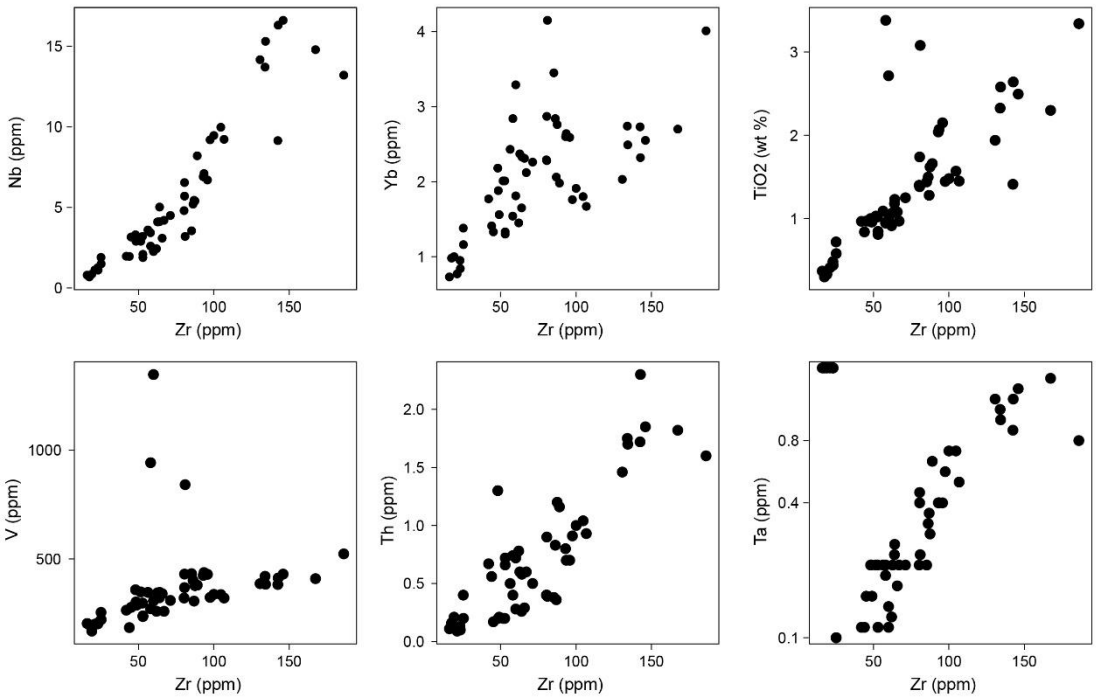

Figure 2. Correlation between Zr and elements used in the below described diagrams (Nb, Yb, Ti, V, Th and Ta).

Supplementary Material 3

Table 3. U-Pb-Hf analytical results for sample DC-09A.

	Sample	Spot	Content (ppm)		Th/U	U–Pb isotopic ratios									U–Pb ages (Ma)					Con %	Lu–Hf data						
			U	Th		$^{207}Pb/^{235}U$	1σ	$^{206}Pb/^{238}U$	1σ	Err. Corr	$^{238}U/^{206}Pb$	1σ	$^{207}Pb/^{206}Pb$	1σ	$^{207}Pb/^{206}Pb$	1σ	$^{206}Pb/^{238}U$	1σ			$^{176}Hf/^{177}Hf$	± (2s)	$^{176}Lu/^{177}Hf$	± (2s)	$^{176}Hf/^{177}Hf$ (t)	ε Hf (t)	± (2s)
Apiaí Terrane	DC-09A	1.1	417	312	0.77	2.4225	2.59	0.2124	1.17	0.45	4.7081	1.17	0.0827	2.31	1262	45	1240	13	102	0.28235	0.000067	0.004	0.00023	0.282253502	9.0347751	2.36929116
		2.1	674	1053	1.61	2.6473	1.01	0.2272	0.96	0.95	4.4010	0.96	0.0845	0.30	1304	6	1320	11	99	0.2824	0.000076	0.005	0.0001	0.282281142	11.827328	2.68755415
		3.1	729	1039	1.47	2.7823	0.99	0.2352	0.96	0.96	4.2511	0.96	0.0858	0.26	1333	5	1362	12	98	0.28231	0.000078	0.004	0.00026	0.282212621	10.355824	2.75827926
		4.1	1008	1417	1.45	1.8906	1.55	0.1792	1.09	0.70	5.5819	1.09	0.0765	1.10	1109	22	1062	11	104	0.28234	0.00006	0.004	0.00029	0.282257982	5.1441802	2.12175328
		5.1	687	750	1.13	2.6665	0.99	0.2292	0.95	0.96	4.3637	0.95	0.0844	0.27	1302	5	1330	11	98	0.28239	0.00013	0.004	9.8E-05	0.282294381	12.53107	4.5971321
		6.1	434	433	1.03	2.5561	1.99	0.2206	0.99	0.50	4.5332	0.99	0.0840	1.72	1293	34	1284	12	101	0.28231	0.000073	0.002	0.00055	0.282259452	10.251009	2.58146649
		7.1	681	670	1.02	2.4226	1.05	0.2139	0.96	0.91	4.6751	0.96	0.0821	0.43	1249	8	1249	11	100	no value	no value	no value	no value	no value	no value	no value
		8.1	787	678	0.89	2.1451	1.31	0.1955	0.95	0.73	5.1148	0.95	0.0796	0.89	1186	18	1151	10	103	no value	no value	no value	no value	no value	no value	no value
		9.1	1180	857	0.75	2.0313	3.71	0.1896	2.11	0.57	5.2756	2.11	0.0777	3.05	1139	61	1118	22	102	0.28221	0.0001	0.002	0.00014	0.28215985	2.936988	3.53625546
		10.1	318	198	0.64	2.5425	1.22	0.2217	1.01	0.83	4.5113	1.01	0.0832	0.67	1274	13	1290	12	99	no value	no value	no value	no value	no value	no value	no value
		11.1	392	404	1.06	2.7834	1.17	0.2373	1.11	0.95	4.2139	1.11	0.0851	0.37	1317	7	1373	14	96	0.28242	0.00015	0.003	0.00022	0.282335463	14.960701	5.30438319
		12.1	1347	1361	~~1.04~~	1.3289	2.43	0.1367	1.57	0.65	4.51133	1.01	0.0705	1.84	943	38	826	12	114	no value	no value	no value	no value	no value	no value	no value

U–Pb data corrected for non-radiogenic Pb based on measured 204Pb. SHRIMP data.
Anomalous disregarded ε Lu–Hf data are in red

Table 4. U-Pb analytical results for sample FM-06.

	Sample	Spot	Content (ppm)		Th/U	U–Pb isotopic ratios									U–Pb ages (Ma)				Con %
			U	Th		$^{207}Pb/^{235}U$	1σ	$^{206}Pb/^{238}U$	1σ %	Err. Corr	$^{238}U/^{206}Pb$	1σ	$^{207}Pb/^{206}Pb$	1σ	$^{207}Pb/^{206}Pb$	1σ	$^{206}Pb/^{238}U$	1σ	
Apiaí Terrane	FM-06	1.1	796	758	0.98	2.5734	0.847	0.2207	0.79	0.93	4.5314937	0.79	0.0846	0.31	1306	6	1285	9	102
		2.1	528	551	1.08	2.4889	0.9	0.2150	0.81	0.90	4.6517826	0.8119	0.0840	0.39	1292	8	1255	9	103
		3.1	421	399	0.98	2.5665	0.941	0.2210	0.83	0.88	4.5246282	0.8253	0.0842	0.45	1298	9	1287	10	101
		4.1	829	1218	1.52	2.6316	0.932	0.2266	0.89	0.96	4.4133216	0.892	0.0842	0.27	1298	5	1317	11	99
		5.1	480	508	1.09	2.5891	0.947	0.2223	0.82	0.87	4.4977885	0.8219	0.0845	0.47	1303	9	1294	10	101
		6.1	493	508	1.06	2.5353	0.899	0.2196	0.82	0.91	4.5534731	0.8175	0.0837	0.37	1286	7	1280	9	101
		7.1	322	254	0.82	2.6374	0.953	0.2275	0.85	0.89	4.3948933	0.8482	0.0841	0.43	1294	8	1322	10	98
		8.1	374	373	1.03	2.5055	1.017	0.2175	0.83	0.82	4.5971432	0.8321	0.0835	0.58	1282	11	1269	10	101
		9.1	141	113	0.82	2.5676	1.408	0.2228	0.96	0.68	4.4877581	0.9572	0.0836	1.03	1283	20	1297	11	99
		10.1	117	72	0.63	2.5697	1.431	0.2205	0.98	0.69	4.5358539	0.9849	0.0845	1.04	1305	20	1284	11	102
		11.1	223	162	0.75	2.5786	1.049	0.2194	0.87	0.83	4.5586688	0.8734	0.0853	0.58	1321	11	1279	10	103
		12.1	694	658	0.98	2.6046	1.064	0.2240	0.91	0.86	4.4650849	0.9132	0.0843	0.55	1301	11	1303	11	100
		13.1	599	784	1.35	2.5639	0.864	0.2205	0.8	0.93	4.5352771	0.7999	0.0843	0.33	1300	6	1284	9	101
		14.1	55	32	0.61	2.6231	2.036	0.2217	1.21	0.59	4.5103701	1.2076	0.0858	1.64	1334	32	1291	14	103
		15.1	249	219	0.91	2.7599	1.228	0.2363	0.87	0.71	4.2326209	0.8699	0.0847	0.87	1309	17	1367	11	96
		16.1	286	230	0.83	2.5747	1.044	0.2220	0.86	0.82	4.504589	0.8581	0.0841	0.59	1295	12	1292	10	100
		17.1	536	653	1.26	2.5986	0.878	0.2241	0.81	0.92	4.4619587	0.8082	0.0841	0.34	1295	7	1304	10	99
		18.1	447	386	0.89	2.4780	1.046	0.2134	0.82	0.78	4.6861929	0.8183	0.0842	0.65	1298	13	1247	9	104
		18.2	192	131	0.71	2.5816	1.084	0.2213	0.91	0.84	4.5186922	0.9056	0.0846	0.60	1307	12	1289	11	101
		19.1	268	367	1.41	2.5740	1.108	0.2239	0.86	0.78	4.465474	0.8619	0.0834	0.70	1278	14	1303	10	98
		20.1	604	645	1.10	2.5443	0.864	0.2185	0.8	0.92	4.5763817	0.7994	0.0844	0.33	1303	6	1274	9	102

U–Pb data corrected for non-radiogenic Pb based on measured 204Pb. SHRIMP data.

Table 5. U-Pb-Hf analytical results for sample GI-14.

	Sample	Spot	Content (ppm)		Th/U	U–Pb isotopic ratios										U–Pb ages (Ma)						%	Lu–Hf data						
			U	Th		$^{207}Pb/^{235}U$	2σ	$^{206}Pb/^{238}U$	2σ	Err. Corr	$^{238}U/^{206}Pb$	2σ	$^{207}Pb/^{206}Pb$	2σ	Err. Corr	$^{207}Pb/^{235}U$	2σ	$^{206}Pb/^{238}U$	2σ	$^{207}Pb/^{206}Pb$	2σ	conc	$^{176}Hf/^{177}Hf$	± (2s) int	$^{176}Lu/^{177}Hf$	± (2s) int	$^{176}Hf/^{177}Hf$ (t)	ε Hf (t)	± (2s)
Apiaí Terrane	GI-14	1	180	116	0.65	7.367	0.235	0.395	0.011	0.598	2.539	0.070	0.135	0.002	0.187	2155	29	2145	49	2154	29	100	0.281166	0.00003	0.000792	0.00005	0.281133	-10.0	1.1
		2	177	156	0.88	7.713	0.249	0.402	0.011	0.644	2.489	0.064	0.139	0.002	0.242	2197	29	2179	51	2210	28	101	0.281117	0.00004	0.001146	0.00005	0.281070	-11.4	1.4
		3	162	98	0.60	7.584	0.249	0.399	0.011	0.572	2.518	0.070	0.138	0.002	0.367	2182	29	2162	51	2199	30	101	0.281115	0.00003	0.000755	0.00006	0.281083	-11.3	1.2
		4	851	1272	1.50	2.461	0.102	0.189	0.007	0.760	5.333	0.209	0.094	0.002	0.474	1259	30	1113	39	1513	48	113	~~0.282894~~	~~0.00029~~	~~0.005344~~	~~0.00022~~	~~0.282782~~	~~24.9~~	~~10.3~~
		5	574	549	0.96	2.693	0.088	0.230	0.006	0.649	4.358	0.123	0.085	0.001	0.171	1325	24	1333	34	1312	33	99	0.282223	0.00006	0.003036	0.00007	0.282146	7.4	2.1
		6	711	712	1.00	2.553	0.083	0.217	0.006	0.763	4.619	0.127	0.085	0.001	0.422	1287	24	1264	33	1323	33	102	0.282221	0.00008	0.003162	0.00007	0.282146	5.7	2.8
		7	1471	800	0.54	1.368	0.062	0.066	0.002	-0.556	15.207	0.533	0.152	0.008	0.806	872	26	414	14	2324	88	211	~~0.282502~~	~~0.00008~~	~~0.002441~~	~~0.00049~~	~~0.282483~~	~~-1.5~~	~~2.9~~
		8	1489	591	0.40	1.419	0.060	0.068	0.002	-0.610	14.717	0.534	0.152	0.007	0.889	895	25	426	15	2343	83	210	~~0.282416~~	~~0.00008~~	~~0.001972~~	~~0.00026~~	~~0.282400~~	~~-4.1~~	~~3.0~~
		9	420	517	1.23	2.957	0.223	0.251	0.039	0.591	3.990	0.385	0.082	0.004	0.114	1391	55	1428	205	1228	101	97	~~0.292793~~	~~0.02717~~	~~0.002956~~	~~0.00020~~	~~0.292713~~	~~384.4~~	~~960.9~~
		10	177	61	0.35	5.696	0.202	0.310	0.009	0.753	3.234	0.097	0.134	0.002	0.212	1928	31	1741	47	2142	32	111	~~0.281168~~	~~0.00004~~	~~0.000896~~	~~0.00005~~	~~0.281138~~	~~-19.1~~	~~1.4~~
		11	246	140	0.57	4.297	0.186	0.248	0.010	0.846	4.047	0.152	0.125	0.003	0.121	1688	37	1428	50	2027	39	118	~~0.281322~~	~~0.00005~~	~~0.000707~~	~~0.00001~~	~~0.281303~~	~~-20.4~~	~~1.8~~
		12	724	742	1.03	2.567	0.088	0.217	0.006	0.814	4.613	0.133	0.085	0.001	-0.035	1289	26	1268	34	1321	33	102	0.282176	0.00007	0.003238	0.00013	0.282099	4.2	2.4
		13	872	1091	1.25	2.326	0.079	0.196	0.006	0.870	5.125	0.156	0.086	0.001	0.189	1219	24	1156	32	1332	31	105	0.282361	0.00010	0.003346	0.00003	0.282288	8.3	3.4
		14	587	794	1.35	2.063	0.068	0.180	0.005	0.784	5.570	0.156	0.083	0.001	0.037	1134	23	1068	28	1255	32	106	0.282261	0.00007	0.002900	0.00026	0.282202	3.3	2.6
		15	385	432	1.12	2.220	0.085	0.187	0.006	0.843	5.399	0.189	0.086	0.002	0.162	1184	27	1102	35	1335	39	107	0.282290	0.00010	0.003159	0.00039	0.282224	4.8	3.4
		16	964	1256	1.30	1.946	0.066	0.172	0.005	0.786	5.833	0.183	0.082	0.001	0.583	1096	23	1022	30	1242	35	107	0.282327	0.00009	0.003148	0.00002	0.282267	4.5	3.3
		17	791	851	1.08	2.323	0.077	0.199	0.006	0.729	5.033	0.146	0.084	0.001	0.180	1219	23	1172	30	1298	32	104	0.282298	0.00007	0.003749	0.00020	0.282215	6.1	2.5
		18	258	259	1.00	4.132	0.148	0.252	0.008	0.458	3.979	0.126	0.119	0.003	0.555	1659	29	1450	41	1931	43	114	~~0.281751~~	~~0.00007~~	~~0.001106~~	~~0.00018~~	~~0.281720~~	~~-5.1~~	~~2.3~~
		~~19~~	~~6~~	~~5~~	~~0.72~~	~~-2479.686~~	~~2178.869~~	~~-9.967~~	~~9.248~~	~~0.590~~	~~74.710~~	~~24.141~~	~~0.221~~	~~0.050~~	~~0.258~~	~~1768~~	~~277~~	~~252~~	~~89~~	~~2300~~	~~308~~	~~701~~	~~0.277104~~	~~0.01696~~	~~0.002700~~	~~0.00016~~	~~0.277091~~	~~-195.9~~	~~599.8~~
		~~20~~	~~0~~	~~0~~	~~0.39~~	~~-2554.392~~	~~886.631~~	~~-4.835~~	~~1.915~~	~~0.115~~	~~-11.575~~	~~29.240~~	~~-0.288~~	~~0.201~~	~~0.043~~	~~7038~~	~~366~~	~~6495~~	~~419~~	~~3417~~	~~371~~	~~108~~	~~0.179304~~	~~0.09505~~	~~0.002013~~	~~0.00098~~	~~0.179045~~	~~-3570.1~~	~~3361.2~~
		21	394	401	1.02	2.558	0.086	0.220	0.006	0.698	4.551	0.130	0.084	0.001	0.158	1287	25	1283	33	1288	35	100	0.282275	0.00007	0.002774	0.00028	0.282208	8.4	2.6
		22	386	404	1.05	2.446	0.083	0.212	0.006	0.477	4.734	0.137	0.083	0.002	0.266	1255	24	1239	32	1279	35	101	0.282248	0.00007	0.002870	0.00030	0.282181	6.4	2.6
		23	305	200	0.66	17.921	0.613	0.576	0.017	0.886	1.747	0.052	0.226	0.004	0.044	2982	33	2929	69	3022	26	102	0.280845	0.00006	0.000884	0.00007	0.280796	-3.7	2.1
		24	873	1536	1.76	2.432	0.077	0.208	0.006	0.672	4.812	0.125	0.085	0.001	0.308	1251	23	1218	30	1311	31	103	0.282349	0.00007	0.004127	0.00007	0.282254	8.5	2.5
		25	525	533	1.02	2.470	0.080	0.213	0.006	0.725	4.705	0.129	0.084	0.001	0.079	1262	23	1246	31	1293	31	101	0.282283	0.00006	0.003430	0.00009	0.282202	7.3	2.1
		26	1107	1134	1.02	1.745	0.060	0.155	0.005	0.723	6.463	0.190	0.082	0.002	0.340	1024	22	931	26	1236	36	110	0.282236	0.00013	0.002708	0.00010	0.282189	-0.3	4.5
		27	969	1185	1.22	2.617	0.083	0.226	0.006	0.582	4.427	0.122	0.084	0.001	0.282	1305	23	1315	32	1296	31	99	0.282281	0.00007	0.004244	0.00005	0.282176	8.0	2.4
		28	601	634	1.06	2.645	0.087	0.228	0.006	0.387	4.400	0.121	0.085	0.002	0.283	1312	24	1322	33	1306	34	99	0.282282	0.00007	0.002661	0.00017	0.282215	9.5	2.5
		29	416	397	0.96	2.488	0.083	0.213	0.006	0.377	4.700	0.121	0.085	0.002	0.218	1267	24	1244	30	1321	34	102	0.282167	0.00008	0.002051	0.00016	0.282118	4.3	3.0
		30	436	474	1.09	2.395	0.080	0.200	0.006	0.581	5.009	0.143	0.087	0.002	0.203	1240	24	1175	30	1361	37	106	0.282172	0.00009	0.002796	0.00044	0.282110	2.5	3.2
		31	505	465	0.92	2.385	0.081	0.211	0.006	0.661	4.756	0.139	0.083	0.002	0.236	1237	24	1234	32	1268	35	100	0.282285	0.00007	0.002957	0.00007	0.282216	7.6	2.6
		32	445	414	0.93	2.333	0.079	0.204	0.006	0.613	4.923	0.137	0.084	0.002	0.260	1221	24	1194	31	1299	35	102	0.282234	0.00008	0.003076	0.00005	0.282165	4.8	2.9
		33	1379	1320	0.96	1.752	0.101	0.151	0.008	0.950	6.734	0.363	0.085	0.002	0.028	1023	38	908	44	1306	37	113	~~0.282333~~	~~0.00020~~	~~0.003451~~	~~0.00025~~	~~0.282274~~	~~2.2~~	~~7.2~~
		34	944	1142	1.21	2.433	0.079	0.213	0.006	0.734	4.700	0.132	0.084	0.001	0.163	1251	23	1246	32	1286	32	100	0.282208	0.00006	0.002590	0.00019	0.282147	5.4	2.1
		35	110	62	0.57	7.366	0.246	0.398	0.011	0.624	2.520	0.072	0.135	0.002	0.244	2152	30	2160	52	2168	31	100	0.281208	0.00007	0.000666	0.00003	0.281181	-7.9	2.4
		36	162	189	1.17	7.391	0.241	0.406	0.011	0.638	2.472	0.067	0.134	0.002	0.280	2157	29	2197	51	2147	30	98	0.281130	0.00004	0.000946	0.00006	0.281090	-10.3	1.4
		37	1225	1938	1.58	2.102	0.081	0.194	0.006	0.712	5.157	0.158	0.079	0.002	-0.061	1148	27	1145	32	1179	43	100	~~0.269621~~	~~0.00981~~	~~0.002071~~	~~0.00020~~	~~0.269577~~	~~-442.6~~	~~347.0~~
		38	348	312	0.90	2.356	0.139	0.212	0.009	0.491	4.758	0.218	0.082	0.004	0.228	1226	43	1237	48	1232	93	99	~~0.280916~~	~~0.01218~~	~~0.002441~~	~~0.00006~~	~~0.280859~~	~~-40.5~~	~~430.8~~
		39	1675	2205	1.32	1.359	0.075	0.117	0.006	0.949	8.714	0.484	0.086	0.002	0.158	868	33	712	35	1328	40	122	~~0.281330~~	~~0.00865~~	~~0.004160~~	~~0.00026~~	~~0.281274~~	~~-37.6~~	~~305.9~~
		40	759	891	1.17	2.500	0.086	0.216	0.006	0.731	4.638	0.132	0.085	0.002	-0.030	1270	25	1262	33	1310	35	101	~~0.281179~~	~~0.00898~~	~~0.003777~~	~~0.00019~~	~~0.281089~~	~~-31.8~~	~~317.7~~
		41	262	269	1.03	2.337	0.086	0.209	0.006	0.630	4.797	0.134	0.083	0.002	-0.062	1223	28	1222	32	1259	42	100	~~0.279205~~	~~0.00508~~	~~0.003264~~	~~0.00014~~	~~0.279130~~	~~-102.2~~	~~179.7~~

U–Pb data with error 2 sigma absolute propagate value
Anomalous disregarded Ɛ Lu–Hf data are in red
Disconcordant data higher than 10 % are strikethrough
Spot 19 and 20 were not consider

Table 6. U-Pb-Hf analytical results for sample WSP-04.

	Sample	Spot	Content (ppm)		Th/U	U–Pb isotopic ratios										U–Pb ages (Ma)						% conc	Lu–Hf data						
			U	Th		$^{207}Pb/^{235}U$	2σ	$^{206}Pb/^{238}U$	2σ	Err. Corr	$^{238}U/^{206}Pb$	2σ	$^{207}Pb/^{206}Pb$	2σ	Err. Corr	$^{207}Pb/^{235}U$	2σ	$^{206}Pb/^{238}U$	2σ	$^{207}Pb/^{206}Pb$	2σ		$^{176}Hf/^{177}Hf$	± (2s) int	$^{176}Lu/^{177}Hf$	± (2s) int	$^{176}Hf/^{177}Hf$ (t)	ε Hf (t)	± (2s)
Apiaí Terrane	WSP-04	1	506	549	1.09	2.524	0.082	0.222	0.006	0.523	4.516	0.119	0.084	0.001	0.228	1278	24	1291	32	1287	33	99	0.282291	0.00007	0.003760	0.00006	0.2821997	8.3	2.4
		2	96	52	0.54	2.312	0.086	0.204	0.006	0.290	4.920	0.140	0.084	0.002	0.388	1212	26	1197	32	1268	53	101	0.282192	0.00005	0.000631	0.00003	0.2821775	5.4	1.8
		3	297	320	1.08	2.578	0.083	0.228	0.006	0.541	4.408	0.121	0.083	0.001	0.237	1293	24	1321	32	1271	33	98	0.282276	0.00007	0.004103	0.00013	0.2821732	8.0	2.4
		4	498	356	0.72	2.580	0.081	0.227	0.006	0.383	4.414	0.112	0.084	0.001	0.352	1295	23	1316	32	1286	31	98	0.282251	0.00005	0.002385	0.00003	0.2821914	8.6	1.7
		5	584	534	0.91	2.412	0.077	0.212	0.006	0.498	4.722	0.129	0.084	0.001	0.306	1246	22	1241	31	1287	32	100	0.282241	0.00060	0.003276	0.00017	0.2821641	5.9	21.3
		6	327	347	1.06	2.499	0.080	0.220	0.006	0.450	4.563	0.124	0.084	0.001	0.258	1270	23	1280	31	1278	33	99	0.282304	0.00007	0.003996	0.00005	0.2822074	8.3	2.4
		7	405	323	0.80	2.435	0.086	0.212	0.006	0.662	4.710	0.139	0.084	0.002	0.052	1251	25	1242	32	1294	39	101	0.282310	0.00007	0.002088	0.00016	0.2822607	9.3	2.6
		8	430	357	0.83	2.450	0.080	0.214	0.006	0.335	4.672	0.127	0.084	0.002	0.300	1256	24	1252	31	1292	37	100	0.282263	0.00007	0.002286	0.00007	0.2822085	7.7	2.3
		9	298	312	1.05	2.503	0.080	0.220	0.006	0.403	4.551	0.121	0.084	0.001	0.249	1272	23	1283	31	1280	34	99	0.282338	0.00007	0.003372	0.00004	0.2822563	10.1	2.4
		10	224	194	0.86	2.490	0.081	0.220	0.006	0.351	4.549	0.125	0.083	0.001	0.295	1267	23	1284	31	1267	35	99	0.282265	0.00005	0.002303	0.00004	0.2822087	8.4	1.7
		11	187	184	0.98	2.391	0.079	0.213	0.006	0.341	4.715	0.134	0.083	0.002	0.371	1238	24	1243	31	1255	38	100	0.282262	0.00006	0.002226	0.00027	0.2822096	7.5	2.1
		12	198	172	0.87	2.489	0.081	0.220	0.006	0.408	4.562	0.123	0.083	0.001	0.142	1267	24	1281	31	1268	35	99	0.282301	0.00005	0.003035	0.00010	0.2822280	9.0	1.7
		13	214	195	0.91	2.512	0.082	0.221	0.006	0.282	4.538	0.122	0.084	0.001	0.235	1274	23	1285	31	1273	35	99	0.282255	0.00005	0.003216	0.00014	0.2821772	7.3	1.8
		14	161	129	0.80	2.494	0.082	0.220	0.006	0.325	4.553	0.124	0.084	0.002	0.298	1270	23	1283	32	1271	38	99	0.282251	0.00005	0.002157	0.00003	0.2821983	8.1	1.9
		15	244	200	0.82	2.521	0.083	0.222	0.006	0.336	4.513	0.123	0.083	0.002	0.262	1276	24	1291	32	1274	37	99	0.282266	0.00007	0.003099	0.00007	0.2821901	7.9	2.6
		16	131	101	0.77	2.451	0.090	0.217	0.006	0.475	4.619	0.134	0.083	0.002	0.137	1254	26	1264	33	1255	44	99	0.282234	0.00006	0.001684	0.00016	0.2821937	7.4	2.0
		17	142	166	1.17	2.574	0.132	0.223	0.010	0.749	4.603	0.222	0.085	0.003	0.304	1286	37	1295	55	1302	59	99	0.282220	0.00008	0.001523	0.00017	0.2821827	7.8	2.8
		18	164	129	0.79	2.528	0.082	0.221	0.006	0.263	4.528	0.125	0.084	0.002	0.324	1280	25	1289	32	1279	36	99	0.282254	0.00006	0.002367	0.00011	0.2821962	8.1	2.1
		19	377	450	1.19	2.555	0.084	0.223	0.006	0.461	4.481	0.121	0.084	0.002	0.293	1287	24	1301	32	1286	35	99	0.282346	0.00010	0.003471	0.00034	0.2822608	10.7	3.7
		20	361	424	1.17	2.545	0.087	0.222	0.006	0.408	4.522	0.126	0.084	0.002	0.277	1284	25	1290	33	1286	40	99	0.280889	0.00408	0.003823	0.00037	0.2807963	-41.5	144.1
		21	516	424	0.82	2.582	0.081	0.225	0.006	0.464	4.441	0.117	0.084	0.001	0.198	1295	23	1309	32	1282	31	99	0.282236	0.00004	0.002744	0.00009	0.2821679	7.6	1.6
		22	623	509	0.82	2.539	0.080	0.224	0.006	0.518	4.478	0.121	0.083	0.001	0.270	1283	23	1301	32	1266	31	99	0.282278	0.00004	0.002843	0.00005	0.2822080	8.8	1.3
		23	447	405	0.91	2.568	0.081	0.224	0.006	0.476	4.467	0.120	0.084	0.001	0.266	1291	23	1304	32	1282	31	99	0.282248	0.00005	0.003298	0.00006	0.2821666	7.4	1.7
		24	761	770	1.01	2.554	0.090	0.221	0.007	0.302	4.534	0.145	0.085	0.002	0.661	1287	26	1288	37	1298	49	100	0.282284	0.00005	0.002461	0.00014	0.2822244	9.1	1.8
		25	94	41	0.44	2.506	0.088	0.220	0.006	0.594	4.560	0.129	0.083	0.002	0.149	1272	25	1283	34	1260	41	99	0.282146	0.00003	0.000452	0.00003	0.2821353	5.8	1.1
		26	84	38	0.46	2.655	0.093	0.228	0.006	0.269	4.411	0.125	0.085	0.002	0.181	1311	26	1323	34	1299	42	99	0.282125	0.00004	0.000505	0.00005	0.2821124	5.9	1.4
		27	181	166	0.92	2.450	0.080	0.216	0.006	0.318	4.644	0.123	0.083	0.001	0.287	1256	24	1259	31	1258	36	100	0.282212	0.00006	0.002414	0.00015	0.2821545	6.0	2.1
		28	97	72	0.75	2.487	0.084	0.218	0.006	0.340	4.615	0.127	0.083	0.002	0.320	1265	25	1270	32	1259	41	100	0.282226	0.00004	0.001430	0.00019	0.2821921	7.5	1.4
		29	251	186	0.74	2.563	0.083	0.225	0.006	0.369	4.451	0.120	0.083	0.001	0.218	1290	24	1309	32	1264	36	99	0.282206	0.00004	0.001451	0.00013	0.2821703	7.6	1.4
		30	385	467	1.21	2.569	0.082	0.223	0.006	0.428	4.484	0.122	0.083	0.001	0.225	1291	23	1299	31	1272	32	99	0.282305	0.00007	0.003556	0.00034	0.2822177	9.1	2.3
		31	401	465	1.16	2.535	0.080	0.220	0.006	0.430	4.547	0.121	0.083	0.001	0.258	1281	23	1283	31	1273	31	100	0.282310	0.00005	0.003511	0.00030	0.2822248	9.0	1.8
		32	199	181	0.91	2.376	0.085	0.208	0.006	0.531	4.831	0.142	0.083	0.002	0.316	1233	26	1218	34	1264	46	101	0.282268	0.00007	0.001747	0.00039	0.2822283	7.6	2.5
		33	177	133	0.75	2.554	0.086	0.222	0.006	0.323	4.503	0.121	0.083	0.002	0.281	1286	25	1292	32	1271	39	100	0.282207	0.00005	0.001956	0.00006	0.2821594	6.9	1.8
		34	339	300	0.89	2.547	0.081	0.221	0.006	0.343	4.542	0.122	0.084	0.001	0.348	1286	22	1285	31	1277	33	100	0.282224	0.00006	0.002951	0.00001	0.2821520	6.4	2.1
		35	553	732	1.32	2.620	0.084	0.228	0.006	0.633	4.399	0.121	0.083	0.001	0.051	1305	23	1324	32	1266	32	99	0.282315	0.00006	0.003725	0.00037	0.2822217	9.8	2.0
		36	537	799	1.49	2.410	0.079	0.211	0.006	0.570	4.745	0.128	0.083	0.001	0.121	1244	24	1235	31	1260	34	101	0.282396	0.00006	0.005496	0.00011	0.2822683	9.4	2.2
		37	121	89	0.74	2.642	0.087	0.228	0.006	0.316	4.392	0.117	0.084	0.002	0.325	1311	25	1325	33	1279	38	99	0.282201	0.00004	0.001435	0.00003	0.2821651	7.8	1.4
		38	213	304	1.42	2.547	0.084	0.216	0.006	0.435	4.634	0.130	0.085	0.002	0.174	1284	24	1261	32	1314	37	102	0.282343	0.00007	0.003998	0.00037	0.2822476	9.3	2.5
		39	818	738	0.90	2.383	0.077	0.213	0.006	0.572	4.711	0.130	0.081	0.001	0.217	1237	23	1243	31	1221	33	100	0.282312	0.00007	0.004327	0.00008	0.2822101	7.5	2.4
		40	917	859	0.94	2.187	0.083	0.191	0.006	0.847	5.272	0.194	0.083	0.002	0.183	1174	27	1125	35	1263	37	104	0.282163	0.00118	0.002548	0.00010	0.2821088	1.3	41.8
		41	294	263	0.90	2.499	0.085	0.218	0.006	0.329	4.601	0.126	0.083	0.002	0.280	1270	25	1270	32	1260	40	100	0.280012	0.00721	0.002496	0.00025	0.2799519	-71.9	254.9
		42	188	202	1.07	2.532	0.082	0.221	0.006	0.343	4.528	0.121	0.082	0.001	0.205	1279	24	1289	31	1249	35	99	0.282301	0.00006	0.003711	0.00004	0.2822105	8.6	2.0
		43	135	130	0.96	2.549	0.084	0.220	0.006	0.311	4.558	0.124	0.084	0.002	0.228	1284	24	1281	32	1280	38	100	0.282292	0.00005	0.002690	0.00003	0.2822274	9.0	1.8
		44	309	305	0.99	2.529	0.085	0.218	0.006	0.337	4.588	0.117	0.084	0.002	0.297	1279	24	1270	32	1282	38	101	0.282301	0.00006	0.001701	0.00020	0.2822598	9.9	2.2
		45	166	135	0.81	2.618	0.085	0.226	0.006	0.352	4.429	0.116	0.083	0.001	0.251	1304	24	1314	32	1273	35	99	0.282271	0.00005	0.002092	0.00003	0.2822188	9.5	1.6
		46	54	29	0.54	2.629	0.102	0.223	0.006	0.264	4.498	0.130	0.084	0.002	0.195	1301	28	1298	33	1275	54	100	0.282206	0.00004	0.000699	0.00008	0.2821891	8.1	1.5
		47	40	15	0.38	2.563	0.097	0.222	0.006	0.254	4.542	0.128	0.084	0.002	0.311	1284	27	1290	34	1257	51	99	0.282169	0.00004	0.000437	0.00002	0.2821584	6.8	1.3
		48	616	126	0.20	0.872	0.032	0.104	0.003	0.494	9.666	0.287	0.060	0.001	0.111	637	18	637	18	615	44	100	0.282088	0.00003	0.000075	0.00002	0.2820875	-10.5	1.1
		49	420	115	0.27	0.846	0.029	0.099	0.003	0.542	10.128	0.287	0.062	0.001	0.269	622	16	609	17	654	43	102	0.282138	0.00004	0.000226	0.00002	0.2821356	-9.4	1.4
		50	808	80	0.10	0.960	0.037	0.102	0.003	0.503	9.778	0.283	0.067	0.002	-0.039	682	19	629	17	846	53	109	0.282184	0.00007	0.000097	0.00002	0.2821828	-7.3	2.6
		51	322	55	0.17	0.980	0.046	0.100	0.003	0.348	10.031	0.341	0.071	0.003	0.178	695	22	616	19	940	72	113	~~0.282392~~	~~0.00036~~	~~0.000120~~	~~0.00004~~	~~0.2823905~~	~~-0.2~~	~~12.6~~
		52	281	65	0.23	1.046	0.049	0.107	0.004	0.494	9.437	0.320	0.071	0.002	0.156	724	25	653	21	963	66	111	~~0.282127~~	~~0.00006~~	~~0.000051~~	~~0.00002~~	~~0.2821264~~	~~-8.7~~	~~2.0~~

Table 7. U-Pb-Hf analytical results for sample DC-22D.

	Sample	Spot	Content (ppm)		Th/U	U–Pb isotopic ratios									U–Pb ages (Ma)				Con %	Lu–Hf data						
			U	Th		$^{207}Pb/^{235}U$	1σ	$^{206}Pb/^{238}U$	1σ %	Err. Corr	$^{238}U/^{206}Pb$	1σ	$^{207}Pb/^{206}Pb$	1σ	$^{207}Pb/^{206}Pb$	1σ	$^{206}Pb/^{238}U$	1σ		$^{176}Hf/^{177}Hf$	± (2s)	$^{176}Lu/^{177}Hf$	± (2s)	$^{176}Hf/^{177}Hf$ (t)	ε Hf (t)	± (2s)
Embu Terrane	DC-22D	1	488	654	1.39	1.5392	1.12	0.1578	0.98	0.88	6.3364	0.98	0.0707	0.54	950	11	945	9	101	0.282417	0.00006	0.00247	0.00017	0.2823731	6.5658251	2.121753275
		2	276	339	1.27	1.3845	2.16	0.1448	1.02	0.47	6.9048	1.02	0.0693	1.91	909	39	872	8	104	0.282412	0.00004	0.00111	0.00014	0.282393807	5.6518071	1.273051965
		3	555	826	1.54	1.4226	1.22	0.1500	0.98	0.80	6.6682	0.98	0.0688	0.74	893	15	901	8	99	0.282423	0.00005	0.0017	0.0001	0.282394203	6.320493	1.591314957
		4	487	823	1.75	1.4173	1.16	0.1493	0.98	0.84	6.6976	0.98	0.0688	0.63	894	13	897	8	100	0.282466	0.00007	0.00148	0.00011	0.282441032	7.8969307	2.369291158
		~~5~~	~~no value~~	~~no value~~	~~no value~~	~~no value~~	~~no value~~	~~no value~~	~~no value~~	~~no value~~	~~no value~~	~~no value~~	~~no value~~	~~no value~~	~~no value~~	~~no value~~	~~no value~~	~~no value~~	~~no value~~	~~0.282466~~	~~0.00007~~	~~0.00223~~	~~0.00042~~	~~0.282422918~~	~~10.174064~~	~~2.510741376~~
		6	543	1027	1.95	1.4256	1.09	0.1503	0.97	0.89	6.6528	0.97	0.0688	0.51	892	10	903	8	99	0.28273	0.00020	0.00175	0.00029	0.282700289	17.211586	7.072510918
		7	338	445	1.36	1.4392	1.25	0.1511	1.00	0.80	6.6178	1.00	0.0691	0.75	901	16	907	8	99	0.282419	0.00005	0.001714	0.000053	0.282389757	6.3079794	1.909577948
		8	363	596	1.70	1.4736	2.13	0.1520	1.00	0.47	6.5772	1.00	0.0703	1.88	937	38	912	9	103	0.28244	0.00004	0.001987	0.000082	0.282405907	6.9956979	1.414502184
		9	145	167	1.19	1.4410	3.57	0.1499	1.12	0.31	6.6670	1.12	0.0697	3.39	919	70	901	9	102	0.282484	0.00005	0.001056	0.000057	0.282466113	8.8673057	1.69740262
		10	800	3330	4.30	1.4159	1.06	0.1490	0.95	0.90	6.7130	0.95	0.0689	0.45	897	9	895	8	100	0.28255	0.00014	0.00243	0.0002	0.282509094	10.26545	4.950757643
		11	241	188	0.81	1.3157	1.64	0.1417	1.03	0.62	7.0532	1.03	0.0673	1.28	847	27	855	8	99	0.282385	0.00005	0.000834	0.000077	0.282371602	4.4776456	1.69740262
		12	600	1028	1.77	1.4272	1.07	0.1495	0.97	0.91	6.6909	0.97	0.0693	0.45	906	9	898	8	101	0.282577	0.00007	0.0034	0.00023	0.282519585	10.700197	2.475378821
		13	816	2024	2.56	1.4101	2.72	0.1481	1.06	0.39	6.7478	1.06	0.0690	2.51	899	52	890	9	101	0.282453	0.00006	0.00237	0.00014	0.282413313	6.7664833	2.227840939
		14	779	1373	1.82	1.3328	1.08	0.1423	0.96	0.89	7.0251	0.96	0.0679	0.49	866	10	858	8	101	0.282463	0.00009	0.0022	0.00014	0.282427519	6.53395	3.147267359
		15	224	292	1.34	1.3945	2.02	0.1461	1.05	0.52	6.8436	1.04	0.0692	1.73	905	36	879	9	103	no value	no value	no value	no value	no value	no value	no value

U–Pb data corrected for non-radiogenic Pb based on measured 204Pb.

Supplementary Material 3

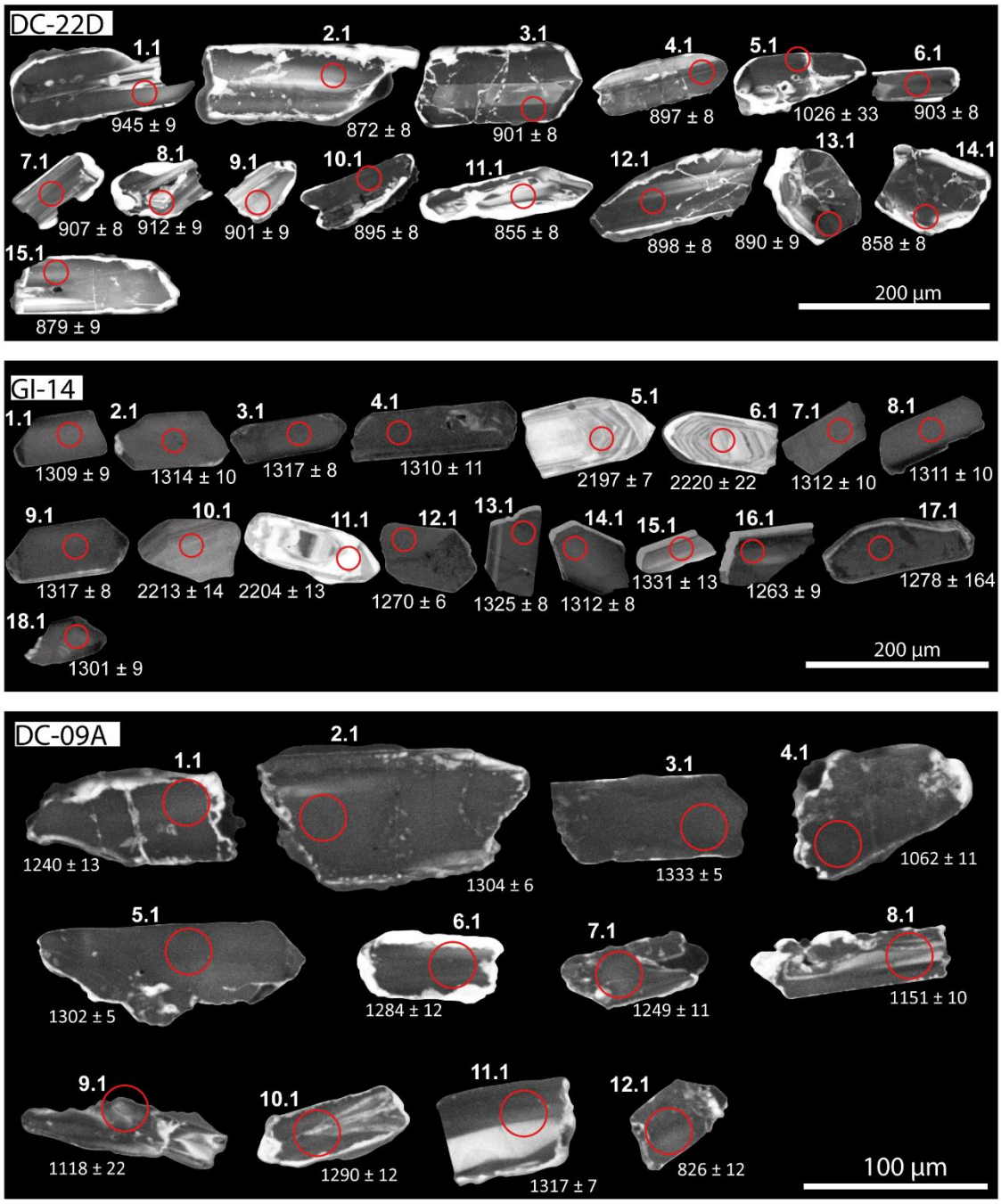

Figure 2. Cathodoluminescence images of zircon analysed for U-Pb-Hf isotopes.

Supplementary Material 4

Table 8. Sm–Nd whole rock analytical data of the analyzed mafic rocks.

Sample	Sm (ppm)	Nd (ppm)	$^{147}Sm/^{144}Nd$	Error1	$^{143}Nd/^{144}Nd$	Error (2s)	$f_{Sm/Nd}$	$e_{Nd(0)}$	T_{DM}	$e_{Nd(t)}$	T
DC-22D	2.151	7.435	0.1750	0.0010	0.512548	0.000006	-0.11	-1.76	1941	0.73	899
DC-09A	3.902	15.903	0.1484	0.0009	0.512427	0.000005	-0.25	-4.12	1433	3.75	1277
FM-06	3.268	9.812	0.2014	0.0012	0.512882	0.000004	0.02	4.77	1948	3.99	1294
FM-08A	3.546	14.153	0.1515	0.0009	0.512444	0.000004	-0.23	-3.79	1464	3.84	1277
WSP-13	5.121	19.158	0.1616	0.0010	0.512450	0.000005	-0.18	1.73	1727	2.21	1314

APPENDIX B – SUPPLEMNETARY MATERIAL OF CHAPTER 4

Supplementary Material A. Analytical methods and materials

A.1. Mineral chemistry

The chemical compositions of minerals were determined with a JEOL JXA-FE-8530 EMPA (electron microprobe analyser) at the University of São Paulo (Brazil). The operating conditions were 15.0 kV accelerating voltage, and a 20 nA beam current. The beam diameter for biotite, muscovite, garnet and ilmenite spot analysis was set to 5 µm. For feldspars and cordierite, the beam diameter was 10 µm. X-ray compositional maps of Fe, Ca, Mn, Al and Ti in garnet were obtained under operating conditions of 15.0 kV accelerating voltage, 300 nA beam current and a dwell time of 25 ms.

A.2. Isochemical phase diagram modelling

Isochemical phase equilibria diagrams were constructed for bulk compositions representative of the main subaluminous metapelitic rocks from the Embu Complex using the Perple_X software (Connolly, 2005) and the internally consistent thermodynamic database of Holland and Powell (2011) (hp11ver.dat, tc-ds61in Perple_X). The minerals involved in phase diagram construction include: garnet, orthopyroxene, white mica, staurolite, biotite, ilmenite, cordierite, feldspar, chlorite, spinel and silicate liquid (melt). The following solution models were used: Gt(W), Bi(W), Mica(W), St(W), Opx(W), Crd(W), Ctd(W), Chl(W), Ilm(W), melt(W) (White et al., 2014),feldspar (Fuhrman and Lindsley, 1988) and Sp(WPC) (White et al., 2002) . The H_2O content was estimated so that the modelled rock composition was saturated in H_2O immediately below the solidus (cf., White et al., 2001) and the contents of P_2O_5 was neglected. Fe^{3+} was set in each modelled bulk composition to reproduce the contents of observed Fe^{3+}-bearing phases in studied thin sections and also considering their influence on measured X_{Mg} values of Fe-Mg minerals (e.g., garnet, biotite). The calculations were undertaken in the NCKFMASHTO chemical model system (Na_2O-CaO-K_2O-FeO-MgO-Al_2O_3-SiO_2-H_2O-TiO_2-O_2) for samples 45A, 12A and 10A and in the MnNCKFMASHTO chemical model for samples 42A and 44A. For sample 45A, the modeled bulk composition was recalculated by adding the corresponding amount of 8 vol.% of melt, taking the melt composition produced in experimental melting of a metapelite sample under conditions

of 750 ºC, 6 kbar and 1 wt.% of added water (Patiño Douce and Harris, 1998). The recalculated bulk rock composition is present in supplementary information S3.

The bulk rock compositions were determined by X-ray fluorescence analysis using a PANalytical AXIOS MAX Advanced X-ray fluorescence (XRF) spectrometer at the University of São Paulo (Brazil).

A.3. U-Pb geochronology and trace element analysis

Monazite, zircon and apatite were analyzed for trace element compositions and U-Pb isotopic ages. Zircon grains from samples of orthogneiss and metasedimentary rocks were separated using standard mineral separation techniques including heavy liquids, before being mounted in epoxy and polished. Monazite and apatite were measured in situ in thin section. Cathodoluminescence images were obtained on the zircon mounts using a FEI-QUANTA 250 FEG scanning electron microscope equipped with a Centaurus Mono CL3+ spectroscope at the University of São Paulo, Brazil.

Zircon grains from three metasedimentary rocks (FM-27, AN-26A, AN-47) were analyzed for U-Pb at the University of São Paulo, Brazil. Analysis on samples AN-26A and AN-47 were performed on a Finnigan Neptune LA-MC-ICP-MS equipped with 9 Faraday detectors, 6 multi-ion counting and 1 secondary electron multiplier. The operating conditions were 60 seconds of ablation time, 6 mJ laser energy, 25% T attenuator value 6 Hz repetition rate and 29 µm spot size. Elemental fractionation and instrumental mass discrimination for LA-MC-ICP-MS analyses were calibrated using the standard zircon GJ-1 and monitored by measurements of NIST 612 glass, following the procedures described in (Sato et al., 2014). Raw data were reduced off-line with corrections for background, instrumental mass bias drift and common Pb. Analysis of sample FM-27 was carried out using a SHRIMP-IIe machine at the University of São Paulo, Brazil. Correction for common Pb was made based on the measured ^{204}Pb. The U-Pb ratios obtained by SHRIMP were calibrated against the standard zircon Temora (^{206}Pb/^{238}U age of 417 Ma, Black et al., 2004), and followed the procedures described by (Williams, 1997). U-Pb ages were calculated using the Isoplot 3.0 program (Ludwig, 2003).

U-Pb ages and trace element compositions of monazite (45A, 12A, 10A, FM02B), apatite (sample FM02B) and zircon from a metasedimentary unit (sample 45A) were obtained via Laser Ablation Split-Stream at the Monash Isotopia Facility, School of Earth,

Atmosphere and Environment, Monash University. An ASI-RESOlution ArF 193 nm excimer laser ablation system was coupled to a Thermo Scientific iCAP-Q Quadruple-Inductively Coupled Plasma Mass Spectrometer (ICPMS) for trace elements and a Thermo Scientific iCAP-TQ Triple-Quadruple ICPMS for U-Pb ages. For zircon and monazite, the laser parameters were as follows: a spot size of 30 µm, fluence of ~4 J.cm-2 at 8 Hz. For apatite, a 30 µm spot size was used, with a fluence of 8 J.cm-2 at 8 Hz. Trace element compositions were obtained with a background of 20 seconds prior to ablation, followed by a 30 second ablation. All data reduction was performed in the Iolite 3 software package (Paton et al., 2011), using built-in Data Reduction schemes. During all sessions standards were interspersed with unknowns, for zircon U-Pb ages Plesovice was the primary standard with Temora 1 (417 Ma, Black et al., 2003), GJ1 (601 Ma, Jackson et al., 2004) and Mud Tank (732 Ma, Black and Gulson, 1978) as quality control and for monazite and apatite the primary standards was MADel, with 44069 (425 Ma, Aleinikoff et al., 2006) as secondary standard. For the trace element analyses the NIST 610 glass standard was used as primary, with samples standardized to Ca during data reduction, while NIST 612, BCR-2 an ATHO-G were used as quality control standards. Concentrations have been normalized to chondrite (McDonough and Sun, 1995).

A.4. In situ Rb-Sr dating

In situ biotite and muscovite Rb-Sr analysis were performed on two different samples (45A, 12A). Isotopic data were carried by Laser Ablation ICPMS at the Monash Isotopia Facility, School of Earth, Atmosphere and Environment, Monash University. The micas were analysed using a Thermo ICAPTQ Triple Quadrupole ICP-MS The mass spectrometer was coupled with an ASI Resolution 193 nm excimer laser equipped with a dual volume Laurin Technic S155 ablation cell. The minerals were ablated in a He atmosphere with laser operated at a repetition rate 10 Hz, 100 µm spot size and approximately 3 Jcm^{-2} of laser energy at the sample. Each analysis began with 20 second measurement of the gas background, followed by 30s with the laser switched on ablating the sample.

It has been shown that Triple Quadropole ICPMS technology is efficient in dealing with isobaric interferences, and in specific it has been shown that is useful for in-situ Rb-Sr geochronology where ^{87}Rb and ^{87}Sr directly overlap. The introduction of an oxydising gas such as O_2 or N_2O into the mass spectrometer ion path, promotes Sr oxydisation but

leaves Rb essentially unaffected, allowing the possibility of measuring Sr isotopes as oxydised reaction products and overcoming the isobaric interference of ^{87}Rb with ^{87}Sr (Hogmalm et al., 2017; Murphy et al., 2020). The analyses used N_2O as a reaction gas as being that more efficient than O_2 in oxydising Sr (Hogmalm et al., 2017; Murphy et al., 2020) and analysed the following masses: ^{39}K, ^{41}K, $^{43}Ca^{16}O$, $^{44}Ca^{16}O$, ^{85}Rb, $^{86}Sr^{16}O$, $^{87}Sr^{16}O$, $^{88}Sr^{16}O$. Dwell time for ^{39}K, ^{41}K, $^{43}Ca^{16}O$, $^{44}Ca^{16}O$ was 5 ms, for ^{85}Rb 50 ms, $^{86}Sr^{16}O$, $^{87}Sr^{16}O$ 120 ms and for $^{88}Sr^{16}O$ 20 ms.

The raw data was reduced using the Iolite 3 software (Paton et al., 2011) and the final integrated raw counts were exported and further processed using an excel spreadsheet for drift correction and the calculation of the $^{87}Rb/^{86}Sr$ and $^{87}Sr/^{86}Sr$. For the $^{87}Sr/^{86}Sr$, NIST 610 was used as the main primary calibration standard whereas for the $^{87}Rb/^{86}Sr$ the Mica-Mg pressed pellet was used. The recommended values used for these standards are reported by (Hogmalm et al., 2017). The analytical uncertainties were estimated using the internal and external precision obtained during the course of analyses of the calibration standards. For the $^{87}Sr/^{86}Sr$, the external precision of NIST 610 of all the analytical sessions (24 analyses) was added in quadratic addition to the internal precision of selected single analyses of the same standard. For the $^{87}Rb/^{86}Sr$, the same statistical approach was used but in this case the uncertainties were estimated using internal and external precision of the Mica-Mg (24 analyses) standard. Relative uncertainties ranged between 1.55 - 2.03% for the $^{87}Rb/^{86}Sr$ and 0.53% for the $^{87}Sr/^{86}Sr$, both at 1 sigma level.

References:

Aleinikoff, J.N., Schenck, W.S., Plank, M.O., Srogi, L.A., Fanning, C.M., Kamo, S.L., Bosbyshell, H., 2006. Deciphering igneous and metamorphic events in high-grade rocks of the Wilmington complex, Delaware: Morphology, cathodoluminescence and backscattered electron zoning, and SHRIMP U-Pb geochronology of zircon and monazite. Bulletin of the Geological Society of America 118, 39–64. https://doi.org/10.1130/B25659.1

Alkmim, F.F., Marshak, S., Pedrosa-Soares, A.C., Peres, G.G., Cruz, S.C.P., Whittington, A., 2006. Kinematic evolution of the Araçuaí-West Congo orogen in Brazil and Africa: Nutcracker tectonics during the Neoproterozoic assembly of Gondwana. Precambrian Research 149, 43–64. https://doi.org/10.1016/j.precamres.2006.06.007

Almeida, F.F.M. De, Hasui, Y., Brito Neves, B.B. De, Fuck, R.A., 1981. Brazilian structural provinces: An introduction. Earth-Science Reviews 17, 1–29. https://doi.org/10.1016/0012-8252(81)90003-9

Almeida, F.F.M., Amaral, G., Cordani, U.G., Kawashita, K., 1973. The Precambrian Evolution of the South American Cratonic Margin South of the Amazon River. The South Atlantic 1, 411–446. https://doi.org/10.1007/978-1-4684-3030-1_11

Almeida, F.F.M., Hasui, Y., 1984. O pré-cambriano do Brasil.

Alsop, G.I., Holdsworth, R.E., 2004. Shear zones — an introduction and overview. Geological Society, London, Special Publications 224, 1 LP – 9. https://doi.org/10.1144/GSL.SP.2004.224.01.01

Alves, A., Janasi, V. de A., Campos Neto, M. da C., 2016. Sources of granite magmatism in the Embu Terrane (Ribeira Belt, Brazil): Neoproterozoic crust recycling constrained by elemental and isotope (Sr-Nd-Pb) geochemistry. Journal of South American Earth Sciences 68, 205–223. https://doi.org/10.1016/j.jsames.2015.10.014

Alves, A., Janasi, V. de A., Campos Neto, M. da C., Heaman, L., Simonetti, A., 2013. U-Pb geochronology of the granite magmatism in the embu terrane: Implications for the evolution of the central ribeira belt, SE Brazil. Precambrian Research 230, 1–12. https://doi.org/10.1016/j.precamres.2013.01.018

Amaral, L., Caxito, F. de A., Pedrosa-Soares, A.C., Queiroga, G., Babinski, M., Trindade, R., Lana, C., Chemale, F., 2020. The Ribeirão da Folha ophiolite-bearing accretionary wedge (Araçuaí orogen, SE Brazil): New data for Cryogenian plagiogranite and metasedimentary rocks. Precambrian Research 336, 105522. https://doi.org/10.1016/j.precamres.2019.105522

Arena, K.R., Hartmann, L.A., Lana, C., 2017. Tonian emplacement of ophiolites in the southern Brasiliano Orogen delimited by U-Pb-Hf isotopes of zircon from metasomatites. Gondwana Research 49, 296–332. https://doi.org/10.1016/j.gr.2017.05.018

Babinski, M., Tassinari, C.C.G., Nutman, A.P., Sato, K., Pimentel, M.M., Iyer, S.S., 2001. U/Pb shrimp zircon ages of migmatites from the basement of the Embú Complex, Ribeira Fold Belt, Brazil: indications for ~1.4-1.3 Ga Pb-Pb and Rb-Sr "isochron" ages of no geological meaning. III South American Symposium on Isotope Geology. Pucón.

Bartoli, O., 2017. Phase equilibria modelling of residual migmatites and granulites: An

evaluation of the melt-reintegration approach. Journal of Metamorphic Geology 35, 919–942. https://doi.org/10.1111/jmg.12261

Basei, M.A.S., Frimmel, H.E., Nutman, A.P., Preciozzi, F., 2008. West Gondwana amalgamation based on detrital zircon ages from Neoproterozoic Ribeira and Dom Feliciano belts of South America and comparison with coeval sequences from SW Africa. Geological Society, London, Special Publications 294, 239–256.

Basei, M.A.S., Siga, O., Machiavelli, A., Mancini, F., 1992. Evolução tectônica dos terrenos entre os cinturões ribeira e dom feliciano (PR-SC). Revista Brasileira de Geociências 22, 216–221.

Bell, E.A., Boehnke, P., Barboni, M., Harrison, T.M., 2019. Tracking chemical alteration in magmatic zircon using rare earth element abundances. Chemical Geology 510, 56–71. https://doi.org/10.1016/j.chemgeo.2019.02.027

Black, L.P., Gulson, B.L., 1978. The age of the Mud Tank carbonatite, Strangways Range, Northern Territory. BMR J. Austral. Geol. Geophy. 3, 227–232. https://doi.org/10.1016/j.apenergy.2015.11.040

Black, L.P., Kamo, S.L., Allen, C.M., Aleinikoff, J.N., Davis, D.W., Korsch, R.J., Foudoulis, C., 2003. TEMORA 1: a new zircon standard for Phanerozoic U-Pb geochronology. Chemical Geology 155–170.

Bose, S., Ghosh, G., Kawaguchi, K., Das, K., Mondal, A.K., Banerjee, A., 2021. Zircon and monazite geochronology from the Rengali-Eastern Ghats Province: Implications for the tectonic evolution of the eastern Indian terrane. Precambrian Research 355, 106080. https://doi.org/10.1016/j.precamres.2020.106080

Boynton, W. V., 1984. Cosmochemistry of the rare earth elements: meteorite studies. Rare Earth Element Geochemistry. Elsevier B.V., 63–114. https://doi.org/10.1016/b978-0-444-42148-7.50008-3

Brito Neves, B.B., Campos Neto, M.D.C., Fuck, R.A., 1999. From Rodinia to Western Gondwana: An approach to the Brasiliano-Pan African cycle and orogenic collage. Episodes 22, 155–166. https://doi.org/10.18814/epiiugs/1999/v22i3/002

Brito Neves, B.B. de, Fuck, R.A., 2013. Neoproterozoic evolution of the basement of the South-American platform. Journal of South American Earth Sciences 47, 72–89. https://doi.org/10.1016/j.jsames.2013.04.005

Brito Neves, B.B. de, Fuck, R.A., Campanha, G.A. da C., 2021. Basement inliers of the Brasiliano structural provinces of South America. Journal of South American Earth Sciences 110, 103392. https://doi.org/10.1016/j.jsames.2021.103392

Brito Neves, B.B. de, Fuck, R.A., Pimentel, M.M., 2014. The Brasiliano collage in South America: a review. Brazilian Journal of Geology 44, 493–518. https://doi.org/10.5327/Z2317-4889201400030010

Brown, M., 2009. Metamorphic patterns in orogenic systems and the geological record. Geological Society, London, Special Publications 318, 37 LP – 74. https://doi.org/10.1144/SP318.2

Cabrita, D., Salamuni, E., Lagoeiro, L., 2017. Fabric evolution of polydeformed orthogneisses and quartzites along the Curitiba Shear Zone, Curitiba Domain, Southern Brazil. Journal of South American Earth Sciences 77. https://doi.org/10.1016/j.jsames.2017.05.010

Cabrita, D.I.G., Faleiros, F.M., Cawood, P.A., Campanha, G.A.C., Yogi, M.T.A.G., Wainwright, A.N., Raveggi, M., Almeida, V. V., 2021. Petrochronological constraints and tectonic implications of Tonian metamorphism in the Embu Complex , Ribeira Belt , Brazil. Precambrian Research 363. https://doi.org/10.1016/j.precamres.2021.106315

Caltabellota, F.P., Lopes, A.P., Brumatti, M., Rodrigues da Silva, A.D., Lima, R.A.P., Severino, R.R., Andrade, J.J.C., Palmeira, L.C.M., Mapa, F.B., Marque, I.P., Turra, B.B., Costa, V.S., Campos, F.F., Ferrari, V.C., Mendes, D., 2017. Mapa Geológico de Integração do ARIM Vale do Ribeira (SP e PR). Escala 1:250.000.

Campanha, G.A. da C., 2002. O Papel do Sistema de Zonas de Cisalhamento Transcorrentes na Configuração da Porção Meridional da Faixa Ribeira. University of São Paulo.

Campanha, G.A. da C., 1991. Tectônica Proterozóica no Alto e Médio Vale do Ribeira, estados de São Paulo e Paraná. Universidade de São Paulo.

Campanha, G.A. da C., Brito Neves, B.B., 2004. Frontal and oblique tectonics in the Brazilian Shield. Episodes 27, 255–259. https://doi.org/10.1016/S1342-937X(05)70391-9

Campanha, G.A. da C., Faleiros, F.M., Basei, M.A.S., Tassinari, C.C.G., Nutman, A., Vasconcelos, P., 2015. Geochemistry and age of mafic rocks from the Votuverava Group, southern Ribeira Belt, Brazil: Evidence for 1490Ma oceanic back-arc magmatism. Precambrian Research 266, 530–550. https://doi.org/10.1016/j.precamres.2015.05.026

Campanha, G.A. da C., Sadowski, G.R., 2002. Determinações da deformação finita em rochas metassedimentares da faixa ribeira na região de Iporanga e Apiaí, SP. Revista

Brasileira de Geociências 32, 107–118.

Campanha, G.A. da C., Sadowski, G.R., 1999. Tectonics of the southern portion of the Ribeira Belt (Apiai Domain). Precambrian Research 98, 31–51. https://doi.org/10.1016/S0301-9268(99)00027-3

Campanha, G.A.C., Basei, M.S., Faleiros, F.M., Nutman, A.P., 2016. The Mesoproterozoic to early Neoproterozoic passive margin Lajeado Group and Apiaí Gabbro, Southeastern Brazil. Geoscience Frontiers 7, 683–694. https://doi.org/10.1016/j.gsf.2015.08.004

Campanha, G.A.C., Faleiros, F.M., Cawood, P.A., Cabrita, D.I.G., Ribeiro, B. V, Basei, M.A.S., 2019. The Tonian Embu Complex in the Ribeira Belt (Brazil): revision , depositional age and setting in Rodinia and West Gondwana. Precambrian Research 320, 31–45. https://doi.org/10.1016/j.precamres.2018.10.010

Campanha, G.A.C., Gimenez Filho, A., Caetano, S.L.V., Pires, F.A., Dantas, A.S.L., Teixeira, A.L., Dehira, L.K., 1986. Geologia e estratigrafia da região das folhas Iporanga e Gruta do Diabo, Vale do Ribeira, São Paulo. Congresso Brasileiro de Geologia. Sociedade Brasileira de Geologia, Goiânia, 1058–1073.

Campos Neto, M. da C., Figueiredo, M.C.., 1995. The Rio Doce Orogeny, Southeastern Brazil. Journal of South American Earth Sciences 8, 143–162. https://doi.org/10.1016/0895-9811(95)00002-W

Campos Neto, M.D.C., 2000. Orogenic systems from Southwestern Gondwana: an approach to Brasiliano Pan African cycle and orogenic collage in Southeastern Brazil. Tectonic Evolution of South America. Rio de Janeiro, 335–365.

Cavalcante, C., Lagoeiro, L., Fossen, H., Egydio-Silva, M., Morales, L.F.G., Ferreira, F., Conte, T., 2018. Temperature constraints on microfabric patterns in quartzofeldsphatic mylonites, Ribeira belt (SE Brazil). Journal of Structural Geology 115, 243–262. https://doi.org/10.1016/j.jsg.2018.07.013

Cawood, P.A., Hawkesworth, C.J., Dhuime, B., 2012. Detrital zircon record and tectonic setting. Geology 40, 875–878. https://doi.org/10.1130/G32945.1

Cawood, P.A., Strachan, R.A., Pisarevsky, S.A., Gladkochub, D.P., Murphy, J.B., 2016. Linking collisional and accretionary orogens during Rodinia assembly and breakup: Implications for models of supercontinent cycles. Earth and Planetary Science Letters 449, 118–126. https://doi.org/10.1016/j.epsl.2016.05.049

Caxito, F.A., Heilbron, M., Valeriano, C.M., Bruno, H., Pedrosa-Soares, A., Alkmim, F.F., Chemale, F., Hartmann, L.A., Dantas, E., Basei, M.A.S., 2021. Integration of

elemental and isotope data supports a neoproterozoic adamastor ocean realm. Geochemical Perspectives Letters 17, 6–10. https://doi.org/10.7185/GEOCHEMLET.2106

Ceccato, A., Pennacchioni, G., Menegon, L., Bestmann, M., 2017. Crystallographic control and texture inheritance during mylonitization of coarse grained quartz veins. Lithos 290–291, 210–227. https://doi.org/10.1016/j.lithos.2017.08.005

Cerva-Alves, T., Hartmann, L.A., Remus, M. V.D., Lana, C., 2020. Integrated ophiolite and arc evolution, southern Brasiliano Orogen. Precambrian Research 341, 105648. https://doi.org/10.1016/j.precamres.2020.105648

Chetty, T.R.K., 2017. Chapter 1 - Orogens. In: Chetty, T.R.K.B.T.-P.O. of I. (Ed.), Proterozoic Orogens of India: A Critical Window to Gondwana. Elsevier, 1–34. https://doi.org/https://doi.org/10.1016/B978-0-12-804441-4.00001-8

Chu, N.C., Taylor, R.N., Chavagnac, V., Nesbitt, R.W., Boella, R.M., Milton, J.A., German, C.R., Bayon, G., Burton, K., 2002. Hf isotope ratio analysis using multi-collector inductively coupled plasma mass spectrometry: An evaluation of isobaric interference corrections. Journal of Analytical Atomic Spectrometry 17, 1567–1574. https://doi.org/10.1039/b206707b

Condie, K.C., 2003. Supercontinents, superplumes and continental growth: The Neoproterozoic record. Geological Society Special Publication 206, 1–21. https://doi.org/10.1144/GSL.SP.2003.206.01.02

Connolly, J.A.D., 2005. Computation of phase equilibria by linear programming: A tool for geodynamic modeling and its application to subduction zone decarbonation. Earth and Planetary Science Letters 236, 524–541. https://doi.org/10.1016/j.epsl.2005.04.033

Conte, T., Cavalcante, C., Lagoeiro, L.E., Fossen, H., Silveira, C.S., 2020. Quartz textural analysis from an anastomosing shear zone system: Implications for the tectonic evolution of the Ribeira belt, Brazil. Journal of South American Earth Sciences 103, 102750. https://doi.org/10.1016/j.jsames.2020.102750

Cordani, U.G., Coutinho, J.M. V, Nutman, A.P., 2002. Geochronological constraints on the evolution of the Embu Complex São Paulo, Brazil. Journal of South American Earth Sciences 14, 903–910. https://doi.org/10.1016/S0895-9811(01)00083-9

Corrales, F.F.P., Dussin, I.A., Heilbron, M., Bruno, H., Bersan, S., Valeriano, C.M., Pedrosa-Soares, A.C., Tedeschi, M., 2020. Coeval high Ba-Sr arc-related and OIB Neoproterozoic rocks linking pre-collisional magmatism of the Ribeira and Araçuaí

orogenic belts, SE-Brazil. Precambrian Research 337, 105476. https://doi.org/10.1016/j.precamres.2019.105476

Costa, R.V. da, Johannes Trouw, R.A., Marimon, R.S., Nepomuceno, F., Mendes, J.C., Dantas, E., 2020. São Bento do Sapucaí Shear Zone: Constraining age and P-T conditions of a collisional Neoproterozoic oblique shear zone, Ribeira Orogen, Brazil. Journal of South American Earth Sciences 98, 102418. https://doi.org/10.1016/j.jsames.2019.102418

Costa, R.V., Trouw, R.A.J., Mendes, J.C., Geraldes, M., Tavora, A., Nepomuceno, F., de Araújo Junior, E.B., 2017. Proterozoic evolution of part of the Embu Complex , eastern S a state , SE Brazil. Journal of South American Earth Sciences 79, 170–188. https://doi.org/10.1016/j.jsames.2017.08.003

Cota de Freitas, N., Almeida, J., Heilbron, M., Cutts, K., Dussin, I., 2021. The Cabo Frio Thrust: A folded suture zone, Ribeira belt, SE Brazil. Journal of Structural Geology 149, 104379. https://doi.org/https://doi.org/10.1016/j.jsg.2021.104379

Cury, L.F., Kaulfuss, G.A., Siga Júnior, O., Basei, M.A.S., Harara, O.M., Sato, K., 2002. Idades U-Pb (Zircões) de 1.75 Ga em granitóides alcalinos deformados dos núcleos Betara e Tigre: evidências de regimes extensionais do estateriano na Faixa Apiaí. Geologia USP - Serie Cientifica 2, 95–108. https://doi.org/10.5327/S1519-874X2002000100009

Da Silva, L.C., McNaughton, N.J., Armstrong, R., Hartmann, L.A., Fletcher, I.R., 2005. The neoproterozoic Mantiqueira Province and its African connections: A zircon-based U-Pb geochronologic subdivision for the Brasiliano/Pan-African systems of orogens. Precambrian Research 136, 203–240. https://doi.org/10.1016/j.precamres.2004.10.004

Deer, W.A., Howie, R.A., Zussman, J., 2013. An introduction to the rock-forming minerals.

Depaolo, D.J., 1981. Neodymium isotopes in the Colorado Front Range and crust-mantle evolution in the Proterozoic. Nature 291, 193–196. https://doi.org/10.1038/291193a0

Ducea, M.N., Saleeby, J.B., Bergantz, G., 2015. The architecture, chemistry, and evolution of continental magmatic arcs. Annual Review of Earth and Planetary Sciences 43, 299–331. https://doi.org/10.1146/annurev-earth-060614-105049

Duffles, P., Trouw, R.A.J., Mendes, J.C., Gerdes, A., Vinagre, R., 2016. U-Pb age of detrital zircon from the Embu sequence, Ribeira belt, Se Brazil. Precambrian

Research 278, 69–86. https://doi.org/10.1016/j.precamres.2016.03.007

Egydio-Silva, M., Vauchez, A., Bascou, J., Hippertt, J., 2002. High-temperature deformation in the Neoproterozoic transpressional Ribeira belt, southeast Brazil. Tectonophysics 352, 203–224. https://doi.org/10.1016/S0040-1951(02)00197-X

Faleiros, F.M., 2008. Evolução de Terrenos Tectono-Metamórficos da Serrania do Ribeira e Planalto Alto Turvo (SP, PR). Universidade de São Paulo.

Faleiros, F.M., Campanha, G.A. da C., Bello, R.M. da S., Fuzikawa, K., 2010. Quartz recrystallization regimes, c-axis texture transitions and fluid inclusion reequilibration in a prograde greenschist to amphibolite facies mylonite zone (Ribeira Shear Zone, SE Brazil). Tectonophysics 485, 193–214. https://doi.org/10.1016/j.tecto.2009.12.014

Faleiros, F.M., Campanha, G.A. da C., Martins, L., Vlach, S., Vasconcelos, P.M., 2011a. Ediacaran high-pressure collision metamorphism and tectonics of the southern Ribeira Belt (SE Brazil): Evidence for terrane accretion and dispersion during Gondwana assembly. Precambrian Research 189, 263–291. https://doi.org/10.1016/j.precamres.2011.07.013

Faleiros, F.M., Campanha, G.A.C., Pavan, M., Almeida, V. V., Rodrigues, S.W.O., Araújo, B.P., 2016. Short-lived polyphase deformation during crustal thickening and exhumation of a collisional orogen (Ribeira Belt, Brazil). Journal of Structural Geology 93, 106–130. https://doi.org/10.1016/j.jsg.2016.10.006

Faleiros, F.M., Ferrari, V.C., Costa, V.S., Da Cruz Campanha, G.A., 2011b. Geochemistry and Petrogenesis of Metabasites from the Votuverava Group (Apiaí Terrane, Southern Ribeira Belt): Evidence of a Calymmian Back-arc Basin. Geologia USP - Serie Cientifica 11, 135–155. https://doi.org/10.5327/Z1519-874X2011000200008

Faleiros, F.M., Morais, S.M., Costa, V.S., 2012. Geologia e recursos minerais da folha Apiaí SG.22-X-B-V: escala 1:100.000: estados de São Paulo e Paraná.

Faleiros, F.M., Ribeiro, B. V, Campanha, G.A.C., Cawood, P.A., Cabrita, D.I.G., Yogi, M.T.A.G., Milani, L.A., Lemos-Santos, D. V, Almeida, V. V, Rodrigues, S.W.O., Malta, I.S., Forero-Ortega, A.J., 2022. Strain Partitioning along Terrane Bounding and Intraterrane Shear Zones: Constraints from a Long-Lived Transpressional System in West Gondwana (Ribeira Belt, Brazil). Lithosphere 2021, 2103213. https://doi.org/10.2113/2022/2103213

Fassbinder, E., 1990. Análise estrutural da Falha Lancinha, Estado do Paraná.

Universidade de São Paulo.

Fernandes, A.J., 1991. O Complexo Embu no Leste do Estado de São Paulo: Contribuição ao Conhecimento da Litoestratigrafia e da Evolução Estrutural e Metamórfica. Universidade de São Paulo.

Forero-Ortega, A.J., Campanha, G.A.C., Faleiros, F.M., Yogi, M.T.A.G., 2020. Pure shear-dominated transpression and vertical extrusion in a strike-slip fault splay from the Itapirapuã Shear Zone, Ribeira Belt, Brazil. Tectonophysics 786, 228455. https://doi.org/10.1016/j.tecto.2020.228455

Forero-Ortega, A.J., Faleiros, F.M., 2018. Ediacaran (570-615 Ma) back-arc basin basaltic volcanism in the ltaiacoca Group, Ribeira Belt, Brazil: a remnant of the Adamastor Ocean. South American Symposium on Isotope Geology. Cochabamba.

Fossen, H., Cavalcante, C., Konopásek, J., Meira, V.T., de Almeida, R.P., Hollanda, M.H.B.M., Trompette, R., 2020. A critical discussion of the subduction-collision model for the Neoproterozoic Araçuaí-West Congo orogen. Precambrian Research 343. https://doi.org/10.1016/j.precamres.2020.105715

Fossen, H., Cavalcante, G.C.G., 2017. Shear zones – A review., Earth-Science Reviews. https://doi.org/10.1016/j.earscirev.2017.05.002

Fuck, R.A., Brito Neves, B.B., Schobbenhaus, C., 2008. Rodinia descendants in South America. Precambrian Research 160, 108–126. https://doi.org/10.1016/j.precamres.2007.04.018

Fuhrman, M.L., Lindsley, D.H., 1988. Ternary-Feldspar Modeling and Thermometry. American Mineralogist 73, 201–215.

Gain, S.E.M., Gréau, Y., Henry, H., Belousova, E., Dainis, I., Griffin, W.L., O'Reilly, S.Y., 2019. Mud Tank Zircon: Long-Term Evaluation of a Reference Material for U-Pb Dating, Hf-Isotope Analysis and Trace Element Analysis. Geostandards and Geoanalytical Research 43, 339–354. https://doi.org/10.1111/ggr.12265

Gilgannon, J., Fusseis, F., Menegon, L., Regenauer-Lieb, K., Buckman, J., 2017. Hierarchical creep cavity formation in an ultramylonite and implications for phase mixing. Solid Earth 8, 1193–1209. https://doi.org/10.5194/se-8-1193-2017

Giraldo, S.J., Trouw, R.A.J., Duffles, P., Vinagre da Costa, R., Ibañez Mejia, M., Schwantes Marimon, R., 2019. Structural analysis combined with new geothermobarometric and geochronological results of the Além Paraíba shear zone, between Três Rios and Bananal, Ribeira Orogen, SE Brazil. Journal of South American Earth Sciences 90, 118–136.

https://doi.org/10.1016/j.jsames.2018.11.018

Gray, D.R., Foster, D.A., Meert, J.G., Goscombe, B.D., Armstrong, R., Trouw, R.A.J., Passchier, C.W., 2008. A Damara orogen perspective on the assembly of southwestern Gondwana. Geological Society Special Publication 294, 257–278. https://doi.org/10.1144/SP294.14

Guillot, S., Hattori, K., Agard, P., Schwartz, S., Vidal, O., 2009. Exhumation Processes in Oceanic and Continental Subduction Contexts: A Review. Subduction Zone Geodynamics. 103–118. https://doi.org/10.1007/978-3-540-87974-9

Hackspacher, P.C., Dantas, E.L., Spoladore, Â., Fetter, A.H., Oliveira, M.A.F. de, 2000. Evidence of Neoproterozoic Backarc Basin Development in the Central Ribeira Belt, Southeastern Brazil: New Geochronological and Geochemical Constraints From the São Roque - Açungui Groups. Revista Brasileira de Geociências 30, 110–114.

Hamilton, P.J., O'Nions, R.K., Bridgwater, D., Nutman, A., 1983. Sm-Nd studies of Archaean metasediments and metavolcanics from West Greenland and their implications for the Earth's early history. Earth and Planetary Science Letters 62, 263–272. https://doi.org/10.1016/0012-821X(83)90089-4

Hartmann, L.A., Werle, M., Michelin, C.R.L., Lana, C., Queiroga, G.N., Castro, M.P., Arena, K.R., 2019. Proto-Adamastor ocean crust (920 Ma) described in Brasiliano Orogen from coetaneous zircon and tourmaline. Geoscience Frontiers 10, 1623–1633. https://doi.org/10.1016/j.gsf.2018.09.018

Heilbron, M., Machado, N., 2003. Timing of terrane accretion in the Neoproterozoic-Eopaleozoic Ribeira orogen (SE Brazil). Precambrian Research 125, 87–112.

Heilbron, M., Oliveira, C., Lobato, M., De Morisson Valeriano, C., Dussin, I., Dantas, E., Simonetti, A., Bruno, H., Corrales, F., Socoloff, E., 2019. The Barreiro suite in the central Ribeira Belt (SE-Brazil): A late Tonian tholeiitic intraplate magmatic event in the distal passive margin of the São Francisco Paleocontinent. Brazilian Journal of Geology 49, 1–21. https://doi.org/10.1590/2317-4889201920180129

Heilbron, M., Valeriano, C.D.M., Peixoto, C., Neubauer, F., Dussin, I., Corrales, F., Bruno, H., Cesar, J., Almeida, H. De, Guilherme, L., 2020. Neoproterozoic magmatic arc systems of the central Ribeira belt, SE-Brazil, in the context of the West-Gondwana pre-collisional history: A review. Journal of South American Earth Sciences 102710. https://doi.org/10.1016/j.jsames.2020.102710

Heilbron, M., Valeriano, C.M., Tassinari, C.C.G., Almeida, J., Tupinambá, M., Siga Jr, O., Trouw, R., 2008. Correlation of Neoproterozoic terranes between Ribeira Belt,

SE Brazil and its African counterpart: comparative tectonic evolution and open questions., West Gondwana: Pre-Cenozoic Correlations Across the South Atlantic Region. https://doi.org/10.1144/SP294.12

Henrique-Pinto, R., De Assis Janasi, V., Da Cruz Campanha, G.A., 2018. U-Pb dating, Lu-Hf isotope systematics and chemistry of zircon from the Morro do Polvilho meta-trachydacite: Constraints on sources of magmatism and on the depositional age of the São Roque Group. Geologia USP - Serie Cientifica 18, 45–56. https://doi.org/10.11606/issn.2316-9095.v18-125793

Henrique-Pinto, R., Janasi, V.A., Vasconcellos, A.C.B.C., Sawyer, E.W., Barnes, S., Basei, M.A.S., Tassinari, C.C.G., 2015. Zircon provenance in meta-sandstones of the São Roque Domain : Implications for the Proterozoic evolution of the Ribeira Belt , SE Brazil. Precambrian Research 256, 271–288. https://doi.org/10.1016/j.precamres.2014.11.014

Hippertt, J., Egydio-Silva, M., 1996. New polygonal grains formed by dissolution-redeposition in quartz mylonite. Journal of Structural Geology 18, 1345–1352. https://doi.org/10.1016/S0191-8141(96)00047-8

Hogmalm, K.J., Zack, T., Karlsson, A.K.O., Sjöqvist, A.S.L., Garbe-Schönberg, D., 2017. In situ Rb-Sr and K-Ca dating by LA-ICP-MS/MS: An evaluation of N2O and SF6 as reaction gases. Journal of Analytical Atomic Spectrometry 32, 305–313. https://doi.org/10.1039/c6ja00362a

Holland, T.J.B., Powell, R., 2011. An improved and extended internally consistent thermodynamic dataset for phases of petrological interest, involving a new equation of state for solids. Journal of Metamorphic Geology 29, 333–383. https://doi.org/10.1111/j.1525-1314.2010.00923.x

Hollocher, K., Robinson, P., Walsh, E., Roberts, D., 2012. Geochemistry of amphibolite-facies volcanics and gabbros of the støren nappe in extensions west and southwest of Trondheim, Western Gneiss Region, Norway: A key to correlations and paleotectonic settings. American Journal of Science 312, 357–416. https://doi.org/10.2475/04.2012.01

Jackson, S.E., Pearson, N.J., Griffin, W.L., Belousova, E.A., 2004. The application of laser ablation-inductively coupled plasma-mass spectrometry to in situ U-Pb zircon geochronology. Chemical Geology 211, 47–69. https://doi.org/10.1016/j.chemgeo.2004.06.017

Jäger, E, 1979. Introduction to Geochronology BT - Lectures in Isotope Geology. In:

Jäger, Emilie, Hunziker, J.C. (Eds.). Springer Berlin Heidelberg, Berlin, Heidelberg, 1–12.

Janasi, V. de A., Alves, A., Vlach, S.R.F., Leite, R.J., 2003. Granitos Peraluminosos da Porção Central da Faixa Ribeira, Estado de São Paulo: Sucessivos Eventos de Reciclagem da Crosta Continental no Neoproterozóico. Geologia USP - Serie Cientifica 3, 13–24.

Janasi, V. de A., Andrade, S., Vasconcellos, A.C.B.C., Henrique-Pinto, R., Ulbrich, H.H.G.J., 2016. Timing and sources of granite magmatism in the Ribeira Belt, SE Brazil: Insights from zircon in situ U–Pb dating and Hf isotope geochemistry in granites from the São Roque Domain. Journal of South American Earth Sciences 68, 224–247. https://doi.org/10.1016/j.jsames.2015.11.009

Janasi, V. de A., Ulbrich, H.H.G.J., 1991. Late Proterozoic granitoid magmatism in the state of São Paulo, southeastern Brazil. Precambrian Research 51, 351–374.

Janasi, V.A., Leite, R.J., Van Schmus, W.R., 2001. U-Pb chronostratigraphy of the granitic magmatism in the Agudos Grandes Batholith (West of São Paulo, Brazil) - Implications for the evolution of the Ribeira Belt. Journal of South American Earth Sciences 14, 363–376. https://doi.org/10.1016/S0895-9811(01)00034-7

Janoušek, V., Farrow, C.M., Erban, V., 2006. Interpretation of whole-rock geochemical data in igneous geochemistry: Introducing Geochemical Data Toolkit (GCDkit). Journal of Petrology 47, 1255–1259. https://doi.org/10.1093/petrology/egl013

Juliani, C., Hackspacher, P., Dantas, E.L., Fetter, A.H., 2000. the Mesoproterozoic Volcano-Sedimentary Serra Do Itaberaba Group of the Central Ribeira Belt, São Paulo State, Brazil: Implications for the Age of the Overlying São Roque Group. Revista Brasileira de Geociências 30, 082–086. https://doi.org/10.25249/0375-7536.2000301082086

Kelsey, D.E., Clark, C., Hand, M., 2008. Thermobarometric modelling of zircon and monazite growth in melt-bearing systems: Examples using model metapelitic and metapsammitic granulites. Journal of Metamorphic Geology 26, 199–212. https://doi.org/10.1111/j.1525-1314.2007.00757.x

Kilian, R., Heilbronner, R., Stünitz, H., 2011. Quartz grain size reduction in a granitoid rock and the transition from dislocation to diffusion creep. Journal of Structural Geology 33, 1265–1284. https://doi.org/10.1016/j.jsg.2011.05.004

Konopásek, J., Cavalcante, C., Fossen, H., Janoušek, V., 2020. Adamastor – an ocean that never existed? Earth-Science Reviews 205, 103201.

https://doi.org/10.1016/j.earscirev.2020.103201

Leandro, R., 2016. Caracterização Tectonoestratigráfica da Sequência Terrígena da Formação Capiru Na Região de Morro Grande, Colombo - Pr., Dissertação de Mestrado. Universidade Federal do Paraná. https://doi.org/10.1017/CBO9781107415324.004

Leite, R.J., 2003. Petrogênese e geocronologia U-Pb do magmatismo granítico tardi- a pós-orogênico no batólito Agudos Grandes (SP). Universidade de São Paulo.

Leite, R.J., Heaman, L.M., de Assis Janasi, V., Martins, L., Creaser, R.A., 2007. The late- to postorogenic transition in the Neoproterozoic Agudos Grandes Granite Batholith (Apiaí Domain, SE Brazil): Constraints from geology, mineralogy, and U-Pb geochronology. Journal of South American Earth Sciences 23, 193–212. https://doi.org/10.1016/j.jsames.2006.09.022

Li, Z.X., Bogdanova, S. V., Collins, A.S., Davidson, A., De Waele, B., Ernst, R.E., Fitzsimons, I.C.W., Fuck, R.A., Gladkochub, D.P., Jacobs, J., Karlstrom, K.E., Lu, S., Natapov, L.M., Pease, V., Pisarevsky, S.A., Thrane, K., Vernikovsky, V., 2008. Assembly, configuration, and break-up history of Rodinia: A synthesis. Precambrian Research 160, 179–210. https://doi.org/10.1016/j.precamres.2007.04.021

Lobato, M., Heilbron, M., Torós, B., Ragatky, D., Dantas, E., 2015. Provenance of the Neoproterozoic high-grade metasedimentary rocks of the arc-related Oriental Terrane of the Ribeira belt: Implications for Gondwana amalgamation. Journal of South American Earth Sciences 63, 260–278. https://doi.org/10.1016/j.jsames.2015.07.019

Ludwig, K.R., 2003. A Geochronological Toolkit for Microsoft Excel. Berkeley Geochronology Center, Special Publication. 4, 71.

Machado, R., Dehler, N.M., Vasconcelos, P., 2007. 40Ar/39Ar ages (600-570 Ma) of the Serra do Azeite transtensional shear zone: Evidence for syncontractional extension in the Cajati area, southern Ribeira belt. Anais Da Academia Brasileira de Ciencias 79, 713–723.

Maurer, V.C., 2016. Caracterização geocronológica (U-Pb), geoquímica e isotópica 9Sr, Nd, Hf) do Complexo Rio Capivari no Terreno Embu. Universidade de São Paulo.

Meira, V.T., 2014. Evolução Tectono-Metamórfica Neoproterozóica dos Complexos Embu e Costeiro no Contexto de Formação do Gondwana Ocidental (Leste do Estado de São Paulo). Universidade de São Paulo.

Meira, V.T., Garcia-Casco, A., Hyppolito, T., Juliani, C., Schorscher, J.H.D., 2019a.

Tectono-Metamorphic Evolution of the Central Ribeira Belt, Brazil: A Case of Late Neoproterozoic Intracontinental Orogeny and Flow of Partially Molten Deep Crust During the Assembly of West Gondwana. Tectonics 38, 3182–3209. https://doi.org/10.1029/2018TC004959

Meira, V.T., García-Casco, A., Juliani, C., Almeida, R.P., Schorscher, J.H.D., 2015. The role of intracontinental deformation in supercontinent assembly: Insights from the Ribeira Belt, Southeastern Brazil (Neoproterozoic West Gondwana). Terra Nova 27, 206–217. https://doi.org/10.1111/ter.12149

Meira, V.T., Garcia-Casco, A., Juliani, C., Schorscher, J.H.D., 2019b. Late Tonian within-plate mafic magmatism and Ediacaran partial melting and magmatism in the Costeiro Domain, Central Ribeira Belt, Brazil. Precambrian Research 334, 105440. https://doi.org/10.1016/j.precamres.2019.105440

Mora, C.A.S., Campanha, G.A. da C., Wemmer, K., 2013. Microstructures and K-Ar illite fine-fraction ages of the cataclastic rocks associated to the Camburu Shear Zone, Ribeira Belt, Southeastern Brazil. Brazilian Journal of Geology 43, 607–622. https://doi.org/10.5327/z2317-48892013000400003

Mori, P.E., Reeves, S., Correia, C.T., Haukka, M., 1999. Development of a fused glass disc XRF facility and comparison with pressed powder pellet technique at Instituto de Geociências, São Paulo University. Revista Brasileira de Geociencias 29, 441–446. https://doi.org/10.5327/rbg.v29i3.715

Mullen, E.D., 1983. MnO/TiO2/P2O5: a minor element discriminant for basaltic rocks of oceanic environments and its implications for petrogenesis. Earth and Planetary Science Letters 62, 53–62. https://doi.org/10.1016/0012-821X(83)90070-5

Murphy, D.T., Allen, C.M., Ghidan, O., Dickson, A., Hu, W.P., Briggs, E., Holder, P.W., Armstrong, K.F., 2020. Analysing Sr isotopes in low-Sr samples such as single insects with inductively coupled plasma tandem mass spectrometry using N2O as a reaction gas for in-line Rb separation. Rapid Communications in Mass Spectrometry 34, 1–12. https://doi.org/10.1002/rcm.8604

Navarro, M.S., Andrade, S., Ulbrich, H., Gomes, C.B., Girardi, V.A.V., 2008. The direct determination of rare earth elements in basaltic and related rocks using ICP-MS: Testing the efficiency of microwave oven sample decomposition procedures. Geostandards and Geoanalytical Research 32, 167–180. https://doi.org/10.1111/j.1751-908X.2008.00840.x

Neumann, B., 2000. Texture development of recrystallised quartz polycrystals unravelled

by orientation and misorientation characteristics. Journal of Structural Geology 22, 1695–1711. https://doi.org/10.1016/S0191-8141(00)00060-2

O'Sullivan, G., Chew, D., Kenny, G., Henrichs, I., Mulligan, D., 2020. The trace element composition of apatite and its application to detrital provenance studies. Earth-Science Reviews 201, 103044. https://doi.org/10.1016/j.earscirev.2019.103044

O'Sullivan, G.J., Thakurdin, Y., Bolhar, R., Horváth, P., Hoare, B.C., Collerson, K.D., 2021. The Great Falls Tectonic Zone after the assembly of Laurentia: evidence for long-term tectonic stability from xenolith apatite. Lithos 384–385, 105977. https://doi.org/10.1016/j.lithos.2021.105977

Orihashi, Y., Nakai, S., Hirata, T., 2008. U-Pb age determination for seven standard zircons using inductively coupled plasma-mass spectrometry coupled with frequency quintupled Nd-YAG (λ = 213 nm) laser ablation system: Comparison with LA-ICP-MS zircon analyses with a NIST glass reference materia. Resource Geology 58, 101–123. https://doi.org/10.1111/j.1751-3928.2008.00052.x

Oriolo, S., Oyhantçabal, P., Wemmer, K., Siegesmund, S., 2017. Contemporaneous assembly of Western Gondwana and final Rodinia break-up: Implications for the supercontinent cycle. Geoscience Frontiers 8, 1431–1445. https://doi.org/10.1016/j.gsf.2017.01.009

Oyhantçabal, P., Wagner-Eimer, M., Wemmer, K., Schulz, B., Frei, R., Siegesmund, S., 2012. Paleo- and Neoproterozoic magmatic and tectonometamorphic evolution of the Isla Cristalina de Rivera (Nico Pérez Terrane, Uruguay). International Journal of Earth Sciences 101, 1745–1762. https://doi.org/10.1007/s00531-012-0757-4

Passarelli, C.R., Basei, M.A.S., Prazeres-Filho, H.J., Siga, O., Szabó, G.A.J., Marco-Neto, J., 2007. Structural and geochronological constraints on the evolution of the Juréia Massif, Registro Domain, State of São Paulo, Brazil. Anais Da Academia Brasileira de Ciencias 79, 441–455. https://doi.org/10.1590/s0001-37652007000300008

Passarelli, C.R., Basei, M.A.S., Wemmer, K., Siga Júnior, O., Oyhantc, P., 2011. Major shear zones of southern Brazil and Uruguay : escape tectonics in the eastern border of Rio de La plata and Paranapanema cratons during the Western Gondwana amalgamation. International Journal of Earth Sciences 100, 391–414. https://doi.org/10.1007/s00531-010-0594-2

Passarelli, C.R., Verma, S.K., Mcreath, I., Basei, M.Â.S., Siga Júnior, O., 2019. Tracing the history from Rodinia break-up to the Gondwana amalgamation in the Embu

Terrane, southern Ribeira Belt, Brazil. Lithos. https://doi.org/10.1016/j.lithos.2019.05.024

Passchier, C.W., Trouw, R.A.J., 2005. Microtectonics. Springer Berlin Heidelberg.

Patiño Douce, A.E., Harris, N., 1998. Experimental constraints on Himalayan anatexis. Journal of Petrology 39, 689–710. https://doi.org/10.1093/petroj/39.4.689

Paton, C., Hellstrom, J., Paul, B., Woodhead, J., Hergt, J., 2011. Iolite: Freeware for the visualisation and processing of mass spectrometric data. Journal of Analytical Atomic Spectrometry 26, 2508–2518. https://doi.org/10.1039/c1ja10172b

Payne, J.L., Hand, M., Barovich, K.M., Wade, B.P., 2008. Temporal constraints on the timing of high-grade metamorphism in the northern Gawler Craton: Implications for assembly of the Australian Proterozoic. Australian Journal of Earth Sciences 55, 623–640. https://doi.org/10.1080/08120090801982595

Pearce, J.A., 2008. Geochemical fingerprinting of oceanic basalts with applications to ophiolite classification and the search for Archean oceanic crust. Lithos 100, 14–48. https://doi.org/10.1016/j.lithos.2007.06.016

Pearce, J.A., 1996. A User's Guide to Basalto Discriminant Diagrams., Geological Association of Canada, Short Course Notes.

Pearce, J.A., Cann, J.R., 1973. Tectonic setting of basic volcanic rocks determined using trace element analyses. Earth and Planetary Science Letters 19, 290–300. https://doi.org/10.1016/0012-821X(73)90129-5

Pearce, J.A., Thirlwall, M.F., Ingram, G., Murton, B.J., Arculus, R.J., Van Der Laan, S.R., 1992. Isotopic evidence for the origin of boninites and related rocks drilled in the Izu-Bonin (Ogasawara) Forearc, Leg 125. Proc., Scientific Results, ODP, Leg 125, Bonin/Mariana Region 125, 237–262. https://doi.org/10.2973/odp.proc.sr.125.134.1992

Pearce, T.H., Gorman, B.E., Birkett, T.C., 1975. The TiO_2-K_2O-P_2O_5 Diagram: A Method of Discriminating Between Oceanic and Non-Oceanic Basalts. Earth and Planetary Science Letters 24, 419–426.

Peixoto, C. de A., Heilbron, M., Ragatky, D., Armstrong, R., Dantas, E., de Morisson Valeriano, C., Simonetti, A., 2017. Tectonic evolution of the Juvenile Tonian Serra da Prata magmatic arc in the Ribeira belt, SE Brazil: Implications for early west Gondwana amalgamation. Precambrian Research 302, 221–254. https://doi.org/10.1016/j.precamres.2017.09.017

Percival, J.J., Konopásek, J., Anczkiewicz, R., Ganerød, M., Sláma, J., de Campos, R.S.,

Bitencourt, M. de F., 2022. Tectono-Metamorphic Evolution of the Northern Dom Feliciano Belt Foreland, Santa Catarina, Brazil: Implications for Models of Subduction-Driven Orogenesis. Tectonics 41, e2021TC007014. https://doi.org/https://doi.org/10.1029/2021TC007014

Perrotta, M.M., 1996. POTENCIAL AURÍFERO DE UMA REGIÃO NO VALE DO RIBEIRA , SÃO PAULO , ESTIMADO POR MODELAGEM DE DADOS GEOLÓGICOS , SISTEMA DE INFORMAÇÕES GEOGRÁFICAS . Mônica Mazzini Perrotta Tese de Doutoramento Programa de Pós-Graduação em Geoquími. Universidade de São Paulo.

Perrotta, M.M., Salvador, E.D., Lopes, R.C., D'Agostino, L.Z., Peruffo, N., Gomes, S.D., Sachs, L.L.B., Meira, V.T., Garcia, M.G.M., Lacerda Filho, J.V., 2005. Mapa geológico do estado de São Paulo. Escala: 1:750.000.

Pertille, J., Hartmann, L.A., Santos, J.O.S., N.J., M., Armstrong, R., 2017. Reconstructing the Cryogenian–Ediacaran evolution of the Porongos fold and thrust belt, Southern Brasiliano Orogen, based on Zircon U–Pb–Hf–O isotopes. International Geology Review 59, 1532–1560. https://doi.org/10.1080/00206814.2017.1285257

Philipp, R.P., Pimentel, M.M., Chemale, F., 2016. Tectonic evolution of the Dom Feliciano Belt in Southern Brazil: Geological relationships and U-Pb geochronology. Brazilian Journal of Geology 46, 83–104. https://doi.org/10.1590/2317-4889201620150016

Pinto, V.M., Debruyne, D., Hartmann, L.A., Queiroga, G.N., Lana, C., Fragoso César, B.A.M., Porcher, C., Castro, M.P., Laux, J., 2021. Metamorphic evolution of a Tonian eclogite associated with an island arc of the southern Brasiliano Orogen. Precambrian Research 366. https://doi.org/10.1016/j.precamres.2021.106414

Polat, A., Hofmann, A.W., Rosing, M.T., 2002. Boninite-like volcanic rocks in the 3.7-3.8 Ga isua greenstone belt, West Greenland: Geochemical evidence for intra-oceanic subduction zone processes in the early earth. Chemical Geology 184, 231–254. https://doi.org/10.1016/S0009-2541(01)00363-1

Porada, H., 1989. Pan-African rifting and orogenesis in Southern Equatorial Africa and Eastern Brazil. Precambrian Research 44, 103–136. https://doi.org/10.1016/0301-9268(89)90078-8

Porcher, C., Egydio-silva, M., Fernandes, L., Vauchez, A., 1995. Dados prelimineres do metamorfismo M1 da Faixa Ribeira: Região de Três Rios e Santo Antônio de Pádua (RJ). V Simpósio Nacional de Estudos Tectônicos. Gramado, 71–73.

Prazeres Filho, H.J. dos, 2005. Caracterização geológica e petrogenética do batólito granítico Três Córregos (PR-SP): geoquímica isotópica (Nd-Sr-Pb), idades (ID-TIMS/SHRIMP) e d18'O em zircão. https://doi.org/10.11606/T.44.2005.tde-29102015-131336

Ramsay, J.G., 1980. Shear zone geometry: A review. Journal of Structural Geology 2, 83–99. https://doi.org/10.1016/0191-8141(80)90038-3

Ribeiro, B. V., Finch, M.A., Cawood, P.A., Faleiros, F.M., Murphy, T.D., Simpson, A., Glorie, S., Tedeschi, M., Armit, R., Barrote, V.R., 2021. From microanalysis to supercontinents: insights from the Rio Apa Terrane into the Mesoproterozoic SW Amazonian Craton evolution during Rodinia assembly. Journal of Metamorphic Geology. https://doi.org/10.1111/jmg.12641

Ribeiro, B. V., Lagoeiro, L., Faleiros, F.M., Hunter, N.J.R., Queiroga, G., Raveggi, M., Cawood, P.A., Finch, M., Campanha, G.A.C., 2020a. Strain localization and fluid-assisted deformation in apatite and its influence on trace elements and U–Pb systematics. Earth and Planetary Science Letters 545, 116421. https://doi.org/10.1016/j.epsl.2020.116421

Ribeiro, B. V., Mulder, J.A., Faleiros, F.M., Kirkland, C.L., Cawood, P.A., O'Sullivan, G., Campanha, G.A.C., Finch, M.A., Weinberg, R.F., Nebel, O., 2020b. Using apatite to resolve the age and protoliths of mid-crustal shear zones: A case study from the Taxaquara Shear Zone, SE Brazil. Lithos 378–379, 105817. https://doi.org/10.1016/j.lithos.2020.105817

Ribeiro, B. V, Faleiros, F.M., Campanha, G.A.C., Lagoeiro, L., Weinberg, R.F., Hunter, N.J.R., 2019. Tectonophysics Kinematics , nature of deformation and tectonic setting of the Taxaquara Shear Zone , a major transpressional zone of the Ribeira Belt (SE Brazil). Tectonophysics 751, 83–108. https://doi.org/10.1016/j.tecto.2018.12.025

Ricardo, B.S., Faleiros, F.M., Moraes, R., Siga Júnior, O., Campanha, G.A.C., 2020. Tectonic implications of juxtaposed high- and low-pressure metamorphic field gradient rocks in the Turvo-Cajati Formation, Curitiba Terrane, Ribeira Belt, Brazil. Precambrian Research 345, 105766. https://doi.org/10.1016/j.precamres.2020.105766

Rubatto, D., Hermann, J., Berger, A., Engi, M., 2009. Protracted fluid-induced melting during Barrovian metamorphism in the Central Alps. Contributions to Mineralogy and Petrology 158, 703–722. https://doi.org/10.1007/s00410-009-0406-5

Sadowski, G.R., 1991. A megafalha de Cubatão no Sudeste Brasileiro. Boletim IG, Instituto de Geociências 22, 15–28.

Sadowski, G.R., Motidome, M.J., 1987. Brazilian megafaults. Revista Geologica de Chile 31, 61–75.

Sadowski, H.G.R.&, 1976. Considerações sobre a estratigrafia do Pré-Cambriano na Região de São Paulo. Boletim IG, Instituto de Geociências 9, 107–112.

Santiago, R., Caxito, F. de A., Pedrosa-Soares, A., Neves, M.A., Dantas, E.L., 2020. Tonian island arc remnants in the northern Ribeira orogen of Western Gondwana: The Caxixe batholith (Espírito Santo, SE Brazil). Precambrian Research 351, 105944. https://doi.org/10.1016/j.precamres.2020.105944

Santos, L. da R., Leandro, R., Bahniuk, A., Cury, L.F., 2018. Low-temperature metamorphism in the Capiru Formation, Morro Grande Synform, Southern Ribeira Belt. Brazilian Journal of Geology 48, 95–113. https://doi.org/10.1590/2317-4889201820170090

Santosh, M., Maruyama, S., Sato, K., 2009. Anatomy of a Cambrian suture in Gondwana: Pacific-type orogeny in southern India? Gondwana Research 16, 321–341. https://doi.org/10.1016/j.gr.2008.12.012

Sato, K., Siga, O., Da Silva, J.A., McReath, I., Dunyi, L., Iizuka, T., Rino, S., Hirata, T., Sproesser, W., Basei, M.A.S., 2009. In situ isotopic analyses of U and Pb in zircon by remotely operated SHRIMP II, and Hf by LA-ICP-MS: An example of dating and genetic evolution of zircon by 176Hf/177Hf from the Ita quarry in the Atuba Complex, Se Brazil. Geologia USP - Serie Cientifica 9, 61–69.

Sato, K., Siga, O., Nutman, A.P., Basei, M.A.S., McReath, I., Kaulfuss, G., 2003. The Atuba Complex, Southern South American platform: Archean components and paleoproterozoic to neoproterozoic tectonothermal events. Gondwana Research 6, 251–263. https://doi.org/10.1016/S1342-937X(05)70974-6

Sawyer, E.W., 2008. Atlas of Migmatites. Canadian Science Publishing. https://doi.org/10.1139/9780660197876

Schulz, B., 2021. Monazite Microstructures and Their Interpretation in Petrochronology. Frontiers in Earth Science 9. https://doi.org/10.3389/feart.2021.668566

Shervais, J.W., 1982. TiV plots and the petrogenesis of modern and ophiolitic lavas. Earth and Planetary Science Letters 59, 101–118. https://doi.org/10.1016/0012-821X(82)90120-0

Siga Junior, O., 1995. Domínios Tectônicos do Sudeste do Paraná e Nordeste de Santa

Catarina: Geocronologia e Evolução crustal. Universidade de São Paulo.

Siga Júnior, O., Angelo, Basei, S., Sato, K., Passarelli, C.R., Nutman, A., Mcreath, I., Prazeres Filho, H.J. dos, 2011a. Calymmian (1 .50 e 1.45 Ga) magmatic records in Votuverava and Perau sequences , south-southeastern Brazil : Zircon ages and Nd e Sr isotopic geochemistry. Journal of South American Earth Sciences 32, 301–308. https://doi.org/10.1016/j.jsames.2011.03.015

Siga Júnior, O., Basei, M.A.S., Nutman, A., Sato, K., McReath, I., Passarelli, C.R., Liu, D., 2011b. Extensional and Colisional Magmatic Records in the Apiaí Terrane, South-Southeastern Brazil: Integration of Geochronological U-Pb Zircon Ages. Geologia USP - Serie Cientifica 11, 149–175.

Siga Júnior, O., Basei, M.A.S., Passarelli, C.R., Sato, K., Cury, L.F., McReath, I., 2009. Lower and Upper Neoproterozoic magmatic records in Itaiacoca Belt (Paraná-Brazil): Zircon ages and lithostratigraphy studies. Gondwana Research 15, 197–208. https://doi.org/10.1016/j.gr.2008.11.002

Siga Júnior, O., Basei, M.A.S., Reis Neto, J.M., Machiavelli, A., Harara, O.M., 1995. O complexo Atuba: um cinturão paleoproterozóico intensamente retrabalhado no Neoproterozóico. Boletim IG-USP. Série Científica 26, 69. https://doi.org/10.11606/issn.2316-8986.v26i0p69-98

Siga Júnior, O., Cury, L.F., Mcreath, I., Maria, L., Leite, D.A., Sato, K., Basei, M.A.S., Passarelli, C.R., 2011c. Geology and geochronology of the Betara region in south-southeastern Brazil: Evidence for possible Statherian (1.80 – 1.75 Ga) and Calymmian (1.50 –1.45 Ga) extension events. Gondwana Research 19, 260–274. https://doi.org/10.1016/j.gr.2010.06.003

Silva, B.Y.B., 2017. Evolução Tectônica Da Porção Central Do Terreno Embu Ao Norte Da Zona De Cisalhamento Taxaquara-Guararema Terreno Embu Ao Norte Da Zona De Cisalhamento Taxaquara-Guararema. University of São Paulo.

Sláma, J., Košler, J., Condon, D.J., Crowley, J.L., Gerdes, A., Hanchar, J.M., Horstwood, M.S.A., Morris, G.A., Nasdala, L., Norberg, N., Schaltegger, U., Schoene, B., Tubrett, M.N., Whitehouse, M.J., 2008. Plešovice zircon - A new natural reference material for U-Pb and Hf isotopic microanalysis. Chemical Geology 249, 1–35. https://doi.org/10.1016/j.chemgeo.2007.11.005

Sobrinho, J.M.A., Janasi, V.A., Simonetti, A., 2011. The Ilha Anchieta Quartz Monzonite : the southernmost expression of ca . 500 Ma post-collisional magmatism in the Ribeira Belt. Anais Da Academia Brasileira de Ciencias 83, 891–906.

Spear, F.S., Kohn, M.J., Cheney, J.T., 1999. P -T paths from anatectic pelites. Contributions Mineral Petrology 134, 17–32.

Stallard, A., Shelley, D., 1995. Quartz c-axes parallel to stretching directions in very low-grade metamorphic rocks. Tectonophysics 249, 31–40. https://doi.org/10.1016/0040-1951(95)00040-T

Stein, D.P., Campanha, G.A. da C., Fernandes, L.A., 1983. Geologia da Folha Pilar do Sul (SF.23-Y-C-IV-4). Estado de São Paulo. São Paulo.

Stipp, M., Stünitz, H., Heilbronner, R., Schmid, S.M., 2002. The eastern Tonale fault zone: A "natural laboratory" for crystal plastic deformation of quartz over a temperature range from 250 to 700 °C. Journal of Structural Geology 24, 1861–1884. https://doi.org/10.1016/S0191-8141(02)00035-4

Sun, S.S., McDonough, W.F., 1989. Chemical and isotopic systematics of oceanic basalts: Implications for mantle composition and processes. Geological Society Special Publication 42, 313–345. https://doi.org/10.1144/GSL.SP.1989.042.01.19

Tassinari, C.C.G., 1988. As idades das rochas e dos eventos metamórficos da porção sudeste do estado de São Paulo e sua evolução crustal. Universidade de São Paulo.

Tassinari, C.C.G., Campos Neto, M. da C., 1988. Precambrian continental crust evolution of Southeastern São Paul State, Brazil, based on isotopic evidence. Geochim. Brasil 2, 175–183.

Tassinari, C.C.G., Munhá, J.M.U., Ribeiro, A., Correia, C.T., 2001. Neoproterozoic oceans in the Ribeira belt (southeastern Brazil): The Pirapora do bom Jesus ophiolitic complex. Episodes 24, 245–251. https://doi.org/10.18814/epiiugs/2001/v24i4/004

Thomson, S.N., Gehrels, G.E., Ruiz, J., Buchwaldt, R., 2012. Routine low-damage apatite U-Pb dating using laser ablation-multicollector- ICPMS. Geochemistry, Geophysics, Geosystems 13, 1–23. https://doi.org/10.1029/2011GC003928

Torquato, J.R., Cordani, 1981. Brazil-Africa geological links. Earth Science Reviews 17, 155–176. https://doi.org/10.1016/0012-8252(81)90010-6

Trouw, R.A.J., Peternel, R., Ribeiro, A., Heilbron, M., Vinagre, R., Duffles, P., Trouw, C.C., Fontainha, M., Kussama, H.H., 2013. A new interpretation for the interference zone between the southern Brasília belt and the central Ribeira belt, SE Brazil. Journal of South American Earth Sciences 48, 43–57. https://doi.org/10.1016/j.jsames.2013.07.012

Tsunogae, T., Uthup, S., Nyirongo, M.W., Takahashi, K., Rahman, M.S., Liu, Q.,

Takamura, Y., Tsutsumi, Y., 2021. Neoproterozoic crustal growth in southern Malawi: New insights from petrology, geochemistry, and U–Pb zircon geochronology, and implications for the Kalahari Craton–Congo Craton amalgamation. Precambrian Research 352, 106007. https://doi.org/10.1016/j.precamres.2020.106007

Tupinambá, M., Heilbron, M., Valeriano, C., Júnior, R.P., de Dios, F.B., Machado, N., Silva, L.G. do E., de Almeida, J.C.H., 2012. Juvenile contribution of the Neoproterozoic Rio Negro Magmatic Arc (Ribeira Belt, Brazil): Implications for Western Gondwana amalgamation. Gondwana Research 21, 422–438. https://doi.org/10.1016/j.gr.2011.05.012

Vauchez, A., Tommasi, A., Silva, A., Trompette, R., 1992. Tectônica de escape na terminação de um craton: A Faixa Ribeira. Congresso Brasileiro de Geologia. 373–374.

Vermeesch, P., 2018. IsoplotR: A free and open toolbox for geochronology. Geoscience Frontiers 9, 1479–1493. https://doi.org/10.1016/j.gsf.2018.04.001

Viegas, G., Menegon, L., Archanjo, C., 2016. Brittle grain-size reduction of feldspar, phase mixing and strain localization in granitoids at mid-crustal conditions (Pernambuco shear zone, NE Brazil). Solid Earth 7, 375–396. https://doi.org/10.5194/se-7-375-2016

Vieira, S.R.S.S., 1996. Estudo de processos metamórfico-metassomáticos nos Complexos Embu e Pilar no Bloco Juquitiba, SP. Universidade de São Paulo.

Vlach, S., 2008. Mineralogia, análise e datação de monazita com microssonda eletrônica e aplicações. Universidade de São Paulo.

Weber, W., Siga Junior, O., Sato, K., Neto, J.M. dos R., Basei, M.Â.S., Nutman, A.P., 2004. A Formação Água Clara na região de Araçaíba-SP: registro de uma bacia Mesoproterozoica. Boletim IG, Instituto de Geociências, USP 4, 101–110.

Werle, M., Hartmann, L.A., Queiroga, G.N., Lana, C., Pertille, J., Michelin, C.R.L., Remus, M.V.D., Roberts, M., Castro, M.P., Leandro, C.G., Savian, J.F., 2020. Oceanic crust and mantellic evidence on the evolution of tonian-cryogenian ophiolites, southern Brasiliano Orogen. Precambrian Research 351, 105979. https://doi.org/10.1016/j.precamres.2020.105979

White, R.W., Powell, R., Halpin, J.A., 2004. Spatially-focussed melt formation in aluminous metapelites from Broken Hill, Australia. Journal of Metamorphic Geology 22, 825–845. https://doi.org/10.1111/j.1525-1314.2004.00553.x

White, R.W., Powell, R., Holland, T.J.B., 2001. Calculation of partial melting equilibria in the system Na2O-CaO-K2O-FeO-MgO-Al2O3-SiO2-H2O (NCKFMASH). Journal of Metamorphic Geology 19, 139–153. https://doi.org/10.1046/j.0263-4929.2000.00303.x

White, R.W., Powell, R., Johnson, T.E., 2014. The effect of Mn on mineral stability in metapelites revisited: New a-x relations for manganese-bearing minerals. Journal of Metamorphic Geology 32, 809–828. https://doi.org/10.1111/jmg.12095

Williams, I.S., 1997. U-Th-Pb Geochronology by Ion Microprobe., Applications of Microanalytical Techniques to Understanding Mineralizing Processes. https://doi.org/10.5382/Rev.07.01

Wilson, M., 1989. Igneous Petrogenesis, Journal of Chemical Information and Modeling. Chapman & Hall.

Wilson, M. (B. M., 2007. Igneous petrogenesis. Dordrecht : Springer, [2007] ©2007.

Xia, L., Li, X., 2019. Basalt geochemistry as a diagnostic indicator of tectonic setting. Gondwana Research 65, 43–67. https://doi.org/10.1016/j.gr.2018.08.006

Xia, L.Q., 2014. The geochemical criteria to distinguish continental basalts from arc related ones. Earth-Science Reviews 139, 195–212. https://doi.org/10.1016/j.earscirev.2014.09.006

Yogi, M.T., 2019. Thermobaric and kinematic evolution of Anta Gorda Anticlinorium , Ribeira Belt : metamorphism record and shear deformation in a transpressional setting. São Paulo University.

Supplementary Information B. Petrographic and microstructural descriptions of the analysed samples for phase equilibria modelling and geochronology

Below, seven samples representative of the main lithotypes of the Embu Complex are described in detail: 45A, 12A, 10A, FM02B, FM27, AN26A, AN47.

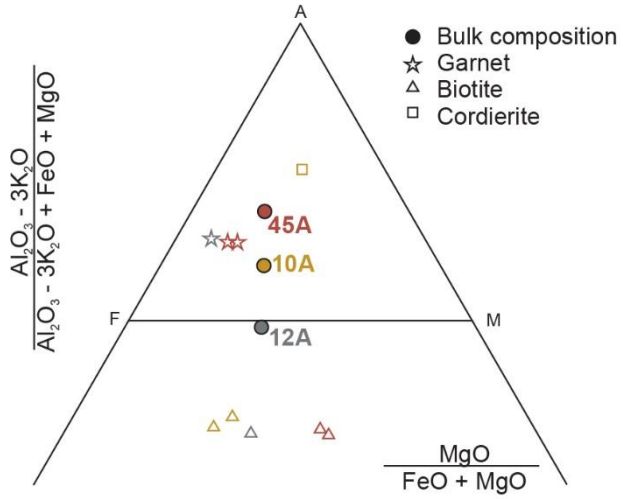

Figure 0.1. AFM compatibility diagram of the modelled metapelitic samples from the Embu Complex.

Sample 45A has a medium to coarse-grained (20 to 1500 µm) granolepidoblastic texture. A S_{cs} foliation is defined by the preferred orientation of biotite and garnet. The metamorphic mineral assemblage is represented by biotite (50 %), quartz (20 %), garnet (15 %) and sillimanite (15 %). Plagioclase, zircon, monazite and opaque minerals occur as accessory minerals. Biotite has a grain size between 20 and 500 µm and the large part of the crysyals occur in the matrix with plaque forms oriented parallel to the foliation with a reddish pleochroism. Sometimes it presents inclusions of opaque minerals and appears intergrowned with quartz in the matrix. Ocassionally, a brownish biotite without an apparent cleavage occur on garnet rims and on the matrix. Quartz occurs as anhedral crystals filling the interstices of the biotite and plagioclase in the matrix and sometimes is present as garnet inclusions. The grain size varies between 5 and 450 µm. Additionally, garnet occurs as rounded porfiroblasts (50 to 1500 µm) parallel to the S_{cs} foliation. It presents fractures orthogonal to the foliation and has quartz and opaque minerals inclusions. It presents irregular rims and sometimes they occur interlobated with quartz, biotite and sillimanite and sometimes are partially replaced by retrograde biotite along with fractures.

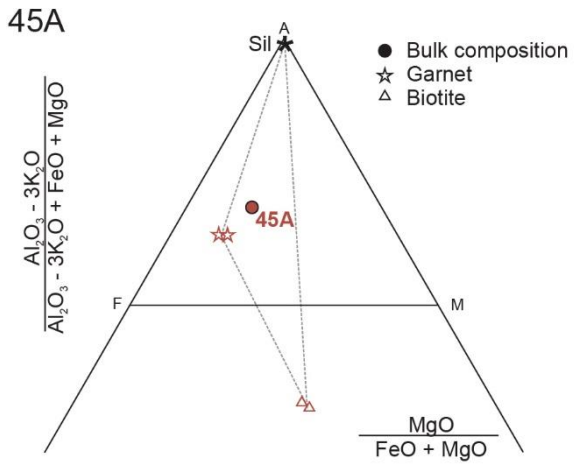

Figure 2. AFM compatibility diagram for the 45A sample.

Sample 12A has a medium to coarse-grained (50 to 2500 µm) granolepidoblastic texture. The S_{cs} foliation is defined by the preferred orientation of biotite and sillimanite. The metamorphic mineral assemblage is represented by quartz (45 %) + biotite (30 %) + sillimanite (10 %) + garnet (5 %) + K-feldspar (3 %) + leucosome (2 %). Zircon, monazite and opaque minerals occur as accessory minerals. Quartz has a grain size between 50 to 5000 µm with a subhedral to euhedral texture. Some grains have diffuse rims, being interpreted as an evidence of partial melting (Fig. 5e). Some crystals occur intergrown with K-feldspar, biotite and sillimanite or as K-feldspar inclusions. Biotite occurs as plates oriented according to foliation, preferably distributed around garnet or intergrown with sillimanite and quartz. Garnet porfiroblasts (50 to 2500 µm) have an anhedral texture being replaced by quartz and biotite. K-feldspar present subhedral to euhedral crystals. Some grains have a grain size up to 100 µm and occur dispersed in the matrix and other occur has subhedral porfiroblasts with a grain size up to 1500 µm. It is often intergrown with quartz grains and some grains contain rounded quartz inclusions. The leucosome has a coarse-grained granobastic texture (500 to 2500 µm) and is composed of unsegregated quartz and K-feldspar. K-feldspar with rounded quartz inclusions are frequent. It is interpreted to have formed by in situ partial melting.

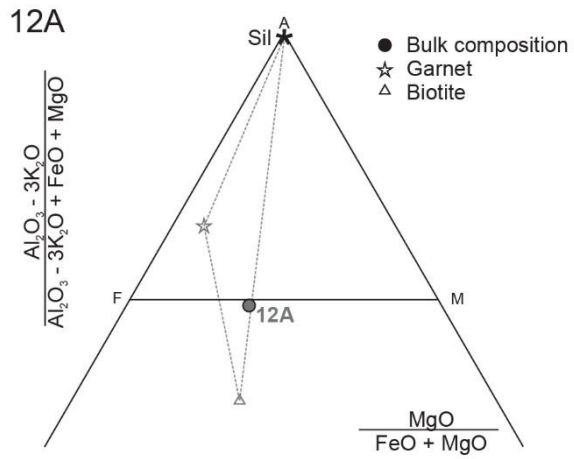

Figure 3. AFM compatibility diagram for the 12A sample.

Sample 10A corresponds to a transitional vein-structured migmatite. The residue is formed by biotite + sillimanite + cordierite + K-feldspar + plagioclase + quartz + ilmenite, and presents a fine to medium-grained lepidoblastic texture. The preferred orientation of biotite + muscovite + sillimanite defines the S_{cs} foliation. The leucosome presents a medium to coarse-grained granoblastic texture and occurs as in situ and in-source leucosomes according to the classification of Sawyer (2008) . In situ leucosomes are composed of quartz + plagioclase + cordierite with grains up to 0.5 mm. Cordierite occurs as a matrix phase with sillimanite inclusions. In-source leucosomes are composed of quartz + plagioclase + K-feldspar with grains up to 2 mm.

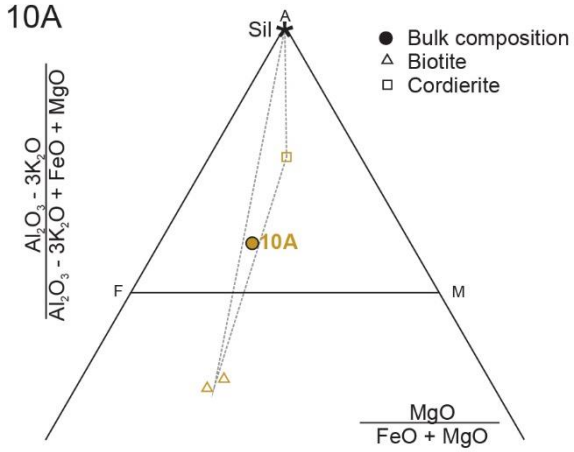

Figure 4. AFM compatibility diagram for the 10A sample.

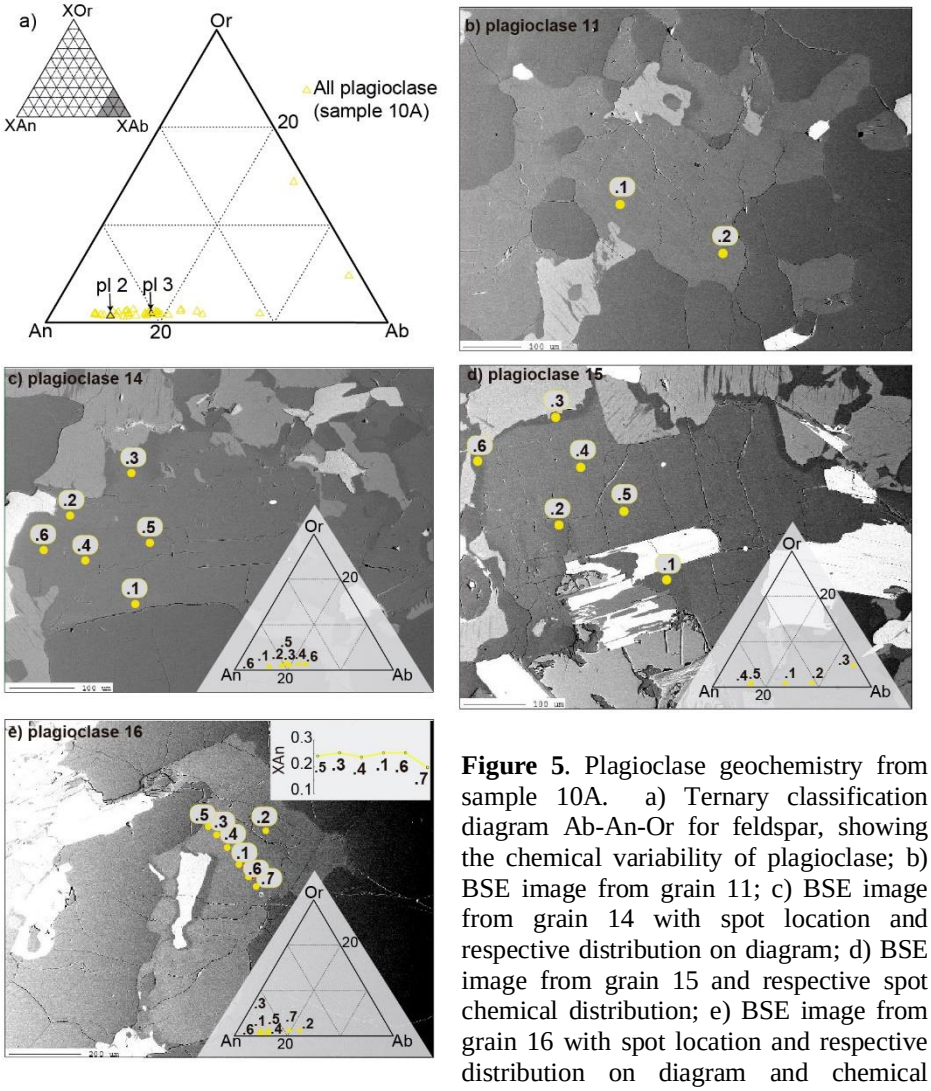

Figure 5. Plagioclase geochemistry from sample 10A. a) Ternary classification diagram Ab-An-Or for feldspar, showing the chemical variability of plagioclase; b) BSE image from grain 11; c) BSE image from grain 14 with spot location and respective distribution on diagram; d) BSE image from grain 15 and respective spot chemical distribution; e) BSE image from grain 16 with spot location and respective distribution on diagram and chemical profile.

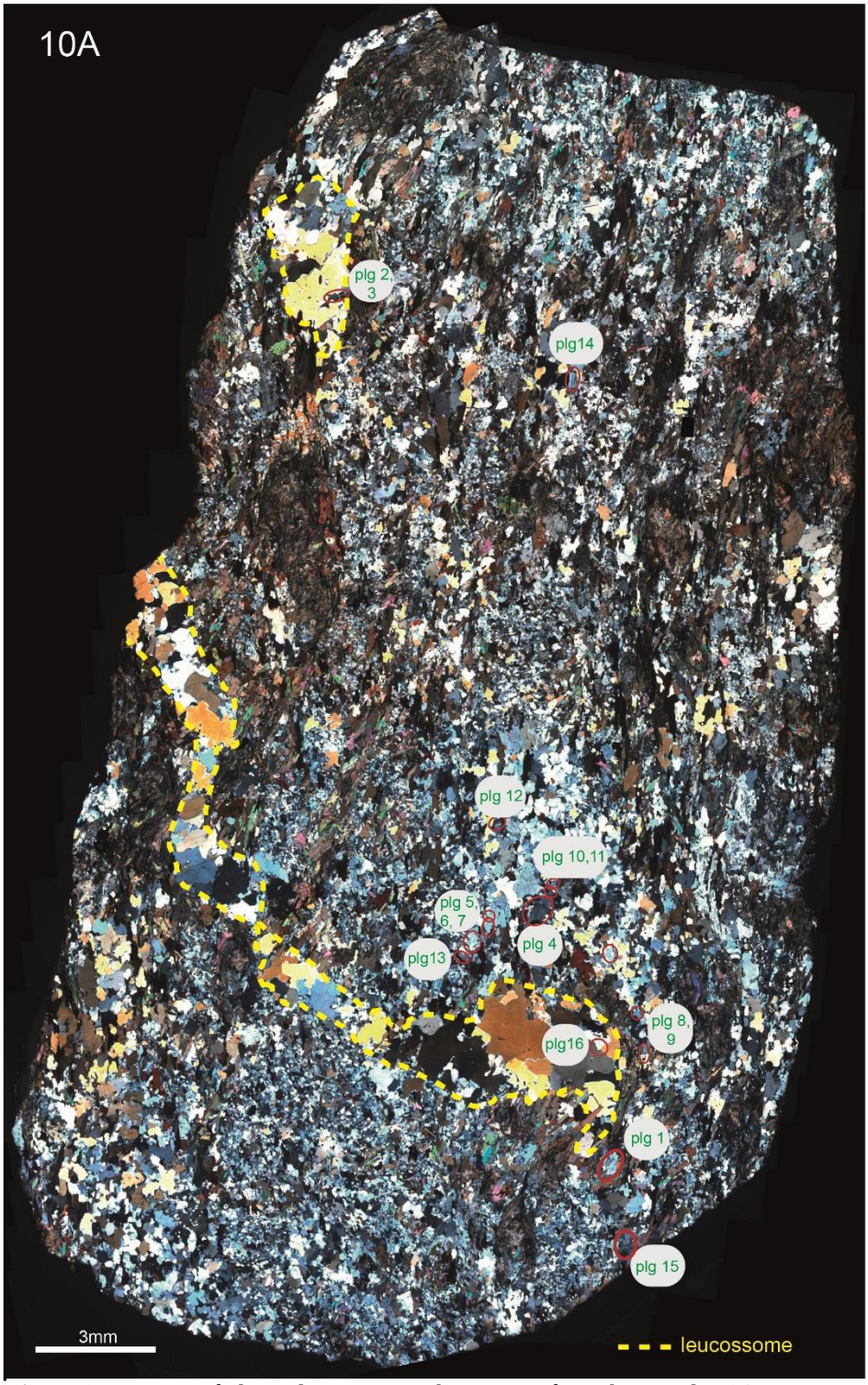

Figure 6. Location of plagioclase spots on thin section from the sample 10A.

Sample FM02B is a darkish medium to coarse-grained gneiss with an incipient S_{cs} defined by the preferred orientation of biotite. The metamorphic mineral assemblage is mainly composed of quartz, plagioclase, K-feldspar, biotite, garnet and sillimanite. Zircon, monazite, apatite and opaque minerals occur as accessory minerals.

Sample FM-27 is a migmatitic paragneiss representative of the regionally the most abundant lithotype of the Embu Complex. The rock presents a centimeter-thick compositional layering defined by alternating granitic leucosome and residual neosome composed of biotite, quartz, plagioclase, garnet, sillimanite, and subordinate muscovite. A schistosity (S_{cs}) parallel to the layering is primarily defined by preferred orientation of biotite and sillimanite. There is a S_2 schistosity defined by elongated quartz grains near perpendicular to and associated with folds defined by S_{cs} curvature. Quartz aggregates present core-and-mantle microstructures with elongated porphyroclasts mantled by aggregates of very fine-grained recrystallised grains, both oriented along the S_2. Recrystallised grains present a bimodal distribution of grain sizes, within the intervals 5 to 20 and 40 to 60 μm. The porphyroclasts present subgrains of the same size as the larger recrystallised grains.

Samples AN26A and AN47 are schistose quartzites with an interlobate granoblastic texture hosted by banded migmatitic paragneiss with residual neosome composed of biotite, quartz, sillimanite, plagioclase and K-feldspar and granitic leucosome.

Supplementary Information C. Table 1a. Biotite compositions (EMPA). Cations are calculated based on 11 oxygens.

Sample	12A										
Mineral	bt1	bt2	bt3	bt4	bt5	bt6	bt7	bt8	bti1.1	bti1.2	bti2.1
SiO_2	34.43	34.64	34.02	34.45	34.25	34.47	34.40	34.31	34.10	33.97	34.22
Al_2O_3	19.09	19.37	19.26	19.11	19.17	19.38	18.93	18.93	18.91	19.18	18.62
FeO	21.14	20.74	20.84	21.06	20.99	20.78	20.89	20.86	20.53	20.11	21.21
MnO	0.18	0.11	0.14	0.13	0.17	0.18	0.12	0.15	0.17	0.17	0.14
ZnO	0.02	0.02	0.08	0.04	0.11	0.05	0.04	0.10	0.06	0.07	0.07
Cl	0.01	0.03	0.00	0.00	0.02	0.00	0.01	0.03	0.00	0.01	0.00
K_2O	9.91	10.23	9.89	10.13	10.14	9.95	10.31	9.98	9.80	10.01	10.01
CaO	0.01	0.01	0.05	0.03	0.04	0.02	0.02	0.00	0.00	0.00	0.02
TiO_2	3.76	3.28	3.28	3.76	3.62	3.29	3.29	3.51	3.43	3.37	4.02
BaO	0.05	0.00	0.03	0.07	0.04	0.01	0.03	0.02	0.05	0.07	0.06
F	0.05	0.07	0.05	0.05	0.08	0.07	0.07	0.07	0.05	0.06	0.04
Na_2O	0.08	0.12	0.12	0.09	0.09	0.07	0.09	0.10	0.14	0.07	0.07
MgO	7.35	7.69	7.68	7.41	7.61	7.56	7.67	7.67	7.72	7.62	7.18
Total	96.08	96.30	95.45	96.33	96.32	95.83	95.88	95.72	94.96	94.71	95.66
O=F	0.05	0.06	0.05	0.04	0.07	0.06	0.07	0.06	0.05	0.05	0.04
O=Cl	0.00	0.01	0.00	0.00	0.01	0.00	0.00	0.01	0.00	0.00	0.00
Total	96.03	96.23	95.40	96.28	96.25	95.76	95.81	95.66	94.92	94.66	95.62
Si	2.64	2.64	2.62	2.63	2.62	2.64	2.64	2.64	2.64	2.63	2.64
Al	1.72	1.74	1.75	1.72	1.73	1.75	1.72	1.72	1.72	1.75	1.69
Fe^{2+}	1.35	1.32	1.34	1.35	1.34	1.33	1.34	1.34	1.33	1.30	1.37
Mn	0.01	0.01	0.01	0.01	0.01	0.01	0.01	0.01	0.01	0.01	0.01
Zn	0.00	0.00	0.00	0.00	0.01	0.00	0.00	0.01	0.00	0.00	0.00
Cl	0.00	0.00	0.00	0.00	0.00	0.00	0.00	0.00	0.00	0.00	0.00
K	0.97	1.00	0.97	0.99	0.99	0.97	1.01	0.98	0.97	0.99	0.99
Ca	0.00	0.00	0.00	0.00	0.00	0.00	0.00	0.00	0.00	0.00	0.00
Ti	0.22	0.19	0.19	0.22	0.21	0.19	0.19	0.20	0.20	0.20	0.23
Ba	0.00	0.00	0.00	0.00	0.00	0.00	0.00	0.00	0.00	0.00	0.00
F	0.01	0.02	0.01	0.01	0.02	0.02	0.02	0.02	0.01	0.01	0.01
Na	0.01	0.02	0.02	0.01	0.01	0.01	0.01	0.01	0.02	0.01	0.01
Mg	0.84	0.87	0.88	0.84	0.87	0.86	0.88	0.88	0.89	0.88	0.83
Total	7.78	7.81	7.81	7.79	7.82	7.79	7.83	7.81	7.80	7.80	7.78
X_{Fe}	0.62	0.60	0.60	0.61	0.61	0.61	0.60	0.60	0.60	0.60	0.62
X_{Mg}	0.38	0.40	0.40	0.39	0.39	0.39	0.40	0.40	0.40	0.40	0.38

$X_{Fe} = Fe^{2+}/(Fe^{2+} + Mg)$

bti2.2	bti3.1	bti3.2	bti4.1	bti4.2	btr1	btr2	btr3	btr4	btr5	btr6
34.01	34.14	34.18	34.36	34.04	33.46	34.11	33.68	34.07	33.81	34.17
18.66	19.03	19.29	19.59	19.60	19.16	19.14	19.12	18.86	19.11	19.03
21.27	21.24	20.80	20.36	20.66	20.43	20.71	20.59	21.25	20.95	20.88
0.14	0.16	0.16	0.14	0.13	0.09	0.14	0.13	0.14	0.14	0.10
0.06	0.06	0.09	0.08	0.04	0.05	0.05	0.08	0.07	0.05	0.08
0.01	0.01	0.01	0.00	0.01	0.01	0.01	0.00	0.02	0.02	0.00
10.00	9.77	9.93	9.92	9.73	9.88	10.13	10.15	10.05	9.99	9.90
0.01	0.01	0.01	0.02	0.00	0.00	0.00	0.00	0.00	0.00	0.00
3.76	3.53	3.59	3.35	3.17	3.32	3.42	3.66	3.28	3.47	3.39
0.08	0.04	0.03	0.06	0.13	0.04	0.06	0.07	0.04	0.05	0.03
0.05	0.07	0.04	0.07	0.07	0.06	0.07	0.06	0.08	0.05	0.05
0.05	0.11	0.07	0.06	0.10	0.09	0.07	0.08	0.10	0.09	0.12
7.41	7.43	7.33	7.68	7.55	8.01	7.85	7.79	7.64	7.39	7.76
95.52	95.60	95.53	95.69	95.23	94.61	95.74	95.40	95.58	95.11	95.51
0.05	0.06	0.04	0.06	0.06	0.06	0.06	0.05	0.07	0.05	0.04
0.00	0.00	0.00	0.00	0.00	0.00	0.00	0.00	0.00	0.00	0.00
95.47	95.54	95.49	95.62	95.17	94.55	95.68	95.34	95.51	95.06	95.47
2.63	2.63	2.63	2.63	2.63	2.60	2.62	2.60	2.63	2.62	2.63
1.70	1.73	1.75	1.77	1.78	1.76	1.73	1.74	1.72	1.75	1.73
1.38	1.37	1.34	1.30	1.33	1.33	1.33	1.33	1.37	1.36	1.35
0.01	0.01	0.01	0.01	0.01	0.01	0.01	0.01	0.01	0.01	0.01
0.00	0.00	0.01	0.00	0.00	0.00	0.00	0.00	0.00	0.00	0.00
0.00	0.00	0.00	0.00	0.00	0.00	0.00	0.00	0.00	0.00	0.00
0.99	0.96	0.98	0.97	0.96	0.98	0.99	1.00	0.99	0.99	0.97
0.00	0.00	0.00	0.00	0.00	0.00	0.00	0.00	0.00	0.00	0.00
0.22	0.20	0.21	0.19	0.18	0.19	0.20	0.21	0.19	0.20	0.20
0.00	0.00	0.00	0.00	0.00	0.00	0.00	0.00	0.00	0.00	0.00
0.01	0.02	0.01	0.02	0.02	0.02	0.02	0.01	0.02	0.01	0.01
0.01	0.02	0.01	0.01	0.01	0.01	0.01	0.01	0.01	0.01	0.02
0.85	0.85	0.84	0.88	0.87	0.93	0.90	0.90	0.88	0.85	0.89
7.80	7.80	7.78	7.79	7.79	7.83	7.82	7.83	7.83	7.81	7.81
0.62	0.62	0.61	0.60	0.61	0.59	0.60	0.60	0.61	0.61	0.60
0.38	0.38	0.39	0.40	0.39	0.41	0.40	0.40	0.39	0.39	0.40

Sample	42A															
Mineral	bt1	bt2	bt3	bt4	bt5	bt6	bt7	bt8	bt9	bt10	bt11	bti1	bti2	bti3	bti4	bti5
SiO_2	34.35	44.73	34.45	34.59	34.19	34.39	34.27	34.09	34.70	34.47	34.22	33.98	34.14	33.90	34.34	34.30
Al_2O_3	19.01	37.10	19.12	19.05	19.38	19.24	19.29	19.31	18.80	19.25	19.27	19.22	19.10	19.09	19.32	19.30
FeO	22.95	1.27	23.03	22.65	23.10	22.95	23.00	23.15	22.70	23.11	22.81	22.62	23.20	23.15	23.07	22.87
MnO	0.30	0.01	0.30	0.25	0.25	0.26	0.32	0.29	0.28	0.29	0.28	0.28	0.28	0.27	0.32	0.27
ZnO	0.02	0.01	0.01	0.03	0.07	0.04	0.08	0.07	0.05	0.04	0.07	0.07	0.07	0.05	0.06	0.04
Cl	0.05	0.01	0.05	0.09	0.03	0.02	0.03	0.07	0.06	0.03	0.05	0.02	0.05	0.05	0.05	0.05
K_2O	9.84	10.65	9.98	9.79	9.80	9.94	9.89	9.86	9.85	9.89	9.77	9.81	9.98	9.88	9.92	9.96
CaO	0.00	0.00	0.01	0.02	0.00	0.00	0.00	0.01	0.00	0.00	0.04	0.00	0.00	0.00	0.00	0.00
TiO_2	1.75	0.70	1.79	1.51	1.88	1.84	1.62	1.65	1.52	1.55	1.60	1.60	1.88	1.87	1.87	1.58
BaO	0.08	0.13	0.12	0.03	0.10	0.03	0.05	0.04	0.04	0.09	0.05	0.08	0.08	0.05	0.00	0.07
F	0.09	0.00	0.09	0.07	0.07	0.08	0.04	0.08	0.08	0.07	0.09	0.06	0.06	0.06	0.05	0.05
Na_2O	0.10	0.76	0.09	0.09	0.09	0.09	0.10	0.10	0.09	0.11	0.11	0.09	0.08	0.10	0.08	0.09
MgO	7.79	0.58	7.88	8.17	7.78	8.01	7.88	7.89	8.09	8.02	7.97	7.76	7.70	7.82	7.82	7.78
Total	96.32	95.94	96.92	96.33	96.74	96.89	96.58	96.60	96.25	96.92	96.32	95.59	96.61	96.29	96.91	96.36
O=F	0.08	0.00	0.08	0.06	0.06	0.07	0.04	0.07	0.07	0.06	0.08	0.06	0.05	0.05	0.05	0.05
O=Cl	0.01	0.00	0.01	0.02	0.01	0.00	0.01	0.01	0.01	0.01	0.01	0.00	0.01	0.01	0.01	0.01
Total	96.23	95.93	96.83	96.25	96.67	96.81	96.53	96.51	96.17	96.85	96.23	95.53	96.55	96.23	96.84	96.30
Si	2.65	2.97	2.64	2.66	2.63	2.64	2.64	2.63	2.67	2.64	2.64	2.64	2.63	2.62	2.63	2.64
Al	1.73	2.90	1.73	1.73	1.75	1.74	1.75	1.75	1.71	1.74	1.75	1.76	1.74	1.74	1.75	1.75
Fe^{2+}	1.48	0.07	1.48	1.46	1.48	1.47	1.48	1.49	1.46	1.48	1.47	1.47	1.50	1.50	1.48	1.47
Mn	0.02	0.00	0.02	0.02	0.02	0.02	0.02	0.02	0.02	0.02	0.02	0.02	0.02	0.02	0.02	0.02
Zn	0.00	0.00	0.00	0.00	0.00	0.00	0.00	0.00	0.00	0.00	0.00	0.00	0.00	0.00	0.00	0.00
Cl	0.01	0.00	0.01	0.01	0.00	0.00	0.00	0.01	0.01	0.00	0.01	0.00	0.01	0.01	0.01	0.01
K	0.97	0.90	0.98	0.96	0.96	0.97	0.97	0.97	0.97	0.97	0.96	0.97	0.98	0.97	0.97	0.98
Ca	0.00	0.00	0.00	0.00	0.00	0.00	0.00	0.00	0.00	0.00	0.00	0.00	0.00	0.00	0.00	0.00
Ti	0.10	0.03	0.10	0.09	0.11	0.11	0.09	0.10	0.09	0.09	0.09	0.09	0.11	0.11	0.11	0.09
Ba	0.00	0.00	0.00	0.00	0.00	0.00	0.00	0.00	0.00	0.00	0.00	0.00	0.00	0.00	0.00	0.00
F	0.02	0.00	0.02	0.02	0.02	0.02	0.01	0.02	0.02	0.02	0.02	0.02	0.01	0.01	0.01	0.01
Na	0.01	0.10	0.01	0.01	0.01	0.01	0.01	0.02	0.01	0.02	0.02	0.01	0.01	0.02	0.01	0.01
Mg	0.90	0.06	0.90	0.94	0.89	0.92	0.90	0.91	0.93	0.92	0.92	0.90	0.89	0.90	0.89	0.89
Total	7.89	7.04	7.90	7.89	7.88	7.89	7.89	7.91	7.89	7.90	7.90	7.89	7.90	7.90	7.89	7.89
X_{Fe}	0.62	0.55	0.62	0.61	0.62	0.62	0.62	0.62	0.61	0.62	0.62	0.62	0.63	0.62	0.62	0.62
X_{Mg}	0.38	0.45	0.38	0.39	0.38	0.38	0.38	0.38	0.39	0.38	0.38	0.38	0.37	0.38	0.38	0.38

Sample	44A													
Mineral	bt1	bt2	bt3	bt4	bt5	bt6	bt7.1	bt7.2	bt8	bt9	bt10	bt12	bti1.1	bt1.2
SiO_2	34.13	33.99	34.36	33.94	33.97	33.96	34.44	33.63	34.05	33.96	33.99	34.22	33.97	34.00
Al_2O_3	19.30	19.05	19.42	19.15	19.28	19.05	19.40	18.67	19.06	19.12	19.06	19.26	19.58	19.62
FeO	23.28	23.53	23.41	23.11	23.29	23.39	23.01	22.80	22.93	22.88	22.89	23.37	22.40	22.19
MnO	0.18	0.21	0.21	0.15	0.22	0.16	0.14	0.14	0.17	0.14	0.15	0.15	0.18	0.14
ZnO	0.07	0.07	0.07	0.02	0.05	0.07	0.12	0.05	0.05	0.07	0.02	0.06	0.03	0.05
Cl	0.04	0.00	0.03	0.04	0.03	0.03	0.04	0.01	0.04	0.02	0.03	0.02	0.01	0.00
K_2O	9.76	9.45	9.55	9.58	9.53	9.66	9.52	9.07	9.47	9.34	9.33	9.62	9.71	9.54
CaO	0.01	0.00	0.00	0.05	0.02	0.00	0.00	0.07	0.00	0.00	0.00	0.02	0.04	0.02
TiO_2	1.69	2.35	1.81	2.00	1.71	1.93	1.72	1.96	1.92	1.84	1.66	1.65	2.75	2.74
BaO	0.10	0.16	0.10	0.14	0.08	0.14	0.12	0.09	0.16	0.12	0.11	0.12	0.06	0.14
F	0.04	0.03	0.06	0.05	0.06	0.04	0.06	0.04	0.01	0.04	0.04	0.04	0.05	0.05
Na_2O	0.07	0.10	0.07	0.05	0.07	0.07	0.05	0.05	0.05	0.06	0.06	0.05	0.10	0.12
MgO	7.57	7.27	7.46	7.56	7.66	7.59	7.63	7.69	7.51	7.56	7.78	7.41	7.07	7.08
Total	96.23	96.21	96.54	95.84	95.97	96.10	96.25	94.27	95.43	95.15	95.12	95.99	95.94	95.68
O=F	0.04	0.03	0.05	0.04	0.05	0.03	0.05	0.04	0.01	0.03	0.03	0.04	0.04	0.04
O=Cl	0.01	0.00	0.01	0.01	0.01	0.01	0.01	0.00	0.01	0.00	0.01	0.00	0.00	0.00
Total	96.18	96.19	96.49	95.79	95.91	96.06	96.19	94.23	95.41	95.12	95.07	95.95	95.90	95.64
Si	2.64	2.63	2.64	2.63	2.63	2.63	2.65	2.64	2.65	2.65	2.65	2.65	2.62	2.63
Al	1.76	1.74	1.76	1.75	1.76	1.74	1.76	1.73	1.75	1.76	1.75	1.76	1.78	1.79
Fe^{2+}	1.50	1.52	1.51	1.50	1.51	1.52	1.48	1.50	1.49	1.49	1.49	1.51	1.45	1.43
Mn	0.01	0.01	0.01	0.01	0.01	0.01	0.01	0.01	0.01	0.01	0.01	0.01	0.01	0.01
Zn	0.00	0.00	0.00	0.00	0.00	0.00	0.01	0.00	0.00	0.00	0.00	0.00	0.00	0.00
Cl	0.00	0.00	0.00	0.01	0.00	0.00	0.01	0.00	0.00	0.00	0.00	0.00	0.00	0.00
K	0.96	0.93	0.94	0.95	0.94	0.95	0.93	0.91	0.94	0.93	0.93	0.95	0.96	0.94
Ca	0.00	0.00	0.00	0.00	0.00	0.00	0.00	0.01	0.00	0.00	0.00	0.00	0.00	0.00
Ti	0.10	0.14	0.10	0.12	0.10	0.11	0.10	0.12	0.11	0.11	0.10	0.10	0.16	0.16
Ba	0.00	0.00	0.00	0.00	0.00	0.00	0.00	0.00	0.00	0.00	0.00	0.00	0.00	0.00
F	0.01	0.01	0.01	0.01	0.01	0.01	0.01	0.01	0.00	0.01	0.01	0.01	0.01	0.01
Na	0.01	0.02	0.01	0.01	0.01	0.01	0.01	0.01	0.01	0.01	0.01	0.01	0.01	0.02
Mg	0.87	0.84	0.86	0.87	0.88	0.88	0.88	0.90	0.87	0.88	0.90	0.86	0.81	0.82
Total	7.88	7.84	7.85	7.86	7.87	7.87	7.85	7.84	7.84	7.84	7.85	7.86	7.82	7.81
X_{Fe}	0.63	0.64	0.64	0.63	0.63	0.63	0.63	0.62	0.63	0.63	0.62	0.64	0.64	0.64
X_{Mg}														

Sample	45A											
Mineral	bt1	bt2	bt3	bt4	bt5	bt6	bt7	bt8	bt9	bt10	bt11	bt12
SiO_2	35.59	35.53	35.26	35.72	35.51	35.72	35.41	35.55	35.87	35.57	35.75	35.45
Al_2O_3	18.28	18.37	18.14	18.32	18.38	18.20	18.52	18.04	18.75	18.31	18.50	18.33
FeO	16.89	17.18	17.44	16.94	16.83	16.25	16.37	16.76	16.50	16.88	16.15	16.68
MnO	0.01	0.04	0.03	0.00	0.00	0.02	0.01	0.04	0.01	0.01	0.01	0.00
ZnO	0.06	0.03	0.08	0.00	0.05	0.00	0.07	0.04	0.05	0.07	0.02	0.06
Cl	0.00	0.00	0.00	0.01	0.04	0.02	0.03	0.01	0.02	0.02	0.03	0.03
K_2O	10.29	10.05	9.99	10.15	9.97	10.09	10.29	10.17	9.92	10.29	10.42	10.20
CaO	0.00	0.01	0.02	0.01	0.00	0.03	0.00	0.00	0.00	0.03	0.03	0.00
TiO_2	4.27	3.79	4.12	4.07	4.01	3.88	4.08	3.93	3.73	4.09	3.78	4.12
BaO	0.08	0.16	0.13	0.24	0.13	0.12	0.09	0.11	0.01	0.19	0.10	0.12
F	0.10	0.08	0.07	0.09	0.08	0.09	0.10	0.10	0.08	0.09	0.08	0.09
Na_2O	0.16	0.19	0.14	0.15	0.20	0.19	0.14	0.17	0.24	0.17	0.15	0.16
MgO	11.58	11.43	11.28	11.59	11.54	11.84	11.59	11.95	11.88	11.59	11.90	11.51
Total	97.31	96.85	96.70	97.29	96.75	96.44	96.70	96.87	97.05	97.30	96.91	96.74
O=F	0.09	0.07	0.07	0.08	0.07	0.08	0.09	0.09	0.07	0.08	0.07	0.08
O=Cl	0.00	0.00	0.00	0.00	0.01	0.00	0.01	0.00	0.00	0.00	0.01	0.01
Total	97.22	96.77	96.64	97.21	96.67	96.36	96.60	96.78	96.97	97.22	96.83	96.66
Si	2.64	2.65	2.64	2.65	2.65	2.66	2.64	2.65	2.65	2.64	2.65	2.64
Al	1.60	1.61	1.60	1.60	1.61	1.60	1.63	1.58	1.63	1.60	1.62	1.61
Fe^{2+}	1.05	1.07	1.09	1.05	1.05	1.01	1.02	1.04	1.02	1.05	1.00	1.04
Mn	0.00	0.00	0.00	0.00	0.00	0.00	0.00	0.00	0.00	0.00	0.00	0.00
Zn	0.00	0.00	0.00	0.00	0.00	0.00	0.00	0.00	0.00	0.00	0.00	0.00
Cl	0.00	0.00	0.00	0.00	0.01	0.00	0.00	0.00	0.00	0.00	0.00	0.00
K	0.97	0.96	0.95	0.96	0.95	0.96	0.98	0.97	0.94	0.97	0.99	0.97
Ca	0.00	0.00	0.00	0.00	0.00	0.00	0.00	0.00	0.00	0.00	0.00	0.00
Ti	0.24	0.21	0.23	0.23	0.22	0.22	0.23	0.22	0.21	0.23	0.21	0.23
Ba	0.00	0.00	0.00	0.01	0.00	0.00	0.00	0.00	0.00	0.01	0.00	0.00
F	0.02	0.02	0.02	0.02	0.02	0.02	0.02	0.02	0.02	0.02	0.02	0.02
Na	0.02	0.03	0.02	0.02	0.03	0.03	0.02	0.02	0.03	0.02	0.02	0.02
Mg	1.28	1.27	1.26	1.28	1.28	1.32	1.29	1.33	1.31	1.28	1.32	1.28
Total	7.83	7.83	7.82	7.82	7.82	7.82	7.83	7.85	7.82	7.84	7.84	7.83
X_{Fe}	0.45	0.46	0.46	0.45	0.45	0.43	0.44	0.44	0.44	0.45	0.43	0.45
X_{Mg}	0.55	0.54	0.54	0.55	0.55	0.57	0.56	0.56	0.56	0.55	0.57	0.55

Sample	10A												
Mineral	bt1	bt2	bt3	bt4.1	bt4.2	bt4.3	bt5	bt6	bt7	bt8	bt9	bt10	bti1
SiO_2	33.66	33.98	33.95	34.23	34.11	34.18	33.90	33.75	33.78	34.10	34.06	33.99	33.55
Al_2O_3	20.64	20.89	20.81	20.96	21.17	21.37	20.05	20.28	20.71	20.60	20.43	20.39	20.68
FeO	22.49	22.42	22.12	22.20	22.55	22.03	23.38	22.56	22.39	21.74	22.08	22.26	22.78
MnO	0.13	0.16	0.15	0.13	0.12	0.13	0.11	0.16	0.15	0.13	0.14	0.17	0.14
ZnO	0.05	0.01	0.10	0.07	0.05	0.04	0.07	0.03	0.01	0.06	0.08	0.06	0.03
Cl	0.02	0.05	0.03	0.04	0.04	0.04	0.07	0.04	0.06	0.04	0.03	0.03	0.02
K_2O	10.17	10.19	10.05	9.97	10.06	9.92	10.11	9.82	10.09	9.91	9.96	10.14	10.09
CaO	0.02	0.00	0.01	0.00	0.00	0.03	0.00	0.05	0.00	0.00	0.01	0.02	0.03
TiO_2	3.69	3.49	3.66	2.86	2.87	2.60	3.58	2.69	2.91	2.53	2.86	2.76	3.31
BaO	0.07	0.13	0.00	0.12	0.04	0.02	0.07	0.08	0.06	0.07	0.03	0.02	0.02
F	0.07	0.04	0.02	0.07	0.05	0.06	0.07	0.08	0.08	0.05	0.08	0.06	0.07
Na_2O	0.13	0.09	0.10	0.11	0.14	0.13	0.06	0.12	0.13	0.11	0.12	0.09	0.10
MgO	5.89	5.91	5.77	6.67	6.73	6.83	6.01	6.86	6.79	6.96	7.04	6.59	6.18
Total	97.03	97.37	96.77	97.43	97.92	97.39	97.48	96.50	97.15	96.32	96.91	96.59	96.99
O=F	0.06	0.04	0.02	0.06	0.05	0.06	0.06	0.07	0.07	0.04	0.07	0.05	0.06
O=Cl	0.00	0.01	0.01	0.01	0.01	0.01	0.02	0.01	0.01	0.01	0.01	0.01	0.00
Total	96.96	97.32	96.75	97.35	97.86	97.32	97.41	96.42	97.07	96.27	96.83	96.53	96.92
Si	2.57	2.59	2.59	2.59	2.58	2.59	2.59	2.59	2.58	2.61	2.60	2.61	2.57
Al	1.86	1.87	1.87	1.87	1.88	1.91	1.81	1.84	1.86	1.86	1.84	1.84	1.87
Fe^{2+}	1.44	1.43	1.41	1.41	1.42	1.39	1.49	1.45	1.43	1.39	1.41	1.43	1.46
Mn	0.01	0.01	0.01	0.01	0.01	0.01	0.01	0.01	0.01	0.01	0.01	0.01	0.01
Zn	0.00	0.00	0.01	0.00	0.00	0.00	0.00	0.00	0.00	0.00	0.00	0.00	0.00
Cl	0.00	0.01	0.00	0.01	0.00	0.00	0.01	0.00	0.01	0.01	0.00	0.00	0.00
K	0.99	0.99	0.98	0.96	0.97	0.96	0.99	0.96	0.98	0.97	0.97	0.99	0.99
Ca	0.00	0.00	0.00	0.00	0.00	0.00	0.00	0.00	0.00	0.00	0.00	0.00	0.00
Ti	0.21	0.20	0.21	0.16	0.16	0.15	0.21	0.16	0.17	0.15	0.16	0.16	0.19
Ba	0.00	0.00	0.00	0.00	0.00	0.00	0.00	0.00	0.00	0.00	0.00	0.00	0.00
F	0.02	0.01	0.01	0.02	0.01	0.02	0.02	0.02	0.02	0.01	0.02	0.01	0.02
Na	0.02	0.01	0.01	0.02	0.02	0.02	0.01	0.02	0.02	0.02	0.02	0.01	0.01
Mg	0.67	0.67	0.66	0.75	0.76	0.77	0.68	0.79	0.77	0.79	0.80	0.75	0.71
Total	7.80	7.79	7.76	7.81	7.82	7.81	7.81	7.84	7.84	7.82	7.83	7.83	7.82
X_{Fe}	0.68	0.68	0.68	0.65	0.65	0.64	0.69	0.65	0.65	0.64	0.64	0.65	0.67
X_{Mg}	0.32	0.32	0.32	0.35	0.35	0.36	0.31	0.35	0.35	0.36	0.36	0.35	0.33

Table 1b. Muscovite compositions (EMPA). Cations are calculated based on 11 oxygens.

Sample	12A										
Mineral	ms1	ms2	ms3	ms4	ms5.1	ms5.2	ms6.1	ms6.2	ms7	ms8	ms9
SiO_2	44.88	44.79	44.38	45.12	44.86	44.79	44.85	44.46	44.32	45.4	44.87
Al_2O_3	36.28	35.88	36.04	36.13	36.41	36.38	35.73	35.86	35.42	36.61	36.33
FeO	1.47	1.55	1.4	1.44	1.59	1.47	1.38	1.47	1.49	1.45	1.29
MnO	0	0.011	0	0.017	0.007	0.008	0	0	0	0.006	0.012
ZnO	0	0.003	0.062	0.032	0	0.022	0.009	0	0	0.011	0.031
Cl	0.006	0.005	0	0	0.003	0	0	0	0	0.014	0.041
K_2O	11.36	10.91	11.23	10.8	11.17	10.91	11.27	11.04	10.9	11.42	11.14
CaO	0	0	0	0	0.013	0	0	0	0.031	0.013	0
TiO_2	0.833	0.962	1.075	1.071	0.83	0.933	0.891	1.04	1.063	0.733	1.318
BaO	0.032	0.088	0.019	0.055	0.018	0.107	0.144	0.051	0.115	0.003	0.059
F	0.037	0.014	0.005	0.005	0.011	0.02	0.003	0.016	0.011	0.013	0.006
Na_2O	0.37	0.384	0.451	0.38	0.439	0.435	0.304	0.423	0.412	0.333	0.341
MgO	0.591	0.642	0.585	0.597	0.566	0.575	0.624	0.636	0.656	0.606	0.519
Total	95.860	95.238	95.248	95.647	95.917	95.649	95.205	94.996	94.417	96.612	95.957
O=F	0.033	0.012	0.004	0.004	0.010	0.018	0.003	0.014	0.010	0.012	0.005
O=Cl	0.001	0.001	0.000	0.000	0.001	0.000	0.000	0.000	0.000	0.003	0.009
Total	95.826	95.224	95.244	95.643	95.907	95.631	95.202	94.982	94.407	96.597	95.942
Si	2.993	3.002	2.981	3.005	2.989	2.989	3.011	2.990	3.000	3.001	2.985
Al	2.851	2.834	2.852	2.836	2.859	2.861	2.827	2.842	2.825	2.852	2.849
Fe^{2+}	0.082	0.087	0.079	0.080	0.089	0.082	0.077	0.083	0.084	0.080	0.072
Mn	0.000	0.001	0.000	0.001	0.000	0.000	0.000	0.000	0.000	0.000	0.001
Zn	0.000	0.000	0.003	0.002	0.000	0.001	0.000	0.000	0.000	0.001	0.002
Cl	0.001	0.001	0.000	0.000	0.000	0.000	0.000	0.000	0.000	0.002	0.005
K	0.966	0.933	0.962	0.918	0.949	0.929	0.965	0.947	0.941	0.963	0.945
Ca	0.000	0.000	0.000	0.000	0.001	0.000	0.000	0.000	0.002	0.001	0.000
Ti	0.042	0.048	0.054	0.054	0.042	0.047	0.045	0.053	0.054	0.036	0.066
Ba	0.001	0.002	0.000	0.001	0.000	0.003	0.004	0.001	0.003	0.000	0.002
F	0.008	0.003	0.001	0.001	0.002	0.004	0.001	0.003	0.002	0.003	0.001
Na	0.048	0.050	0.059	0.049	0.057	0.056	0.040	0.055	0.054	0.043	0.044
Mg	0.059	0.064	0.059	0.059	0.056	0.057	0.062	0.064	0.066	0.060	0.051
Total	7.051	7.025	7.050	7.007	7.044	7.029	7.033	7.039	7.032	7.041	7.022

Sample	42A												44A
Mineral	ms1	ms2	ms3	ms4	ms5	ms6	ms7	ms8	ms9.1	ms9.2	ms10	ms11	msi1
SiO_2	45	45.92	45.73	44.99	44.7	44.98	44.83	45.28	44.88	45.74	45.24	45	44.55
Al_2O_3	37.12	35.19	35.92	37.33	37.53	36.99	37.21	37.64	36.67	37.4	37.22	36.76	36.78
FeO	0.984	1.57	1.33	0.929	1.018	1.264	1.21	0.811	1.264	1.093	1.035	1.216	0.997
MnO	0	0.038	0.02	0.011	0	0.018	0	0.009	0.004	0.028	0.023	0.02	0.018
ZnO	0	0.012	0	0	0	0	0	0.007	0.024	0.005	0	0.012	0
Cl	0	0	0	0	0	0	0.019	0	0.022	0.005	0.003	0.021	0
K_2O	10.69	11.49	10.77	10.7	10.7	10.99	10.75	10.59	10.62	10.83	10.82	10.75	10.15
CaO	0	0	0	0.032	0	0	0	0	0	0.015	0	0	0.013
TiO_2	0.535	0.499	0.313	0.507	0.475	0.587	0.445	0.619	0.559	0.592	0.598	0.61	0.454
BaO	0.16	0.256	0.287	0.167	0.152	0.093	0.16	0.083	0.196	0.101	0.049	0.112	0.312
F	0.021	0.002	0.022	0.007	0.006	0.005	0.028	0.007	0.031	0.019	0.019	0.014	0
Na_2O	0.782	0.375	0.699	0.841	0.771	0.713	0.364	0.597	0.796	0.632	0.769	0.857	1.005
MgO	0.56	1.074	0.82	0.484	0.468	0.533	0.564	0.473	0.626	0.553	0.467	0.64	0.494
Total	95.852	96.426	95.910	95.998	95.819	96.173	95.580	96.115	95.693	97.012	96.245	96.011	94.772
O=F	0.019	0.002	0.020	0.006	0.005	0.004	0.025	0.006	0.028	0.017	0.017	0.012	0.000
O=Cl	0.000	0.000	0.000	0.000	0.000	0.000	0.004	0.000	0.005	0.001	0.001	0.005	0.000
Total	95.833	96.424	95.890	95.992	95.814	96.169	95.551	96.109	95.660	96.994	96.227	95.994	94.772
Si	2.986	3.051	3.040	2.981	2.968	2.983	2.983	2.986	2.990	2.997	2.990	2.988	2.989
Al	2.903	2.756	2.814	2.915	2.937	2.891	2.918	2.925	2.879	2.888	2.899	2.876	2.908
Fe^{2+}	0.055	0.087	0.074	0.051	0.057	0.070	0.067	0.045	0.070	0.060	0.057	0.068	0.056
Mn	0.000	0.002	0.001	0.001	0.000	0.001	0.000	0.001	0.000	0.002	0.001	0.001	0.001
Zn	0.000	0.001	0.000	0.000	0.000	0.000	0.000	0.000	0.001	0.000	0.000	0.001	0.000
Cl	0.000	0.000	0.000	0.000	0.000	0.000	0.002	0.000	0.002	0.001	0.000	0.002	0.000
K	0.905	0.974	0.913	0.904	0.906	0.930	0.913	0.891	0.902	0.905	0.912	0.910	0.869
Ca	0.000	0.000	0.000	0.002	0.000	0.000	0.000	0.000	0.000	0.001	0.000	0.000	0.001
Ti	0.027	0.025	0.016	0.025	0.024	0.029	0.022	0.031	0.028	0.029	0.030	0.030	0.023
Ba	0.004	0.007	0.007	0.004	0.004	0.002	0.004	0.002	0.005	0.003	0.001	0.003	0.008
F	0.004	0.000	0.005	0.001	0.001	0.001	0.006	0.001	0.007	0.004	0.004	0.003	0.000
Na	0.101	0.048	0.090	0.108	0.099	0.092	0.047	0.076	0.103	0.080	0.099	0.110	0.131
Mg	0.055	0.106	0.081	0.048	0.046	0.053	0.056	0.047	0.062	0.054	0.046	0.063	0.049
Total	7.040	7.057	7.041	7.043	7.043	7.053	7.019	7.005	7.050	7.024	7.039	7.056	7.034

Table 1c. Garnet compositions (EMPA). Cations are calculated based on 12 oxygens.

Sample	12A									
Mineral	gr1.1	gr1.2	gr1.3	gr1.4	gr1.5	gr1.6	gr1.7	gr1.8	gr1.9	gr1.10
SiO_2	37.1	36.81	36.95	37.06	36.98	36.72	37	36.94	36.91	36.63
Al_2O_3	21.38	21.36	21.38	21.37	21.31	21.34	21.44	21.41	21.31	21.43
FeO	33.8	33.31	33.69	34.03	33.87	33.25	33.62	33.62	33.77	33.28
MnO	4.55	4.63	4.62	4.65	4.64	4.82	4.87	4.85	5.04	4.99
CaO	0.624	0.64	0.647	0.618	0.659	0.63	0.635	0.652	0.654	0.664
Cr_2O_3	0	0	0	0	0.004	0.041	0	0.005	0	0.01
TiO_2	0.024	0.006	0	0	0.017	0.01	0.004	0	0.017	0.023
MgO	3.12	3.06	3.08	3.05	3.04	3.07	3	3.02	2.94	2.98
Total	100.599	99.815	100.367	100.778	100.52	99.881	100.569	100.497	100.641	100.007
Si	2.979	2.976	2.975	2.975	2.975	2.970	2.974	2.972	2.970	2.962
Al	2.023	2.035	2.028	2.022	2.021	2.034	2.031	2.030	2.021	2.042
Fe^{2+}	2.269	2.252	2.268	2.284	2.279	2.249	2.260	2.262	2.273	2.250
Mn	0.309	0.317	0.315	0.316	0.316	0.330	0.332	0.330	0.344	0.342
Ca	0.054	0.055	0.056	0.053	0.057	0.055	0.055	0.056	0.056	0.058
Cr	0.000	0.000	0.000	0.000	0.000	0.003	0.000	0.000	0.000	0.001
Ti	0.001	0.000	0.000	0.000	0.001	0.001	0.000	0.000	0.001	0.001
Mg	0.373	0.369	0.370	0.365	0.365	0.370	0.359	0.362	0.353	0.359
Total	8.009	8.006	8.011	8.015	8.013	8.011	8.010	8.013	8.018	8.015
X_{Alm}	0.755	0.752	0.754	0.757	0.755	0.749	0.752	0.751	0.751	0.748
X_{Pyr}	0.124	0.123	0.123	0.121	0.121	0.123	0.120	0.120	0.117	0.119
X_{Gros}	0.018	0.019	0.019	0.018	0.019	0.018	0.018	0.019	0.019	0.019
X_{Sps}	0.103	0.106	0.105	0.105	0.105	0.110	0.110	0.110	0.114	0.114

$X_{Alm} = Fe^{2+}/(Fe^{2+} + Mg + Mn + Ca)$; $X_{Pyr} = Mg/(Fe^{2+} + Mg + Mn + Ca)$; $X_{Gros} = Ca/(Fe^{2+} + Mg + Mn + Ca)$; $X_{Sps} = Mn/(Fe^{2+} + Mg + Mn + Ca)$

gr1.11	gr1.12	gr1.13	gr1.14	gr1.15	gr1.16	gr1.17	gr1.18	gr1.19	gr1.20	gr1.21
36.88	36.8	36.77	37.07	36.67	36.85	36.72	36.75	36.75	36.63	36.83
21.25	21.23	21.35	21.34	21.35	21.5	21.07	21.1	21.21	21.21	20.99
34.18	33.76	33.47	33.56	33.83	33.72	34.08	33.37	34.12	33.35	33.3
5.01	4.98	5.12	5.1	5.27	5.26	5.49	5.53	5.34	5.41	5.53
0.645	0.646	0.665	0.673	0.622	0.655	0.58	0.643	0.617	0.658	0.653
0.037	0.018	0	0	0.018	0.007	0.014	0.029	0.01	0.037	0.027
0.007	0.034	0.047	0.023	0.006	0.026	0.038	0.032	0	0.051	0.026
2.98	2.96	2.86	2.86	2.88	2.76	2.78	2.67	2.68	2.67	2.67
100.989	100.428	100.281	100.626	100.645	100.777	100.772	100.124	100.726	100.017	100.026
2.964	2.969	2.968	2.980	2.957	2.963	2.964	2.977	2.965	2.969	2.985
2.012	2.018	2.031	2.022	2.029	2.038	2.004	2.014	2.017	2.026	2.005
2.297	2.277	2.259	2.256	2.281	2.267	2.300	2.260	2.302	2.261	2.257
0.341	0.340	0.350	0.347	0.360	0.358	0.375	0.379	0.365	0.371	0.380
0.056	0.056	0.058	0.058	0.054	0.056	0.050	0.056	0.053	0.057	0.057
0.002	0.001	0.000	0.000	0.001	0.000	0.001	0.002	0.001	0.002	0.002
0.000	0.002	0.003	0.001	0.000	0.002	0.002	0.002	0.000	0.003	0.002
0.357	0.356	0.344	0.343	0.346	0.331	0.335	0.322	0.322	0.323	0.323
8.029	8.020	8.013	8.007	8.028	8.016	8.031	8.013	8.026	8.013	8.010
0.753	0.752	0.750	0.751	0.750	0.753	0.752	0.749	0.757	0.751	0.748
0.117	0.118	0.114	0.114	0.114	0.110	0.109	0.107	0.106	0.107	0.107
0.018	0.018	0.019	0.019	0.018	0.019	0.016	0.018	0.018	0.019	0.019
0.112	0.112	0.116	0.116	0.118	0.119	0.123	0.126	0.120	0.123	0.126

	42A												
	gr1.1	gr1.2	gr1.3	gr1.4	gr1.5	gr1.6	gr1.7	gr1.8	gr2.1	gr2.2	gr3.1	gr3.2	gr3.3
SiO_2	36.21	36.01	36.17	35.75	36.55	36.1	35.91	35.72	35.85	36.12	35.89	36.01	36
Al_2O_3	21.84	21.69	21.69	21.45	21.47	21.72	21.47	21.43	21.56	21.57	21.35	21.5	21.54
FeO	31.99	32.05	32.01	32.36	31.9	31.88	32.03	31.2	32.58	32.4	31.58	32.4	31.78
MnO	8.12	8.09	8.05	8.47	8.45	8.2	8.61	10.08	7.52	7.6	9.54	7.7	8.14
CaO	0.56	0.584	0.685	0.636	0.729	0.68	0.704	0.618	0.56	0.607	0.591	0.558	0.683
Cr_2O_3	0	0.003	0.032	0	0.022	0	0.008	0	0	0.021	0.037	0.014	0.001
TiO_2	0	0	0	0	0	0	0	0.015	0.008	0.013	0.026	0	0.008
MgO	2.22	2.31	2.38	2.2	2.35	2.32	2.13	1.572	2.42	2.36	1.643	2.31	2.36
Total	100.94	100.736	101.017	100.866	101.47	100.9	100.862	100.636	100.498	100.69	100.657	100.493	100.512
Si	2.925	2.918	2.921	2.906	2.940	2.919	2.916	2.916	2.914	2.926	2.926	2.926	2.923
Al	2.079	2.071	2.064	2.055	2.035	2.070	2.054	2.062	2.065	2.060	2.052	2.059	2.061
Fe^{2+}	2.161	2.172	2.162	2.200	2.145	2.156	2.175	2.130	2.214	2.195	2.153	2.201	2.157
Mn	0.555	0.555	0.551	0.583	0.576	0.562	0.592	0.697	0.518	0.521	0.659	0.530	0.560
Ca	0.048	0.051	0.059	0.055	0.063	0.059	0.061	0.054	0.049	0.053	0.052	0.049	0.059
Cr	0.000	0.000	0.002	0.000	0.001	0.000	0.001	0.000	0.000	0.001	0.002	0.001	0.000
Ti	0.000	0.000	0.000	0.000	0.000	0.000	0.000	0.001	0.000	0.001	0.002	0.000	0.000
Mg	0.267	0.279	0.287	0.267	0.282	0.280	0.258	0.191	0.293	0.285	0.200	0.280	0.286
Total	8.036	8.046	8.046	8.066	8.042	8.046	8.057	8.052	8.053	8.042	8.045	8.045	8.046
X_{Alm}	0.713	0.710	0.707	0.708	0.700	0.705	0.705	0.693	0.720	0.719	0.703	0.719	0.705
X_{Pyr}	0.088	0.091	0.094	0.086	0.092	0.092	0.084	0.062	0.095	0.093	0.065	0.091	0.093
X_{Gros}	0.016	0.017	0.019	0.018	0.020	0.019	0.020	0.018	0.016	0.017	0.017	0.016	0.019
X_{Sps}	0.183	0.182	0.180	0.188	0.188	0.184	0.192	0.227	0.168	0.171	0.215	0.173	0.183

gr3.4	gr3.5	gr3.6	gr3.7	gr3.8	gr3.9	gr3.10	gr4.1	gr4.2	gr5	gr6.1	gr6.2	gr7.1	gr7.2	gr7.3
36.08	35.97	35.8	36.12	36.28	36	36.37	35.93	36.07	35.88	35.89	36.2	36.19	35.96	35.99
21.41	21.49	21.49	21.58	21.58	21.45	21.51	21.43	21.58	21.5	21.63	21.58	21.59	21.58	21.62
31.77	31.8	31.91	31.51	31.39	31.78	31.87	32.16	32.05	32.14	32	32.3	31.55	31.63	31.72
8.26	8.39	8.21	8.36	8.29	8.23	8.11	7.85	8.15	7.88	8.04	8.07	8.24	8.29	8.15
0.676	0.703	0.651	0.681	0.696	0.685	0.739	0.757	0.712	0.713	0.761	0.728	0.702	0.686	0.724
0.021	0.018	0	0.002	0.001	0.037	0.003	0	0.011	0.002	0.013	0.017	0.025	0.02	0.062
0.001	0.023	0.019	0.002	0.013	0	0.044	0.014	0.023	0.008	0.047	0.037	0.015	0	0
2.37	2.34	2.22	2.41	2.48	2.35	2.31	2.24	2.27	2.33	2.27	2.25	2.33	2.39	2.33
100.588	100.733	100.301	100.666	100.729	100.532	100.956	100.381	100.866	100.453	100.65	101.182	100.641	100.556	100.596
2.928	2.918	2.917	2.926	2.933	2.924	2.937	2.924	2.921	2.918	2.913	2.923	2.931	2.918	2.919
2.048	2.055	2.064	2.060	2.056	2.053	2.047	2.055	2.059	2.060	2.069	2.054	2.060	2.064	2.067
2.156	2.157	2.174	2.134	2.122	2.158	2.152	2.188	2.170	2.185	2.171	2.181	2.136	2.147	2.151
0.568	0.576	0.567	0.574	0.568	0.566	0.555	0.541	0.559	0.543	0.553	0.552	0.565	0.570	0.560
0.059	0.061	0.057	0.059	0.060	0.060	0.064	0.066	0.062	0.062	0.066	0.063	0.061	0.060	0.063
0.001	0.001	0.000	0.000	0.000	0.002	0.000	0.000	0.001	0.000	0.001	0.001	0.002	0.001	0.004
0.000	0.001	0.001	0.000	0.001	0.000	0.003	0.001	0.001	0.000	0.003	0.002	0.001	0.000	0.000
0.287	0.283	0.270	0.291	0.299	0.285	0.278	0.272	0.274	0.282	0.275	0.271	0.281	0.289	0.282
8.047	8.053	8.050	8.044	8.038	8.048	8.036	8.047	8.048	8.052	8.050	8.047	8.037	8.049	8.046
0.702	0.701	0.709	0.698	0.696	0.703	0.706	0.713	0.708	0.711	0.709	0.711	0.702	0.700	0.704
0.093	0.092	0.088	0.095	0.098	0.093	0.091	0.089	0.089	0.092	0.090	0.088	0.092	0.094	0.092
0.019	0.020	0.019	0.019	0.020	0.019	0.021	0.022	0.020	0.020	0.022	0.021	0.020	0.019	0.021
0.185	0.187	0.185	0.188	0.186	0.184	0.182	0.176	0.182	0.177	0.180	0.180	0.186	0.186	0.183

	44A												
	gr1.1	gr1.2	gr1.3	gr1.4	gr1.5	gr1.6	gr2.1	gr2.2	gr2.3	gr3	gr4.1	gr4.2	gr5.1
SiO_2	35.84	35.96	35.97	35.83	36.03	35.64	35.66	35.81	35.76	36.09	35.93	35.8	35.76
Al_2O_3	21.36	21.42	21.31	21.4	21.36	21.25	21.34	21.26	21.22	21.07	21.31	21.36	21.27
FeO	35.85	36.48	36.36	36.26	36.46	36.5	36.46	36.32	36.11	34.75	35.6	35.29	36.18
MnO	4.35	3.08	3.07	3.65	3.55	3.66	3.67	3.67	4.27	5.73	4.88	5.48	4.48
CaO	0.769	0.781	0.781	0.608	0.601	0.607	0.703	0.712	0.707	0.837	0.698	0.869	0.692
Cr_2O_3	0.025	0.012	0.013	0.008	0	0.002	0.002	0	0	0.005	0.018	0	0
TiO_2	0.044	0	0.009	0	0	0.003	0.032	0.022	0.012	0	0	0.016	0.038
MgO	2.1	2.42	2.39	2.18	2.18	2.1	2.19	2.11	1.98	1.83	1.89	1.76	2
Total	100.338	100.153	99.903	99.936	100.181	99.762	100.057	99.904	100.059	100.312	100.326	100.575	100.419
Si	2.923	2.928	2.935	2.929	2.937	2.924	2.917	2.931	2.928	2.947	2.933	2.921	2.920
Al	2.053	2.056	2.050	2.061	2.052	2.055	2.057	2.051	2.047	2.027	2.050	2.054	2.047
Fe^{2+}	2.445	2.484	2.481	2.478	2.485	2.504	2.494	2.486	2.472	2.373	2.430	2.407	2.471
Mn	0.300	0.212	0.212	0.253	0.245	0.254	0.254	0.254	0.296	0.396	0.337	0.379	0.310
Ca	0.067	0.068	0.068	0.053	0.052	0.053	0.062	0.062	0.062	0.073	0.061	0.076	0.061
Cr	0.002	0.001	0.001	0.001	0.000	0.000	0.000	0.000	0.000	0.000	0.001	0.000	0.000
Ti	0.003	0.000	0.001	0.000	0.000	0.000	0.002	0.001	0.001	0.000	0.000	0.001	0.002
Mg	0.255	0.294	0.291	0.266	0.265	0.257	0.267	0.257	0.242	0.223	0.230	0.214	0.243
Total	8.047	8.043	8.039	8.040	8.037	8.048	8.053	8.043	8.048	8.039	8.042	8.051	8.054
X_{Alm}	0.797	0.812	0.813	0.813	0.815	0.816	0.811	0.812	0.805	0.774	0.795	0.783	0.801
X_{Pyr}	0.083	0.096	0.095	0.087	0.087	0.084	0.087	0.084	0.079	0.073	0.075	0.070	0.079
X_{Gros}	0.022	0.022	0.022	0.017	0.017	0.017	0.020	0.020	0.020	0.024	0.020	0.025	0.020
X_{Sps}	0.098	0.069	0.070	0.083	0.080	0.083	0.083	0.083	0.096	0.129	0.110	0.123	0.100

gr5.2	gr5.3	gr6.1	gr6.2	gr6.3	gr6.4	gr7.1	gr7.2	gr7.3	gr7.4	gr8.1	gr8.2	gr8.3
35.91	35.91	35.92	36.07	36.24	35.76	35.96	36.12	36.05	36.08	35.88	35.92	35.78
21.24	21.5	21.33	21.27	21.29	21.33	21.55	21.37	21.57	21.36	21.47	21.49	21.33
36.6	35.71	36.2	36.25	36.81	36.83	36.19	36.1	36.5	36.59	35.71	36.89	36.59
3.44	5.14	3.85	3.32	3.45	3.56	3.78	3.27	3.19	3.44	4.76	3.38	3.43
0.587	0.592	0.619	0.604	0.68	0.613	0.698	0.619	0.612	0.641	0.608	0.626	0.63
0	0.023	0.004	0.024	0	0.017	0	0	0	0.013	0	0.014	0
0.002	0.01	0.004	0.032	0	0.009	0	0	0.013	0	0	0.003	0.043
2.17	1.89	2.11	2.31	2.28	2.18	2.26	2.51	2.48	2.35	2	2.29	2.3
99.949	100.776	100.038	99.88	100.75	100.299	100.438	99.989	100.415	100.473	100.428	100.612	100.103
2.936	2.921	2.934	2.944	2.939	2.920	2.924	2.941	2.926	2.933	2.924	2.919	2.922
2.047	2.061	2.053	2.046	2.035	2.052	2.065	2.051	2.064	2.046	2.062	2.058	2.053
2.503	2.429	2.473	2.474	2.497	2.514	2.460	2.458	2.478	2.487	2.434	2.507	2.499
0.238	0.354	0.266	0.229	0.237	0.246	0.260	0.225	0.219	0.237	0.329	0.233	0.237
0.051	0.052	0.054	0.053	0.059	0.054	0.061	0.054	0.053	0.056	0.053	0.055	0.055
0.000	0.001	0.000	0.002	0.000	0.001	0.000	0.000	0.000	0.001	0.000	0.001	0.000
0.000	0.001	0.000	0.002	0.000	0.001	0.000	0.000	0.001	0.000	0.000	0.000	0.003
0.265	0.229	0.257	0.281	0.276	0.265	0.274	0.305	0.300	0.285	0.243	0.277	0.280
8.040	8.047	8.039	8.030	8.043	8.053	8.044	8.034	8.041	8.044	8.045	8.051	8.049
0.819	0.793	0.811	0.815	0.814	0.816	0.805	0.808	0.812	0.812	0.796	0.816	0.814
0.087	0.075	0.084	0.093	0.090	0.086	0.090	0.100	0.098	0.093	0.079	0.090	0.091
0.017	0.017	0.018	0.017	0.019	0.017	0.020	0.018	0.017	0.018	0.017	0.018	0.018
0.078	0.116	0.087	0.076	0.077	0.080	0.085	0.074	0.072	0.077	0.107	0.076	0.077

gr8.4	gr9.1	gr9.2	gr9.3	gr9.4	gr10.1	gr10.2	gr10.3	gr11.1	gr11.2	gr11.3	gr11.4	gr11.5	gri1
36.29	35.91	35.98	36.04	35.91	35.93	35.95	35.91	35.99	35.92	35.63	35.99	35.71	35.82
21.3	21.35	21.37	21.2	21.39	21.48	21.38	21.37	21.5	21.25	21.36	21.44	21.25	21.35
35.45	36.16	36.02	36.61	36.24	36.36	36.06	35.05	36.62	36.05	36.3	36.5	35.89	34.91
4.9	4.2	3.46	3.4	3.83	4.4	4.09	5.43	3.6	3.95	4.11	3.96	4.82	5.87
0.83	0.702	0.578	0.59	0.669	0.76	0.753	0.732	0.582	0.621	0.613	0.598	0.573	0.662
0.017	0	0.011	0.01	0.014	0.007	0.018	0.007	0.005	0	0.005	0.02	0	0.006
0.028	0.031	0.066	0.013	0.001	0	0.025	0	0.017	0.003	0.016	0	0	0
1.89	2.21	2.52	2.49	2.23	2.04	2.07	1.85	2.42	2.33	2.05	2.2	2.15	1.79
100.705	100.563	100.004	100.353	100.283	100.976	100.346	100.349	100.734	100.124	100.084	100.708	100.394	100.408
2.947	2.923	2.932	2.934	2.927	2.917	2.929	2.930	2.920	2.931	2.917	2.924	2.917	2.925
2.038	2.048	2.052	2.034	2.054	2.055	2.053	2.055	2.056	2.044	2.061	2.053	2.046	2.055
2.407	2.461	2.454	2.492	2.470	2.468	2.457	2.392	2.484	2.460	2.485	2.480	2.452	2.384
0.337	0.289	0.239	0.234	0.264	0.302	0.282	0.375	0.247	0.273	0.285	0.272	0.333	0.406
0.072	0.061	0.050	0.051	0.058	0.066	0.066	0.064	0.051	0.054	0.054	0.052	0.050	0.058
0.001	0.000	0.001	0.001	0.001	0.000	0.001	0.000	0.000	0.000	0.000	0.001	0.000	0.000
0.002	0.002	0.004	0.001	0.000	0.000	0.002	0.000	0.001	0.000	0.001	0.000	0.000	0.000
0.229	0.268	0.306	0.302	0.271	0.247	0.251	0.225	0.293	0.283	0.250	0.266	0.262	0.218
8.032	8.052	8.038	8.048	8.046	8.056	8.042	8.042	8.051	8.046	8.052	8.049	8.060	8.047
0.790	0.799	0.805	0.809	0.806	0.800	0.804	0.783	0.808	0.801	0.808	0.808	0.792	0.778
0.075	0.087	0.100	0.098	0.088	0.080	0.082	0.074	0.095	0.092	0.081	0.087	0.085	0.071
0.024	0.020	0.017	0.017	0.019	0.021	0.022	0.021	0.016	0.018	0.017	0.017	0.016	0.019
0.111	0.094	0.078	0.076	0.086	0.098	0.092	0.123	0.080	0.089	0.093	0.089	0.108	0.132

	45A												
	gr1.1	gr1.2	gr1.3	gr1.4	gr1.5	gr1.6	gr1.7	gr1.8	gr1.9	gr1.10	gr1.11	gr1.12	gr1.13
SiO_2	37.59	37.96	38.13	38.12	38.43	37.84	37.96	38.1	38.33	38.1	38.07	38.24	37.84
Al_2O_3	21.92	22.1	22	21.99	22.03	22.17	21.96	22.07	22	22.05	22.06	22.11	21.96
FeO	34.17	33.42	33.23	32.75	32.48	32.99	32.85	33.17	32.61	32.95	32.71	33.36	33.82
MnO	0.955	0.888	0.887	0.949	0.861	0.918	0.907	0.935	0.925	0.936	0.913	0.951	0.92
CaO	0.779	0.786	0.826	0.781	0.768	0.69	0.684	0.712	0.732	0.864	0.818	0.852	0.764
Cr_2O_3	0.014	0.003	0.012	0.013	0.012	0.02	0.003	0.026	0.009	0.06	0.026	0.026	0.013
TiO_2	0.027	0.001	0	0.022	0.007	0.01	0.014	0	0.016	0.033	0.017	0.065	0.007
MgO	5.21	5.98	5.99	5.94	6.13	6.33	6.13	6.26	6.23	6.04	6.06	6.07	5.33
Total	100.665	101.139	101.075	100.565	100.717	100.969	100.508	101.274	100.853	101.033	100.674	101.675	100.654
Si	2.968	2.969	2.981	2.989	3.001	2.959	2.980	2.971	2.992	2.977	2.981	2.973	2.981
Al	2.040	2.037	2.027	2.032	2.027	2.043	2.031	2.028	2.024	2.030	2.036	2.026	2.038
Fe^{2+}	2.256	2.185	2.172	2.147	2.121	2.157	2.156	2.163	2.129	2.153	2.142	2.169	2.227
Mn	0.064	0.059	0.059	0.063	0.057	0.061	0.060	0.062	0.061	0.062	0.061	0.063	0.061
Ca	0.066	0.066	0.069	0.066	0.064	0.058	0.058	0.059	0.061	0.072	0.069	0.071	0.064
Cr	0.001	0.000	0.001	0.001	0.001	0.001	0.000	0.002	0.001	0.004	0.002	0.002	0.001
Ti	0.002	0.000	0.000	0.001	0.000	0.001	0.001	0.000	0.001	0.002	0.001	0.004	0.000
Mg	0.613	0.697	0.698	0.694	0.714	0.738	0.717	0.728	0.725	0.704	0.708	0.704	0.626
Total	8.010	8.013	8.006	7.993	7.985	8.018	8.004	8.014	7.994	8.004	7.999	8.010	7.999
X_{Alm}	0.752	0.727	0.725	0.723	0.718	0.716	0.721	0.718	0.715	0.720	0.719	0.722	0.748
X_{Pyr}	0.204	0.232	0.233	0.234	0.241	0.245	0.240	0.242	0.244	0.235	0.238	0.234	0.210
X_{Gros}	0.022	0.022	0.023	0.022	0.022	0.019	0.019	0.020	0.021	0.024	0.023	0.024	0.022
X_{Sps}	0.021	0.020	0.020	0.021	0.019	0.020	0.020	0.021	0.021	0.021	0.020	0.021	0.021

gr2.1	gr2.2	gr3	gr4.1	gr4.2	gr4.3	gr4.4	gr5.1	gr5.2	gr5.3	gr5.4	gr6	gr7.1	gr7.2
36.88	36.87	36.97	37.04	37.06	37.02	37.05	36.86	36.87	37.1	36.88	37.02	36.96	37.11
22.03	22.22	22.18	21.95	22.13	22.06	21.92	21.98	22.02	22.07	22.04	21.96	22.08	22.06
34.78	34.03	34.36	34.38	33.49	33.32	33.85	34.36	34.03	33.64	33.48	33.98	33.42	33.5
1.054	0.974	0.979	0.991	0.917	1.009	0.983	1.004	0.964	0.943	0.985	0.92	0.922	0.928
0.881	0.795	0.839	0.815	0.789	0.714	0.836	0.767	0.801	0.778	0.76	0.823	0.818	0.849
0.028	0.022	0.046	0	0	0.024	0.026	0.007	0	0.019	0.009	0	0.038	0.02
0.036	0.04	0.015	0.036	0.023	0.031	0	0.029	0.037	0.018	0	0.014	0	0.01
5.3	5.87	5.53	5.53	6.17	6.22	5.66	5.45	5.81	6.14	6.11	5.68	6.3	6.17
100.989	100.82	100.918	100.741	100.579	100.398	100.325	100.456	100.532	100.707	100.264	100.396	100.538	100.649
2.919	2.911	2.920	2.931	2.924	2.925	2.938	2.926	2.920	2.926	2.921	2.934	2.918	2.927
2.055	2.067	2.065	2.047	2.058	2.054	2.048	2.056	2.055	2.051	2.058	2.051	2.054	2.050
2.302	2.247	2.269	2.275	2.209	2.202	2.244	2.281	2.254	2.218	2.218	2.252	2.206	2.209
0.071	0.065	0.065	0.066	0.061	0.068	0.066	0.068	0.065	0.063	0.066	0.062	0.062	0.062
0.075	0.067	0.071	0.069	0.067	0.060	0.071	0.065	0.068	0.066	0.064	0.070	0.069	0.072
0.002	0.001	0.003	0.000	0.000	0.001	0.002	0.000	0.000	0.001	0.001	0.000	0.002	0.001
0.002	0.002	0.001	0.002	0.001	0.002	0.000	0.002	0.002	0.001	0.000	0.001	0.000	0.001
0.625	0.691	0.651	0.652	0.726	0.733	0.669	0.645	0.686	0.722	0.722	0.671	0.742	0.725
8.050	8.052	8.045	8.043	8.046	8.045	8.038	8.044	8.050	8.047	8.049	8.040	8.054	8.047
0.749	0.732	0.742	0.743	0.721	0.719	0.736	0.746	0.734	0.723	0.722	0.737	0.717	0.720
0.204	0.225	0.213	0.213	0.237	0.239	0.219	0.211	0.223	0.235	0.235	0.220	0.241	0.236
0.024	0.022	0.023	0.023	0.022	0.020	0.023	0.021	0.022	0.021	0.021	0.023	0.022	0.023
0.023	0.021	0.021	0.022	0.020	0.022	0.022	0.022	0.021	0.021	0.022	0.020	0.020	0.020

gr7.3	gr7.4	gr8	gr9.1	gr9.2	gr9.3	gr9.4	gr10.1	gr10.2	gr10.3	gr10.4	gr11.1	gr11.2	gr11.3
37.06	36.86	37.07	37.03	36.83	36.67	36.83	36.62	36.79	36.86	36.76	36.92	36.96	36.84
22.02	21.98	21.98	22.1	22.18	22	22.17	21.86	22.13	22.11	21.91	21.97	22.11	22.02
33.2	33.52	33.49	33.46	33.49	33.28	33.47	35.31	33.82	33.5	34.58	34.79	33.49	34.91
0.962	0.928	0.886	0.911	0.894	0.875	0.97	1.046	0.955	0.967	1.014	0.963	0.968	0.984
0.833	0.83	0.805	0.854	0.849	0.886	0.898	0.786	0.8	0.808	0.867	0.839	0.7	0.774
0	0.018	0	0.005	0.003	0.029	0	0.031	0	0.026	0.012	0.02	0.008	0.012
0.001	0.011	0.002	0.042	0	0.036	0.015	0.036	0.022	0.007	0.032	0.011	0	0
6.08	5.89	6.15	6.11	6.2	6.15	5.96	4.73	5.96	6.06	5.46	5.58	6	5.19
100.156	100.037	100.382	100.512	100.447	99.926	100.313	100.42	100.477	100.337	100.635	101.093	100.236	100.73
2.934	2.927	2.931	2.924	2.912	2.914	2.917	2.924	2.913	2.918	2.918	2.918	2.927	2.924
2.054	2.057	2.048	2.057	2.067	2.060	2.069	2.057	2.065	2.063	2.050	2.046	2.063	2.059
2.198	2.226	2.214	2.209	2.214	2.211	2.216	2.358	2.239	2.218	2.296	2.299	2.218	2.317
0.064	0.062	0.059	0.061	0.060	0.059	0.065	0.071	0.064	0.065	0.068	0.064	0.065	0.066
0.071	0.071	0.068	0.072	0.072	0.075	0.076	0.067	0.068	0.069	0.074	0.071	0.059	0.066
0.000	0.001	0.000	0.000	0.000	0.002	0.000	0.002	0.000	0.002	0.001	0.001	0.001	0.001
0.000	0.001	0.000	0.002	0.000	0.002	0.001	0.002	0.001	0.000	0.002	0.001	0.000	0.000
0.718	0.697	0.725	0.719	0.731	0.729	0.704	0.563	0.703	0.715	0.646	0.657	0.708	0.614
8.039	8.043	8.045	8.045	8.055	8.053	8.048	8.044	8.053	8.049	8.054	8.058	8.041	8.046
0.720	0.728	0.722	0.722	0.720	0.719	0.724	0.771	0.728	0.723	0.744	0.744	0.727	0.756
0.235	0.228	0.236	0.235	0.238	0.237	0.230	0.184	0.229	0.233	0.210	0.213	0.232	0.200
0.023	0.023	0.022	0.024	0.023	0.025	0.025	0.022	0.022	0.022	0.024	0.023	0.019	0.021
0.021	0.020	0.019	0.020	0.019	0.019	0.021	0.023	0.021	0.021	0.022	0.021	0.021	0.022

Table 1d. K-feldspar compositions (EMPA). Cations are calculated based on 8 oxygens.

Sample	DC012A														
Mineral	kf1.1	kf1.2	kf1.3	kf2.1	kf2.2	kf3.1	kf3.2	kf4	kf5	kf6	kf7.1	kf7.2	kf8.1	kf8.2	kf8.3
SiO_2	65.18	64.89	65.00	65.22	65.05	65.07	65.26	65.01	65.11	65.08	64.82	64.70	64.93	64.89	65.05
Al_2O_3	19.18	19.18	19.16	19.14	19.10	19.21	19.24	19.11	19.09	19.28	19.38	19.18	19.09	19.19	19.10
FeO	0.00	0.02	0.02	0.04	0.01	0.04	0.05	0.00	0.00	0.05	0.00	0.00	0.00	0.01	0.00
MnO	0.01	0.01	0.00	0.00	0.00	0.01	0.00	0.00	0.02	0.00	0.00	0.00	0.00	0.01	0.01
K_2O	14.41	14.45	14.44	14.81	15.06	14.51	14.43	14.41	14.53	15.20	14.29	14.31	14.90	14.83	14.90
CaO	0.04	0.01	0.06	0.00	0.03	0.04	0.05	0.04	0.04	0.00	0.05	0.04	0.00	0.00	0.00
SrO	0.09	0.09	0.08	0.07	0.10	0.08	0.07	0.12	0.05	0.10	0.08	0.06	0.11	0.11	0.11
TiO_2	0.02	0.04	0.00	0.02	0.00	0.05	0.02	0.03	0.02	0.02	0.02	0.00	0.01	0.00	0.04
BaO	0.31	0.38	0.44	0.44	0.38	0.45	0.46	0.51	0.34	0.39	0.38	0.34	0.38	0.36	0.40
Na_2O	1.48	1.48	1.25	1.03	0.92	1.39	1.37	1.41	1.34	0.94	1.36	1.41	0.98	1.01	1.07
MgO	0.00	0.02	0.00	0.00	0.00	0.00	0.03	0.01	0.00	0.00	0.00	0.00	0.00	0.00	0.02
Total	100.72	100.56	100.46	100.77	100.66	100.85	100.98	100.64	100.54	101.06	100.39	100.03	100.40	100.42	100.70
Si	2.98	2.97	2.98	2.98	2.98	2.97	2.98	2.98	2.98	2.97	2.97	2.97	2.98	2.98	2.98
Al	1.03	1.04	1.03	1.03	1.03	1.03	1.03	1.03	1.03	1.04	1.05	1.04	1.03	1.04	1.03
Fe_{2+}	0.00	0.00	0.00	0.00	0.00	0.00	0.00	0.00	0.00	0.00	0.00	0.00	0.00	0.00	0.00
Mn	0.00	0.00	0.00	0.00	0.00	0.00	0.00	0.00	0.00	0.00	0.00	0.00	0.00	0.00	0.00
K	0.84	0.84	0.84	0.86	0.88	0.85	0.84	0.84	0.85	0.89	0.84	0.84	0.87	0.87	0.87
Ca	0.00	0.00	0.00	0.00	0.00	0.00	0.00	0.00	0.00	0.00	0.00	0.00	0.00	0.00	0.00
Sr	0.00	0.00	0.00	0.00	0.00	0.00	0.00	0.00	0.00	0.00	0.00	0.00	0.00	0.00	0.00
Ti	0.00	0.00	0.00	0.00	0.00	0.00	0.00	0.00	0.00	0.00	0.00	0.00	0.00	0.00	0.00
Ba	0.01	0.01	0.01	0.01	0.01	0.01	0.01	0.01	0.01	0.01	0.01	0.01	0.01	0.01	0.01
Na	0.13	0.13	0.11	0.09	0.08	0.12	0.12	0.13	0.12	0.08	0.12	0.13	0.09	0.09	0.09
Mg	0.00	0.00	0.00	0.00	0.00	0.00	0.00	0.00	0.00	0.00	0.00	0.00	0.00	0.00	0.00
Total	4.99	5.00	4.98	4.98	4.98	4.99	4.99	4.99	4.99	4.99	4.98	4.99	4.98	4.98	4.99
X_{An}	0.00	0.00	0.00	0.00	0.00	0.00	0.00	0.00	0.00	0.00	0.00	0.00	0.00	0.00	0.00
X_{ab}	0.13	0.13	0.12	0.10	0.08	0.13	0.13	0.13	0.12	0.09	0.13	0.13	0.09	0.09	0.10
X_{Or}	0.86	0.86	0.88	0.90	0.91	0.87	0.87	0.87	0.88	0.91	0.87	0.87	0.91	0.91	0.90

X_{An} = Ca/(Ca + Na + K); X_{Ab} = Na/(Ca + Na + K); X_{Or} = K/(Ca + Na + K)

						WSP10-A				
kf8.4	kf8.5	kf8.6	kf9.1	kf9.2		kf1.1	kf1.2	kf2.1	kf3	kf4
64.760	64.660	64.960	64.480	64.360	SiO_2	63.670	64.000	63.930	64.600	64.510
19.150	19.210	19.190	19.000	19.160	Al_2O_3	19.120	18.730	18.800	18.810	18.770
0.03	0.03	0.04	0.00	0.00	FeO	0.03	0.26	0.16	0.15	0.11
0.000	0.000	0.009	0.000	0.018	MnO	0.000	0.002	0.010	0.000	0.000
14.770	14.890	14.850	14.840	15.060	K_2O	15.730	15.520	15.130	15.110	15.570
0.000	0.024	0.029	0.000	0.000	CaO	0.000	0.004	0.013	0.002	0.000
0.100	0.078	0.079	0.078	0.078	SrO	0.024	0.089	0.085	0.032	0.071
0.000	0.010	0.025	0.000	0.000	TiO_2	0.000	0.043	0.000	0.019	0.047
0.394	0.403	0.385	0.379	0.334	BaO	0.327	0.386	0.371	0.328	0.289
1.028	1.064	0.943	1.026	0.925	Na_2O	1.105	0.874	1.151	1.304	1.132
0.008	0.000	0.000	0.000	0.000	MgO	0.000	0.050	0.059	0.000	0.000
100.241	100.367	100.516	99.804	99.934	Total	100.012	99.983	99.726	100.377	100.516
2.977	2.971	2.977	2.978	2.971	Si	2.954	2.968	2.967	2.975	2.973
1.037	1.040	1.036	1.034	1.042	Al	1.045	1.024	1.028	1.021	1.019
0.001	0.001	0.002	0.000	0.000	Fe_{2+}	0.001	0.010	0.006	0.006	0.004
0.000	0.000	0.000	0.000	0.001	Mn	0.000	0.000	0.000	0.000	0.000
0.866	0.873	0.868	0.874	0.887	K	0.931	0.918	0.896	0.888	0.915
0.000	0.001	0.001	0.000	0.000	Ca	0.000	0.000	0.001	0.000	0.000
0.003	0.002	0.002	0.002	0.002	Sr	0.001	0.002	0.002	0.001	0.002
0.000	0.000	0.001	0.000	0.000	Ti	0.000	0.001	0.000	0.001	0.002
0.007	0.007	0.007	0.007	0.006	Ba	0.006	0.007	0.007	0.006	0.005
0.092	0.095	0.084	0.092	0.083	Na	0.099	0.079	0.104	0.116	0.101
0.001	0.000	0.000	0.000	0.000	Mg	0.000	0.003	0.004	0.000	0.000
4.983	4.991	4.979	4.988	4.992	Total	5.038	5.012	5.015	5.013	5.022
0.000	0.001	0.001	0.000	0.000	X_{An}	0.000	0.000	0.001	0.000	0.000
0.096	0.098	0.088	0.095	0.085	X_{ab}	0.096	0.079	0.104	0.116	0.100
0.904	0.901	0.911	0.905	0.915	X_{Or}	0.904	0.921	0.896	0.884	0.900

kf5	kf6.1	kf6.2	kf7	kf8	kf9	kf10	kf11	kf12	kf13
64.000	64.530	64.000	65.360	65.530	65.520	65.130	65.290	65.320	65.550
18.950	18.830	18.790	19.080	19.260	19.280	19.320	19.190	19.200	19.150
0.37	0.01	0.05	0.06	0.02	0.03	0.00	0.08	0.17	0.08
0.000	0.000	0.000	0.004	0.007	0.012	0.013	0.002	0.000	0.000
14.490	14.960	15.830	14.740	15.040	15.310	14.810	15.760	15.730	15.620
0.005	0.020	0.007	0.028	0.006	0.000	0.016	0.037	0.001	0.027
0.056	0.047	0.061	0.045	0.038	0.067	0.030	0.057	0.039	0.066
0.027	0.000	0.000	0.000	0.026	0.000	0.023	0.009	0.008	0.000
0.241	0.248	0.324	0.196	0.306	0.330	0.305	0.263	0.321	0.292
1.620	1.480	0.963	1.760	1.480	1.460	1.580	1.135	1.204	1.162
0.133	0.000	0.000	0.006	0.005	0.014	0.000	0.000	0.000	0.000
99.933	100.122	100.036	101.281	101.726	102.022	101.227	101.834	102.013	101.961
2.957	2.976	2.968	2.975	2.972	2.969	2.967	2.969	2.966	2.974
1.032	1.023	1.027	1.023	1.030	1.030	1.037	1.028	1.028	1.024
0.014	0.000	0.002	0.002	0.001	0.001	0.000	0.003	0.006	0.003
0.000	0.000	0.000	0.000	0.000	0.000	0.001	0.000	0.000	0.000
0.854	0.880	0.937	0.856	0.870	0.885	0.861	0.914	0.911	0.904
0.000	0.001	0.000	0.001	0.000	0.000	0.001	0.002	0.000	0.001
0.002	0.001	0.002	0.001	0.001	0.002	0.001	0.002	0.001	0.002
0.001	0.000	0.000	0.000	0.001	0.000	0.001	0.000	0.000	0.000
0.004	0.004	0.006	0.003	0.005	0.006	0.005	0.005	0.006	0.005
0.145	0.132	0.087	0.155	0.130	0.128	0.140	0.100	0.106	0.102
0.009	0.000	0.000	0.000	0.000	0.001	0.000	0.000	0.000	0.000
5.019	5.019	5.029	5.018	5.012	5.022	5.013	5.022	5.025	5.016
0.000	0.001	0.000	0.001	0.000	0.000	0.001	0.002	0.000	0.001
0.145	0.131	0.085	0.153	0.130	0.127	0.139	0.098	0.104	0.101
0.855	0.868	0.915	0.845	0.870	0.873	0.860	0.900	0.896	0.897

Table 1e. Plagioclase compositions (EMPA). Cations are calculated based on 8 oxygens.

Sample	DC044A												
Mineral	plg1.1	plg1.2	plg2.1	plg2.2	plg2.3	plg3	plg4	plg5	plg6.1	plg6.2	plg7	plg8	plg9.1
SiO_2	63.83	63.83	64.15	64.5	64.2	64.48	64.2	64.07	64.61	63.76	64.26	63.92	64.47
Al_2O_3	22.05	22.3	22.07	21.88	22.1	21.95	21.94	22.19	22.08	22.27	22.11	22.04	21.83
FeO	0.001	0.022	0.005	0.010	0.040	0.013	0.000	0.004	0.040	0.031	0.008	0.017	0.005
MnO	0.009	0	0.008	0.005	0.002	0.009	0.012	0.014	0.02	0.006	0.003	0.004	0.006
K_2O	0.079	0.08	0.1	0.064	0.112	0.103	0.14	0.084	0.082	0.085	0.102	0.066	0.1
CaO	3.03	3.08	2.77	2.54	2.81	2.65	2.58	2.88	2.72	3.07	2.63	2.69	2.7
SrO	0.074	0.1	0.132	0.055	0.091	0.124	0.077	0.105	0.112	0.085	0.085	0.087	0.126
TiO_2	0.022	0.02	0	0.005	0	0	0	0.04	0	0.02	0	0	0.001
BaO	0.038	0.014	0	0.027	0.024	0	0	0.014	0.058	0	0.06	0.024	0
Na_2O	9.88	9.82	9.96	10.13	10.05	10.02	10.12	10	10.08	9.89	10.06	9.97	10.09
MgO	0	0	0	0	0	0	0	0	0	0	0	0	0
Total	99.013	99.27	99.196	99.217	99.433	99.351	99.069	99.4	99.807	99.219	99.318	98.82	99.329
Si	2.843	2.836	2.850	2.861	2.847	2.858	2.855	2.842	2.853	2.835	2.851	2.849	2.860
Al	1.157	1.168	1.155	1.144	1.155	1.147	1.150	1.160	1.149	1.167	1.156	1.158	1.141
Fe^{2+}	0.000	0.001	0.000	0.000	0.002	0.000	0.000	0.000	0.001	0.001	0.000	0.001	0.000
Mn	0.000	0.000	0.000	0.000	0.000	0.000	0.000	0.001	0.001	0.000	0.000	0.000	0.000
K	0.004	0.005	0.006	0.004	0.006	0.006	0.008	0.005	0.005	0.005	0.006	0.004	0.006
Ca	0.145	0.147	0.132	0.121	0.133	0.126	0.123	0.137	0.129	0.146	0.125	0.128	0.128
Sr	0.002	0.003	0.003	0.001	0.002	0.003	0.002	0.003	0.003	0.002	0.002	0.002	0.003
Ti	0.001	0.001	0.000	0.000	0.000	0.000	0.000	0.001	0.000	0.001	0.000	0.000	0.000
Ba	0.001	0.000	0.000	0.000	0.000	0.000	0.000	0.000	0.001	0.000	0.001	0.000	0.000
Na	0.853	0.846	0.858	0.871	0.864	0.861	0.872	0.860	0.863	0.852	0.865	0.862	0.868
Mg	0.000	0.000	0.000	0.000	0.000	0.000	0.000	0.000	0.000	0.000	0.000	0.000	0.000
Total	5.006	5.005	5.004	5.004	5.010	5.002	5.010	5.009	5.005	5.009	5.007	5.004	5.006
X_{An}	0.144	0.147	0.132	0.121	0.133	0.127	0.123	0.137	0.129	0.146	0.125	0.129	0.128
X_{Ab}	0.851	0.848	0.862	0.875	0.861	0.867	0.870	0.859	0.866	0.849	0.869	0.867	0.866
X_{Or}	0.004	0.005	0.006	0.004	0.006	0.006	0.008	0.005	0.005	0.005	0.006	0.004	0.006

X_{An} = Ca/(Ca + Na + K); X_{Ab} = Na/(Ca + Na + K); X_{Or} = K/(Ca + Na + K)

plg9.2	plg9.3	plg9.4	plg9.5	plg10.1	plg10.2	plg10.3	plg11.1	plg11.2	plg11.3	plg11.4	plg12.1	plg12.2	plg13.1	plg13.2
64.87	64.64	64.44	63.87	64.63	64.6	64.49	63.97	64.39	63.99	64.03	63.92	64.07	64.07	64.13
21.94	21.99	21.99	22.06	22	21.93	21.92	22.08	22.09	22.13	21.95	22.31	22.17	22.07	22.24
0.018	0.015	0.028	0.048	0.212	0.061	0.079	0.021	0.000	0.000	0.031	0.104	0.031	0.008	0.040
0.009	0.011	0	0.008	0.029	0	0	0	0.005	0	0.01	0.012	0.005	0.006	0.005
0.128	0.13	0.124	0.093	0.103	0.108	0.082	0.095	0.117	0.107	0.155	0.076	0.068	0.097	0.078
2.63	2.6	2.76	2.62	2.75	2.5	2.61	2.99	2.8	2.82	2.79	2.96	2.91	2.81	2.94
0.096	0.097	0.082	0.06	0.054	0.073	0.055	0.103	0.067	0.055	0.102	0.124	0.106	0.095	0.13
0	0.028	0	0	0.005	0	0.018	0	0	0	0.014	0.049	0	0.007	0.043
0	0	0	0	0	0	0.061	0.019	0.01	0	0	0.014	0.024	0	0
10.23	10.17	10.11	10.16	9.99	10.12	10.2	10	10.2	10.06	10.13	9.92	10.03	10.11	9.9
0.009	0	0	0	0.007	0	0.006	0	0.003	0	0	0	0	0	0
99.932	99.682	99.537	98.924	99.803	99.4	99.53	99.279	99.682	99.162	99.215	99.503	99.417	99.273	99.511
2.860	2.857	2.853	2.846	2.854	2.861	2.856	2.843	2.848	2.844	2.847	2.834	2.842	2.846	2.841
1.140	1.145	1.148	1.158	1.145	1.145	1.144	1.156	1.152	1.159	1.150	1.166	1.159	1.155	1.161
0.001	0.001	0.001	0.002	0.008	0.002	0.003	0.001	0.000	0.000	0.001	0.004	0.001	0.000	0.002
0.000	0.000	0.000	0.000	0.001	0.000	0.000	0.000	0.000	0.000	0.000	0.000	0.000	0.000	0.000
0.007	0.007	0.007	0.005	0.006	0.006	0.005	0.005	0.007	0.006	0.009	0.004	0.004	0.005	0.004
0.124	0.123	0.131	0.125	0.130	0.119	0.124	0.142	0.133	0.134	0.133	0.141	0.138	0.134	0.140
0.002	0.002	0.002	0.002	0.001	0.002	0.001	0.003	0.002	0.001	0.003	0.003	0.003	0.002	0.003
0.000	0.001	0.000	0.000	0.000	0.000	0.001	0.000	0.000	0.000	0.000	0.002	0.000	0.000	0.001
0.000	0.000	0.000	0.000	0.000	0.000	0.001	0.000	0.000	0.000	0.000	0.000	0.000	0.000	0.000
0.874	0.871	0.868	0.878	0.855	0.869	0.876	0.862	0.875	0.867	0.873	0.853	0.863	0.871	0.850
0.001	0.000	0.000	0.000	0.000	0.000	0.000	0.000	0.000	0.000	0.000	0.000	0.000	0.000	0.000
5.010	5.009	5.010	5.016	5.000	5.003	5.010	5.012	5.016	5.012	5.017	5.008	5.011	5.014	5.003
0.124	0.123	0.130	0.124	0.131	0.119	0.123	0.141	0.131	0.133	0.131	0.141	0.138	0.132	0.140
0.869	0.870	0.863	0.871	0.863	0.874	0.872	0.854	0.863	0.861	0.860	0.855	0.859	0.862	0.855
0.007	0.007	0.007	0.005	0.006	0.006	0.005	0.005	0.007	0.006	0.009	0.004	0.004	0.005	0.004

plg14.1	plg14.2	plg14.3	plg15.1	plg15.2	plg16.1	plg16.2	plg16.3	plg17.1	plg17.2	plg17.3	plg18	plg19.1	plg19.2
64.05	64.16	64.01	63.98	64.6	64.25	64.25	63.65	64.36	64.26	64.16	64.07	64.49	64.51
22.2	22.3	22.38	22.26	21.88	22.19	22.13	22.22	22.64	22.23	22.23	22.24	22.15	22.07
0.030	0.055	0.033	0.149	0.022	0.098	0.042	0.171	0.111	0.112	0.000	0.089	0.049	0.058
0	0.023	0.005	0.007	0	0.004	0.001	0.004	0.017	0.007	0	0	0	0
0.083	0.09	0.085	0.08	0.151	0.078	0.081	0.115	0.096	0.082	0.108	0.077	0.09	0.115
2.94	2.96	3.27	3.03	2.57	2.99	2.9	3.23	3.3	2.84	2.87	2.84	2.93	2.76
0.076	0.08	0.131	0.114	0.072	0.073	0.09	0.068	0.108	0.092	0.087	0.072	0.092	0.098
0	0	0	0.002	0	0	0.025	0	0	0	0	0.018	0.031	0.021
0.056	0	0.002	0.034	0	0	0	0	0.016	0	0	0	0	0.006
9.99	9.84	9.69	9.78	10.21	9.87	10.03	9.96	9.67	9.97	9.89	10	9.95	10.09
0	0	0	0	0	0	0	0	0	0	0	0	0	0
99.428	99.514	99.611	99.453	99.508	99.565	99.554	99.437	100.33	99.606	99.346	99.416	99.787	99.734
2.841	2.841	2.835	2.838	2.860	2.844	2.845	2.828	2.830	2.844	2.845	2.841	2.848	2.851
1.161	1.164	1.168	1.164	1.142	1.158	1.155	1.164	1.173	1.159	1.162	1.162	1.153	1.150
0.001	0.002	0.001	0.006	0.001	0.004	0.002	0.006	0.004	0.004	0.000	0.003	0.002	0.002
0.000	0.001	0.000	0.000	0.000	0.000	0.000	0.000	0.001	0.000	0.000	0.000	0.000	0.000
0.005	0.005	0.005	0.005	0.009	0.004	0.005	0.007	0.005	0.005	0.006	0.004	0.005	0.006
0.140	0.140	0.155	0.144	0.122	0.142	0.138	0.154	0.155	0.135	0.136	0.135	0.139	0.131
0.002	0.002	0.003	0.003	0.002	0.002	0.002	0.002	0.003	0.002	0.002	0.002	0.002	0.003
0.000	0.000	0.000	0.000	0.000	0.000	0.001	0.000	0.000	0.000	0.000	0.001	0.001	0.001
0.001	0.000	0.000	0.001	0.000	0.000	0.000	0.000	0.000	0.000	0.000	0.000	0.000	0.000
0.859	0.845	0.832	0.841	0.876	0.847	0.861	0.858	0.824	0.855	0.850	0.860	0.852	0.865
0.000	0.000	0.000	0.000	0.000	0.000	0.000	0.000	0.000	0.000	0.000	0.000	0.000	0.000
5.010	5.001	4.999	5.000	5.011	5.001	5.008	5.019	4.996	5.005	5.002	5.008	5.002	5.008
0.139	0.142	0.156	0.146	0.121	0.143	0.137	0.151	0.158	0.135	0.137	0.135	0.139	0.130
0.856	0.853	0.839	0.850	0.870	0.853	0.858	0.843	0.837	0.860	0.856	0.861	0.856	0.863
0.005	0.005	0.005	0.005	0.008	0.004	0.005	0.006	0.005	0.005	0.006	0.004	0.005	0.006

Sample	WSP10.A													
Mineral	plg1	plg2	plg3	plg4.1	plg4.2	plg5.1	plg5.2	plg5.3	plg6.1	plg6.2	plg7	plg8	plg9	plg10
SiO_2	61.38	61.14	62.14	62.45	61.72	62.17	62.56	62.95	62.56	61.48	61.01	62.43	60.89	60.92
Al_2O_3	24.16	24.22	23.56	23.51	23.72	23.64	23.6	23.19	23.48	24.1	24.32	23.6	24.51	24.34
FeO	0.027	0.138	0.015	0.016	0.033	0.199	0.119	0.058	0.043	0.027	0.015	0.000	0.000	0.006
MnO	0.016	0.018	0	0.001	0	0	0	0.01	0.008	0.029	0.023	0.006	0.019	0
K_2O	0.15	0.122	0.174	0.194	0.234	0.145	0.141	0.132	0.176	0.194	0.149	0.158	0.151	0.139
CaO	4.91	5.1	4.29	4.28	4.57	4.67	4.34	3.98	4.18	4.91	5.3	4.22	5.28	5.21
SrO	0.036	0.064	0.053	0.03	0.044	0.089	0.082	0.031	0.059	0.073	0.076	0.023	0.005	0.048
TiO_2	0.041	0.042	0.036	0	0	0.006	0.068	0.015	0.019	0	0	0.031	0	0
BaO	0	0	0	0	0	0	0	0	0.044	0.01	0	0.017	0	0.022
Na_2O	8.78	8.59	9.1	9.12	8.99	8.89	9.09	9.35	9.21	8.89	8.54	9.05	8.52	8.65
MgO	0	0.004	0	0	0	0.013	0	0	0	0	0	0	0	0
Total	99.503	99.452	99.369	99.603	99.315	99.844	100.012	99.722	99.783	99.716	99.436	99.535	99.375	99.335
Si	2.736	2.729	2.769	2.775	2.755	2.760	2.770	2.791	2.776	2.737	2.724	2.774	2.719	2.723
Al	1.269	1.274	1.237	1.231	1.248	1.237	1.231	1.212	1.228	1.265	1.280	1.236	1.290	1.282
Fe^{2+}	0.001	0.005	0.001	0.001	0.001	0.007	0.004	0.002	0.002	0.001	0.001	0.000	0.000	0.000
Mn	0.001	0.001	0.000	0.000	0.000	0.000	0.000	0.000	0.000	0.001	0.001	0.000	0.001	0.000
K	0.009	0.007	0.010	0.011	0.013	0.008	0.008	0.007	0.010	0.011	0.008	0.009	0.009	0.008
Ca	0.234	0.244	0.205	0.204	0.219	0.222	0.206	0.189	0.199	0.234	0.254	0.201	0.253	0.250
Sr	0.001	0.002	0.001	0.001	0.001	0.002	0.002	0.001	0.002	0.002	0.002	0.001	0.000	0.001
Ti	0.001	0.001	0.001	0.000	0.000	0.000	0.002	0.001	0.001	0.000	0.000	0.001	0.000	0.000
Ba	0.000	0.000	0.000	0.000	0.000	0.000	0.000	0.000	0.001	0.000	0.000	0.000	0.000	0.000
Na	0.759	0.743	0.786	0.786	0.778	0.765	0.780	0.804	0.792	0.767	0.739	0.780	0.738	0.750
Mg	0.000	0.000	0.000	0.000	0.000	0.001	0.000	0.000	0.000	0.000	0.000	0.000	0.000	0.000
Total	5.011	5.006	5.009	5.008	5.016	5.004	5.004	5.007	5.010	5.019	5.009	5.001	5.009	5.014
X_{An}	0.234	0.245	0.205	0.204	0.216	0.223	0.207	0.189	0.199	0.231	0.253	0.203	0.253	0.248
X_{Ab}	0.757	0.748	0.785	0.785	0.770	0.769	0.785	0.804	0.792	0.758	0.738	0.788	0.738	0.744
X_{Or}	0.009	0.007	0.010	0.011	0.013	0.008	0.008	0.007	0.010	0.011	0.008	0.009	0.009	0.008

plg11.1	plg11.2	plg12	plg13	plg14.1	plg14.2	plg14.3	plg14.4	plg14.5	plg14.6	plg15.1	plg15.2	plg15.3	plg15.4	plg15.5
62.58	62.08	62.14	61.91	61.44	62.15	62.42	63.06	62.17	63.64	63.78	64.91	67.45	61.67	62
23.33	23.81	23.63	23.92	24.18	23.54	23.5	22.99	23.48	22.82	22.86	21.79	19.84	23.99	23.94
0.000	0.030	0.056	0.101	0.010	0.430	0.049	0.010	0.037	0.065	0.220	0.047	0.165	0.021	0.055
0.005	0.01	0.004	0.014	0.012	0.01	0.007	0	0.005	0.009	0.019	0.002	0	0.001	0.016
0.15	0.113	0.115	0.17	0.113	0.162	0.147	0.214	0.199	0.194	0.144	0.164	0.866	0.202	0.219
4.18	4.73	4.38	4.75	4.86	4.27	4.11	3.71	4.13	3.4	3.36	2.28	0.216	4.75	4.71
0.072	0.044	0.076	0.066	0.065	0.061	0.024	0.057	0.06	0.048	0.039	0.047	0	0.014	0.08
0.011	0	0	0.001	0.018	0.001	0	0.009	0.002	0	0.004	0	0	0.048	0
0	0.022	0.04	0.006	0.029	0.038	0.009	0.001	0.092	0.076	0	0	0.003	0.041	0.036
9.16	8.89	9.1	9.04	8.7	8.87	9.3	9.47	9.07	9.6	9.74	10.35	11.19	8.94	8.94
0	0	0	0	0	0.107	0	0	0	0	0	0	0.057	0	0
99.488	99.732	99.549	99.989	99.428	99.688	99.571	99.523	99.251	99.859	100.191	99.596	99.806	99.678	100.002
2.783	2.758	2.765	2.748	2.739	2.763	2.775	2.801	2.774	2.815	2.812	2.869	2.967	2.745	2.751
1.223	1.247	1.239	1.251	1.270	1.233	1.231	1.203	1.235	1.190	1.188	1.135	1.028	1.258	1.252
0.000	0.001	0.002	0.004	0.000	0.016	0.002	0.000	0.001	0.002	0.008	0.002	0.006	0.001	0.002
0.000	0.000	0.000	0.001	0.000	0.000	0.000	0.000	0.000	0.000	0.001	0.000	0.000	0.000	0.001
0.009	0.006	0.007	0.010	0.006	0.009	0.008	0.012	0.011	0.011	0.008	0.009	0.049	0.011	0.012
0.199	0.225	0.209	0.226	0.232	0.203	0.196	0.177	0.197	0.161	0.159	0.108	0.010	0.226	0.224
0.002	0.001	0.002	0.002	0.002	0.002	0.001	0.001	0.002	0.001	0.001	0.001	0.000	0.000	0.002
0.000	0.000	0.000	0.000	0.001	0.000	0.000	0.000	0.000	0.000	0.000	0.000	0.000	0.002	0.000
0.000	0.000	0.001	0.000	0.001	0.001	0.000	0.000	0.002	0.001	0.000	0.000	0.000	0.001	0.001
0.790	0.766	0.785	0.778	0.752	0.764	0.801	0.815	0.784	0.823	0.833	0.887	0.954	0.771	0.769
0.000	0.000	0.000	0.000	0.000	0.007	0.000	0.000	0.000	0.000	0.000	0.000	0.004	0.000	0.000
5.005	5.004	5.010	5.018	5.004	4.999	5.014	5.011	5.006	5.006	5.010	5.011	5.018	5.016	5.013
0.200	0.226	0.209	0.223	0.234	0.208	0.195	0.176	0.199	0.162	0.159	0.108	0.010	0.224	0.223
0.792	0.768	0.785	0.768	0.759	0.782	0.797	0.812	0.790	0.827	0.833	0.883	0.942	0.764	0.765
0.009	0.006	0.007	0.009	0.006	0.009	0.008	0.012	0.011	0.011	0.008	0.009	0.048	0.011	0.012

plg16.1	plg16.2	plg16.3	plg16.4	plg16.5	plg16.6	plg16.7	plg17	plg18	plg19	plg20	plg21
61.2	62.98	60.68	61.41	60.99	60.41	62.7	63.42	62.49	63.09	63.27	62.8
24.42	22.99	24.4	24.01	24	24.33	23.25	24.15	24.13	24.04	23.95	24.29
0.025	0.076	0.000	0.008	0.028	0.213	0.000	0.031	0.171	0.249	0.258	0.042
0.018	0	0.015	0.001	0.022	0.005	0	0.022	0.02	0.003	0.016	0.009
0.134	0.23	0.17	0.205	0.116	0.162	0.183	0.193	0.122	0.146	0.129	0.109
5.27	3.66	5.35	4.94	5.06	5.21	4.16	4.14	4.54	4.32	4.11	4.79
0.084	0.055	0.069	0.087	0.069	0.022	0.069	0.044	0.035	0.009	0.083	0.049
0.004	0	0.036	0.042	0	0	0	0	0	0.046	0.038	0
0	0.023	0	0	0	0.016	0.06	0.005	0	0	0.013	0
8.57	9.4	8.68	8.73	8.78	8.43	9.23	9.24	8.95	8.95	9.14	8.85
0	0	0	0	0	0.032	0	0	0	0.073	0.095	0
99.728	99.423	99.401	99.434	99.069	98.853	99.652	101.248	100.477	100.955	101.132	100.944
2.724	2.800	2.714	2.740	2.733	2.715	2.785	2.770	2.754	2.764	2.769	2.754
1.281	1.205	1.286	1.263	1.268	1.288	1.217	1.243	1.253	1.241	1.235	1.255
0.001	0.003	0.000	0.000	0.001	0.008	0.000	0.001	0.006	0.009	0.009	0.002
0.001	0.000	0.001	0.000	0.001	0.000	0.000	0.001	0.001	0.000	0.001	0.000
0.008	0.013	0.010	0.012	0.007	0.009	0.010	0.011	0.007	0.008	0.007	0.006
0.251	0.174	0.256	0.236	0.243	0.251	0.198	0.194	0.214	0.203	0.193	0.225
0.002	0.001	0.002	0.002	0.002	0.001	0.002	0.001	0.001	0.000	0.002	0.001
0.000	0.000	0.001	0.001	0.000	0.000	0.000	0.000	0.000	0.002	0.001	0.000
0.000	0.000	0.000	0.000	0.000	0.000	0.001	0.000	0.000	0.000	0.000	0.000
0.740	0.810	0.753	0.755	0.763	0.734	0.795	0.783	0.765	0.760	0.775	0.752
0.000	0.000	0.000	0.000	0.000	0.002	0.000	0.000	0.000	0.005	0.006	0.000
5.008	5.007	5.023	5.010	5.017	5.009	5.009	5.004	5.002	4.993	4.999	4.997
0.252	0.175	0.252	0.235	0.240	0.252	0.197	0.196	0.217	0.209	0.198	0.229
0.741	0.812	0.739	0.753	0.753	0.738	0.792	0.793	0.776	0.783	0.795	0.765
0.008	0.013	0.010	0.012	0.007	0.009	0.010	0.011	0.007	0.008	0.007	0.006

Table 1f. Cordierite compositions (EMPA). Cations are calculated based on 18 oxygens.

Sample	WSP10-A					
Mineral	crd1	crd2	crd3	crd4.1	crd4.2	crd4.3
SiO_2	48.41	48.17	47.98	47.97	47.8	47.78
Al_2O_3	33.42	33.22	33.19	33.25	33.01	33.09
FeO	11.410	11.329	10.996	11.311	10.942	11.401
MnO	0.405	0.363	0.374	0.358	0.378	0.33
K_2O	0	0.009	0.009	0.071	0.064	0.028
CaO	0	0.025	0	0	0.027	0
SrO	0	0.012	0	0.045	0	0.009
TiO_2	0.046	0	0	0	0	0
BaO	0.035	0.037	0	0.017	0.024	0
Na_2O	0.17	0.217	0.238	0.251	0.231	0.253
MgO	6.4	6.26	6.34	6.1	6.39	6.15
Total	101.576	100.912	100.361	100.642	100.093	100.32
Si	4.832	4.839	4.840	4.834	4.838	4.829
Al	3.931	3.933	3.946	3.948	3.938	3.942
Fe^{2+}	0.953	0.952	0.928	0.954	0.927	0.964
Mn	0.034	0.031	0.032	0.031	0.032	0.028
K	0.000	0.001	0.001	0.009	0.008	0.004
Ca	0.000	0.003	0.000	0.000	0.003	0.000
Sr	0.000	0.001	0.000	0.003	0.000	0.001
Ti	0.003	0.000	0.000	0.000	0.000	0.000
Ba	0.001	0.001	0.000	0.001	0.001	0.000
Na	0.033	0.042	0.047	0.049	0.045	0.050
Mg	0.952	0.937	0.953	0.916	0.964	0.927
Total	10.740	10.740	10.747	10.744	10.757	10.744
X_{Mg}	0.50	0.50	0.51	0.49	0.51	0.49

$X_{Mg} = Mg/(Fe^{2+} + Mg)$

Table 2. X-ray bulk rock composition (wt%):

	12A	45A	45A (recalculated)	10A
SiO_2	68.59	72.05	72.94	56.36
TiO_2	0.981	0.804	0.72	0.911
Al_2O_3	14.11	13.54	13.83	22.06
Fe_2O_3	6.17	8.9	-	9.11
MnO	0.041	0.172	-	0.086
MgO	1.99	2.28	2.15	2.7
CaO	0.06	0.17	0.2	0.29
Na_2O	0.28	0.07	0.42	1.02
K_2O	4.43	1.1	1.24	5.5
P_2O_5	0.045	0.02	-	0.096
LOI	2.35	0.64	-	1.39
Total	99.04	99.74	-	99.52

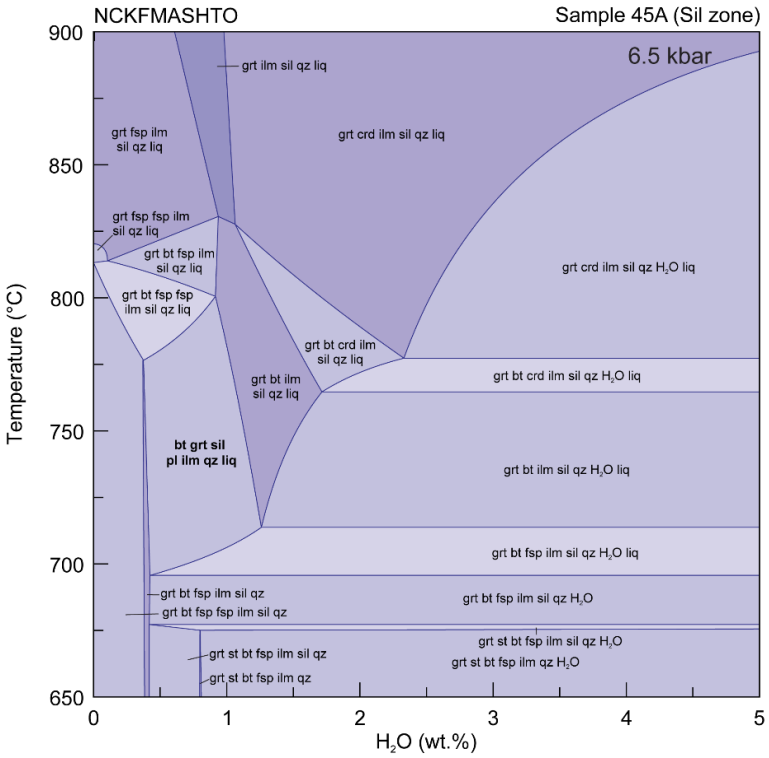

wt.% Na_2O = 0.42 CaO = 0.20 K_2O = 1.25 FeO = 7.59 MgO = 2.17 Al_2O_3 = 13.95
SiO_2 = 73.59 H_2O = 0.00 TiO_2 = 0.77 O_2 = 0.05

wt.% Na_2O = 0.40 CaO = 0.19 K_2O = 1.19 FeO = 7.21 MgO = 2.06 Al_2O_3 = 13.26
SiO_2 = 69.91 H_2O = 5.00 TiO_2 = 0.73 O_2 = 0.05

Figure 7. Calculated T-H_2O section of sample 45A at 6.5 kbar.

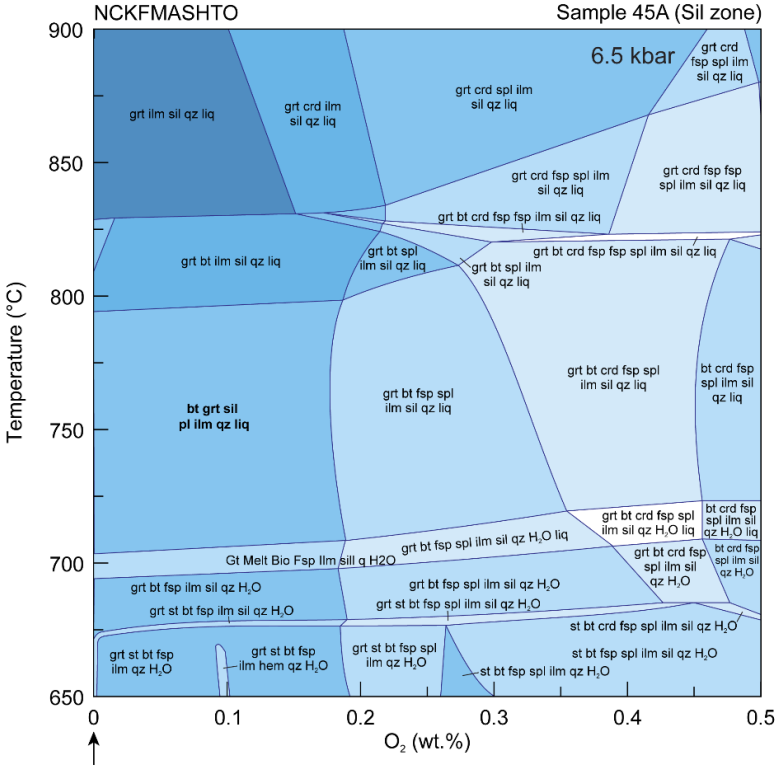

wt.% Na_2O = 0.42 CaO = 0.20 K_2O = 1.24 FeO = 7.52 MgO = 2.15 Al_2O_3 = 13.83
SiO_2 = 72.92 H_2O = 0.95 TiO_2 = 0.76 O_2 = 0.00

wt.% Na_2O = 0.42 CaO = 0.20 K_2O = 1.23 FeO = 7.49 MgO = 2.14 Al_2O_3 = 13.76
SiO_2 = 72.56 H_2O = 0.95 TiO_2 = 0.76 O_2 = 0.50

Figure 8. Calculated T-O_2 section of sample 45A at 6.5 kbar.

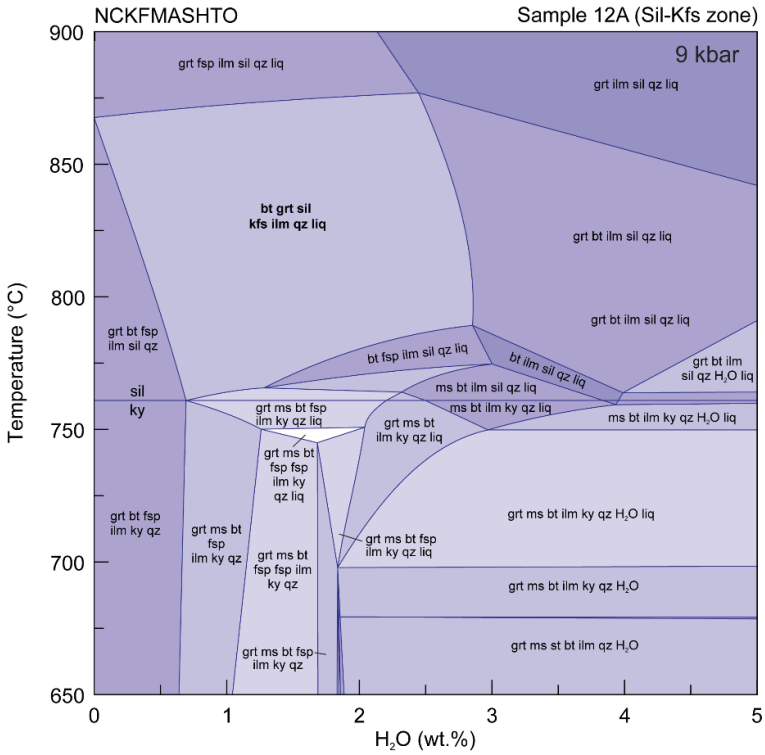

wt.% Na_2O = 0.30 CaO = 0.06 K_2O = 4.61 FeO = 5.78 MgO = 2.07 Al_2O_3 = 14.69 SiO_2 = 71.42 H_2O = 0.00 TiO_2 = 1.02 O_2 = 0.05

wt.% Na_2O = 0.28 CaO = 0.06 K_2O = 4.38 FeO = 5.49 MgO = 1.97 Al_2O_3 = 13.96 SiO_2 = 67.85 H_2O = 5.00 TiO_2 = 0.97 O_2 = 0.05

Figure 9. Calculated T-H_2O section of sample 12A at 9 kbar.

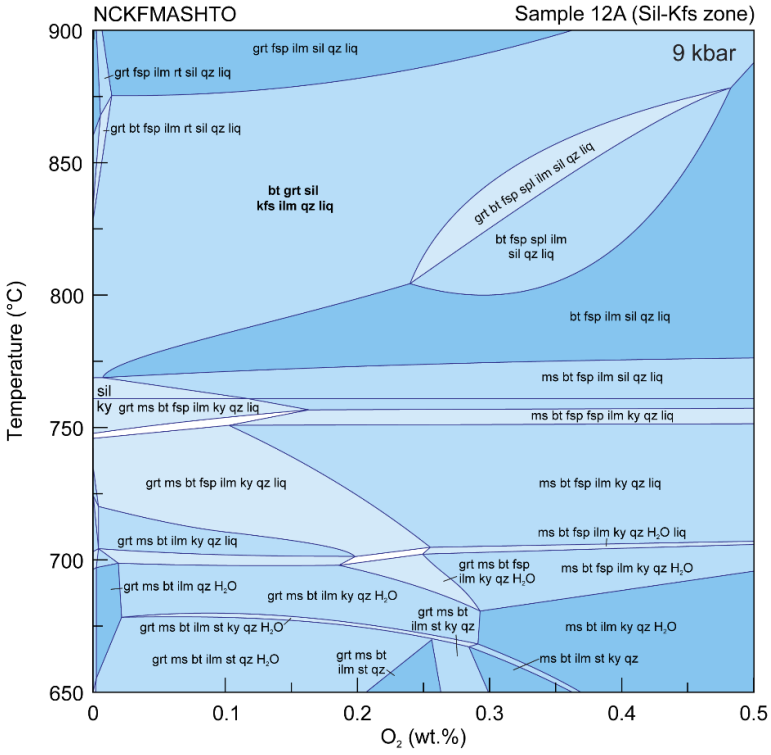

wt.% Na_2O = 0.29 CaO = 0.06 K_2O = 4.52 FeO = 5.67 MgO = 2.03 Al_2O_3 = 14.42 SiO_2 = 70.10 H_2O = 1.90 TiO_2 = 1.00 O_2 = 0.00

wt.% Na_2O = 0.29 CaO = 0.06 K_2O = 4.50 FeO = 5.64 MgO = 2.02 Al_2O_3 = 14.35 SiO_2 = 69.75 H_2O = 1.90 TiO_2 = 1.00 O_2 = 0.50

Figure 10. Calculated T-O_2 section of sample 12A at 9 kbar.

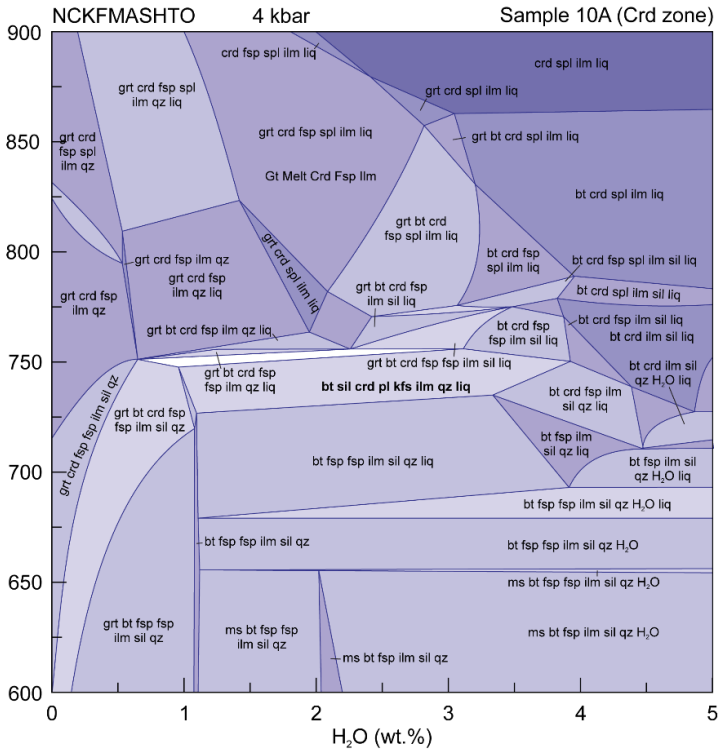

wt.% Na_2O = 1.06 CaO = 0.30 K_2O = 5.66 FeO = 8.44 MgO = 2.78 Al_2O_3 = 22.73 SiO_2 = 58.06 H_2O = 0.00 TiO_2 = 0.93 O_2 = 0.05

wt.% Na_2O = 1.00 CaO = 0.28 K_2O = 5.38 FeO = 8.02 MgO = 2.64 Al_2O_3 = 21.59 SiO_2 = 55.15 H_2O = 5.00 TiO_2 = 0.89 O_2 = 0.05

Figure 11. Calculated T-H_2O section of sample 10A at 4 kbar.

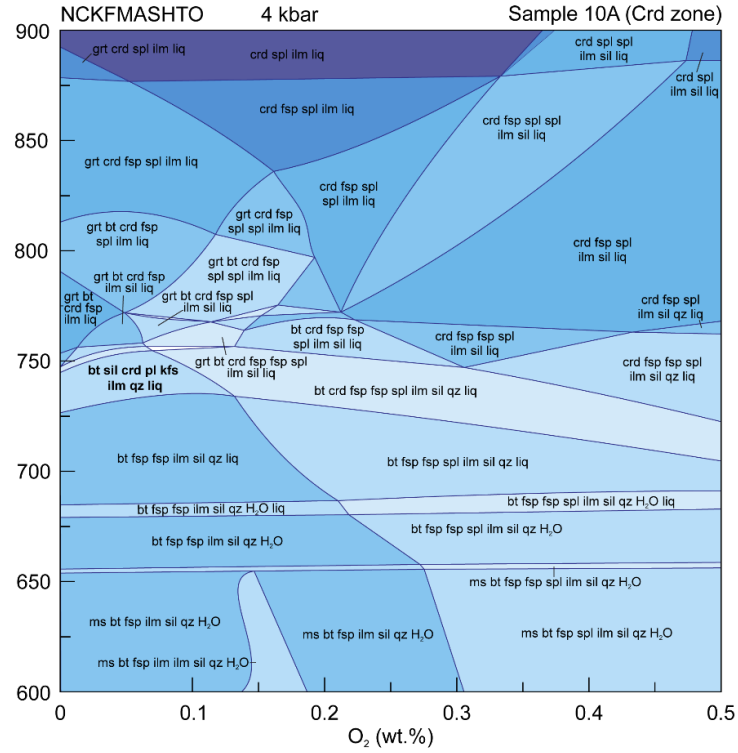

wt.% Na_2O = 1.03 CaO = 0.29 K_2O = 5.52 FeO = 8.24 MgO = 2.71 Al_2O_3 = 22.18 SiO_2 = 56.66 H_2O = 2.45 TiO_2 = 0.91 O_2 = 0.00

wt.% Na_2O = 1.03 CaO = 0.29 K_2O = 5.50 FeO = 8.19 MgO = 2.70 Al_2O_3 = 22.07 SiO_2 = 56.37 H_2O = 2.45 TiO_2 = 0.91 O_2 = 0.50

Figure 12. Calculated T-O_2 section of sample 10A at 4 kbar.

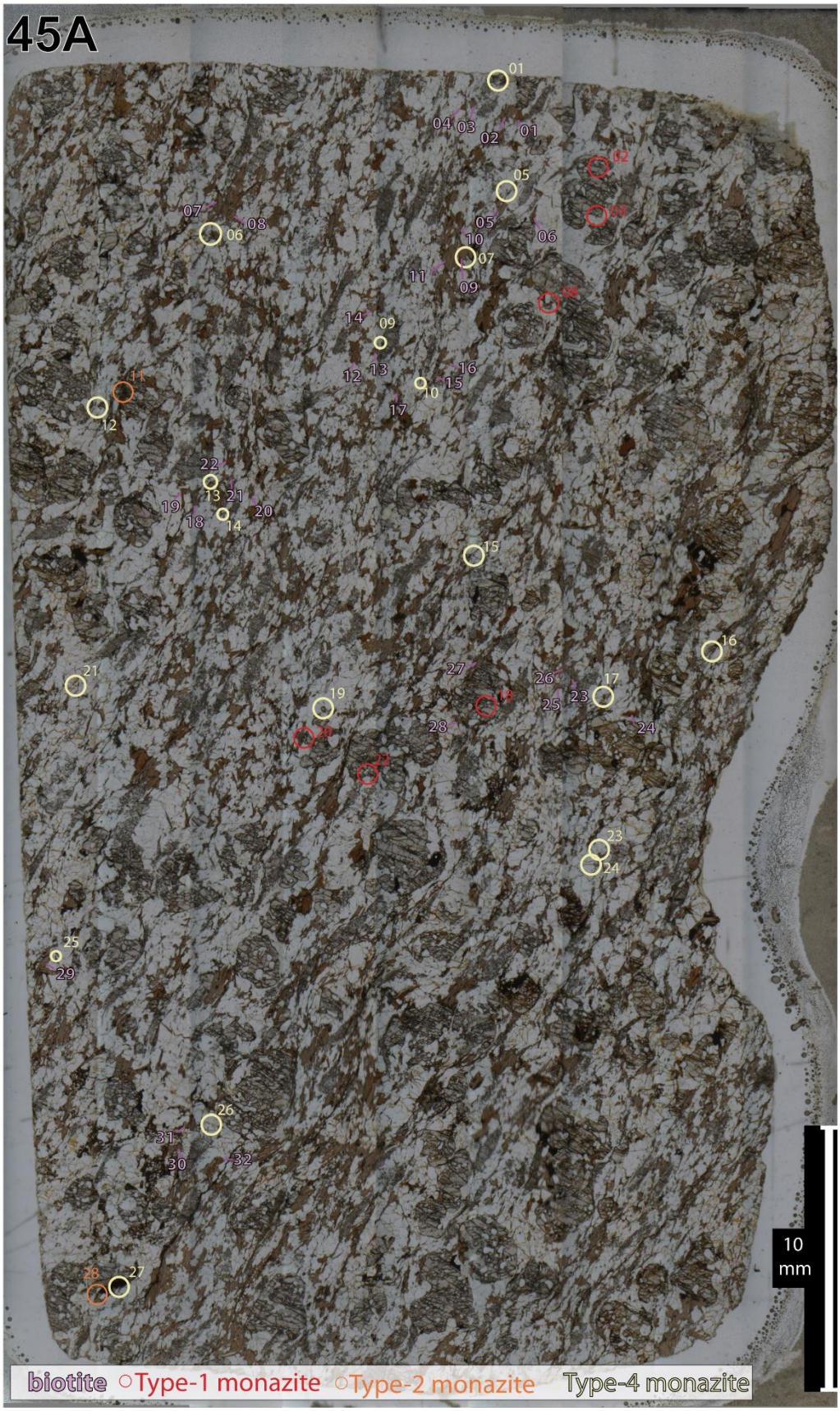

Figure 13. Location of biotite and monazite grains on thin section from the sample 45A under plane-polarised light.

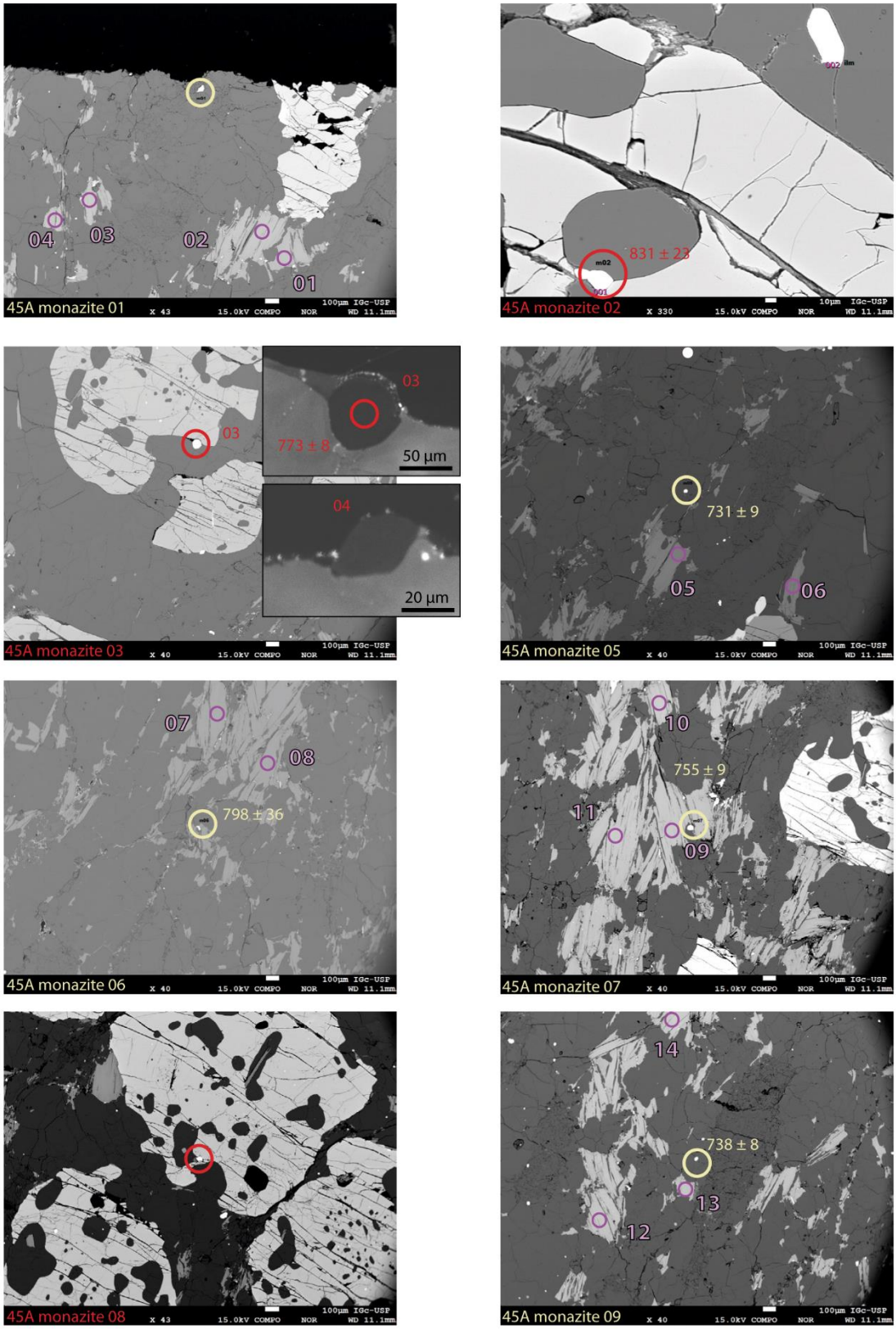

Figure 14. Backscattered electron image (BSE) pointing the location of analyzed biotite and monazite grains for sample 45A.

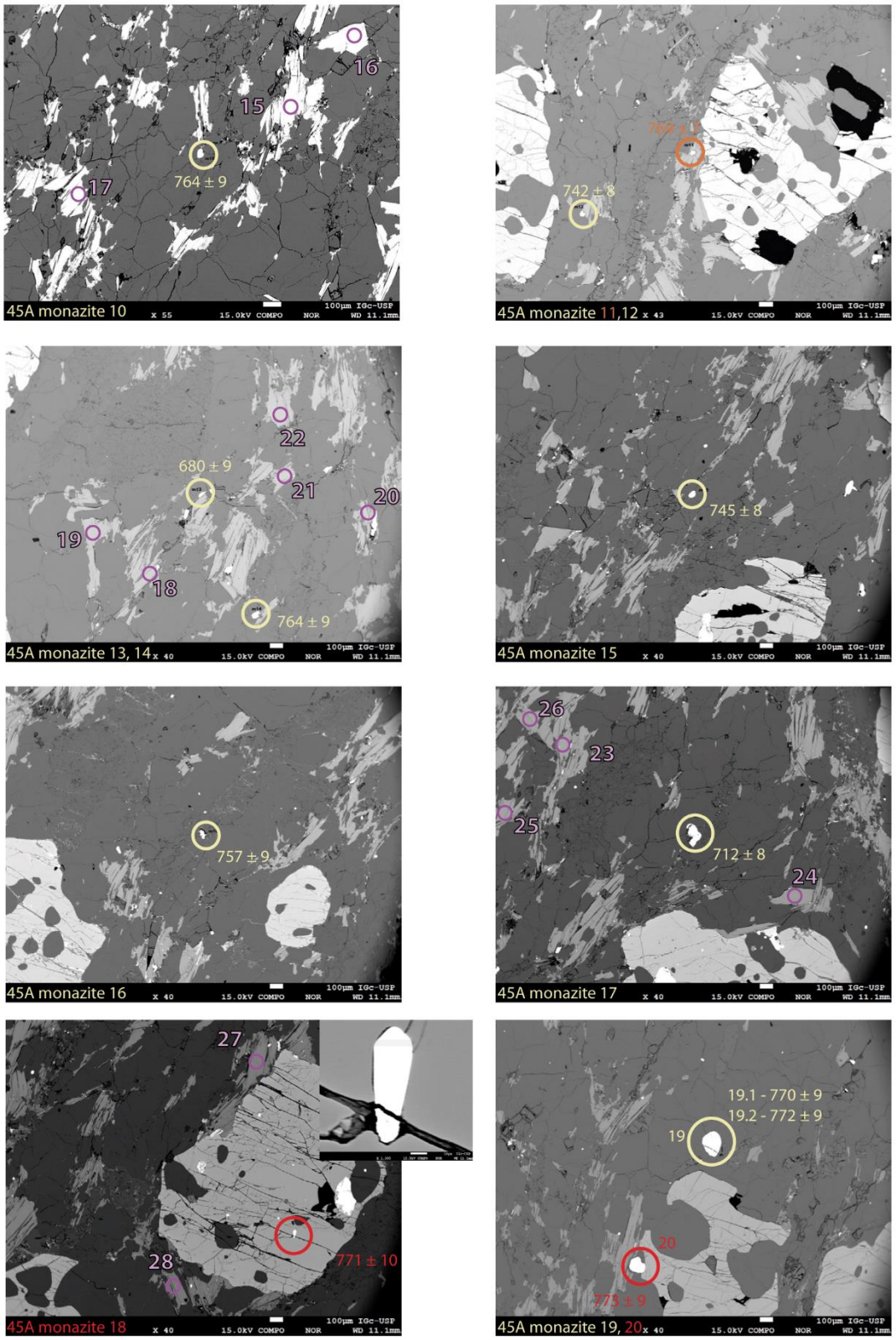

Figure 14. cont.

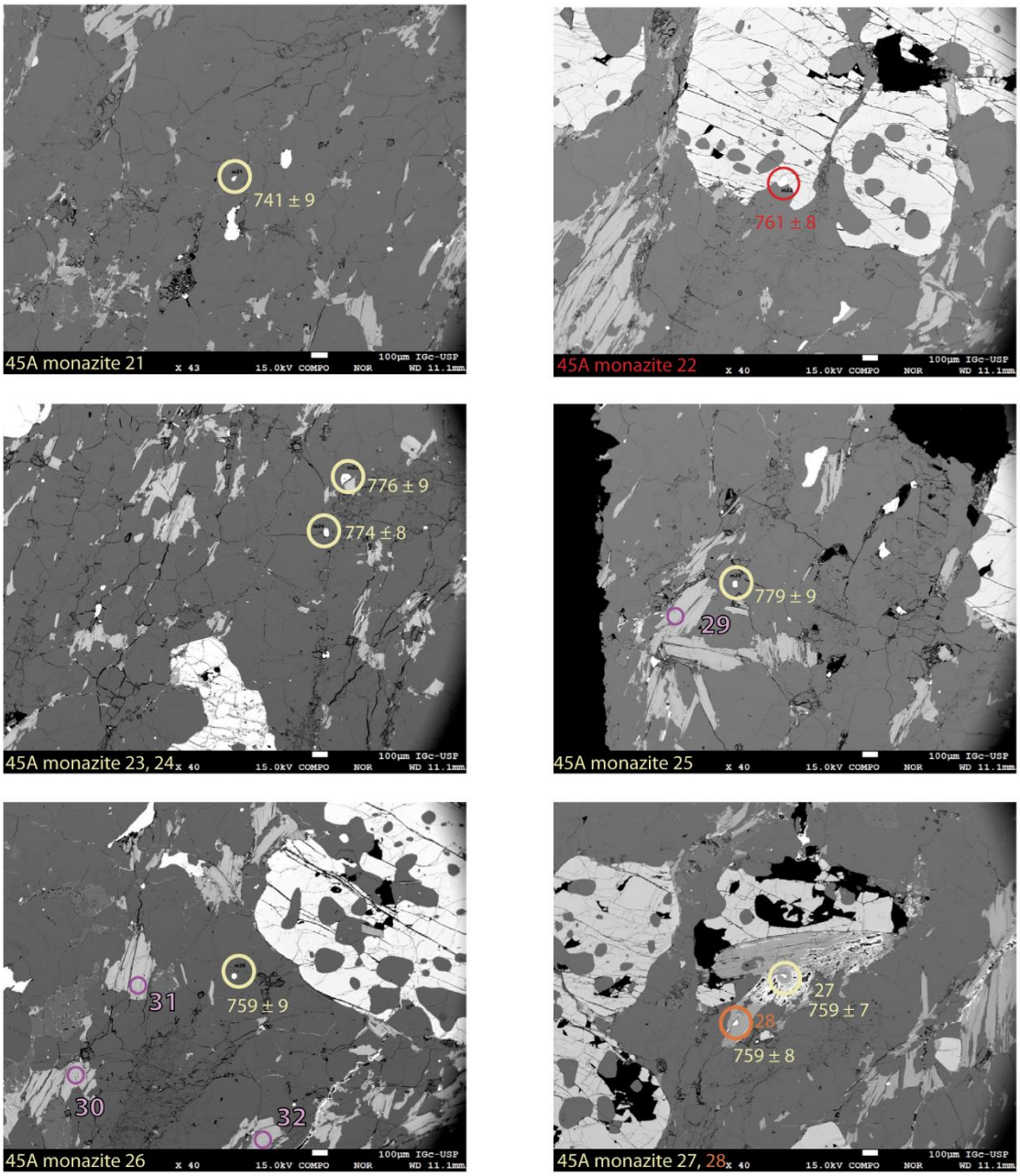

Figure 14. cont.

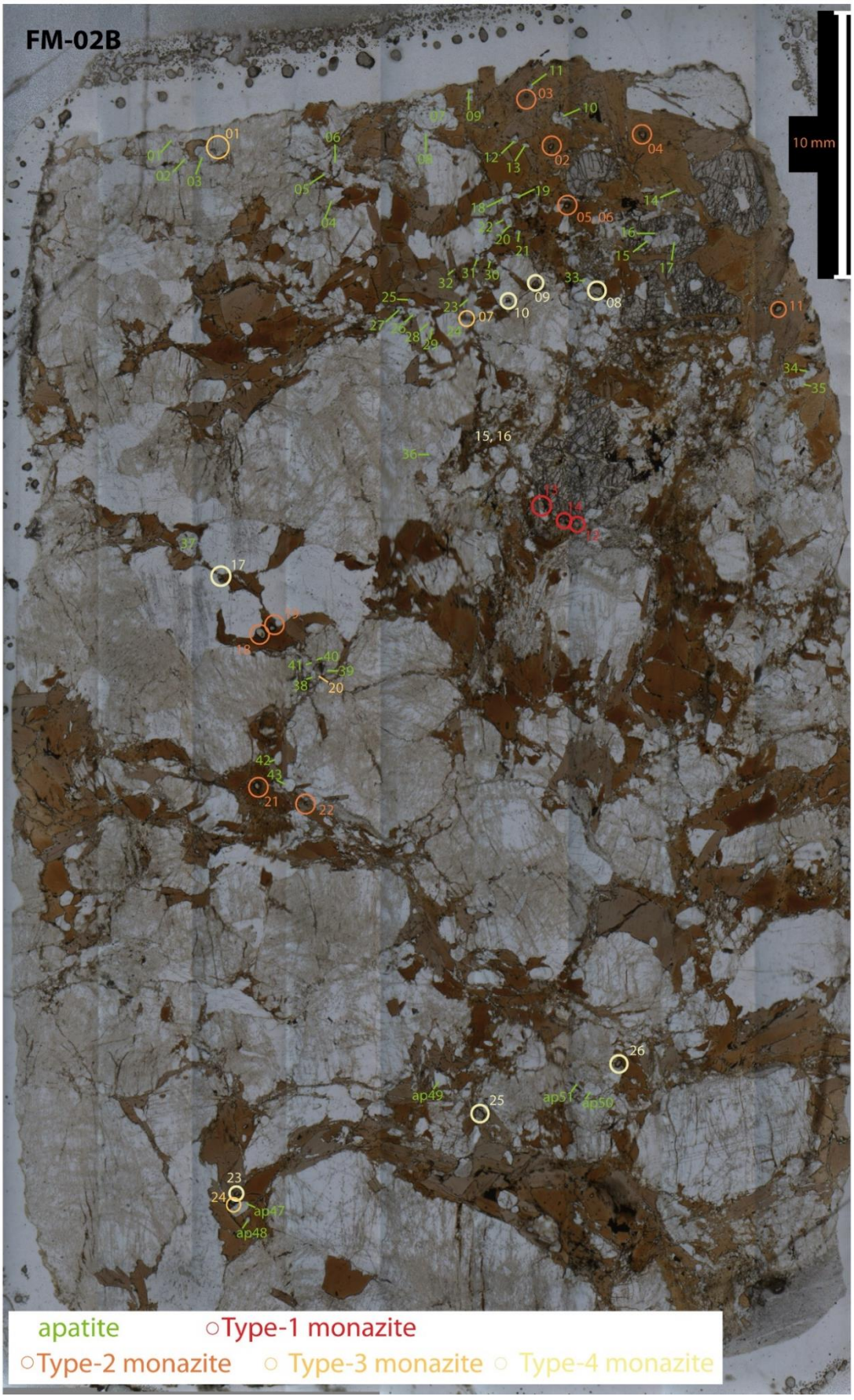

Figure 15. Location of apatite and monazite grains on thin section from the sample FM-02B under plane-polarised light.

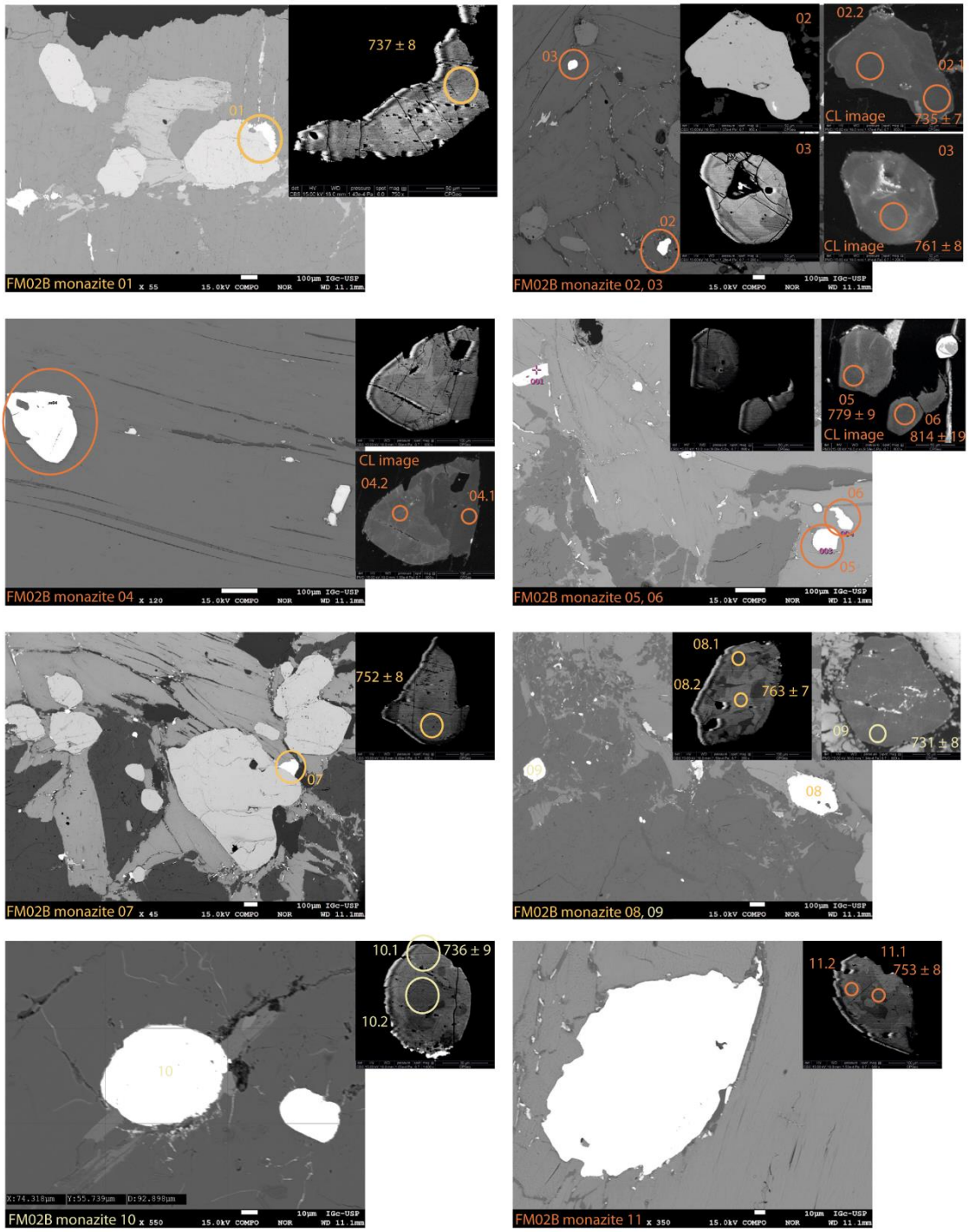

Figure 16. Backscattered electron image (BSE) pointing the location of analyzed apatite and monazite grains for sample FM-02B.

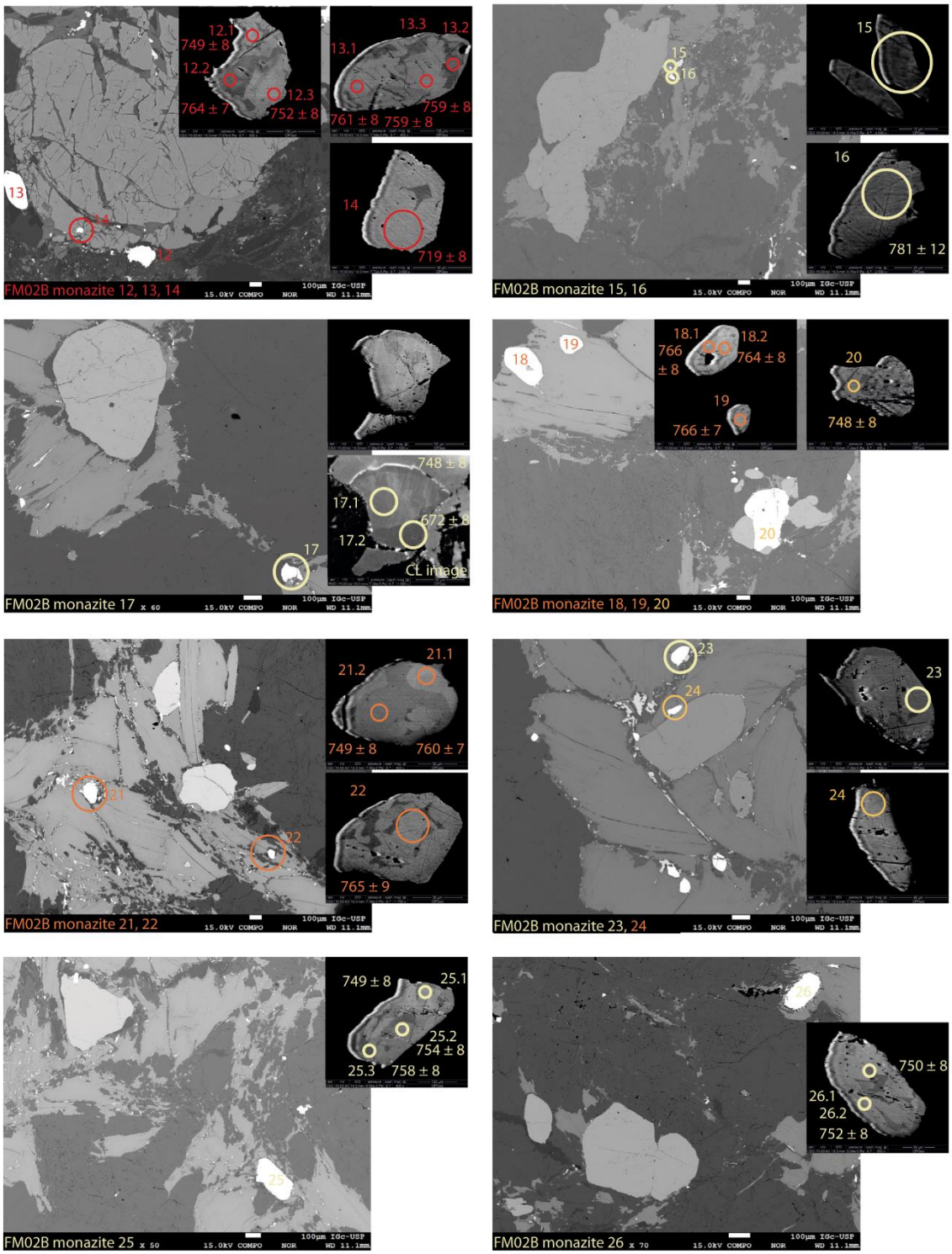

Figure 16. Cont.

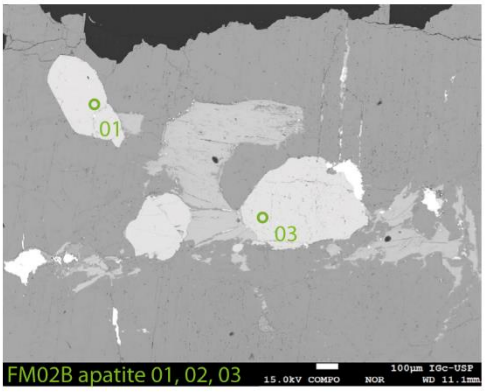

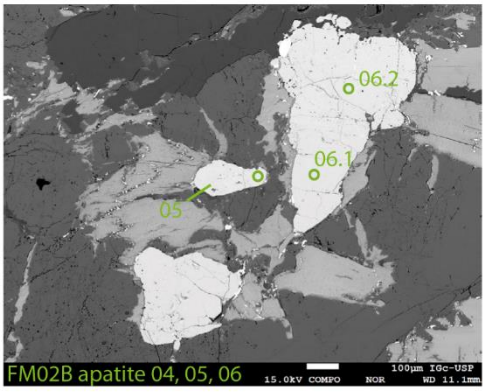

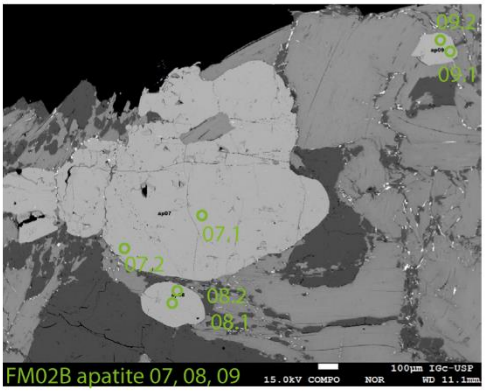

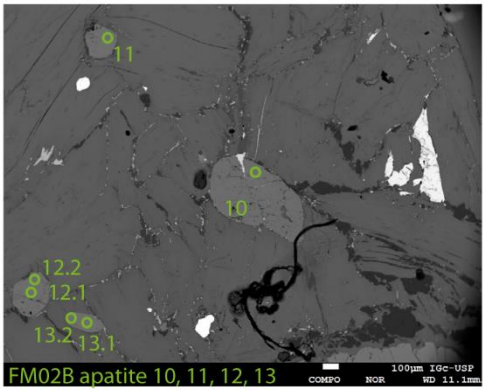

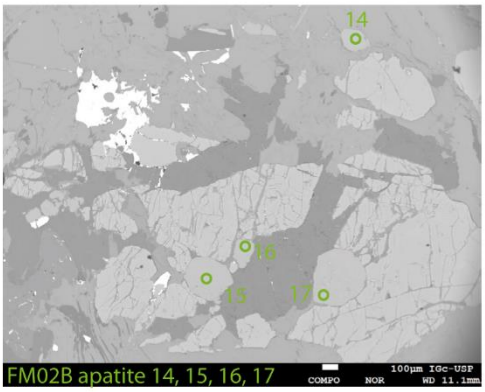

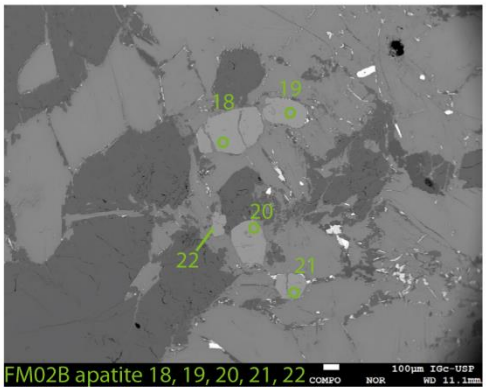

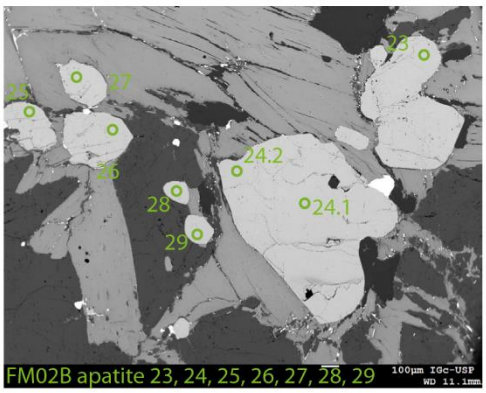

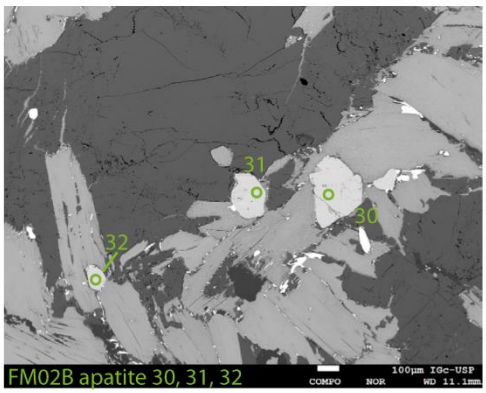

Figure 16. Cont.

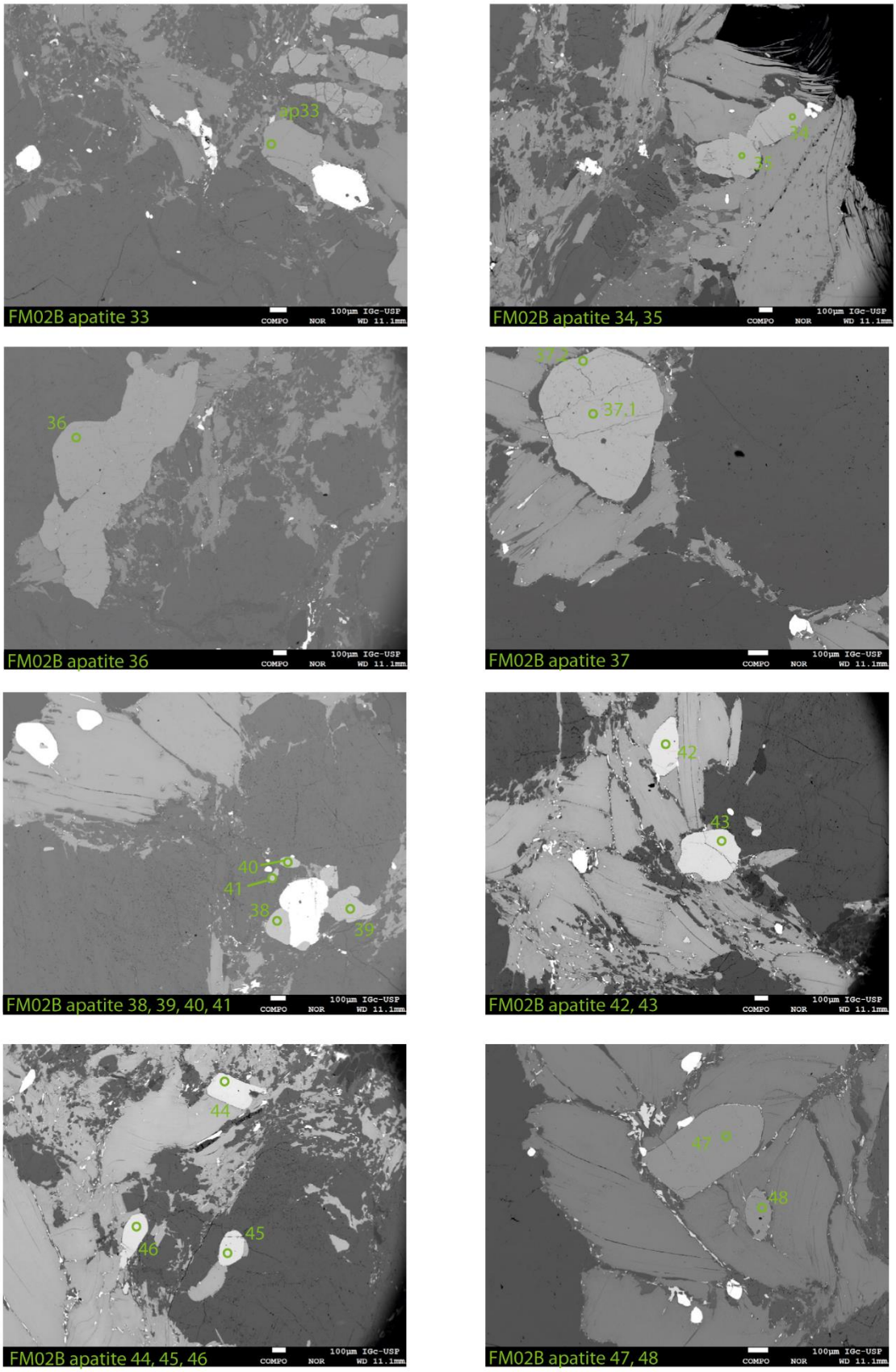

Figure 16. Cont.

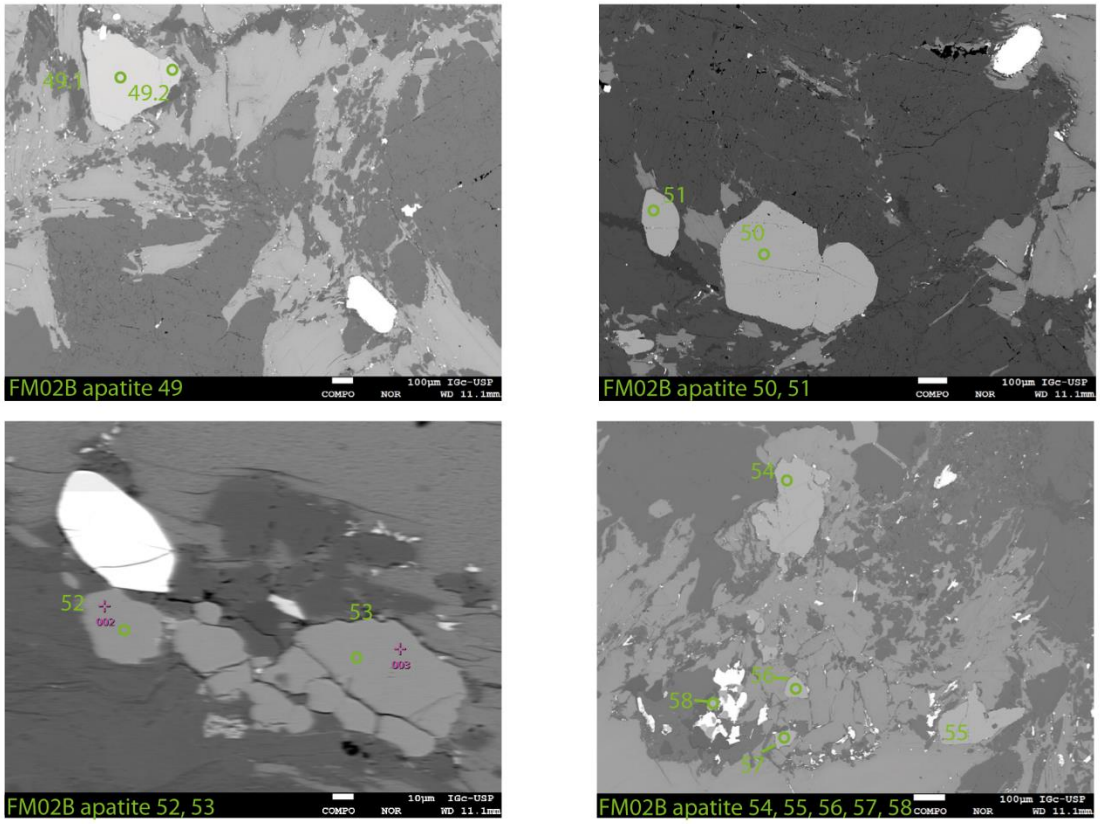

Figure 16. Cont.

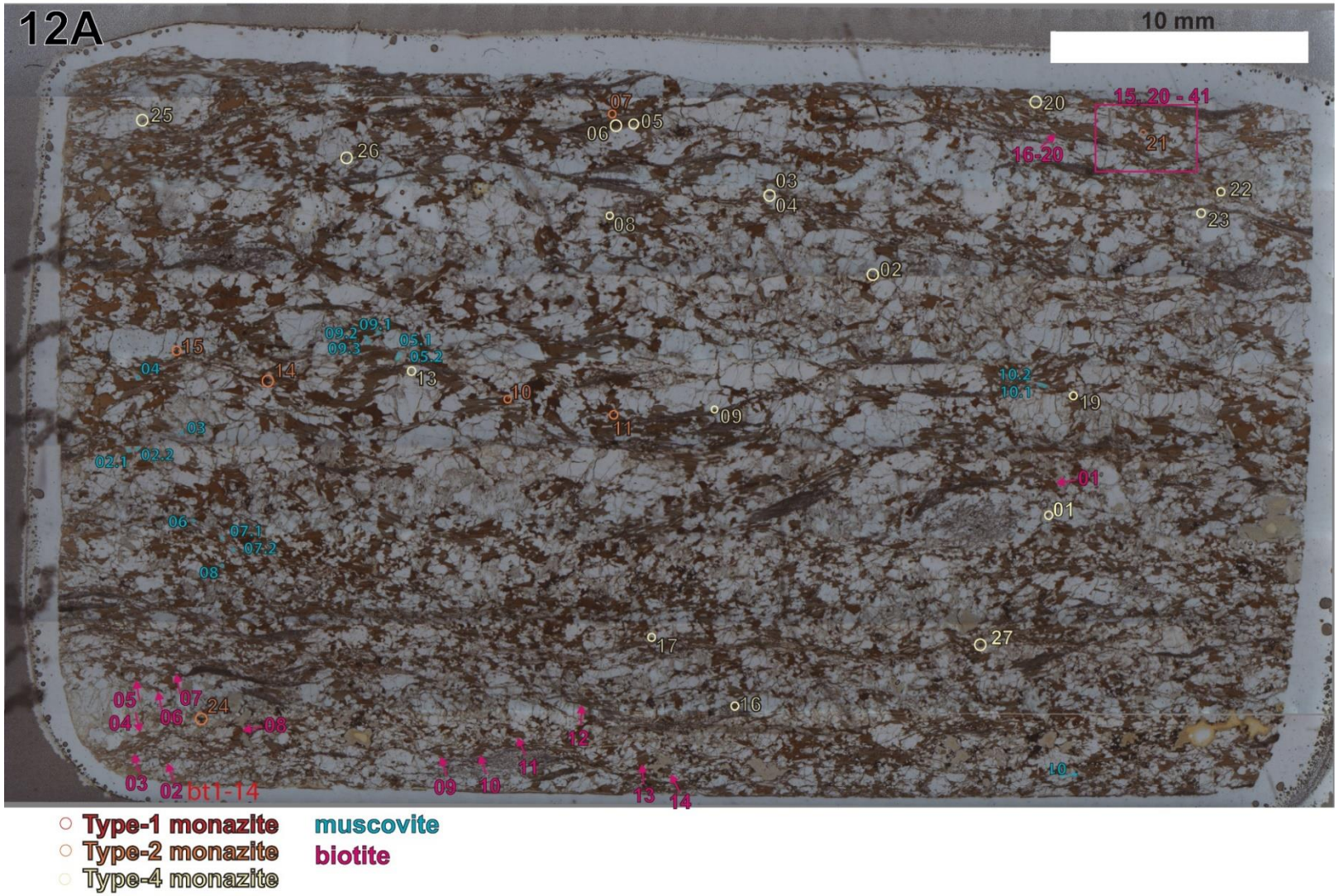

Figure 17. Location of muscovite, biotite and monazite grains on thin section from the sample 12A under plane-polarised light.

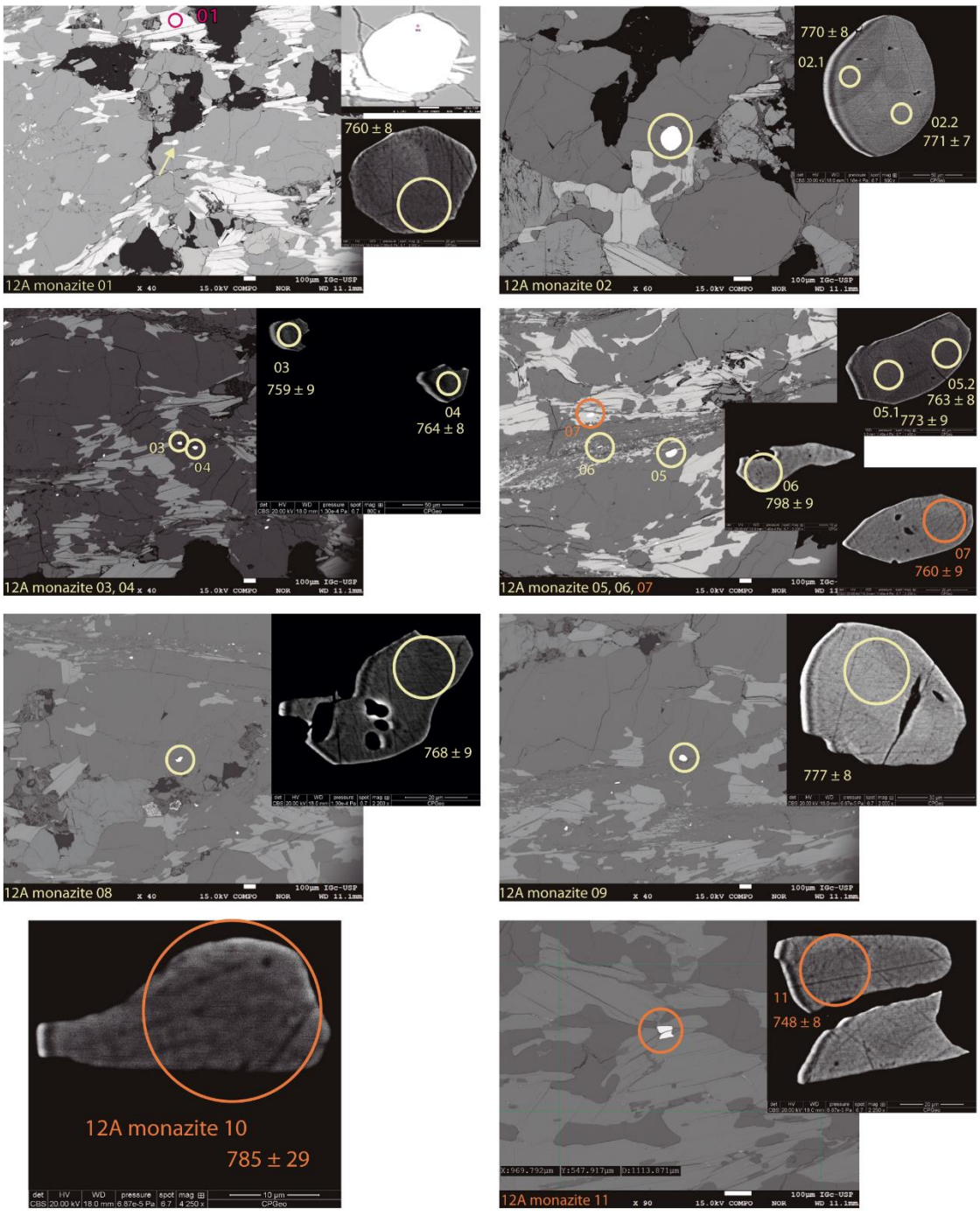

Figure 18. Backscattered electron image (BSE) pointing the location of analyzed muscovite, biotite and monazite grains for sample 12A.

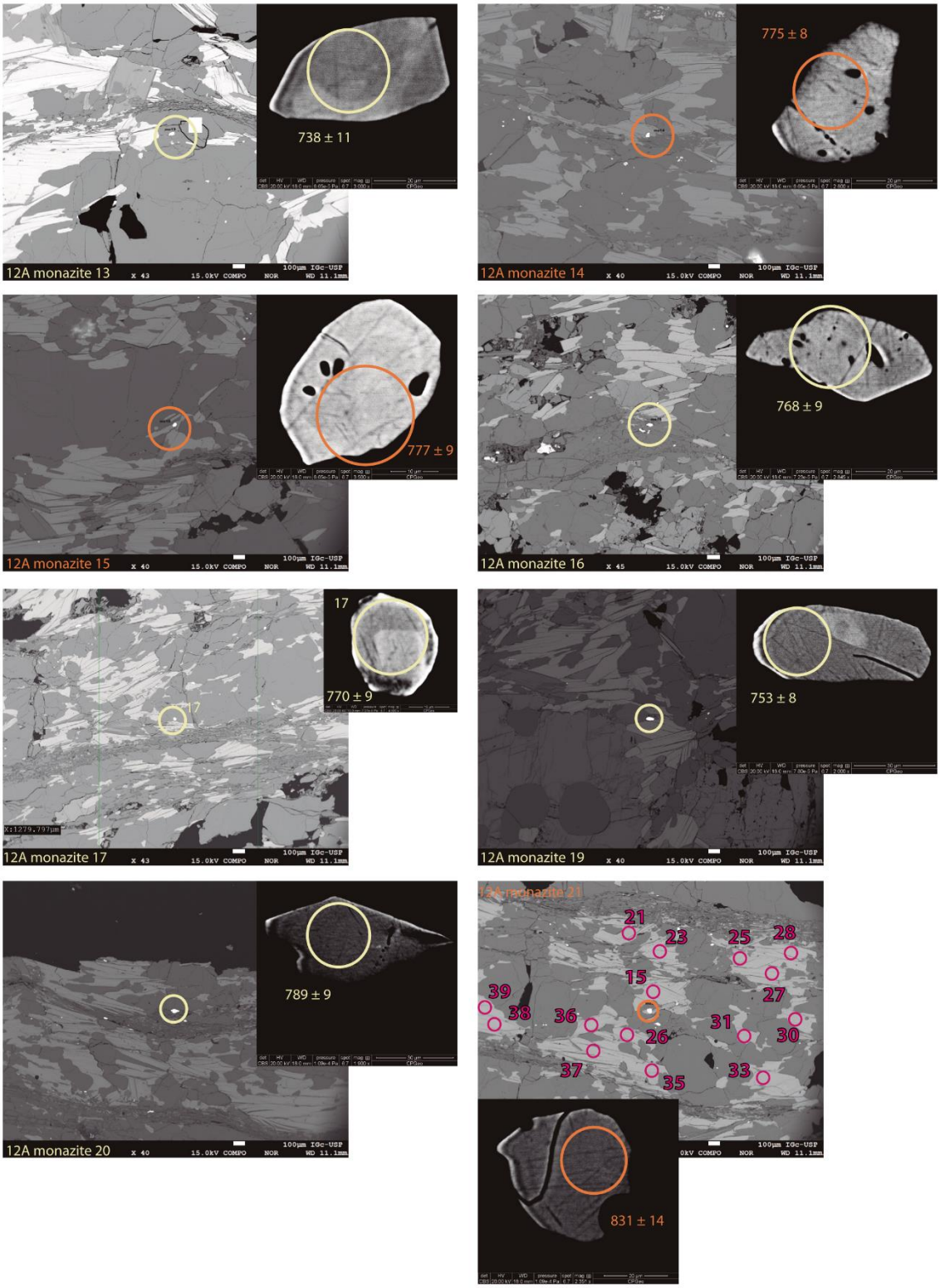

Figure 18. Cont.

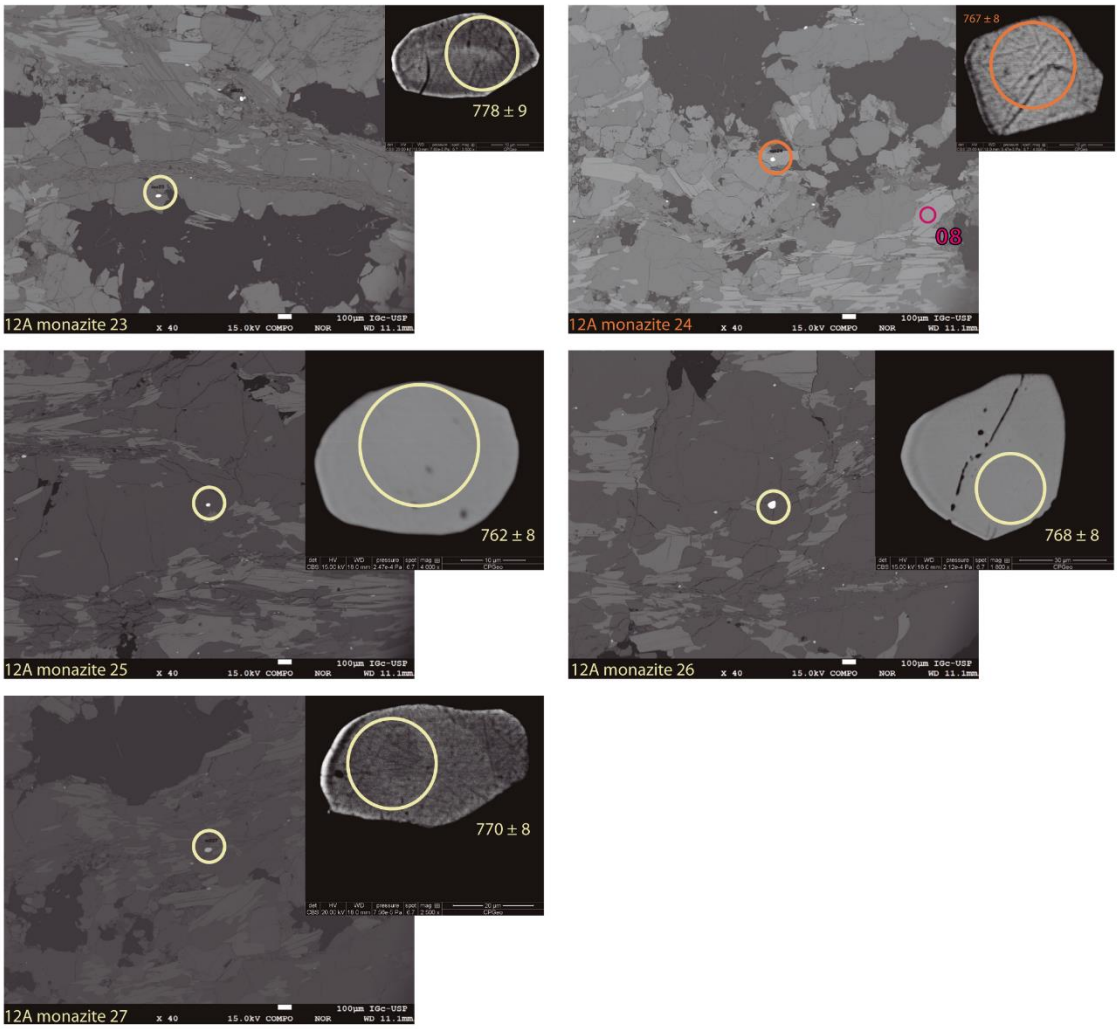

Figure 18. Cont.

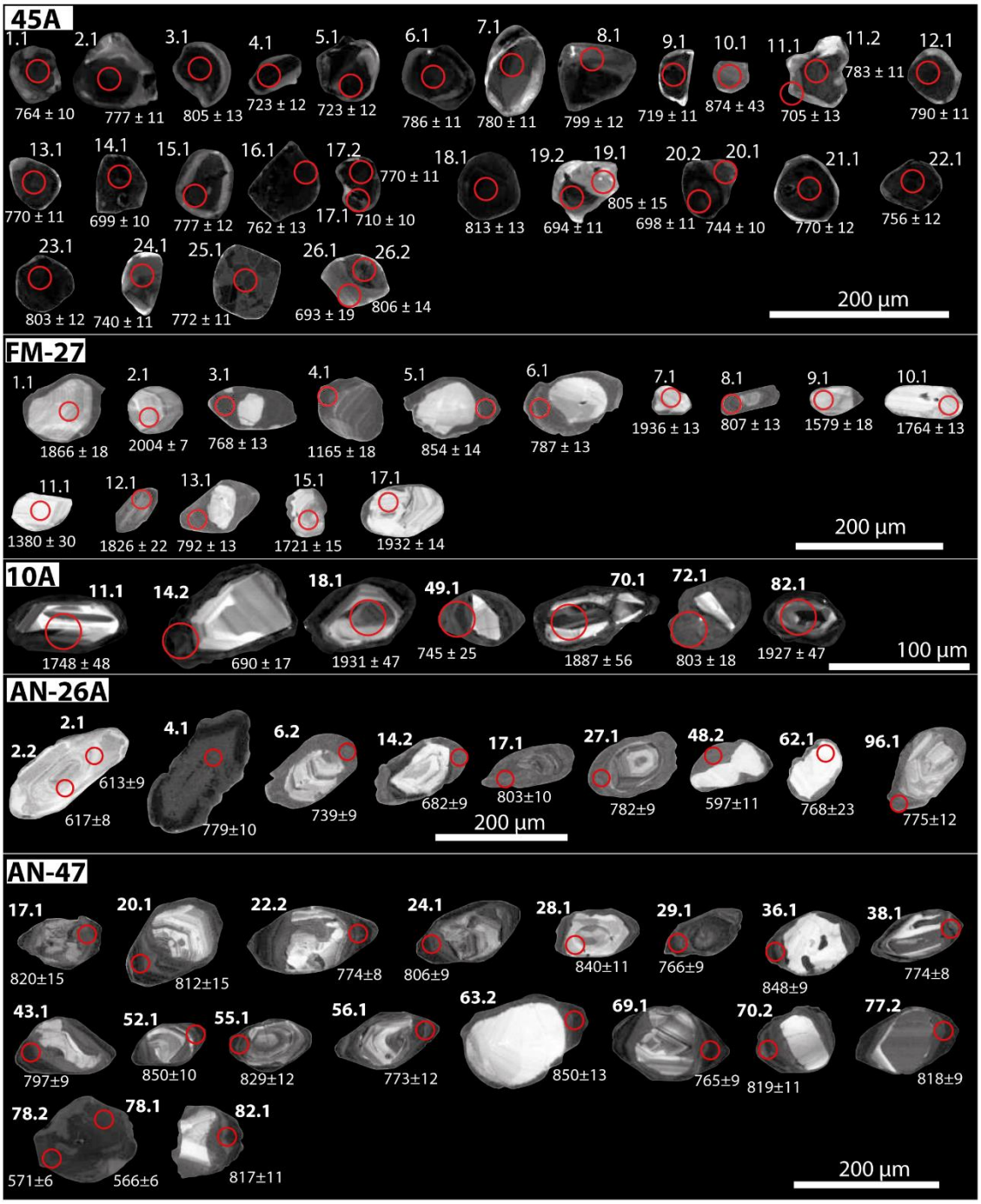

Figure 19. Cathodoluminescence images of selected zircon grains from metasedimentary samples from the Embu Complex. Red circles show the position of analytic spots with their identification numbers and ages in Ma, respectively. Reported ages are $^{206}Pb/^{238}U$ and $^{207}Pb/^{206}Pb$ ages for zircon domains younger and older than 1000 Ma, respectively.

Table 3. Analytical LA-ICP-MS U/Pb results from in situ monazite from Embu Complex.

Sample-Spot	Textural domain	Isotopic ratios								Age (Ma)*						Conc.
		207Pb/235U	2σ	206Pb/238U	2σ	err. corr.	238U/206Pb	2σ	207Pb/206Pb	2σ	207Pb/206Pb	2σ	206Pb/238U	2σ	207Pb/235U	2σ	
12A-01	Type-4	1.0940	0.03	0.1251	0.0015	0.48	7.9936	0.10	0.06	0.001	756	40	760	8	749	15	99%
12A-02.1	Type-4	1.1120	0.03	0.1269	0.0015	0.49	7.8802	0.09	0.06	0.001	765	37	770	8	758	14	98%
12A-02.2	Type-4	1.2250	0.03	0.127	0.0013	0.58	7.8740	0.08	0.07	0.001	779	35	771	7	811	15	105%
12A-03	Type-4	1.1010	0.03	0.125	0.0016	0.41	8.0000	0.10	0.07	0.001	782	40	759	9	754	14	99%
12A-04	Type-4	1.1010	0.03	0.1259	0.0014	0.42	7.9428	0.09	0.07	0.001	767	39	764	8	753	14	99%
12A-05.1	Type-4	1.1120	0.03	0.1274	0.0015	0.37	7.8493	0.09	0.07	0.001	773	40	773	9	759	14	98%
12A-05.2	Type-4	1.1920	0.03	0.1257	0.0014	0.46	7.9554	0.09	0.06	0.001	726	38	763	8	796	15	104%
12A-06	Type-4	1.1610	0.03	0.1318	0.0015	0.32	7.5873	0.09	0.07	0.001	791	41	798	9	781	15	98%
12A-07	Type-2	1.0880	0.03	0.1251	0.0015	0.43	7.9936	0.10	0.06	0.001	756	37	760	9	748	13	98%
12A-08	Type-4	1.0930	0.03	0.1265	0.0015	0.31	7.9051	0.09	0.06	0.001	747	42	768	9	749	15	98%
12A-09	Type-4	1.1260	0.03	0.1282	0.0014	0.43	7.8003	0.09	0.07	0.001	782	38	777	8	765	14	98%
12A-10	Type-2	1.1930	0.07	0.1295	0.0050	0.27	7.7220	0.30	0.07	0.004	900	##	785	29	794	33	101%
12A-11	Type-2	1.0700	0.03	0.1231	0.0014	0.53	8.1235	0.09	0.06	0.001	747	34	748	8	738	13	99%
12A-13	Type-4	1.0900	0.06	0.1213	0.0019	0.32	8.2440	0.13	0.07	0.003	805	68	738	11	745	25	101%
12A-14	Type-2	1.1320	0.03	0.1277	0.0014	0.30	7.8309	0.09	0.07	0.001	780	42	775	8	768	15	99%
12A-15	Type-2	1.1330	0.03	0.1281	0.0016	0.54	7.8064	0.10	0.07	0.001	771	38	777	9	768	15	99%
12A-16	Type-4	1.1480	0.03	0.1265	0.0016	0.40	7.9051	0.10	0.07	0.001	818	44	768	9	775	16	101%
12A-17	Type-4	1.1680	0.04	0.1269	0.0016	0.38	7.8802	0.10	0.07	0.001	776	46	770	9	784	16	102%
12A-19	Type-4	1.1240	0.03	0.1239	0.0014	0.61	8.0710	0.09	0.06	0.001	760	37	753	8	764	15	101%
12A-20	Type-4	1.1850	0.03	0.1302	0.0015	0.55	7.6805	0.09	0.07	0.001	771	36	789	9	793	15	100%
12A-21	Type-2	1.2750	0.04	0.1376	0.0025	0.67	7.2674	0.13	0.07	0.001	815	44	831	14	832	17	100%
12A-22	Type-4	1.5100	0.20	0.1349	0.0035	0.92	7.4129	0.19	0.08	0.006	972	99	815	20	872	47	107%
12A-23	Type-4	1.1730	0.04	0.1283	0.0015	0.31	7.7942	0.09	0.07	0.002	790	49	778	9	786	16	101%
12A-24	Type-2	1.1290	0.03	0.1264	0.0014	0.54	7.9114	0.09	0.06	0.001	759	35	767	8	767	15	100%
12A-25	Type-4	1.1340	0.03	0.1255	0.0014	0.03	7.9681	0.09	0.07	0.002	775	52	762	8	769	15	101%
12A-26	Type-4	1.1370	0.03	0.1265	0.0014	0.33	7.9051	0.09	0.07	0.001	789	42	768	8	771	15	100%
12A-27	Type-4	1.1320	0.03	0.1269	0.0014	0.35	7.8802	0.09	0.07	0.001	778	43	770	8	768	15	100%

45A-01	Type-4	1.206	0.03	0.1236	0.0015	0.43	8.0906	0.1	0.06	0.001	760	40	751	8	802	15	107%
45A-02	Type-1	1.234	0.06	0.1377	0.0041	0.57	7.2622	0.22	0.07	0.003	828	82	831	23	816	27	98%
45A-03	Type-1	1.157	0.03	0.1274	0.0014	0.31	7.8493	0.09	0.06	0.001	733	47	773	8	779	16	101%
45A-05	Type-4	1.095	0.03	0.1202	0.0016	0.48	8.3195	0.11	0.06	0.001	744	37	731	9	750	14	103%
45A-06	Type-4	1.177	0.09	0.1323	0.0066	0.27	7.5586	0.38	0.06	0.004	740	##	798	36	790	34	99%
45A-07	Type-4	1.151	0.04	0.1242	0.0016	0.32	8.0515	0.1	0.07	0.002	766	53	755	9	777	18	103%
45A-08	Type-1	1.17	0.04	0.1215	0.0017	0.36	8.2305	0.12	0.07	0.002	847	57	739	10	784	18	106%
45A-09	Type-4	1.118	0.03	0.1214	0.0014	0.62	8.2372	0.09	0.07	0.001	773	35	738	8	761	14	103%
45A-10	Type-4	1.094	0.03	0.1259	0.0015	0.39	7.9428	0.09	0.06	0.001	747	41	764	9	749	14	98%
45A-11	Type-2	1.179	0.03	0.1268	0.0013	0.29	7.8864	0.08	0.07	0.001	807	41	769	7	791	15	103%
45A-12	Type-4	1.088	0.03	0.1221	0.0014	0.51	8.1900	0.09	0.06	0.001	721	39	742	8	746	15	101%
45A-13	Type-4	1.003	0.03	0.1112	0.0015	0.49	8.9928	0.12	0.06	0.001	759	43	680	9	704	15	104%
45A-14	Type-4	1.143	0.04	0.1258	0.0015	0.36	7.9491	0.09	0.07	0.002	777	49	764	9	772	16	101%
45A-15	Type-4	1.137	0.04	0.1225	0.0014	0.34	8.1633	0.09	0.07	0.002	828	48	745	8	769	16	103%
45A-16	Type-4	1.114	0.03	0.1246	0.0015	0.34	8.0257	0.1	0.07	0.001	764	45	757	9	759	15	100%
45A-17	Type-4	1.022	0.03	0.1168	0.0014	0.53	8.5616	0.1	0.06	0.001	737	36	712	8	715	14	100%
45A-18	Type-1	1.126	0.03	0.1272	0.0017	0.46	7.8616	0.11	0.07	0.001	765	45	771	10	764	16	99%
45A-19.1	Type-4	1.168	0.04	0.1268	0.0015	0.33	7.8864	0.09	0.07	0.002	778	50	770	9	784	17	102%
45A-19.2	Type-4	1.219	0.04	0.1273	0.0016	0.21	7.8555	0.1	0.06	0.002	741	53	772	9	807	17	105%
45A-20	Type-1	1.184	0.04	0.1274	0.0016	0.39	7.8493	0.1	0.07	0.002	784	48	773	9	791	17	102%
45A-21	Type-4	1.122	0.03	0.1219	0.0015	0.63	8.2034	0.1	0.06	0.001	765	38	741	9	764	16	103%
45A-22	Type-1	1.179	0.03	0.1253	0.0015	0.40	7.9808	0.1	0.07	0.001	805	43	761	8	789	16	104%
45A-23	Type-4	1.178	0.04	0.128	0.002	0.35	7.8125	0.1	0.06	0.002	749	50	776	9	788	17	102%
45A-24	Type-4	1.188	0.03	0.1276	0.002	0.47	7.8370	0.09	0.07	0.001	783	39	774	8	795	15	103%
45A-25	Type-4	1.201	0.04	0.1285	0.002	0.35	7.7821	0.1	0.07	0.001	779	47	779	9	799	16	103%
45A-26	Type-4	1.171	0.03	0.1249	0.002	0.46	8.0064	0.1	0.07	0.001	790	42	759	9	785	16	103%
45A-27	Type-4	1.148	0.03	0.125	0.001	0.44	8.0000	0.08	0.06	0.001	753	36	759	7	776	14	102%
45A-28	Type-2	1.17	0.03	0.1249	0.001	0.52	8.0064	0.09	0.07	0.001	788	39	759	8	785	15	103%
FM02B-01	Type-3	1.103	0.03	0.1211	0.001	0.63	8.2576	0.09	0.06	0.001	733	33	737	8	754	14	102%

FM02B-02.1	Type-2/core	1.097	0.03	0.1208	0.001	0.68	8.2781	0.09	0.06	0.001	732	31	735	7	752	14	102%
FM02B-02.2	Type-2/overg.	1.228	0.03	0.1264	0.001	0.40	7.9114	0.08	0.06	0.001	747	38	767	8	812	15	106%
FM02B-03	Type-2	1.157	0.03	0.1254	0.001	0.47	7.9745	0.09	0.06	0.001	760	38	761	8	779	15	102%
FM02B-04.1	Type-2	1.83	0.16	0.1298	0.003	0.78	7.7042	0.15	0.10	0.007	1400	##	786	15	1015	52	129%
FM02B-04.2	Type-2	1.243	0.03	0.1252	0.001	0.40	7.9872	0.09	0.07	0.001	799	40	760	8	820	16	108%
FM02B-05	Type-2	1.173	0.03	0.1285	0.002	0.49	7.7821	0.09	0.06	0.001	748	39	779	9	787	15	101%
FM02B-06	Type-2	1.213	0.04	0.1343	0.003	0.88	7.4460	0.18	0.06	0.001	762	36	814	19	803	19	99%
FM02B-07	Type-3	1.096	0.03	0.1237	0.001	0.56	8.0841	0.09	0.06	0.001	736	35	752	8	752	13	100%
FM02B-08.1	Type-3	1.123	0.03	0.1256	0.001	0.50	7.9618	0.08	0.06	0.001	750	35	763	7	763	14	100%
FM02B-08.2	Type-3	1.213	0.03	0.1244	0.001	0.44	8.0386	0.07	0.06	0.001	752	33	756	7	806	14	107%
FM02B-09	Type-4	1.074	0.03	0.1202	0.001	0.54	8.3195	0.09	0.06	0.001	751	35	731	8	740	14	101%
FM02B-10.1	Type-4	1.071	0.03	0.121	0.002	0.65	8.2645	0.11	0.06	0.001	736	34	736	9	738	14	100%
FM02B-10.2	Type-4	1.226	0.03	0.1245	0.002	0.62	8.0321	0.1	0.07	0.001	778	36	756	9	812	15	107%
FM02B-11.1	Type-2	1.1	0.03	0.1238	0.001	0.62	8.0775	0.09	0.06	0.001	750	32	753	8	753	14	100%
FM02B-11.2	Type-2	1.202	0.03	0.1234	0.001	0.52	8.1037	0.09	0.06	0.001	765	35	750	8	801	14	107%
FM02B-12.1	Type-1	1.101	0.03	0.1232	0.001	0.49	8.1169	0.09	0.07	0.001	769	37	749	8	753	14	101%
FM02B-12.2	Type-1	1.063	0.03	0.1258	0.001	0.43	7.9491	0.08	0.06	0.001	770	34	764	7	735	13	96%
FM02B-12.3	Type-1	1.056	0.03	0.1237	0.001	0.36	8.0841	0.09	0.07	0.001	790	40	752	8	731	14	97%
FM02B-13.1	Type-1	1.118	0.03	0.1252	0.001	0.33	7.9872	0.08	0.07	0.001	763	42	761	8	761	15	100%
FM02B-13.2	Type-1	1.05	0.03	0.125	0.001	0.50	8.0000	0.08	0.06	0.001	749	35	759	8	729	13	96%
FM02B-13.3	Type-1	1.077	0.03	0.125	0.001	0.31	8.0000	0.09	0.07	0.001	778	42	759	8	741	14	98%
FM02B-14	Type-1	1.044	0.03	0.1181	0.001	0.49	8.4674	0.1	0.06	0.001	757	37	719	8	725	14	101%
FM02B-15	Type-4	1.2	0.11	0.1211	0.006	0.50	8.2576	0.38	0.07	0.005	920	##	736	32	785	47	107%
FM02B-16	Type-4	1.13	0.03	0.1288	0.002	0.70	7.7640	0.13	0.06	0.001	749	41	781	12	766	16	98%
FM02B-17.1	Type-4	1.125	0.03	0.1231	0.001	0.39	8.1235	0.09	0.07	0.001	835	40	748	8	764	15	102%
FM02B-17.2	Type-4	1.051	0.1	0.1099	0.001	0.85	9.0992	0.12	0.07	0.004	834	76	672	8	701	28	104%
FM02B-18.1	Type-2	1.12	0.03	0.1262	0.001	0.51	7.9239	0.08	0.07	0.001	772	38	766	8	762	15	99%
FM02B-18.2	Type-2	1.092	0.03	0.1258	0.001	0.50	7.9491	0.08	0.06	0.001	763	38	764	8	748	14	98%
FM02B-19	Type-2	1.116	0.03	0.1262	0.001	0.46	7.9239	0.08	0.07	0.001	780	36	766	7	760	14	99%
FM02B-20	Type-3	1.072	0.03	0.123	0.001	0.48	8.1301	0.09	0.06	0.001	750	35	748	8	740	14	99%

FM02B-21.1	Type-2	1.129	0.03	0.1251	0.001	0.41	7.9936	0.08	0.06	0.001	720	38	760	7	767	14	101%
FM02B-21.2	Type-2	1.076	0.03	0.1232	0.001	0.34	8.1169	0.09	0.06	0.001	759	36	749	8	742	13	99%
FM02B-22	Type-2	1.16	0.03	0.1261	0.002	0.48	7.9302	0.09	0.06	0.001	754	35	765	9	782	14	102%
FM02B-23	Type-4	1.51	0.14	0.1278	0.002	0.56	7.8247	0.12	0.08	0.006	1080	##	775	11	905	48	117%
FM02B-24	Type-3	1.248	0.05	0.1226	0.001	0.41	8.1566	0.09	0.07	0.002	895	56	745	7	818	20	110%
FM02B-25.1	Type-4	1.092	0.03	0.1233	0.001	0.43	8.1103	0.09	0.06	0.001	744	35	749	8	749	14	100%
FM02B-25.2	Type-4	1.109	0.03	0.1241	0.001	0.58	8.0580	0.09	0.06	0.001	745	33	754	8	757	13	100%
FM02B-25.3	Type-4	1.127	0.03	0.1249	0.001	0.63	8.0064	0.08	0.06	0.001	751	32	758	8	766	14	101%
FM02B-26.1	Type-4	1.151	0.03	0.1234	0.002	0.02	8.1037	0.1	0.06	0.001	728	38	750	8	777	14	104%
FM02B-26.2	Type-4	1.078	0.03	0.1238	0.001	0.56	8.0775	0.08	0.06	0.001	733	35	752	8	743	14	99%

Sample name + x.y: grain number followed by analysis number
* Not corrected for common Pb
2σ is an standard absolute value (STDEV/SQRT)

Table 4. Analytical LA-ICP-MS REE results (ppm) from in situ monazites.

Sample-Spot	Type	Ce	Pr	Nd	Sm	Eu	Gd	Tb	Dy	Ho	Er	Tm	Yb	Lu	Ta
12A-m01	Type-4	20010	2322	9510	1791	59.3	1440	174.2	721	91.8	146.2	11.52	45.8	4.12	0.161
12A-m02.1	Type-4	19330	2219	8750	1621	83.5	1201	137.4	547	69.4	113.9	9.19	38.07	3.37	0.129
12A-m02.2	Type-4	19800	2301	9380	1826	109.7	1377	160.9	659	82.5	131.6	10.77	44.5	3.876	0.138
12A-m03	Type-4	20380	2399	9720	1815	60.5	1385	158.3	651	84.9	140.5	11.24	44.9	3.99	0.15
12A-m04	Type-4	20150	2353	9630	1853	68.6	1497	181.2	722	86.7	132.1	9.7	38.74	3.474	0.172
12A-m05.1	Type-4	20300	2370	9590	1832	52.8	1413	167.6	706	92.7	157	12.85	52.7	4.7	0.163
12A-m05.2	Type-4	20260	2364	9600	1869	48.8	1542	189.4	783	94	139.5	10.07	39	3.44	0.15
12A-m06	Type-4	20030	2332	9440	1824	96.5	1392	161.6	637	76.9	119.8	9.2	36.61	3.23	0.15
12A-m07	Type-2	20220	2359	9600	1894	70.7	1612	203.3	807	92.7	128.9	8.71	31.86	2.85	0.189
12A-m08	Type-4	19350	2227	8920	1688	154.6	1362	167.9	668	80	121.2	8.91	35.7	3.14	0.142
12A-m09	Type-4	19750	2271	9160	1737	84.7	1251	143.6	565	69.3	108.2	8.55	34.4	2.98	0.112
12A-m10	Type-2	19010	2200	8800	1690	477	1300	153	570	60.2	84.2	5.9	24.4	2.32	0.074
12A-m11	Type-2	19680	2271	9180	1801	142	1483	177.1	674	76.2	110.3	7.85	30.61	2.691	0.128
12A-m13	Type-4	19940	2308	9520	1834	114	1442	159	562	61.2	92.8	7.06	29.4	2.72	0.1
12A-m14	Type-2	20190	2366	9560	1790	85.9	1344	152.7	600	73.7	117.4	9.18	36.8	3.17	0.12
12A-m15	Type-2	20150	2353	9640	1826	67.2	1441	167.2	653	78.8	122.8	9.35	37.3	3.32	0.152
12A-m16	Type-4	20160	2372	9680	1829	120	1363	152.9	603	73.7	114.4	8.81	34.7	3	0.127
12A-m17	Type-4	20280	2397	9740	1850	74.6	1398	157.4	621	75.7	118.2	9.07	37	3.11	0.123
12A-m19	Type-4	20070	2329	9480	1861	76.2	1616	202.2	789	87	114.9	7.25	26.38	2.331	0.146
12A-m20	Type-4	19710	2283	9220	1750	86.6	1277	145.9	580	71.2	112.8	8.83	36.49	3.13	0.136
12A-m21	Type-2	19920	2330	9210	1793	59.3	1485	182.9	714	82.2	119.7	8.25	33.9	3.25	0.134
12A-m22	Type-4	19420	2220	8920	1692	119	1289	146.1	568	70	110.1	8.8	36.8	3.16	0.135
12A-m23	Type-4	19950	2324	9420	1781	73	1310	145.9	565	68.9	108.4	8.21	33.35	2.796	0.122
12A-m24	Type-2	19820	2299	9170	1799	67.5	1435	179.6	761	98.1	159.7	12.84	53	4.81	0.152
12A-m25	Type-4	20040	2348	9540	1819	91.5	1371	157.2	629	77.6	122.1	9.46	39	3.36	0.133

12A-m26	Type-4	19880	2324	9350	1778	119	1355	158.1	631	77.5	121.8	9.3	38.5	3.33	0.128
12A-m27	Type-4	20070	2358	9530	1805	65.9	1450	176.1	707	83	120.3	8.44	31.46	2.775	0.136
45A-m01	Type-4	19790	2158	8290	1343	22.77	583	27.7	44.2	2.81	5.62	0.138	1.228	0.099	0.0069
45A-m02	Type-1	19680	2169	8400	1514	121	1033	87	258	25.9	37.7	2.43	10.2	0.75	0.051
45A-m03	Type-1	20110	2246	8950	1681	17.77	1281	105.9	225.7	14.43	15.57	0.575	3.58	0.355	0.0267
45A-m05	Type-4	20100	2218	8690	1524	68.4	841	57.4	122.9	8.74	11.15	0.379	2.21	0.222	0.0146
45A-m06	Type-4	20050	2221	8770	1681	153	1248	117.8	314	23.9	25.7	1.11	4.92	0.508	0.051
45A-m07	Type-4	20080	2216	8610	1392	25.8	657	34.2	55.7	3.48	6.23	0.15	1.39	0.114	0.0134
45A-m08	Type-1	20250	2262	8920	1601	68	1175	106	253	17.7	19	0.82	4.03	0.42	0.034
45A-m09	Type-4	20250	2258	8810	1551	25.85	756	39.2	64.4	4.07	7.16	0.212	1.63	0.142	0.0081
45A-m10	Type-4	19780	2178	8430	1353	22.7	598	28.3	41.8	2.49	5.45	0.099	1.17	0.092	0.0051
45A-m11	Type-2	20290	2250	8760	1644	83.5	1175	109.6	326	32.5	47.2	3.22	12.8	1.076	0.059
45A-m12	Type-4	20050	2228	8690	1566	52.7	875	58.3	124.2	9.29	12.61	0.504	2.68	0.241	0.0151
45A-m13	Type-4	20170	2244	8880	1754	153.5	1310	121.6	322	24.4	25.3	1.097	4.65	0.467	0.06
45A-m14	Type-4	20260	2239	8760	1309	13.69	445	16.39	19.3	1.143	4.3	0.045	0.763	0.0506	< LOD
45A-m15	Type-4	20360	2253	8860	1543	40.6	869	54.1	98.8	6.08	8.49	0.261	1.95	0.187	0.0135
45A-m16	Type-4	20360	2269	8850	1372	17.5	490	19.4	25.5	1.52	4.79	0.0582	0.874	0.068	0.0045
45A-m17	Type-4	20050	2240	8800	1584	163.5	1023	91.4	230.8	16.9	18.92	0.778	3.55	0.391	0.0237
45A-m18	Type-1	20270	2259	8830	1548	64.1	934	74.3	205	20.6	30.1	1.83	7.27	0.573	0.0413
45A-m19.1	Type-4	20390	2272	8940	1565	14.71	943	61.1	109.5	6.38	8.49	0.237	1.91	0.202	0.0126
45A-m19.2	Type-4	20400	2258	8800	1522	13.74	827	45.4	70.3	3.84	6.36	0.139	1.556	0.137	0.0073
45A-m20	Type-1	20840	2332	9150	1589	12.4	747	35.16	46.1	2.435	5.45	0.106	1.34	0.121	< LOD
45A-m21	Type-4	20140	2236	8730	1544	71	876	61.2	132	9.4	12.1	0.43	2.37	0.231	0.0135
45A-m22	Type-1	19610	2141	8420	1668	20.39	1537	135.3	274.7	16.53	16.23	0.579	3.81	0.436	0.0284
45A-m23	Type-4	20570	2306	9160	1617	19.3	993	70.7	151.6	10.74	13.9	0.582	2.9	0.278	0.0232
45A-m24	Type-4	20030	2197	8550	1458	26.4	680	33.5	53	3.22	5.97	0.138	1.33	0.114	0.0083
45A-m25	Type-4	20310	2268	8870	1510	12.2	857	52	89	5.3	7.5	0.196	1.72	0.164	0.0103

45A-m26	Type-4	20320	2279	8980	1547	88	901	70.8	207	22.3	35.4	2.47	10	0.841	0.0461
45A-m27	Type-4	19980	2223	8750	1722	58.6	1080	67	121	7.7	10	0.339	2.43	0.228	0.0124
45A-m28	Type-2	19960	2206	8720	1882	112.3	1569	122.9	257	16.5	17.14	0.671	4.38	0.406	0.083
FM02B-01	Type-3	19990	2292	9130	1746	44.2	1384	148.9	476	46.2	58.2	3.19	11.3	1.07	0.086
FM02B-02.1	Type-2/core	21680	2616	10740	2250	72.8	1788	180.6	497	39.46	38.9	1.406	5.36	0.588	0.0643
FM02B-02.2	Type-2/overg.	20120	2290	9130	1826	77.2	1474	159.7	523	46.86	51.64	2.628	9.57	0.893	0.081
FM02B-03	Type-2	20520	2398	9610	1917	56.7	1507	159.8	491	44.6	51.9	2.55	8.95	0.827	0.129
FM02B-04.1	Type-2	25050	3370	14960	3434	120.8	2810	285	794	65	64.9	2.48	9.62	1.021	0.109
FM02B-04.2	Type-2	19390	2172	8450	1568	54.74	1194	121.2	364	30.42	33.74	1.705	7.13	0.716	0.0497
FM02B-05	Type-2	19900	2256	8910	1665	70.3	1299	135.5	424	37.9	43.2	2.2	8.58	0.81	0.073
FM02B-06	Type-2	20330	2343	9420	1790	54.8	1380	132	352	25.88	25.54	0.933	3.96	0.477	0.049
FM02B-07	Type-3	19930	2261	8960	1635	40.25	1276	137.6	434	38.8	43.2	2.08	7.32	0.672	0.0757
FM02B-08.1	Type-3	19680	2209	8691	1491	33.85	1171	135.5	469	44.5	52.1	2.75	9.37	0.896	0.082
FM02B-08.2	Type-3	20190	2309	9140	1712	43.3	1360	151.4	509	50.7	63.2	3.71	12.93	1.204	0.087
FM02B-09	Type-4	20270	2350	9400	1799	50.5	1369	127.7	323.4	23.81	23.6	0.804	3.68	0.409	0.0405
FM02B-10.1	Type-4	20360	2348	9390	1810	46.39	1365	125	319	24.4	26.5	1.09	4.57	0.496	0.0462
FM02B-10.2	Type-4	19880	2273	8920	1688	52.5	1325	145.1	490	47.1	54.7	2.89	9.58	0.881	0.085
FM02B-11.1	Type-2	19980	2269	8910	1675	45.55	1345	148.5	474.5	42.56	45.67	1.97	6.43	0.621	0.084
FM02B-11.2	Type-2	20280	2341	9280	1781	46.2	1328	123	305.5	21.99	20.71	0.672	3.31	0.36	0.046
FM02B-12.1	Type-1	20110	2283	9090	1706	43.69	1364	149	492	47.22	59.4	3.34	11.32	1.072	0.088
FM02B-12.2	Type-1	19960	2266	8990	1617	34.4	1301	157.3	577	57.69	71	4.159	13.97	1.275	0.111
FM02B-12.3	Type-1	20200	2307	9170	1757	68.6	1375	145	460.2	40.96	44.84	2.26	8.48	0.762	0.0707
FM02B-13.1	Type-1	19970	2289	9070	1678	59.3	1288	132.7	417	36.8	40.5	1.98	7.04	0.671	0.064
FM02B-13.2	Type-1	19940	2267	8960	1657	37.34	1331	158.3	566	56.8	69.8	4.04	13.57	1.16	0.088
FM02B-13.3	Type-1	20480	2363	9470	1878	72.1	1476	157.5	497.6	43.23	46.8	2.314	8.65	0.82	0.0787
FM02B-14	Type-1	20390	2339	9520	1871	57.6	1428	135.2	359	26	25.3	0.852	4.14	0.472	0.041
FM02B-15	Type-4	33100	5220	26900	7920	367	7300	780	2300	185	167	7.1	20.8	2.15	1.09

FM02B-16	Type-4	22890	2862	11960	2589	91.2	2108	208.4	585	47.6	47.8	1.61	5.72	0.67	0.249
FM02B-17.1	Type-4	20240	2305	9110	1726	50.93	1300	118.6	296.8	20.86	19.3	0.6	3.11	0.361	0.0358
FM02B-17.2	Type-4	25010	3431	15680	4133	185.1	3550	370	1025	78.9	75	2.884	11.88	1.305	0.135
FM02B-18.1	Type-2	19250	2147	8300	1500	60.3	1162	120.5	376.1	33.17	37.36	1.853	6.98	0.682	0.0549
FM02B-18.2	Type-2	20120	2308	9210	1810	75.2	1432	153.8	488	43.03	47.31	2.431	9.63	0.839	0.08
FM02B-19	Type-2	19830	2265	8970	1715	68.4	1359	139.8	435.8	37.62	41.58	2.057	7.89	0.769	0.0674
FM02B-20	Type-3	19880	2269	9090	1714	44.23	1359	135.6	371	28.61	27.59	0.954	3.8	0.452	0.0435
FM02B-21.1	Type-2	19890	2258	8930	1659	46.3	1263	120.8	318.1	23.21	22.16	0.713	3.2	0.366	0.0396
FM02B-21.2	Type-2	19840	2245	8840	1680	45.04	1329	148.3	477.6	42.68	45.82	1.912	6.54	0.629	0.069
FM02B-22	Type-2	20000	2267	9030	1716	53.3	1331	137.6	417	35.5	39.1	1.85	7.05	0.689	0.091
FM02B-23	Type-4	20070	2251	8800	1612	44.7	1266	138.2	447	40.71	44.9	2.06	6.83	0.64	< LOD
FM02B-24	Type-3	21420	2568	10590	2133	68.7	1639	159.1	427	32.27	31.68	1.116	4.66	0.547	0.056
FM02B-25.1	Type-4	20110	2303	9150	1746	46.13	1365	141.3	394.9	30.23	27.43	0.882	3.9	0.431	0.0503
FM02B-25.2	Type-4	20090	2290	9050	1754	42.33	1446	168	544	48.44	48.21	1.772	5.81	0.587	0.075
FM02B-25.3	Type-4	19900	2257	8920	1700	40.8	1399	173.5	654	70.8	90	4.99	15.76	1.336	0.122
FM02B-26.1	Type-4	20260	2305	9150	1710	45.32	1305	128.2	363	30.1	32.7	1.37	5.15	0.547	0.0501
FM02B-26.2	Type-4	19660	2227	8750	1637	45.25	1233	117.6	311.7	23.02	22.15	0.733	3.34	0.367	0.0375

Table 5. U-Pb analytical results (LA-MC-ICP-MS) of the metasedimentary rocks of the Embu Complex. Monash University.

Sample / Spot	U (ppm)	Th (ppm)	Th/U	Isotopic ratios							Age (Ma)*						% Conc
				$^{207}Pb/^{206}Pb$	2σ	$^{207}Pb/^{235}U$	2σ	$^{206}Pb/^{238}U$	2σ	err corr	$^{206}Pb/^{238}U$	2σ	$^{207}Pb/^{206}Pb$	2σ	$^{207}Pb/^{235}U$	2σ	
45A-01.1	816	29	0.04	.065	0.002	1.138	0.04	.126	0.002	.07	764	10	760	63	770	17	101
45A-02.1	704	21	0.03	.065	0.002	1.151	0.04	.128	0.002	.32	777	11	755	58	776	17	100
45A-03.1	534	38	0.07	.066	0.002	1.206	0.04	.133	0.002	.54	805	13	772	63	801	19	100
45A-04.1	524	20	0.04	.064	0.002	1.050	0.04	.119	0.002	.25	723	12	718	69	730	16	101
45A-05.1	859	35	0.04	.065	0.002	1.057	0.04	.117	0.002	.53	713	10	758	62	731	17	103
45A-06.1	949	47	0.05	.064	0.002	1.161	0.03	.130	0.002	.41	786	11	749	58	782	17	100
45A-07.1	765	24	0.03	.065	0.002	1.155	0.04	.129	0.002	.36	780	11	752	61	778	17	100
45A-08.1	550	27	0.05	.064	0.002	1.172	0.04	.132	0.002	.36	799	12	723	66	785	19	98
45A-09.1	771	43	0.06	.064	0.002	1.042	0.03	.118	0.002	.42	719	11	717	62	723	17	101
45A-10.1	524	49	0.09	.068	0.002	1.388	0.11	.146	0.008	.92	874	43	856	79	870	44	100
~~45A-11.1~~	~~265~~	~~12~~	~~0.04~~	~~.068~~	~~0.003~~	~~1.090~~	~~0.05~~	~~.116~~	~~0.002~~	~~.44~~	~~705~~	~~13~~	~~837~~	~~83~~	~~744~~	~~25~~	~~106~~
45A-11.2	704	27	0.04	.064	0.002	1.148	0.04	.129	0.002	.29	783	11	732	61	775	17	99
45A-12.1	764	29	0.04	.066	0.002	1.190	0.04	.130	0.002	.42	790	11	791	59	794	17	100
45A-13.1	781	52	0.07	.066	0.002	1.168	0.04	.127	0.002	.43	770	11	806	60	784	17	102
45A-14.1	748	34	0.05	.065	0.002	1.039	0.03	.115	0.002	.43	699	10	771	59	722	16	103
45A-15.1	573	18	0.03	.065	0.002	1.159	0.04	.128	0.002	.40	777	12	775	65	779	18	100
45A-16.1	708	32	0.04	.067	0.002	1.165	0.05	.125	0.002	.09	762	13	812	68	781	21	102
45A-17.1	740	28	0.04	.064	0.002	1.035	0.03	.116	0.002	.29	710	10	734	62	720	17	101
45A-17.2	627	27	0.04	.064	0.002	1.122	0.04	.127	0.002	.37	770	11	729	66	764	18	99
45A-18.1	637	41	0.06	.067	0.002	1.244	0.04	.134	0.002	.59	813	13	813	61	818	20	101
45A-19.1	531	48	0.09	.066	0.002	1.217	0.05	.133	0.003	.66	805	15	784	68	804	22	100
45A-19.2	350	10	0.03	.064	0.002	1.002	0.04	.114	0.002	.21	694	11	716	77	702	19	101
45A-20.1	745	17	0.02	.065	0.002	1.085	0.03	.122	0.002	.35	744	10	748	58	745	16	100

45A-20.2	668	25	0.04	.065	0.002	1.020	0.03	.114	0.002	.42	698	11	753	62	712	17	102
45A-21.1	752	49	0.06	.065	0.002	1.140	0.04	.127	0.002	.43	770	12	771	63	771	17	100
45A-22.1	759	38	0.05	.068	0.002	1.172	0.04	.124	0.002	.70	756	12	863	61	784	20	104
45A-23.1	676	31	0.05	.064	0.002	1.159	0.04	.132	0.002	.43	803	12	717	63	780	18	97
45A-24.1	465	9	0.02	.065	0.002	1.091	0.04	.122	0.002	.39	740	11	763	65	747	18	101
45A-25.1	684	40	0.06	.066	0.002	1.153	0.04	.127	0.002	.35	772	11	793	60	777	17	101
~~45A-26.1~~	~~102~~	~~2~~	~~0.02~~	~~.072~~	~~0.005~~	~~1.102~~	~~0.07~~	~~.114~~	~~0.003~~	~~.10~~	~~693~~	~~19~~	~~840~~	~~140~~	~~741~~	~~34~~	~~107~~
45A-26.2	892	43	0.05	.071	0.002	1.304	0.05	.133	0.002	.76	806	14	941	65	843	23	105
10A-01.1	193	249	1.29	0.122	0.0036	5.790	0.21	0.342	0.0077	0.68	1896	37	1967	53	1939	32	102
10A-02.1	339	31	0.09	0.123	0.0032	6.270	0.2	0.365	0.0068	0.72	2006	32	1993	46	2010	28	100
~~10A-03.1~~	~~435~~	~~68~~	~~0.16~~	~~0.080~~	~~0.0029~~	~~1.800~~	~~0.12~~	~~0.158~~	~~0.0067~~	~~0.91~~	~~940~~	~~37~~	~~1182~~	~~72~~	~~1024~~	~~43~~	~~109~~
~~10A-04.1~~	~~571~~	~~95~~	~~0.17~~	~~0.101~~	~~0.0035~~	~~2.231~~	~~0.09~~	~~0.161~~	~~0.0055~~	~~0.73~~	~~963~~	~~31~~	~~1624~~	~~68~~	~~1187~~	~~28~~	~~123~~
~~10A-05.1~~	~~932~~	~~263~~	~~0.28~~	~~0.089~~	~~0.0028~~	~~2.028~~	~~0.1~~	~~0.162~~	~~0.0053~~	~~0.92~~	~~966~~	~~30~~	~~1398~~	~~61~~	~~1115~~	~~36~~	~~115~~
~~10A-06.1~~	~~2210~~	~~146~~	~~0.07~~	~~0.082~~	~~0.0037~~	~~1.750~~	~~0.15~~	~~0.151~~	~~0.0086~~	~~0.87~~	~~903~~	~~48~~	~~1204~~	~~87~~	~~999~~	~~52~~	~~111~~
10A-07.1	251	166	0.66	0.115	0.0032	5.220	0.18	0.324	0.0067	0.76	1811	32	1872	50	1851	30	102
10A-08.1	685	667	0.97	0.187	0.0049	12.670	0.43	0.490	0.011	0.80	2570	48	2710	44	2652	33	103
10A-09.1	685	26	0.04	0.073	0.0023	1.443	0.052	0.145	0.0034	0.48	870	19	999	66	904	22	104
~~10A-10.1~~	~~483~~	~~109~~	~~0.23~~	~~0.109~~	~~0.0037~~	~~3.730~~	~~0.25~~	~~0.242~~	~~0.011~~	~~0.96~~	~~1392~~	~~60~~	~~1749~~	~~70~~	~~1538~~	~~62~~	~~110~~
10A-11.1	294	246	0.84	0.107	0.0029	4.520	0.19	0.302	0.0093	0.89	1696	46	1748	48	1721	36	101
~~10A-12.1~~	~~301~~	~~238~~	~~0.79~~	~~0.112~~	~~0.0038~~	~~4.010~~	~~0.24~~	~~0.254~~	~~0.011~~	~~0.93~~	~~1464~~	~~53~~	~~1822~~	~~62~~	~~1619~~	~~51~~	~~111~~
~~10A-13.1~~	~~720~~	~~155~~	~~0.22~~	~~0.087~~	~~0.0035~~	~~1.890~~	~~0.12~~	~~0.156~~	~~0.0053~~	~~0.87~~	~~931~~	~~30~~	~~1352~~	~~79~~	~~1068~~	~~43~~	~~115~~
~~10A-14.1~~	~~348~~	~~84~~	~~0.24~~	~~0.088~~	~~0.0027~~	~~2.248~~	~~0.11~~	~~0.182~~	~~0.006~~	~~0.91~~	~~1074~~	~~33~~	~~1372~~	~~58~~	~~1182~~	~~36~~	~~110~~
10A-14.2	363	3	0.01	0.065	0.0032	1.012	0.052	0.113	0.0029	0.36	690	17	741	100	706	26	102
~~10A-15.1~~	~~1010~~	~~458~~	~~0.45~~	~~0.099~~	~~0.0034~~	~~2.910~~	~~0.17~~	~~0.213~~	~~0.0087~~	~~0.87~~	~~1242~~	~~46~~	~~1593~~	~~66~~	~~1379~~	~~43~~	~~111~~
~~10A-16.1~~	~~510~~	~~138~~	~~0.27~~	~~0.103~~	~~0.0035~~	~~3.560~~	~~0.22~~	~~0.248~~	~~0.01~~	~~0.91~~	~~1427~~	~~54~~	~~1661~~	~~65~~	~~1526~~	~~52~~	~~107~~
~~10A-17.1~~	~~594~~	~~118~~	~~0.20~~	~~0.097~~	~~0.0026~~	~~2.800~~	~~0.14~~	~~0.207~~	~~0.0085~~	~~0.92~~	~~1207~~	~~45~~	~~1549~~	~~51~~	~~1340~~	~~37~~	~~111~~
10A-18.1	241	195	0.81	0.119	0.0031	5.550	0.2	0.338	0.0073	0.83	1878	34	1931	47	1904	31	101

10A-19.1	445	58	0.13	0.104	0.0029	2.921	0.12	0.201	0.0054	0.85	1178	29	1690	53	1378	31	117
10A-19.2	443	95	0.22	0.114	0.003	4.250	0.16	0.266	0.0056	0.86	1518	29	1863	48	1677	31	110
10A-20.1	402	253	0.63	0.118	0.0031	5.290	0.17	0.321	0.0063	0.69	1794	31	1925	47	1863	28	104
10A-21.1	596	144	0.24	0.108	0.0039	4.070	0.24	0.267	0.0092	0.92	1524	47	1748	71	1626	52	107
10A-22.1	521	77	0.15	0.077	0.0026	1.589	0.083	0.145	0.0048	0.69	873	27	1117	75	954	32	109
10A-23.1	1252	500	0.40	0.090	0.0034	2.170	0.15	0.170	0.0076	0.97	1007	42	1401	80	1147	52	114
10A-24.1	1320	194	0.15	0.094	0.0031	2.400	0.15	0.179	0.0074	0.97	1057	40	1514	60	1216	46	115
10A-25.1	1050	76	0.07	0.092	0.0046	2.010	0.15	0.154	0.0052	0.87	922	29	1397	100	1093	50	119
10A-26.1	724	48	0.07	0.089	0.0037	2.100	0.17	0.164	0.0084	0.96	978	46	1374	85	1114	58	114
10A-27.1	557	163	0.29	0.089	0.0037	1.950	0.16	0.153	0.0077	0.95	914	43	1371	80	1067	55	117
10A-28.1	730	333	0.46	0.091	0.0037	2.210	0.14	0.175	0.0063	0.83	1037	35	1415	81	1174	44	113
10A-29.1	1100	113	0.10	0.075	0.0028	1.543	0.08	0.147	0.0039	0.83	883	22	1057	75	940	32	106
10A-30.1	840	135	0.16	0.098	0.0032	2.710	0.18	0.195	0.009	0.97	1143	49	1562	64	1302	52	114
10A-31.1	452	85	0.19	0.111	0.003	3.890	0.16	0.250	0.0072	0.92	1435	38	1805	51	1605	35	112
10A-32.1	514	269	0.52	0.107	0.0042	4.070	0.31	0.267	0.014	0.97	1520	74	1723	80	1606	75	106
10A-33.1	1370	640	0.47	0.105	0.0029	3.290	0.14	0.224	0.0066	0.87	1299	35	1708	48	1469	34	113
10A-34.1	1150	209	0.18	0.195	0.0048	10.470	0.41	0.385	0.0097	0.96	2098	46	2779	41	2466	40	118
10A-35.1	933	136	0.15	0.074	0.0022	1.439	0.053	0.138	0.0028	0.75	835	16	1045	58	902	23	108
10A-36.1	858	79	0.09	0.080	0.0036	1.950	0.19	0.164	0.0097	0.98	975	53	1148	91	1045	63	107
10A-37.1	646	145	0.22	0.098	0.003	3.060	0.14	0.222	0.0062	0.90	1291	33	1599	52	1413	37	109
10A-38.1	583	87	0.15	0.077	0.0029	1.618	0.1	0.147	0.0053	0.94	884	30	1090	76	959	40	108
10A-39.1	641	154	0.24	0.114	0.0031	4.020	0.19	0.251	0.0082	0.95	1440	42	1862	49	1629	39	113
10A-40.1	724	60	0.08	0.094	0.0031	1.870	0.069	0.143	0.0027	0.45	863	15	1483	62	1067	24	124
10A-41.1	329	353	1.07	0.110	0.0039	4.200	0.25	0.275	0.0092	0.89	1563	47	1767	79	1653	54	106
10A-42.1	1043	89	0.09	0.098	0.0027	2.684	0.088	0.197	0.0032	0.72	1158	17	1574	52	1321	25	114
10A-43.1	658	100	0.15	0.083	0.0034	1.880	0.13	0.160	0.0058	0.94	954	32	1225	84	1053	45	110
10A-44.1	408	184	0.45	0.114	0.004	4.180	0.31	0.261	0.013	0.96	1487	65	1840	64	1647	60	111
10A-45.1	564	24	0.04	0.163	0.0051	4.950	0.21	0.218	0.0062	0.75	1269	33	2480	53	1807	38	142

~~10A-46.1~~	~~681~~	~~345~~	~~0.51~~	~~0.155~~	~~0.0068~~	~~5.370~~	~~0.43~~	~~0.248~~	~~0.011~~	~~0.91~~	~~1425~~	~~57~~	~~2383~~	~~81~~	~~1865~~	~~71~~	~~131~~
~~10A-47.1~~	~~554~~	~~113~~	~~0.20~~	~~0.089~~	~~0.003~~	~~2.420~~	~~0.17~~	~~0.191~~	~~0.0094~~	~~0.97~~	~~1120~~	~~51~~	~~1389~~	~~66~~	~~1218~~	~~54~~	~~109~~
~~10A-48.1~~	~~488~~	~~51~~	~~0.10~~	~~0.076~~	~~0.0036~~	~~1.550~~	~~0.11~~	~~0.143~~	~~0.0051~~	~~0.88~~	~~861~~	~~29~~	~~1056~~	~~100~~	~~934~~	~~45~~	~~108~~
10A-49.1	234	1	0.01	0.067	0.0052	1.110	0.077	0.123	0.0045	0.38	745	25	750	160	752	38	101
~~10A-50.1~~	~~666~~	~~51~~	~~0.08~~	~~0.084~~	~~0.0032~~	~~1.880~~	~~0.11~~	~~0.158~~	~~0.0049~~	~~0.89~~	~~944~~	~~27~~	~~1271~~	~~72~~	~~1056~~	~~40~~	~~112~~
10A-51.1	495	800	1.62	0.117	0.0031	5.240	0.2	0.321	0.0071	0.91	1790	35	1904	49	1864	30	104
~~10A-52.1~~	~~578~~	~~219~~	~~0.38~~	~~0.094~~	~~0.0037~~	~~2.640~~	~~0.22~~	~~0.194~~	~~0.011~~	~~0.98~~	~~1136~~	~~59~~	~~1455~~	~~84~~	~~1261~~	~~65~~	~~111~~
~~10A-53.1~~	~~1384~~	~~960~~	~~0.69~~	~~0.108~~	~~0.0027~~	~~3.390~~	~~0.11~~	~~0.226~~	~~0.0045~~	~~0.78~~	~~1310~~	~~24~~	~~1754~~	~~46~~	~~1498~~	~~26~~	~~114~~
~~10A-54.1~~	~~936~~	~~197~~	~~0.21~~	~~0.092~~	~~0.0042~~	~~2.630~~	~~0.29~~	~~0.195~~	~~0.014~~	~~0.99~~	~~1140~~	~~73~~	~~1415~~	~~89~~	~~1246~~	~~77~~	~~109~~
~~10A-55.1~~	~~703~~	~~88~~	~~0.13~~	~~0.085~~	~~0.0034~~	~~1.860~~	~~0.11~~	~~0.156~~	~~0.0049~~	~~0.84~~	~~936~~	~~27~~	~~1289~~	~~76~~	~~1055~~	~~39~~	~~113~~
10A-56.1	802	63	0.08	0.069	0.003	1.242	0.099	0.129	0.0066	0.81	781	37	860	93	806	44	103
~~10A-58.1~~	~~551~~	~~170~~	~~0.31~~	~~0.098~~	~~0.0028~~	~~3.000~~	~~0.13~~	~~0.221~~	~~0.0057~~	~~0.88~~	~~1290~~	~~28~~	~~1569~~	~~55~~	~~1400~~	~~37~~	~~109~~
10A-59.1	233	207	0.89	0.118	0.0033	5.550	0.21	0.334	0.008	0.86	1853	39	1922	48	1900	34	103
~~10A-60.1~~	~~2108~~	~~261~~	~~0.12~~	~~0.175~~	~~0.0046~~	~~8.040~~	~~0.35~~	~~0.329~~	~~0.0094~~	~~0.96~~	~~1829~~	~~46~~	~~2603~~	~~42~~	~~2231~~	~~40~~	~~122~~
10A-61.1	243	119	0.49	0.118	0.0037	5.490	0.28	0.332	0.012	0.89	1843	57	1910	57	1881	48	102
~~10A-62.1~~	~~648~~	~~133~~	~~0.21~~	~~0.098~~	~~0.0026~~	~~2.572~~	~~0.087~~	~~0.188~~	~~0.0035~~	~~0.77~~	~~1109~~	~~19~~	~~1575~~	~~51~~	~~1289~~	~~25~~	~~116~~
~~10A-63.1~~	~~442~~	~~184~~	~~0.42~~	~~0.101~~	~~0.0031~~	~~2.930~~	~~0.13~~	~~0.207~~	~~0.0058~~	~~0.87~~	~~1214~~	~~31~~	~~1638~~	~~56~~	~~1385~~	~~35~~	~~114~~
~~10A-64.1~~	~~538~~	~~259~~	~~0.48~~	~~0.113~~	~~0.0033~~	~~4.250~~	~~0.2~~	~~0.269~~	~~0.0077~~	~~0.89~~	~~1532~~	~~39~~	~~1837~~	~~53~~	~~1673~~	~~39~~	~~109~~
~~10A-65.1~~	~~1573~~	~~1122~~	~~0.71~~	~~0.112~~	~~0.0032~~	~~4.240~~	~~0.19~~	~~0.271~~	~~0.0081~~	~~0.92~~	~~1545~~	~~42~~	~~1829~~	~~53~~	~~1681~~	~~38~~	~~109~~
~~10A-66.1~~	~~769~~	~~454~~	~~0.59~~	~~0.103~~	~~0.0032~~	~~3.460~~	~~0.15~~	~~0.244~~	~~0.0063~~	~~0.77~~	~~1409~~	~~33~~	~~1667~~	~~59~~	~~1515~~	~~34~~	~~108~~
10A-67.1	688	483	0.70	0.119	0.0034	5.380	0.25	0.326	0.013	0.91	1815	63	1938	50	1884	38	104
~~10A-68.1~~	~~780~~	~~175~~	~~0.22~~	~~0.078~~	~~0.0026~~	~~1.787~~	~~0.077~~	~~0.164~~	~~0.0041~~	~~0.65~~	~~978~~	~~23~~	~~1134~~	~~70~~	~~1037~~	~~29~~	~~106~~
~~10A-69.1~~	~~502~~	~~382~~	~~0.76~~	~~0.072~~	~~0.0056~~	~~0.946~~	~~0.09~~	~~0.091~~	~~0.0016~~	~~0.59~~	~~562.2~~	~~9.2~~	~~890~~	~~130~~	~~664~~	~~41~~	~~118~~
10A-70.1	402	274	0.68	0.116	0.0035	4.960	0.26	0.305	0.011	0.95	1712	55	1887	56	1790	52	105
~~10A-71.1~~	~~1043~~	~~263~~	~~0.25~~	~~0.114~~	~~0.0029~~	~~4.298~~	~~0.14~~	~~0.269~~	~~0.0054~~	~~0.89~~	~~1536~~	~~28~~	~~1863~~	~~45~~	~~1689~~	~~28~~	~~110~~
10A-72.1	397	17	0.04	0.069	0.0025	1.255	0.059	0.133	0.0032	0.61	803	18	879	78	820	27	102

~~10A-73.1~~	~~843~~	~~428~~	~~0.51~~	~~0.115~~	~~0.0029~~	~~4.478~~	~~0.14~~	~~0.279~~	~~0.0051~~	~~0.86~~	~~1591~~	~~24~~	~~1881~~	~~45~~	~~1724~~	~~27~~	~~108~~
~~10A-74.1~~	~~641~~	~~271~~	~~0.42~~	~~0.170~~	~~0.0049~~	~~7.630~~	~~0.39~~	~~0.320~~	~~0.01~~	~~0.97~~	~~1782~~	~~52~~	~~2546~~	~~52~~	~~2159~~	~~52~~	~~121~~
10A-75.1	529	290	0.55	0.095	0.0029	3.090	0.17	0.233	0.0088	0.95	1347	46	1509	58	1412	45	105
~~10A-76.1~~	~~796~~	~~359~~	~~0.45~~	~~0.113~~	~~0.0028~~	~~4.103~~	~~0.13~~	~~0.260~~	~~0.0053~~	~~0.88~~	~~1492~~	~~26~~	~~1847~~	~~45~~	~~1651~~	~~27~~	~~111~~
~~10A-77.1~~	~~1151~~	~~242~~	~~0.21~~	~~0.119~~	~~0.0029~~	~~4.760~~	~~0.14~~	~~0.287~~	~~0.0047~~	~~0.80~~	~~1625~~	~~24~~	~~1942~~	~~44~~	~~1776~~	~~25~~	~~109~~
~~10A-78-1~~	~~713~~	~~214~~	~~0.30~~	~~0.105~~	~~0.0033~~	~~3.140~~	~~0.19~~	~~0.211~~	~~0.0089~~	~~0.96~~	~~1231~~	~~47~~	~~1694~~	~~60~~	~~1413~~	~~50~~	~~115~~
~~10A-79.1~~	~~1086~~	~~569~~	~~0.52~~	~~0.106~~	~~0.003~~	~~3.760~~	~~0.22~~	~~0.252~~	~~0.011~~	~~0.97~~	~~1444~~	~~56~~	~~1726~~	~~53~~	~~1562~~	~~50~~	~~108~~
~~10A-80.1~~	~~654~~	~~326~~	~~0.50~~	~~0.092~~	~~0.0037~~	~~2.770~~	~~0.2~~	~~0.212~~	~~0.0094~~	~~0.95~~	~~1233~~	~~51~~	~~1443~~	~~82~~	~~1317~~	~~58~~	~~107~~
~~10A-81.1~~	~~817~~	~~55~~	~~0.07~~	~~0.074~~	~~0.0024~~	~~1.441~~	~~0.064~~	~~0.140~~	~~0.0032~~	~~0.77~~	~~842~~	~~18~~	~~1033~~	~~67~~	~~901~~	~~27~~	~~107~~
10A-82.1	429	328	0.76	0.118	0.003	5.380	0.22	0.326	0.0093	0.91	1813	45	1927	47	1870	35	103
~~10A-83.1~~	~~394~~	~~149~~	~~0.38~~	~~0.105~~	~~0.003~~	~~2.890~~	~~0.14~~	~~0.199~~	~~0.0069~~	~~0.90~~	~~1165~~	~~37~~	~~1709~~	~~50~~	~~1371~~	~~36~~	~~118~~
~~10A-84.1~~	~~796~~	~~275~~	~~0.35~~	~~0.096~~	~~0.0029~~	~~2.490~~	~~0.11~~	~~0.187~~	~~0.0049~~	~~0.90~~	~~1104~~	~~27~~	~~1536~~	~~55~~	~~1261~~	~~34~~	~~114~~
~~10A-85.1~~	~~698~~	~~175~~	~~0.25~~	~~0.110~~	~~0.0038~~	~~4.320~~	~~0.26~~	~~0.275~~	~~0.012~~	~~0.95~~	~~1558~~	~~62~~	~~1810~~	~~61~~	~~1663~~	~~63~~	~~107~~
~~10A-86.1~~	~~665~~	~~80~~	~~0.12~~	~~0.185~~	~~0.0054~~	~~7.680~~	~~0.4~~	~~0.300~~	~~0.011~~	~~0.94~~	~~1686~~	~~54~~	~~2692~~	~~47~~	~~2178~~	~~48~~	~~129~~

Table 6. U-Pb zircon analytical results (SHRIMP) of the metasedimentary (FM27) rock of the Embu Complex

Spot	Content (ppm)		Th/U	Isotopic ratios							Age (Ma)				% Disc
	U	Th		$^{207}Pb/^{206}Pb$	1σ	$^{207}Pb/^{235}Pb$	1σ	$^{206}Pb/^{238}U$	1σ	err corr	$^{207}Pb/^{206}Pb$	1σ	$^{206}Pb/^{238}U$	1σ	
~~FM27-1.1~~	~~390~~	~~116~~	~~0.31~~	~~.119~~	~~0.4~~	~~4.49~~	~~2.0~~	~~.2853~~	~~1.7~~	~~0.87~~	~~1866~~	~~18~~	~~1618~~	~~25~~	~~15~~
FM27-2.1	391	254	0.67	.123	0.3	6.35	1.8	.3736	1.7	0.98	2004	7	2046	30	-2
FM27-3.1	1116	24	0.02	.071	0.5	1.13	2.4	.1266	1.8	0.72	772	35	768	13	1
~~FM27-4.1~~	~~945~~	~~93~~	~~0.10~~	~~.086~~	~~0.3~~	~~2.30~~	~~1.8~~	~~.1980~~	~~1.7~~	~~0.96~~	~~1298~~	~~9~~	~~1165~~	~~18~~	~~11~~
~~FM27-5.1~~	~~838~~	~~43~~	~~0.05~~	~~.074~~	~~0.4~~	~~1.41~~	~~1.9~~	~~.1417~~	~~1.7~~	~~0.92~~	~~994~~	~~15~~	~~854~~	~~14~~	~~16~~
FM27-6.1	874	6	0.01	.071	0.5	1.17	2.4	.1299	1.7	0.74	778	34	787	13	-1
~~FM27-7.1~~	~~178~~	~~136~~	~~0.79~~	~~.121~~	~~0.5~~	~~5.33~~	~~1.9~~	~~.3256~~	~~1.8~~	~~0.92~~	~~1936~~	~~13~~	~~1817~~	~~28~~	~~7~~
FM27-8.1	1502	19	0.01	.067	0.5	1.21	1.8	.1334	1.7	0.95	806	12	807	13	0
FM27-9.1	210	58	0.29	.101	0.5	3.72	2.0	.2761	1.8	0.88	1579	18	1572	25	0
FM27-10.1	174	197	1.17	.109	0.6	4.75	1.9	.3196	1.8	0.93	1764	13	1788	28	-1
FM27-11.1	102	65	0.66	.092	0.8	2.92	2.4	.2413	1.8	0.76	1380	30	1393	23	-1
~~FM27-12.1~~	~~605~~	~~146~~	~~0.25~~	~~.118~~	~~0.3~~	~~3.96~~	~~2.1~~	~~.2576~~	~~1.7~~	~~0.82~~	~~1826~~	~~22~~	~~1477~~	~~23~~	~~24~~
FM27-13.1	745	10	0.01	.066	0.5	1.18	1.8	.1307	1.7	0.96	798	11	792	13	1
FM27-15.1	251	213	0.88	.109	0.5	4.36	1.9	.3002	1.7	0.90	1721	15	1692	26	2
FM27-17.1	159	51	0.33	.120	0.7	5.66	1.9	.3466	1.8	0.92	1932	14	1918	30	1

Table 7. Zircon U/Pb analytical results (LA-MC-ICP-MS) from sample AN26A and AN47 of the Embu Complex. São Paulo University.

Sample / Spot	U (ppm)	Th (ppm)	Th/U	Isotopic ratios							Age (204corr)						% Conc
				$^{207}Pb/^{206}Pb$	1σ	$^{207}Pb/^{235}U$	1σ	$^{206}Pb/^{238}U$	1σ	err corr	$^{206}Pb/^{238}U$	1σ	$^{207}Pb/^{206}Pb$	1σ	$^{208}Pb/^{232}Th$	1σ	
AN26A-2.1	248	25	0.10	.061	0.002	0.8412	0.03	0.0997	0.002	0.26	613	9	646	7	62	15	98
AN26A-2.2	315	274	0.87	.060	0.002	0.8371	0.02	0.1005	0.001	0.99	617	8	618	52	618	12	99
AN26A-4.1	869	4	0.00	.065	0.001	1.1812	0.02	0.1320	0.002	0.84	799	1	771	38	792	11	100
AN26A-6.2	336	3	0.01	.064	0.002	1.0717	0.03	0.1214	0.002	0.94	739	9	743	51	74	13	99
AN26A-14.2	278	24	0.09	.062	0.002	0.9558	0.03	0.1115	0.002	0.83	682	9	679	6	681	14	100
AN26A-17.2	319	1	0.00	.065	0.002	1.1926	0.03	0.1327	0.002	0.54	803	1	781	58	797	15	100
AN26A-27.1	236	3	0.01	.065	0.002	1.1507	0.03	0.1290	0.002	0.94	782	9	765	57	778	16	100
AN26A-48.2	179	43	0.24	.061	0.002	0.8153	0.03	0.0971	0.002	0.74	597	11	636	73	605	16	98
AN26A-62.1	74	63	0.84	.065	0.004	1.1271	0.07	0.1266	0.004	0.80	768	23	761	127	766	31	100
AN26A-96.1	232	21	0.09	.067	0.003	1.1824	0.05	0.1277	0.002	0.76	775	12	842	77	792	21	97
AN47-17.1	394	34	0.09	.066	0.002	1.2327	0.04	0.1357	0.003	0.88	820	15	802	68	816	17	100
AN47-20.1	352	10	0.03	.066	0.002	1.2195	0.04	0.1342	0.003	0.87	812	15	804	73	81	18	100
AN47-22.2	600	63	0.11	.065	0.002	1.1436	0.03	0.1276	0.002	0.64	774	8	775	5	774	13	99
AN47-24.1	467	50	0.11	.066	0.002	1.2030	0.03	0.1331	0.002	0.48	806	9	792	57	802	15	100
AN47-28.1	228	30	0.13	.070	0.002	1.3326	0.05	0.1391	0.002	0.95	840	11	913	67	860	19	97
AN47-29.1	407	93	0.23	.066	0.002	1.1493	0.03	0.1261	0.002	0.97	766	9	809	56	777	15	98
AN47-36.1	431	98	0.23	.067	0.002	1.3036	0.05	0.1405	0.002	0.21	848	9	846	66	847	19	100
AN47-38.1	358	101	0.28	.067	0.002	1.1812	0.04	0.1277	0.001	0.86	774	8	841	68	792	18	97

AN47-43.1	574	73	0.13	.064	0.002	1.1692	0.03	0.1317	0.002	0.81	797	9	755	66	786	16	101
AN47-52.1	432	44	0.10	.067	0.002	1.3062	0.04	0.1410	0.002	0.98	850	1	844	71	848	18	100
AN47-55.1	529	28	0.05	.067	0.002	1.2617	0.03	0.1372	0.002	0.97	829	12	829	61	829	16	100
AN47-56.1	509	16	0.03	.066	0.002	1.1604	0.03	0.1274	0.002	0.95	773	12	808	62	782	15	98
AN47-63.2	679	40	0.06	.065	0.002	1.2600	0.04	0.1410	0.002	0.96	850	13	769	61	828	16	102
AN47-69.1	1030	24	0.02	.066	0.003	1.1487	0.05	0.1260	0.002	0.92	765	9	809	83	777	22	98
AN47-70.2	405	32	0.08	.065	0.003	1.2056	0.06	0.1354	0.002	0.98	819	11	760	114	803	28	101
AN47-77.2	764	59	0.08	.066	0.002	1.2240	0.04	0.1352	0.002	0.92	818	9	795	77	812	2	100
AN47-78.1	4091	370	0.09	.060	0.002	0.7528	0.02	0.0917	0.001	0.79	566	6	587	65	570	13	99
AN47-78.2	5123	847	0.17	.060	0.002	0.7662	0.02	0.0926	0.001	0.77	571	6	604	65	578	13	98
AN47-82.1	392	11	0.03	.066	0.003	1.2209	0.05	0.1352	0.002	0.68	817	11	791	9	810	23	100

Table 8. Zircon analytical LA-ICP-MS REE (ppm) results from 45A and 10A samples.

Sample-Spot	La	Ce	Pr	Nd	Sm	Eu	Gd	Tb	Dy	Ho	Er	Tm	Yb	Lu
45A-1	0.36	1.34	0.2	1.58	3.32	0.8	15.2	2.64	12.1	2.01	4.83	0.84	6.4	1.1
45A-2	0.179	0.68	0.122	0.92	2.67	0.65	19.5	5.88	41.8	8.23	22.08	3.21	23.16	4.26
45A-3	1.67	5.9	0.92	4.6	2.96	5.2	14.5	5.1	45.4	11.03	39.1	7.29	63.2	12.1
45A-4	0.196	0.7	0.122	0.91	2.18	0.44	10.6	2.17	14.3	2.88	7.47	1.14	8.17	1.39
45A-5	0.92	4.9	0.83	4.6	4.71	1.14	17.3	3.32	17.5	3.31	9.4	1.52	12.8	2.14
45A-6	0.184	0.84	0.165	1.23	2.55	1	20.47	8.13	73.2	16.35	47.5	6.64	46.6	7.63
45A-7	0.112	0	0.091	0.74	2.26	0.36	13.15	3.54	24	4.8	13.9	2.15	15.9	2.78
45A-8	0	0.371	0.0126	0.221	1.52	0.049	12.41	4.6	38.6	8.98	27.8	4.39	31.5	5.24
45A-9	0.107	0.77	0.083	1.15	4.07	0.337	19.1	3.38	17.9	2.94	7.01	1.02	7.24	1.2
45A-10	0.0112	5.21	0.099	2.01	4.68	0.78	28.6	9.6	109	37.4	166	31.8	277	53.3
~~45A-11.1~~	~~2.02~~	~~4.2~~	~~0.82~~	~~6.1~~	~~4.4~~	~~1.85~~	~~10.8~~	~~3.24~~	~~25.8~~	~~5.96~~	~~22~~	~~4.47~~	~~34.3~~	~~6.7~~
45A-11.2	0	0.466	0	0.6	2.9	0.161	13.33	2.18	11.09	1.5	4.03	0.581	4.43	0.823
45A-12	0.77	2.9	0.54	3.6	3.28	3.4	16.6	4.81	41	9.27	30.8	5.2	39.8	7.2
45A-13	2.09	5.4	1.09	5.6	4.78	7	11.5	2.16	14.4	3.21	13.2	2.9	32	6.6
45A-14	0.075	0.617	0.054	0.81	3.42	0.274	17.2	3.3	19.19	3.24	8.42	1.168	8.72	1.4
45A-15	0	0.359	0	0.38	2.41	0.141	11.24	2.24	12.5	2	4.67	0.66	4.67	0.79
45A-16	0	0.83	0.094	1.17	3.1	0.96	12.6	1.97	10.1	1.5	3.72	0.591	4.49	0.797
45A-17.1	0.074	0.542	0.041	0.524	2.06	0.134	8.35	1.212	6.46	0.88	2.05	0.304	2.46	0.346
45A-17.2	0.06	0.439	0.022	0.372	1.67	0.066	6.1	1.16	5.6	1.02	2.33	0.35	2.63	0.431
45A-18	0.0089	0.51	0	0.35	1.28	0.066	11.89	4.55	45.9	10.82	34.74	5.34	39.7	6.34
45A-19.1	0.055	2.09	0.053	0.54	1.51	0.344	11.29	3.74	36.6	10.3	43	8.9	82	16.6
45A-19.2	0.48	1.61	0.366	2.11	1.91	0.82	8.4	2.43	18.4	4.32	13.49	2.28	18.4	3.51
45A-20.1	0.301	1.06	0.201	1.35	2.14	1.35	11.82	3.58	26.9	6.36	18.6	2.93	23.2	4.42
45A-20.2	1.16	4.15	0.8	4.16	2.82	6.3	15.4	4.61	38.1	9.19	25.6	3.99	31.6	5.56
45A-21	1.01	2.3	0.31	2.7	1.86	0.45	10.1	2.99	21.9	4.89	13.3	2.26	18.2	3.4

45A-22	0.8	2.26	0.41	2.61	3.56	4	15.5	3.98	26.5	6.18	20.6	4.1	37	7.4
45A-23	0	0	0.014	0.33	2.16	0.174	11.3	1.8	9.3	1.63	4.8	0.87	8.5	1.62
45A-24	0.027	0.398	0	0	4.56	1.11	25.4	8.12	71.7	18.32	60.5	10.48	81.8	14.48
45A-25	0.37	1.39	0.29	1.77	3.15	1.35	12.54	2.12	11.9	2.48	8	1.61	15	2.84
~~45A-26.1~~	~~0.76~~	~~1.03~~	~~0.311~~	~~1.34~~	~~1.03~~	~~0.6~~	~~6.6~~	~~3.07~~	~~35.7~~	~~11.9~~	~~45.9~~	~~9.2~~	~~74.9~~	~~14.8~~
45A-26.2	4.13	12.4	2.63	12.6	6.3	13	20.3	5.37	45.9	12.5	48.8	11.4	121	26.2
10A-1	10	55	2.9	17	8.4	1.58	29.5	9.5	113	43.2	197	43	420	85.3
10A-2	0.039	0.89	0.083	1.51	5.31	0.213	28.8	6.64	42.6	7.7	19.1	2.74	20.2	3.3
~~10A-3~~	~~1.86~~	~~3.9~~	~~0.96~~	~~7.5~~	~~5.8~~	~~2.6~~	~~29.5~~	~~8.73~~	~~109~~	~~39.9~~	~~183~~	~~42.6~~	~~449~~	~~91~~
~~10A-4~~	~~3.83~~	~~21.5~~	~~3.18~~	~~20.1~~	~~10.2~~	~~2.58~~	~~26.7~~	~~7.9~~	~~92~~	~~33.8~~	~~157~~	~~34.4~~	~~355~~	~~76~~
~~10A-5~~	~~3.03~~	~~26.3~~	~~2.11~~	~~12.7~~	~~7.16~~	~~3.91~~	~~18.1~~	~~6.01~~	~~78~~	~~33.6~~	~~178~~	~~44.4~~	~~494~~	~~109.9~~
~~10A-6~~	~~4.59~~	~~19.3~~	~~2.58~~	~~14.1~~	~~7.2~~	~~4.25~~	~~18.9~~	~~6~~	~~88~~	~~43.9~~	~~273~~	~~75~~	~~920~~	~~251~~
10A-7	0.073	31.4	0.149	1.91	3.81	1.76	20.2	6.98	82.5	33.1	159	35.4	355	76.7
10A-8	0.32	8.9	0.18	1.65	1.99	0.43	10.8	4.09	51.6	21.1	103	23.5	231	49.9
10A-9	1.57	4.6	0.5	2.98	1.56	0.64	5	2.66	45.4	22.7	134	39.8	472	112.8
~~10A-10~~	~~0.334~~	~~7.4~~	~~0.242~~	~~1.96~~	~~2.47~~	~~1.11~~	~~11.2~~	~~4.36~~	~~57~~	~~23~~	~~116.7~~	~~28.6~~	~~301~~	~~66.2~~
10A-11	15	74	3.2	17	8.8	2.02	30.9	10.27	116.9	44.9	202	44	405	83.7
~~10A-12~~	~~1.21~~	~~55~~	~~0.75~~	~~6.8~~	~~8.4~~	~~1.93~~	~~29.2~~	~~8.4~~	~~84~~	~~29.3~~	~~129~~	~~28.1~~	~~275~~	~~59.5~~
~~10A-13~~	~~3.4~~	~~17.3~~	~~1.22~~	~~5.6~~	~~1.3~~	~~0.86~~	~~8.3~~	~~3.54~~	~~39.6~~	~~16.3~~	~~86~~	~~23~~	~~269~~	~~58~~
~~10A-14.1~~	~~2.9~~	~~30.2~~	~~1.54~~	~~9~~	~~6.6~~	~~1.27~~	~~20.8~~	~~6.74~~	~~80.8~~	~~30.2~~	~~143.7~~	~~33.7~~	~~345~~	~~76.9~~
10A-14.2	4.7	5.4	1.35	6.2	0.64	0.46	4	2.46	33.5	16.5	89	27.8	360	81
~~10A-15~~	~~0.185~~	~~32.2~~	~~0.213~~	~~2.67~~	~~4.2~~	~~1.55~~	~~22.7~~	~~8.2~~	~~108~~	~~47.6~~	~~243~~	~~61.3~~	~~639~~	~~147.6~~
~~10A-16~~	~~12~~	~~21.1~~	~~5.9~~	~~48~~	~~24.7~~	~~12.9~~	~~87~~	~~24.3~~	~~237~~	~~73~~	~~279~~	~~56.6~~	~~510~~	~~106~~
~~10A-17~~	~~1.09~~	~~13.4~~	~~0.76~~	~~5.3~~	~~4.93~~	~~1.33~~	~~23.4~~	~~7.89~~	~~97.6~~	~~39.9~~	~~192~~	~~44.9~~	~~448~~	~~102.3~~
10A-18	0.75	39.5	1.02	6.89	5.01	1.69	21.5	6.9	78.5	30.2	140.8	31.8	308	64.2
~~10A-19.1~~	~~0.406~~	~~3.09~~	~~0.138~~	~~1.76~~	~~3.15~~	~~0.281~~	~~18.6~~	~~7.13~~	~~95.4~~	~~38.9~~	~~184~~	~~41.7~~	~~410~~	~~88.2~~

10A-19.2	0.291	4.86	0.147	1.35	2.19	0.238	13.89	5.31	70.6	28.53	136.8	30.14	289	60
10A-20	0.58	34.2	0.35	2.95	4.09	0.484	17.7	6.39	78.5	30.6	146	33.2	325	68.4
10A-21	1.34	17.1	1.04	8.9	5.7	1.13	14.4	4.9	58.8	24.5	127	31.3	333	76
10A-22	3.69	18.8	3.8	21.2	8.9	3.91	17.8	5.73	71.5	30.4	163	42.4	462	105
10A-23	1.31	66	1.15	10.5	13.6	5.13	56	18	209	80	387	89	911	219
10A-24	2.35	10.5	1.65	9.7	5.6	2.38	15.2	5.8	75	32.4	173	44.6	505	114
10A-25	3.3	8	1.61	7.9	3.46	2.41	10	3.85	60	30	178	49.8	591	142
10A-26	2.3	4.7	0.77	6.3	1.67	0.96	4.6	1.89	32	15.1	92	26.9	334	77.8
10A-27	1.76	49.8	0.99	6.5	5.43	1.51	25.3	8.2	104	43.3	220	51.3	548	123.6
10A-28	1.37	55	0.82	5.9	5.5	2.66	21	7.4	91	39	206	52.2	576	134
10A-29	0.88	10.5	0.43	1.92	1.03	0.73	5.9	2.66	40.6	21.8	131	37.1	465	118
10A-30	1.34	9.8	1.47	12	14.2	4.3	52	17.1	178	58	236	50.3	507	101.4
10A-31	0.67	4.91	0.277	2.86	4.66	0.9	21.2	6.04	57.6	19.3	82.6	19.8	216	47.1
10A-32	0.8	27.5	0.8	6.1	2.74	1.24	10.1	3.37	43.1	18.5	100	25	281	63.5
10A-33	49	121	18.8	110	37	12.3	61	16.3	163	60	268	59	620	135
10A-34	11	30.1	5.57	33.7	13.2	7.5	29.9	7.9	80	29.3	140	32	351	78
10A-35	1.53	19.2	1.28	7.6	3.87	2.07	12.3	4.79	66.2	32.3	183	49	580	140
10A-36	0.74	6.8	0.35	2.16	1.27	0.68	6.4	3.15	46.9	23.1	138	39.1	465	113
10A-37	0.31	14.1	0.032	0.78	1.01	0.337	6.5	2.87	41.8	20	109	29.9	350	79
10A-38	0.37	4.6	0.205	1.3	1.52	0.55	7.4	3.42	49.3	23	126.6	35.3	419	97.1
10A-39	5.3	16.8	4.7	28.9	12.6	7.9	30.5	11	134	54.8	255	57.3	557	113
10A-40	0.86	8.1	0.89	5.2	3.17	0.6	6.4	3.17	49	23	132	39.5	490	116
10A-41	3.79	76	1.73	13	11.8	3.96	44.4	15.2	170	65.8	303	65.1	630	138
10A-42	2.02	7.9	0.99	5.2	3.06	1.79	8	3.28	49.2	23.9	138	39.1	470	110
10A-43	1.86	14.9	1.56	9	4.45	1.03	10.5	3.64	54	23.8	139	38.6	469	115.8
10A-44	1.34	27.9	0.46	4.5	4.5	1.69	18.6	5.56	64.9	27.5	147	36.7	402	95.6

10A-45	2.4	6.7	1.56	9.4	4.2	2.8	10	4.25	62.2	26.6	142	39.5	431	95
10A-46	3	32.7	1.62	11.3	7.9	2.75	26.8	7.4	86	33	154	35.4	370	71
10A-47	0.47	10.1	0.164	1.55	1.99	0.321	11.7	4.64	64.5	26.3	138	32.9	342	71.6
10A-48	0.97	6.1	0.56	3.42	2.69	1.62	10.5	4.9	69	31	174	46.2	522	117
10A-49	0.39	0.69	0.22	1.7	0	0.42	2.7	1.51	28.4	13.7	78	23.7	266	61
10A-50	14.1	15.5	4	20.3	6.5	4.97	12.6	4.07	56.1	24.5	142.5	39	433	96.5
10A-51	7.5	138	4.7	31.9	20.2	6.1	70	21.8	253	93	421	89.8	823	164
10A-52	12	50	2.1	15	4.1	1.03	18.5	6.8	92	38.7	202	50.1	530	112.5
10A-53	8.8	67.4	7.1	42.7	17	6.82	35	9.8	111.6	43.3	221	53.9	587	133.4
10A-54	1.22	13.6	0.76	5.98	4.6	0.86	19.7	6.8	90	39.3	216	53.5	582	125
10A-55	1.63	11.8	0.61	2.61	1.55	0.62	7.2	3.69	59.1	25.6	150	41.4	478	101
10A-56	0.07	3.3	0.21	1.88	0.68	0.2	4.1	2.3	40.4	18.3	101	30	364	73
10A-58	3.21	33.2	3.5	16.7	10.7	11.2	28.1	9.06	113	45.2	234	56.2	569	123
10A-59	0.39	32.3	0.45	4.28	5.61	1.28	25.9	8.07	90.5	33.9	157	33.3	309	63.4
10A-60	4.31	13.7	3.8	22	8.8	6.5	14.8	4.14	52.3	22.9	138	40.2	462	104
10A-61	0.9	15	0.62	5.2	6.49	0.8	26.7	8.89	103.3	40.9	198	42.8	416	88
10A-62	3.1	22.7	1.34	7.7	4.2	0.89	14.3	5.5	73.4	32.3	177.7	46.1	499	111.6
10A-63	0.66	28.5	0.24	2.73	3.5	1.23	17.3	7.2	93	39.7	205	49	499	106
10A-64	0.38	34.2	0.36	3.6	5	1.75	18.6	6.2	71	27.5	134	32.7	325	73.8
10A-65	2.9	40	0.91	5.5	3.54	1.29	14.8	5.1	65	27.5	140	36.6	421	95
10A-66	1.54	6.7	0.94	6.7	3.8	2.33	12.5	4.2	61	25.2	136	35.8	418	97
10A-67	0.42	12.6	0.42	5	8.2	1.54	39	11.6	141	55	252	58	622	136
10A-68	3.35	15.9	2.78	16	7.2	3.36	16.5	5.69	71	28.4	147	36.9	446	100
10A-69	20.4	96	7.9	36.1	11.6	1.91	26.3	7.4	84.4	33.2	149.9	33.4	336	70.5
10A-70	0.241	22	0.413	5.4	6.4	1	24.8	7	76	26.9	115	25.5	262	54.6
10A-71	1.48	5.4	1.42	9.6	7.2	3.75	21.7	6.3	69.8	23.1	102	23.2	247	51.3

10A-72	0.55	0	0.196	1	0.85	0.43	6.8	2.88	44.2	23.8	133.5	38.3	481	113.2
~~10A-73~~	~~17~~	~~54~~	~~4.6~~	~~21~~	~~8.4~~	~~1.58~~	~~29.2~~	~~8.9~~	~~102~~	~~40.2~~	~~186~~	~~43.8~~	~~464~~	~~98.2~~
~~10A-74~~	~~2.35~~	~~38.9~~	~~1.76~~	~~10.3~~	~~5~~	~~2.22~~	~~13.5~~	~~4.73~~	~~66.7~~	~~29.4~~	~~160.6~~	~~43.3~~	~~494~~	~~113.3~~
10A-75	0.66	29.1	0.86	8.7	7.6	1.54	25.2	8.1	96	38.3	176	39.9	410	82.6
~~10A-76~~	~~1.88~~	~~30.6~~	~~1.61~~	~~10.2~~	~~9.4~~	~~2.49~~	~~42.6~~	~~13.06~~	~~158~~	~~59.8~~	~~255~~	~~51.7~~	~~488~~	~~94.6~~
~~10A-77~~	~~3.03~~	~~10.7~~	~~2.33~~	~~15.1~~	~~10.9~~	~~3.81~~	~~44.7~~	~~15.8~~	~~202~~	~~79.3~~	~~353~~	~~76.4~~	~~729~~	~~147~~
~~10A-78~~	~~3.52~~	~~33.3~~	~~3.03~~	~~19.4~~	~~11.9~~	~~4.66~~	~~35.1~~	~~10.1~~	~~108.7~~	~~38.4~~	~~170~~	~~39.8~~	~~424~~	~~88.3~~
~~10A-79~~	~~2.43~~	~~44.9~~	~~2.14~~	~~15.3~~	~~11~~	~~2.49~~	~~43.1~~	~~11.6~~	~~150~~	~~56.5~~	~~250~~	~~57.3~~	~~571~~	~~113~~
~~10A-80~~	~~0.65~~	~~22~~	~~0.307~~	~~2.85~~	~~4.1~~	~~0.74~~	~~19.3~~	~~7.1~~	~~89~~	~~36.1~~	~~174~~	~~44.4~~	~~481~~	~~100~~
~~10A-81~~	~~0.99~~	~~5.5~~	~~0.52~~	~~3.41~~	~~2.08~~	~~0.72~~	~~9.2~~	~~3.8~~	~~60.7~~	~~27.7~~	~~150~~	~~41.5~~	~~496~~	~~111~~
10A-82	2.59	59.4	1.7	11.2	6.4	3.1	21	7.09	86.7	34.8	169	39.8	427	92.6
~~10A-83~~	~~3~~	~~37~~	~~1.11~~	~~6.5~~	~~4.98~~	~~1.88~~	~~21.7~~	~~7.84~~	~~106.9~~	~~46~~	~~231.3~~	~~55.5~~	~~581~~	~~125.2~~
~~10A-84~~	~~1.42~~	~~16.6~~	~~0.79~~	~~6.1~~	~~5~~	~~1.04~~	~~18.5~~	~~6.5~~	~~84~~	~~33.9~~	~~165~~	~~40.1~~	~~449~~	~~96~~
~~10A-85~~	~~0.54~~	~~8.6~~	~~0.243~~	~~2.23~~	~~3.33~~	~~0.71~~	~~20~~	~~8.6~~	~~122~~	~~50.3~~	~~247~~	~~56.6~~	~~562~~	~~120~~
~~10A-86~~	~~7.2~~	~~24.1~~	~~5.9~~	~~33.3~~	~~12.9~~	~~10~~	~~21.6~~	~~5.9~~	~~67~~	~~25.9~~	~~132~~	~~31.8~~	~~356~~	~~78~~

U/Pb disconcordant data (>5%) are strikethrough

Table 9. Analytical LA-ICP-MS U/Pb results from apatite (Sample FM02B)

Sample-Spot	U (ppm)	Th (ppm)	Th/U	Isotopic ratios									
				$^{207}Pb/^{235}Pb$	2σ	$^{206}Pb/^{238}U$	2σ	Err Corr	$^{238}U/^{206}Pb$	2σ	$^{207}Pb/^{206}Pb$	2σ	Err Corr
FM02B-01	22	0.1	218	8.8	1.7	0.160	0.02	0.40	6.250	0.70	0.399	0.08	0.84
FM02B-03	8	0.4	23	12	2.2	0.185	0.02	0.54	5.405	0.47	0.477	0.08	0.02
FM02B-05	31	0.1	224	3.8	0.62	0.107	0.00	0.21	9.311	0.35	0.260	0.04	0.47
FM02B-06.1	7	0.1	70	14.45	2.4	0.208	0.01	0.50	4.808	0.25	0.507	0.08	0.54
FM02B-06.2	9	0.1	89	13.19	2.1	0.198	0.01	0.40	5.045	0.22	0.486	0.07	0.33
FM02B-07.1	41	0.2	215	8.28	1.6	0.180	0.02	0.87	5.556	0.46	0.320	0.05	-0.46
FM02B-07.2	12	0.0	1523	13.14	2.1	0.211	0.01	0.36	4.751	0.23	0.466	0.07	0.52
FM02B-08.1	16	0.2	105	8.31	1.4	0.161	0.01	0.27	6.219	0.29	0.386	0.06	0.41
FM02B-08.2	15	0.3	48	7.63	1.3	0.155	0.01	0.24	6.472	0.34	0.369	0.06	0.54
~~FM02B-09.1~~	~~9~~	~~3.7~~	~~3~~	~~28~~	~~6.9~~	~~0.299~~	~~0.05~~	~~0.46~~	~~3.344~~	~~0.53~~	~~0.710~~	~~0.16~~	~~0.42~~
~~FM02B-09.2~~	~~51~~	~~0.6~~	~~89~~	~~3.75~~	~~0.6~~	~~0.159~~	~~0.06~~	~~0.50~~	~~6.289~~	~~2.53~~	~~0.210~~	~~0.03~~	~~0.51~~
FM02B-10	7	2.5	3	23.1	4	0.289	0.02	0.64	3.460	0.24	0.581	0.09	0.32
FM02B-11	16	0.2	79	10.95	1.8	0.181	0.01	0.27	5.534	0.25	0.453	0.07	0.47
FM02B-12.1	79	2.5	32	2.36	0.38	0.102	0.00	0.52	9.785	0.32	0.168	0.03	0.01
FM02B-12.2	20	0.4	52	9	1.4	0.167	0.01	0.38	5.999	0.21	0.388	0.06	0.38
FM02B-13.1	41	1.3	32	3.82	0.62	0.127	0.00	0.61	7.893	0.29	0.221	0.03	-0.03
FM02B-14	5	1.5	3	27.6	4.9	0.341	0.03	0.63	2.933	0.25	0.643	0.11	0.38
FM02B-15	41	0.5	90	3.52	0.57	0.110	0.00	0.49	9.058	0.33	0.238	0.04	0.09
FM02B-16	8	0.1	75	12.17	2.1	0.178	0.01	0.09	5.624	0.29	0.523	0.09	-0.01
FM02B-17	16	0.1	141	8.53	1.4	0.159	0.01	0.32	6.285	0.27	0.401	0.06	0.49
FM02B-18	14	0.1	144	8.58	1.4	0.161	0.01	0.33	6.207	0.28	0.396	0.06	0.28
FM02B-19	11	0.1	162	10.67	1.8	0.174	0.01	0.47	5.754	0.29	0.455	0.07	0.40
FM02B-20	12	0.1	176	9.26	1.5	0.169	0.01	0.36	5.903	0.30	0.419	0.07	0.57
FM02B-21	8	4.7	2	26.7	7.1	0.324	0.05	0.80	3.086	0.50	0.581	0.11	-0.20
FM02B-23	19	0.0	419	10.78	1.7	0.190	0.01	0.60	5.271	0.23	0.416	0.06	0.35
FM02B-24.1	47	0.2	291	5.11	0.81	0.144	0.00	0.41	6.969	0.22	0.262	0.04	0.15
FM02B-24.2	20	0.3	68	10.04	1.6	0.184	0.01	0.39	5.432	0.23	0.404	0.06	0.48
FM02B-25	26	0.1	258	6.3	1	0.145	0.01	0.50	6.916	0.31	0.317	0.05	0.08

FM02B-27	15	0.1	150	8.77	1.4	0.153	0.01	0.35	6.536	0.32	0.425	0.07	0.62
FM02B-28	11	0.1	114	14.21	2.3	0.218	0.01	0.25	4.589	0.20	0.492	0.07	0.59
FM02B-29	17	0.1	268	10.82	1.7	0.190	0.01	0.50	5.263	0.21	0.420	0.06	0.62
FM02B-30	13	0.1	96	12.22	2.1	0.191	0.01	0.31	5.225	0.26	0.472	0.08	0.41
FM02B-31	19	0.4	51	6.91	1.1	0.142	0.01	0.25	7.042	0.32	0.365	0.06	0.50
FM02B-32	13	0.0	290	8.19	1.3	0.156	0.01	0.24	6.414	0.30	0.387	0.06	0.46
FM02B-33	7	0.1	67	16.16	2.6	0.221	0.01	0.41	4.525	0.23	0.537	0.08	0.60
FM02B-34	10	0.1	149	14.9	2.5	0.217	0.01	0.59	4.608	0.30	0.519	0.08	0.40
FM02B-35	7	0.3	22	16.96	2.8	0.228	0.01	0.40	4.386	0.23	0.565	0.09	0.50
FM02B-36	32	0.0	8205	13.7	2.4	0.231	0.01	0.85	4.329	0.26	0.417	0.07	-0.53
FM02B-37.1	71	0.8	92	3.97	0.64	0.135	0.00	0.58	7.407	0.25	0.212	0.03	0.00
fM02B-37.2	14	0.1	116	11.82	1.9	0.191	0.01	0.36	5.233	0.26	0.464	0.07	0.58
FM02B-38	34	0.6	58	4.91	0.8	0.140	0.01	0.40	7.143	0.26	0.256	0.04	0.18
~~FM02B-39~~	~~5~~	~~0.6~~	~~8~~	~~46.3~~	~~7.7~~	~~0.665~~	~~0.04~~	~~0.57~~	~~1.504~~	~~0.08~~	~~0.509~~	~~0.08~~	~~0.42~~
FM02B-40	30	0.6	52	4.95	0.79	0.119	0.00	0.27	8.439	0.28	0.304	0.05	0.49
FM02B-41	13	0.1	191	9.57	1.6	0.168	0.01	0.65	5.963	0.30	0.414	0.06	0.09
~~FM02B-42~~	~~18~~	~~0.1~~	~~182~~	~~9.01~~	~~1.6~~	~~0.184~~	~~0.03~~	~~0.53~~	~~5.435~~	~~0.80~~	~~0.840~~	~~0.93~~	~~0.21~~
FM02B-43	11	0.1	149	11.55	1.9	0.201	0.01	0.53	4.975	0.25	0.430	0.07	0.33
FM02B-44	22	0.0	807	7.33	1.2	0.158	0.01	0.26	6.313	0.24	0.341	0.05	0.53
FM02B-45	15	0.1	150	9.06	1.5	0.168	0.01	0.28	5.942	0.26	0.405	0.06	0.43
FM02B-46	55	0.2	235	3.23	0.51	0.116	0.00	0.12	8.643	0.25	0.205	0.03	0.47
FM02B-47	28	0.5	58	8.03	1.3	0.167	0.01	0.53	6.002	0.23	0.350	0.05	0.35
FM02B-48	11	0.2	54	11.01	1.8	0.173	0.01	0.35	5.790	0.33	0.475	0.07	0.52
FM02B-49.1	18	0.4	43	9.8	1.6	0.182	0.01	0.51	5.507	0.22	0.395	0.06	0.20
FM02B-49.2	12	0.4	31	9.9	1.6	0.160	0.01	0.30	6.258	0.29	0.464	0.07	0.47
FM02B-50	23	0.0	1547	7.89	1.3	0.182	0.01	0.38	5.501	0.19	0.316	0.05	0.36
FM02B-51	14	0.1	142	7.55	1.2	0.155	0.01	0.31	6.472	0.31	0.370	0.06	0.44
FM02B-52	0	0.0	3	21.6	4.8	0.274	0.03	0.35	3.650	0.41	0.592	0.13	0.41
~~FM02B-53~~	~~177~~	~~2.3~~	~~76~~	~~6.89~~	~~1.4~~	~~0.182~~	~~0.01~~	~~0.84~~	~~5.507~~	~~0.30~~	~~0.249~~	~~0.04~~	~~-0.59~~
FM02B-54	3	1.4	2	98	25	1.030	0.22	0.91	0.971	0.21	0.694	0.11	0.59
FM02B-56	11	1.6	7	11.14	1.8	0.196	0.01	0.36	5.110	0.26	0.417	0.07	0.44
FM02B-57	14	1.0	14	9.63	1.5	0.177	0.01	0.29	5.637	0.25	0.402	0.06	0.59
FM02B-58	7	0.8	9	19.1	3.5	0.251	0.03	0.50	3.984	0.40	0.569	0.10	0.54

Sample name + x.y: grain number followed by analysis number
2σ is an standard absolute value (STDEV/SQRT)
Visible discordant data are strikethrough

Table 10. Rb/Sr isotope analyses results of the metasedimentary rocks of the Embu Complex

	$^{87}Rb/^{86}Sr$	1σ*	$^{87}Sr/^{86}Sr$	1σ*
45A-m01	0.00398	1.55	0.73754	0.53
45A-m02.1	0.00072	1.55	0.73196	0.53
45A-m02.2	0.00067	1.55	0.72774	0.53
45A-m03	0.00289	1.55	0.74377	0.53
45A-m04	0.00129	1.55	0.72719	0.53
45A-m05	0.01046	1.55	0.75310	0.53
45A-m06	0.00768	1.55	0.73586	0.53
45A-bt01	544.2144612	2.03	5.363669232	0.53
45A-bt02	543.227654	2.03	5.73653072	0.53
45A-bt03	517.1455212	2.03	5.307830405	0.53
45A-bt04	481.9918168	2.03	5.100153666	0.53
45A-bt05	508.6719947	2.03	5.292668576	0.53
45A-bt06	480.3199398	2.03	5.166703529	0.53
45A-bt07	488.7593862	2.03	5.211948103	0.53
45A-bt08	401.0747743	2.03	4.438641257	0.53
45A-bt09	340.3971321	2.03	3.951888352	0.53
45A-bt10	361.4448298	2.03	4.20390101	0.53
45A-bt11	338.9450926	2.03	3.893768428	0.53
45A-bt12	364.4539276	2.03	4.087019328	0.53
45A-bt13	402.0072422	2.03	4.106126682	0.53
45A-bt14	433.841444	2.03	4.620325896	0.53
45A-bt15	417.4188598	2.03	4.526371788	0.53
45A-bt16	517.9115645	2.03	5.277361915	0.53
45A-bt17	420.4825489	2.03	4.371107907	0.53
45A-bt18	474.965389	2.03	4.761298799	0.53
45A-bt19	331.7616342	2.03	3.731764387	0.53
45A-bt20.1	403.1809173	2.03	4.422830974	0.53
45A-bt20.2	371.1619778	2.03	4.133433008	0.53
45A-bt21	775.7076489	2.03	7.135222233	0.53
45A-bt22	439.360694	2.03	4.800848993	0.53
45A-bt23	451.6587244	2.03	4.679454764	0.53
45A-bt24	912.7687754	2.03	8.317024423	0.53
45A-bt25	592.3085079	2.03	5.819758929	0.53
45A-bt26	556.3149961	2.03	5.507902593	0.53
45A-bt27	582.0671159	2.03	5.844441697	0.53
45A-bt28	465.4884172	2.03	5.034579763	0.53
45A-bt29	234.2399688	2.03	2.723462865	0.53
45A-bt30	504.0653682	2.03	4.629426075	0.53
45A-bt31	428.1988704	2.03	4.393231774	0.53
45A-bt32	410.4948088	2.03	4.332515642	0.53
45A-bt33	361.2840349	2.03	4.045555804	0.53

45A-bt34	832.3467587	2.03	7.427462278	0.53
45A-bt35	380.3688217	2.03	4.182180096	0.53
45A-bt average	**474.17**		**4.9050**	
45A-m average	**0.00395**			
12A-bt001	907.00	2.03	8.8315	0.53
12A-bt002.1	1448.61	2.03	14.0533	0.53
12A-bt002.2	1475.50	2.03	14.4070	0.53
12A-bt003	1431.05	2.03	13.8585	0.53
12A-bt004	1363.14	2.03	13.4778	0.53
12A-bt005	1428.49	2.03	13.5376	0.53
12A-bt006.1	1012.49	2.03	9.9138	0.53
12A-bt006.2	957.50	2.03	9.3445	0.53
12A-bt007	907.76	2.03	8.8480	0.53
12A-bt008	923.97	2.03	9.3682	0.53
12A-bt009	1426.21	2.03	13.4301	0.53
12A-bt010	1335.46	2.03	13.0456	0.53
12A-bt011.1	1165.25	2.03	11.4442	0.53
12A-bt011.2	1426.86	2.03	13.5210	0.53
12A-bt012	1031.15	2.03	9.9640	0.53
12A-bt013	1405.03	2.03	13.0394	0.53
12A-bt014	912.85	2.03	8.7379	0.53
12A-bt015	1041.47	2.03	10.4884	0.53
12A-bt016	415.55	2.03	4.1222	0.53
12A-bt017	882.24	2.03	8.9112	0.53
12A-bt018.1	651.90	2.03	6.6457	0.53
12A-bt018.2	675.97	2.03	6.8269	0.53
12A-bt019	1553.28	2.03	14.5400	0.53
12A-bt020	2467.22	2.03	22.8764	0.53
12A-bt021	535.67	2.03	5.5857	0.53
12A-bt023	837.68	2.03	8.0664	0.53
12A-bt024	1746.10	2.03	16.6936	0.53
12A-bt025	704.93	2.03	6.8934	0.53
12A-bt026	621.14	2.03	6.0854	0.53
12A-bt027	829.35	2.03	8.4046	0.53
12A-bt028	862.37	2.03	8.6476	0.53
12A-bt029	841.08	2.03	8.0285	0.53
12A-bt030	1163.90	2.03	11.5559	0.53
12A-bt031	729.48	2.03	7.7038	0.53
12A-bt032	926.04	2.03	8.8650	0.53
12A-bt033	754.22	2.03	7.8624	0.53
12A-bt034	852.29	2.03	8.1034	0.53
12A-bt035	560.35	2.03	5.1673	0.53
12A-bt036	655.39	2.03	6.5705	0.53
12A-bt037	606.23	2.03	6.2202	0.53
12A-bt038	344.39	2.03	3.6483	0.53
12A-bt039.1	910.17	2.03	9.1915	0.53
12A-bt039.2	877.42	2.03	8.2988	0.53

12A-m01	0.07130	1.55	0.75279	0.53
12A-m02	0.04259	1.55	0.74041	0.53
12A-m03	0.04359	1.55	0.74231	0.53
12A-m04	0.04476	1.55	0.74686	0.53
12A-m05	0.04678	1.55	0.74336	0.53
12A-m06	0.05137	1.55	0.74259	0.53
12A-m07	0.04125	1.55	0.74727	0.53
12A-bt average	**1014.0506**		**9.8797**	
12A-mn average	**0.04881**			
12A-ms01	32.25	1.55	1.0423	0.53
12A-ms02.1	30.26	1.55	1.0222	0.53
12A-ms02.2	29.81	1.55	1.0355	0.53
12A-ms03	32.10	1.55	1.0440	0.53
12A-ms04	30.10	1.55	1.0208	0.53
12A-ms05.1	31.45	1.55	1.0384	0.53
12A-ms05.2	33.62	1.55	1.0842	0.53
12A-ms06	31.90	1.55	1.0581	0.53
12A-ms07.1	30.54	1.55	1.0183	0.53
12A-ms07.2	32.58	1.55	1.0440	0.53
12A-ms08	29.09	1.55	1.0127	0.53
12A-ms09.1	31.52	1.55	1.0294	0.53
12A-ms09.2	32.47	1.55	1.0436	0.53
12A-ms09.3	34.41	1.55	1.0735	0.53
12A-ms10.1	31.73	1.55	1.0230	0.53
12A-ms10.2	31.58	1.55	1.0420	0.53
12A-m01	0.07130	1.55	0.75279	0.53
12A-m02	0.04259	1.55	0.74041	0.53
12A-m03	0.04359	1.55	0.74231	0.53
12A-m04	0.04476	1.55	0.74686	0.53
12A-m05	0.04678	1.55	0.74336	0.53
12A-m06	0.05137	1.55	0.74259	0.53
12A-m07	0.04125	1.55	0.74727	0.53
12A-ms average	**31.5886**		**1.0395**	
12A-mn average	**0.0488**			

*1σ is in percentage

APPENDIX C – SUPPLEMNETARY MATERIAL OF CHAPTER 5

Supplementary Material 1

Methods

1. Electron backscatter diffraction (EBSD)

Electron backscatter diffraction analyses were performed to collected crystallographic preferred orientation of recrystallized quartz in order to identify the dominant deformation mechanisms during mylonite development. During petrographic description, representative areas of deformational microstructures in the thin section were selected for the analysis. For EBSD analyses, a final polishing stage was done in the polished thin sections using a colloidal silica solution in order to remove surface damage. After that, they were carbon coated. EBSD analyses were performed in a JEOL 7001 FE SEM with an EBSD detector (AZTec acquisition software, Oxford Instruments) at Plymouth Electron Microscopy Centre (PEMC), United Kingdom. The setup used a 70º tilt in the microscope chamber to the horizontal position, voltage of 20 kV, probe current of 12 nA and working distance of 20 mm. The step size ranged from 0.8 to 1.5 μm, and was chosen according to subgrain and recrystallized grain size allowing a maximum population of grains to be measured.

Raw EBSD data were processed using HKL Channel 5 software (Oxford Instruments), with a noise reduction being applied in all maps. Subsets with one-point-per-grain were generated to plot the pole figures of the following crystallographic directions and planes: <001> (c axes); {100} (m, prism planes); ⟨110⟩ (a axes); {101} (r rhomb planes); and {011'} (z rhomb planes). Pole figures are oriented with the X parallel to the stretching lineation, and the Z parallel to the pole to the foliation. Pole figures and misorientation axis distribution in crystal coordinates are presented in the lower hemisphere stereographic projections and contoured with a half width of 15° using multiple uniform distribution technique. Misorientation data are displayed as misorientation angle distribution histograms, showing the relative frequency of misorientation angles.

2. Isochemical phase equilibria modeling

Isochemical phase diagrams were constructed for bulk compositions using the Perple_X 6.7.7 (Connolly, 2005) and the internally consistent thermodynamic database of (Holland

and Powell, 2011) (hp11ver.dat in Perple_X) (hp11ver.dat, tc-ds61in Perple_X). The minerals involved in pseudosection construction include mica, staurolite, biotite, chlorite, garnet, ilmenite, feldspar, cordierite and epidote. The following solution models were used: Mica(W), St(W), Bi(W), Chl(W), Gt(W) and Crd(W) (White et al., 2014), Ilm (WPH), feldspar (Fuhrman and Lindsley, 1988), and Ep (HP11). The H_2O was considered as a saturated component and the low content of P_2O_5 and MnO were neglected. The calculations were undertaken in the NCKFMASHTO chemical model system (Na_2O-CaO-K_20-FeO-MgO-Al_2O_3-SiO_2-H_2O-TiO_2-O_2), using the measured bulk rock composition. The bulk rock compositions were determined by X-ray fluorescence analysis using a PANalytical AXIOS MAX Advanced X-ray fluorescence (XRF) spectrometer at the University of São Paulo (Brazil). Fe^{3+} was considered in each modelled bulk composition due to the presence of Fe^{3+} minerals. To constrain Fe^{3+} contents, we used a T-X_{O2} diagram with X_{O2} range of 0-0.15 wt. % for sample DC-33C and 0-0.4 wt. % for sample DC-41B, coupled with epidote and ilmenite mode isopleths. The chemical compositions of minerals were determined with a JEOL JXA-FE-8530 EMPA (electron microprobe analyser) at the University of São Paulo (Brazil). The operating conditions were 15.0 kV accelerating voltage, and a 20 nA beam current with a beam diameter of 5µm.

3. Trace element analysis and U–Pb geochronology

In order to constrain the elements mobility and timing of deformation of the CSZ, apatite and zircon grains were analyzed for trace element compositions and U–Pb isotopic ages. Apatite grains from five samples were analyzed: samples DC37B and DC41B were measured in situ in thin section and samples DC39A, DC46D, DC76B were measured in mount. Zircon grains from four samples (DC41D, DC46D, DC59A, DC76B) were analyzed in mount for U–Pb geochronology and trace element composition. For the mounts, apatite and zircon grains were separated using standard mineral separation techniques, including heavy liquids, and mounted in rounded epoxy mounts and polished. For the apatite and zircon in mounts cathodoluminescence (CL) images were obtained using a Philips FEI XL30 scanning electron microscope equipped with a Gatan CL detector at the Earth-Sciences Electron Microscopy and in-situ X-ray Microanalysis at the University of Melbourne, Australia. For the apatite analysed in situ in thin section,the backscattered electron (BSE) and CL images were acquired using a FEI-QUANTA 250 FEG scanning electron microscope equipped with a Centaurus Mono CL3+ spectroscope

of the Research Center for Geochronology and Isotopic Geochemistry (CPGeo) at the University of São Paulo, Brazil. BSE and CL images of selected apatite and zircon from CSZ mylonites are outlined in Supplementary Information 3.

U–Pb isotopes and trace element analyses were carried out using a laser ablation split-stream inductively coupled plasma mass spectrometer (LASS-ICP-MS) at the Monash Isotopia Facility, School of Earth, Atmosphere and Environment, Monash University, Australia. The experiments used an ASI-RESOlution ArF 193 nm excimer laser ablation system coupled to a Thermo Scientific iCAP-Q Quadruple ICP-MS for trace elements and a Thermo Scientific iCAP-TQ Triple-Quadruple ICP-MS for U–Pb isotopes. The laser operating conditions for apatite and zircon U–Pb and REE data are described in Table 1. For zircon U–Pb analyses we employed Plesovice zircon (337 ± 0.4 Ma, Sláma et al., 2008) as primary standard and Temora 1 (417 ± 0.2 Ma, Black et al., 2003) and GJ-1 zircons (601 Ma, Jackson et al., 2004) as secondary standards. For apatite U–Pb analyses, we used MADel monazite as primary standard (516 Ma, Payne et al., 2008) and 44069 monazite (425 ± 0.4 Ma, Aleinikoff et al., 2006) and Madagascar apatite (485 Ma, Thomson et al., 2012) as secondary standards. For both trace element minerals analyses, the NIST 610 glass was used as primary standard, with NIST 612, BCR2, ATHO and BHVO used as secondary standards. During all sessions, standards were interspersed with unknowns. Data reduction was performed in the Iolite 3 software package (Paton et al., 2011), using the U_Pb_Geochron4 and Trace_Elements data reduction schemes. ^{42}Ca and ^{14}Si were used as internal calibration for apatite and zircon, respectively.

For both minerals, U–Pb ages were calculated using the IsoplotR program (version 3.7) (Vermeesch, 2018). For the apatite grains, the ^{204}Pb non-corrected radiogenic isotopes ratios were plotted in the Tera-Wasserburg Concordia diagrams and the ages calculated from the lower intercept of discordia model-1. For the zircon grains, all data was plotted in the Wetherill Concordia diagrams. Ages and respective uncertainties are stated as 2 σ (95 % confidence). Isotopic data are presented in Supplementary Information 4.

Table 1. Laser operation conditions for apatite and zircon U–Pb and REE.

	Zircon	Apatite
Energy	4 mJ	6 mJ
Frequency	8 Hz	
Atenuator	50%	25%
Ablation time	20 sec (background) + 30 sec (ablation) + 15 sec cleaning	
Spot size	25 µm	30 µm

Supplementary Material 2

Table 2. X-ray fluorescence bulk rock composition (wt%).

	DC-33C	DC-41B
SiO_2	73.04	67.66
TiO_2	0.18	0.56
Al_2O_3	14.35	13.67
FeO	1.38	3.9
MgO	0.33	2.31
CaO	0.96	0.99
Na_2O	3.65	1.39
K_2O	4.82	6.24
Total	98.71	96.72

Table 3.1. Biotite compositions (EMPA) in mass%. Cations are calculated based on 11 oxygens.

Sample	DC-33B			Sample	DC-41B									
Mineral	bt1	bt2	bt aver.	Mineral	bt1	bt2	bt3	bt4	bt5	bt6	bt7	bt8	bt9	bt aver.
SiO_2	37.10	36.84	36.97	SiO_2	37.64	39.47	37.45	37.61	37.44	35.61	37.58	37.53	37.10	37.49
Al_2O_3	17.34	17.46	17.40	Al_2O_3	16.95	17.21	16.54	17.26	17.26	16.26	16.93	16.94	16.43	16.86
FeO	20.72	20.36	20.54	FeO	17.00	17.14	17.92	17.34	17.57	17.39	16.77	16.44	17.48	17.23
MnO	0.39	0.40	0.40	MnO	0.35	0.36	0.35	0.36	0.31	0.33	0.33	0.35	0.38	0.35
ZnO	0.06	0.08	0.07	ZnO	0.08	0.05	0.02	0.05	0.09	0.01	0.06	0.07	0.05	0.05
Cl	0.02	0.00	0.01	Cl	0.00	0.00	0.02	0.02	0.00	0.00	0.02	0.01	0.02	0.01
K_2O	9.29	9.44	9.37	K_2O	8.53	8.15	9.37	8.87	8.57	9.07	9.00	9.10	9.54	8.91
CaO	0.10	0.06	0.08	CaO	0.12	0.11	0.06	0.11	0.12	0.03	0.08	0.12	0.00	0.08
TiO_2	1.17	0.98	1.08	TiO_2	0.81	0.95	1.04	0.84	0.85	0.94	0.98	0.96	1.03	0.93
BaO	0.08	0.01	0.05	BaO	0.02	0.07	0.12	0.02	0.05	0.02	0.09	0.00	0.01	0.04
F	0.38	0.38	0.38	F	0.66	0.63	0.59	0.66	0.53	0.64	0.61	0.67	0.65	0.63
Na_2O	0.08	0.08	0.08	Na_2O	0.04	0.05	0.06	0.14	0.06	0.08	0.06	0.06	0.06	0.07
MgO	8.02	8.43	8.23	MgO	11.11	10.69	11.60	11.29	11.13	11.64	11.22	11.34	11.52	11.28
Total	94.75	94.53	94.64	Total	93.30	94.88	95.13	94.57	93.97	92.02	93.73	93.58	94.26	93.94
O=F	0.34	0.34	0.34	O=F	0.58	0.56	0.52	0.59	0.47	0.57	0.54	0.59	0.58	0.56
O=Cl	0.00	0.00	0.00	O=Cl	0.00	0.00	0.01	0.01	0.00	0.00	0.00	0.00	0.00	0.00
Total	94.41	94.19	94.30	Total	92.72	94.32	94.61	93.97	93.50	91.45	93.19	92.98	93.68	93.38
Si	2.85	2.84	2.85	Si	2.87	2.94	2.83	2.84	2.84	2.79	2.86	2.86	2.83	2.85
Al total	1.57	1.59	1.58	Al total	1.52	1.51	1.47	1.54	1.55	1.50	1.52	1.52	1.48	1.51
Al iv	1.15	1.16	1.15	Al iv	1.13	1.06	1.17	1.16	1.16	1.21	1.14	1.14	1.17	1.15
Al vi	0.42	0.42	0.42	Al vi	0.39	0.45	0.31	0.38	0.39	0.29	0.38	0.38	0.31	0.36
Fe^{2+}	1.33	1.31	1.32	Fe^{2+}	1.08	1.07	1.13	1.10	1.12	1.14	1.07	1.05	1.12	1.10
Mn	0.03	0.03	0.03	Mn	0.02	0.02	0.02	0.02	0.02	0.02	0.02	0.02	0.02	0.02
Zn	0.00	0.00	0.00	Zn	0.00	0.00	0.00	0.00	0.00	0.00	0.00	0.00	0.00	0.00
Cl	0.00	0.00	0.00	Cl	0.00	0.00	0.00	0.00	0.00	0.00	0.00	0.00	0.00	0.00
K	0.91	0.93	0.92	K	0.83	0.77	0.90	0.85	0.83	0.91	0.87	0.88	0.93	0.87
Ca	0.01	0.01	0.01	Ca	0.01	0.01	0.00	0.01	0.01	0.00	0.01	0.01	0.00	0.01
Ti	0.07	0.06	0.06	Ti	0.05	0.05	0.06	0.05	0.05	0.06	0.06	0.05	0.06	0.05

Ba	0.00	0.00	0.00	Ba	0.00	0.00	0.00	0.00	0.00	0.00	0.00	0.00	0.00	0.00
F	0.09	0.09	0.09	F	0.16	0.15	0.14	0.16	0.13	0.16	0.15	0.16	0.16	0.15
Na	0.01	0.01	0.01	Na	0.01	0.01	0.01	0.02	0.01	0.01	0.01	0.01	0.01	0.01
Mg	0.92	0.97	0.94	Mg	1.26	1.19	1.31	1.27	1.26	1.36	1.27	1.29	1.31	1.28
Total	9.37	9.41	9.39	Total	9.34	9.23	9.37	9.40	9.36	9.45	9.36	9.38	9.40	9.36
X_{Fe}	0.59	0.58	0.58	X_{Fe}	0.46	0.47	0.46	0.46	0.47	0.46	0.46	0.45	0.46	0.46
X_{Mg}	0.41	0.42	0.42	X_{Mg}	0.54	0.53	0.54	0.54	0.53	0.54	0.54	0.55	0.54	0.54

$X_{Fe} = Fe^{2+}/(Fe^{2+} + Mg)$

Table 3.2. Muscovite compositions (EMPA) in mass%. Cations are calculated based on 11 oxygens.

Sample	DC-33B				DC-41B							
Mineral	ms1	ms2	ms3	ms aver.	ms1	ms2	ms3	ms4	ms5	ms6	ms7	ms aver.
SiO_2	52.17	49.05	51.34	50.85	49.67	48.75	47.36	47.73	47.9	47.52	47.39	48.05
Al_2O_3	29.15	31.77	29.59	30.17	30.45	30.35	30.34	30.9	30.99	30.5	30.78	30.62
FeO	2.3	3.52	2.64	2.82	2.93	3.04	3.77	2.88	3.01	3.26	2.8	3.10
MnO	0.015	0.08	0.033	0.04	0.025	0.042	0.031	0.04	0.057	0.052	0.085	0.05
ZnO	0.005	0	0.024	0.01	0	0.006	0.009	0	0.039	0.008	0	0.01
Cl	0.011	0.008	0	0.01	0.011	0	0.011	0.006	0	0.018	0	0.01
K_2O	6.58	8.87	8.7	8.05	10.54	10.66	10.63	10.78	10.81	10.46	10.81	10.67
CaO	0.143	0.089	0.15	0.13	0.02	0.019	0.02	0.026	0.028	0.032	0	0.02
TiO_2	0.026	0.075	0.187	0.10	0.199	0.085	0.329	0.195	0.152	0.137	0.165	0.18
BaO	0.093	0.066	0.107	0.09	0.304	0.203	0.295	0.293	0.255	0.288	0.259	0.27
F	0.113	0.119	0.089	0.11	0.127	0.109	0.188	0.101	0.183	0.118	0.159	0.14
Na_2O	2.81	0.557	1.95	1.77	0.168	0.265	0.137	0.146	0.131	0.133	0.147	0.16
MgO	1.112	1.77	1.528	1.47	2.15	2.4	2.73	2.22	2.41	2.36	2.33	2.37
Total	94.529	95.973	96.338	95.61	96.595	95.928	95.849	95.316	95.965	94.886	94.925	95.64
O=F	0.100	0.106	0.079	0.10	0.113	0.097	0.167	0.090	0.163	0.105	0.141	0.13
O=Cl	0.002	0.002	0.000	0.00	0.002	0.000	0.002	0.001	0.000	0.004	0.000	0.00
Total	94.426	95.865	96.259	95.52	96.480	95.831	95.679	95.225	95.802	94.777	94.784	95.51
Si	3.440	3.240	3.370	3.35	3.284	3.255	3.187	3.212	3.204	3.215	3.204	3.22
Al total	2.265	2.473	2.289	2.34	2.373	2.388	2.406	2.451	2.443	2.432	2.452	2.42
Al iv	0.560	0.760	0.630	0.65	0.716	0.745	0.813	0.788	0.796	0.785	0.796	0.78
Al vi	1.706	1.713	1.659	1.69	1.656	1.642	1.593	1.663	1.647	1.646	1.656	1.64
Fe^{2+}	0.127	0.194	0.145	0.16	0.162	0.170	0.212	0.162	0.168	0.184	0.158	0.17
Mn	0.001	0.004	0.002	0.00	0.001	0.002	0.002	0.002	0.003	0.003	0.005	0.00
Zn	0.000	0.000	0.001	0.00	0.000	0.000	0.000	0.000	0.002	0.000	0.000	0.00
Cl	0.001	0.001	0.000	0.00	0.001	0.000	0.001	0.001	0.000	0.002	0.000	0.00
K	0.554	0.747	0.728	0.68	0.889	0.908	0.912	0.925	0.922	0.903	0.932	0.91
Ca	0.010	0.006	0.011	0.01	0.001	0.001	0.001	0.002	0.002	0.002	0.000	0.00

Ti	0.001	0.004	0.009	0.00	0.010	0.004	0.017	0.010	0.008	0.007	0.008	0.01
Ba	0.002	0.002	0.003	0.00	0.008	0.005	0.008	0.008	0.007	0.008	0.007	0.01
F	0.024	0.025	0.018	0.02	0.027	0.023	0.040	0.021	0.039	0.025	0.034	0.03
Na	0.359	0.071	0.248	0.23	0.022	0.034	0.018	0.019	0.017	0.017	0.019	0.02
Mg	0.109	0.174	0.150	0.14	0.212	0.239	0.274	0.223	0.240	0.238	0.235	0.24
Total	9.160	9.415	9.263	9.28	9.362	9.418	9.485	9.487	9.499	9.468	9.507	9.46

Table 3.3. K-feldspar compositions (EMPA) in mass%. Cations are calculated based on 8 oxygens.

Sample	DC-33B																		
Mineral	kf1	kf2	kf3	kf4	kf5	kf6	kf7	kfr1	kfr2	kfr3	kfr4	kfr5	kfr6	kfr7	kfr8	kfr9	kfr10	kfr11	kfr12
SiO_2	65.05	65.09	65.07	64.95	64.83	65.20	65.41	65.02	65.16	64.79	65.03	64.83	65.23	65.30	65.44	65.11	65.25	64.78	65.5
Al_2O_3	18.89	18.88	18.95	18.95	18.81	18.82	18.82	18.99	18.80	18.96	18.72	18.77	18.87	18.90	18.87	18.71	18.71	18.76	18.7
Fe_2O_3	0.00	0.04	0.05	0.03	0.02	0.02	0.01	0.02	0.01	0.02	0.02	0.00	0.04	0.01	0.00	0.02	0.02	0.01	0.01
MnO	0.00	0.00	0.00	0.01	0.00	0.02	0.01	0.00	0.00	0.00	0.01	0.00	0.00	0.00	0.01	0.02	0.02	0.00	0.01
K_2O	16.09	15.74	15.89	15.82	15.62	16.08	16.10	15.66	15.90	15.69	16.15	15.49	15.96	16.05	15.89	16.18	16.26	16.30	16.1
CaO	0.02	0.01	0.00	0.00	0.01	0.00	0.00	0.00	0.00	0.03	0.02	0.04	0.00	0.00	0.00	0.00	0.00	0.02	0.01
SrO	0.04	0.05	0.05	0.04	0.03	0.04	0.10	0.07	0.04	0.12	0.06	0.06	0.06	0.01	0.04	0.00	0.05	0.05	0.06
TiO_2	0.00	0.04	0.09	0.00	0.00	0.02	0.00	0.02	0.02	0.00	0.01	0.03	0.00	0.06	0.03	0.03	0.06	0.01	0.03
BaO	0.21	0.07	0.18	0.09	0.25	0.13	0.09	0.29	0.11	0.55	0.03	0.27	0.25	0.12	0.11	0.01	0.02	0.17	0.10
Na_2O	0.29	0.35	0.36	0.32	0.42	0.26	0.32	0.43	0.34	0.34	0.25	0.38	0.40	0.38	0.37	0.34	0.28	0.30	0.30
MgO	0.00	0.00	0.00	0.01	0.03	0.01	0.00	0.01	0.00	0.00	0.00	0.00	0.00	0.01	0.00	0.00	0.00	0.00	0.01
Total	101	100	101	100	100	101	101	101	100	101	100	100	101	101	101	100	101	100	101
Si	2.99	2.99	2.98	2.99	2.99	2.99	2.99	2.99	2.99	2.98	2.99	2.99	2.99	2.99	2.99	2.99	2.99	2.99	3.00
Al	1.02	1.02	1.02	1.03	1.02	1.02	1.02	1.03	1.02	1.03	1.02	1.02	1.02	1.02	1.02	1.01	1.01	1.02	1.01
Fe_{2+}	0.00	0.00	0.00	0.00	0.00	0.00	0.00	0.00	0.00	0.00	0.00	0.00	0.00	0.00	0.00	0.00	0.00	0.00	0.00
Mn	0.00	0.00	0.00	0.00	0.00	0.00	0.00	0.00	0.00	0.00	0.00	0.00	0.00	0.00	0.00	0.00	0.00	0.00	0.00
K	0.94	0.92	0.93	0.93	0.92	0.94	0.94	0.92	0.93	0.92	0.95	0.91	0.93	0.94	0.93	0.95	0.95	0.96	0.94
Ca	0.00	0.00	0.00	0.00	0.00	0.00	0.00	0.00	0.00	0.00	0.00	0.00	0.00	0.00	0.00	0.00	0.00	0.00	0.00
Sr	0.00	0.00	0.00	0.00	0.00	0.00	0.00	0.00	0.00	0.00	0.00	0.00	0.00	0.00	0.00	0.00	0.00	0.00	0.00
Ti	0.00	0.00	0.00	0.00	0.00	0.00	0.00	0.00	0.00	0.00	0.00	0.00	0.00	0.00	0.00	0.00	0.00	0.00	0.00
Ba	0.00	0.00	0.00	0.00	0.00	0.00	0.00	0.01	0.00	0.01	0.00	0.00	0.00	0.00	0.00	0.00	0.00	0.00	0.00
Na	0.03	0.03	0.03	0.03	0.04	0.02	0.03	0.04	0.03	0.03	0.02	0.03	0.04	0.03	0.03	0.03	0.03	0.03	0.03
Mg	0.00	0.00	0.00	0.00	0.00	0.00	0.00	0.00	0.00	0.00	0.00	0.00	0.00	0.00	0.00	0.00	0.00	0.00	0.00
Total	4.99	4.97	4.98	4.98	4.98	4.98	4.98	4.98	4.98	4.98	4.98	4.97	4.98	4.98	4.98	4.99	4.99	5.00	4.98
X_{An}	0.00	0.00	0.00	0.00	0.00	0.00	0.00	0.00	0.00	0.00	0.00	0.00	0.00	0.00	0.00	0.00	0.00	0.00	0.00
X_{ab}	0.03	0.03	0.03	0.03	0.04	0.02	0.03	0.04	0.03	0.03	0.02	0.04	0.04	0.03	0.03	0.03	0.03	0.03	0.03
X_{Or}	0.97	0.97	0.97	0.97	0.96	0.98	0.97	0.96	0.97	0.97	0.98	0.96	0.96	0.97	0.97	0.97	0.97	0.97	0.97

Sample	DC-41B						
Mineral	kf1	kf2	kf3	kf4.1	kf4.2	kf5	kf6
SiO2	64.65	65.03	64.56	64.78	64.52	64.98	64.82
Al2O3	18.97	18.97	19.07	19.03	19.11	18.95	19.09
Fe2O3	0.05	0.03	0.00	0.00	0.04	0.01	0.02
MnO	0.01	0.00	0.01	0.01	0.01	0.00	0.02
K2O	15.84	15.42	15.39	15.35	15.47	15.66	15.51
CaO	0.00	0.00	0.05	0.00	0.00	0.00	0.00
SrO	0.09	0.10	0.12	0.07	0.06	0.10	0.05
TiO2	0.00	0.00	0.00	0.00	0.02	0.00	0.05
BaO	0.51	0.44	0.87	0.66	0.60	0.48	0.53
Na2O	0.43	0.63	0.50	0.59	0.47	0.48	0.55
MgO	0.01	0.00	0.01	0.00	0.01	0.00	0.00
Total	101	101	101	100	100	101	101
Si	2.98	2.98	2.97	2.98	2.97	2.98	2.98
Al	1.03	1.03	1.04	1.03	1.04	1.03	1.03
Fe2+	0.00	0.00	0.00	0.00	0.00	0.00	0.00
Mn	0.00	0.00	0.00	0.00	0.00	0.00	0.00
K	0.93	0.90	0.90	0.90	0.91	0.92	0.91
Ca	0.00	0.00	0.00	0.00	0.00	0.00	0.00
Sr	0.00	0.00	0.00	0.00	0.00	0.00	0.00
Ti	0.00	0.00	0.00	0.00	0.00	0.00	0.00
Ba	0.01	0.01	0.02	0.01	0.01	0.01	0.01
Na	0.04	0.06	0.04	0.05	0.04	0.04	0.05
Mg	0.00	0.00	0.00	0.00	0.00	0.00	0.00
Total	4.99	4.98	4.98	4.98	4.98	4.98	4.98
XAn	0.00	0.00	0.00	0.00	0.00	0.00	0.00
Xab	0.04	0.06	0.05	0.06	0.04	0.04	0.05
XOr	0.96	0.94	0.95	0.94	0.96	0.96	0.95

X_{An} = Ca/(Ca + Na + K); X_{Ab} = Na/(Ca + Na + K); X_{Or} = K/(Ca + Na + K)

Supplementary Material 3

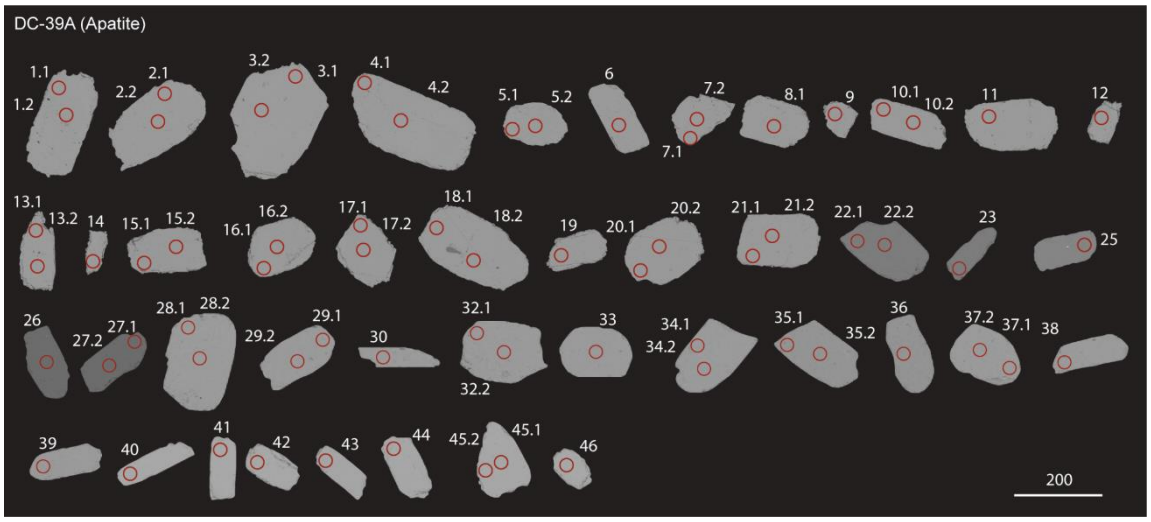

Figure 1. Cathodoluminescence images of apatite grains from samples DC-39A. Red circles show the position of analytic spots.

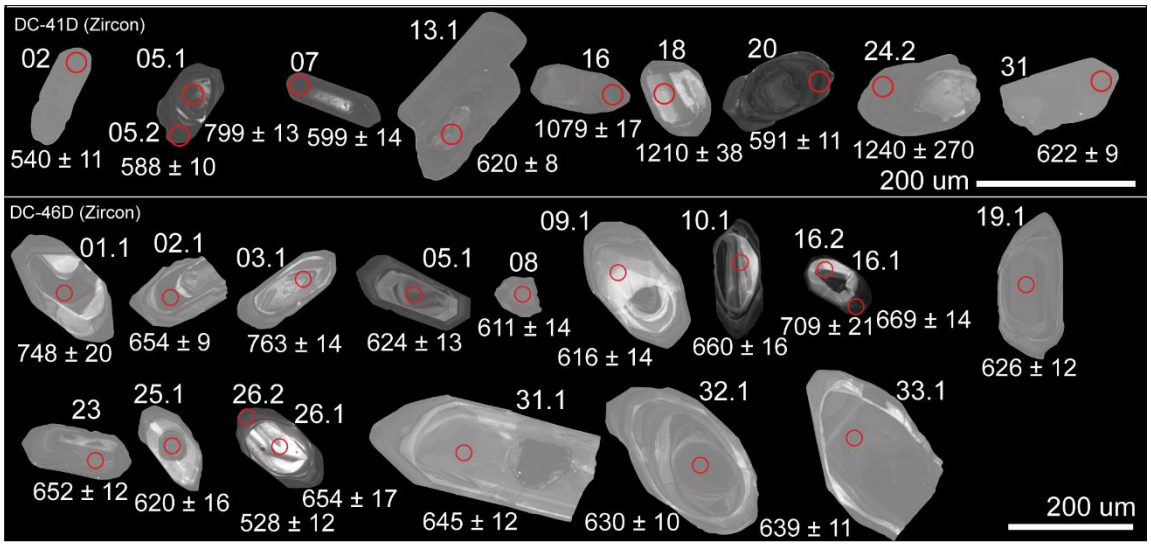

Figure 2. Cathodoluminescence images of selected zircon grains from samples DC-41D and DC-46D. Red circles show the position of analytic spots with their identification numbers and ages in Ma, respectively. Reported ages are $^{206}Pb/^{238}U$ and $^{207}Pb/^{206}Pb$ ages for zircon domains younger and older than 1000 Ma, respectively.

Table 4. Apatite analytical LA-ICP-MS U-Pb results from Cubatão Shear Zone mylonites.

Sample	Spot	Isotopic ratios										Ages (Ma)*					
		$^{207}Pb/^{235}Pb$	2σ	$^{206}Pb/^{238}U$	2σ	Err Corr	$^{238}U/^{206}Pb$	2σ	$^{207}Pb/^{206}Pb$	2σ	Err Corr	$^{207}Pb/^{235}U$	2σ	$^{206}Pb/^{238}U$	2σ	$^{207}Pb/^{206}Pb$	2σ
DC-37B	1	4.14	0.68	0.123	0.00	0.26	8.137	0.28	0.251	0.04	0.30	1660	140	746	25	3144	230
	2	5.12	0.91	0.127	0.01	0.48	7.899	0.44	0.295	0.05	0.12	1802	140	767	40	3370	240
	3	5.00	0.83	0.133	0.01	0.56	7.547	0.32	0.269	0.04	0.12	1802	150	801	32	3298	250
	4	5.69	0.93	0.134	0.01	0.36	7.440	0.35	0.313	0.05	0.47	1911	140	811	36	3481	230
	6.1	5.50	0.90	0.131	0.00	0.18	7.663	0.28	0.307	0.05	0.38	1878	150	790	27	3447	250
	6.2	12.14	2.10	0.180	0.01	0.30	5.556	0.34	0.493	0.08	0.46	2592	160	1075	67	4140	260
	7	4.81	0.78	0.124	0.00	0.23	8.091	0.32	0.281	0.04	0.48	1772	140	750	28	3332	250
	8	5.65	0.91	0.133	0.01	0.25	7.496	0.34	0.310	0.05	0.50	1915	140	805	34	3489	240
	9	7.66	1.20	0.151	0.01	0.30	6.609	0.31	0.370	0.06	0.52	2170	150	906	39	3748	250
	10.1	8.73	1.40	0.162	0.01	0.35	6.165	0.29	0.396	0.06	0.37	2284	160	966	42	3852	220
	10.2	3.90	0.63	0.118	0.00	0.08	8.511	0.30	0.242	0.04	0.44	1596	130	715	24	3065	250
	11	26.20	4.70	0.341	0.03	0.69	2.933	0.26	0.597	0.10	0.42	3323	190	1860	140	4440	270
	12	20.60	3.50	0.255	0.02	0.69	3.922	0.25	0.589	0.09	0.25	3090	170	1470	85	4446	240
	13.1	16.90	2.90	0.234	0.02	0.72	4.274	0.27	0.546	0.09	0.30	2894	180	1344	77	4280	260
	13.2	3.75	0.60	0.117	0.00	0.11	8.518	0.30	0.234	0.04	0.54	1568	130	715	24	3022	250
	14	5.56	0.91	0.134	0.01	0.31	7.491	0.30	0.302	0.05	0.36	1883	140	807	31	3413	250
	16	5.16	0.85	0.129	0.01	0.41	7.734	0.31	0.289	0.04	0.35	1827	140	782	30	3363	240
	17.1	11.98	2.00	0.187	0.01	0.53	5.350	0.27	0.479	0.08	0.35	2566	160	1109	53	4090	240
	17.2	3.65	0.59	0.117	0.00	0.42	8.584	0.33	0.227	0.03	0.31	1551	130	710	26	2999	240
	18.1	6.40	1.10	0.146	0.01	0.47	6.873	0.43	0.322	0.05	0.40	2019	150	873	50	3529	230
	18.2	10.75	1.70	0.178	0.01	0.36	5.612	0.28	0.454	0.07	0.56	2498	170	1053	49	4044	240
	19	4.48	0.73	0.125	0.00	0.24	7.981	0.29	0.260	0.04	0.30	1705	130	760	27	3182	250
	20	5.58	0.92	0.136	0.01	0.39	7.331	0.32	0.297	0.05	0.34	1890	140	823	33	3401	250
	21	145.00	26.00	1.320	0.12	0.97	0.758	0.07	0.796	0.12	0.10	4973	190	5230	330	4953	260

	22	8.31	1.40	0.151	0.01	0.60	6.627	0.34	0.392	0.06	0.34	2240	150	903	43	3830	250
	23	11.43	1.90	0.184	0.01	0.31	5.444	0.28	0.456	0.07	0.41	2521	160	1091	54	4020	250
	25.1	10.25	1.70	0.172	0.01	0.51	5.817	0.27	0.432	0.07	0.33	2422	150	1020	45	3970	250
	25.2	6.28	1.00	0.137	0.01	0.21	7.294	0.32	0.334	0.05	0.55	1994	140	826	34	3566	260
	26	11.06	1.80	0.175	0.01	0.37	5.721	0.28	0.457	0.07	0.45	2494	160	1036	47	4046	240
	30	8.34	1.50	0.159	0.01	0.18	6.301	0.32	0.376	0.06	0.42	2229	160	947	44	3750	260
	31	27.60	5.00	0.317	0.03	0.79	3.155	0.33	0.663	0.11	0.46	3364	180	1750	150	4620	270
	32	30.60	5.90	0.332	0.06	0.01	3.012	0.52	0.730	0.16	0.69	3470	210	1820	270	4730	430
	33	10.38	1.70	0.168	0.01	0.49	5.949	0.28	0.449	0.07	0.47	2460	160	999	43	4060	240
	34	35.30	5.80	0.374	0.02	0.73	2.674	0.14	0.677	0.10	0.14	3612	170	2037	92	4676	240
	35	32.20	6.40	0.322	0.03	0.91	3.106	0.29	0.700	0.11	0.18	3450	180	1770	140	4720	260
	36	82.00	20.00	0.690	0.11	0.59	1.449	0.23	0.870	0.18	0.41	4440	230	3350	410	5110	410
	37	6.81	1.10	0.149	0.01	0.36	6.725	0.33	0.337	0.05	0.40	2045	160	891	41	3570	270
	38	5.38	0.87	0.129	0.01	0.23	7.776	0.34	0.302	0.05	0.49	1867	140	783	33	3443	240
	39	7.38	1.20	0.142	0.01	0.15	7.067	0.34	0.380	0.06	0.57	2125	150	851	38	3750	250
	40	9.63	1.60	0.168	0.01	0.33	5.956	0.28	0.408	0.06	0.58	2376	150	1011	47	3910	250
	41	11.05	1.80	0.176	0.01	0.39	5.685	0.28	0.461	0.07	0.34	2503	160	1041	47	4058	240
	44	20.90	3.90	0.273	0.02	0.50	3.663	0.30	0.577	0.10	0.37	3081	180	1540	110	4370	300
	49	4.18	0.68	0.119	0.00	0.29	8.425	0.32	0.256	0.04	0.37	1651	140	722	26	3176	250
	50	3.12	0.51	0.112	0.00	0.39	8.969	0.33	0.202	0.03	0.16	1432	140	681	24	2800	270
	1.1	4.08	0.65	0.126	0.00	0.51	7.924	0.27	0.227	0.03	0.17	1635	130	765	25	3011	250
	1.2	5.49	0.89	0.140	0.00	0.35	7.163	0.25	0.276	0.04	0.21	1867	140	841	28	3278	240
	2.1	5.70	0.90	0.142	0.00	0.33	7.067	0.22	0.285	0.04	0.44	1919	140	855	26	3364	230
DC-39A	2.2	7.92	1.20	0.159	0.01	0.25	6.281	0.22	0.355	0.05	0.50	2213	150	951	32	3700	230
	3.1	6.55	1.00	0.151	0.00	0.19	6.636	0.21	0.305	0.05	0.51	2042	140	904	26	3475	230
	3.2	8.19	1.30	0.166	0.01	0.58	6.035	0.20	0.339	0.05	0.03	2228	150	987	30	3618	230
	4.1	9.65	1.50	0.172	0.01	0.25	5.817	0.19	0.388	0.06	0.51	2387	150	1021	31	3840	230
	4.2	2.93	0.46	0.118	0.00	0.23	8.467	0.22	0.172	0.03	0.34	1385	120	719	18	2552	250
	5.1	2.70	0.42	0.116	0.00	0.05	8.628	0.22	0.162	0.02	0.46	1323	120	706	17	2442	260

5.2	8.54	1.40	0.167	0.01	0.31	5.995	0.22	0.358	0.05	0.50	2276	150	992	33	3713	230
6	6.95	1.10	0.154	0.01	0.35	6.494	0.22	0.319	0.05	0.51	2098	140	922	29	3533	230
7.1	13.18	2.10	0.208	0.01	0.25	4.803	0.18	0.449	0.07	0.59	2674	150	1216	42	4042	220
7.2	6.47	1.00	0.148	0.00	0.28	6.780	0.22	0.310	0.05	0.41	2044	150	886	27	3490	230
8.1	10.23	1.70	0.182	0.01	0.5	5.498	0.28	0.399	0.06	0.36	2431	160	1073	50	3861	230
8.2	5.97	1.00	0.141	0.01	0.37	7.117	0.31	0.289	0.05	0.31	1944	150	853	38	3370	260
9	6.14	0.98	0.141	0.00	0.38	7.117	0.23	0.305	0.05	0.33	1978	140	846	25	3466	240
10.1	7.01	1.20	0.155	0.01	0.64	6.468	0.30	0.317	0.05	0.11	2085	140	924	40	3501	240
11	7.34	1.20	0.155	0.01	0.35	6.460	0.24	0.335	0.05	0.47	2141	140	926	32	3618	240
13.1	6.37	1.10	0.151	0.01	0.37	6.609	0.31	0.295	0.05	0.51	2002	140	906	39	3392	240
13.2	5.28	0.83	0.136	0.00	0.23	7.364	0.23	0.277	0.04	0.47	1856	140	820	25	3311	240
15.1	12.61	2.10	0.214	0.01	0.39	4.673	0.28	0.431	0.07	0.53	2624	160	1241	67	3940	250
15.2	6.34	1.00	0.144	0.01	0.42	6.969	0.26	0.308	0.05	0.32	1996	140	863	30	3467	240
16.1	4.65	0.82	0.134	0.01	0.79	7.452	0.33	0.245	0.04	0.34	1737	140	810	33	3117	250
16.2	3.20	0.51	0.117	0.00	0.37	8.576	0.22	0.197	0.03	0.06	1440	120	710	18	2761	250
17.1	11.30	2.10	0.190	0.01	0.88	5.263	0.33	0.397	0.06	0.43	2412	170	1132	68	3814	250
17.2	11.69	1.90	0.202	0.01	0.38	4.958	0.18	0.423	0.06	0.31	2551	150	1182	39	3969	230
18.1	4.95	0.78	0.133	0.00	0.36	7.502	0.24	0.271	0.04	0.38	1798	130	805	24	3283	240
18.2	5.27	0.83	0.137	0.00	0.24	7.321	0.23	0.283	0.04	0.45	1859	130	824	24	3354	240
20.1	7.31	1.20	0.159	0.01	0.14	6.285	0.25	0.340	0.05	0.53	2126	150	949	35	3623	250
20.2	16.84	2.70	0.234	0.01	0.39	4.268	0.18	0.533	0.08	0.57	2907	160	1358	52	4306	240
21.1	8.10	1.30	0.164	0.01	0.33	6.083	0.23	0.360	0.06	0.30	2215	140	979	34	3705	220
21.2	14.83	2.40	0.217	0.01	0.44	4.617	0.19	0.509	0.08	0.48	2792	160	1266	49	4236	230
22.2	4.46	0.71	0.127	0.00	0.06	7.905	0.24	0.260	0.04	0.47	1716	130	767	22	3216	230
23	2.40	0.39	0.111	0.00	0.14	9.025	0.28	0.159	0.03	0.29	1237	120	677	20	2410	270
24	12.08	1.90	0.198	0.01	0.57	5.043	0.21	0.451	0.07	0.27	2588	160	1168	46	4054	230
25	8.11	1.30	0.170	0.01	0.26	5.875	0.22	0.356	0.05	0.53	2229	140	1011	36	3688	230
26	3.25	0.51	0.120	0.00	0.28	8.333	0.24	0.200	0.03	0.39	1463	120	730	20	2802	250
27.1	4.69	0.74	0.134	0.00	0.35	7.468	0.23	0.261	0.04	0.35	1757	140	811	24	3218	240
27.2	4.74	0.74	0.136	0.00	0.34	7.380	0.23	0.261	0.04	0.49	1769	130	818	24	3223	230

	28.1	4.38	0.69	0.129	0.00	0.32	7.734	0.23	0.252	0.04	0.39	1701	140	783	22	3165	240
	28.2	5.65	0.90	0.137	0.00	0.14	7.278	0.25	0.308	0.05	0.53	1907	140	829	27	3456	240
	29.1	6.00	0.95	0.141	0.01	0.3	7.107	0.26	0.316	0.05	0.58	1962	130	847	29	3525	250
	29.2	15.67	2.50	0.231	0.01	0.49	4.331	0.19	0.508	0.08	0.47	2835	150	1333	54	4221	220
	30	17.46	2.80	0.239	0.01	0.37	4.181	0.17	0.544	0.08	0.57	2946	160	1383	56	4341	250
	31	4.60	0.84	0.131	0.01	0.74	7.616	0.35	0.245	0.04	0.48	1684	150	794	34	3060	250
	32.1	6.26	0.98	0.142	0.00	0.25	7.057	0.23	0.330	0.05	0.47	2005	140	853	26	3581	230
	32.2	14.18	2.30	0.224	0.01	0.47	4.470	0.18	0.467	0.07	0.46	2741	150	1297	47	4121	240
	33	6.64	1.10	0.143	0.01	0.22	6.974	0.26	0.348	0.05	0.48	2049	150	862	30	3651	230
	34.1	7.09	1.10	0.149	0.00	0.23	6.711	0.22	0.350	0.05	0.56	2109	140	894	28	3673	230
	34.2	7.13	1.10	0.158	0.01	0.33	6.337	0.22	0.337	0.05	0.43	2118	140	943	30	3626	230
	35.1	6.55	1.00	0.151	0.01	0.38	6.623	0.24	0.319	0.05	0.41	2039	140	905	30	3534	230
	35.2	10.59	1.70	0.186	0.01	0.35	5.371	0.20	0.422	0.06	0.43	2472	150	1099	38	3950	230
	36	4.40	0.74	0.131	0.00	0.53	7.634	0.26	0.240	0.04	0.03	1661	140	792	25	3038	260
	37.1	14.72	2.40	0.225	0.01	0.62	4.444	0.20	0.488	0.07	0.23	2775	170	1302	54	4170	230
	37.2	16.94	2.70	0.245	0.01	0.33	4.087	0.17	0.518	0.08	0.54	2925	160	1406	51	4258	230
	38	3.48	0.56	0.123	0.00	0.57	8.137	0.25	0.206	0.03	0.03	1509	120	749	23	2839	250
	39	6.52	1.00	0.148	0.01	0.25	6.770	0.23	0.327	0.05	0.50	2034	140	887	29	3569	230
	40	17.94	2.90	0.258	0.01	0.66	3.876	0.20	0.512	0.08	0.26	2945	160	1471	67	4264	230
	41	2.59	0.41	0.115	0.00	0.2	8.688	0.24	0.165	0.02	0.45	1295	110	702	18	2478	250
	42	3.12	0.49	0.121	0.00	0.13	8.285	0.22	0.189	0.03	0.33	1427	120	735	18	2693	260
	43	10.18	1.60	0.185	0.01	0.41	5.411	0.19	0.407	0.06	0.33	2438	160	1091	35	3901	230
	44	2.91	0.46	0.118	0.00	0.33	8.503	0.23	0.182	0.03	0.33	1381	120	716	19	2635	240
	45.1	10.87	1.70	0.187	0.01	0.5	5.350	0.21	0.438	0.07	0.65	2495	150	1102	40	3991	250
	45.2	17.30	3.00	0.251	0.02	0.8	3.984	0.29	0.499	0.08	0.15	2882	170	1428	88	4200	230
DC-41B	1	84.00	31.00	0.850	0.25	0.97	1.176	0.35	0.650	0.12	0.82	3970	470	3520	770	4550	340
	2	47.70	12.00	0.526	0.10	0.86	1.901	0.35	0.655	0.12	0.14	3880	240	2650	400	4590	320
	4	37.60	6.70	0.395	0.04	0.84	2.532	0.24	0.709	0.12	0.15	3684	190	2130	170	4750	280
	5	3.60	0.59	0.116	0.01	0.08	8.651	0.37	0.227	0.04	0.53	1539	130	704	29	2990	240

7	98.00	26.00	0.900	0.18	0.97	1.111	0.22	0.725	0.11	0.45	4280	300	3800	560	4800	260
8	19.40	3.60	0.265	0.03	0.4	3.774	0.40	0.572	0.11	0.69	3013	180	1500	140	4340	300
9	5.80	1.90	0.136	0.02	0.95	7.353	0.87	0.292	0.06	0.75	1820	200	813	87	3260	260
10	67.80	12.00	0.617	0.05	0.8	1.621	0.13	0.798	0.12	0.23	4253	190	3060	200	4956	270
11	22.90	4.70	0.242	0.02	0.5	4.132	0.38	0.633	0.11	0.39	3180	180	1390	110	4560	280
12	42.00	12.00	0.443	0.09	0.95	2.257	0.46	0.614	0.10	0.34	3400	290	2210	370	4470	290
13	12.90	2.40	0.205	0.01	0.41	4.878	0.33	0.454	0.08	0.23	2647	170	1202	72	4060	250
14	22.20	4.70	0.226	0.02	0.66	4.425	0.35	0.720	0.20	0.32	3100	180	1306	96	4750	450
15	16.50	4.20	0.214	0.03	0.9	4.673	0.61	0.504	0.09	0.24	2690	220	1230	140	4170	280
17	23.40	6.60	0.305	0.05	0.97	3.279	0.57	0.480	0.08	0.66	2830	260	1620	240	4030	270
18	5.31	0.89	0.133	0.01	0.39	7.502	0.38	0.299	0.05	0.13	1862	170	806	38	3480	220
19	8.13	1.40	0.150	0.01	0.23	6.689	0.40	0.411	0.07	0.54	2240	160	895	50	3890	250
20.1	5.92	1.20	0.139	0.01	0.76	7.215	0.47	0.308	0.05	0.23	1910	160	834	51	3410	260
21	4.97	1.10	0.135	0.01	0.85	7.418	0.47	0.248	0.04	0.64	1700	160	812	48	3070	270
22	5.32	1.10	0.137	0.01	0.87	7.315	0.42	0.270	0.05	0.63	1820	170	824	44	3240	290
23	10.91	1.90	0.162	0.01	0.36	6.158	0.38	0.480	0.08	0.39	2479	160	967	55	4140	260
24	2.47	0.40	0.110	0.00	0.27	9.074	0.29	0.160	0.02	0.19	1254	120	674	20	2430	290
25.1	5.55	1.10	0.145	0.01	0.81	6.887	0.42	0.267	0.04	0.45	1860	160	871	49	3190	240
25.2	10.85	1.80	0.177	0.01	0.58	5.643	0.32	0.434	0.07	0.49	2479	160	1047	56	4006	240
26	10.94	1.90	0.178	0.01	0.25	5.618	0.41	0.463	0.08	0.53	2495	170	1050	70	4040	260
27	19.20	3.40	0.244	0.02	0.72	4.098	0.32	0.587	0.10	0.39	3024	180	1395	97	4410	260
28.1	9.80	3.40	0.167	0.02	0.98	5.988	0.86	0.339	0.07	0.84	2130	260	980	130	3480	320
28.2	3.44	0.57	0.120	0.00	0.32	8.306	0.33	0.201	0.03	0.30	1499	130	732	27	2806	270
29	5.79	0.98	0.153	0.01	0.55	6.557	0.38	0.276	0.04	0.21	1932	150	912	48	3291	260
30	6.44	1.10	0.145	0.01	0.2	6.897	0.36	0.321	0.05	0.55	2036	150	870	43	3544	240
31	10.50	2.10	0.167	0.01	0.86	5.988	0.47	0.454	0.07	0.08	2391	150	987	72	4000	250
32.1	3.90	0.86	0.122	0.01	0.97	8.170	0.42	0.217	0.04	0.84	1520	160	743	36	2800	280
32.2	11.95	2.00	0.191	0.02	0.51	5.236	0.41	0.455	0.07	0.60	2578	180	1119	82	4040	230
33	5.85	1.20	0.147	0.01	0.18	6.803	0.60	0.288	0.05	0.46	1880	160	879	69	3320	250
34	4.17	0.68	0.125	0.01	0.26	8.032	0.36	0.238	0.04	0.58	1652	140	755	32	3061	260

	35	2.20	0.35	0.108	0.00	0.08	9.225	0.26	0.143	0.02	0.36	1178	110	663	18	2225	270
	36	2.15	0.35	0.106	0.00	0.31	9.443	0.30	0.142	0.02	0.23	1154	110	649	20	2214	270
	37	1.92	0.31	0.102	0.00	0.05	9.766	0.28	0.132	0.02	0.38	1081	110	628	17	2079	270
	38	7.73	1.30	0.164	0.01	0.03	6.098	0.36	0.337	0.06	0.69	2190	150	976	53	3570	240
	39	9.60	2.20	0.174	0.02	0.79	5.747	0.66	0.383	0.07	0.01	2350	190	1030	110	3800	250
	40	12.36	2.10	0.192	0.01	0.27	5.208	0.33	0.476	0.08	0.55	2609	170	1125	64	4110	250
	41	11.11	1.90	0.177	0.01	0.26	5.647	0.32	0.451	0.07	0.52	2502	160	1048	56	4020	250
	42	14.60	3.60	0.210	0.03	0.85	4.762	0.66	0.477	0.08	0.06	2690	210	1210	140	4080	270
	43	5.43	0.89	0.133	0.01	0.2	7.530	0.32	0.293	0.05	0.46	1895	170	803	33	3410	250
	44	20.00	3.70	0.261	0.02	0.47	3.831	0.34	0.566	0.10	0.37	3060	190	1490	110	4350	280
	45	5.30	1.40	0.132	0.01	0.9	7.576	0.63	0.264	0.05	0.58	1750	200	796	62	3100	300
	1	22.80	3.70	0.286	0.02	0.51	3.497	0.21	0.612	0.10	0.59	3190	170	1604	86	4494	240
	2.1	7.68	1.30	0.163	0.01	0.63	6.127	0.26	0.344	0.05	0.09	2155	150	972	37	3615	230
	2.2	15.27	2.50	0.221	0.01	0.5	4.523	0.20	0.512	0.08	0.09	2799	150	1296	56	4213	230
	3.1	11.56	1.90	0.184	0.01	0.18	5.450	0.29	0.465	0.07	0.57	2548	160	1083	53	4100	260
	3.2	12.13	2.00	0.200	0.01	0.38	5.000	0.21	0.450	0.07	0.46	2581	150	1172	44	4029	240
	4.1	16.60	2.80	0.227	0.02	0.39	4.405	0.29	0.551	0.09	0.37	2873	180	1307	77	4330	270
	4.2	23.80	4.10	0.295	0.02	0.45	3.390	0.24	0.602	0.10	0.51	3197	150	1663	100	4450	250
	5.1	7.86	1.30	0.163	0.01	0.24	6.143	0.25	0.357	0.05	0.23	2178	150	970	36	3681	230
	5.2	6.89	1.10	0.153	0.01	0.38	6.519	0.27	0.332	0.05	0.45	2083	140	918	35	3603	250
	6.1	4.38	0.70	0.130	0.00	0.22	7.716	0.24	0.247	0.04	0.42	1695	130	785	23	3131	250
	6.2	12.90	2.10	0.211	0.01	0.42	4.748	0.22	0.463	0.07	0.46	2651	160	1233	53	4070	220
	7.1	7.40	1.20	0.154	0.01	0.29	6.494	0.24	0.353	0.05	0.51	2145	140	922	31	3694	230
	7.2	6.84	1.10	0.152	0.01	0.58	6.592	0.28	0.337	0.05	0.16	2066	150	908	36	3582	230
	8.1	38.50	7.00	0.410	0.03	0.7	2.439	0.20	0.681	0.11	0.23	3693	180	2200	150	4690	250
	8.2	28.30	4.70	0.331	0.02	0.42	3.021	0.16	0.643	0.10	0.42	3389	160	1828	83	4566	250
	9	25.20	4.30	0.293	0.02	0.58	3.413	0.22	0.649	0.10	0.29	3248	170	1641	93	4570	260
	10	10.37	1.70	0.187	0.01	0.76	5.359	0.25	0.422	0.06	0.07	2450	150	1098	47	3939	220
	11.1	4.24	0.70	0.133	0.00	0.6	7.524	0.26	0.235	0.04	0.11	1654	120	806	27	3036	230
DC-46D																	

11.2	3.64	0.58	0.121	0.00	0.19	8.237	0.26	0.222	0.03	0.48	1546	120	738	22	2956	250
12	22.70	3.80	0.297	0.02	0.36	3.367	0.19	0.577	0.09	0.45	3187	180	1677	89	4380	250
13	8.49	1.40	0.166	0.01	0.63	6.013	0.28	0.369	0.06	0.13	2231	150	988	42	3724	240
14	13.51	2.20	0.220	0.01	0.4	4.545	0.23	0.464	0.07	0.34	2686	160	1274	58	4090	230
15.1	12.21	2.00	0.199	0.01	0.49	5.020	0.23	0.455	0.07	0.32	2589	150	1166	49	4060	240
15.2	10.08	1.70	0.184	0.01	0.56	5.426	0.29	0.399	0.06	0.15	2367	180	1085	52	3812	250
16.1	3.97	0.63	0.127	0.00	0.28	7.893	0.28	0.237	0.04	0.41	1631	130	768	26	3054	240
16.2	5.87	0.97	0.140	0.01	0.49	7.123	0.30	0.310	0.05	0.17	1932	150	845	33	3489	250
17	12.39	2.00	0.199	0.01	0.5	5.023	0.22	0.468	0.07	0.45	2622	150	1166	46	4100	220
18	6.14	1.00	0.147	0.01	0.43	6.821	0.29	0.306	0.05	0.22	1952	140	880	34	3421	240
19.1	4.26	0.69	0.127	0.00	0.25	7.862	0.25	0.248	0.04	0.29	1673	140	774	24	3125	240
19.2	9.99	1.70	0.183	0.01	0.49	5.470	0.25	0.415	0.06	0.25	2406	160	1079	44	3918	230
20	9.77	1.70	0.186	0.01	0.48	5.368	0.28	0.392	0.06	0.19	2384	160	1097	52	3817	250
21	3.73	0.60	0.126	0.00	0.28	7.918	0.27	0.223	0.03	0.31	1572	130	765	24	2943	250
22	5.75	0.97	0.142	0.01	0.52	7.022	0.30	0.292	0.05	0.08	1874	160	860	35	3320	250
23	22.10	3.70	0.293	0.02	0.54	3.413	0.20	0.574	0.09	0.36	3153	170	1638	85	4384	240
24	16.15	2.60	0.236	0.01	0.23	4.237	0.20	0.521	0.08	0.56	2852	160	1358	58	4246	230
25	8.10	1.30	0.161	0.01	0.41	6.231	0.29	0.382	0.06	0.41	2225	150	956	41	3801	240
26.1	12.53	2.10	0.209	0.01	0.86	4.794	0.21	0.446	0.07	0.16	2607	150	1224	51	4027	230
26.2	5.05	0.82	0.135	0.00	0.48	7.424	0.26	0.280	0.04	0.19	1811	140	813	27	3313	230
27	9.66	1.50	0.173	0.01	0.29	5.787	0.23	0.422	0.06	0.55	2397	150	1025	37	3948	230
28	6.39	1.00	0.151	0.01	0.24	6.614	0.28	0.321	0.05	0.43	1999	150	905	36	3484	250
29.1	10.45	1.70	0.181	0.01	0.54	5.519	0.23	0.428	0.06	0.26	2450	150	1070	41	3962	240
29.2	10.61	1.70	0.179	0.01	0.51	5.587	0.24	0.429	0.07	0.16	2445	160	1063	43	3964	230
30	12.90	2.10	0.202	0.01	0.47	4.958	0.25	0.490	0.08	0.41	2634	160	1178	56	4128	240
31.1	4.26	0.69	0.127	0.00	0.36	7.849	0.25	0.248	0.04	0.16	1660	130	772	23	3104	230
31.2	3.83	0.61	0.123	0.00	0.5	8.123	0.24	0.232	0.04	0.59	1585	130	748	21	3034	240
32	8.17	1.30	0.167	0.01	0.45	5.977	0.24	0.367	0.06	0.37	2229	150	994	37	3735	220
33	5.26	0.85	0.135	0.00	0.29	7.424	0.27	0.293	0.04	0.38	1852	140	813	27	3386	240
34	6.30	1.00	0.147	0.01	0.42	6.784	0.26	0.321	0.05	0.35	2010	140	888	33	3532	230

	35.1	4.92	0.78	0.137	0.00	0.22	7.289	0.24	0.269	0.04	0.44	1792	140	828	25	3244	240
	35.2	19.30	3.30	0.256	0.02	0.66	3.906	0.23	0.562	0.09	0.23	3002	160	1456	75	4361	230
	36	30.80	5.30	0.375	0.03	0.51	2.667	0.18	0.633	0.10	0.45	3461	170	2030	120	4530	260
	37	6.68	1.10	0.149	0.01	0.34	6.711	0.25	0.326	0.05	0.42	2048	140	894	31	3555	240
	38	4.54	0.73	0.130	0.00	0.3	7.710	0.27	0.254	0.04	0.37	1720	130	785	26	3149	240
	39	5.44	0.86	0.138	0.00	0.2	7.231	0.22	0.284	0.04	0.41	1876	140	834	24	3352	240
	40	16.17	2.60	0.241	0.01	0.4	4.149	0.19	0.492	0.07	0.48	2862	160	1390	61	4181	240
	41.1	12.82	2.10	0.207	0.01	0.48	4.831	0.28	0.462	0.07	0.49	2624	160	1204	64	4059	250
	41.2	17.96	2.90	0.256	0.01	0.39	3.906	0.21	0.519	0.08	0.51	2962	160	1460	69	4262	250
	42.1	9.90	1.90	0.177	0.01	0.82	5.650	0.38	0.369	0.06	0.27	2294	160	1060	67	3690	250
	42.2	29.30	5.00	0.333	0.03	0.59	3.003	0.23	0.635	0.10	0.47	3415	170	1830	110	4560	270
	43	4.12	0.66	0.129	0.00	0.27	7.740	0.25	0.229	0.03	0.38	1641	130	783	24	2987	240
	44	15.61	2.50	0.227	0.01	0.36	4.405	0.23	0.503	0.08	0.56	2823	160	1311	61	4211	250
	45	5.36	0.89	0.145	0.01	0.33	6.916	0.29	0.264	0.04	0.31	1838	140	868	34	3185	260
	46	15.09	2.50	0.227	0.01	0.44	4.405	0.23	0.481	0.07	0.36	2798	160	1311	62	4129	240
	47	8.17	1.30	0.159	0.01	0.51	6.274	0.25	0.367	0.05	0.34	2232	150	951	36	3745	230
	48	8.25	1.30	0.166	0.01	0.51	6.020	0.24	0.350	0.05	0.46	2234	150	988	37	3669	230
	49	14.60	2.60	0.209	0.01	0.45	4.785	0.27	0.492	0.08	0.03	2693	190	1229	65	4110	260
	2.1	42.10	7.60	0.511	0.07	0.56	1.957	0.26	0.642	0.11	0.46	3250	200	2230	220	3980	310
	2.2	69.00	16.00	0.660	0.11	0.8	1.515	0.25	0.761	0.13	0.32	3621	180	2000	130	4800	290
	4.1	24.80	4.20	0.333	0.02	0.52	3.003	0.17	0.543	0.08	0.98	4240	210	2600	740	5610	1000
	4.2	60.30	10.00	0.564	0.04	0.83	1.773	0.12	0.783	0.12	0.67	3090	240	1970	240	3960	440
	6.1	43.00	7.10	0.429	0.02	0.59	2.331	0.13	0.759	0.12	0.03	4090	210	2800	220	4870	350
	6.2	72.00	24.00	0.690	0.19	0.92	1.449	0.40	0.766	0.13	0.04	4050	280	2870	270	4730	400
	7	14.59	2.40	0.257	0.01	0.7	3.891	0.18	0.433	0.07	0.51	3804	170	2290	110	4856	270
	8.1	48.00	8.30	0.560	0.04	0.72	1.786	0.11	0.629	0.10	0.46	3655	180	2410	180	4500	270
	8.2	45.80	8.30	0.503	0.06	0.5	1.988	0.25	0.750	0.18	0.05	4120	220	2790	240	4910	340
	9	35.60	5.90	0.394	0.03	0.55	2.538	0.16	0.672	0.10	0.56	3220	280	2300	380	3840	460

DC-76B

10.2	64.90	14.00	0.510	0.16	0.67	1.961	0.62	1.090	0.46	0.57	4064	180	2800	230	4890	300
12	72.00	22.00	0.530	0.15	0.23	1.887	0.53	1.040	0.36	0.50	4330	200	3370	350	4990	290
13.2	28.90	4.80	0.314	0.02	0.55	3.185	0.18	0.670	0.11	0.81	2690	620	1980	720	3290	490
14.1	31.00	5.10	0.371	0.03	0.43	2.695	0.19	0.626	0.10	0.29	4007	150	2770	150	4781	260
14.2	54.30	9.50	0.541	0.04	0.87	1.848	0.13	0.727	0.11	0.46	3622	170	2063	96	4663	250
15.1	37.30	6.70	0.459	0.04	0.6	2.179	0.19	0.616	0.10	0.67	3490	160	2010	120	4528	240
15.2	25.20	5.10	0.420	0.05	0.39	2.381	0.28	0.452	0.09	0.31	2763	150	1469	60	3974	230
18.1	54.00	10.00	0.500	0.05	0.54	2.000	0.20	0.780	0.14	0.23	2710	190	1870	160	3450	310
19.1	15.00	10.00	0.360	0.16	0.98	2.778	1.23	0.272	0.08	0.71	3797	190	2630	290	4570	300
19.2	23.40	5.80	0.431	0.08	0.07	2.320	0.45	0.400	0.12	0.09	4109	190	2860	160	4921	270
20.1	32.50	6.50	0.440	0.07	0.22	2.273	0.35	0.610	0.15	0.50	3427	170	1769	95	4670	270
20.2	23.90	4.20	0.372	0.03	0.51	2.688	0.20	0.478	0.08	0.14	3889	170	2860	150	4544	250
21.2	50.50	8.30	0.484	0.03	0.57	2.066	0.12	0.749	0.11	0.57	3180	160	1826	79	4186	230
22.1	36.10	6.00	0.381	0.02	0.51	2.625	0.14	0.666	0.10	0.53	4010	200	2590	210	4910	320
22.2	37.20	6.10	0.400	0.02	0.59	2.500	0.15	0.686	0.11	0.68	3580	230	2320	300	4440	370
24.1	69.00	27.00	0.565	0.06	0.94	1.770	0.18	0.850	0.27	0.51	3646	170	2120	140	4730	270
24.2	48.70	8.00	0.630	0.19	0.5	1.587	0.48	0.590	0.22	0.53	4330	290	2720	610	5500	820
26	22.41	3.60	0.327	0.02	0.45	3.058	0.15	0.496	0.08	0.66	3920	210	2600	270	4830	410
27.1	59.50	13.00	0.546	0.06	0.66	1.832	0.19	0.778	0.15	0.39	4046	180	2860	210	4810	280
27.2	59.00	13.00	0.550	0.06	0.57	1.818	0.18	0.770	0.15	0.02	4166	160	2980	140	4830	250
28	37.00	6.60	0.369	0.03	0.63	2.710	0.21	0.740	0.12	0.46	3659	170	2140	110	4678	260
29.1	56.00	14.00	0.563	0.06	0.56	1.776	0.20	0.710	0.15	0.52	3963	170	2510	120	4831	270
31.1	62.10	10.00	0.593	0.04	0.84	1.686	0.10	0.742	0.11	0.99	3965	160	3120	730	4440	550
31.2	18.37	2.90	0.254	0.01	0.4	3.937	0.19	0.531	0.08	0.50	3626	170	2140	120	4652	250
32	56.50	10.00	0.569	0.05	0.73	1.757	0.16	0.740	0.12	0.90	4260	430	2880	240	5080	600
33.1	14.70	3.00	0.340	0.03	0.39	2.941	0.29	0.316	0.06	0.79	4230	200	3160	370	4860	300
33.2	21.00	5.10	0.359	0.05	0.5	2.786	0.40	0.450	0.13	0.34	4300	290	3330	680	4890	310
35	16.10	2.70	0.368	0.02	0.34	2.717	0.13	0.321	0.05	0.42	3256	170	1840	94	4340	280

36	36.10	6.10	0.390	0.03	0.66	2.564	0.19	0.709	0.11	0.60	3215	180	2020	130	4080	250
37	73.80	14.00	0.714	0.10	0.48	1.401	0.19	0.799	0.14	0.28	2857	170	2014	79	3548	240
39	55.700	9.70	0.555	0.06	0.53	1.802	0.19	0.774	0.13	0.58	2992	160	1455	60	4287	230

Sample name + x.y: grain number followed by analysis number

* Not corrected for common Pb

2σ is an standard absolute value (STDEV/SQRT)

Table 5. Apatite analytical LA-ICP-MS REE (ppm) results from Cubatão Shear Zone mylonites.

Sample	Spot	La	Ce	Pr	Nd	Sm	Eu	Gd	Tb	Dy	Ho	Er	Tm	Yb	Lu
DC-37B	1	501	1653	263.8	1547	617	89	934	180	1197	247	647	83	480	57
	2	277	1127	210.0	1354	571	68	803	145	896	178	444	56	315	37
	3	340	1213	210.0	1345	552	68	768	133	824	159	391	49	271	32
	4	352	1307	235.0	1524	649	84	866	152	928	176	434	54	307	36
	6.1	490	1620	262.8	1561	627	90	930	176	1178	244	636	82	466	56
	6.2	315	1015	160.9	946	369	53	551	106	689	146	363	47	260	32
	7	445	1452	234.0	1397	562	81	846	159	1064	222	575	75	422	51
	8	439	1441	232.3	1399	564	81	832	156	1031	213	539	69	394	47
	9	171	756	149.8	1033	481	69	778	146	950	193	485	59	322	37
	10.1	343	1126	185.8	1116	445	64	659	124	821	171	437	56	313	38
	10.2	363	1330	229.3	1442	617	90	939	178	1179	240	611	78	436	52
	11	192	676	114.6	712	303	45	444	81	522	102	260	35	205	24
	12	212	779	137.1	858	349	49	518	90	560	110	265	31	171	20
	13.1	256	826	132.9	797	309	45	457	83	544	112	283	36	200	24
	13.2	559	1861	301.0	1797	719	103	1059	202	1340	278	720	93	544	65
	14	222	933	171.9	1157	516	69	742	133	823	155	371	45	238	27
	15	33	119	22.7	172	113	38	245	47	302	56	128	15	84	9
	16	411	1379	231.5	1421	615	81	903	166	1059	209	517	63	357	42
	17.1	220	743	126.0	759	302	43	436	80	520	107	277	35	193	23
	17.2	481	1649	279.0	1691	685	98	1007	192	1275	264	677	88	505	61
	18.1	357	1148	188.0	1143	463	70	680	128	843	172	436	55	309	37
	18.2	343	1084	173.1	1020	417	60	619	117	777	162	418	54	308	37
	19	440	1511	257.4	1602	662	94	970	179	1157	232	578	73	417	49
	20	371	1230	202.1	1225	511	86	781	148	977	192	471	59	334	40
	21	237	723	119.3	743	316	56	475	86	562	110	271	34	201	24
	22	297	1028	177.7	1096	454	72	645	114	715	139	332	43	241	29
	23	304	996	166.1	1001	408	60	596	108	702	140	350	44	244	29

24	27	43	4.2	18	3	1	2	0	2	0	1	0	1	0
25.1	304	1013	170.5	1053	445	64	677	123	805	162	410	51	287	33
25.2	356	1170	190.9	1174	488	71	744	141	912	189	484	62	348	41
26	357	1166	190.9	1159	492	72	738	136	890	180	450	57	318	38
30	282	1030	189.1	1257	619	85	928	168	1024	191	459	56	322	37
31	238	817	143.2	918	428	56	642	111	682	129	315	39	222	27
33	365	1354	249.9	1668	818	107	1167	208	1283	237	567	72	411	47
34	327	1124	207.6	1365	648	85	918	162	959	177	420	52	299	36
35	212	894	175.0	1185	576	73	820	144	851	158	378	46	261	30
36	91	422	89.5	660	329	44	445	71	397	67	146	17	93	11
37	143	669	134.4	944	443	71	694	129	842	168	420	53	289	35
38	342	1150	192.2	1176	501	74	762	145	958	199	507	66	382	47
39	145	594	116.9	792	395	68	630	118	737	146	354	44	241	28
40	256	972	172.6	1090	483	73	757	141	921	186	476	60	345	41
41	99	465	105.1	835	485	73	743	128	746	133	309	38	215	25
42	38	163	35.5	298	185	32	297	49	276	47	106	13	71	8
43	30	160	44.2	407	279	44	446	71	389	66	148	18	94	11
44	72	320	74.3	618	413	74	655	110	621	106	237	28	153	17
45	56	226	54.1	450	284	54	440	73	404	68	147	17	95	11
46	35	1650	7.0	17	0	2	5	1	3	1	3	0	3	0
47	50	0	26.0	200	73	14	109	21	141	27	70	10	50	5
48	104	0	81.7	570	273	51	398	66	375	66	147	16	88	10
49	384	1326	214.3	1346	573	83	860	156	1023	203	527	66	378	46
50	333	1180	215.0	1407	653	98	984	177	1141	226	566	70	404	49
51	30	136	0.0	0	0	1	0	0	2	0	2	0	2	0
1.1	252	788	130.5	788	281	29	354	56	367	81	239	37	257	36
1.2	272	806	127.5	737	240	23	283	45	286	63	184	28	197	28
2.1	229	679	108.7	638	241	26	332	57	385	89	262	39	265	38
2.2	293	794	121.4	677	228	22	302	50	337	77	227	34	239	34

DC-39A

3.1	249	849	134.9	767	291	29	369	64	401	81	218	31	213	30
4.1	194	551	85.4	493	172	21	227	37	243	55	165	26	186	27
4.2	547	1515	220.5	1171	361	39	431	69	439	98	287	45	323	47
5.1	358	1036	161.2	916	312	39	420	72	489	117	359	57	417	61
5.2	263	724	107.1	582	184	22	238	41	265	63	191	30	216	32
6	211	598	89.8	499	175	21	257	47	334	84	273	44	307	45
7.1	187	531	84.6	489	179	19	249	41	275	64	185	28	191	28
7.2	277	800	126.2	714	254	24	338	56	374	86	253	39	269	38
8.1	221	645	100.5	581	193	17	241	37	230	50	140	20	137	20
8.2	279	867	141.3	832	285	26	360	57	356	77	216	32	218	32
9	202	603	99.8	598	233	23	325	53	339	72	205	30	204	29
10.1	185	623	105.0	643	254	28	326	57	347	70	185	27	177	25
11	271	805	125.1	690	229	20	281	44	265	57	160	23	161	24
13.1	193	685	120.7	736	287	25	356	58	356	73	195	29	193	27
13.2	247	874	151.4	886	346	28	421	70	433	89	244	36	246	35
15.1	96	329	61.1	404	165	17	229	37	235	51	141	20	126	18
15.2	191	609	100.5	604	222	21	297	49	314	69	198	29	196	28
16.1	382	1214	189.0	1054	337	34	413	69	461	104	316	49	346	50
17.1	215	634	98.7	574	206	21	277	45	297	67	196	29	202	29
18.1	328	1000	154.8	854	283	27	347	55	348	76	217	33	226	33
18.2	377	1081	159.8	854	268	24	322	51	316	67	194	29	200	29
20.1	155	462	77.5	464	182	23	258	44	298	68	201	31	211	31
20.2	218	608	93.5	531	179	17	237	39	257	60	178	27	190	27
21.1	179	514	83.4	495	188	23	269	47	315	71	208	31	214	31
21.2	230	634	94.6	523	173	17	226	38	254	59	175	26	181	26
22.2	236	732	119.3	720	266	27	364	60	405	93	278	42	294	42
23	379	1172	187.1	1096	390	42	502	85	561	125	380	59	423	61
24	277	766	112.1	595	181	20	218	35	221	50	147	23	162	24
25	104	307	49.3	297	121	23	220	47	371	100	333	55	399	57
26	369	1094	175.0	1013	376	33	490	80	513	111	315	48	329	47

	27.1	259	877	146.0	834	320	32	409	71	446	92	252	37	249	36
	27.2	295	976	160.8	907	339	30	423	72	450	93	256	38	257	37
	28.1	302	904	143.3	800	288	28	390	65	429	98	288	43	298	43
	28.2	296	860	134.7	750	258	25	340	56	371	83	242	36	253	37
	29.1	258	801	128.6	751	270	25	340	54	335	72	204	30	209	30
	29.2	209	614	96.3	557	191	16	231	36	219	47	131	19	131	20
	30	205	567	85.3	479	158	17	199	31	200	45	134	21	146	21
	31	255	761	116.0	653	224	27	321	57	402	100	315	50	356	52
	32.1	273	800	123.5	702	241	24	303	48	307	67	192	29	199	29
	32.2	241	682	101.8	570	185	16	225	35	214	46	131	19	130	19
	33	228	666	102.9	584	190	19	256	44	311	75	221	33	222	31
	34.1	224	657	107.7	613	210	24	267	44	286	64	190	30	208	30
	34.2	336	958	141.5	757	245	25	291	47	302	67	198	31	223	32
	35.1	181	559	95.2	584	229	27	320	54	371	86	251	38	264	38
	35.2	266	748	112.9	653	221	20	292	47	318	75	227	34	240	35
	36	171	497	76.1	446	172	27	271	53	399	103	346	57	420	59
	37.1	228	662	101.4	579	189	20	223	35	223	49	143	22	158	23
	37.2	268	745	112.9	598	185	18	216	33	203	45	131	20	144	21
	38	366	1063	163.9	939	319	33	430	74	519	123	374	57	395	57
	39	219	669	112.0	687	270	22	357	57	351	74	202	29	195	28
	40	83	230	35.1	206	76	15	126	25	195	52	176	29	204	30
	41	449	1321	203.3	1136	382	39	488	79	513	116	348	55	402	58
	42	401	1146	175.3	967	351	35	463	78	504	111	319	48	328	48
	43	193	627	105.2	605	226	19	286	47	293	61	168	24	164	24
	44	423	1266	200.2	1154	409	43	548	97	704	169	508	76	516	75
	45.1	232	643	96.3	518	172	18	226	37	245	57	176	28	199	29
	45.2	211	564	83.7	463	152	17	202	33	217	51	155	24	173	25
DC-41B	1	31	86	16.3	131	78	9	118	22	139	26	69	9	47	6
	2	30	77	11.0	90	43	5	81	13	70	14	26	4	25	3

3	27	47	5.6	20	3	1	5	1	3	1	2	0	2	0
4	19	45	8.6	68	52	6	91	18	116	23	56	7	36	5
5	31	125	30.8	249	158	15	237	44	278	55	138	17	96	12
6	31	50	6.0	22	8	2	7	1	9	2	4	0	4	1
7	15	61	16.1	143	99	11	167	31	201	40	99	12	64	8
8	13	39	8.7	75	55	6	94	17	105	20	49	5	29	4
9	23	90	23.9	199	144	17	233	44	290	58	145	17	96	12
10	63	124	26.7	182	96	14	126	22	121	21	46	5	27	3
11	20	57	14.4	118	92	11	164	31	201	40	103	12	66	9
12	20	75	18.9	179	132	15	228	42	275	54	135	16	88	11
13	21	66	14.1	130	100	12	171	32	207	41	103	12	67	9
14	28	67	14.3	112	79	14	127	24	157	32	81	11	57	8
15	21	94	24.8	220	170	17	261	49	325	64	158	20	105	13
17	14	65	16.1	146	108	17	190	36	236	48	122	15	85	11
18	19	107	30.9	290	184	20	285	54	359	72	189	23	132	16
19	9	44	12.7	128	114	17	216	43	292	60	150	18	97	13
20.1	139	491	85.8	487	148	18	141	20	113	21	54	7	45	6
21	56	251	60.0	483	246	22	323	55	330	63	149	18	101	13
22	39	168	43.3	358	203	22	292	51	308	59	148	18	103	13
23	23	73	19.8	174	126	16	218	42	268	53	131	16	84	10
24	84	342	71.7	507	219	32	280	47	286	57	145	19	110	15
25.1	26	104	25.5	217	141	22	231	43	277	55	138	17	95	12
25.2	20	94	24.3	206	146	20	244	46	299	60	149	18	98	12
26	29	115	30.9	256	178	25	304	54	347	72	175	22	118	15
27	17	65	17.9	154	111	15	193	36	231	46	113	14	73	9
28.1	30	148	39.6	335	180	17	256	47	316	64	163	20	115	14
28.2	19	94	26.5	257	174	19	295	57	372	75	189	24	129	16
29	16	75	21.2	200	154	19	268	53	347	70	174	21	118	14
30	12	65	19.6	187	145	18	256	50	333	67	166	20	106	13
31	12	61	18.3	165	128	15	214	42	268	56	134	16	87	11

32.1	23	116	32.6	304	222	25	378	74	490	99	250	31	173	21
32.2	21	62	14.9	125	86	10	140	28	185	36	91	11	62	8
33	14	72	20.6	191	134	15	220	42	279	55	139	17	94	11
34	39	124	37.0	293	170	17	259	49	324	65	165	21	115	14
35	23	116	33.6	302	209	22	338	66	435	88	223	28	154	19
36	29	140	38.1	329	216	22	329	62	413	83	211	27	145	18
37	30	138	36.4	320	228	25	376	75	498	100	251	31	171	21
38	19	78	20.9	175	126	16	205	38	239	47	116	14	76	10
39	32	97	20.4	141	72	12	96	17	99	19	47	6	35	5
40	17	64	18.5	167	127	18	230	42	268	54	132	16	84	11
41	16	65	17.4	155	110	16	189	35	224	45	112	14	72	9
42	12	51	13.9	140	109	16	199	38	242	49	124	15	77	10
43	19	88	22.7	195	131	12	199	36	235	47	114	14	76	9
44	25	97	22.8	188	111	12	166	31	195	39	96	12	67	8
45	43	176	41.4	309	164	15	224	40	252	49	123	15	89	11
1	113	407	78.0	503	193	15	233	38	206	39	99	13	89	14
2.1	192	547	90.4	534	227	34	328	58	346	68	177	23	144	20
2.2	151	416	67.7	395	165	24	237	40	243	48	123	16	100	13
3.1	150	450	75.6	466	197	24	270	46	264	50	127	17	105	15
3.2	161	468	78.8	476	198	23	269	45	264	50	127	17	105	14
4.1	45	197	41.4	283	125	16	170	28	161	31	77	10	59	8
4.2	63	235	43.9	293	120	14	163	27	152	29	72	9	55	8
5.1	173	528	94.4	588	248	28	329	54	310	58	147	20	124	17
5.2	194	600	105.4	673	279	30	368	61	340	63	160	21	135	19
6.1	206	645	113.9	746	313	52	404	67	395	78	197	26	154	21
6.2	116	348	60.8	400	158	26	203	32	191	37	92	12	70	9
7.1	142	483	89.3	557	242	28	333	57	335	65	168	22	136	19
7.2	195	629	108.4	666	287	31	379	65	381	74	188	25	155	21
8.1	200	715	124.9	730	247	14	275	44	239	42	105	14	87	12

DC-46D

8.2	200	689	122.0	687	232	13	260	42	220	39	96	13	80	12
9	129	428	75.4	438	159	15	198	31	165	29	71	8	55	7
10	190	571	94.6	565	241	34	333	55	332	65	164	20	124	17
11.1	116	367	67.1	452	229	34	365	68	451	98	268	38	245	33
11.2	135	435	80.4	545	281	46	448	85	572	124	344	48	309	42
12	65	240	44.6	290	117	14	157	26	143	27	66	8	53	7
13	131	441	82.9	556	249	36	338	55	317	63	156	20	115	15
14	143	400	65.8	382	163	29	222	38	230	46	113	14	84	11
15.1	151	444	74.4	455	195	25	263	44	254	50	123	15	93	12
15.2	179	531	90.1	536	228	31	315	52	308	60	148	19	112	15
16.1	207	648	115.1	750	344	50	469	78	466	93	234	29	174	23
16.2	148	484	89.1	589	267	41	373	61	361	72	179	22	129	17
17	128	356	59.5	355	149	29	217	37	230	45	115	15	86	12
18	195	604	104.4	656	290	46	415	70	420	84	211	27	157	21
19.1	235	748	135.3	848	353	41	471	78	457	88	225	30	187	26
19.2	147	463	81.2	513	207	25	275	45	257	50	125	16	99	14
20	110	405	77.1	514	221	24	290	50	284	54	135	18	114	16
21	155	590	113.7	727	314	39	419	72	421	80	202	27	170	24
22	186	571	102.4	655	299	47	424	71	422	84	212	27	158	21
23	102	325	56.1	342	141	17	189	33	185	36	91	12	76	10
24	30	145	35.1	275	154	24	227	40	229	43	110	15	93	13
26.1	189	628	113.1	696	277	28	355	60	340	64	162	22	134	19
26.2	227	785	139.1	854	347	35	434	74	419	78	201	27	171	24
27	346	1184	204.4	1123	385	21	427	69	378	66	169	23	152	22
28	103	337	60.0	380	177	36	265	45	282	56	143	18	106	14
29.1	137	418	73.8	470	212	30	291	48	282	55	136	17	102	14
29.2	152	452	78.7	501	220	29	298	50	287	56	138	18	104	14
30	57	248	54.0	376	183	25	255	43	244	46	115	15	95	13
31.1	200	601	101.3	622	281	44	411	75	451	89	231	31	196	27
31.2	260	769	126.8	740	307	44	442	78	470	92	238	32	198	28

	32	104	339	57.8	350	149	26	222	41	261	56	153	21	140	20
	33	147	510	92.3	594	261	28	350	61	355	70	176	23	147	20
	34	192	624	109.3	651	283	35	387	68	403	78	200	26	167	23
	35.1	228	669	111.3	658	277	36	386	67	395	75	193	26	161	22
	35.2	119	349	57.9	350	148	20	209	35	205	39	99	13	79	11
	36	94	316	57.8	365	142	13	180	29	160	30	75	10	59	8
	37	200	583	96.8	601	258	34	367	63	369	73	189	25	155	21
	38	164	594	111.5	725	311	37	419	70	402	77	195	26	163	22
	39	170	573	104.2	646	281	33	392	68	409	80	207	28	174	24
	40	141	434	74.0	448	181	18	248	41	242	50	128	16	101	14
	41.1	95	358	69.5	456	188	19	241	39	221	41	102	14	85	12
	41.2	114	420	78.3	493	184	14	223	36	195	36	88	12	71	10
	42.1	136	487	91.5	582	234	24	300	50	276	51	128	17	108	15
	42.2	71	261	51.1	338	137	14	178	29	159	29	72	9	58	8
	43	222	697	120.4	750	325	41	454	78	451	87	219	29	185	26
	44	86	289	51.1	325	141	19	198	34	198	39	96	13	80	11
	45	57	196	37.8	273	144	21	230	42	279	59	164	23	144	20
	46	99	342	62.2	397	161	17	214	36	205	39	96	13	78	11
	47	150	453	77.5	491	208	35	275	45	265	53	133	17	103	13
	48	170	565	102.4	625	264	27	342	59	331	62	156	21	133	18
	49	57	249	49.6	350	158	16	205	34	193	36	89	12	71	10
	1	728	1544	190.3	856	151	43	137	18	107	22	66	9	59	8
	2.1	1169	2450	294.5	1290	212	58	176	20	102	19	45	6	32	4
	2.2	698	1522	192.0	889	164	49	165	23	140	31	94	14	86	11
DC-76B	3	1	3	0.6	5	2	1	8	2	23	8	33	6	43	7
	4.2	976	2120	269.0	1257	229	67	221	30	180	39	115	17	108	14
	5	129	275	42.3	221	51	20	60	7	56	12	30	4	32	4
	6.1	453	1013	130.5	618	116	34	120	16	98	22	64	9	59	7
	6.2	506	1152	147.4	685	129	37	124	16	94	20	54	8	49	6

7	1090	2302	287.2	1268	220	63	188	23	119	22	56	7	45	5
8.1	834	1818	226.5	1022	179	51	156	19	99	19	46	6	36	4
8.2	1011	2209	280.2	1224	212	58	178	21	104	18	42	5	29	4
9	572	1189	146.7	657	115	34	112	15	90	19	56	8	51	7
10.1	795	1711	213.0	944	164	45	138	16	84	16	39	5	29	4
10.2	947	2087	264.6	1192	208	57	176	21	106	20	48	6	34	4
11.1	15	29	4.5	27	8	2	11	2	13	4	11	1	6	1
12	701	1508	190.0	845	148	42	133	17	96	19	53	8	47	6
13.1	590	1240	152.0	692	114	33	102	12	66	13	34	4	28	3
13.2	1893	4240	539.0	2419	434	121	384	50	280	58	158	22	142	18
14.1	714	1511	187.5	828	144	41	131	17	96	20	56	8	49	6
14.2	1036	2290	288.2	1302	228	65	200	25	141	29	80	11	72	9
15.1	1069	2250	277.0	1205	208	57	176	21	111	21	55	7	44	6
15.2	1139	2350	285.0	1240	209	57	173	20	101	18	44	5	31	4
16.1	315	729	95.3	463	97	28	104	15	101	23	70	11	66	9
16.2	304	714	96.0	476	105	30	118	18	119	28	84	12	79	10
18.1	351	802	106.6	509	106	31	112	16	104	24	69	10	62	8
18.2	389	800	102.0	460	86	26	84	12	79	17	51	8	48	6
19.1	981	2080	254.6	1108	184	49	152	17	81	14	32	4	20	3
19.2	980	2079	253.4	1122	187	50	154	17	85	15	33	4	21	3
20.1	1087	2322	287.0	1275	216	60	184	22	110	21	51	7	39	5
20.2	1370	2929	360.8	1571	264	71	216	25	120	21	47	5	29	4
21.1	91	207	27.8	137	32	10	39	6	45	10	32	5	29	4
21.2	1785	3816	469.5	2076	357	85	314	40	229	47	130	18	117	15
22.1	841	1843	230.9	1067	193	54	175	23	134	28	78	11	71	9
22.2	1290	2806	348.9	1552	272	76	234	29	156	30	80	11	69	8
23	343	770	98.8	468	98	33	103	15	99	23	66	10	64	8
24.1	411	993	136.7	678	143	43	153	23	142	32	96	14	91	11

24.2	838	1864	238.8	1074	189	52	159	19	96	18	42	5	31	4
25	139	312	43.8	244	77	21	101	15	90	19	53	7	42	5
26	360	1480	265.2	1546	555	60	760	145	1055	248	714	101	629	86
27.1	1018	2110	253.0	1077	182	50	153	19	95	18	46	6	36	5
27.2	960	2028	247.2	1089	184	53	159	19	105	21	54	8	45	6
28	397	1038	143.0	704	157	34	166	25	162	39	118	18	115	15
29.1	526	1134	142.0	656	128	39	137	21	133	31	89	13	82	10
30.1	11	24	3.5	18	9	4	26	7	77	27	110	19	133	18
30.2	7	17	2.4	14	9	4	25	7	76	26	106	18	120	17
31.1	913	3110	486.0	2490	525	149	489	66	382	81	225	32	204	30
31.2	951	3188	486.0	2469	504	141	457	59	331	68	189	26	164	24
32	920	2002	243.7	1084	194	52	168	20	109	21	54	7	44	6
33.1	1150	2277	293.1	1274	209	56	173	19	93	16	36	4	24	3
33.2	1170	2222	298.0	1299	216	58	175	20	96	17	38	4	24	3
34	1007	2213	270.1	1188	207	56	182	22	121	24	62	8	52	7
35	175	915	185.2	1117	305	22	320	46	269	55	144	19	120	17
36	523	1156	146.1	671	129	37	133	18	116	26	77	12	76	10
37	602	1357	174.8	819	155	45	152	21	125	28	79	11	73	9
38	746	1627	204.9	915	162	45	141	17	90	18	46	6	39	5
39	677	1489	188.0	854	155	45	142	19	109	24	66	10	61	7
40.1	902	1840	220.0	973	164	47	146	18	96	20	51	7	43	5

Table 6. U-Pb zircon analytical results results from Cubatão Shear Zone mylonites.

Sample	Spot	Content (ppm)		Th/U	Isotopic ratios										Age (Ma)*						Con.
		U	Th		$^{207}Pb/^{235}Pb$	2σ	$^{206}Pb/^{238}U$	2σ	err corr	$^{238}U/^{206}Pb$	2σ	$^{207}Pb/^{206}Pb$	2σ	err corr	$^{207}Pb/^{235}U$	2σ	$^{206}Pb/^{238}U$	2σ	$^{207}Pb/^{206}Pb$	2σ	
DC-41D	2	426	92	0.22	0.7490	0.030	0.0872	0.0018	0.283	11.468	0.24	0.062	0.002	0.286	565	18	540	11	617	83	105%
DC-41D	5.1	488	332	0.68	1.1960	0.041	0.1320	0.0023	0.457	7.576	0.13	0.065	0.002	0.149	796	19	799	13	747	67	100%
DC-41D	5.2	690	61	0.09	0.8330	0.039	0.0955	0.0018	0.071	10.471	0.20	0.062	0.003	0.312	612	21	588	10	658	96	104%
DC-41D	31	1513	428	0.28	0.8470	0.024	0.1013	0.0015	0.329	9.874	0.15	0.060	0.002	0.353	623	13	622	9	614	54	100%
Hydrothermal zircons (LREE-I < 30)																					
DC-41D	3	952	104	0.11	0.9390	0.036	0.0991	0.0019	0.651	10.091	0.19	0.068	0.002	-0.137	672	19	609	11	861	66	110%
DC-41D	7	830	62	0.07	0.7810	0.039	0.0906	0.0024	0.197	11.038	0.29	0.062	0.003	0.366	583	22	559	14	670	100	104%
DC-41D	13.1	988	191	0.19	0.8690	0.027	0.1010	0.0014	0.221	9.899	0.14	0.062	0.002	0.200	634	15	620	8	651	63	102%
DC-41D	16	641	121	0.19	1.9540	0.061	0.1820	0.0032	0.629	5.495	0.10	0.077	0.002	0.105	1099	22	1079	17	1120	56	102%
DC-41D	18	251	173	0.69	2.4600	0.140	0.2067	0.007	0.667	4.838	0.16	0.086	0.004	-0.141	1251	42	1210	38	1323	82	103%
DC-41D	20	1200	111	0.09	0.8420	0.034	0.0961	0.0019	0.613	10.406	0.21	0.063	0.002	-0.008	618	19	591	11	688	77	105%
DC-41D	21.2	315	17	0.06	0.8160	0.059	0.0908	0.003	0.401	11.013	0.36	0.063	0.004	0.105	601	33	560	18	710	150	107%
DC-41D	22.2	439	73	0.17	0.7250	0.031	0.0850	0.0016	0.384	11.765	0.22	0.061	0.003	0.098	555	20	526	10	623	90	106%
DC-41D	24.2	2	0	0.01	2.8000	2.500	0.2130	0.052	0.100	4.695	1.15	0.120	0.120	0.917	1210	650	1240	270	900	2100	98%
DC-41D	29	801	42	0.05	0.9760	0.038	0.1047	0.0021	0.640	9.551	0.19	0.067	0.002	-0.124	688	19	642	12	813	67	107%
DC-41D	10.1	614	470	0.77	1.2660	0.041	0.1282	0.0022	0.360	7.800	0.13	0.071	0.002	0.309	829	18	777	12	940	62	107%
Discordant data																					
DC-41D	1	627	100	0.16	1.0200	0.037	0.0955	0.0019	0.100	10.471	0.21	0.077	0.003	0.538	711	19	588	11	1084	77	121%
DC-41D	4	4510	170	0.04	0.6980	0.027	0.0633	0.0012	0.791	15.810	0.30	0.079	0.002	-0.312	536	16	395	7	1160	56	136%
DC-41D	6	1071	175	0.16	1.0370	0.043	0.1011	0.0016	0.311	9.891	0.16	0.074	0.003	0.064	718	22	621	10	984	84	116%
DC-41D	8	4600	312	0.07	0.6170	0.026	0.0557	0.002	0.814	17.953	0.64	0.080	0.002	0.160	485	17	349	12	1174	59	139%
DC-41D	9.1	959	105	0.11	1.1960	0.047	0.1132	0.0025	0.760	8.834	0.20	0.076	0.002	-0.175	794	22	691	15	1071	60	115%
DC-41D	9.2	591	70	0.12	1.1840	0.056	0.0849	0.0034	0.452	11.779	0.47	0.103	0.005	0.515	790	26	524	20	1621	89	151%
DC-41D	10.2	834	109	0.13	1.0710	0.046	0.0674	0.0019	0.232	14.837	0.42	0.115	0.005	0.543	736	23	421	12	1836	89	175%
DC-41D	11.1	1133	233	0.21	1.2100	0.046	0.0858	0.0013	0.100	11.650	0.18	0.102	0.004	0.577	802	21	531	8	1621	74	151%
DC-41D	11.2	519	123	0.24	1.4050	0.053	0.0728	0.0022	0.189	13.736	0.42	0.142	0.007	0.674	891	23	453	13	2218	75	197%

DC-41D	12.1	256	144	0.56	1.3070	0.050	0.1183	0.0025	0.347	8.453	0.18	0.079	0.003	0.285	847	22	721	14	1155	69	117%
DC-41D	12.2	1510	309	0.20	0.8460	0.031	0.0844	0.0032	0.100	11.848	0.45	0.075	0.006	0.936	620	17	522	19	1020	130	119%
DC-41D	13.2	1157	169	0.15	1.1850	0.045	0.0756	0.0019	0.100	13.228	0.33	0.115	0.006	0.804	790	21	469	12	1835	92	168%
DC-41D	14	631	137	0.22	0.9520	0.037	0.0955	0.0018	0.436	10.471	0.20	0.072	0.002	0.131	679	19	588	11	960	73	116%
DC-41D	15.1	829	55	0.07	0.9730	0.037	0.0731	0.0017	0.366	13.680	0.32	0.096	0.004	0.445	687	19	454	10	1527	74	151%
DC-41D	15.2	465	151	0.33	1.1040	0.044	0.1090	0.0028	0.552	9.174	0.24	0.072	0.002	0.185	751	21	666	16	992	72	113%
DC-41D	17.1	1113	168	0.15	0.9860	0.037	0.0971	0.0018	0.393	10.299	0.19	0.073	0.003	0.185	694	19	597	11	1003	72	116%
DC-41D	17.2	1390	96	0.07	0.9730	0.039	0.0827	0.0014	0.302	12.092	0.20	0.085	0.004	0.410	688	20	512	8	1284	81	134%
DC-41D	19.1	684	111	0.16	1.2190	0.051	0.1058	0.0024	0.134	9.452	0.21	0.083	0.003	0.283	807	23	648	14	1239	80	125%
DC-41D	19.2	1973	88	0.04	1.0650	0.041	0.0991	0.0016	0.119	10.091	0.16	0.078	0.003	0.288	733	20	609	9	1103	72	120%
DC-41D	21.1	1470	71	0.05	0.9420	0.037	0.0890	0.002	0.348	11.236	0.25	0.076	0.003	0.275	671	19	550	12	1080	74	122%
DC-41D	22.1	592	231	0.39	1.1610	0.044	0.0948	0.0021	0.145	10.549	0.23	0.089	0.004	0.450	779	21	583	13	1373	77	134%
DC-41D	23	433	128	0.30	0.9280	0.049	0.0918	0.0026	0.611	10.893	0.31	0.073	0.003	-0.107	660	26	566	16	974	87	117%
DC-41D	24.1	950	69	0.07	1.0610	0.044	0.0870	0.0052	0.017	11.494	0.69	0.099	0.009	0.941	731	22	536	31	1420	150	136%
DC-41D	25	560	100	0.18	0.8800	0.050	0.0858	0.0021	0.036	11.655	0.29	0.075	0.004	0.250	641	29	531	12	1020	120	121%
DC-41D	26	688	61	0.09	0.8570	0.048	0.0505	0.0029	0.100	19.802	1.14	0.131	0.011	0.785	624	25	317	18	2010	150	197%
DC-41D	27	272	34	0.13	2.8100	0.440	0.0910	0.016	0.889	10.989	1.93	0.239	0.017	0.277	1330	110	558	93	3070	120	238%
DC-41D	28.1	330	28	0.08	2.3200	0.430	0.0980	0.021	0.762	10.204	2.19	0.187	0.014	0.177	1150	110	590	120	2720	150	195%
DC-41D	28.2	591	96	0.16	1.0310	0.037	0.1024	0.002	0.075	9.766	0.19	0.073	0.003	0.593	717	19	628	12	976	72	114%
DC-41D	30	307	73	0.24	1.0840	0.046	0.1019	0.0044	0.263	9.814	0.42	0.080	0.005	0.820	741	22	624	26	1110	110	119%
DC-41D	32	323	200	0.62	1.9800	0.120	0.1146	0.0021	0.409	8.726	0.16	0.124	0.007	-0.124	1090	39	699	12	1929	100	156%
DC-46D	2.1	1077	51	0.05	0.9270	0.027	0.1068	0.0015	0.272	9.365	0.13	0.062	0.002	0.295	665	14	654	9	670	59	102%
DC-46D	5.1	461	43	0.09	0.9100	0.042	0.1016	0.0022	0.692	9.843	0.21	0.064	0.002	-0.221	652	22	624	13	712	75	104%
DC-46D	8	382	128	0.34	0.8590	0.039	0.0992	0.0023	0.426	10.081	0.23	0.062	0.003	0.300	626	21	611	14	636	90	102%
DC-46D	9.1	106	220	2.08	0.8280	0.050	0.1003	0.0023	0.198	9.970	0.23	0.059	0.003	0.137	610	28	616	14	510	130	99%
DC-46D	16.1	286	130	0.45	0.9870	0.044	0.1094	0.0025	0.328	9.141	0.21	0.065	0.003	0.207	695	22	669	14	736	89	104%
DC-46D	16.2	81	217	2.69	1.0780	0.069	0.1163	0.0036	0.230	8.598	0.27	0.066	0.004	0.203	728	34	709	21	710	130	103%
DC-46D	24.1	176	70	0.40	1.4930	0.068	0.1437	0.0039	0.515	6.959	0.19	0.075	0.003	0.127	926	28	864	22	1021	85	107%
DC-46D	25.1	312	58	0.18	0.8790	0.045	0.1011	0.0027	0.414	9.891	0.26	0.062	0.003	0.131	636	25	620	16	626	99	103%
DC-46D	26.1	69	119	1.74	0.9060	0.068	0.1069	0.0029	0.171	9.355	0.25	0.061	0.005	0.215	637	37	654	17	490	160	97%

DC-46D	31.1	238	168	0.71	0.9200	0.040	0.1052	0.0021	0.176	9.506	0.19	0.063	0.003	0.234	658	21	645	12	649	90	102%
Hydrothermal zircons (LREE-I < 30)																					
DC-46D	1.1	550	357	0.65	1.1020	0.044	0.1228	0.0034	0.697	8.143	0.23	0.064	0.002	0.126	750	21	748	20	739	67	100%
DC-46D	3.1	180	89	0.49	1.1910	0.051	0.1257	0.0025	0.125	7.955	0.16	0.068	0.003	0.332	791	24	763	14	826	91	104%
DC-46D	7.2	495	45	0.09	0.7980	0.031	0.0896	0.0016	0.092	11.161	0.20	0.065	0.003	0.632	593	17	553	9	717	83	107%
DC-46D	10.1	529	820	1.55	0.9470	0.044	0.1078	0.0028	0.664	9.276	0.24	0.063	0.002	-0.070	676	23	660	16	690	75	102%
DC-46D	18	93	148	1.59	0.7380	0.049	0.0980	0.0028	0.094	10.204	0.29	0.055	0.004	0.312	561	29	602	16	330	140	93%
DC-46D	19.1	311	67	0.22	0.8790	0.037	0.1019	0.002	0.215	9.814	0.19	0.062	0.003	0.240	639	20	626	12	631	88	102%
DC-46D	23	375	358	0.95	0.9590	0.039	0.1064	0.002	0.412	9.398	0.18	0.064	0.002	0.109	679	20	652	12	717	80	104%
DC-46D	25.2	1069	134	0.13	0.7730	0.025	0.0879	0.0015	0.386	11.377	0.19	0.063	0.002	0.228	581	15	543	9	695	63	107%
DC-46D	26.2	423	37	0.09	0.7380	0.045	0.0854	0.0021	0.623	11.710	0.29	0.062	0.004	0.053	557	26	528	12	630	120	105%
DC-46D	32.1	1314	381	0.29	0.8770	0.030	0.1027	0.0016	0.526	9.737	0.15	0.061	0.002	-0.050	638	16	630	10	633	65	101%
DC-46D	33.1	430	248	0.58	0.9080	0.034	0.1043	0.0019	0.250	9.588	0.17	0.063	0.002	0.288	653	18	639	11	667	74	102%
Discordant data																					
DC-46D	1.2	409	44	0.11	0.9530	0.036	0.0932	0.0016	0.139	10.730	0.18	0.073	0.003	0.282	677	19	574	10	1005	76	118%
DC-46D	2.2	389	42	0.11	0.9400	0.047	0.0924	0.002	0.441	10.823	0.23	0.074	0.004	-0.025	671	27	570	12	1000	100	118%
DC-46D	3.2	466	53	0.11	0.8110	0.044	0.0882	0.0022	0.073	11.338	0.28	0.066	0.004	0.344	608	25	545	13	790	130	112%
DC-46D	4.1	873	84	0.10	1.1000	0.049	0.1041	0.0017	0.456	9.606	0.16	0.076	0.003	-0.133	748	23	638	10	1045	77	117%
DC-46D	4.2	713	141	0.20	1.0920	0.043	0.0845	0.0015	0.353	11.834	0.21	0.093	0.003	0.066	747	21	523	9	1465	69	143%
DC-46D	5.2	688	64	0.09	0.6180	0.024	0.0696	0.0013	0.206	14.374	0.27	0.064	0.003	0.301	486	15	434	8	694	81	112%
DC-46D	6.1	1633	257	0.16	1.1400	0.040	0.0972	0.0023	0.100	10.288	0.24	0.086	0.004	0.870	770	19	598	13	1273	87	129%
DC-46D	6.2	742	102	0.14	0.6040	0.021	0.0684	0.0012	0.189	14.620	0.26	0.062	0.002	0.537	479	13	426	7	676	74	112%
DC-46D	7.1	53	101	1.92	1.6560	0.110	0.0916	0.0026	0.105	10.917	0.31	0.132	0.009	0.295	970	42	564	15	2010	120	172%
DC-46D	9.2	375	39	0.10	1.1680	0.067	0.0845	0.002	0.100	11.834	0.28	0.100	0.006	0.506	783	30	523	12	1560	120	150%
DC-46D	10.2	436	149	0.34	0.8540	0.031	0.0899	0.0017	0.005	11.123	0.21	0.068	0.003	0.500	624	17	555	10	842	80	112%
DC-46D	11.1	895	128	0.14	1.5600	0.110	0.0968	0.0015	0.230	10.331	0.16	0.116	0.009	-0.061	934	43	596	9	1770	120	157%
DC-46D	11.2	956	203	0.21	0.9380	0.032	0.0937	0.0015	0.022	10.672	0.17	0.072	0.002	0.438	670	16	577	9	966	69	116%
DC-46D	12.1	592	148	0.25	1.1100	0.068	0.0948	0.0025	0.100	10.549	0.28	0.087	0.006	0.511	745	32	584	15	1200	130	128%
DC-46D	12.2	949	84	0.09	0.9420	0.033	0.0641	0.0017	0.100	15.601	0.41	0.108	0.005	0.801	672	17	400	10	1728	84	168%
DC-46D	13.1	259	203	0.78	0.9710	0.041	0.0997	0.0021	0.204	10.030	0.21	0.070	0.003	0.262	684	22	613	12	881	85	112%
DC-46D	13.2	585	76	0.13	0.9560	0.037	0.0905	0.0018	0.229	11.050	0.22	0.075	0.003	0.268	678	19	558	10	1063	75	121%
DC-46D	14.2	487	60	0.12	0.8680	0.041	0.0858	0.0026	0.380	11.655	0.35	0.074	0.003	0.342	634	23	530	15	984	90	120%
DC-46D	15.1	753	267	0.35	0.9940	0.050	0.0981	0.0014	0.100	10.192	0.15	0.073	0.004	0.284	703	26	603	8	966	100	117%

DC-46D	15.1	239	108	0.45	1.1570	0.089	0.0914	0.0027	0.982	10.941	0.32	0.089	0.006	-0.927	766	43	564	16	1340	130	136%
DC-46D	15.2	573	45	0.08	0.8840	0.043	0.0854	0.0016	0.143	11.710	0.22	0.073	0.004	0.294	640	24	528	10	989	99	121%
DC-46D	17.1	1080	1550	1.44	1.1930	0.052	0.0953	0.0022	0.100	10.493	0.24	0.092	0.005	0.812	792	24	586	13	1366	100	135%
DC-46D	17.2	800	103	0.13	0.9400	0.046	0.0847	0.0017	0.044	11.806	0.24	0.080	0.004	0.357	667	23	524	10	1118	95	127%
DC-46D	19.2	514	79	0.15	0.8600	0.040	0.0895	0.0017	0.491	11.173	0.21	0.069	0.003	-0.134	625	21	553	10	836	85	113%
DC-46D	20.1	948	120	0.13	0.8170	0.029	0.0874	0.0014	0.479	11.442	0.18	0.067	0.002	-0.056	606	16	540	9	812	64	112%
DC-46D	20.2	358	156	0.44	1.1370	0.047	0.0908	0.0016	0.258	11.013	0.19	0.090	0.004	0.147	766	22	560	9	1374	77	137%
DC-46D	21.1	346	101	0.29	1.0590	0.042	0.0985	0.0024	0.293	10.152	0.25	0.078	0.003	0.306	734	21	605	14	1116	81	121%
DC-46D	21.2	384	28	0.07	0.9160	0.058	0.0955	0.0027	0.244	10.471	0.30	0.069	0.004	0.253	655	30	588	16	870	120	111%
DC-46D	22.1	549	275	0.50	1.3900	0.170	0.0991	0.0026	0.300	10.091	0.26	0.104	0.012	-0.085	848	58	609	16	1440	160	139%
DC-46D	22.2	257	31	0.12	0.8290	0.036	0.0883	0.002	0.447	11.325	0.26	0.068	0.003	0.160	610	20	545	12	833	94	112%
DC-46D	24.2	831	293	0.35	1.3250	0.062	0.0792	0.0017	0.063	12.626	0.27	0.122	0.006	0.254	853	27	491	10	1950	91	174%
DC-46D	27.1	683	193	0.28	1.5740	0.071	0.1129	0.003	0.638	8.857	0.24	0.099	0.003	-0.093	952	27	689	18	1596	64	138%
DC-46D	27.2	732	51	0.07	0.8340	0.032	0.0899	0.0015	0.403	11.123	0.19	0.066	0.002	0.090	616	18	555	9	816	70	111%
DC-46D	28.1	2230	251	0.11	2.5900	0.190	0.0748	0.0036	0.421	13.369	0.64	0.256	0.015	0.505	1265	48	464	21	3110	120	273%
DC-46D	28.2	1100	168	0.15	1.3600	0.110	0.0981	0.0038	0.877	10.194	0.39	0.099	0.005	-0.643	869	48	603	22	1563	92	144%
DC-46D	29	289	47	0.16	0.8780	0.061	0.0888	0.002	0.190	11.261	0.25	0.071	0.005	0.096	634	33	548	12	880	140	116%
DC-46D	30	480	31	0.07	1.1900	0.190	0.0930	0.008	0.874	10.753	0.92	0.087	0.007	-0.196	766	74	572	46	1280	150	134%
DC-46D	31.2	776	156	0.20	0.9620	0.040	0.0825	0.0018	0.299	12.121	0.26	0.085	0.003	0.173	683	21	511	11	1277	78	134%
DC-46D	32.2	438	28	0.06	0.8070	0.041	0.0691	0.0012	0.121	14.482	0.25	0.083	0.004	0.345	596	22	430	8	1219	95	138%
DC-46D	33.2	168	26	0.15	0.8060	0.044	0.0862	0.0027	0.100	11.601	0.36	0.067	0.004	0.533	596	25	533	16	790	130	112%
DC-39A	7.1	1141	208	0.18	6.5080	0.180	0.3416	0.0048	0.726	2.927	0.04	0.139	0.003	0.059	2047	23	1894	23	2215	41	108%
DC-39A	10.1	546	32	0.06	5.4700	0.270	0.3110	0.011	0.959	3.215	0.11	0.128	0.004	0.100	1889	47	1743	56	2064	49	108%
Concordant and hydrothermal zircons (LREE-I < 30)																					
DC-39A	2.1	210	160	0.76	6.7600	0.230	0.3462	0.0081	0.374	2.889	0.07	0.143	0.005	0.311	2077	32	1914	39	2249	51	109%
DC-39A	6.1	1438	139	0.10	0.9100	0.040	0.0976	0.0023	0.100	10.246	0.24	0.071	0.005	0.835	653	20	600	14	860	110	109%
DC-39A	11.1	627	71	0.11	6.6000	0.210	0.3541	0.009	0.820	2.824	0.07	0.137	0.004	0.531	2055	29	1951	43	2177	45	105%
DC-39A	13.1	650	306	0.47	0.8390	0.029	0.1007	0.0017	0.433	9.930	0.17	0.061	0.002	0.093	617	16	618	10	615	69	100%
DC-39A	15	545	237	0.43	0.8280	0.028	0.0971	0.0016	0.014	10.299	0.17	0.062	0.002	0.586	611	15	598	9	670	74	102%
DC-39A	19.1	359	176	0.49	7.2500	0.230	0.3908	0.0074	0.795	2.559	0.05	0.135	0.003	0.082	2138	28	2125	35	2164	42	101%
DC-39A	20	286	75	0.26	1.4760	0.086	0.1471	0.0058	0.843	6.798	0.27	0.072	0.003	0.100	905	37	882	33	955	78	103%

DC-39A	22.1	291	78	0.27	9.9400	0.320	0.4229	0.009	0.808	2.365	0.05	0.173	0.004	0.318	2426	30	2271	41	2577	43	107%
DC-39A	22.2	157	69	0.44	10.6400	0.520	0.4170	0.015	0.948	2.398	0.09	0.184	0.005	0.100	2469	47	2237	71	2683	45	110%
DC-39A	24	369	298	0.81	8.9700	0.290	0.4037	0.0097	0.587	2.477	0.06	0.162	0.004	0.100	2329	31	2182	45	2476	40	107%
Discordant data used in the discordia trend																					
DC-39A	7.2	419	248	0.59	6.1500	0.200	0.3207	0.0063	0.837	3.118	0.06	0.140	0.004	0.100	1992	29	1792	31	2223	42	111%
DC-39A	8.2	210	48	0.23	5.5200	0.250	0.3020	0.011	0.886	3.311	0.12	0.134	0.004	0.175	1893	38	1696	52	2143	50	112%
DC-39A	11.2	555	72	0.13	2.3200	0.230	0.1610	0.01	0.983	6.211	0.39	0.098	0.005	0.100	1145	71	957	56	1524	91	120%
DC-39A	27.1	509	89	0.17	1.7700	0.220	0.1346	0.0086	0.978	7.429	0.47	0.086	0.006	0.100	952	74	809	48	1210	120	118%
Discordant data (common-Pb & Pb loss)																					
DC-39A	1.1	623	15	0.02	2.4800	0.190	0.1242	0.0058	0.876	8.052	0.38	0.141	0.006	0.100	1226	55	752	33	2204	73	163%
DC-39A	1.2	1500	841	0.56	4.5600	0.280	0.1355	0.0047	0.786	7.380	0.26	0.243	0.010	0.100	1712	48	817	27	3110	64	210%
DC-39A	2.2	996	97	0.10	1.3160	0.065	0.0849	0.0018	0.100	11.779	0.25	0.112	0.006	0.477	845	26	525	10	1846	98	161%
DC-39A	3.1	375	62	0.16	7.4800	0.300	0.3379	0.008	0.884	2.959	0.07	0.160	0.005	0.100	2164	37	1874	39	2454	49	115%
DC-39A	3.2	336	68	0.20	0.9950	0.052	0.0635	0.0015	0.428	15.748	0.37	0.112	0.005	0.159	693	26	397	9	1785	88	175%
DC-39A	4	1025	182	0.18	0.9700	0.035	0.0520	0.0018	0.100	19.231	0.67	0.141	0.007	0.841	686	18	326	11	2183	89	210%
DC-39A	5.1	787	202	0.26	1.2260	0.044	0.0580	0.0019	0.420	17.241	0.56	0.158	0.006	0.676	810	20	363	12	2403	68	223%
DC-39A	5.2	1402	142	0.10	1.2960	0.082	0.0840	0.0024	0.016	11.905	0.34	0.117	0.008	0.546	833	35	520	14	1770	120	160%
DC-39A	6.2	4040	252	0.06	2.3560	0.096	0.0637	0.0011	0.373	15.711	0.27	0.270	0.010	0.051	1222	29	398	7	3286	60	307%
DC-39A	8.1	1160	32	0.03	1.2530	0.085	0.0965	0.0041	0.804	10.363	0.44	0.095	0.004	0.100	819	38	594	24	1512	83	138%
DC-39A	8.3	270	21	0.08	1.4630	0.089	0.0666	0.0015	0.093	15.015	0.34	0.161	0.010	0.318	906	35	416	9	2425	110	218%
DC-39A	9	777	79	0.10	1.2500	0.110	0.1083	0.0052	0.942	9.234	0.44	0.082	0.004	0.100	801	49	662	30	1195	100	121%
DC-39A	10.2	365	83	0.23	1.1870	0.071	0.0838	0.0021	0.100	11.933	0.30	0.107	0.007	0.594	790	34	519	13	1630	130	152%
DC-39A	12	1341	1300	0.97	1.4500	0.100	0.0619	0.0018	0.768	16.155	0.47	0.168	0.009	0.100	888	41	387	11	2468	89	229%
DC-39A	13.2	44	8	0.17	1.8100	0.210	0.0724	0.0041	0.100	13.812	0.78	0.199	0.028	0.582	1022	74	450	24	2600	250	227%
DC-39A	14	694	105	0.15	3.8600	0.220	0.2080	0.01	0.965	4.808	0.23	0.135	0.004	0.240	1575	52	1209	56	2158	51	130%
DC-39A	16	1906	2210	1.16	1.8100	0.076	0.0678	0.0016	0.808	14.749	0.35	0.195	0.006	0.100	1042	27	423	10	2774	48	246%
DC-39A	17	723	162	0.22	0.9120	0.046	0.0608	0.0021	0.633	16.447	0.57	0.110	0.004	0.109	651	24	380	13	1760	72	171%
DC-39A	18	794	193	0.24	5.0500	0.180	0.2658	0.008	0.918	3.762	0.11	0.139	0.004	0.526	1824	30	1516	42	2215	43	120%
DC-39A	19.2	593	780	1.32	1.5500	0.110	0.0596	0.0022	0.673	16.779	0.62	0.188	0.010	0.100	942	42	373	13	2682	87	253%
DC-39A	21	426	120	0.28	1.0210	0.059	0.0934	0.0021	0.100	10.707	0.24	0.084	0.007	0.847	705	27	575	12	1150	140	123%

DC-39A	23.1	452	116	0.26	1.6420	0.088	0.0665	0.0045	0.855	15.038	1.02	0.189	0.009	0.864	975	34	413	27	2704	78	236%
DC-39A	23.2	590	75	0.13	6.5700	0.280	0.3080	0.011	0.950	3.247	0.12	0.156	0.004	0.144	2040	41	1724	55	2403	42	118%
DC-39A	25.1	330	42	0.13	1.5000	0.120	0.0718	0.0025	0.301	13.928	0.48	0.152	0.012	0.443	904	43	447	15	2260	140	202%
DC-39A	25.2	663	56	0.08	4.2280	0.140	0.2363	0.0061	0.783	4.232	0.11	0.133	0.004	0.850	1677	28	1366	32	2138	57	123%
DC-39A	26.1	1184	48	0.04	1.3770	0.041	0.0770	0.0016	0.143	12.987	0.27	0.131	0.004	0.673	879	18	478	9	2094	57	184%
DC-39A	26.2	950	134	0.14	4.0900	0.220	0.2110	0.014	0.647	4.739	0.31	0.159	0.013	0.689	1647	44	1219	78	2300	110	135%
DC-39A	27.2	1029	116	0.11	1.2010	0.046	0.0737	0.0017	0.100	13.569	0.31	0.123	0.006	0.780	799	22	459	10	1932	87	174%

Table 7. Zircon analytical LA-ICP-MS REE (ppm) results from Cubatão Shear Zone mylonites.

Sample	Spot	La	Ce	Pr	Nd	Sm	Eu	Gd	Tb	Dy	Ho	Er	Tm	Yb	Lu
DC-41D	2	0.90	19.60	0.53	3.58	3.54	1.49	11.80	5.31	63.20	28.30	144.00	34.10	340.00	74.20
DC-41D	5.1	0.03	5.32	0.20	3.96	7.68	0.63	43.10	16.10	179.00	75.90	334.00	66.60	585.00	119.30
DC-41D	5.2	0.47	7.40	0.09	0.95	0.59	0.15	4.50	1.84	28.00	13.00	74.00	18.50	205.00	48.30
DC-41D	31	0.22	20.20	0.16	1.41	2.35	0.39	14.70	6.12	80.60	33.80	171.60	39.00	388.00	82.10
Hydrothermal zircons (LREE-I < 30)															
DC-41D	3	6.07	39.90	4.07	24.30	17.10	4.77	35.40	9.20	71.10	24.60	109.20	24.90	253.90	60.00
DC-41D	7	10.40	66.00	6.30	34.00	15.00	34.00	26.00	8.30	67.00	22.50	82.00	15.90	131.00	26.10
DC-41D	13.1	3.06	26.50	2.34	18.00	10.20	4.01	19.10	5.04	60.30	21.40	102.20	24.10	242.00	51.70
DC-41D	16	36.00	119.00	16.00	76.00	17.00	0.40	27.00	6.60	74.00	25.60	112.00	24.60	227.00	43.30
DC-41D	18	5.00	33.50	3.66	25.50	17.70	4.09	44.90	11.90	125.00	41.40	169.00	35.00	310.00	60.90
DC-41D	20	5.30	31.30	4.20	28.50	14.90	7.30	26.00	6.50	59.30	19.00	84.00	19.90	198.00	42.80
DC-41D	21.2	4.70	40.00	2.60	17.30	10.00	2.50	15.60	6.10	40.00	14.60	65.00	13.10	140.00	32.00
DC-41D	22.2	1.48	19.30	1.26	6.70	5.30	1.38	13.40	4.34	56.20	22.20	116.00	27.30	282.00	60.20
DC-41D	24.2	8.00	13.00	0.00	17.00	0.00	12.10	11.00	2.80	5.40	5.10	4.30	1.60	16.00	5.60
DC-41D	29	6.70	40.40	6.40	37.70	18.80	3.52	27.30	5.57	47.80	16.40	77.40	16.90	165.00	34.20
DC-41D	10.1	1.03	15.20	0.89	8.00	7.00	6.50	27.60	8.26	106.70	39.40	173.00	35.30	318.00	62.60
Discordant data															
DC-41D	1	12.40	56.00	6.80	32.20	13.50	3.39	24.80	7.69	76.50	31.30	144.00	32.80	317.00	69.70
DC-41D	4	66.00	510.00	47.60	286.00	157.00	83.30	271.00	56.20	366.00	95.50	310.00	55.40	470.00	85.80
DC-41D	6	12.60	229.00	8.00	44.00	28.90	8.50	46.00	12.90	103.00	33.60	143.00	31.70	301.00	63.50
DC-41D	8	168.00	1160.00	108.00	564.00	316.00	63.80	409.00	93.00	592.00	142.00	466.00	84.70	710.00	125.00
DC-41D	9.1	6.75	42.40	4.92	32.40	16.80	3.58	27.60	5.48	56.10	17.90	80.80	19.10	188.00	39.50
DC-41D	9.2	59.40	381.00	40.80	262.00	158.00	59.00	221.00	44.60	325.00	69.00	226.00	43.20	380.00	69.60
DC-41D	10.2	74.00	422.00	58.00	348.00	223.00	59.00	289.00	58.00	406.00	84.00	271.00	52.70	457.00	82.00
DC-41D	11.1	65.00	730.00	44.00	258.00	148.00	38.70	196.00	39.70	315.00	72.70	262.00	54.60	512.00	103.20
DC-41D	11.2	166.00	1050.00	126.00	760.00	461.00	104.00	546.00	117.00	804.00	161.00	505.00	92.00	777.00	132.00
DC-41D	12.1	9.90	51.00	5.90	34.60	16.00	3.14	30.40	7.49	84.10	29.13	130.40	27.90	262.90	54.30
DC-41D	12.2	65.00	280.00	44.00	260.00	170.00	43.00	220.00	46.00	350.00	76.00	269.00	52.00	445.00	85.00
DC-41D	13.2	44.60	173.00	31.40	182.00	118.00	24.50	160.00	33.30	257.00	59.20	218.00	45.40	422.00	86.10

DC-41D	14	7.10	42.10	5.27	42.20	23.90	8.30	43.30	9.90	105.00	33.50	145.00	31.20	301.00	62.50
DC-41D	15.1	67.00	317.00	50.60	319.00	171.00	39.80	231.00	47.80	350.00	72.00	234.00	45.10	375.00	71.00
DC-41D	15.2	34.20	92.00	15.90	89.00	35.80	5.27	53.90	11.30	109.20	34.20	144.20	30.20	276.10	56.30
DC-41D	17.1	22.20	87.00	17.00	100.00	59.00	23.80	101.00	19.50	172.00	45.70	172.00	34.80	314.00	63.20
DC-41D	17.2	54.00	177.00	37.80	229.00	145.00	48.90	199.00	41.70	297.00	63.00	207.00	39.30	345.00	64.30
DC-41D	19.1	54.00	143.00	17.80	91.00	40.30	8.50	58.00	13.20	106.00	30.90	124.50	27.00	253.00	53.70
DC-41D	19.2	22.00	127.00	11.70	74.00	38.00	12.30	57.00	13.30	117.00	32.40	123.00	26.40	239.00	45.60
DC-41D	21.1	34.30	299.00	24.00	137.00	63.00	24.10	77.00	16.50	135.00	37.10	149.00	29.30	265.00	50.40
DC-41D	22.1	13.10	72.00	10.00	64.40	36.60	14.20	75.90	19.50	185.00	63.40	266.00	51.00	460.00	89.80
DC-41D	23	8.50	70.00	7.60	47.70	30.40	11.30	54.00	14.10	129.00	41.70	181.00	36.20	345.00	71.00
DC-41D	24.1	76.00	520.00	54.00	320.00	185.00	69.00	260.00	49.00	315.00	75.00	283.00	58.00	560.00	112.00
DC-41D	25	11.50	142.00	7.40	44.00	25.00	14.80	42.00	9.20	75.00	23.50	110.00	24.20	247.00	51.00
DC-41D	26	394.00	2520.00	251.00	1460.00	850.00	165.00	1060.00	230.00	1470.00	298.00	890.00	146.00	1170.00	189.00
DC-41D	27	340.00	3300.00	231.00	1440.00	860.00	310.00	1170.00	260.00	1660.00	330.00	1080.00	148.00	1210.00	190.00
DC-41D	28.1	500.00	2080.00	343.00	1940.00	1120.00	251.00	1410.00	292.00	1710.00	359.00	1110.00	170.00	1480.00	203.00
DC-41D	28.2	9.70	44.00	5.70	35.00	20.90	4.56	34.60	9.30	87.60	29.30	134.00	28.50	281.00	59.90
DC-41D	30	17.00	140.00	12.80	80.00	54.00	13.00	84.00	16.30	139.00	41.30	174.00	34.00	310.00	66.20
DC-41D	32	8.50	34.00	5.50	36.50	27.00	8.10	54.90	14.00	124.00	39.60	169.00	33.60	305.00	62.40
DC-46D	2.1	0.19	5.80	0.15	1.16	1.01	0.53	5.17	2.40	39.00	17.10	90.30	21.40	218.00	46.10
DC-46D	5.1	0.18	4.90	0.23	1.61	2.61	0.52	12.50	4.40	40.50	10.47	34.50	6.30	57.00	11.30
DC-46D	8	0.03	18.70	0.05	0.94	2.17	0.57	14.80	6.50	93.00	41.00	210.00	50.00	490.00	95.00
DC-46D	9.1	0.00	29.10	0.05	1.06	1.88	0.32	9.01	3.35	37.80	15.26	72.70	17.00	166.10	34.30
DC-46D	16.1	0.04	19.90	0.05	0.65	1.09	0.20	6.78	2.90	37.90	16.37	80.30	18.73	181.10	37.10
DC-46D	16.2	0.03	23.10	0.03	0.55	1.36	0.19	8.62	3.33	48.10	19.27	97.60	22.06	222.00	42.48
DC-46D	24.1	0.05	4.68	0.07	1.06	1.78	0.29	11.20	3.57	46.20	16.80	82.10	18.00	194.00	43.00
DC-46D	25.1	0.06	9.70	0.04	0.73	1.85	0.25	8.62	2.48	25.50	7.65	31.60	6.02	55.60	10.80
DC-46D	26.1	0.04	14.30	0.21	3.53	6.19	1.75	27.10	8.34	99.80	34.40	154.50	31.70	298.00	57.70
DC-46D	31.1	0.00	39.00	0.07	1.26	2.55	0.23	14.30	6.15	74.10	32.60	152.40	35.40	340.00	72.20
Hydrothermal zircons (LREE-I < 30)															
DC-46D	1.1	22.00	102.00	9.30	50.00	21.90	3.50	61.00	17.50	206.00	73.00	335.00	70.00	665.00	130.20
DC-46D	3.1	2.84	41.50	3.64	23.00	10.96	2.02	26.40	7.96	106.30	43.40	209.60	45.00	430.00	87.00
DC-46D	7.2	3.60	27.00	4.10	23.00	12.60	3.00	15.30	3.10	23.40	6.90	27.90	7.47	79.10	18.00

DC-46D	10.1	0.38	40.10	0.80	9.50	12.00	0.63	43.40	13.70	140.00	49.50	202.00	39.70	346.00	67.00
DC-46D	18	0.09	25.80	0.38	6.49	10.80	2.97	33.30	8.06	72.70	20.00	75.00	13.56	115.00	20.30
DC-46D	19.1	0.04	7.67	0.09	1.23	3.89	0.87	15.51	3.18	23.40	4.84	15.53	2.42	20.40	3.65
DC-46D	23	4.05	35.10	4.40	31.00	21.80	6.00	48.80	11.20	109.00	31.90	130.00	24.90	228.00	43.00
DC-46D	25.2	2.87	28.90	2.12	11.90	6.70	1.77	10.00	2.13	21.30	6.62	34.60	8.55	104.40	21.88
DC-46D	26.2	1.52	14.40	1.27	7.90	5.10	1.76	10.30	2.06	20.40	6.90	36.70	9.90	110.00	24.00
DC-46D	32.1	12.00	210.00	13.90	81.00	36.00	12.50	51.00	15.60	130.00	49.10	209.60	42.90	353.00	65.20
DC-46D	33.1	0.98	56.00	0.72	4.78	4.24	1.14	13.30	4.31	44.60	17.70	82.30	19.00	182.00	38.90
Discordant data															
DC-46D	1.2	2.91	32.40	3.02	20.30	11.50	3.00	14.50	2.83	24.60	6.30	26.50	6.52	71.80	17.20
DC-46D	2.2	7.80	197.00	8.60	56.00	34.00	11.00	41.00	8.10	56.00	11.30	40.00	8.30	84.00	18.10
DC-46D	3.2	6.10	64.00	6.30	37.00	23.00	5.30	26.00	5.40	41.00	9.60	39.10	9.50	101.00	22.40
DC-46D	4.1	8.10	133.00	7.70	48.90	31.50	8.10	37.30	10.00	107.50	38.00	194.00	49.60	543.00	114.40
DC-46D	4.2	27.10	342.00	24.00	136.00	76.00	19.10	78.00	15.00	105.00	20.60	69.00	13.10	131.00	25.30
DC-46D	5.2	1.56	21.00	1.60	8.50	6.30	1.48	8.30	2.02	16.40	5.40	26.30	6.37	75.00	19.30
DC-46D	6.1	27.90	420.00	30.80	182.00	108.00	27.40	114.00	23.90	160.00	44.00	175.00	39.10	393.00	84.00
DC-46D	6.2	0.95	29.30	1.05	6.20	4.10	1.10	7.00	1.61	14.20	4.61	20.80	5.36	61.90	16.20
DC-46D	7.1	8.78	67.80	7.83	52.90	37.00	9.00	56.50	11.66	76.20	15.31	41.30	6.24	44.90	7.07
DC-46D	9.2	16.60	170.00	17.00	102.00	57.00	12.60	64.00	13.80	88.00	16.80	50.80	10.10	88.00	18.80
DC-46D	10.2	8.50	119.00	9.10	54.30	33.10	8.60	38.60	8.40	59.90	15.20	54.30	10.90	97.40	19.00
DC-46D	11.1	5.50	59.60	4.50	27.80	20.50	5.40	34.40	11.70	134.70	55.90	284.00	71.90	746.00	153.00
DC-46D	11.2	9.00	71.50	9.40	80.20	47.30	40.60	43.50	6.48	42.70	10.97	40.40	8.54	83.40	17.70
DC-46D	12.1	38.00	300.00	37.00	211.00	118.00	27.00	119.00	20.90	127.00	25.00	74.40	12.80	108.00	17.70
DC-46D	12.2	150.00	744.00	124.00	681.00	363.00	92.10	380.00	76.20	426.00	76.20	205.00	35.30	308.00	58.20
DC-46D	13.1	4.46	82.90	4.64	28.60	21.40	4.39	35.80	11.56	115.10	43.40	201.70	47.00	463.00	96.90
DC-46D	13.2	4.01	46.90	3.97	24.10	13.60	3.52	18.30	4.36	30.80	9.30	40.70	9.73	111.70	26.70
DC-46D	14.1	7.30	60.30	4.01	24.00	11.70	2.01	25.50	7.68	84.00	31.50	140.20	29.20	267.00	52.30
DC-46D	14.2	18.00	203.00	17.50	108.00	69.00	15.80	84.00	18.70	114.00	23.20	75.90	14.90	138.00	29.20
DC-46D	15.1	1.13	22.10	1.12	7.60	5.80	1.23	11.40	3.65	41.30	16.33	81.40	19.93	213.30	49.70
DC-46D	15.2	10.40	81.00	10.00	55.00	20.50	8.30	29.00	5.60	40.00	10.50	43.20	10.30	112.00	23.80
DC-46D	17.1	81.00	570.00	64.00	370.00	192.00	44.00	225.00	39.00	262.00	54.00	169.00	27.90	222.00	37.30
DC-46D	17.2	25.00	120.00	17.50	104.00	56.00	14.30	68.00	10.30	65.00	13.00	46.00	9.50	100.00	20.20
DC-46D	19.2	2.18	16.80	1.87	12.50	9.20	2.17	12.80	2.71	22.60	5.12	21.90	5.16	57.80	13.60

DC-46D	20.1	4.80	37.00	4.00	24.50	15.80	3.30	19.00	3.90	33.30	8.39	36.00	8.97	101.70	22.64
DC-46D	20.2	4.39	33.90	3.61	23.80	18.90	4.19	37.50	9.57	88.50	25.00	103.50	20.80	199.00	38.20
DC-46D	21.1	4.10	54.00	4.10	22.10	14.70	3.04	31.90	8.95	90.10	24.40	92.20	16.50	148.00	26.30
DC-46D	21.2	4.10	57.00	2.60	14.40	8.90	2.10	13.30	3.10	25.30	8.10	35.10	9.60	111.40	24.00
DC-46D	22.1	140.00	300.00	35.00	150.00	47.00	13.00	64.00	13.00	129.00	37.60	162.00	32.40	316.00	61.00
DC-46D	22.2	2.04	18.40	2.30	16.70	12.80	2.75	13.90	2.49	21.80	5.60	25.60	6.11	76.10	18.20
DC-46D	24.2	72.20	1060.00	61.40	363.00	169.00	46.50	162.00	25.40	157.00	29.20	89.00	14.70	133.00	24.20
DC-46D	27.1	9.20	98.00	9.30	66.00	50.00	19.30	83.00	18.80	156.00	51.60	221.00	47.50	450.00	95.50
DC-46D	27.2	6.08	68.00	7.10	48.60	33.30	10.70	41.10	8.30	60.00	13.40	50.60	11.10	118.60	23.60
DC-46D	28.1	262.00	3320.00	262.00	1420.00	820.00	207.00	860.00	187.00	1060.00	216.00	650.00	121.00	1003.00	173.00
DC-46D	28.2	9.50	103.00	9.00	51.00	32.50	8.10	37.40	7.90	51.00	10.80	36.40	7.60	73.00	17.10
DC-46D	29	1.38	13.20	1.36	6.30	5.00	1.08	7.70	1.59	14.90	4.90	23.70	5.80	64.00	16.20
DC-46D	30	35.00	184.00	26.80	129.00	66.00	18.60	79.00	19.70	133.00	30.90	103.00	20.50	187.00	37.70
DC-46D	31.2	8.20	86.00	8.40	52.90	25.90	22.20	29.80	6.30	38.10	10.05	38.50	8.26	82.10	20.30
DC-46D	32.2	32.00	330.00	26.60	161.00	98.00	23.10	115.00	25.30	154.00	33.10	107.00	22.90	214.00	42.50
DC-46D	33.2	1.93	11.50	0.99	6.00	3.40	0.66	4.80	1.64	9.60	3.45	16.60	4.13	50.60	13.60
DC-39A	7.1	0.18	24.60	0.15	1.03	2.61	0.26	12.80	4.59	56.10	21.75	100.60	21.83	204.60	40.90
DC-39A	10.1	0.00	0.49	0.02	0.60	2.39	0.16	18.40	6.22	53.20	13.60	45.40	8.10	63.00	11.70
Concordant and hydrothermal zircons (LREE-I < 30)															
DC-39A	2.1	3.34	44.40	2.17	14.30	9.35	2.06	19.50	5.47	51.00	18.01	82.50	18.40	190.90	42.50
DC-39A	6.1	45.00	370.00	23.00	105.00	47.00	8.10	68.00	13.90	115.00	27.60	95.00	15.70	135.00	20.20
DC-39A	11.1	17.30	137.00	8.40	56.00	20.80	3.40	39.00	10.60	96.00	25.40	87.00	15.50	126.00	21.10
DC-39A	13.1	2.09	0.00	1.35	10.15	10.04	1.64	31.90	9.47	106.90	36.60	167.00	36.90	354.00	75.20
DC-39A	15	1.62	39.10	0.98	6.30	6.30	1.12	21.00	6.28	73.30	25.70	116.60	25.40	243.00	49.60
DC-39A	19.1	3.90	28.50	1.81	10.30	4.56	0.91	17.80	5.14	59.50	21.70	105.60	23.70	243.00	52.40
DC-39A	20	21.00	13.00	3.20	15.30	7.90	1.28	36.50	12.10	142.00	55.50	234.00	46.20	403.00	78.20
DC-39A	22.1	5.60	36.30	3.16	15.70	11.30	10.07	20.10	5.65	58.90	21.80	97.20	20.97	200.20	43.60
DC-39A	22.2	38.00	34.00	10.40	47.00	8.20	3.21	17.40	4.70	51.10	19.40	86.80	19.20	184.00	39.70
DC-39A	24	3.10	43.00	2.60	12.60	11.00	3.10	34.70	10.40	112.70	43.20	184.00	37.80	341.00	68.10
Discordant data used in the discordia trend															
DC-39A	7.2	0.12	40.40	0.22	2.87	6.52	1.93	30.30	9.62	108.10	40.30	178.60	37.10	352.00	73.30
DC-39A	8.2	3.44	40.80	2.37	12.50	6.30	1.77	12.00	3.22	33.30	12.20	57.30	13.70	144.00	33.60

DC-39A	11.2	0.95	15.70	0.53	2.81	2.41	0.29	8.97	3.09	36.20	13.31	62.70	14.00	134.00	27.80
DC-39A	27.1	3.30	35.50	2.51	14.00	8.90	1.39	20.80	6.17	66.30	25.90	117.00	25.40	237.00	48.10
Discordant data (common-Pb & Pb loss)															
DC-39A	1.1	22.70	275.00	16.30	81.80	41.30	9.40	49.90	9.74	72.70	17.10	63.80	11.60	105.40	20.10
DC-39A	1.2	133.00	1190.00	92.00	515.00	241.00	55.20	266.00	51.90	346.00	75.90	252.00	46.70	432.00	81.80
DC-39A	2.2	34.90	293.00	22.10	108.00	49.00	9.90	61.00	14.10	110.00	28.00	103.00	19.20	175.00	31.70
DC-39A	3.1	5.20	36.70	3.15	18.90	11.20	9.30	26.10	6.40	55.00	16.70	69.00	14.00	135.00	27.00
DC-39A	3.2	29.20	186.00	20.00	107.00	53.90	10.50	63.10	14.00	107.00	27.60	108.40	22.50	220.00	45.30
DC-39A	4	155.00	725.00	90.00	475.00	245.00	56.00	304.00	65.10	448.00	102.00	349.00	65.60	593.00	104.90
DC-39A	5.1	175.00	990.00	117.00	640.00	307.00	55.90	358.00	70.00	468.00	98.00	310.00	56.70	494.00	87.20
DC-39A	5.2	108.00	870.00	72.00	397.00	177.00	29.60	193.00	37.60	248.00	55.10	173.00	29.30	243.00	38.30
DC-39A	6.2	414.00	2950.00	243.00	1290.00	579.00	154.10	651.00	118.00	754.00	157.00	468.00	80.80	671.00	117.00
DC-39A	8.1	32.00	192.00	20.80	106.00	49.00	10.20	57.00	11.90	89.00	24.40	96.00	19.90	171.00	33.10
DC-39A	8.3	213.00	1300.00	128.00	600.00	247.00	51.00	278.00	57.00	372.00	81.00	249.00	49.00	432.00	84.00
DC-39A	9	12.44	94.20	8.76	42.60	20.30	3.97	28.10	6.76	57.40	16.20	61.00	12.50	111.00	20.90
DC-39A	10.2	27.00	170.00	15.00	71.00	31.00	5.80	36.00	8.00	70.00	20.10	84.00	18.10	181.00	37.20
DC-39A	12	382.00	1480.00	259.00	1300.00	585.00	108.00	688.00	136.00	911.00	186.00	559.00	94.00	769.00	131.00
DC-39A	13.2	410.00	1920.00	280.00	1600.00	740.00	118.00	700.00	130.00	850.00	158.00	480.00	94.00	840.00	169.00
DC-39A	14	45.00	285.00	36.50	194.00	96.00	16.80	118.00	23.70	162.00	36.90	116.00	22.90	211.00	41.10
DC-39A	16	245.00	1260.00	160.00	869.00	491.00	136.00	637.00	106.20	682.00	133.90	401.00	71.10	579.00	95.10
DC-39A	17	55.00	320.00	29.10	147.00	67.00	13.40	79.00	17.80	141.00	34.30	122.00	25.40	248.00	46.30
DC-39A	18	58.00	235.00	35.00	191.00	88.00	15.70	107.00	21.00	167.00	47.80	178.00	38.00	358.00	71.00
DC-39A	19.2	325.00	1300.00	215.00	1150.00	536.00	101.00	565.00	115.00	710.00	148.00	429.00	71.00	576.00	100.00
DC-39A	21	20.00	140.00	10.10	45.00	20.00	4.00	46.00	8.20	76.00	28.40	117.00	24.30	228.00	46.30
DC-39A	23.1	160.00	1060.00	99.00	533.00	257.00	48.20	276.00	53.60	343.00	73.20	212.00	36.70	314.00	57.50
DC-39A	23.2	23.00	157.00	13.90	65.00	37.00	10.10	52.00	11.20	88.00	25.40	98.00	21.10	201.00	41.80
DC-39A	25.1	131.00	700.00	80.00	423.00	206.00	41.20	243.00	52.00	331.00	85.00	302.00	59.00	501.00	98.00
DC-39A	25.2	26.00	132.00	13.90	77.00	38.00	27.20	59.00	12.10	85.00	21.00	74.00	15.80	153.00	31.60
DC-39A	26.1	158.00	880.00	108.00	540.00	261.00	47.50	293.00	61.00	412.00	90.00	272.00	49.00	393.00	62.00
DC-39A	26.2	106.00	570.00	56.00	290.00	143.00	23.60	160.00	32.00	210.00	48.00	147.00	26.60	226.00	44.00
DC-39A	27.2	170.00	900.00	99.00	530.00	251.00	48.00	300.00	61.00	410.00	93.00	284.00	51.00	440.00	81.00